RĪGAS TEHNISKĀ UNIVERSITĀTE

Abhishek Rajesh Indurkar

AMORFI KALCIJA FOSFĀTI UN TO NANOKOMPOZĪTI

Promocijas darbs

AMORPHOUS CALCIUM PHOSPHATES AND THEIR NANOCOMPOSITES

Doctoral Thesis

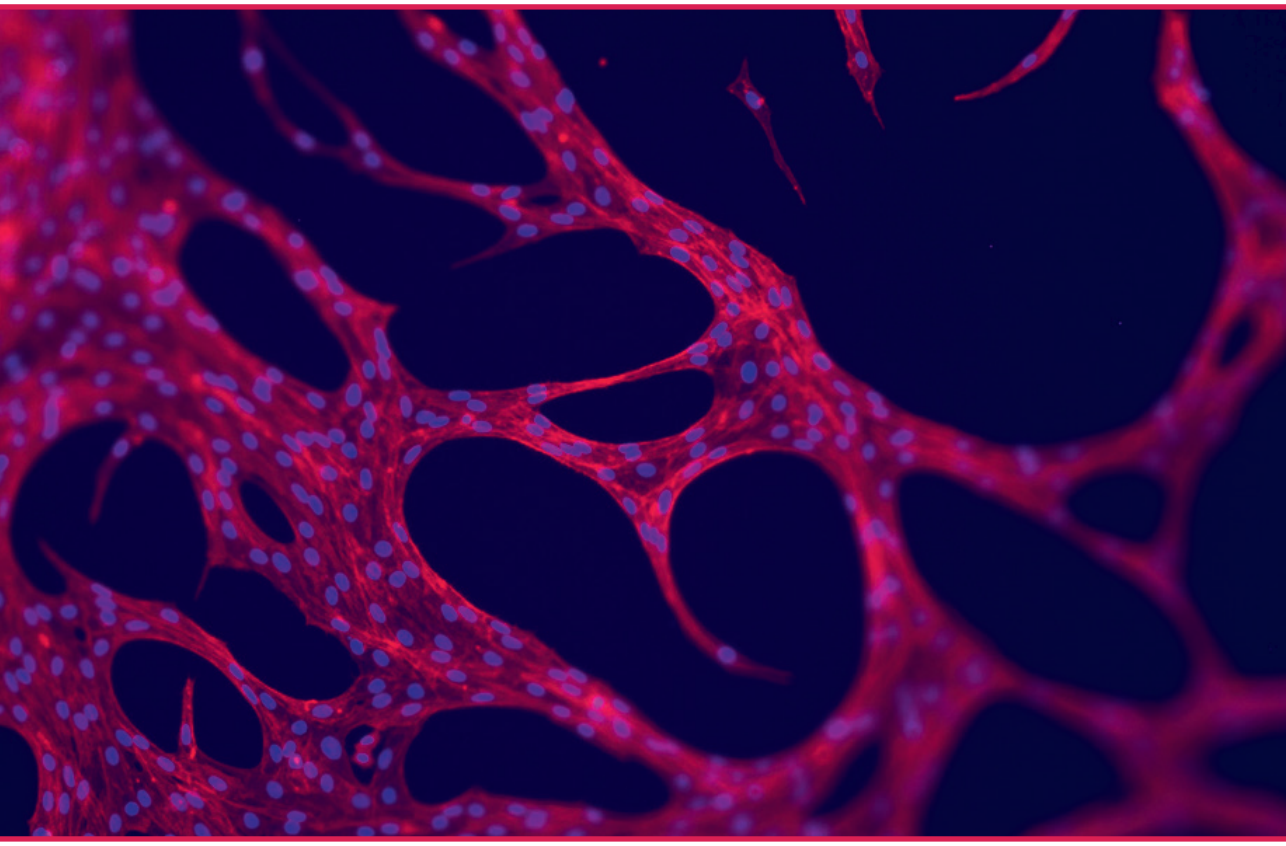

RTU Izdevniecība
RTU Press
Rīga 2024

RĪGAS TEHNISKĀ UNIVERSITĀTE
Dabaszinātņu un tehnoloģiju fakultāte
Biomateriālu un bioinženierijas institūts

RIGA TECHNICAL UNIVERSITY
Faculty of Natural Sciences and Technology
Institute of Biomaterials and Bioengineering

Abhishek Rajesh Indurkar
Doktora studiju programmas "Ķīmija, materiālu zinātne un inženierija" doktorant
Doctoral Student of the Study Programme "Chemistry, Materials Science and Engineering"

AMORFI KALCIJA FOSFĀTI UN TO NANOKOMPOZĪTI

Promocijas darba

AMORPHOUS CALCIUM PHOSPHATES AND THEIR NANOCOMPOSITES

Doctoral Thesis

Zinātniskais vadītājs
profesors *Dr. sc. ing.* Jānis Ločs

Līdzvadītājs
Dr. sc. ing. Kristaps Rubenis

RTU Izdevniecība / RTU Press
Rīga 2024 / Riga 2024

Indurkar A. R. Amorfi kalcija fosfāti
un to nanokompozīti. Promocijas darba kopsavilkums. Rīga: RTU Izdevniecība, 2024. 237 lpp.

Indurkar A. R. Amorphous Calcium Phosphates and Their Nanocomposites. Summary of the Doctoral Thesis. Riga: RTU Press, 2024. 237 p.

Publicēts saskaņā ar promocijas padomes "RTU P-02" 2024. gada 28. augusta lēmumu, protokols Nr. 040309.2.2/6.

Published in accordance with the decision of the Promotion Council "P-02" on 28th August 2024, Minutes No. 04030-9.2.2/6.

Šis projekts ir saņēmis finansējumu no Eiropas Savienības pētniecības un inovāciju programmas "Apvārsnis 2020" saskaņā ar līgumu Nr. 857287 (BBCE – Baltijas Biomateriālu ekselences centrs).

This project has received funding from the European Union's Horizon 2020 research and innovation programme under the grant agreement No. 857287 (BBCE – Baltic Biomaterials Centre of Excellence).

PROMOCIJAS DARBS IZVIRZĪTS ZINĀTNES DOKTORA GRĀDA IEGŪŠANAI RĪGAS TEHNISKAJĀ UNIVERSITĀTĒ

Promocijas darbs zinātnes doktora (*Ph. D.*) grāda iegūšanai tiek publiski aizstāvēts 2024. gada 28. augustā plkst. 10.00 Rīgas Tehniskās universitātes Dabaszinātņu un tehnoloģiju fakultātē, Paula Valdena ielā 3/7, 272. auditorijā.

OFICIĀLIE RECENZENTI

Profesors Sergejs Gaidukovs
Rīgas Tehniskā universitāte

Dr. Antons Sizovs
Latvijas Organiskās sintēzes institūts, Latvija

Profesore *Jagoda Litowczenko-Cybulska*
Poznaņas Adama Mickeviča universitāte, Polija

APSTIPRINĀJUMS

Apstiprinu, ka esmu izstrādājis šo promocijas darbu, kas iesniegts izskatīšanai Rīgas Tehniskajā universitātē zinātnes doktora (*Ph. D.*) grāda iegūšanai. Promocijas darbs zinātniskā grāda iegūšanai nav iesniegts nevienā citā universitātē.

Abhishek Rajesh Indurkar … … … … … … … … … … … …. (paraksts)

Datums: … … … … … … … … … …

Promocijas darbs ir uzrakstīts kā rakstu krājums. To veido kopsavilkums latviešu un angļu valodā un astoņas publikācijas. Publikācijas ir rakstītas angļu valodā un ietver elektroniski pieejamu papildu informāciju.

SATURS

PATEICĪBA 5
SAĪSINĀJUMI 6
PROMOCIJAS DARBA VISPĀRĒJS RAKSTUROJUMS 7
IEVADS 7
MĒRĶIS 8
AIZSTĀVĀMĀS TĒZES 8
ZINĀTNISKĀ NOVITĀTE 8
PRAKTISKĀ NOZĪME 8
PROMOCIJAS DARBA STRUKTŪRA 8
SCI PUBLIKĀCIJAS, KURĀS PREZENTĒTI PROMOCIJAS DARBA REZULTĀTI 10
Publicētās 10
Iesniegtas publicēšanai 10
ZINĀTNISKĀS KONFERENCES, KURĀS PREZENTĒTI PROMOCIJAS DARBA REZULTĀTI 10
AUTORA PERSONĪGAIS IEGULDĪJUMS 12
PROMOCIJAS DARBA IZSTRĀDES GAITĀ SAGATAVOTO UN PUBLICĒTO ZINĀTNISKO PUBLIKĀCIJU SAVSTARPĒJĀ SAISTĪBA 12
PROMOCIJAS DARBA REZULTĀTI 13
LITERATŪRAS APSKATS 13
MAZO ORGANISKO MOLEKULU IZVĒLE 15
MOM SATUROŠA AKF SINTĒZE 16
SINTĒZES REZULTĀTĀ IEGŪTO AKF ĪPAŠĪBAS 18
SINTEZĒTO AKF KRISTALIZĀCIJAS KINĒTIKA ŪDENS VIDĒ 19
SINTEZĒTO AKF RAKSTUROŠANA *IN VITRO* 22
NANOKOMPOZĪTA BIOTINTE 24
NANOKOMPOZĪTU HIDROGELI 29
DUBULTTĪKLA NANOKOMPOZĪTHIDROGELI 31
SECINĀJUMI 37
IZMANTOTĀ LITERATŪRA 38

PATEICĪBA

Sirsnīgs paldies visiem, kuri palīdzēja izstrādāt šo promocijas darbu, sniedzot atbalstu un iedrošinājumu!

Liels paldies pētījumu līdzautoriem! Jūsu ieguldījums un atbalsts ievērojami uzlaboja šī promocijas darba kvalitāti. Jūsu ieguldījums ir nenovērtējams.

Sirsnīgi pateicos promocijas darba vadītājiem par ieteikumiem, mentorēšanu un pacietību! Viņu izpratnei un iedrošinājumam bija izšķiroša nozīme, veidojot manu pētniecības ceļu.

Liels paldies maniem vecākiem! Jūsu nelokāmais atbalsts un ticība manām spējām bija pastāvīgs motivācijas avots. Jūsu upurēšanās un uzmundrinājumi ir likuši pamatus maniem akadēmiskajiem sasniegumiem. Es ļoti pateicos savai sievai par atbalstu, sapratni un iedrošinājumu šajā izaicinošajā, bet piepildītajā ceļojumā! Viņas klātbūtne ir mans balsts, un man ir prieks dalīties šajā sasniegumā ar viņu.

Visbeidzot – gribu atzīt Dieva dievišķo vadību un svētību. Spēks un izturība, ko atradu grūtajos brīžos, liecina par viņa žēlastību.

Nobeigumā vēlos pateikties visiem, kas veicinājuši manu akadēmisko darbību. Jūsu kopējais ieguldījums un atbalsts ir darījis to jēgpilnu un atalgotu.

SAĪSINĀJUMI

MOM – mazas organiskās molekulas
CaP – kalcija fosfāts
Ap –apatīts
HA – hidroksiapatīts
AKF – amorfais kalcija fosfāts
AKF_CL – amorfais kalcija fosfāts, kura sintēzei izmantots $CaCl_2$
AKF_NIT – amorfais kalcija fosfāts, kura sintēzei izmantots $Ca(NO_3)_2$
AKF_ACE – acetātu saturošs amorfais kalcija fosfāts
AKF_ASK – askorbātu saturošs amorfais kalcija fosfāts
AKF_CIT – citrātu saturošs amorfais kalcija fosfāts
AKF_GLU – glutamātu saturošs amorfais kalcija fosfāts
AKF_ITN – itakonātu saturošs amorfais kalcija fosfāts
ADA-GEL – alginmāts-didehīds-želatīns
VT – viens tīkls
DT – dubulttīkls
FBS – fosfāta buferšķīdums
α-MEM – Minimum Essential Medium
P123 – Pluronic P123
GELMA – želatīna metakrilāts
PAM – poliakrilamīds
APS – amonija persulfāts
TMED –tetrametiletilēndiamīns
MCŠ – mezenhimālās cilmes šūnas
LFS – liellopa fetālais serums
FTIS – Furjē transformāciju infrasarkanā spektroskopija
VEA - viskoelastīgo īpašību apgabals

PROMOCIJAS DARBA VISPĀRĒJS RAKSTUROJUMS

IEVADS

Lai risinātu dažādas problēmas, tostarp nelaimes gadījumu un vēža ārstēšanas sekas, kā arī veiktu kosmētiskus uzlabojumus, pasaulē katru gadu tiek veiktas vairāk nekā 4,5 miljoni rekonstruktīvas ķirurģiskas operācijas [1]. Globālās saslimstības datu analīze liecina, ka aptuveni 1,71 miljardam cilvēku visā pasaulē ir muskuļu un skeleta sistēmas slimības [2]. Kaulaudu ārstēšanai un aizvietošanai ir nepieciešami efektīvi biomateriāli. Kaulaudu unikālās īpašības, tos veidojošās fāzes un to strukturālā mijiedarbība dažādos hierarhijas līmeņos ir ļoti sarežģīta. Tāpēc atdarināt dabīgos kaulaudus un iegūt biomateriālus, kuru īpašības būtu salīdzināmas ar dabīgajiem kauliem, ir sarežģīti [3].

Šā iemesla dēļ alotransplantāts joprojām ir "zelta" standarts ar kaulaudiem saistītu slimību ārstēšanā [4]. Alotransplantātiem ir vairāki trūkumi, tāpēc ir liela nepieciešamība pēc sintētiskajiem materiāliem, kas ir līdzīgi dabīgajam kaulam [5]. Kauls ir nanokompozītmateriāls, kas sastāv no neorganiskās un organiskās fāzes. Neorganisko fāzi galvenokārt veido kalcija fosfāts (CaP), savukārt organisko fāzi galvenokārt veido kolagēns.

Kaulu neorganiskā fāze veidojas procesos, kas saistīti ar šūnu mitohondrijiem. Šo procesu rezultātā vispirms veidojas amorfais kalcija fosfāts (AKF), kas kolagēna klātbūtnē transformējas uz vāji kristāliskā apatīta (Ap) fāzi [6]. Mitohondrijos AKF ir saistīts ar organisko savienojumu, kas regulē starpfibrilāro kolagēna mineralizāciju. Organisku savienojumu sānu grupas (karboksilgrupas vai hidroksilgrupas) var mijiedarboties ar CaP virsmu [7]. Organiskie savienojumi var aizkavēt AKF kristalizāciju un transformāciju uz Ap, kavējot kristalizācijas centru veidošanos un augšanu, un tiem ir būtiska nozīme starpfibrilārajā kolagēna mineralizācijas procesā [8]. Šī promocijas darba mērķis ir izstrādāt mazas organiskās molekulas (MOM) saturošus AKF un tos saturošus hidrogelus, kas būtu lietojami kaulaudu reģenerācijā. Pētījumos tika izmantotas piecas MOM, kas dabīgi sastopamas arī mitohondrijos. Šīm MOM ir liela nozīme kaulaudu atjaunošanā, un tām ir dažādas funkcionālās grupas.

Promocijas darba primārais mērķis bija izstrādāt sintēzes metodi MOM saturošu AKF iegūšanai un analizēt MOM ietekmi uz AKF īpašībām – daļiņu izmēru, morfoloģiju, patieso blīvumu, īpatnējo virsmas laukumu (ĪVL), kristalizācijas kinētiku, kā arī citosaderību. Pēc tam sintezētie MOM saturošie AKF tika izmantoti kā neorganiska pildviela organiskā matricā, veidojot nanokompozītus.

Nanokompozītbiotinte tika iegūta, pievienojot MOM saturošus AKF kā neorganisku pildvielu algināta dialdehīda-želatīna (*ADA-GEL*) organiskajai matricei. Citrātu saturošais AKF (AKF_CIT) bija efektīvākā pildviela izdrukāto konstrukciju strukturālās integritātes nodrošināšanai. Pēc tam, izmantojot ķīmisko šķērssaistīšanu, tika izstrādāts viena tīkla (VT) nanokompozīthidrogels, kas sastāvēja no želatīna metakrilāta (*GELMA*) un AKF_CIT.

Papildus tika izveidots AKF_CIT saturošs poliakrilamīda (PAM) – *Pluronic P123* (*P123*) – *GELMA* dubulttīkla (DT) nanokompozīthidrogels. Vispirms tika izvērtēta *P123* ietekme uz PAM-*GELMA* hidrogela mehāniskajām īpašībām, pēc tam tika analizēta AKF_CIT ietekme uz PAM-*GELMA*-*P123* hidrogelu mehāniskajām un reoloģiskajām īpašībām, kā arī novērtēts to formas atmiņas efekts.

Visi promocijas darba izstrādes gaitā iegūtie AKF un AKF saturošie hidrogeli ir citosaderīgi, kas liecina, ka potenciāli tos var izmantot kaulaudu reģenerācijai.

MĒRĶIS

Promocijas darba mērķis bija iegūt MOM saturošus AKF, izpētīt to īpašības un raksturotcitosaderību, kā arī izmantot tos kā pildvielas nanokompozīthidrogelu iegūšanai un novērtētiegūto nanokompozīthidrogelu mehāniskās un reoloģiskās īpašības, kā arī citosaderību. Mērķasasniegšanai definēti vairāki uzdevumi.

Izstrādāt sintēzes metodi MOM saturošu AKF iegūšanai.

Noskaidrot MOM ietekmi uz AKF īpašībām un transformācijas kinētiku uz vāji kristālisko Ap ūdens vidē (dejonizētā ūdenī, fosfāta buferšķīdumā (FBS) un šūnu kultūras barotnē Minimum Essential Medium (α-MEM)), kā arī AKF citosaderību.

Biotintē, VT un DT hidrogelā iekļaut sintēžu rezultātā iegūtos AKF un izpētīt iegūto nanokompozīthidrogelu īpašības.

AIZSTĀVĀMĀS TĒZES

1. MOM iekļaušana AKF ietekmē tā īpašības, transformācijas kinētiku uz Ap, kā arī citosaderību.
2. Ūdens mediētas AKF transformācijas ātrumu uz Ap ietekmē ūdens vides sastāvs (dejonizēts ūdens, *FBS* un *α-MEM*).
3. AKF pievienošana biotintei, VT un DT hidrogeliem uzlabo to reoloģiskās, mehāniskās un strukturālās īpašības, vienlaikus saglabājot citosaderību.

ZINĀTNISKĀ NOVITĀTE

1. Izstrādāta viena soļa slapjā ķīmiskās sintēzes metode tīra un MOM (piemēram, acetātu, askorbātu, citrātu, itakonātu un glutamātu) saturoša AKF sintēzei.
2. Pirmo reiz sintezēts acetātu, askorbātu un itakonātu saturošs AKF.
3. Pirmo reizi raksturota MOM ietekme uz ūdens mediētas AKF transformācijas kinētiku uz Ap.
4. Izstrādāta jauna AKF saturoša biotinte, kā arī AKF saturoši VT un DT hidrogeli.
5. Izveidots jauna sastāva PAM-*GELMA-P123* hidrogels.

PRAKTISKĀ **NOZĪME**

1. Izstrādāto metodi var izmantot arī citu MOM saturošu AKF sintēzei.
2. Specifiskam lietojumam AKF transformācijas kinētiku uz Ap var pielāgot, izmantojot noteiktu MOM un ūdens vides kombināciju.
3. DT hidrogela mehāniskās īpašības var kontrolēt, modulējot *P123* koncentrāciju PAM-*GELMA* hidrogelā.

PROMOCIJAS DARBA STRUKTŪRA

1. Promocijas darbs veidots kā tematiski vienota zinātnisko publikāciju kopa, kur iekļauti pētījumi, kas veltīti MOM saturošu AKF sintēzei un sintezēto AKF saturošas biotintes, VT un DT hidrogelu izstrādei. Katra publikāciju kopas zinātniskā publikācija ir oriģinālpētījums, kurā atspoguļotas jaunas zināšanas. Kopā šīs publikācijas apraksta

pētījumu par jaunu pieeju MOM saturošu AKF sintezēšanai un tos saturošu nanokompozītu izstrādi.

2. Pirms eksperimentālā darba sākšanas veikts literatūras apskats (promocijas darba autora 1. publikācija) par dažādu CaP veidu fizikālajām īpašībām, bioloģisko sastopamību un sintēzi, kā arī to lietošanu kaulaudu reģenerācijā. Literatūras izpētes rezultātā secināts, ka ķīmiski tīra, kristāliska CaP iegūšanai nepieciešama augsta sintēzes temperatūra vai apstrāde. AKF ir metastabila CaP forma, tāpēc to nevar saķepināt augstā temperatūrā.
3. Promocijas darba autora 2. publikācijā AKF tika sintezēts, izmantojot šķīdināšanas-nogulsnēšanas metodi. No sintezētā AKF pulvera tika iegūti paraugi ar augstu relatīvo blīvumu, to uniaksiāli presējot 1250 MPa līdz 1500 MPa spiedienā istabas temperatūrā. Iegūtie paraugi saglabāja AKF fāzi.
4. Dabīgais kaulu Ap ir nestohiometrisks un strukturāli nesakārtots. Tāpēc mērķis bija izprast kaulu Ap veidošanās mehānismu, kā arī kolagēna un organisko molekulu lomu mineralizācijas procesa regulēšanā (promocijas darba autora 3. publikācija). Dabīgais AKF veidojas procesos, kas saistīti ar šūnu mitohondrijiem. AKF mitohondrijos ir saistīts ar organisku savienojumu. Organisko savienojumu sānu grupas (karboksila un hidroksila grupu) regulē Ap nukleāciju un kolagēna intrfibrilāro mineralizāciju. Balstoties literatūras apskatā, tika atlasītas piecas MOM, kas sastopamas šūnu mitohondrijos, kurām ir dažādas funkcionālajās grupas un kas ir nozīmīgas kaulu fizioloģijā. Šīs MOM tika izmantotas MOM saturošu AKF sintēzei, kas bija promocijas darba galvenais mērķis.
5. Promocijas darba autora 4. publikācijā galvenā uzmanība tika pievērsta vienas pakāpes slapjās ķīmiskās metodes izstrādei AKF_ACE un AKF_CIT sintēzei. 4. publikācijā aprakstītā autora izstrādātā sintēzes metode pēc tam tika izmantota, lai sintezētu arī AKF_GLU, AKF_ITA un AKF_ASK (promocijas darba autora 5. publikācija). Sintēžu rezultātā iegūtie AKF tika raksturoti ar dažādām metodēm. Iegūtie rezultāti demonstrē MOM ietekmi uz AKF īpašībām un citosaderību.
6. Promocijas darba autora 6. publikācijā analizēta AKF daļiņu lieluma, transformācijas kinētikas un MOM ietekme uz *ADA-GEL* hidrogelu un izdrukātajām konstrukcijām. AKF_ACE un AKF_CIT tika izmantoti kā neorganiskā pildviela *ADA-GEL* organiskajā matricē nanokompozīthidrogelu iegūšanai. Nanokompozītu biotintes tika iegūtas, AKF-*ADA-GEL* hidrogeliem pievienojot *MC3T3-E1* šūnas. Gan AKF_ACE, gan AKF_CIT biotintes bija citosaderīgas, tomēr AKF_CIT bija efektīvāka izdrukāto konstrukciju strukturālās integritātes saglabāšanai.
7. Promocijas darba autora 7. publikācijā aprakstīts izstrādātais AKF_CIT saturošs *GELMA* hidrogels, izmantojot ķīmiskās šķērssaistīšanas metodi kā alternatīvu fotošķērssaistīšanai. *In vitro* analīze apstiprināja, ka ķīmiskā šķērssaistīšana un AKF_CIT pievienošana neietekmēja *GELMA* hidrogela citosaderību.
8. Promocijas darba autora 8. publikācijā aprakstīts sintezētais DT hidrogels, kas sastāv no PAM-*GELMA-P123*. Pirmais DT hidrogela tīkls tika iegūts, izmantojot *P123*, otro tīklu veidoja PAM-*GELMA* kopolimērs. Abi PAM-*GELMA* tīkli tika ķīmiski šķērssaistīti. Sākotnēji *P123* koncentrācija PAM-*GELMA* hidrogelā tika pielāgota, lai iegūtu optimālās mehāniskās īpašības. Pēc tam tika analizēta dažādu AKF_CIT koncentrāciju ietekme uz PAM-*GELMA-P123* hidrogela mehāniskajām īpašībām. Papildus tika izpētīts DT nanokompozīthidrogela formas atmiņas efekts.

SCI PUBLIKĀCIJAS, KURĀS PREZENTĒTI PROMOCIJAS DARBA REZULTĀTI

Publicētās

1. **Indurkar, A.,** Choudhary, R., Rubenis, K., & Locs, J. (2021). Advances in sintering techniques for calcium phosphates ceramics. Materials, 14 (20), 6133. (**1. publikācija**) https://doi.org/10.3390/ma14206133.
2. Rubenis, K., Zemjane, S., Vecstaudza, J., Lazdovica, K., Bitenieks, J., Wiecinski, P., **Indurkar, A.,** & Locs, J. (2022). Sintering of amorphous calcium phosphate to near-full density by uniaxial compaction at room temperature. Journal of the European Ceramic Society, 42 (13), 6199–6205. (**2. publikācija**) https://doi.org/10.1016/j.jeurceramsoc.2022.06.041.
3. **Indurkar, A.,** Choudhary, R., Rubenis, K., & Locs, J. (2023). Role of carboxylic organic molecules in interfibrillar collagen mineralization. Frontiers in Bioengineering and Biotechnology, 11, 1150037. (**3. publikācija**) https://doi.org/10.3389/fbioe.2023.1150037.
4. **Indurkar, A.,** Choudhary, R., Rubenis, K., Nimbalkar, M., Sarakovskis, A., Boccaccini, A. R., & Locs, J. (2023). Amorphous calcium phosphate and amorphous calcium phosphate carboxylate: Synthesis and characterization. ACS Omega. (**4. publikācija**) https://doi.org/10.1021/acsomega.3c00796.
5. **Indurkar, A.,** Kudale, P., Rjabovs, K., Heinmaa, I,. Demir, O., Kirejevs, M., Rubenis, K., Chaturbhuj, G., Turks, M,. & Locs, J. (2023). Small Organic Molecules Containing Amorphous Calcium Phosphate: Synthesis, Characterization and Transformation. Frontiers in Bioengineering and Biotechnology, 11. (**5. publikācija**) https://doi.org/10.3389/fbioe.2023.1329752.

Iesniegtas publicēšanai

1. **Indurkar, A.,** Heid, S., Bauer, J., Rubenis, K., Friedrich, O., A., Locs, J., & Boccaccini, A. R. Amorphous Calcium Phosphate Reinforced Alginate-Dialdehyde-Gelatin (Ada-Gel) Bioinks for Biofabrication of Bone Tissue Scaffolds. Tiek recenzēta žurnālā Scientific reports (**6. publikācija*).***
2. **Indurkar, A.,** Rubenis, K., Boccaccini, A. R., & Locs, J. Development of nanocomposite hydrogel using citrate-containing amorphous calcium phosphate and gelatin methacrylate. Iesniegta žurnālā Frontiers Bioengnieering and Biotechnology (**7. publikācija**).
3. **Indurkar, A.,** Rubenis, K., Boccaccini, A. R., & Locs, J. Development and Characterization of Thermoresponsive Double-Network Nanocomposite Hydrogel for Bone Tissue Engineering. Iesniegta žurnālā Macromolecular Materials and Engineering (**8. publikācija**).

ZINĀTNISKĀS KONFERENCES, KURĀS PREZENTĒTI PROMOCIJAS DARBA REZULTĀTI

1. Development of nanocomposite double network hydrogel: Vecstaudza, J., Egle, K., **Indurkar, A.,** Locs, J. 64th International Scientific Conference, Rīgas Tehniskā universitāte, Latvija notika 2023. gada 6. oktobrī. (***Prezentācijas***)

2. Development of nanocomposite double network hydrogel: **Indurkar, A.,** Rubenis, K., Boccaccini, A. R., & Locs, J. 64th International Scientific Conference, Rīgas Tehniskā universitāte, Latvija notika 2023. gada 6. oktobrī. (***Prezentācija***)
3. Amorphous calcium phosphate citrate reinforced gelatin-alginate dialdehyde bioink for bone regeneration: **Indurkar, A.,** Rubenis, K., Boccaccini, A. R., & Locs, J. International Conference on Biofabrication, Saskatūna, Kanāda, notika no 2023. gada 17. līdz 20. septembrim. (***Prezentācija***)
4. Amorphous calcium phosphate citrate reinforced gelatin-alginate dialdehyde bioink for bone regeneration: **Indurkar, A.,** Rubenis, K., Boccaccini, A. R., & Locs, J. FEMS EuroMat 2023, Frankfurte, Vācija, notika no 2023. gada 3. līdz 7. septembrim. (***Prezentācija***)
5. Amorphous calcium phosphate citrate reinforced gelatin-alginate dialdehyde bioink for bone regeneration: **Indurkar, A.,** Rubenis, K., Boccaccini, A. R., & Locs, J. 5th World Congress of Latvian Scientists, Rīga, Latvija, notika no 2023. gada 26. līdz 29. jūnijam. (***Stenda referāts***)
6. Biomimetic synthesis of amorphous calcium phosphate: **Indurkar, A.,** Choudhary, R., Rubenis., & Locs, J. 16th Scandinavian Society of Biomaterials, Roros, Norvēģija notika no 2023. gada 21. līdz 24. martam. (***Stenda referāts***)
7. Tailor-made synthesis of bionic amorphous calcium phosphate: **Indurkar, A.,** Choudhary, R., Rubenis, K., Locs, J. Biomaterials and novel technologies for healthcare 3rd biennial International Conference BIOMAH, Roma, Itālija, notika no 2022. gada 18. līdz 21. oktobrim. (***Prezentācija***)

AUTORA PERSONĪGAIS IEGULDĪJUMS

Šajā promocijas darbā aprakstītie pētījumi ir izstrādāti sadarbībā ar 16 zinātniekiem. Pētījumus uzraudzīja pieredzējuši mentori, kuri sniedza būtisku atbalstu un vērtīgu ieguldījumu. Katrā no publicētajiem pētījumiem autoram bija vadošā loma – gan pētot zinātnisko literatūru, gan veicot pētījumu. Autora personīgais ieguldījums šajā promocijas darbā ietver vienas pakāpes mitrās ķīmiskās sintēzes metodes izstrādi AKF sintēzei (ar un bez MOM) un sintezētā produkta raksturošanu. Sintezētais AKF tika izmantots kā pildviela biotintē, VT un DT hidrogelos.

Promocijas darba izstrādes gaitā liela nozīme bija diskusijām ar līdzautoriem un promocijas darba vadītājiem, kas bija būtiskas, lai pārvarētu dažādus sarežģījumus, kas radās pētniecības gaitā.

PROMOCIJAS DARBA IZSTRĀDES GAITĀ SAGATAVOTO UN PUBLICĒTO ZINĀTNISKO PUBLIKĀCIJU SAVSTARPĒJĀ SAISTĪBA

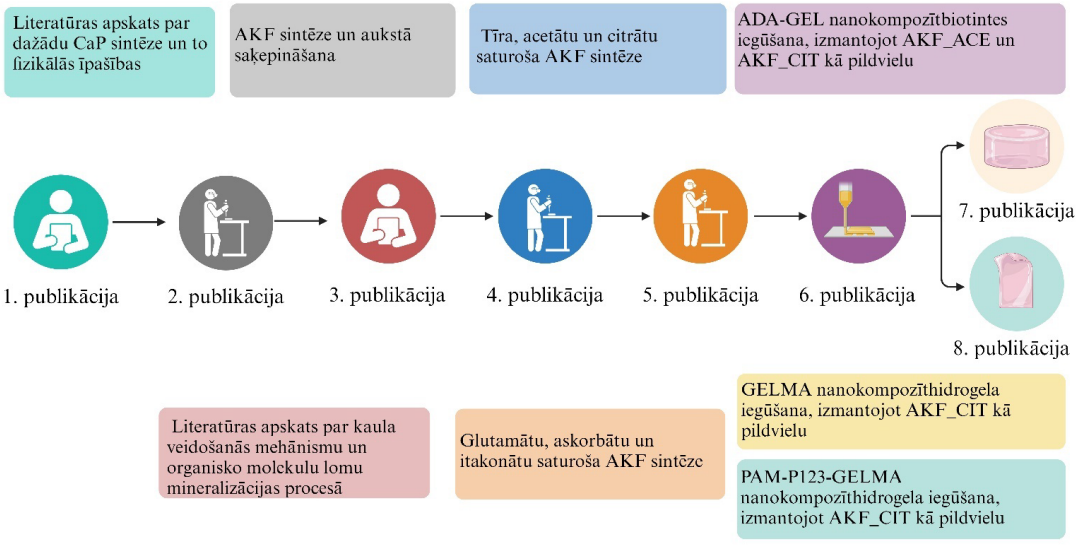

1. att. Promocijas darba izstrādes gaitā sagatavoto un publicēto zinātnisko publikāciju tematika un savstarpējā saistība.

PROMOCIJAS DARBA REZULTĀTI

LITERATŪRAS APSKATS

Kauli (kaulaudi) ir blīva saistaudu forma, kas veido cilvēka skeletu. Kaulaudi sastāv no specifiskām šūnām un matrices, kas pēc masas satur 65–70 % biominerālu un 5–8 % ūdens, savukārt pārējais ir organiskas vielas [9]. Minerālā fāze sastāv no kalcija fosfāta (CaP) – karbonātus saturoša hidroksilapatīta (HA). Organiskā fāze satur 90 % kolagēna un 10 % citu proteīnu.

CaP ir nozīmīga kaulu sastāvdaļa. Pēdējās desmitgadēs gan kaulaudu reģenerācijas pētījumos, gan klīniski izmantoti dažādi biomateriāli, kas satur CaP [10]. Promocijas darba autora 1. zinātniskajā publikācijā ir sniegts visaptverošs pārskats par CaP, piemēram, to fizikālajām īpašībām, bioloģiskajiem aspektiem un to sintēzes metodēm [11]. Apskatīta literatūra par sintēzes metodēm, ko izmanto ķīmiski tīru, stehiometrisku CaP materiālu iegūšanai. Veicot literatūras analīzi, secināts, ka ķīmiski tīra, kristāliska CaP iegūšanai nepieciešama augsta sintēzes temperatūra vai apstrāde augstā temperatūrā.

Sintētiskā HA, kas iegūts augstās temperatūrās, ķīmiskā formula ir $Ca_{10}(PO_4)_6(OH)_2$. Apatīts (Ap), kas sastopams kaulos, veidojas zemā temperatūrā un nav tik kristālisks. To uzskata par vāji kristālisku Ap formu, kas nav stohiometriska viena vai vairāku katjonu (Na^+, K^+, Fe^{2+}, Mg^{2+}, Zn^{2+}, Sr^{2+}) un/vai anjonu (HPO_4^{2-}, CO_3^{2-}, Cl^-, F^-, citrāta) klātbūtnes dēļ tā struktūrā [12]. Piemaisījumi kaula Ap rada spriegumus tā kristālstruktūrā, padarot to mazāk stabilu, taču reaģētspējīgāku [13]. Kaula Ap kristāliem ir unikāla ģeometrija – garums nepārsniedz 30–50 nm, savukārt biezums ir tuvu 2 nm [14]. Promocijas darba autora 3. publikācijā galvenā uzmanība pievērsta kaulu Ap veidošanās mehānisma izpratnei [15].

Amorfais kalcija fosfāts (AKF) ir pirmā CaP fāze, kas veidojas procesos, kas saistīti ar šūnu mitohondrijiem. AKF mitohondrijos ir saistīts ar organisku savienojumu – Hovarda faktoru, kas liecina par kompleksu organiska-neorganiska savienojuma veidošanos. Šis komplekss tiek pārnests uz kolagēna matrici, kur AKF transformējas uz vāji kristālisku Ap.

Kaulu organiskajai komponentei ir fundamentāla nozīme Ap veidošanās procesā. Kā redzams 2. attēlā, kaulos kolagēns ir izkārtots paralēlā zigzagveida masīvā. Kolagēna molekulas cita pret citu ir nobīdītas par attālumu D (67 nm), savukārt attālums starp divām tropokolagēna molekulām ir 40 nm, ko dēvē par atstarpes zonu [16]. Atstarpes zonā notiek AKF nukleācija un transformācija uz Ap. Ap kristālu c ass ir orientēta paralēli kolagēna molekulu garenvirzienam [17].

Agrāk veiktajos pētījumos konstatēts, ka sintētiska AKF/kolagēna kombinācija neizraisa AKF transformāciju uz Ap [18]. Tā rezultātā kļuva skaidrs, ka kolagēns nevar patstāvīgi ierosināt mineralizāciju un tam nepieciešams nukleācijas procesu regulējošs katalizators. Šis katalizators ir organiska molekula ar specifiskām reaktīvām sānu grupām (karboksilgrupa vai hidroksilgrupa), kas izkārtotas stereoķīmiskā formā [8].

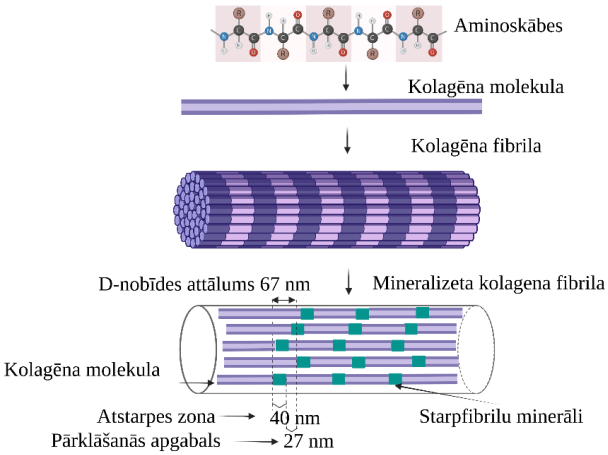

2. att. Kolagēna hierarhiskās struktūras shematisks attēlojums.

Pirmais organiskais savienojums, kura ietekme uz kolagēna starpfibrilāro mineralizāciju tika pētīta, bija poliaspartāts. Poliaspartāta pievienošana uzlaboja mijiedarbību starp CaP un kolagēnu, kā rezultātā kolagēna fibrilās veidojās atsevišķi CaP kristāli. Ja poliaspartāts netika pievienots, veidojās ar kolagēna fibrilām vāji saistīti CaP kristālu klasteri. Poliaspartāts adsorbējas uz CaP virsmas, un CaP kristalizācijas aizkavēšana var būt saistīta ar palēninātu AKF transformāciju uz Ap vai ar mijiedarbību ar kristālisko fāzi, kavējot nukleācijas centru augšanu [7]. Minētais pētījums pierādīja, ka organiskajām molekulām ir fundamentāla nozīme kolagēna starpfibrilārās mineralizācijas regulēšanā.

Zinātniskajā literatūrā izvērtēta dažādu organisko molekulu (proteīnu, polimēru un mazu organisko molekulu (MOM)) ietekme uz CaP sintēzi. Organisko molekulu saraksts, kuru ietekme uz CaP sintēzi pētīta, atrodams promocijas darba autora 3. publikācijā.

AKF dabīgi veidojas procesos, kas saistīti ar šūnu mitohondrijiem (3. A attēls). Šūnu mitohondrijos AKF veido kompleksu ar organisku savienojumu. Literatūrā minēts, ka organiskie savienojumi ar sānu grupām (karboksilgrupu un hidroksilgrupu) var izraisīt Ap nukleāciju [5]. Organisko savienojumu funkcionālajām grupām jābūt ar noteiktu konfigurāciju, lai izraisītu CaP nukleāciju simulētās ķermeņa vides apstākļos. Promocijas darbā pētījumu veikšanai tika izvēlētas piecas MOM, kas sastopamas šūnu mitohondrijos. Šīm MOM ir būtiska nozīme kaulaudu reģenerācijā, un tām ir dažādas funkcionālās grupas, kā redzams 3. B attēlā.

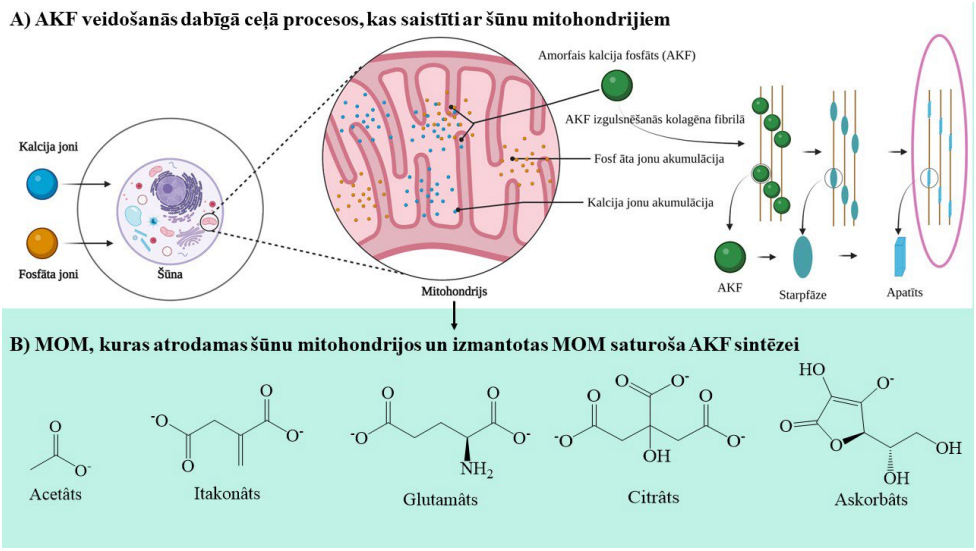

3. att. A) AKF veidošanās procesos, kas saistīti ar šūnu mitohondrijiem;
B) MOM, kas atrodamas šūnu mitohondrijos un izmantotas MOM saturoša AKF sintēzei promocijas darba autora 4. publikācijā.

Acetāts ir monokarboksilsavienojums, kas uzlabo cilmes šūnu diferenciāciju, palielinot histona acetilēšanu un hromatīna veidošanos. Kaulu smadzeņu mezenhimālās cilmes šūnas (MCŠ) regulē kaulaudu reģenerāciju, diferenciējoties par adipocītiem, hondrocītiem un osteoblastiem. Novecojušām MCŠ ir samazināta spēja diferencēties osteogēnajā un hondrogēnajā šūnu līnijā. Acetāts var samazināt novecojušu MCŠ osteoģenēzes defektus [19].

Itakonāts un glutamāts ir dikarboksilsavienojumi, kas sastopami šūnu mitohondrijos. Itakonāts ir metabolīts, kas regulē osteoklastu diferenciāciju un aktivāciju, uztur kaulu homeostāzi un mazina lipopolisaharīdu izraisīta iekaisuma kaulaudu zudumu [20]. Glutamāts ir fundamentāla ārpusšūnas signālmolekula, kas tiek izmantota neirālai un neneirālai signālu pārnesei kaulaudos. Osteoblasti, osteoklasti un kaulu smadzeņu šūnas ekspresē glutamāta receptorus. Glutamāta receptoru aktivācija kontrolē osteoblastu un osteoklastu fenotipu *in vitro* un kaulu masu *in vivo* [21]. Turklāt glutamāts kaulu lūzumu gadījumā palīdz uzturēt slāpekļa līdzsvaru, tādējādi paātrinot kaulu dzīšanas procesu [22].

Citrāts ir trikarboksilsavienojums un būtiska komponente, kas tiek sintezēta Krebsa ciklā. Citrāta klātbūtne kaulos pirmo reizi tika detektēta 1941. gadā [23]. Citrāta koncentrācija kaulos ir 20–80 μmol/g, kas 100–400 reizes pārsniedz tā koncentrāciju mīkstajos audos. Kauli satur 1,6 % citrāta, kas veido 90 % no citrāta, kas ir cilvēka ķermenī [24]. Jaunākie kodolmagnētiskās

rezonanses (KMR) pētījumi ir apstiprinājuši citrāta klātbūtni kaulos [25]. Citrāta un apatīta kompleksā mijiedarbība regulē Ap kristālrežģa orientāciju, daļiņu izmēru un sadalījumu. Citrāta molekulas gareniskā ass ir paralēla Ap virsmai. Trīs citrāta karboksilgrupas atrodas 0,3–0,45 nm attālumā no Ap virsmas. Karboksilgrupu atstatums sakrīt ar kalcija jonu uz apatīta c ass, tāpēc apatīta kristāla augšana tiek kavēta tā šķērsvirzienā, bet turpinās garenvirzienā [26].

Askorbātam (C vitamīnam) ir izšķiroša nozīme kolagēna sintēzē, un tas ir ļoti svarīgs organisks savienojums saistaudos un kaulos [27]. Kolagēns veido kaula struktūru un nodrošina elastību, ļaujot tam izturēt mehānisku slodzi. Bez pietiekama askorbāta daudzuma tiek traucēta kolagēna sintēze, vājinot kaulu struktūru un palielinot kaulu lūzumu iespējamību [28]. Askorbāts ietekmē arī osteogēno šūnu diferenciāciju [29], [30].

Kopumā tādām MOM kā acetātam, itakonātam, glutamātam, citrātam un askorbātam ir izšķiroša nozīme kaulaudu fizioloģijā. Tādēļ šīs MOM tika izmantotas, lai sintezētu MOM saturošu AKF un analizētu to funkcionālo grupu ietekmi uz AKF fizioķīmiskajām īpašībām un citosaderību.

MOM SATUROŠA AKF SINTĒZE

Vienas pakāpes AKF sintēzei var izmantot šķīdināšanas-izgulsnēšanas metodi, vispirms izšķīdinot HA un tad iegūtajam šķīdumam strauji pievienojot bāzi (promocijas darba autora 2. publikācija), kā parādīts 4. A attēlā. Turpretī MOM saturošu AKF sintēzē parasti tiek izmantotas daudzpakāpju metodes, kur MOM pievieno vai nu skābes, vai arī bāzes formā, kā redzams 4. B attēlā.

Sarežģītākais AKF sintēzē ir fosfātu jonu triprotiskais raksturs. Ja AKF sintezēts skābā vidē, tas satur HPO_4^{2-}, nevis PO_4^{3-}, kas negatīvi ietekmē AKF īpašības [31]. *Boskey* un *Posner* pierādīja tādu faktoru kā sintēzes pH, virsmas laukuma, kalcija koncentrācijas, maisīšanas ātruma un šķīduma koncentrācijas ietekmi uz sintēzes rezultātā iegūtā AKF fizikālajām un ķīmiskajām īpašībām (sintēze veikta kontrolētas temperatūras apstākļos 26 °C temperatūrā). AKF sintēzes pH ietekme uz laiku, kas nepieciešams, lai tas transformētos uz Ap, redzama 1. tabulā.

1. tabula

Sintēzes pH ietekme uz AKF transformāciju par Ap [32]

AKF sintēzes pH	**Laiks, kas nepieciešams AKF transformācijai uz Ap (min)**
6,8	16
7,0	30
7,5	48
8,0	120
9,0	135
10,0	280

Zinātniskajā literatūrā aprakstītas dažādas metodes tīra un MOM saturoša AKF sintēzei. Sintēzes veiktas atšķirīgos pH, dažādos maisīšanas ātrumos, reakcijas laikos, atšķirīgos tilpumos, kā arī dažādās kalcija un fosfāta jonu koncentrācijās. Tāpēc ir sarežģīti salīdzināt sintēžu rezultātā iegūtos tīros un MOM saturošos AKF.

Promocijas darba gaitā izstrādāta vienas pakāpes slapjās ķīmiskās sintēzes metode tīra un MOM saturoša AKF iegūšanai, saglabājot nemainīgus sintēzes parametrus, piemēram, sintēzes pH, reakcijas tilpumu, temperatūru, maisīšanas ātrumu un kalcija un fosfātu jonu koncentrāciju. Šī standartizētā pieeja ļauj analizēt MOM ietekmi uz AKF fizikālajām un ķīmiskajām īpašībām.

Promocijas darba izstrādes gaitā (promocijas darba autora 4. publikācija) tīra AKF iegūšanai tika izmantota šāda pieeja: vispirms tika pagatavots kalcija hlorīda vai kalcija nitrāta šķīdums (150 mM 150 ml dejonizēta ūdens), tā pH pielāgots līdz 11,5, izmantojot 3M NaOH šķīdumu. Pēc tam, vienmērīgi maisot ar ātrumu 500 apgr./min., šim šķīdumam tika pievienots identisks apjoms trinātrija fosfāta šķīduma (100 mM 150 ml dejonizēta ūdens), kā redzams 4. C attēlā.

Lai iegūtu MOM saturošu AKF (promocijas darba autora 4. un 5. publikācija), vispirms kalcija glutamāts (150 mM), kalcija acetāts (10 mM) vai kalcija citrāts (150 mM) tika pievienots 150 ml dejonizēta ūdens. Iegūtā šķīduma pH tika pielāgots līdz 11,5, izmantojot 3M NaOH šķīdumu, kam sekoja identiska apjoma trinātrija fosfāta šķīduma pievienošana (100 mM 150 ml dejonizēta ūdens), šķīdumu maisot ar 500 apgr./min. (4. D attēls).

Itakonātu un askorbātu saturošā AKF iegūšanas process redzams 4. C attēlā. 150 ml dejonizēta ūdens tika pievienots kalcija hlorīds (150 mM), itakonskābes anhidrīds (150 mM) vai askorbīnskābe (150 mM). Iegūto šķīdumu pH tika pielāgots līdz 11,5, izmantojot 3M NaOH šķīdumu. Pēc tam tika pievienots identisks apjoms trinātrija fosfāta šķīduma (100 mM 150 ml dejonizēta ūdens), nepārtraukti maisot ar ātrumu 500 apgr./min.

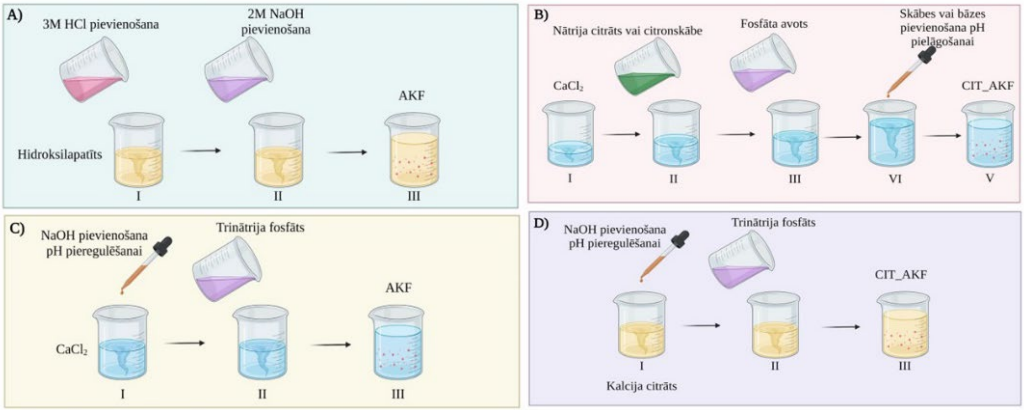

4. att. Tradicionālā sintēzes pieeja tīra (A) un MOM saturoša AKF iegūšanai (B). Promocijas darba gaitā tīra AKF sintēzei izmantots kalcija hlorīda šķīdums (pH pielāgots līdz 11,5 ar 3M NaOH), kuram pēc tam pievienots trinātrija fosfāta šķīdums (C). MOM saturoša AKF sintēzei izmantots attiecīgās MOM kalcija sāls šķīdums, kuram pēc pH pielāgošanas pievienots trinātrija fosfāta šķīdums (D).

Visu sintēžu gadījumā kalcija sāls šķīdumu (arī MOM saturošo) pH tika pielāgots līdz 11,5, izmantojot 3M NaOH. Trinātrija fosfāta šķīduma pH vērtība pēc būtības ir 12. Sajaucot šos šķīdumus, reakcijas pH saglabājās robežās no 10,5 līdz 11,5. Sintēžu reakcijas tilpums, temperatūra, maisīšanas ātrums, kalcija un fosfātu jonu koncentrācija, kā arī skalošanas un žāvēšanas process (centrifugēšana, trīskārtēja skalošana ar destilētu ūdeni, iegūto nogulšņu sasaldēšana, izmantojot šķidro slāpekli un liofilizācija) bija identiski. Gan AKF, gan MOM saturošie AKF tika iegūti līdzīgos apstākļos, kas ļaujot tos savstarpēji salīdzināt un spriest par

MOM ietekmi gan uz AKF fizikālajām un ķīmiskajām īpašībām, gan AKF transformācijas kinētiku uz Ap.

SINTĒZES REZULTĀTĀ IEGŪTO AKF ĪPAŠĪBAS

Promocijas darba autora 4. publikācijā aprakstītas gan sintēzes rezultātā iegūto tīro AKF, gan acetātu un citrātu saturošo AKF īpašības, savukārt 5. publikācijā sniegta informācija par askorbātu, glutamātu un itakonātu saturošajiem AKF.

Visu sintezēto AKF RTG ainas uzrādīja divus platus izliekumus, apliecinot, ka sintēžu rezultātā ir iegūts AKF. Absorbcijas joslu šķelšanās ν_4 PO_4^{3-} raksturīgajā svārstību apgabalā (500–620 cm^{-1}) paraugiem iegūtajos FTIR spektros netika novērota, liecinot par visu sintēzes rezultātā iegūto AKF amorfo dabu.

Visu iegūto AKF cietvielu ^{31}P kodolmagnētiskās rezonanses (KMR) analīze uzrādīja AKF raksturīgo plato pīķi ar Gausa sadalījuma formu, kas centrēts starp 2,2 ppm līdz 6,5 ppm. AKF un attiecīgo MOM funkcionālo grupu klātbūtne tika apstiprināta, izmantojot FTIR un cietvielu ^{13}C KMR analīzi.

Morfoloģija AKF, kura klātbūtne detektēta zebrzivs spuru kaulos, cāļu embriju garajos kaulos un peļu galvaskausos, ir sfēriska vai globulāra, ar izmēru 10–50 nm [33], [34]. 5. attēlā redzama promocijas darba izstrādes gaitā sintezēto tīro un MOM saturošo AKF transmisijas elektronu mikroskopijas (TEM) attēli. Tīrā, acetātu, askorbātu, glutamātu un itakonātu saturošā AKF daļiņām ir sfēriska forma ar diametru ap 20 nm. Novērojams, ka daļiņām ir dobs vidus. Citrātu saturošajam AKF ir globulāra morfoloģija ar diametru ap 40 nm.

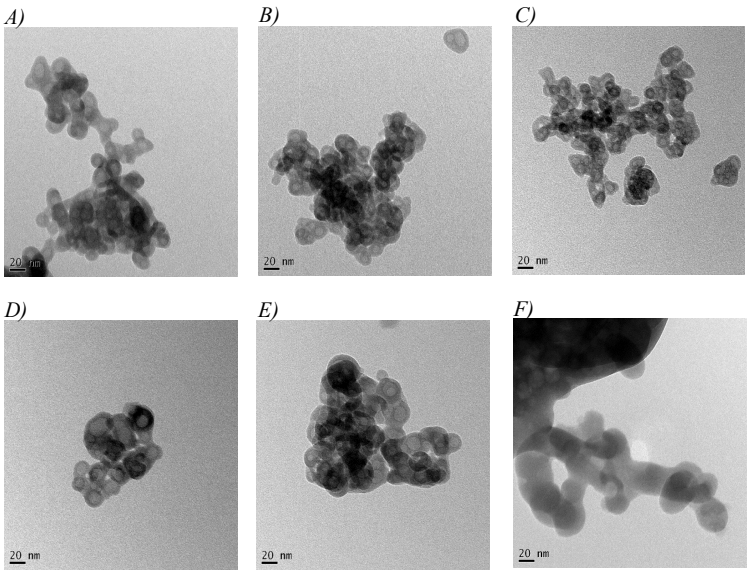

5. att. Promocijas darba izstrādes gaitā sintezēto AKF morfoloģija (mērogs 20 nm). A) tīrs AKF; B) AKF_ACE (acetātu saturošs AKF); C) AKF_ITN (itakonātu saturošs AKF); D) AKF_GLU (glutamātu saturošs AKF; E) AKF_ASK (askorbātu saturošs AKF); F) AKF_CIT (citrātu saturošs AKF).

MOM ietekme uz AKF patieso blīvumu un īpatnējo virsmas laukumu (ĪVL) redzama 2. tabulā. Šajā pētījumā izmantotajām MOM ir dažādas funkcionālās grupas. Acetāts ir

monokarboksilāts, glutamāts un itakonāts ir bikarboksilāts, citrātam ir trīs karboksilāta grupas un hidroksilgrupa, savukārt askorbātam ir hidroksilgrupas. AKF sastāvā esošie kalcija un fosfāta joni var reaģēt ar acetāta, citrāta, itakonāta un glutamāta karboksilāta grupām. Hidroksilgrupas var reaģēt gan ar fosfāta, gan kalcija joniem. Ņemot vērā to, ka sintēzei izmantotajām MOM ir atšķirīgs karboksilātu un hidroksilgrupu skaits un, attiecīgi, to negatīvo lādiņu skaits, tās atšķirīgi reaģē ar AKF sastāvā esošajiem kalcija un fosfāta joniem. 2. tabulā redzamas tīrā un MOM saturošo AKF patiesais blīvums un ĪVL.

2. tabula

Sintēzes rezultātā iegūto AKF patiesais blīvums un ĪVL

Paraugs	**Patiesais blīvums (g/cm^3)**	**ĪVL (m^2/g)**
AKF	2,62	105
Acetātu saturošs AKF	2,47	118
Itakonātu saturošs AKF	2,43	130
Glutamātu saturošs AKF	2,64	92
Askorbātu saturošs AKF	2,82	115
Citrātu saturošs AKF	2,57	62

SINTEZĒTO AKF KRISTALIZĀCIJAS KINĒTIKA ŪDENS VIDĒ

In vitro analīze tiek izmantota, lai noteiktu šūnu atbildes reakciju uz materiālu. Šīs analīzes laikā materiāls tiek pakļauts dažādu šķīdumu iedarbībai. Metastabiliem materiāliem, piemēram, AKF, pirms *in vitro* analīzes veikšanas ir ļoti būtiski novērtēt kristalizācijas kinētiku ūdens vidē. Promocijas darba autora 5. publikācijā aprakstīti visu sintezēto AKF kristalizācijas kinētikas pētījumi. Eksperimenti tika veikti dejonizētā ūdenī, fosfāta buferšķīdumā (*FBS*) un šūnu kultūras barotnē *Minimum Essential Medium* (*α-MEM*).

Līdz šim publicētie pētījumi liecina, ka AKF kristalizācijas kinētiku neietekmē šādi faktori: a) izmantotās buferšķīduma sistēmas veids; b) dažāda veida monovalento jonu klātbūtne; c) AKF saskare ar sintēzes šķīdumu, filtrēšana, žāvēšana vai tā pievienošana tikko pagatavotam buferšķīdumam.

Faktori, kas ietekmē kristalizācijas kinētiku, ir maisīšanas ātrums, sintēzes šķīduma sastāvs, šķīdinātāja veids, piesārņojuma klātbūtne un piedevas (polimetrolīti, fosfolipīdi, poliglikoli, proteīni). Līdz šim veiktajos pētījumos MOM ietekmei uz AKF kristalizāciju pievērsta maza uzmanība [32].

Kristalizācijas eksperimenti vispirms tika veikti dejonizētā ūdenī (6. att.). Acetātu saturošā AKF transformācija uz Ap notika ātrāk nekā tīrā AKF gadījumā. Organiskā savienojuma sānu grupas (karboksilāta vai hidroksilgrupa) nodrošina mijiedarbību ar CaP. Organisko molekulu funkcionālajās grupas var būtiski ietekmēt AKF fizikālās un ķīmiskās īpašības (piemēram, morfoloģiju, daļiņu lielumu, ĪVL un patieso blīvumu).

KMR analīze apstiprināja, ka tīrs AKF satur karbonātu jonus (lādiņš –2). Acetāta lādiņš ir –1. Zinātniskajā literatūrā minēts, ka fluoru saturošs AKF uz Ap transformējas ātrāk nekā tīrs AKF, kas saistāms ar fluora jona negatīvo lādiņu [35], [36]. Acetāta negatīvais lādiņš varēja veicināt ātrāku acetātu saturošā AKF transformāciju uz Ap.

Ir zināms, ka karbonāta jonu klātbūtne AKF struktūrā kavē tā transformēšanos uz Ap [31]. Itakonāts un glutamāts satur divas karboksilāta grupas (katrai lādiņš –1), kā rezultātā to ietekme

varētu būt līdzīga kā karbonātus saturošam AKF. Tāpēc tīra, kā arī glutamātu un itakonātu saturoša AKF transformācijas ātrums uz Ap varēja būt līdzīgs.

Citrāts satur trīs karboksilāta grupas (kopējais negatīvais lādiņš –3). Tā rezultātā citrātu saturošā AKF transformācijas ātrums bija vislēnākais. Askorbāta anjona lādiņš ir –1, kas varēja palēnināt tā transformācijas ātrumu, salīdzinot ar tīru, acetātu, itakonātu un glutamātu saturošu AKF.

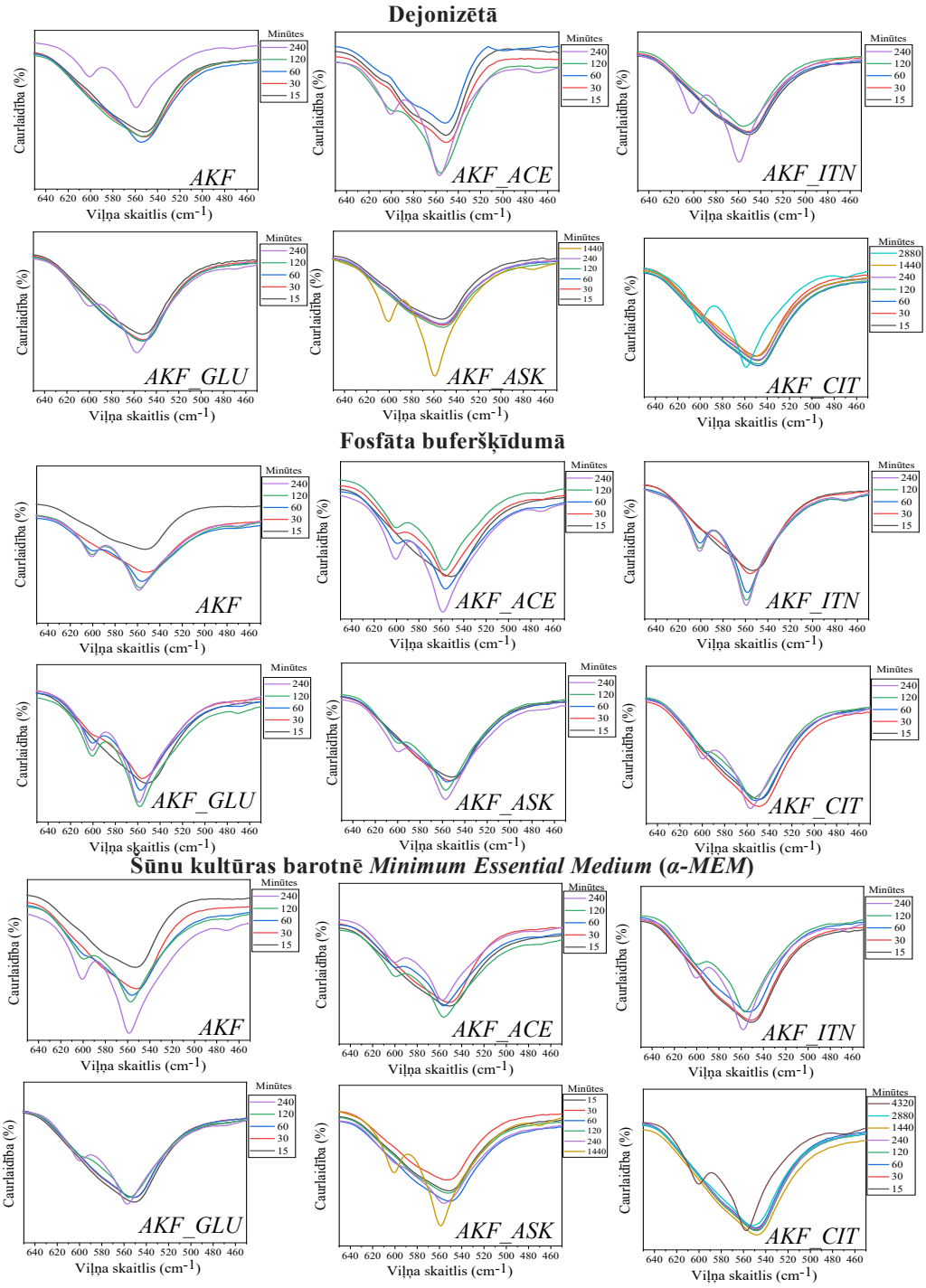

6. att. AKF transformācija uz Ap dažādās ūdens vidēs. Transformācijas kritērijs bija ν_4 PO_4^{3-} svārstību apgabals paraugu FTIS spektros. Paraugi, kuros ν_4 PO_4^{3-} svārstību apgabalā netika novērota skaidra šķelšanās, uzskatīti par amorfiem; paraugi, kuriem novērota šķelšanās ν_4 PO_4^{3-} svārstību apgabalā transformējušies uz Ap.

FBS gadījumā visi sintezētie AKF ātrāk transformējās par Ap. Zinātniskajā literatūrā minēts, ka *FBS* šķīdumā organiskie savienojumi no AKF virsmas izdalās jonu apmaiņas ar fosfātu grupām no *FBS* vides rezultātā. Tā rezultātā pieaug fosfātu koncentrācija AKF, kas samazina tā stabilitāti un izraisa straujāku transformāciju uz Ap fāzi [37]. Fosfātu saturs *α-MEM* vidē ir mazāks nekā *FBS*. Tādēļ transformācijas kinētika bija lēnāka (izņemot citrātu saturošo AKF).

Citrātus saturošais AKF *α-MEM* vidē stabilitāti saglabāja līdz 2880 minūtēm ilgi. Agrāk publicētajos pētījumos minēts, ka ap citrāta stabilizētām zelta nanodaļiņām albumīna serumā veidojas ar proteīniem bagāts slānis. Iespējams, līdzīgi, negatīvi lādētais citrāts no citrāta stabilizētajām AKF daļiņām mijiedarbojas ar fetālo liellopa serumu, kas ir *α-MEM* sastāvā, un tā rezultātā tiek aizkavēta AKF kristalizācija [38], [39].

FTIS analīzes apstiprināja, ka attiecīgo MOM funkcionālās grupas CaP struktūrā saglabājas arī pēc transformācijas. MOM saturošu Ap var iegūt, integrējot sintēzes un transformācijas kinētikas procesus.

SINTEZĒTO AKF RAKSTUROŠANA *IN VITRO*

*S*intezētā AKF raksturošana *in vitro* tika veikta ar osteoblastu prekursoru šūnām, kas iegūtas no peles (*Mus musculus*) galvaskausa (*MC3T3-E1*). Lai veiktu testus ar šūnām, tika sagatavotas AKF suspensijas, pievienojot 10 m/v % AKF daļiņu *α-MEM* videi, kas pēc tam ar ūdens tvaikiem piesātinātā atmosfērā, kas sastāvēja no 95 % gaisa un 5 % CO_2, 37 °C temperatūrā tika inkubēta 24 stundas.

Ekstrakti vispirms tika centrifugēti un pēc tam filtrēti, lai atdalītu cietās daļiņas. Pēc tam tie tika atšķaidīti ar *α-MEM*, lai iegūtu nepieciešamo koncentrāciju – 1 m/v% un 0,1 m/v %. *In vitro* pētījumiem izmantots gan neatšķaidīts ekstrakts, gan ekstraktu atšķaidījumi (1 m/v un 0,1 m/v %). Pēc tam ekstrakti tika pievienoti *MC3T3-E1* saturošām šūnu platēm, kas pēc tam tika inkubētas 48 stundas. *α-MEM* vide tika izmantota kā pozitīvā kontrole. Kā negatīvā kontrole tika izmantota *α-MEM* vide, kas saturēja 6 tilp.% dimetilsulfoksīda. Šūnu dzīvotspējas analizēšanai tika izmantots *WST-8* (*CCK-8*, *Sigma Aldrich*) komplekts.

Promocijas darba autora 4. publikācijā analizēti tīra, kā arī AKF_CIT un AKF_ACE *in vitro* testu rezultāti. Absorbcija, kas reģistrēta no šūnām, kas tika kultivētas pozitīvās kontroles vidē, tika normalizēta līdz 100 %. Šūnas, kas kultivētas ar 10 w/v % AKF_ACE ekstraktu, uzrādīja zemāko šūnu dzīvotspēju. Vislielākā šūnu dzīvotspēja tika novērota 0,1 w/v % AKF_CIT ekstraktā. Starp 10 w/v % koncentrācijas ekstraktiem visaugstāko šūnu dzīvotspēju uzrādīja AKF_CIT ekstrakts, kam sekoja tīrs AKF (AKF_CL un AKF_NIT) un AKF_ACE.

Tā kā visi AKF paraugi (7. att.) uzrādīja šūnu dzīvotspēju virs 70 %, var secināt, ka visi paraugi ir citosaderīgi. *In vitro* analīzes rezultāti liecina, ka AKF_CIT ekstraktos šūnu dzīvotspēja bija visaugstākā, kas liecina, ka šūnu dzīvotspēja pieaug, ja AKF satur citrātus.

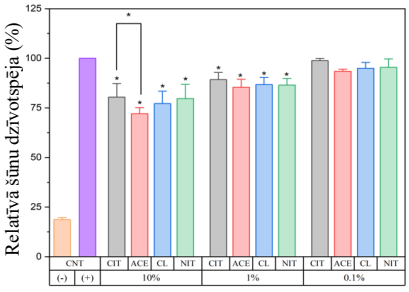

7. att. Atšķirīgu koncentrāciju (10 % m/v, 1 % m/v un 0,1 % m/v) AKF ekstraktos kultivētu *MC3T3-E1* šūnu relatīvā dzīvotspēja (n = 12, CNT – kontrole, trīs atkārtojumi, *p < 0,05). CL un NIT reprezentē tīru AKF paraugus, CIT un ACE – citrātu un acetātu saturošus AKF.

Promocijas darba autora 5. publikācijā aprakstīta *in vitro* analīze, kas veikta askorbātu, glutamātu un itakonātu saturošiem AKF. Pozitīvā un negatīvā kontrole apzīmēta attiecīgi kā CNT+ un CNT–. Iegūtie rezultāti liecināja, ka 10 % w/v AKF_GLU ekstrakts bija citotoksisks. Augsta glutamāta koncentrācija var izraisīt ekscitotoksicitāti un/vai oksidatīvu glutamāta toksicitāti [40], [41]. Tomēr, samazinot AKF_GLU ekstrakta koncentrāciju līdz 1 % w/v, šūnu dzīvotspēja pieauga.

Šūnu dzīvotspēja 10 % AKF_ITN un AKF_ASK ekstraktā bija labāka nekā 10 % AKF_GLU ekstraktā. Līdzīga tendence tika novērota arī 1 % w/v AKF_ITN un AKF_ASK ekstrakta gadījumā. Šūnu dzīvotspēja 10 % w/v un 1 % w/v AKF_ASK ekstraktā bija labāka nekā CNT+ gadījumā.

Askorbātam ir izšķiroša nozīme preosteoblastu diferenciācijā, un tas var būt iemesls lielākai šūnu dzīvotspējai [42], [43]. Kā redzams 8. attēlā, šūnu dzīvotspēja visos AKF ekstraktos (izņemot 10 % w/v AKF_GLU) bija lielāka par 70 %, tāpēc var secināt, ka visi ekstrakti ir citosaderīgi.

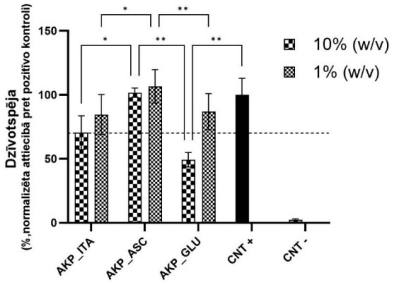

8. att. Relatīvā dzīvotspēja *MC3T3-E1* šūnām, kas kultivētas dažādu koncentrāciju AKF ekstraktos (10 % un 1 % m/v), kas iegūti *α-MEM* vidē. Visi paraugi tika analizēti trīs reizes, un dati norādīti kā vidējā vērtība un standartnovirze. CNT + un CNT – attiecīgi ir pozitīvā un negatīvā kontrole.

NANOKOMPOZĪTA BIOTINTE

Promocijas darba gaitā izstrādātā nanokompozīthidrogela biotinte, kas satur AKF, tika izstrādāta pirmo reizi. Nanokompozīthidrogela biotintes iegūšanai tika izmantots citrātu un acetātu saturošais AKF. Pētījumā analizēta izdrukāto konstrukciju strukturālā integritāte, daļiņu izmēra, kristalizācijas kinētikas un attiecīgā MOM ietekme uz biotintes īpašībām.

Promocijas darba autora 6. publikācijā aprakstīta nanokompozīthidrogela pamatņu biodrukāšana, kas tika veikta trīs posmos – pirmsdrukāšana, drukāšana un pēcdrukāšanas analīze.

Pirmsdrukāšanas posmā tika izvēlēts pamatņu dizains, materiāls un šūnas. Kopumā iegūtas divas nanokompozīta biotintes, kur alginmāta dialdehīda-želatīna (*ADA-GEL*) organiskajā matricē tika iekļauts citrātu un acetātu saturošais AKF.

GEL ir vienpavediena proteīns, kas iegūts kolagēna hidrolītiskās noārdīšanas rezultātā. Tas satur glicīnu, prolīnu un 4-hidroksiprolīna, un tam piemīt līdzīgas biomehāniskās īpašības kā kolagēnam [44]. Alginmāts ir dabīgs polimērs, kas iegūts no brūnajām jūraszālēm, kas sastāv no β-(1-4), kas saistīts ar mannouronskābi, un β-(1-4), kas saistīts ar I-glikuronskābes vienībām. Pie alginmāta nevar piesaistīties šūnas, taču to bieži izmanto kopā ar *GEL*, lai izgatavotu 3D pamatnes [45]. Alginātam nepiemīt spēja mijiedarboties ar *GEL*, tāpēc tas tika pārveidots par alginmāta dialdehīdu (*ADA*). Tā rezultātā tas nodrošināja reaktīvās grupas *GEL* šķērssaistīšanai, nodrošinot Šifa bāzes veidošanos [46].

Otrais solis bija biotinšu drukāšana. Vispirms tika veikta hidrogelu reoloģijas analīze, kā arī veikta biodrukāšanas parametru optimizācija. Amplitūdas tests ir pirmais solis hidrogelu viskoelastīgo īpašību raksturošanā [47].

Visu hidrogelu *VEA* iekļaujas 20 % no maksimālās bīdes deformācijas vērtības, kā redzams 9. A–C attēlā. Papildus visiem hidrogeliem tika veikts frekvences un tecēšanas tests pie 1 % no maksimālās bīdes deformācijas vērtības. Frekvences tests tika veikts, lai analizētu hidrogelu krājuma moduli (G') un zuduma moduli (G"), kā redzams 9. D–F attēlā.

ADA-GEL un AKF saturošā *ADA-GEL* hidrogeliem G'>G", kas ir vēlami konstrukciju biodrukāšanai. Zemākā frekvence, pie kuras tika analizētas hidrogelu G' un G" vērtības, bija 1 Hz. *ADA-GEL* hidrogelā G' un G" bija attiecīgi 99,2 ± 9,3 Pa un 9 ± 1,1 Pa. AKF_ACE saturošajam *ADA-GEL* hidrogelam G' un G" vērtības ir 134,9 ± 16,5 Pa and 6,5 ± 0,5 Pa, savukārt AKF_CIT saturošajam *ADA-GELA* hidrogelam G' un G" vērtības ir attiecīgi 142,6 ± 14,1 Pa un 7,6 ± 1,2 Pa. Visiem iegūtajiem hidrogeliem piemīt neņūtona šķidrumu īpašības (9. G att.).

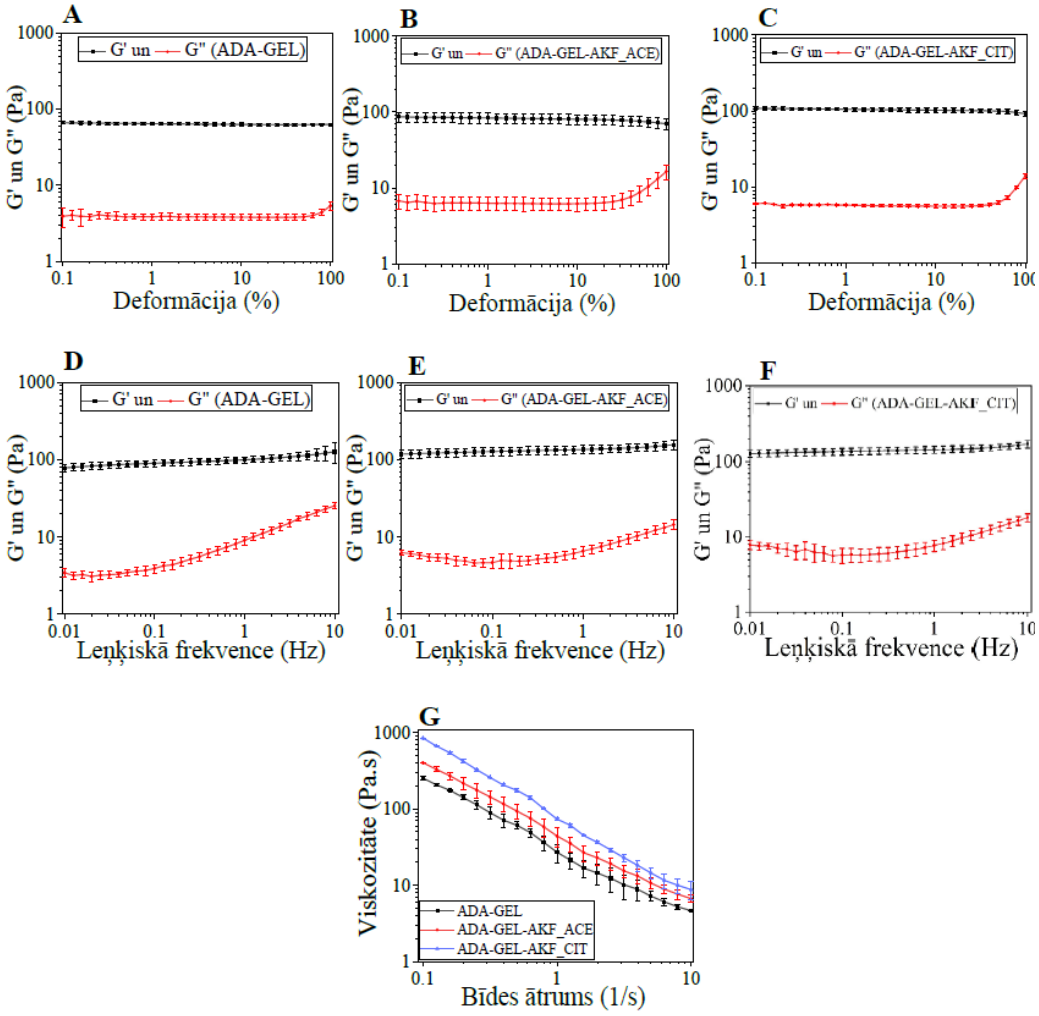

9. att. *ADA-GEL* un *AKF* saturoša *ADA-GEL* hidrogela oscilācijas testi. (A–C) amplitūdas krituma analīze tika veikta, lai novērtētu hidrogela *VEA*. (D–F) frekvenču analīze – lai raksturotu hidrogelu krājuma (G') un (G"). Rezultāti liecina, ka *AKF* pievienošana *ADA-GEL* hidrogelam uzlabo tā G' un G". (G) hidrogela plūstamības analīze veikta, attiecinot viskozitātes.

Drukāšanas parametri tika optimizēti ar izmēģinājuma un kļūdu metodi, izmantojot *ADA-GEL* hidrogelu. Lai optimizētu printēšanas spiedienu un drukāšanas ātrumu, tika izdrukāta 8 x 8 mm^2 konstrukcija – režģis. Sākotnēji drukāšana tika veikta lēnām – ar ātrumu 2 mm/s – pie mainīga spiediena. Drukāšanas ātrums tika optimizēts pēc tam, kad drukāšanas rezultātā tika iegūts nepārtraukts režģis ar viendabīgu acu izmēru, kā redzams 10. attēlā. Optimālais drukāšanas spiediens bija 65 kPa, savukārt ātrums 5 mm/s. Šie drukāšanas parametri tika izmantoti, lai izdrukātu konstrukcijas, izmantojot *ADA-GEL* un AKF saturošu *ADA-GEL* biotinti, kas pēc tam tika šķērssaistītas, izmantojot kalcija hlorīdu un bakteriālo transglutamināzi un iemērktas *α-MEM* vidē.

Trešais posms ir izdrukāto konstrukciju analīze, kuras laikā autors pārliecinājās par izdrukāto konstrukcijas stabilitāti. Drukāšanas indekss un vidējā poru laukuma analīze tika veikta, izmantojot *ImageJ* programmatūru. Agrāk publicētos pētījumos drukāšanas indekss izmantots, lai optimizētu drukāšanas parametrus. Veiktajā pētījumā drukāšanas indekss izmantots, lai raksturotu izdrukāto konstrukciju acu ģeometrijas izmaiņas kā funkciju no laika. Savukārt drukāšanas indeksa rezultāti tika korelēti ar vidējo režģa acs laukumu, kā redzams 11. attēlā.

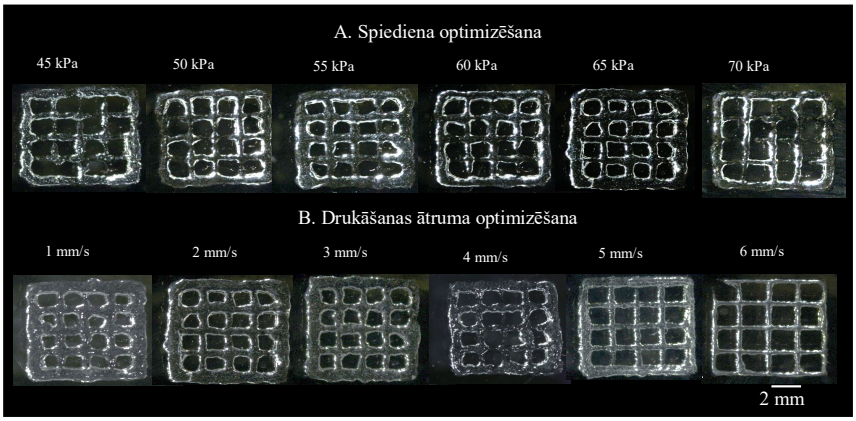

10. att. Izmēģinājuma un kļūdu metodes izmantošana drukāšanas parametru optimizācijai, izmantojot dažādas drukāšanas spiediena un ātruma kombinācijas. A) Vispirms drukāšanas spiediens tika optimizēts pie drukāšanas ātruma 2 mm/s. B) Drukāšans ātrums optimizēts pie spiediena 65 kPa.

Izdrukāto konstrukciju acu ģeometrija tika novērtēta, izmantojot drukāšanas indeksu [48]. Slēgta apgabala cirkularitāte (C) tiek definēta kā:

$$C = \frac{4\pi A}{L^2} \quad (1),$$

kur L – perimetrs, A – režģa acs laukums. Apļa formai ir vislielākā cirkularitāte – $C = 1$, savukārt kvadrāta formai cirkularitāte ir vienāda ar $\pi/4$. Zinātniskajā literatūrā aprakstītajos pētījumos biotintes drukas indekss (*Pr*) kvadrātveida formas porām ir noteikts, izmantojot šādu funkciju [49]:

$$Pr = \frac{\pi}{4}.\frac{1}{C} = \frac{L^2}{16A}. \quad (2)$$

Ideāli saželējušas režģa konstrukcijas acij ir kvadrātveida forma ar *Pr* vērtību 1. $Pr > 1$ liecina par neregulāras acs formas ģeometriju, savukārt $Pr < 1$ apraksta izliektas formas acs ģeometriju [50]. Drukāto *ADA-GEL* un AKF saturoša *ADA-GEL* konstrukciju attēli iegūti, izmantojot stereomikroskopu. Katras režģa konstrukcijas acu cirkularitāte (n = 16) tika analizēta, izmantojot *Image-J* programmatūru, pēc tam aprēķinot *Pr* vērtību [51]. Dati uzrādīti kā vidējā *Pr* vērtība ar standartnovirzi.

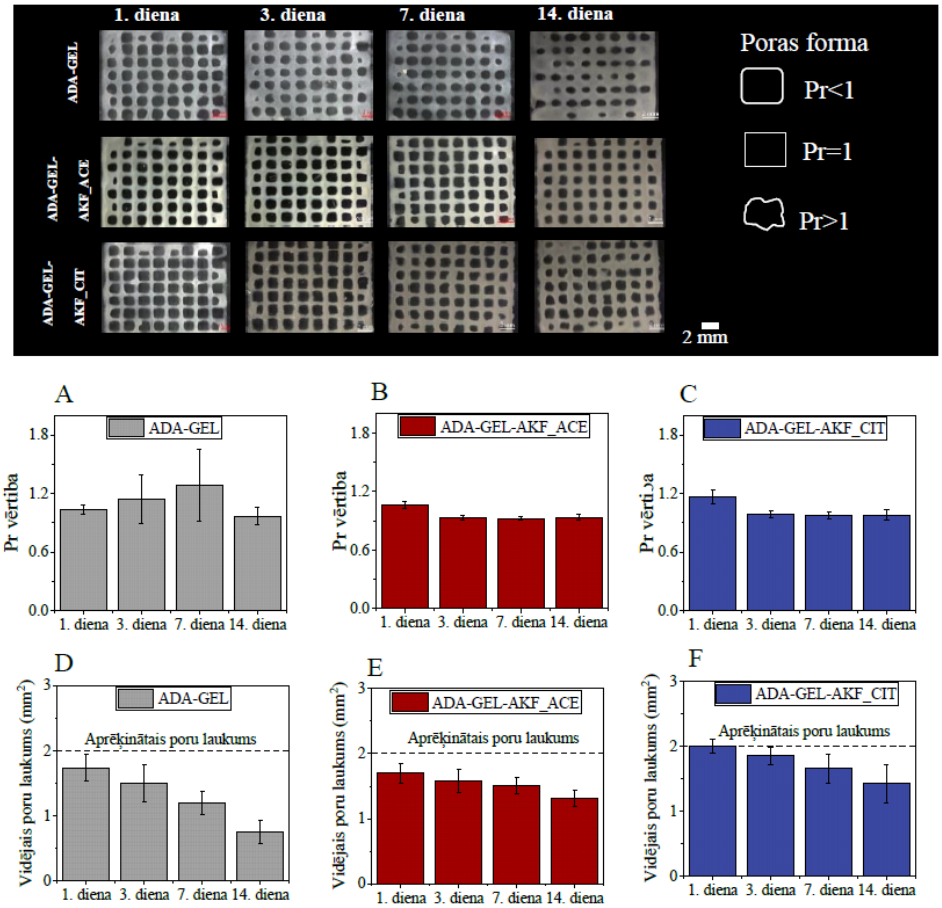

11. att. *ADA-GELA* un AKF saturošas *ADA-GEL* biotintes drukāto konstrukciju pēcdrukas analīze (*ADA-GEL, ADA-GEL*-AKF_*ACE* un *ADA-GEL*-AKF_CIT). Stereomikroskopijas attēlu analīze tika veikta 1., 3., 7. un 14. dienā (mērogs 2 mm). Drukas indekss (*Pr*) un vidējā poru laukuma analīze tika veikta, izmantojot attēlu analīzi programmatūru, atlasot 16 poras. Poru ģeometrija tika novērtēta, analizējot *Pr* vērtību; piemēram, *Pr* < 1 attēlo izliektu, *Pr* = 1 atbilst kvadrātveida, *Pr* > 1 neregulāru iporu ģeometriju. (A–C) demonstrē *Pr* vērtības, (D–F) parāda vidējo biotintes poru laukumu. *ADA-GEL* biotintes uzrāda straujas konformācijas izmaiņas poru ģeometrijā un biotintes vidējā poru laukuma samazināšanos, liecinot par zemu strukturālo stabilitāti, salīdzinot ar AKF saturošajām *ADA-GEL* biotintēm.

AKF_ CIT pievienošana nodrošināja labāku izdrukātās konstrukcijas strukturālo integritāti nekā AKF_ACE pievienošana, kas, iespējams, saistīts ar atšķirīgo kalcija un fosfātu jonu izdalīšanās kinētiku no AKF_CIT un AKF_ACE (12. att.). Jonu izdalīšanās eksperimenti tika veikti 168 stundas (septiņas dienas), lai analizētu kalcija un fosfāta jonu izdalīšanos. Sākotnēji, pirmo stundu laikā, tika novērota strauja kalcija un fosfātu jonu izdalīšanās, kas pēc tam pakāpeniski samazinājās [52], [53]. AKF_CIT uzrādīja augstāku izdalīto jonu koncentrācija. AKF_ACE izdalītais kalcija un fosfātu jonu daudzums bija salīdzinoši neliels – robežās no 1 mM līdz 1,5 mM.

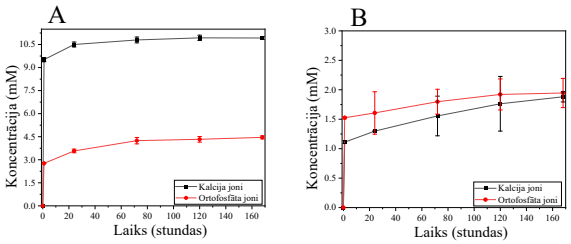

12. att. Fosfātu un kalcija jonu izdalīšanās kinētika. (A) Citrātu saturošs AKF; (B) acetātu saturošs AKF.

Arī AKF daļiņu izmēram var būt būtiska nozīme izdrukātās konstrukcijas strukturālās integritātes nodrošināšanā. AKF_ACE daļiņu izmērs ir mazāks (~ 20 nm) nekā AKF_CIT (~ 40 nm) (detalizētāka informācija atrodama promocijas darba autora 4. publikācijā). Mazāks daļiņu izmērs nodrošina lielāku virsmas laukumu un, attiecīgi, lielāku tendenci daļiņām aglomerēties, kas var negatīvi ietekmēt izdrukātās konstrukcijas strukturālo integritāti [54].

Brīvā citrāta karboksilgrupa potenciāli var reaģēt ar želatīna amīnu grupu, nodrošinot amīda saites veidošanos. Gan *ADA*, gan *GEL* var šķērssaistīt ar citrātu saturošu AKF [55]. Precīzai šķērssaistīšanās mehānisma noteikšanai būtu nepieciešams veikt papildu analīzes.

Izdrukāto konstrukciju raksturošana *in vitro* tika veikta, izmantojot iekrāsošanu ar rodamīna falloidīnu un *DAPI*. 13. attēlā redzams šūnu piesaistīšanās izdrukātajai konstrukcijai pirmajā dienā, kam seko šūnu pagarināšanās, saplūšana un tīklojuma veidošanās nākamo dienu laikā. Konstrukciju virsmu 14. dienā klāja šūnas, kas apstiprina izveidotās nanokomozīta biotintes citosaderību.

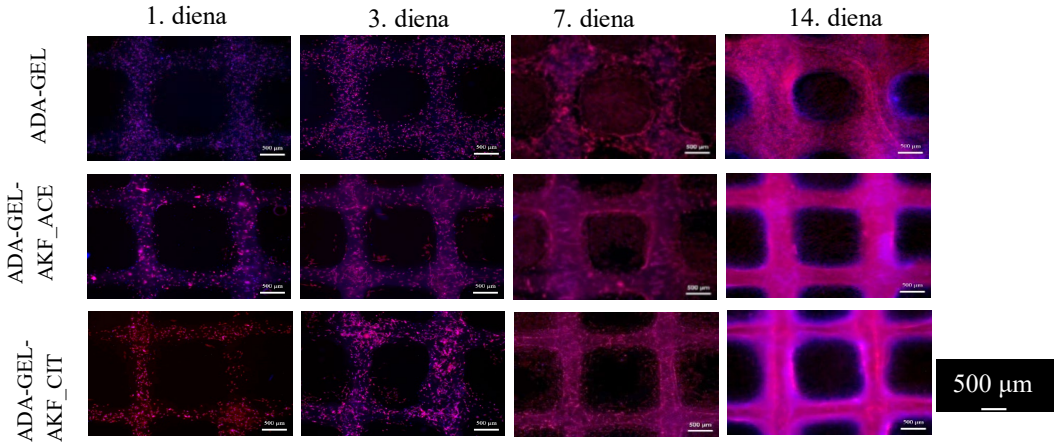

13. att. Epifluorescences mikroskopija rodamīna-faloidīna (sarkanā krāsā) un *DAPI* (zilā krāsā) iekrāsotām *MC3T3-E1* šūnām, kas iekļautas *ADA-GEL* un AKF saturoša *ADA-GEL* konstrukcijās (*ADA-GEL*-AKF_ACE un *ADA-GEL*-AKF_ACE). Mērogs 500 µm.

Lai raksturotu šūnu izplatīšanos izdrukāto konstrukciju tilpumā, izmantota divfotonu mikroskopija. Iegūto divfotonu mikroskopijas attēlu grupu 3D rekonstrukcijas redzamas 14. attēlā. Attēlos redzams, ka šūnu populācija ar laiku pakāpeniski pieaug, apstiprinot rezultātus, kas iegūti ar epifluorescences mikroskopiju.

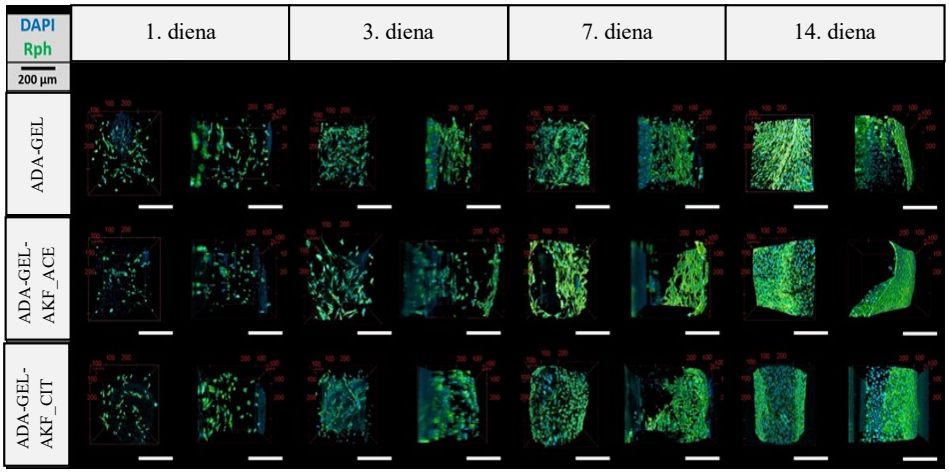

14. att. Trīsdimensionāli rekonstruēti daudzfotonu mikroskopijas attēli kvalitatīvai morfometrijas un šūnu sadalījuma analīzei.

NANOKOMPOZĪTU HIDROGELI

Promocijas darba autora 7. publikācijā aprakstīts nanokompozīthidrogels, kura matricu veido *GELMA*, savukārt pildviela ir AKF. *GELMA* ir pateicīgs materiāls audu inženierijai, ņemot vērā tā biosaderību, bioloģisko noārdīšanos, bioaktivitāti un unikālās šķērssaistīšanās īpašības, kas lietojamas nanokompozītuhidrogelu izgatavošanai [56].

Izplatītākā metode *GELMA* hidrogelu šķērssaistīsanai ir fotošķērssaistīšana, kur tiek izmantota ultravioletā (UV) gaisma un fotoiniciators . *GELMA* šķīdums satur fotoiniciatoru, kas tiek pakļauts UV gaismas iedarbībai. Fotoiniciators absorbē UV gaismu un fotolīzes reakcijas rezultātā ģenerē brīvos radikāļus. Brīvie radikāļi reaģē ar *GELMA* esošajām metakriloila grupām, izraisot radikāļu veidošanos uz *GELMA* molekulām. Radikāļi blakus esošajās *GELMA* molekulās sāk ķēdes reakciju, veidojot kovalentās saites starp metakriloila grupām. Līdzīgā veidā redoksa sistēma izmanto ķīmisko iniciatoru amonija persulfātu (APS) un n,n,n′,n′-tetra metiletilēnadiamīnu (*TEMED*).

Fotošķērssaistīšanai ir trūkumi, piemēram, lēna želēšana un sarežģīts sagatavošanas process [57]. Fotošķērssaistīšanas efektivitāti var būtiski samazināt pildvielas, kas hidrogelu padara necaurspīdīgu, proti, pasliktina tā gaismas caurlaidību, kas traucē fotopolimerizācijas reakcijas procesu un šķērssaistīšanas dziļumu [58]. AKF pievienošanas rezultātā hidrogels kļūst necaurspīdīgs (15. B att.), kas apgrūtina *GELMA* fotošķērsaistīšanas procesu. Lai izstrādātu AKF_CIT saturošus *GELMA* hidrogelus, tika izmantota redoksa ierosināta ķīmiskā šķērssaistīšana, izmantojot APS/*TEMED* [59]. Izgatavotie hidrogeli redzami 15. attēlā. AKF_CIT pievienošana minimāli ietekmēja *GELMA* hidrogela viskoelastiskās īpašības.

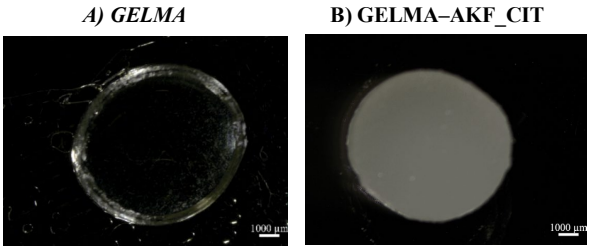

15. att. Iegūtie *GELMA* un *GELMA*-KF_CIT hidrogeli (mērogs 1000 µm).

Amplitūdas testa rezultāti redzami 16. (A–C) attēlā. Hidrogela *VEA* tika analizēts, izmantojot amplitūdas testu apgabalā, kas ir mazāks par 10 % no maksimālās bīdes deformācijas vērtības. Papildu analīze tika veikta zem 1 % no maksimālās bīdes deformācijas vērtības. Nešķērssaistītas *GELMA* krājuma (G") un zuduma modulis (G') bija ļoti zems (mazāks par 0,1 Pa) ar krustošanās punktu (G" = G') 501 %, kas liecina par tās spēju izturēt bīdes spēku izraisītu neatgriezenisku deformāciju. Pēc šķērssaistīšanas *GELMA* hidrogela G' un G" pieauga, savukārt krustošanās punkts samazinājās līdz 125,8 %. AKF_CIT pievienošana *GELMA* hidrogelam uzlaboja moduli, paaugstinot krustošanās punktu līdz 158,4 %, un tā rezultātā uzlabojās hidrogela spēja izturēt bīdes spēku izraisītu neatgriezenisku deformāciju.
Lai novērtētu iegūto hidrogelu viskoelastīgās īpašības, tiem tika veikts frekvences tests (16. (D–F) att.). Hidrogelu G' un G'' tika noteikti pie frekvences 1 Hz (16. A att.). Nešķērssaistītai *GELMA* G' un G" vērtības ir ļoti zemas (attiecīgi, 0,12 Pa un G" 0,016 Pa), kas raksturīgas mehāniski neizturīgam un viegli deformējamam materiālam. Pēc šķērssaistīšanas tās tika uzlabotas, G' sasniedzot 82,6 ± 13 Pa, savukārt G" 2,28 ± 0,5 Pa. Pievienojot AKF_CIT, *GELMA* krājuma un zuduma moduļa vērtības palielinājās, G' sasniedzot 318,8 ± 6,5 Pa, savukārt G" 11,3 ± 0,23 Pa.

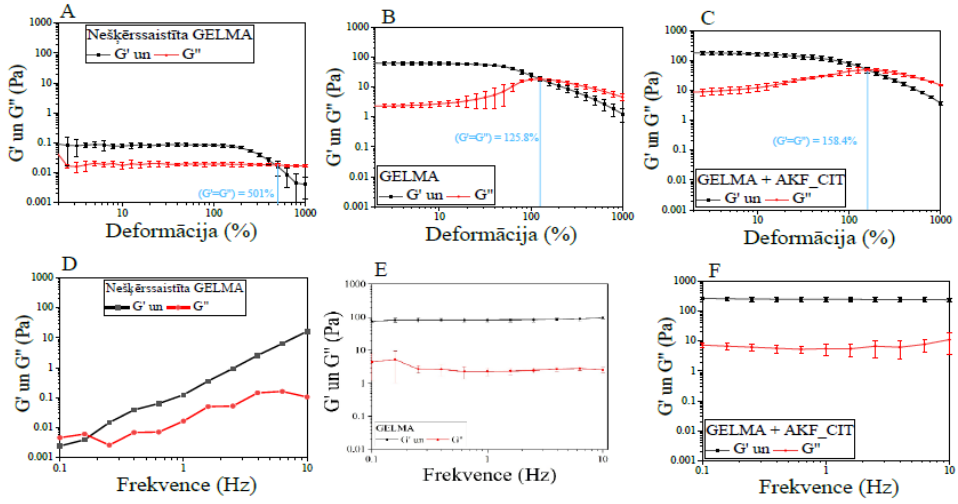

16. att. Hidrogelu viskoelastīgās īpašības tika analizētas, izmantojot oscilācijas testu: (A–C) hidrogela *VEA* tika analizēts ar amplitūdas testu; (D–E) hidrogelu krājuma un zuduma moduļi raksturoti ar frekvences testu.

Izstrādātie VT hidrogeli tika raksturoti *in vitro*, izmantojot iekrāsošanu ar rodamīna falloidīnu un 4′,6-diamidino-2-fenilindolu un *DAPI* (17. att.). Šūnu piesaistīšanās hidrogeliem tika novērota pirmajā dienā. Septītajai dienā šūnas bija vienmērīgi izkliedētas pa visu hidrogelu, apliecinot APS/*TEMED* šķērssaistīšanas paņēmiena citosaderību. Turklāt netika novērota negatīva AKF_CIT ietekme uz *MC3T3-E1* šūnu proliferācijas procesu.

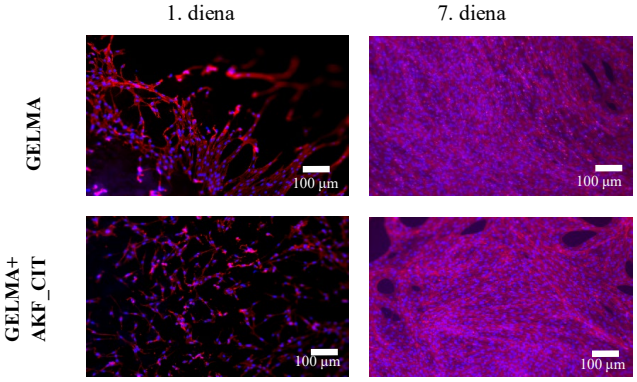

17. att. Epifluorescences mikroskopija rodamīna-faloidīna (sarkanā krāsā) un *DAPI* (zilā krāsā) iekrāsotām *MC3T3-E1* šūnām, kas iekļautas *GELMA* un *GELMA*-AKF_CIT hidrogelos.

DUBULTTĪKLA NANOKOMPOZĪTHIDROGELI

Promocijas darba autora 8. publikācijā aprakstīts dubulttīkla nanokompozīthidrogels (*DTKH*), kurā AKF_CIT iekļauts *P123*-PAM-*GELMA* matricē. Pirmais dubulttīkla hidrogela tīkls tika izveidots, izmantojot *P123*. Otrais tīkls sastāv no PAM un *GELMA* kopolimēriem. Otrā tīkla šķērssaistīšana tika veikta, izmantojot APS un *TEMED* (18. att.).

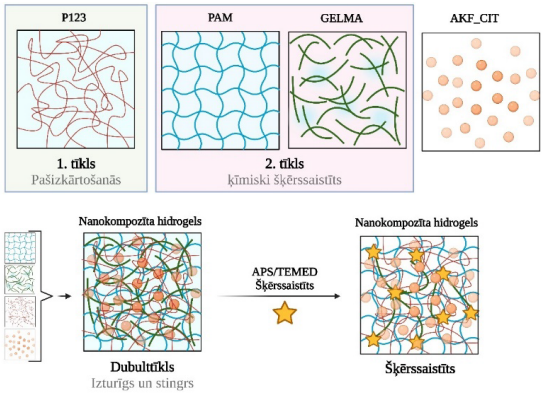

18. att. DT hidrogela iegūšana, izmantojot fizikālo un ķīmisko šķērssaistīšanu. Primāro tīklu veidoja *Pluronic P123*, savukārt sekundāro tīklu – kopolimēra sistēma, kas sastāv no poliakrilamīda-želatīna metakrilāta (PAM-*GELMA*). AKF_CIT izmantota kā neorganiskā pildviela hidrogelā.

Sagatavojot DT nanokompozītu hidrogelus, tika izmantota sistemātiska pieeja; sākotnēji tika pētīta dažādu *P123* (2,5 %, 5 %, 7,5 % un 10 %) koncentrāciju ietekme uz PAM-*GELMA*

mehāniskajām īpašībām (elastības moduli, stiepes stiprību, pagarinājumu stiepē). Starp tiem DT hidrogelam ar 7,5 w/v % *P123* koncentrāciju PAM-*GELMA* bija vislabākās mehāniskās īpašības, tādēļ tas tika izmantots arī nanokompozīta DT hidrogelu izstrādē, hidrogelā iekļaujot dažādas AKF_CIT koncentrācijas (0,75 %, 1,5 % un 3 %).

AKF_CIT saturošais DT hidrogels ar 0,75 w/v% AKF_CIT koncentrāciju (saīsināti DT3-AFK0,75) uzrādīja visaugstvērtīgākās mehāniskās īpašības (19. att.). Šim kompozītam papildus tika izvērtētas reoloģiskās īpašības un citosaderība un salīdzināta ar tīra DT hidrogela (7,5 w/v% *P123*-PAM-*GELMA*, saīsināti DT3) īpašībām.

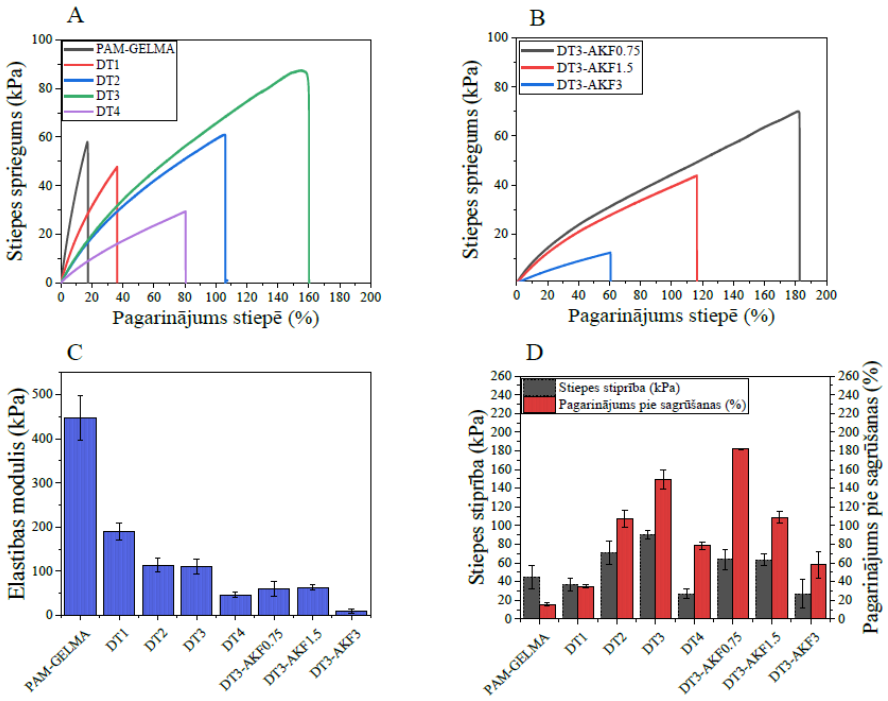

19. att. Iegūto hidrogelu stiepes sprieguma-deformācijas līkne. (A) *P123* koncentrācijas ietekme uz PAM-*GELMA* hidrogela pagarinājumu stiepē. (B) AKF_CIT koncentrācijas ietekme uz DT3 hidrogela pagarinājumu stiepē. (C) Elastības modulis, (D) stiepes izturība un pagarinājums sagraušanas brīdī (%) visiem iegūtajiem hidrogeliem.

Visu sintezēto hidrogelu reoloģijas testi parādīja, ka to G'> G", kas liecina par gelam raksturīgajām īpašībām. Lai novērtētu iegūto hidrogelu viskoelastīgās īpašības, papildus tika veikts frekvences tests (20. A att.). Hidrogelu G' un G" tika analizēts pie frekvences 1 Hz (20. A att.). *P123* ir ļoti zemas G' un G" vērtības (attiecīgi, 1112,3 ± 28,5 Pa), kas atbilst mehāniski neizturīga, mīksta materiāla īpašībām. Savukārt PAM-*GELMA* hidrogelam ir augstas G' un G" vērtības (attiecīgi, 10916,6 ± 625,3 Pa un 4058,6 ± 213,8 Pa), kas atbilst augstai stiprībai un trauslumam. Palielinot PAM-*GELMA* hidrogela *P123* saturu, G' vērtība tika ietekmēta mazāk nekā G" vērtība. G" samazinājums nozīmē, ka deformācijas laikā tiek izkliedēts mazāks enerģijas daudzums, kas liecina, ka hidrogels vairāk izturas elastīgi nekā viskozi. Tādējādi, palielinoties *P123* koncentrācijai, atšķirība starp G' un G" vērtībām liecina par elastības palielināšanos [60]. Šī parādība tika novērota līdz *P123* koncentrācijai 7,5 w/v % PAM-*GELMA*

hidrogelā (DT3). Turpinot palielināt *P123* koncentrāciju līdz 10 w/v % (*DT4*), G' samazināšanās izraisīja G" palielināšanos, ietekmējot hidrogela elastību.

DT3 hidrogeliem ar zemāku AKF_CIT koncentrāciju (0,75 w/v%) G′ vērtība sasniedza 9141 ± 2545 Pa, savukārt G″ 341,3 ± 134,8 Pa. AKF_CIT iekļaušana (0,75 w/v%) samazina G' un G" vērtības, tomēr G' vērtības kritums ir neliels, salīdzinot ar G" vērtības samazināšanos, kas varēja veicināt tā elastīgo īpašību uzlabošanos. AKF_CIT koncentrācijai DT3 hidrogelos pieaugot līdz 1,5 %, G' un G" vērtība būtiski palielinājās (attiecīgi, 17766,6 ± 2689,4 Pa un 1034,9 ± 290,2 Pa), kas uzlaboja hidrogela stingrību. Palielinot AKF_CIT koncentrāciju līdz 3 w/v% G' un G" vērtības dramatiski pieauga (attiecīgi, uz 22523,3 ± 6950 Pa un1422,6 ± 47,6 Pa), kas varēja izraisīt kompozīta mehānisko īpašību pasliktināšanos [61], [62].

Visu sintezēto hidrogelu tan δ analīze redzama 20. C attēlā. Tan δ ir viskoelastīga materiāla G' un G" attiecība, ko bieži izmanto materiāla slāpēšanas īpašību raksturošanai. Tā kvantificē enerģijas daudzumu, kas izkliedēts siltuma veidā. Viskoelastīga materiāla lielāka tan δ vērtība (tuvāka 1) liecina par lielāku enerģijas daļu, kas izkliedēta siltuma veidā, attiecībā pret elastības enerģiju. No otras puses, mazāka tan δ vērtība liecina, ka vairāk saglabāta elastības enerģija, salīdzinot ar enerģiju, kas zaudēta siltuma veidā [47].

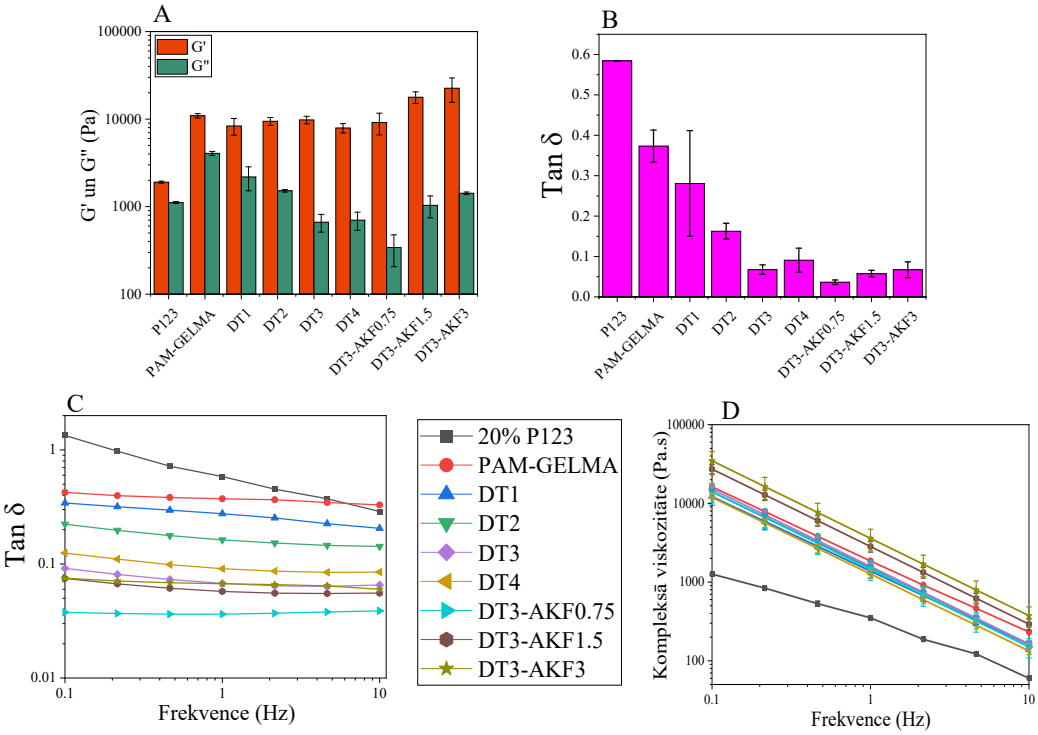

20. att. A) Krājuma (G') un zuduma moduļa (G") analīze pie 1 Hz frekvences. B) Tan δ analīze pie 1 Hz frekvences. C) Visu sintezēto hidrogelu tan δ analīze dažādās frekvencēs. D) Kompleksās viskozitātes analīze.

PAM-*GELMA* hidrogela tan δ vērtība bija 0,37 ± 0,03, analizējot pie 1 Hz frekvences (20. D att.). Palielinoties *P123* koncentrācijai PAM-*GELMA* hidrogelos, tan δ vērtības pieaug

uz attiecīgi 0,28 ± 0,13 DT1, 0,16 ± 0,01 DT2, 0,067 ± 0,01 DT3 un 0,09 ± 0,02 DT4 hidrogelam. Šī analīze liecināja, ka tan δ vērtības samazinājās, līdz *P123* koncentrācija bija 7,5 w/v% PAM-*GELMA* (DT3), ko var attiecināt uz palielinātu elastību [63]. Ja *P123* koncentrācija tika palielināta līdz 10 w/v% PAM-*GELMA* (DT4), slāpēšanas vērtība palielinājās, samazinot elastību.

Nanokompozīthidrogelos tan δ vērtības bija 0,036 ± 0,05 DT3-AKF0.75, 0,057 ± 0,008 DT3-AKF1.5 un 0,067 ± 0,02 (DT3-AKF3). DT3-AKF0.75 tan δ vērtība bija viszemākā, ko var attiecināt uz visaugstāko elastību. Palielinot AKF_CIT koncentrāciju DT3 hidrogelos līdz 1,5 m/v % (DT3-AKF1.5) un 3 m/v % (DT3-AKF3), palielinās tan δ vērtība, ko var attiecināt uz slāpēšanas īpašību samazināšanos. Palielinoties AKF_CIT koncentrācijai, sāk pieaugt tan δ vērtība, kas var ietekmēt šķērssaistīšanās blīvumu un polimēru ķēžu mobilitāti hidrogelā, tādējādi ietekmējot hidrogela kopējās mehāniskās īpašības.

Visu sintezēto hidrogelu kompleksā viskozitāte samazinājās, palielinoties frekvencei. Kompleksas viskozitātes variācijas tika novērotas pie dažādām *P123* un AKF_CIT koncentrācijām PAM-*GELMA* hidrogelā [64]. Kā redzams 20. D attēlā, *P123* koncentrācijas palielināšanās PAM-*GELMA* hidrogelā izraisa ievērojamu kompleksās viskozitātes samazināšanos.

Stiepes testu rezultāti korelē ar oscilācijas bīdes testiem, kas liecina par to, ka *P123* uzlabo PAM-*GELMA* hidrogelu elastību un mehāniskās īpašības. Tomēr *P123* ietekme ir atkarīga no koncentrācijas. Arī AKF_CIT ietekme uz hidrogela īpašībām ir atkarīga no tā koncentrācijas hidrogelā. Pie noteiktas AKF_CIT koncentrācijas novērotā hidrogela elastības pastiprināšanās varētu būt saistīta ar AKF_CIT esošā citrāta pseidošķērssaistīšanos ar *GELMA*. Tomēr, lai apstiprinātu citrāta-*GELMA* mijiedarbību, ir nepieciešamas izvērstākas analīzes. DT3 un nanokompozītmateriāla DT3-AKF0.75 hidrogelam ir augstvērtīgākās mehāniskās īpašības. Tāpēc šiem diviem hidrogeliem tika veiktas papildu analīzes.

Materiāla plūstamības (*creep*) un atjaunošanās īpašības palīdz izprast viskoelastīga materiāla polimēru ķēžu mijiedarbību, kas savukārt palīdz analizēt hidrogela deformācijas mehānismu. Lai novērtētu DT3 hidrogela un DT3-AKF0.75 nanokompozīta polimēru ķēžu mijiedarbības izmaiņas, tika veikta to plūstamības un atjaunošanās analīze (21. A att.). AKF_CIT iekļaušanai DT3 hidrogelā (DT3-AKF0.75) ir pozitīva ietekme uz plūstamības sprieguma samazināšanu. Tas var būt saistīts ar polimēru ķēžu kustīguma samazināšanos AKF_CIT nanodaļiņu pievienošanas rezultātā [65]. Sprieguma relaksācijas līknes redzamas 21. B attēlā. DT3 hidrogelam un DT3-AKF0.75 nanokompozītam raksturīga strauja sprieguma relaksēšana.

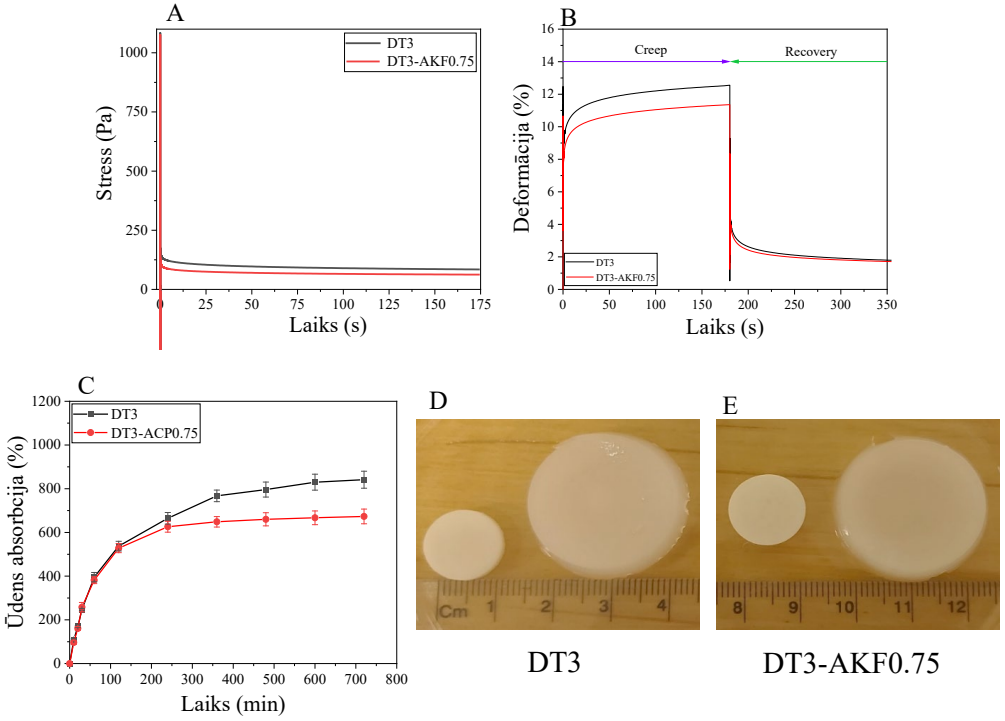

21. att. Šļūdes-atjaunošanās analīze (A), sprieguma relaksācija (B), uzbriešanas spēja C), kā arī žāvētu un uzbriedušu DT3 un DT3-AKF0.75 hidrogelu fotogrāfijas (D un E).

DT3 hidrogela un DT3-AKF0.75 uzbriešanas spēja redzama 21. C attēlā. Gan DT3, gan DT3-AKF0.75 izmērs uzbriešanas rezultātā pieaug divas reizes (21. D un E att.). AKF_CIT pievienošana DT3 hidrogelam ietekmē uzbriešanas kinētiku. DT3-AKF0.75 hidrogelu uzbriešanas spējas samazināšanos var izraisīt tas, ka brīvās polimēru ķēdes kustīgumu kavē AKF_CIT klātbūtne [66].

Formas atmiņas hidrogeliem ir divu veidu šķērssaites. Pirmais tīkls ir kovalenti šķērssaistīts, kas ir būtiski hidrogela struktūras integritātes saglabāšanai. Otrais tīkls ir atgriezeniski fizikāli šķērssaistīts un atbild par pagaidu formas fiksēšanu. Pētītais hidrogels PAM-*GELMA* veido kovalenti šķērssaistītu tīklu [67]. Termojutīgais *P123* augstā temperatūrā (70 °C) veido atgriezeniski šķērssaistītu tīklu, ierosinot formas maiņu, ja hidrogels tiek pakļauts 4 °C temperatūrai, tādējādi nodrošinot formas atmiņu un formas atjaunošanās īpašības, kā redzams 22. attēlā.

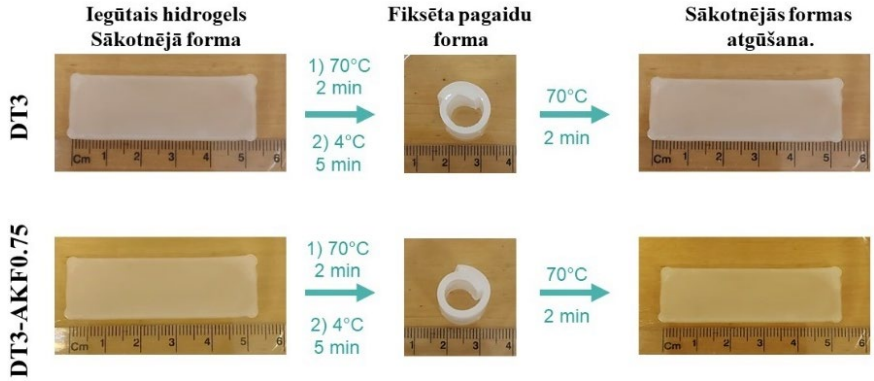

22. att. Temperatūras izraisīts DT3 un DT3-AKF0.75 hidrogelu formas atmiņas efekts

Iegūtā hidrogela un nanokopozīta *in vitro* analīze veikta, izmantojot iekrāsošanu ar rodamīna faloidīnu un *DAPI* (23. att.). Šūnu piesaiste hidrogelam un nanokompozītam tika novērota pirmajā dienā. Trešajā dienā šūnas bija vienmērīgi izplatījās gan pa hidrogelu, gan nanokompozītu. Gan hidrogels, gan nanokompozīts septītajā dienā bija blīvi noklāts ar šūnām, apliecinot iegūtā DT3 un DT3-AKF0.75 citosaderību.

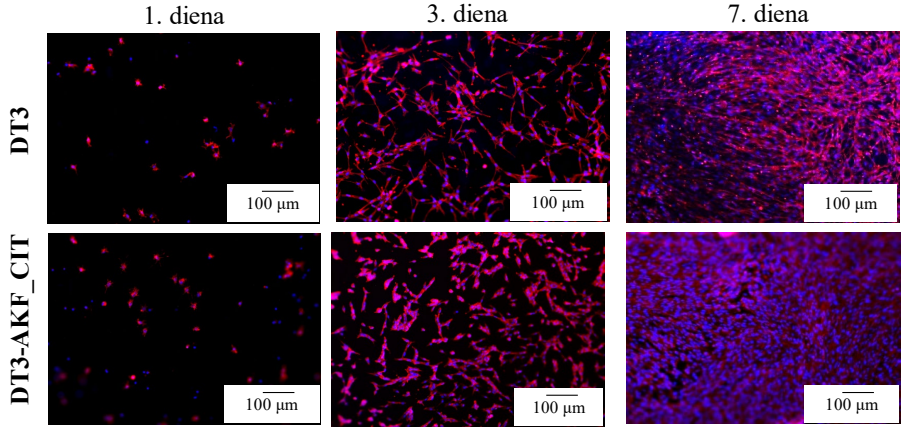

23. att. Epifluorescences mikroskopija rodamīna-faloidīna (sarkanā krāsā) un *DAPI* (zilā krāsā) iekrāsotām *MC3T3-E1* šūnām, kas iekļautas DT3 un NC1DT3 hidrogelos.

SECINĀJUMI

1. Negatīvā lādiņa atšķirības MOM sānu grupās ietekmē MOM mijiedarbību ar AKF, ietekmējot AKF īpašības.

2. Šķīduma mediētas AKF transformācijas kinētiku uz Ap ietekmē šķīduma vides sastāvs. Neskatoties uz to, MOM saturošu AKF transformācijas uz Ap secība dažādu šķīdumu vidēs nemainās: AKF_ACE > > *tīrs* AKF = AKF_ITN = AKF_GLU > > AKF_ASK > AKF_CIT. *FBS* vidē visi sintezētie AKF ātrāk transformējās uz Ap, salīdzinot ar dejonizēta ūdens vidi. *FBS* esošie fosfātu joni nodrošina papildu vietas kalcija jonu saistīšanai, paātrinot AKF transformāciju uz Ap. Transformācija *α-MEM* vidē ir lēnāka nekā *FBS*, kas saistāma ar tā salīdzinoši zemo fosfātu jonu koncentrāciju.

3. Citrātu un acetātu saturoša AKF pievienošana (1 %) *ADA-GEL* hidrogelam palielina gan tā krājuma, gan zuduma moduli (AKF_CIT saturošam *ADA-GEL* G'= 142,6 ± 14,1 Pa un G" = 7,6 ± 1,2 Pa, AKF_ACE saturošam *ADA-GEL* G' = 134,9 ± 16,5 Pa un G" = 6,5 ± 0,5 Pa, savukārt *ADA-GEL* hidrogelam G'= 99,2 ± 9,3 Pa un G" = 9 ± 1,1 Pa). Palielinātais krājuma un zuduma modulis uzlabo izdrukāto konstrukciju strukturālo integritāti. Šis uzlabojums saistāms ar papildu kalcija joniem, ko AKF nodrošina *ADA* šķērssaistīšanai.

4. *GELMA* hidrogela krājuma G' un zuduma G" moduļu vērtības (attiecīgi, 82,6 ± 13 Pa un 2,28 ± 0,5 Pa) var būtiski uzlabot, hidrogelam pievienojot 2 % citrātu saturoša AKF. Tā rezultātā *GELMA* hidrogela G' sasniedza 318,8 ± 6,5 Pa, savukārt G" 11,3 ± 0,23 Pa.

5. AKF_CIT ietekme uz DT3 hidrogela mehāniskajām īpašībām ir atkarīga no tā koncentrācijas hidrogelā. Pievienojot 0,75 w/v % AKF_CIT, tiek palielināta DT3 hidrogela elastība, kas saistāms ar polimēru ķēžu mijiedarbības samazināšanos AKF_CIT ietekmes rezultātā. Pieaugot AKF_CIT koncentrācijai, G' un G" vērtības būtiski palielinās, padarot hidrogelu stingrāku un ietekmējot tā mehāniskās īpašības.

IZMANTOTĀ LITERATŪRA

[1] J. M. Grasman, M. J. Zayas, R. L. Page, and G. D. Pins, "Biomimetic Scaffolds for Regeneration of Volumetric Muscle Loss in Skeletal Muscle Injuries," *Acta Biomater.*, vol. 25, p. 2, Oct. 2015, doi: 10.1016/J.ACTBIO.2015.07.038.

[2] "Musculoskeletal health." Accessed: Dec. 13, 2023. [Online]. Available: https://www.who.int/news-room/fact-sheets/detail/musculoskeletal-conditions

[3] A. R. Amini, C. T. Laurencin, and S. P. Nukavarapu, "Bone Tissue Engineering: Recent Advances and Challenges," *Crit. Rev. Biomed. Eng.*, vol. 40, no. 5, p. 363, 2012, doi: 10.1615/CRITREVBIOMEDENG.V40.I5.10.

[4] A. H. Schmidt, "Autologous bone graft: Is it still the gold standard?," *Injury*, vol. 52, pp. S18–S22, Jun. 2021, doi: 10.1016/J.INJURY.2021.01.043.

[5] O. Petrauskaite *et al.*, "Biomimetic mineralization on a macroporous cellulose-based matrix for bone regeneration," *Biomed Res. Int.*, vol. 2013, 2013, doi: 10.1155/2013/452750.

[6] A. L. Lehninger, "Mitochondria and Calcium Ion Transport THE FIFTH JUBILEE LECTURE," *Biochem. J.*, vol. 119, no. 2, pp. 129–138, 1970.

[7] J. H. Bradt, M. Mertig, A. Teresiak, and W. Pompe, "Biomimetic Mineralization of Collagen by Combined Fibril Assembly and Calcium Phosphate Formation," *Chem. Mater.*, vol. 11, no. 10, pp. 2694–2701, 1999, doi: 10.1021/CM991002P.

[8] A. G. Walton, B. A. Friedman, and A. Schwartz, "Nucleation and mineralization of organic matrices," *J. Biomed. Mater. Res.*, vol. 1, no. 3, pp. 337–354, Sep. 1967, doi: 10.1002/JBM.820010305.

[9] "Biomedical Applications of Inorganic Materials," *Biomed. Appl. Inorg. Mater.*, Dec. 2021, doi: 10.1039/9781788019293.

[10] C. Drouet, "Apatite formation: Why it may not work as planned, and how to conclusively identify apatite compounds," *Biomed Res. Int.*, vol. 2013, 2013, doi: 10.1155/2013/490946.

[11] A. Indurkar, R. Choudhary, K. Rubenis, and J. Locs, "Advances in Sintering Techniques for Calcium Phosphates Ceramics," *Mater. 2021, Vol. 14, Page 6133*, vol. 14, no. 20, p. 6133, Oct. 2021, doi: 10.3390/MA14206133.

[12] H. C. W. Skinner and H. Ehrlich, "Biomineralization," *Treatise Geochemistry Second Ed.*, vol. 10, pp. 105–162, Jan. 2014, doi: 10.1016/B978-0-08-095975-7.00804-4.

[13] I. Cacciotti, "Cationic and anionic substitutions in hydroxyapatite," *Handb. Bioceram. Biocomposites*, pp. 145–211, Jan. 2016, doi: 10.1007/978-3-319-12460-5_7/FIGURES/6.

[14] A. Lotsari, A. K. Rajasekharan, M. Halvarsson, and M. Andersson, "Transformation of amorphous calcium phosphate to bone-like apatite," *Nat. Commun. 2018 91*, vol. 9, no. 1, pp. 1–11, Oct. 2018, doi: 10.1038/s41467-018-06570-x.

[15] A. Indurkar, R. Choudhary, K. Rubenis, and J. Locs, "Role of carboxylic organic molecules in interfibrillar collagen mineralization," *Front. Bioeng. Biotechnol.*, vol. 11, p. 439, Apr. 2023, doi: 10.3389/FBIOE.2023.1150037.

[16] W. J. Landis, F. H. Silver, and J. W. Freeman, "Collagen as a scaffold for biomimetic mineralization of vertebrate tissues," *J. Mater. Chem.*, vol. 16, no. 16, pp. 1495–1503, 2006, doi: 10.1039/B505706J.

[17] W. J. Landis and F. H. Silver, "Mineral Deposition in the Extracellular Matrices of Vertebrate Tissues: Identification of Possible Apatite Nucleation Sites on Type I Collagen," *Cells. Tissues. Organs*, vol. 189, no. 1–4, p. 20, Dec. 2008, doi: 10.1159/000151454.

[18] Y. K. Kim *et al.*, "Mineralisation of reconstituted collagen using polyvinylphosphonic acid/polyacrylic acid templating matrix protein analogues in the presence of calcium, phosphate and hydroxyl ions," *Biomaterials*, vol. 31, no. 25, p. 6618, Sep. 2010, doi: 10.1016/J.BIOMATERIALS.2010.04.060.

[19] A. Pouikli *et al.*, "Chromatin remodeling due to degradation of citrate carrier impairs osteogenesis of aged mesenchymal stem cells," *Nat. Aging 2021 19*, vol. 1, no. 9, pp. 810–825, Sep. 2021, doi: 10.1038/s43587-021-00105-8.

[20] Y. Wang *et al.*, "Aging Relevant Metabolite Itaconate Inhibits Inflammatory Bone Loss," *Front. Endocrinol. (Lausanne).*, vol. 13, Jul. 2022, doi: 10.3389/FENDO.2022.885879/FULL.
[21] K. S. Brakspear and D. J. Mason, "Glutamate signaling in bone," *Front. Endocrinol. (Lausanne).*, vol. 3, no. AUG, 2012, doi: 10.3389/FENDO.2012.00097.
[22] O. Polat, S. S. Kilicoglu, and E. Erdemli, "A controlled trial of glutamine effects on bone healing," *Adv. Ther.*, vol. 24, no. 1, pp. 154–160, May 2007, doi: 10.1007/BF02850003.
[23] F. Dickens, "The citric acid content of animal tissues, with reference to its occurrence in bone and tumour," *Biochem. J.*, vol. 35, no. 8–9, pp. 1011–1023, Sep. 1941, doi: 10.1042/BJ0351011.
[24] D. Granchi, N. Baldini, F. M. Ulivieri, and R. Caudarella, "Role of Citrate in Pathophysiology and Medical Management of Bone Diseases," *Nutrients*, vol. 11, no. 11, 2019, doi: 10.3390/NU11112576.
[25] E. Davies *et al.*, "Citrate bridges between mineral platelets in bone," *Proc. Natl. Acad. Sci. U. S. A.*, vol. 111, no. 14, 2014, doi: 10.1073/PNAS.1315080111/-/DCSUPPLEMENTAL/PNAS.201315080SI.PDF.
[26] B. Xie and G. H. Nancollas, "How to control the size and morphology of apatite nanocrystals in bone," *Proc. Natl. Acad. Sci. U. S. A.*, vol. 107, no. 52, p. 22369, Dec. 2010, doi: 10.1073/PNAS.1017493108.
[27] S. Murad, D. Grove, K. A. Lindberg, G. Reynolds, A. Sivarajah, and S. R. Pinnell, "Regulation of collagen synthesis by ascorbic acid.," *Proc. Natl. Acad. Sci. U. S. A.*, vol. 78, no. 5, p. 2879, 1981, doi: 10.1073/PNAS.78.5.2879.
[28] D. Gunson, K. E. Gropp, and A. Varela, "Bone and Joints," *Haschek Rousseaux's Handb. Toxicol. Pathol. Third Ed. Vol. 1-3*, vol. 1–3, pp. 2761–2858, Jan. 2013, doi: 10.1016/B978-0-12-415759-0.00063-7.
[29] R. Thaler *et al.*, "Vitamin C epigenetically controls osteogenesis and bone mineralization," *Nat. Commun. 2022 131*, vol. 13, no. 1, pp. 1–18, Oct. 2022, doi: 10.1038/s41467-022-32915-8.
[30] P. Aghajanian, S. Hall, M. D. Wongworawat, and S. Mohan, "The Roles and Mechanisms of Actions of Vitamin C in Bone: New Developments," *J. Bone Miner. Res.*, vol. 30, no. 11, p. 1945, Nov. 2015, doi: 10.1002/JBMR.2709.
[31] C. Combes and C. Rey, "Amorphous calcium phosphates: synthesis, properties and uses in biomaterials," *Acta Biomater.*, vol. 6, no. 9, pp. 3362–3378, 2010, doi: 10.1016/J.ACTBIO.2010.02.017.
[32] A. L. Boskey and A. S. Posner, "Conversion of amorphous calcium phosphate to microcrystalline hydroxyapatite. A pH-dependent, solution-mediated, solid-solid conversion," *J. Phys. Chem.*, vol. 77, no. 19, pp. 2313–2317, 1973, doi: 10.1021/J100638A011/SUPPL_FILE/J100638A011_SI_001.PDF.
[33] L. N. Niu *et al.*, "Biomimetic remineralization of dentin," *Dent. Mater.*, vol. 30, no. 1, pp. 77–96, Jan. 2014, doi: 10.1016/J.DENTAL.2013.07.013.
[34] A. J. Hoeher, S. T. Mergelsberg, O. J. Borkiewicz, and F. M. Michel, "Impacts of Initial Ca/P on Amorphous Calcium Phosphate," 2023, doi: 10.1021/acs.cgd.1c00058.
[35] M. Iafisco *et al.*, "Fluoride-doped amorphous calcium phosphate nanoparticles as a promising biomimetic material for dental remineralization," *Sci. Rep.*, vol. 8, no. 1, Dec. 2018, doi: 10.1038/S41598-018-35258-X.
[36] J. M. Ten Cate and J. D. B. Featherstone, "Mechanistic aspects of the interactions between fluoride and dental enamel," *Crit. Rev. Oral Biol. Med.*, vol. 2, no. 3, pp. 283–296, 1991, doi: 10.1177/10454411910020030101.
[37] K. Chatzipanagis *et al.*, "Crystallization of citrate-stabilized amorphous calcium phosphate to nanocrystalline apatite: a surface-mediated transformation," *CrystEngComm*, vol. 18, no. 18, pp. 3170–3173, May 2016, doi: 10.1039/C6CE00521G.
[38] S. Dominguez-Medina, S. McDonough, P. Swanglap, C. F. Landes, and S. Link, "In situ measurement of bovine serum albumin interaction with gold nanospheres," *Langmuir*, vol. 28, no. 24, pp. 9131–9139, Jun. 2012, doi: 10.1021/LA3005213.
[39] G. P. Szekeres and J. Kneipp, "Different binding sites of serum albumins in the protein corona of gold

nanoparticles," *Analyst*, vol. 143, no. 24, pp. 6061–6068, Dec. 2018, doi: 10.1039/C8AN01321G.
[40] D. Schubert and D. Piasecki, "Oxidative Glutamate Toxicity Can Be a Component of the Excitotoxicity Cascade," *J. Neurosci.*, vol. 21, no. 19, p. 7455, Oct. 2001, doi: 10.1523/JNEUROSCI.21-19-07455.2001.
[41] A. A. Kritis, E. G. Stamoula, K. A. Paniskaki, and T. D. Vavilis, "Researching glutamate – induced cytotoxicity in different cell lines: A comparative/collective analysis/study," *Front. Cell. Neurosci.*, vol. 9, p. 131867, Mar. 2015, doi: 10.3389/FNCEL.2015.00091/BIBTEX.
[42] P. W. Hwang and J. A. Horton, "Variable osteogenic performance of MC3T3-E1 subclones impacts their utility as models of osteoblast biology," *Sci. Reports 2019 91*, vol. 9, no. 1, pp. 1–9, Jun. 2019, doi: 10.1038/s41598-019-44575-8.
[43] S. N. Hadzir *et al.*, "Ascorbic acid induces osteoblast differentiation of human suspension mononuclear cells," *Cytotherapy*, vol. 16, no. 5, pp. 674–682, May 2014, doi: 10.1016/J.JCYT.2013.07.013.
[44] T. Fukunishi, T. Shoji, and T. Shinoka, "Nanofiber composites in vascular tissue engineering," *Nanofiber Compos. Biomed. Appl.*, pp. 455–481, Jan. 2017, doi: 10.1016/B978-0-08-100173-8.00018-1.
[45] M. B. Łabowska, K. Cierluk, A. M. Jankowska, J. Kulbacka, J. Detyna, and I. Michalak, "A Review on the Adaption of Alginate-Gelatin Hydrogels for 3D Cultures and Bioprinting," *Materials (Basel).*, vol. 14, no. 4, pp. 1–28, Feb. 2021, doi: 10.3390/MA14040858.
[46] S. Heid *et al.*, "Bioprinting with bioactive alginate dialdehyde-gelatin (ADA-GEL) composite bioinks: Time-dependent in-situ crosslinking via addition of calcium-silicate particles tunes in vitro stability of 3D bioprinted constructs," *Bioprinting*, vol. 26, p. e00200, Jun. 2022, doi: 10.1016/J.BPRINT.2022.E00200.
[47] A. Indurkar, P. Bangde, M. Gore, P. Reddy, R. Jain, and P. Dandekar, "Optimization of guar gum-gelatin bioink for 3D printing of mammalian cells," *Bioprinting*, vol. 20, p. e00101, Dec. 2020, doi: 10.1016/J.BPRINT.2020.E00101.
[48] H. Jongprasitkul, S. Turunen, V. S. Parihar, and M. Kellomäki, "Two-step crosslinking to enhance the printability of methacrylated gellan gum biomaterial ink for extrusion-based 3D bioprinting," *Bioprinting*, vol. 25, Mar. 2022, doi: 10.1016/J.BPRINT.2021.E00185.
[49] S. Kyle, Z. M. Jessop, A. Al-Sabah, and I. S. Whitaker, "'Printability'' of Candidate Biomaterials for Extrusion Based 3D Printing: State-of-the-Art,'" *Adv. Healthc. Mater.*, vol. 6, no. 16, Aug. 2017, doi: 10.1002/ADHM.201700264.
[50] L. Ouyang, "3D Bioprinting of Thermal-Sensitive Bioink," pp. 63–80, 2019, doi: 10.1007/978-981-13-9455-3_5.
[51] W. Rasband, "ImageJ, U.S. National Institutes of Health, Bethesda, Maryland, USA," 2011.
[52] X. Niu, S. Chen, F. Tian, L. Wang, Q. Feng, and Y. Fan, "Hydrolytic conversion of amorphous calcium phosphate into apatite accompanied by sustained calcium and orthophosphate ions release," *Mater. Sci. Eng. C*, vol. 70, pp. 1120–1124, Jan. 2017, doi: 10.1016/J.MSEC.2016.04.095.
[53] X. Niu *et al.*, "Sustained delivery of calcium and orthophosphate ions from amorphous calcium phosphate and poly(L-lactic acid)-based electrospinning nanofibrous scaffold," *Sci. Reports 2017 71*, vol. 7, no. 1, pp. 1–9, Mar. 2017, doi: 10.1038/srep45655.
[54] Y. Cai, S. Y. Chang, S. W. Gan, S. Ma, W. F. Lu, and C. C. Yen, "Nanocomposite bioinks for 3D bioprinting," *Acta Biomater.*, vol. 151, pp. 45–69, Oct. 2022, doi: 10.1016/J.ACTBIO.2022.08.014.
[55] M. Inoue, M. Sasaki, A. Nakasu, M. Takayanagi, and T. Taguchi, "An antithrombogenic citric acid-crosslinked gelatin with endothelialization activity," *Adv. Healthc. Mater.*, vol. 1, no. 5, pp. 573–581, Sep. 2012, doi: 10.1002/ADHM.201200001.
[56] S. Bupphathong, C. Quiroz, W. Huang, P. F. Chung, H. Y. Tao, and C. H. Lin, "Gelatin Methacrylate Hydrogel for Tissue Engineering Applications—A Review on Material Modifications," *Pharmaceuticals*, vol. 15, no. 2, Feb. 2022, doi: 10.3390/PH15020171.
[57] J. Zhang *et al.*, "Injectable In Situ Photocrosslinked Hydrogel Dressing for Infected Wound Healing," *ACS Appl. Bio Mater.*, vol. 6, no. 5, pp. 1992–2002, May 2023, doi:

10.1021/ACSABM.3C00205/SUPPL_FILE/MT3C00205_SI_001.PDF.
[58] Q. Ma, Y. Zhang, V. Launay, M. Le Dot, S. Liu, and J. Lalevée, "How to overcome the light penetration issue in photopolymerization? An example for the preparation of high content iron-containing opaque composites and application in 3D printing," *Eur. Polym. J.*, vol. 165, p. 111011, Feb. 2022, doi: 10.1016/J.EURPOLYMJ.2022.111011.
[59] Y. Stuart, F. Lauren, and A. Brian, "A mechanically robust injectable hydrogel scaffold for adipose-derived stem cell delivery for the treatment of peripheral arterial disease," *Front. Bioeng. Biotechnol.*, vol. 4, 2016, doi: 10.3389/CONF.FBIOE.2016.01.00861/EVENT_ABSTRACT.
[60] H. Chen, S. Hou, H. Ma, X. Li, and Y. Tan, "Controlled gelation kinetics of cucurbit[7]uril-adamantane cross-linked supramolecular hydrogels with competing guest molecules," *Sci. Reports 2016 61*, vol. 6, no. 1, pp. 1–10, Feb. 2016, doi: 10.1038/srep20722.
[61] J. Zaragoza, S. Fukuoka, M. Kraus, J. Thomin, and P. Asuri, "Exploring the Role of Nanoparticles in Enhancing Mechanical Properties of Hydrogel Nanocomposites," *Nanomater. 2018, Vol. 8, Page 882*, vol. 8, no. 11, p. 882, Oct. 2018, doi: 10.3390/NANO8110882.
[62] M. Levin, A. Sonn-Segev, and Y. Roichman, "Structural changes in nanoparticle-hydrogel composites at very low filler concentrations," *J. Chem. Phys.*, vol. 150, no. 6, Feb. 2019, doi: 10.1063/1.5053171/198966.
[63] Z. Jing *et al.*, "Tough, stretchable and compressive alginate-based hydrogels achieved by non-covalent interactions," *RSC Adv.*, vol. 10, no. 40, pp. 23592–23606, Jun. 2020, doi: 10.1039/D0RA03733H.
[64] G. Kaya and F. Oytun, "Rheological properties of İnjectable hyaluronic acid hydrogels for soft tissue engineering applications," *Biointerface Res. Appl. Chem.*, vol. 11, no. 1, pp. 8424–8430, 2021, doi: 10.33263/BRIAC111.84248430.
[65] S. Shojaei, M. Nikuei, V. Goodarzi, M. Hakani, H. A. Khonakdar, and M. R. Saeb, "Disclosing the role of surface and bulk erosion on the viscoelastic behavior of biodegradable poly(ε-caprolactone)/poly(lactic acid)/hydroxyapatite nanocomposites," *J. Appl. Polym. Sci.*, vol. 136, no. 10, p. 47151, Mar. 2019, doi: 10.1002/APP.47151.
[66] B. Y. S. Kumar, A. M. Isloor, G. C. M. Kumar, Inamuddin, and A. M. Asiri, "Nanohydroxyapatite Reinforced Chitosan Composite Hydrogel with Tunable Mechanical and Biological Properties for Cartilage Regeneration," *Sci. Reports 2019 91*, vol. 9, no. 1, pp. 1–13, Nov. 2019, doi: 10.1038/s41598-019-52042-7.
[67] B. Maiti *et al.*, "Thermoresponsive Shape-Memory Hydrogel Actuators Made by Phototriggered Click Chemistry," *Adv. Funct. Mater.*, vol. 30, no. 24, p. 2001683, Jun. 2020, doi: 10.1002/ADFM.202001683.

DOCTORAL THESIS PROPOSED TO RIGA TECHNICAL UNIVERSITY FOR PROMOTION TO THE SCIENTIFIC DEGREE OF DOCTOR OF SCIENCE

To be granted the scientific degree of Doctor of Science (Ph. D.), the present Doctoral Thesis has been submitted for defence at the open meeting of the RTU Promotion Council on 28th August 2024 at the Faculty of Natural Sciences and Technology of Riga Technical University, Paula Valdena Street 3/7, Room 272.

OFFICIAL REVIEWERS

Professor Sergejs Gaidukovs
Riga Technical University

Dr. Antons Sizovs
Latvian Institute of Organic Synthesis

Professor Jagoda Litowczenko-Cybulska
Adam Mickiewicz University in Poznań, Poland

DECLARATION OF ACADEMIC INTEGRITY

I hereby declare that the Doctoral Thesis submitted for review to Riga Technical University for promotion to the scientific degree of Doctor of Science (Ph. D.) is my own. I confirm that this Doctoral Thesis has not been submitted to any other university for promotion to a scientific degree.

Abhishek Rajesh Indurkar ……. (signature)
Date: ……

The Doctoral Thesis has been written as collection of articles. It consists of summary in Latvian and English and with eight publications. Publications are written in English including electronically available supplementary information.

TABLE OF CONTENTS

ACKNOWLEDGEMENT 44
LIST OF ABBREVIATIONS 45
GENERAL OVERVIEW OF THESIS 46
Introduction 46
Aim 47
Thesis to defend 47
Scientific novelty 47
Practical significance 47
Structure of thesis 48
List of appended papers 49
Individual contribution to papers 51
Research roadmap 51
THE MAIN RESULT OF THE THESIS 52
CONCLUSIONS 74
REFERENCES 75

ACKNOWLEDGEMENT

I want to express my sincere gratitude to the individuals who have been instrumental in completing the Thesis, providing unwavering support, gratitude, and encouragement.

To my esteemed co-authors, your contribution and shared commitment to the research have significantly enhanced the depth and quality of this Thesis. Your contribution has been invaluable, and I am grateful for the collective efforts.

My heartfelt thanks to my supervisors for their expert guidance, mentorship, and patience. Their insights and encouragement have been pivotal in shaping the course of my research journey.

To my parents, your unwavering support and belief in my abilities have been a constant source of motivation. Your sacrifices and encouragement have laid the foundation for my academic pursuits. I am deeply grateful to my wife for her enduring support, understanding, and encouragement throughout this challenging yet fulfilling journey. Your presence is my anchor, and I am blessed to share this accomplishment with you.

Finally, I want to acknowledge God's divine guidance and blessings. The strength and resilience I found in the challenging moments was a testament to His grace.

In conclusion, thanks to everyone who has played a role in the academic endeavor. Your collective contribution and support made this journey meaningful and rewarding.

LIST OF ABBREVIATIONS

SOM – Small Organic Molecules
CaP – Calcium Phosphate
Ap – low crystalline apatite
HA – hydroxyapatite
ACP – Amorphous Calcium Phosphate
ACP_CL – amorphous calcium phosphate without any organics
ACP_NIT – amorphous calcium phosphate without any organics
ACP_ACE – acetate-containing amorphous calcium phosphate
ACP_ASC – ascorbate-containing amorphous calcium phosphate
ACP_CIT – citrate-containing amorphous calcium phosphate
ACP_GLU – glutamate-containing amorphous calcium phosphate.
ACP_ITN – itaconate-containing amorphous calcium phosphate.
ADA-GEL – alginate-dialdehyde-gelatin
SN – Single-Network
DN – Double-Network
DI – Deionized
PBS – Phosphate Buffer Saline
α-MEM – Minimum Essential Medium Eagle – alpha modification
P123 – Pluronic P123
GELMA – gelatin methacrylate
PAM – polyacrylamide
APS – ammonium persulfate
TEMED – Tetramethylethylenediamine
MSC – Mesenchymal Stem Cells
FBS – Fetal Bovine Serum

GENERAL OVERVIEW OF THE THESIS

INTRODUCTION

Globally, over 4.5 million reconstructive surgeries are conducted each year to address a range of causes, including accidents, cancer procedures, and cosmetic enhancements [1]. Global Burden Disease data analysis revealed that approximately 1.71 billion people worldwide have musculoskeletal conditions [2]. Consequently, there is a need for effective biomaterial for bone treatment and replacement. The unique characteristics of bone, its constituent phases, and structural relationships at various hierarchical levels are complex. Therefore, replicating it artificially to achieve biomaterials with properties comparable to bone has proven challenging [3].

For this reason, allograft remains a gold standard for treating bone-related disorders [4]. There is a need to develop synthetic materials similar to natural bone [5]. Bone is a nanocomposite material made up of inorganic and organic counterparts. The organic component primarily comprises calcium phosphate (CaP), while the organic content predominantly comprises collagen.

The inorganic content of bone is synthesized through a mitochondrial-dependent cellular mechanism in the form of amorphous calcium phosphate (ACP), which is further nucleated to low-crystalline apatite (Ap) in the presence of collagen [6]. In mitochondria, the ACP is associated with an organic compound that regulates interfibrillar collagen mineralization. The side chains of an organic compound (carboxylate or hydroxyl groups) allow interaction with CaP by surface adsorption [7]. The organic compound delay CaP crystallization can be due to retarding the transformation rate (crystallization) of ACP to Ap or interaction with the crystalline phase by inhibiting the growth of nuclei. Therefore the organic compound becomes a key player in regulating interfibrillar collagen mineralization [8]. The Doctoral Thesis aims to develop small organic molecule-containing ACPs and their nanocomposites as bone substitute materials for improved bone regeneration. Based on this, five synthetic SOMs have been selected with diverse functional groups and used for the development of SOM-containing ACPs. These SOMs are also naturally present in mitochondria and play a role in bone regeneration.

The primary goal was to develop a wet chemical synthesis route for the synthesis of SOM-containing ACP and analyze the impact of SOM on ACP's physiochemical properties (particle size, morphology, true density, specific surface area, and transformation kinetics) and cytocompatibility. Synthetic SOM-containing ACPs were used as inorganic fillers in an organic matrix to develop nanocomposite scaffolds.

Nanocomposite bioink was developed by adding the SOM-containing ACPs as an inorganic filler in an alginate-dialdehyde-gelatin (ADA-GEL) organic matrix wherein citrate-containing ACP (ACP_CIT) was effective in maintaining the structural integrity of the bioprinted scaffolds. Subsequently, a single-network (SN) nanocomposite hydrogel consisting of gelatin methacrylate (GELMA) and ACP_CIT was developed using chemical crosslinking.

Afterwards, a double network (DN) nanocomposite hydrogel of polyacrylamide (PAM), Pluronic P123, GELMA, and ACP_CIT was formulated. Initially, the effect of P123 on the mechanical properties of PAM-GELMA hydrogel was evaluated, followed by analyzing the effect of ACP on the mechanical and rheological properties of PAM-GELMA-P123 hydrogels. Subsequently, their shape memory effect was also evaluated. In conclusion, all the synthesized

ACPs and their nanocomposite bioink, SN, and DN hydrogels demonstrate cytocompatibility, suggesting their potential use in bone tissue regeneration applications.

THE AIM OF THE THESIS

The Thesis aimed to develop SOM-containing ACPs, investigate their physiochemical characteristics and cytocompatibility, employ them as fillers in nanocomposite development, and assess their mechanical and rheological properties. The following tasks were set to fulfil the aim:

1. To develop a wet chemical route for the synthesis of SOM-containing ACP.
2. To examine the influence of SOM on the physiological properties and transformation kinetics of ACP to low-crystalline apatite (Ap) in aqueous media: deionized (DI) water, PBS and α-MEM cell culture media.
3. To incorporate developed ACPs into bioink, SN, and DN hydrogel and investigate the properties of developed nanocomposites.

THESIS TO DEFEND

1. Incorporating SOM in ACP influences its physiochemical properties, transformation kinetics, and cytocompatibility.
2. Solution-mediated transformation of ACP to Ap is affected by the composition of aqueous media (deionized water, PBS, and α-MEM cell culture media).
3. The addition of ACP filler in bioink, SN, and DN hydrogels enhances their rheological, mechanical, and structural properties while maintaining cytocompatibility.

SCIENTIFIC NOVELTY

1. A one-step wet chemical approach was developed to synthesize pure and SOM-containing ACP (such as acetate, ascorbate, citrate, itaconate, and glutamate).
2. New ACPs with acetate, ascorbate, and itaconate were synthesized.
3. For the first time, the influence of SOM on the transformation kinetics of ACP to Ap in different aqueous mediums was evaluated.
4. Novel nanocomposite bioink, SN and DN hydrogel containing ACP were developed.
5. A new formulation of PAM-GELMA-P123 hydrogel was created.

PRACTICAL SIGNIFICANCE

1. The developed synthesis methods can be expanded to include other SOMs in ACP.
2. The transformation kinetics of ACP to Ap can be tailored using a combination of specific SOM and aqueous media for specific applications.
3. DN hydrogel with tailored mechanical properties can be developed by modulating the concentration of P123 in PAM-GELMA hydrogel.

STRUCTURE OF THE THESIS

1. The Thesis is created as a thematically unified set of scientific papers which focus on developing SOM-containing ACPs and their nanocomposites (bioink, SN, and DN hydrogel). Each paper stands on its own, presenting new knowledge and original research. Together, the papers form an extensive long-term body of research to create a new approach for synthesizing SOM-containing ACP and developing its nanocomposites.
2. The study began with an in-depth literature review (***Publication 1***) to understand the physical properties, biological occurrence, and synthesis of various calcium phosphate (CaP) types and their use as bone substitute materials. The examination revealed that achieving pure crystalline CaP requires high-temperature synthesis or treatments. Amorphous calcium phosphate (ACP) is a metastable form of calcium phosphate; therefore, densification at high temperature is not possible.
3. In ***Publication 2,*** ACP was synthesized using the dissolution precipitation method. The obtained ACP powder was sintered to near full density by simple uniaxial pressing at 1250–1500 MPa at room temperature maintaining the amorphous nature.
4. Naturally, the bone apatite is nonstoichiometric and structurally disordered. Therefore, *Publication 3*, focused on understanding the mechanism of bone apatite formation and the role of collagen and organic molecules in regulating mineralization. Naturally, ACP is formed through a mitochondrial-dependent cellular mechanism. Additionally, ACP is associated with an organic compound in the mitochondria. The side chains of organic compounds (carboxyl and hydroxyl groups) regulate Ap nucleation and collagen interfibrillar mineralization. The organic compounds' capability depends on the number of functional groups at specific configurations. Therefore, five SOMs were selected based on different functional groups, natural presence in mitochondria, and role in bone physiology. The primary goal of the Doctoral Thesis was to synthesize the SOM-containing ACP**.**
5. In ***Publication 4***, the focus is on developing a one-step wet chemical approach for the synthesis of pure, acetate (ACP_ACE), and citrate-containing ACP (ACP_CIT). The synthesis approach developed in ***Publication 4*** was further used to synthesize glutamate (ACP_GLU), itaconate (ACP_ITN), and ascorbate-containing ACP (ACP_ASC) in ***Publication 5.*** All the synthesized ACPs were characterized, and the results have shown the impact of SOM on the physiochemical properties and cytocompatibility of ACP.
6. In ***Publication 6***, the effect of ACP's particle size, transformation kinetics, and SOM on ADA-GEL hydrogel and printed scaffold were analyzed. ACP_ACE and ACP_CIT were used as an inorganic filler in the ADA-GEL organic matrix for developing nanocomposite hydrogels. Nanocomposite bioinks were developed by adding MC3T3-E1 cells in the ACP-ADA-GEL hydrogels. Both bioinks comprising ACP_CIT and ACP_ACE were cytocompatible; however, the ACP_CIT was more effective in maintaining the structural integrity of the printed scaffolds.
7. In ***Publication 7***, a nanocomposite SN hydrogel of ACP_CIT and GELMA was developed using a chemical crosslinking approach using APS/TEMED as an alternative to photo-crosslinking. *In vitro* analysis has confirmed that the chemical crosslinking and incorporation of ACP_CIT did not hamper the cytocompatibility of GELMA hydrogel.
8. In ***Publication 8***, a DN thermoresponsive hydrogel consisting of PAM-GELMA-P123 was synthesized. The primary network of DN hydrogel was developed using P123, while the

secondary network consisted of a co-polymer of PAM-GELMA. Both the PAM-GELMA were chemically crosslinked using APS/TEMED. Initially, the concentration of P123 in PAM-GELMA hydrogel was adjusted to achieve optimum mechanical properties. Afterwards, the effect of different concentrations of ACP_CIT on the mechanical properties of PAM-GELMA-P123 hydrogel was analyzed. Additionally, the shape memory effect of the nanocomposite DN hydrogel was examined.

LIST OF APPENDED PAPERS

RESULTS OF THE THESIS WERE PUBLISHED IN SCI SCIENTIFIC PUBLICATIONS

Published

1. **Indurkar, A.,** Choudhary, R., Rubenis, K., & Locs, J. (2021). Advances in sintering techniques for calcium phosphates ceramics. Materials, 14(20), 6133. doi.org/10.3390/ma14206133 (Scopus, Open Access, IF 3.4, Q2, CiteScore 5.2). (***Publication 1***).
2. Rubenis, K., Zemjane, S., Vecstaudza, J., Lazdovica, K., Bitenieks, J., Wiecinski, P., **Indurkar, A.,** & Locs, J. (2022). Sintering of amorphous calcium phosphate to near-full density by uniaxial compaction at room temperature. Journal of the European Ceramic Society, 42(13), 6199–6205. doi.org/10.1016/j.jeurceramsoc.2022.06.041 (Scopus, Open Access, IF 5.7, Q1, CiteScore 10.1) (***Publication 2***)
3. **Indurkar, A.,** Choudhary, R., Rubenis, K., & Locs, J. (2023). Role of carboxylic organic molecules in interfibrillar collagen mineralization. Frontiers in Bioengineering and Biotechnology, 11, 1150037. doi.org/10.3389/fbioe.2023.1150037 (Scopus, Open Access, IF 5.7, Q1, CiteScore 6.7) (***Publication 3***)
4. **Indurkar, A.,** Choudhary, R., Rubenis, K., Nimbalkar, M., Sarakovskis, A., Boccaccini, A. R., & Locs, J. (2023). Amorphous calcium phosphate and amorphous calcium phosphate carboxylate: Synthesis and characterization. ACS Omega. doi.org/10.1021/acsomega.3c00796 (Scopus, Open Access, IF 4.1, Q1, CiteScore 5.9) (***Publication 4***)
5. **Indurkar, A.,** Kudale, P., Rjabovs, K., Heinmaa, I,. Demir, O., Kirejevs, M., Rubenis, K., Chaturbhuj, G., Turks, M., & Locs, J. (2023). Small Organic Molecules Containing Amorphous Calcium Phosphate: Synthesis, Characterization and Transformation. Frontiers in Bioengineering and Biotechnology, 11. doi.org/10.3389/fbioe.2023.1329752 (Scopus, Open Access, IF 5.7, Q1, CiteScore 6.7) (***Publication 5***)

In press (Under review)

1. **Indurkar, A.,** Heid, S., Bauer, J., Rubenis, K., Friedrich, O., Locs, J., & Boccaccini, A. R. Amorphous Calcium Phosphate Reinforced Alginate-Dialdehyde-Gelatin (Ada-Gel) Bioinks for Biofabrication of Bone Tissue Scaffolds (Under review in Scientific reports) (Scopus, Open Access, IF 4.6, Q1, CiteScore 6.9). (***Publication 6***)
2. **Indurkar, A.,** Rubenis, K., Boccaccini, A. R., & Locs, J. Development of nanocomposite hydrogel using citrate-containing amorphous calcium phosphate and gelatin methacrylate (Under review in Frontiers in Bioengineering and Biotechnology) (Scopus, Open Access, IF 5.7, Q1, CiteScore 6.7) (***Publication 7***)

3. **Indurkar, A.,** Rubenis, K., Boccaccini, A. R., & Locs, J. Development and Characterization of Thermoresponsive Double-Network Nanocomposite Hydrogel for Bone Tissue Engineering (Under review in Macromolecular Materials and Engineering) (Scopus, Open Access, IF 3.9, Q1, CiteScore 6.5) (***Publication 8***)

RESULTS OF THE THESIS PRESENTED AT SCIENTIFIC CONFERENCES

1. Development of nanocomposite double network hydrogel: Vecstaudza, J., Egle, K., **Indurkar, A.,** Locs, J. 64th International Scientific Conference of Riga Technical University, Latvia held on 6th October 2023. (***Oral presentation***)
2. Development of nanocomposite double network hydrogel: **Indurkar, A.,** Rubenis, K., Boccaccini, A. R., & Locs, J. 64th International Scientific Conference of Riga Technical University, Latvia, held on 6th October 2023. (***Oral presentation***)
3. Amorphous calcium phosphate citrate reinforced gelatin-alginate dialdehyde bioink for bone regeneration: **Indurkar, A.,** Rubenis, K., Boccaccini, A. R., & Locs, J. International Conference on Biofabrication, Saskatoon, Canada, held on 17th to 20th September 2023. (***Oral presentation***)
4. Amorphous calcium phosphate citrate reinforced gelatin-alginate dialdehyde bioink for bone regeneration: **Indurkar, A.,** Rubenis, K., Boccaccini, A. R., & Locs, J. FEMS EuroMat 2023, Frankfurt, Germany,held on 3rd to 7th September 2023. (***Oral presentation***)
5. Amorphous calcium phosphate citrate reinforced gelatin-alginate dialdehyde bioink for bone regeneration: **Indurkar, A.,** Rubenis, K., Boccaccini, A. R., & Locs, J. 5th World Congress of Latvian Scientists, Riga, Latvia, held on 26th to 29th June 2023. (***Poster presentation***)
6. Biomimetic synthesis of amorphous calcium phosphate: **Indurkar, A.,** Choudhary, R., Rubenis., & Locs, J. 16th Scandinavian Society of Biomaterials, Røros, Norway held on 21st to 24th March 2023. (***Poster presentation***)
7. Tailor-made synthesis of bionic amorphous calcium phosphate: **Indurkar, A.,** Choudhary, R., Rubenis, K., Locs, J. Biomaterials and novel technologies for healthcare 3rd biennial International Conference BIOMAH, Rome, Italy, held on 18th to 21st October 2022. (***Oral presentation***)

INDIVIDUAL CONTRIBUTION TO PAPERS

The papers discussed in this Thesis are co-authored with 16 collaborators and supervised by experienced mentors who provided strong support and valuable input. The author of the Thesis played a pivotal role in each paper, shaping the research and exploring background literature. The author of the Thesis focused on developing a one-step wet chemical approach for synthesizing ACP (with and without SOM) and its characterization. The developed ACPs were used to create nanocomposite bioink, SN, and DN hydrogel.

During the Doctoral Thesis, the author had interactive discussions with the co-authors and supervisors, which has proven vital for overcoming hurdles and navigating the complexity of the research. The collective process has kept the author actively involved with his team. While the author's work and theirs are distinct, all the co-authors and supervisors have propelled the study in this field forward.

RESEARCH ROADMAP

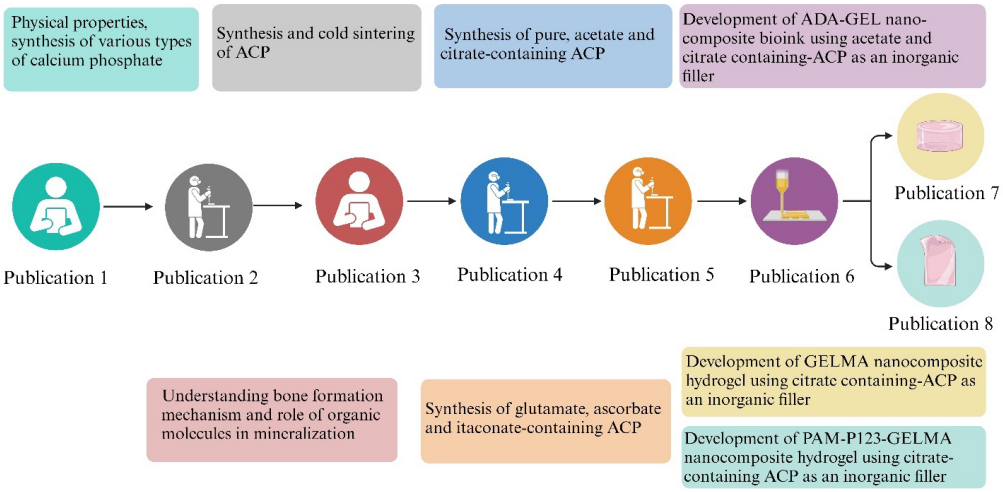

Fig. 1. Roadmap of appended papers for developing SOM-containing ACP and its nanocomposites bioink, SN, and DN hydrogels.

THE MAIN RESULTS OF THE THESIS

LITERATURE SURVEY

Bone is a dense form of connective tissue (osseous tissue) that constitutes the fundamental framework of the human skeletal system. Osseous tissue comprises specialized cells and a matrix comprising 65–70 % biomineral by weight and 5–8 % water, with the rest including organic materials [9]. The mineral phase mainly comprises CaP, the principal component being carbonated hydroxyapatite (cHA). The organic matrix comprises 90 % collagen and 10 % non-collagenous proteins.

CaP is a significant component in bone. In past decades, various CaP biomaterials have been used in bone regeneration studies and clinical applications [10]. Therefore, Publication 1 highlighted a comprehensive overview of CaP materials, such as their physical properties, biological occurrences, and diverse synthesis methods [11]. The examination revealed that achieving pure crystalline CaP requires high-temperature synthesis or treatments, encouraging to review numerous sintering methods for obtaining pure and stoichiometric CaP materials.

Synthetic hydroxyapatite (HA) developed under high temperatures has the chemical formula $Ca_{10}(PO_4)_6(OH)_2$. However, bone apatite formed at low temperatures is not well crystalline and termed a low or poorly crystalline form of calcium apatite that is structurally disordered and nonstoichiometric due to the presence of one or more cationic (Na^+, K^+, Fe^{2+}, Mg^{2+}, Zn^{2+}, Sr^{2+}) and/or anionic (HPO_4^{2-}, CO_3^{2-}, Cl^-, F^-, citrate) species [12]. Such impurities in bone apatite introduce stress into the crystal structure, making it less stable and more reactive [13]. Moreover, bone apatite has a unique geometry where the length does not exceed 30–50 nm while maintaining a thickness close to 2 nm [14]. Therefore, Publication 3 focused on understanding the mechanism of bone apatite formation [15].

The organic component of bone plays a vital role in apatite formation. ACP is the first solid phase of CaP formed by mitochondrial-dependent cellular mechanisms. ACP is associated with an organic compound (Howard factor) in mitochondria, indicating a complex inorganic-organic formation. This complex is transferred onto the collagen matrix, where ACP transforms to low crystalline apatite (Ap).

The organic component of bone plays a crucial role in Ap formation. In bone, collagen is arranged in a parallel staggered array, as shown in Fig. 2. The collagen molecules are shifted by distance D, wherein one D-repeat consists of a complete collagen sequence of 67 nm, and the distance between two tropocollagen subunits measures 40 nm, termed as the gap zone [16]. The gap zone serves as a nucleation site for ACP to Ap transformation, wherein Ap achieves its c-axis orientation parallel to the long axis of collagen [17].

However, previous studies have shown that synthetic combinations of ACP/collagen cannot initiate apatite nucleation [18]. Therefore, it was clear that collagen alone cannot initiate mineralization independently, and a nucleation catalyst regulating the process is present. The nucleation catalyst is an organic molecule of specific reactive side chains (carboxyl or hydroxyl groups) arranged in a stereochemical array [8].

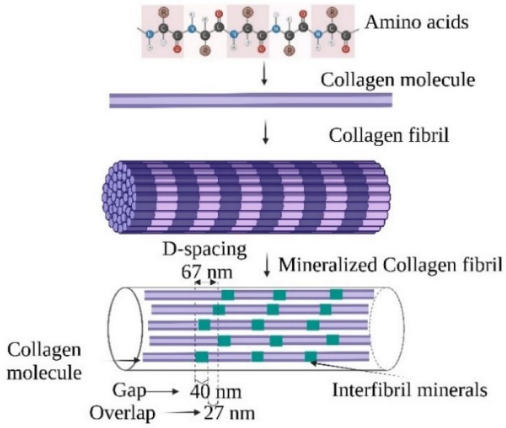

Fig. 2. Schematic illustration of the hierarchical structure of collagen.

Poly-aspartate was the first organic compound analyzed for collagen interfibrillar mineralization. Adding poly-aspartate improves the connection between CaP and collagen, creating separate CaP crystals in the collagen fibril. On the contrary, the absence of poly-aspartate resulted in clusters of CaP crystals loosely bound to collagen fibril. Poly-aspartate interacts with CaP by surface adsorption, and the delay of CaP crystallization can be due to retarding the transformation rate of ACP to Ap or due to interaction with the crystalline phase by inhibition growth of nuclei [7]. This study established the fundamental significance of organic molecules in regulating collagen interfibrillar mineralization.

Subsequently, further research was focused on analyzing different organic molecules (non-collagenous proteins, polymers, and small organic molecules) in developing synthetic CaP. The list of the organic molecules used in developing CaP is highlighted in Publication 3.

Naturally, ACP is formed through a mitochondrial-dependent cellular mechanism, as illustrated in Fig. 3 A). Furthermore, ACP forms a complex with an organic compound in the mitochondria. The literature showed that the side chains of organic compounds (carboxyl and hydroxyl groups) can induce apatite nucleation [5]. The functional groups should have the required configuration to induce CaP nucleation under stimulated body conditions. Therefore, in this study, five synthetic SOMs have been selected that are also naturally present in mitochondria. These SOMs play a role in bone regeneration and have different functional groups, as shown in Fig. 3 B).

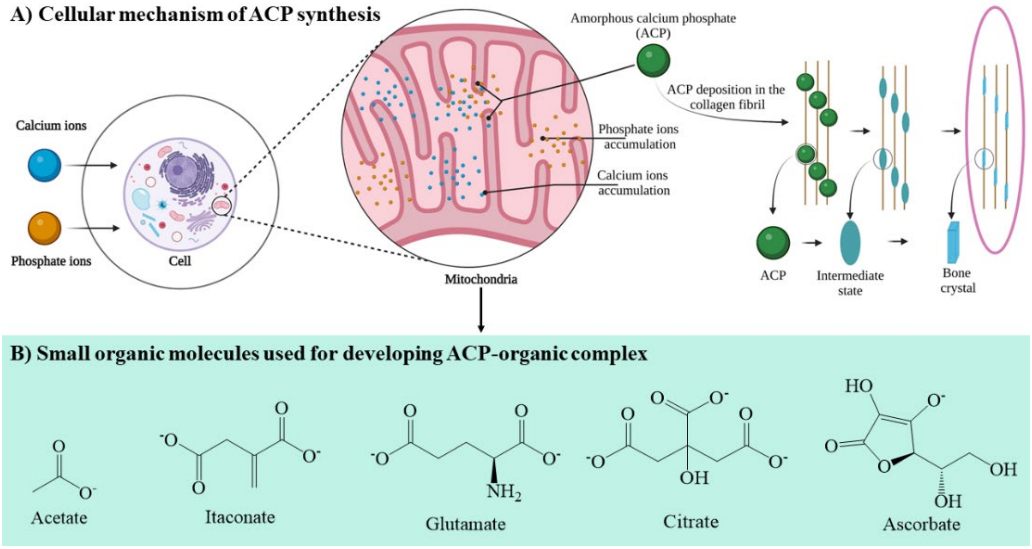

Fig. 3. A) – Formation of ACP by mitochondrial-dependent cellular mechanism. B) – Synthetic SOMs that are also naturally present in mitochondria are used to synthesize SOM-containing ACP.

Acetate is a monocarboxylic compound that enhances stem cell differentiation by increasing histone acetylation and chromatin assembly. Bone marrow mesenchymal stem cells (MSCs) regulate bone regeneration by giving rise to adipocytes, chondrocytes, and osteoblasts. However, aged MSCs have a decreased capacity to differentiate into osteogenic and chondrogenic linage. Treatment of aged MSC by supplementing acetate rescues the osteogenic defects of aged MSC [19].

Itaconate and glutamate are dicarboxylic compounds present in mitochondria. Itaconate is a metabolite that regulates osteoclast differentiation and activation, maintains bone homeostasis, and reduces inflammatory bone loss caused by lipopolysaccharide-induced inflammation [20]. Glutamate is a fundamental extracellular messenger molecule used for neural and non-neural signaling in bone. The osteoblasts, osteoclasts, and bone marrow cells express the glutamate receptors. Activation of glutamate receptors controls the phenotype of osteoblasts and osteoclasts *in vitro* and bone mass *in vivo* [21]. Moreover, glutamate has attained the nitrogen balance in a fractured bone, thus accelerating the bone healing process [22].

Citrate is a tricarboxylic compound and an essential component synthesized in the Kerbs cycle. In 1941, the presence of citrate in bone was first identified [23]. The citrate concentration in bones is 20–80 µmol/g, which is 100–400 folds higher than in most soft tissues. Bone comprises 1.6 %

citrate, and about 90 % of body citrates are found in human bone [24]. Recent NMR studies have shown the presence of citrate in bone [25]. The complex interaction of the citrate with the apatite regulates the Ap's lattice orientation, particle size, and distribution. The long axis of the citrate molecule is parallel to the surface of the apatite. The three carboxylic groups of citrates are at 0.3–0.45 nm from the apatite surface. The spacing of the carboxylic groups matches with the calcium ion along the c-axis of the apatite. Therefore, the crystal growth is inhibited in the direction of thickness but continued in the longitudinal direction [26].

Ascorbate (vitamin C) is crucial in collagen synthesis and is a vital organic compound in connective tissues and bone [27]. Collagen provides structure and flexibility to the bone, enabling it to withstand mechanical stress. Without sufficient ascorbate, collagen synthesis is impaired, weakening the bone structure and increasing susceptibility to bone fractures [28]. Furthermore, osteogenic cell differentiation depends on ascorbate [29], [30].

In summary, SOMs such as acetate, itaconate, glutamate, citrate, and ascorbate play a crucial role in bone physiology. Therefore, these SOMs were used to synthesize SOM-containing ACP, and the effect of different functional groups on the physiochemical properties of ACP and cytocompatibility was analyzed.

SYNTHESIS OF ACP WITH SOM

Initially, the dissolution precipitation method was used to synthesize ACP in one step involving the dissolution of hydroxyapatite and rapid addition of alkali (***Publication 2***), as depicted in Fig. 4 A). However, previous studies have performed the synthesis of SOM-containing ACP by a multi-step approach wherein the SOM was either introduced in its acidic or basic form, as illustrated in Fig. 4 B). Therefore, the aim was to develop a one-step approach to synthesize ACP both with and without SOM.

The complicated step in ACP synthesis is the triprotic nature of phosphate ions. In an acidic solution, ACP contains HPO_4^{2-} instead of PO_4^{3-} therefore compromising the synthesized product (ACP) [31]. ***Boskey and Posner*** have proved the influence of factors such as synthesis pH, surface area, calcium concentration, stirring rate, and slurry concentration on the physiochemical characteristics of synthesized ACP under consistent temperature conditions at 26 °C. The effect of the synthesis pH of ACP on the transformation time to apatite is shown in Table 1.

Table 1

Effect of Synthesis pH on ACP Transformation to Apatite [32]

ACP synthesis pH	Time needed for ACP transformation to apatite (min)
6.8	16
7.0	30
7.5	48
8.0	120
9.0	135
10.0	280

The literature describes various approaches to synthesize pure and SOM-containing ACP. Different approaches have different synthesis parameters, such as pH, stirring rate, reaction time,

volume, and calcium and phosphate ion concentrations. Therefore, comparing pure and SOM-containing ACP becomes problematic when using different synthesis parameters.

In the Doctoral Thesis, a one-step wet chemical synthesis approach of pure and SOM-containing ACP was developed, keeping constant synthesis parameters such as synthesis pH, reaction volume, temperature, stirring rate, and calcium and phosphate ions concentrations. This standardized approach allows us to analyze the effect of SOM on ACP's physiological properties.

The synthesis approach described in Publication 4 for the pure ACP employed the following strategy: calcium chloride or calcium nitrate solutions (150 mM in 150 ml Milli-Q® water) were prepared, and their pH was adjusted to 11.5 using 3M NaOH solution, followed by the addition of an equal amount of trisodium phosphate (100 mM in 150 ml Milli-Q® water) under constant stirring of 500 rpm, as illustrated in Fig. 4 C).

Similarly, for the synthesis of SOM-containing ACP (***Publications 4 and 5***), (150 mM) calcium acetate, (50 mM) calcium citrate, or (150 mM) calcium glutamate was added in 150 ml Milli-Q® water. Their pH was adjusted to 11.5 using 3M NaOH solution, followed by adding an equal amount of trisodium phosphate (100 mM in 150 ml Milli-Q® water) under constant stirring of 500 rpm, as illustrated in Fig. 4 D).

The process for itaconate and ascorbate-containing ACP followed a similar approach, as shown in Fig. 4 D). Calcium chloride (150 mM) and itaconic anhydride (150 mM) or ascorbic acid were added to 150 ml Milli-Q® water. Their pH was adjusted to 11.5 using 3M NaOH solution, followed by adding an equal amount of trisodium phosphate (100 mM in 150 ml Milli-Q® water) under constant stirring of 500 rpm.

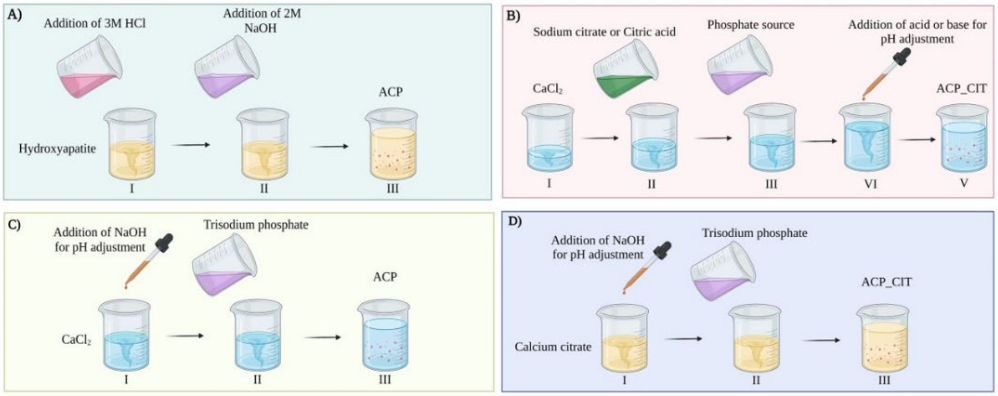

Fig. 4. Traditional synthesis approach for pure ACP (A) and SOM-containing ACP (B). The synthesis approach in which the pH of the calcium chloride solution was adjusted to 11.5 using 3M NaOH, followed by adding trisodium phosphate (C). SOM was consumed as calcium salt, making pH adjustment convenient with marginal pH variation after adding trisodium phosphate (D).

In every synthesis method, the pH of the calcium salt (with or without SOM) was set to 11.5 using 3M NaOH, and trisodium phosphate inherently had a pH of 12. The reaction pH stayed between 10.5 and 11.5 when these solutions were mixed. Moreover, the synthesis reaction volume, temperature, stirring rate, calcium and phosphate ions concentrations, and the downstream process (centrifuge, washing thrice with Milli-Q® water, liquid nitrogen freeing of precipitate, and lyophilization) were the same. As a result, pure and SOM-containing ACPs were produced under

similar conditions, enabling a comparison between them. Moreover, it also allows examining the effect of SOM on physiochemical properties and transformation kinetics of ACP to Ap.

PHYSIOCHEMICAL PROPERTIES OF SYNTHESIZED ACP VARIANTS

Publication 4 outlines the physiochemical characteristics of synthesized pure ACP as well as ACP_CIT and acetate-containing ACP (ACP_ACE). At the same time, ***Publication 5*** provides information on ascorbate (ACP_ASC), glutamate (ACP_GLU), and itaconate-containing ACP (ACP_ITN).

The XRD analysis of all the synthesized ACP variants shows a broad featureless background, showing an X-ray amorphous nature. The splitting in the $v_4\ PO_4^{3-}$ vibration region (500–620 cm^{-1}) in FTIR spectra is not seen, thus confirming the amorphous nature of all the synthesized ACP variants.

The solid-state ^{31}P nuclear magnetic resonance (NMR) analysis of all ACP variants has shown a characteristic broad Gaussian peak centered from 2.2 ppm to 6.5 ppm, corresponding to ACP. The functional groups of ACP and respective SOM were confirmed using FTIR and solid-state ^{13}C nuclear magnetic resonance (NMR) analysis.

The morphology of ACP observed in zebrafish fin, embryonic chicken long bones, and developing mouse calvaria were either spherulite or globular, with particle sizes ranging from 10–50 nm [33], [34]. Figure 5 displays the TEM analysis of the synthesized and SOM-containing ACP variants.

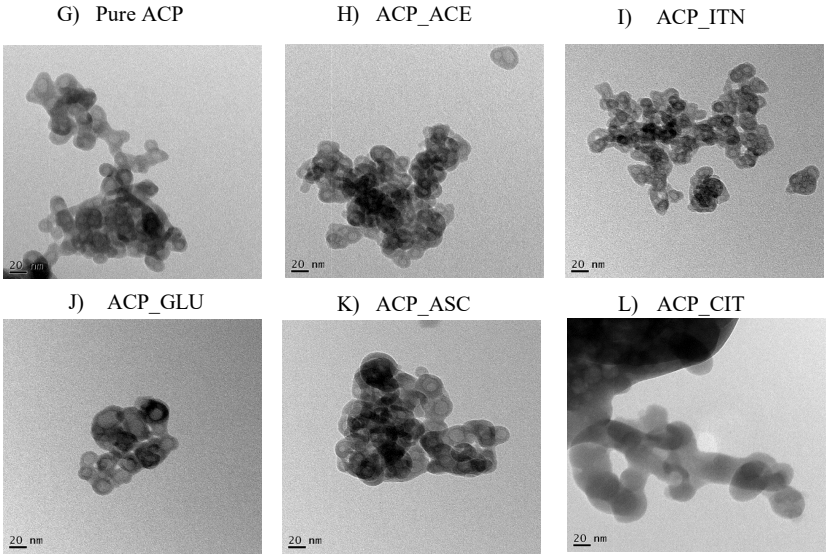

Fig. 5. Morphology and particle size analysis of all the synthesized ACP variants (scale bar of 20 nm): A) – pure ACP, B) ACP_ACE (acetate-containing ACP); C) – ACP_ITN (itaconate-containing ACP); D) – ACP_GLU (glutamate-containing ACP; E) – ACP_ASC (ascorbate-containing ACP); and F) – ACP_CIT (citrate-containing ACP).

The pure ACP, ACP_ACE, ACP_ASC, ACP_GLU, and ACP_ITN have a hollow spherical morphology with particle sizes close to 20 nm. On the other hand, ACP_CIT shows globular morphology with particle size close to 40 nm.

The effect of SOM on ACP's true density and specific surface area is shown in Table 2. The SOM used in this study possesses different functional groups. For instance, acetate is monocarboxylic, glutamate and itaconate is dicarboxylic, citrate contains tricarboxylic and a hydroxyl group, and ascorbate has hydroxyl groups. Both calcium and phosphate ions in ACP can react with the carboxylate group of acetate, citrate, itaconate, and glutamate. Similarly, the hydroxyl group can react with both phosphate and calcium ions. The functional group variations offer diverse negative charges, which react differently with calcium and phosphate ions in ACP. Therefore, the effect of SOM was observed on ACP's morphology, particle size, density, and SSA of ACP.

Table 2

Density and SSA of Synthesized ACP Variants

Sample	True density (g/cm^3)	SSA (m^2/g)
Pure ACP	2.62	105
Acetate-containing ACP	2.47	118
Itaconate-containing ACP	2.43	130
Glutamate-containing ACP	2.64	92
Ascorbate-containing ACP	2.82	115
Citrate-containing ACP	2.57	62

CRYSTALLIZATION KINETICS OF SYNTHESIZED ACPS IN AQUEOUS MEDIUM

In vitro analysis is the primary measure to scrutinize the cellular responses of a material. This examination often involves the material's exposure to diverse solutions. Specifically, for ACP, which is recognized for its metastable nature, a comprehensive investigation of its transformation kinetics in an aqueous medium becomes crucial before evaluating the *in vitro* performance. Therefore, in ***Publication 5***, transformation kinetic experiments of all the synthesized ACPs were performed. The media used were DI water, PBS, and α-MEM medium.

In literature, earlier studies have discovered that the transformation kinetics of ACP to Ap is unaffected by the following factors: a) the nature of the buffer system used, b) the presence of different types of univalent ions, c) the ACPs were in contact with mother liquor or filtered, dried, or added to the fresh buffer. The parameters affecting the transformation kinetics are stirring rate, slurry composition, solvent type, presence of foreign ions, and additives (polyelectrolytes, phospholipids, polyglycols, proteins). In this context, the effect of SOM on ACP to Ap transformation has received relatively less attention [32].

The transformation experiments were initially performed in DI water, as shown in Fig. 6. Results revealed that the transformation of ACP_ACE to Ap was faster than pure ACP. The side chains of an organic compound (carboxylate or hydroxyl groups) allow interaction with CaP by

surface adsorption. The functional groups in organic molecules possess different effects on the physiochemical properties of ACP (morphology, particle size, SSA, and true density of ACP).

NMR analysis has confirmed that pure ACP has carbonate ions with a negative charge of –2. Acetate consists of single carboxylic groups offering a negative charge of –1. Fluoride ions also have a negative charge of –1; therefore, the transformation of ACP to Ap was faster in the presence of fluoride-doped ACP than in pure ACP [35], [36]. The negative charge of –1 in acetate was attributed to the faster transformation of ACP_ACE to Ap. The presence of carbonate ions in ACP is known to retard its conversion to Ap [31]. Similarly, itaconate and glutamate are dicarboxylic compounds with a negative charge of –2 and may behave similarly to carbonate-substituted ACP. Therefore, the transformation rate of pure ACP, ACP_GLU and ACP_ITN was the same.

Citrate is a tricarboxylic compound that can interact with CaP in four ways. The first most accepted interpretation is the interaction of Ca^{2+} with the COO^-, a group of citrates. The second interpretation is the interaction of OH^- of citrate with the phosphate ions. The third possible occurs through the substitution of the phosphate group with citrate anion. The fourth prediction is the interaction of carboxylic groups with phosphate ions. The carboxylate group of citrate has a negative charge of –3 offering multiple interactions with ACP, which can be attributed to the retarded transformation rate of ACP_CIT. In the case of ascorbate anion, the transformation rate was slower than other ACP variants (except ACP_CIT). The ascorbate anion can react with ACP, which may result in complex formation, thus retarding its conversion to Ap.

In PBS, all the synthesized ACPs showed rapid transformation to Ap. Earlier studies have revealed that in the presence of PBS solution, the organic compounds are released from the surface of ACP due to ionic exchange with the phosphate groups in the medium. This leads to an elevated phosphate concentration in ACP, thus reducing stability and rapidly transforming to Ap [37]. The phosphate content in the α-MEM medium was less than in PBS. Therefore, the transformation kinetics were slower (except for the ACP_CIT).

In the case of ACP_CIT, the amorphous nature was kept up to 2880 min in the α-MEM medium. In literature, the interaction of serum albumin with citrate-stabilized gold nanoparticles forms a protein-rich layer around the particle. Similarly, the delayed transformation of ACP_CIT may be due to the interaction of negatively charged citrate with Fetal bovine serum (FBS) present in α-MEM medium [38], [39].

FTIR analysis confirmed that the functional groups of respective SOMs in the transformed Ap were retained. SOM-containing Ap can be developed by integrating the synthesis and transformation kinetics approaches.

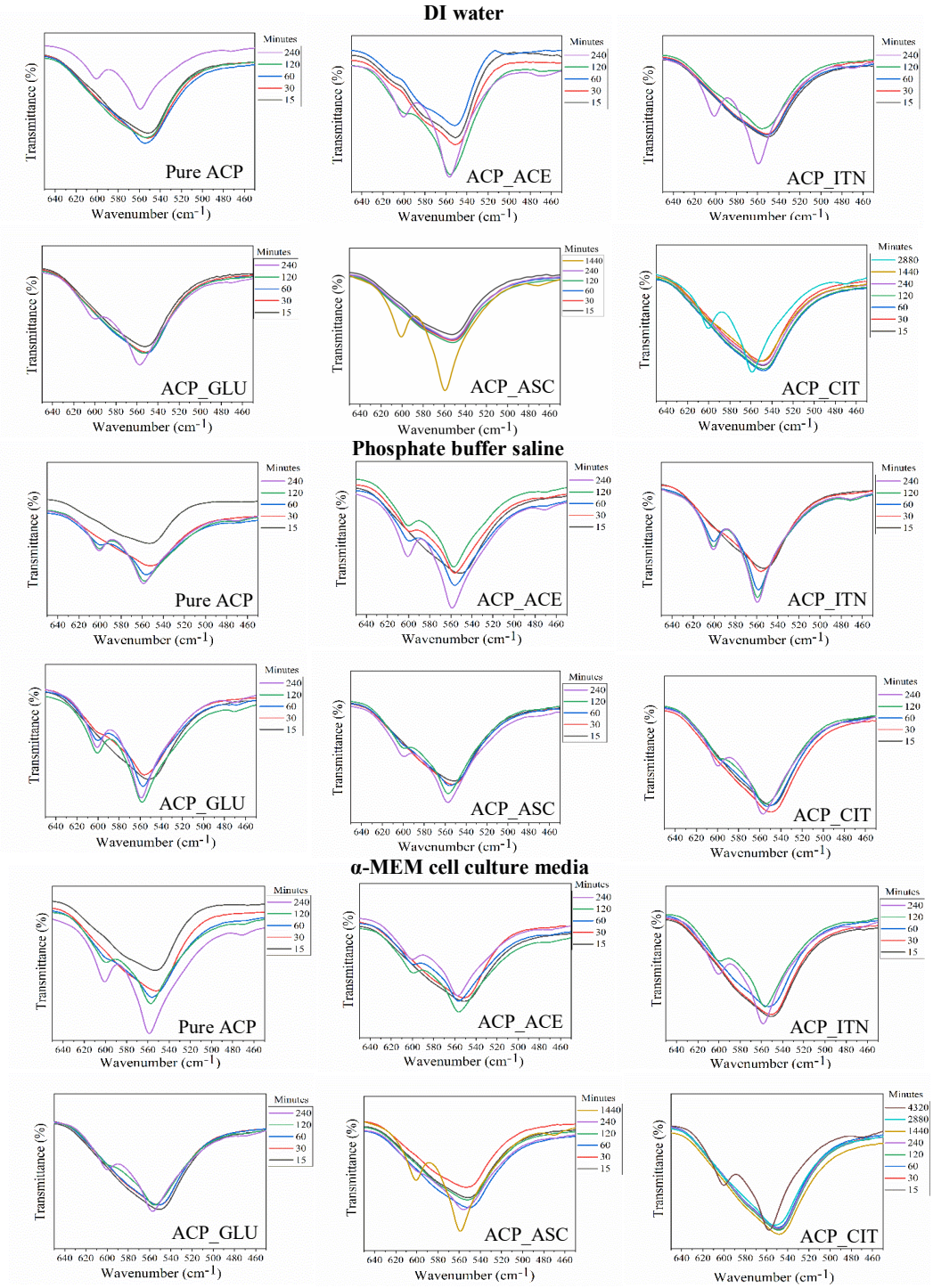

Fig. 6. Transformation kinetics of ACP to Ap in different aqueous mediums. The evaluation was based on $v_4\,PO_4^{3-}$ vibration region. The samples that did not show clear splitting in the $v_4\,PO_4^{3-}$ vibration region was termed amorphous; on the contrary, the samples that showed splitting of the $v_4\,PO_4^{3-}$ vibration region were termed low crystalline apatite.

IN VITRO ANALYSIS OF SYNTHESIZED ACPS

In vitro analysis of synthesized ACPs was performed with an osteoblast precursor cell line derived from mouse (Mus musculus) calvaria (MC3T3-E1). For cellular analysis, suspensions were prepared by adding 10 % w/v ACP precipitate in α-MEM medium and incubated at 37 °C in a humidified atmosphere of 95 % air and 5 % CO_2 for 24 h.

The extracts were collected by centrifugation and filtered to eliminate solid particles. The extracts were diluted with α-MEM medium to get the concentration of 1 % and 0.1 % w/v. For in-vitro analysis three concentrations were tested as follows: 10 %, 1 %, and 0.1 % w/v of each ACP variant. The extracts were then added to MC3T3-E1 containing well plates and incubated for 48 h. The α-MEM medium was added as a positive control. In contrast, the α-MEM medium with 6 vol% DMSO (dimethyl sulfoxide) was used as a negative control. The WST-8 (CCK-8, Sigma Aldrich) kit was used to analyze cell viability.

In ***Publication 4***, *in vitro* analysis of pure ACP, ACP_ACE and ACP_CIT was performed. The absorbance recorded from the positive control cells cultured in only medium was normalized to 100 %. The cells cultured with a 10 % w/v ACP_ACE extract showed the lowest cell viability. In contrast, the highest cell viability was observed in a 0.1 % w/v extract ACP_CIT. In the group of 10 % w/v, ACP_CIT has the highest cell viability, followed by pure ACP (ACP_CL and ACP_NIT) and ACP_ACE.

Since all the ACP samples shown in Fig. 7 exhibited cell viability of more than ~ 70 %, it can be inferred that all the samples were cytocompatible. *In vitro* analysis showed that ACP_CIT possesses maximum cell viability compared to other ACP samples (pure and ACP_ACE). This shows that the association of citrates enhanced the cell viability of ACP.

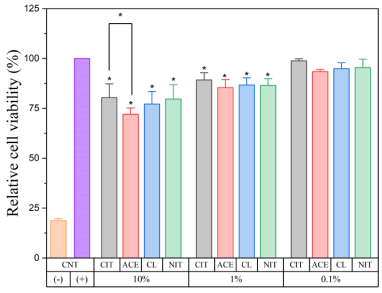

Fig. 7. Relative viability of MC3T3-E1 cells cultured with extract of different ACPs in 10 %, 1 %, 0.1 % w/v cell culture media dilutions (n = 12; CNT = control; samples in triplicate; *p < 0.05). The CL and NIT represent the pure ACP samples, while CIT and ACE represent citrate and acetate-containing ACP.

In ***Publication 5***, *in vitro* analysis of ACP_ASC, ACP_ITN and ACP_GLU was performed. The CNT+ and CNT– were positive and negative controls, respectively. Results revealed that the 10 % w/v ACP_GLU was cytotoxic. Higher glutamate concentration leads to excitotoxicity and or oxidative glutamate toxicity [40], [41]. However, reducing the concentration to 1 % w/v, ACP_GLU improved cell viability.

The 10 % w/v ACP_ITN and ACP_ASC concentration was better than 10 w/v% ACP_GLU. A similar trend was found in 1 w/v% ACP_ITN and ACP_ASC. The cell viability of 10 % and 1 % w/v ACP_ASC was better than CNT+.

Ascorbate is critical for the differentiation of the preosteoblast, and this may explain the higher cell viability [42], [43]. In conclusion, ACP samples (except 10 % w/v ACP_GLU), shown in Fig. 8, exhibited cell viability of more than ~ 70 %. It can be inferred that all the samples were cytocompatible.

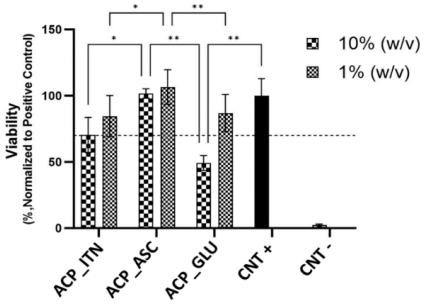

Fig. 8. Relative cell viabilities of MC3T3-E1 cells cultured with extracts of ACP variants (10 % and 1 % w/v) prepared in α-MEM medium. All the samples were analyzed in triplicate, and data is presented in average and standard deviation. The CNT+ and CNT– were positive and negative controls, respectively.

NANOCOMPOSITE BIOINK

The nanocomposite bioink containing ACP was designed for the first time. To analyze the effect of particle size, transformation kinetics, and respective SOM-containing ACP on the printed constructs' bioink properties and structural integrity, citrate and acetate-containing ACP were used for the nanocomposite bioink development.

In ***Publication 6***, bioprinting of the nanocomposite scaffold was performed in three stages: pre-printing, printing, and post-printing analysis.

In the pre-printing stage designing approach, scaffold material and cells were selected. Two nanocomposite bioinks were developed by incorporating ACP_CIT and ACP_ACE in the alginate-dialdehyde and gelatin (ADA-GEL) organic matrix.

GEL is a single-stranded protein obtained from the hydrolytic degradation of collagen. It consists of a large number of glycine, proline, and 4-hydroxyproline residues and displays similar biomechanical properties to collagen [44]. Alginate is a natural polymer obtained from brown seaweed consisting of β-(1-4) linked to mannouronic acid and β-(1-4) linked with I-glucuronic acid units. It lacks a cell attachment site and is often used with GEL to fabricate 3D scaffolds [45]. Alginate lacks binding properties with GEL; therefore, it was modified to alginate dialdehyde (ADA), offering reactive groups for crosslinking GEL by Schiff base formation [46].

The second step was printing, in which the oscillator shear tests and optimization of bioprinting parameters were performed with the hydrogels. The amplitude sweep analysis is the first step in characterizing the linear viscoelastic region (LVE) of the hydrogels [47].

The LVE region of all the synthesized hydrogels falls within 20 % of the strain, as shown in Fig. 9 A–C. Therefore, further analysis was performed at 1 % strain. The frequency sweep analysis

was performed to analyze the storage moduli (G') and loss moduli (G") of the hydrogels, as shown in Fig. 9 D–F.

The formulated hydrogels of ADA-GEL and ACP reinforced ADA-GEL have G' > G", favorable for bioprinting of scaffold. The G' and G" value of hydrogels was analyzed at the lowest frequency of 1 Hz. In the ADA-GEL hydrogel, the G' and G" were 99.2 ± 9.3 Pa and 9 ± 1.1 Pa, respectively. By the addition of ACP_ACE in ADA-GEL hydrogel, the G' and G" of 134.9 ± 16.5 Pa and 6.5 ± 0.5 Pa; on the other hand, incorporation of ACP_CIT in ADA-GEL hydrogel shows G' and G" of 142.6 ± 14.1 Pa and 7.6 ± 1.2 Pa, respectively. The flow behavior of all the formulated hydrogels has non-Newtonian shear thinning properties, as shown in Fig. 9 G.

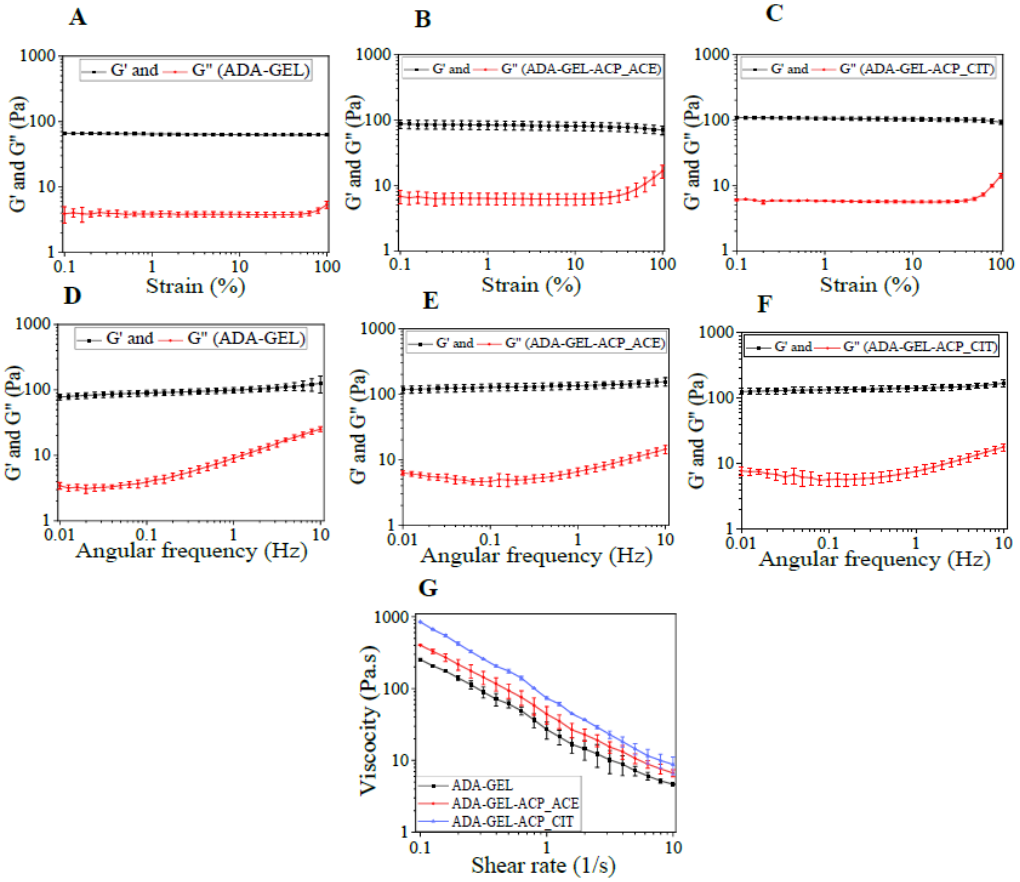

Fig. 9. Oscillatory shear tests of the ADA-GEL and ACP-reinforced ADA-GEL hydrogels. A–C – Amplitude sweep analysis was performed to assess the LVE region of the hydrogel. D–F – Frequency sweep analysis to examine (G') and loss moduli (G") of the hydrogels. Results indicate that reinforcement of ACP in ADA-GEL enhances both G' and loss moduli G" of the ADA-GEL hydrogel. G – A flow behavior analysis of hydrogels was performed using viscosity analysis against shear rate. An increase in the shear rate led to decreased viscosity, revealing the shear-thinning properties of hydrogels.

Further, the printing parameters were optimized by a trial-and-error method using ADA-GEL hydrogel. An 8 × 8 mm^2 construct optimized pressure and printing speed. Initially, the printing

was performed slowly at 2 mm/s, and the pressure was varied. Printing speed was adjusted once the construct with the unbroken grid line and uniform pores were obtained, as shown in Fig. 10.

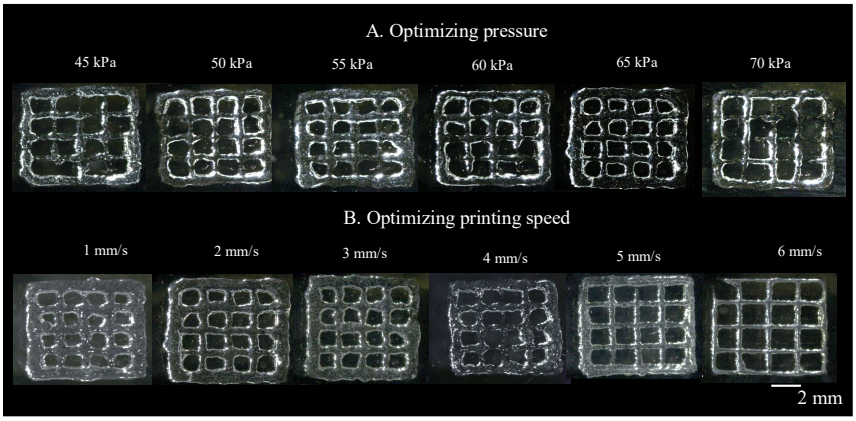

Fig. 10. Trial-and-error approach for evaluating the optimum printing under different printing pressure and speed combinations. A – Initially, the printing pressure was assessed at a slow printing speed of 2 mm/s. B – To overcome this, printing was performed at different speeds, keeping the pressure at 65 kPa.

The optimized printing pressure and speed of 65 kPa and 5 mm/s were used to fabricate constructs with ADA-GEL and ACP-reinforced ADA-GEL bioink, which were further crosslinked (using calcium chloride and microbial transglutaminase) and immersed in α-MEM cell culture media. The third step of post-printing analysis of the construct is essential to ensure the stability of the printed construct. Printability index and average pore area analysis were performed using ImageJ software. The printability index reveals the scaffold's pore geometry, which was analyzed at different day points. Moreover, the results from the printability index were correlated with the average pore area, as shown in Fig. 11.

The pore geometry of the printed constructs was evaluated using the printability index [48]. The circularity (C) of an enclosed area is defined as follows:

$$C = \frac{4\pi A}{L^2} \quad (1),$$

where L is the perimeter, and A is the area of the pore. Circles have the highest circularity where C equals 1, whereas, for the square shape, circularity equals π/4. Therefore, previous studies have defined the bioink printability index (Pr) based on a square shape using the following function [49]:

$$Pr = \frac{\pi}{4}.\frac{1}{C} = \frac{L^2}{16A}. \quad (2)$$

For an ideal gelation condition, the interconnected channels of the constructs would display a square shape with a Pr value of 1. The $Pr > 1$ shows irregular pore geometry, while $Pr < 1$ signifies curved geometry [50]. Optical images of ADA-GEL and ACP-reinforced ADA-GEL constructs were obtained using a stereo microscope. The circularity of pores ($n = 16$) of each construct was

analyzed using ImageJ software (National Institute of Health, Maryland, USA), and *Pr* values were calculated [51]. The data are presented as averages of *Pr* values with standard deviation.

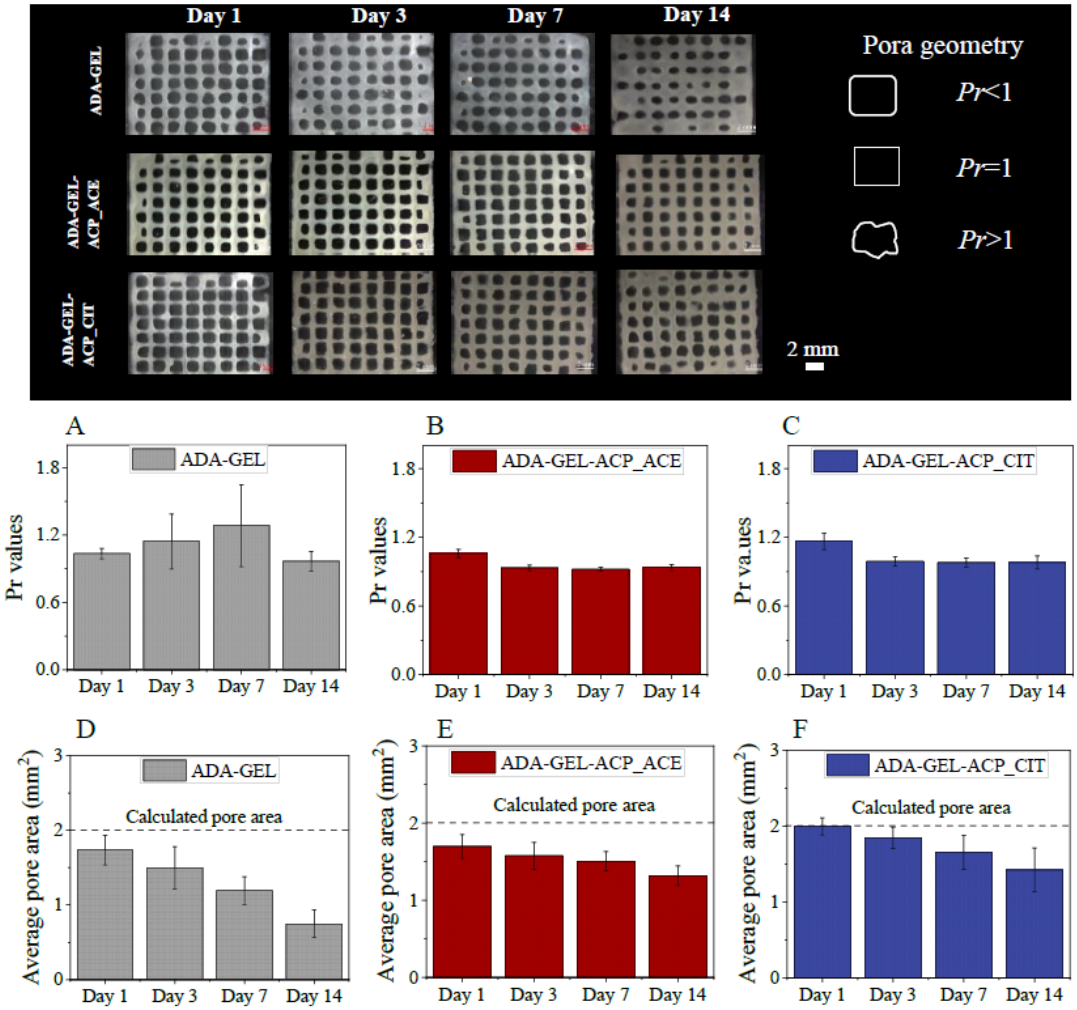

Fig. 11. Post-printing analysis of the printed construct of ADA-GEL and ACP reinforced ADA-GEL bioink (ADA-GEL-ACP_ACE and ADA-GEL-ACP_CIT). Stereo microscopy image analysis was performed on days 1, 3, 7, and 14 (scale bar 2 mm). Printability index (*Pr*) and average pore area analysis were performed using image J analysis by selecting 16 pores. Pore geometry was evaluated by analyzing the *Pr* value; for instance, $Pr < 1$ represents curved, $Pr = 1$ corresponds to square, and $Pr > 1$ resembles variable pore geometry. A–C reveal the *Pr* values. D–F show the average pore area of bioink. ADA-GEL bioinks show rapid conformational changes in pore geometry and reduction in the average pore area of bioink, showing poor structural stability compared to ACP-reinforced ADA-GEL bioinks.

ACP_CIT offers better structural integrity than ACP_ACE, possibly due to the ion release kinetics shown in Fig. 12. The ion release was studied for 168 h (seven days) to analyze calcium and phosphate ion release. Initially, a burst release was observed within the first few hours,

gradually reducing over time [52], [53]. The highest ion release was observed in ACP_CIT, while the calcium and phosphate ions released in ACP_ACE were low, ranging between 1–1.5 mM.

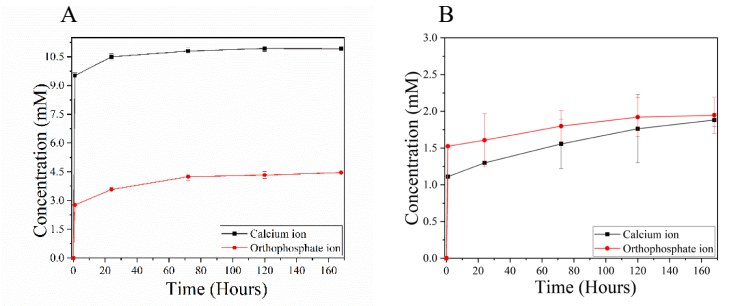

Fig. 12. Kinetic release of phosphate and calcium ions. A) – ACP_CIT and B) – ACP_ACE.

The particle size can also play a crucial role in keeping the structural integrity of the constructs. ACP_ACE has a smaller particle size (~ 20 nm) than ACP_CIT (~ 40 nm) ***(for more details, see Publication 4).*** Smaller particle size provides higher surface area and a higher agglomeration tendency, thus affecting the structural integrity [54].

The carboxylate group of citrates can potentially react with the amine group of gelatins to form amide bond formation. ADA, GEL, or both can be crosslinked with ACP_CIT [55]. However, more advanced analyses are needed to confirm the exact mechanism.

In vitro analysis was performed using Rhodamine phalloidin and DAPI staining. Figure 13 shows cellular attachment on day 1, followed by cell elongation, fusion, and network formation on the consecutive day points. The scaffold surface was covered with cells on day 14, confirming the cytocompatibility of the developed nanocomposite bioink.

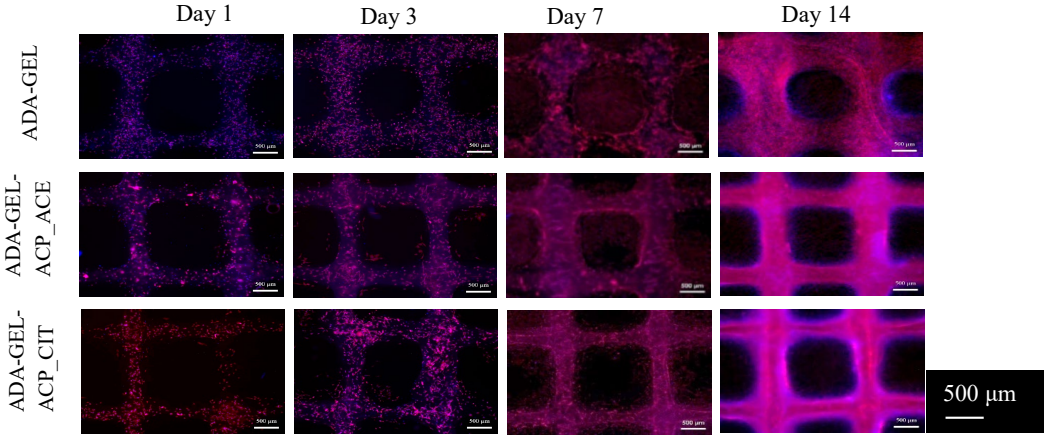

Fig. 13. Epifluorescence microscopy of rhodamine-phalloidin (red) and DAPI (blue) staining of MC3T3-E1 cells embedded in ADA-GEL and ACP reinforced ADA-GEL constructs (ADA-GEL-ACP_ACE and ADA-GEL-ACP_ACE). (Scale bar 500µm).

Two-photon microscopy analyzed the three-dimensional cell distribution within the biofabricated constructs. The 3D reconstructions of the obtained two-photon microscopy image stacks are presented in Fig. 14, showing cell distribution in the scaffolds. The images show that the cell

population gradually grows over time in the scaffolds, supporting the results from the epifluorescence microscopy experiments.

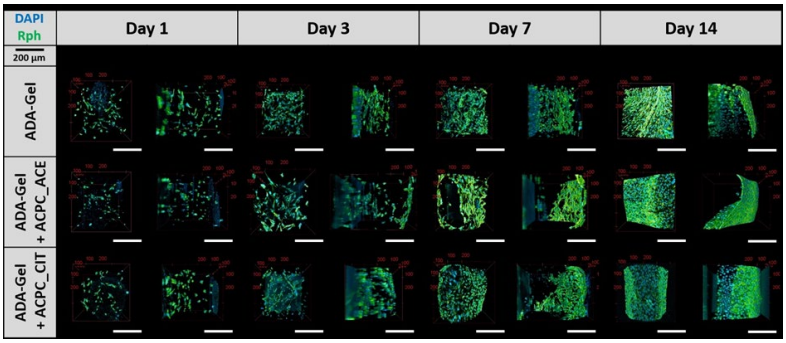

Fig. 14. Three-dimensionally reconstructed multiphoton microscopy images for qualitative morphometry and cell distribution analysis.

NANOCOMPOSITE HYDROGELS

In ***Publication 7***, a nanocomposite hydrogel was developed by incorporating ACP_CIT in the gelatin methacrylate (GELMA) matrix. GELMA is an attractive material in tissue engineering due to its biocompatibility, biodegradability, bioactivity, and unique crosslinking properties in developing nanocomposite hydrogels [56].

A commonly used method for crosslinking GELMA hydrogels is photo-crosslinking, wherein ultraviolet (UV) light and a photo-initiator are used. The GELMA solution has a photo-initiator that is exposed to UV light. The photo-initiator absorbs the UV light and undergoes a photolysis reaction, generating free radicals. The generated free radicals then react with the methacryloyl groups present in GELMA, causing the formation of radicals on the GELMA molecules. The radicals on neighboring GELMA chains start a chain reaction, forming covalent bonds between the methacryloyl groups. Similarly, a redox system uses a chemical initiator, APS and TEMED.

Photo-crosslinking has disadvantages, such as slow in situ gelation and complex preparation processes [57]. One of the significant limitations of photo-crosslinking is the incorporation of fillers that make the hydrogel opaque, which deteriorates light penetration, thus obstructing the photopolymerization reaction process and curing depth [58]. ACP fillers create opaque hydrogel, as shown in Fig. 15 B), which makes photo-crosslinking of GELMA difficult. Therefore, we have utilized the redox initiator chemical crosslinking approach using APS/TEMED to develop GELMA- ACP_CIT hydrogels [59]. The fabricated hydrogels are shown in Fig. 15. Adding ACP_CIT has enhances the viscoelastic properties of GELMA hydrogel.

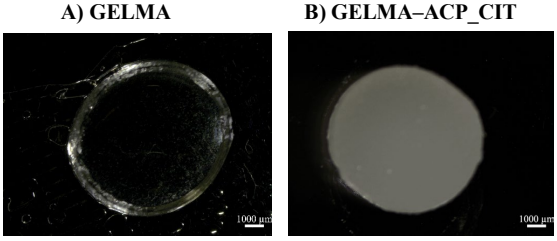

Fig. 15. Fabricated GELMA and GELMA-ACP_CIT hydrogels.

The amplitude sweep is shown in Fig. 16 A–C. The LVE region of the hydrogel was analyzed using amplitude sweep, which falls under 10 % of the stain. Therefore, further analysis was performed under 1 % strain. The storage (G") and loss modulus (G') of the uncrosslinked GELMA was very low (less than 0.1 Pa) with a crossover point (G" = G') of 501 %, indicating its ability to withstand strain-induced irreversible deformation. After cross-linking, the G" and G' of the GELMA hydrogel were enhanced, whereas the crossover point decreased to 125.8 %. Adding ACP-CIT to GELMA hydrogel enhanced the modulus by increasing the crossover point to 158.4 %. The crossover point was enhanced, resulting in hydrogel's ability to withstand strain-induced irreversible deformation.

A frequency sweep analysis was performed to evaluate the viscoelastic properties of the prepared hydrogels, as shown in Fig. 16 D–F. The G' and G" of the hydrogels were analyzed against the frequency of 1 Hz shown in Fig. 16 A. Uncrosslinked GELMA possesses very low G' (0.12 Pa) and G" (0.016 Pa) corresponding to the characteristic of weak and soft material. On the contrary, after crosslinking, the GELMA hydrogel G' (82.6 ± 13 Pa) and G" (2.28 ± 0.5 Pa) were enhanced, corresponding to the increase in strength. Incorporating ACP_CIT have shown further enhancement of G' (318.8 ± 6.5 Pa) and G" (11.3 ± 0.23 Pa) values, conforming reinforcement of GELMA hydrogel.

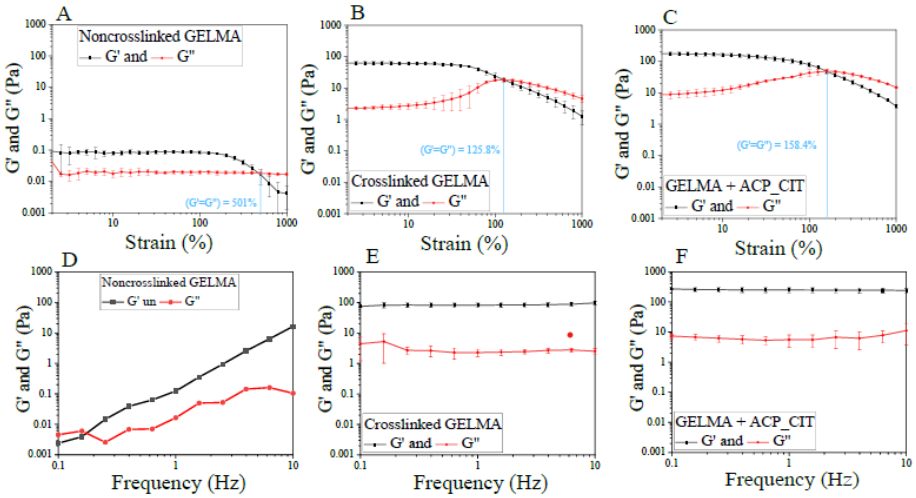

Fig. 16. The viscoelastic properties of the hydrogels were analyzed using oscillatory shear tests: A–C – the LVE region of the hydrogel was analyzed by amplitude sweep; D–F – investigation of storage and loss modulus of the hydrogels by frequency sweep analysis.

The *in vitro* analysis of the developed SN hydrogels was evaluated using rhodamine phalloidin and DAPI staining, as shown in Fig. 17. Cell attachment to the hydrogels was observed on day 1. By day 7, the cells were spread and distributed well on the hydrogel, confirming the cytocompatibility of APS/TEMED crosslinking. Furthermore, ACP_CIT did not harm the proliferation of MC3T3-E1cells.

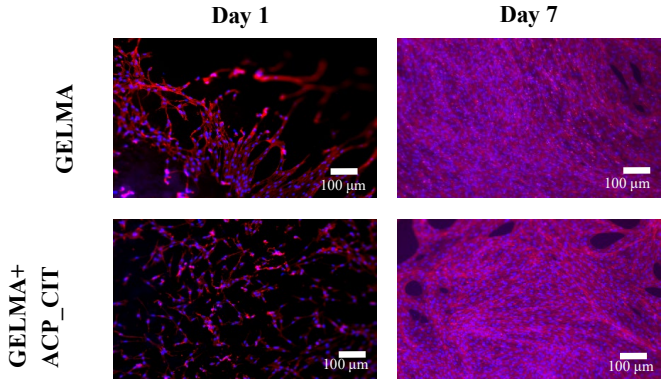

Fig. 17. Fluorescent microscopy of rhodamine-phalloidin (red) and DAPI (blue) staining of MC3T3-E1 cells in GELMA and GELMA-ACP_CIT hydrogels.

NANOCOMPOSITE DOUBLE NETWORK HYDROGELS

In ***Publication 8***, a nanocomposite DN hydrogel consisting of ACP_CIT in a P123-PAM-GELMA matrix was fabricated. The first network of DN hydrogel was created using Pluronic P123. The second network consists of polyacrylamide (PAM) and GELMA co-polymers. The second network was crosslinked using ammonium persulfate (APS) and N,N,N′,N′-Tetramethylethylenediamine (TEMED), as shown in Fig. 18.

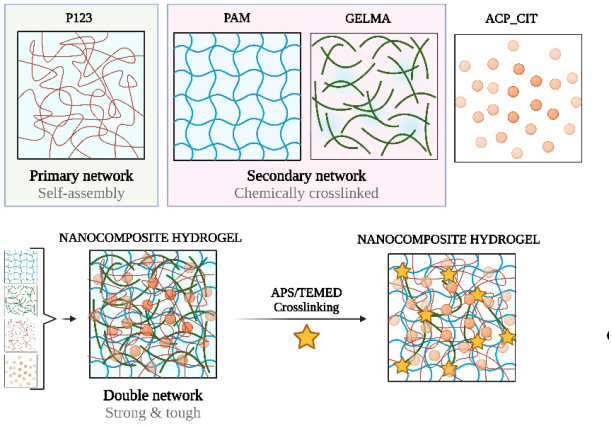

Fig. 18. Development of DN hydrogel by a physical-chemical network. Pluronic P123 self-assembly was used as a primary network, and the secondary network was composed of a co-polymer system made up of polyacrylamide-gelatin methacrylate (PAM-GELMA). Moreover, the ACP_CIT was utilized as an inorganic filler.

A systematic approach was deployed for preparation for DN nanocomposite hydrogels; initially, the impact of varying w/v concentration of P123 (2.5 %, 5 %, 7.5 %, and 10 %) on mechanical properties (Young's modulus, tensile strength, elongation at break) of PAM-GELMA was explored. Amongst these, the DN hydrogel with 7.5 w/v% P123 in PAM-GELMA (DN3) exhibited the highest mechanical properties; therefore, it was further used for the development of

nanocomposite DN hydrogels by incorporating different w/v concentrations of ACP_CIT (0.75 %, 1.5 %, and 3 %) in P123.

The nanocomposite DN hydrogels with 0.75 % w/v ACP_CIT (abbreviated as DN3-ACP0.75) exhibited the highest mechanical properties (as shown in Fig. 19), whose rheological characteristics and cytocompatibility were further evaluated and compared with pristine DN hydrogel (7.5 w/v% P123-PAM-GELMA) (abbreviated as DN3).

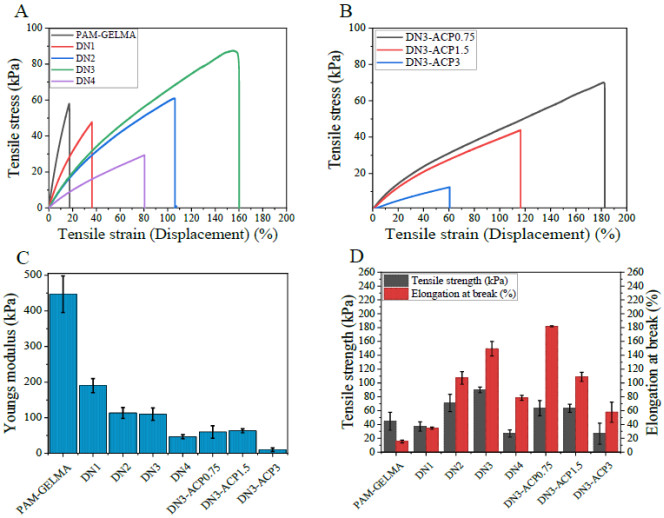

Fig. 19. Tensile stress-strain curve of the prepared hydrogel. A – Analyzing the effect of P123 concentration on the Elongation of the PAM-GELMA hydrogel; B – analyzing the effect of ACP_CIT concentration on the Elongation of the DN3 hydrogel; C – Young's modulus; D – tensile strength, and elongation at break (%) of all the synthesized hydrogels.

The amplitude sweep of all the synthesized hydrogels reveals that the hydrogels possess G' > G", showing gel-like behavior. A frequency sweep analysis was performed to evaluate the viscoelastic properties of the prepared hydrogels ***(for more details, see Publication 8)***. The G' and G" of the hydrogels were analyzed against the frequency of 1 Hz shown in Fig. 20 A. P123 possesses very low G' (1904 ± 50 Pa) and G" (1112.3 ± 28.5 Pa), corresponding to the characteristic of weak and soft material. On the contrary, the PAM-GELMA hydrogel has high G' (10916.6 ± 625.3 Pa) and G" (4058.6 ± 213.8 Pa), corresponding to the high strength and brittle nature. By increasing the P123 in PAM-GELMA hydrogel, the G' value was less affected compared to the G" value. The reduction in G" means less energy is dissipated during deformation, indicating that the hydrogel behaves more elastically and less viscously. Therefore, as the concentration of P123 increases, the difference between the G' and G" values shows increasing elastic behavior [60]. This phenomenon was observed until the P123 concentration of 7.5 w/v% in PAM-GELMA hydrogel (DN3). However, further increasing the P123 concentration to 10 w/v% in PAM-GELMA hydrogel (DN4), the decrease in the G' and increase in G", obstructed the elastic behavior of the hydrogel.

In the case of nanocomposite hydrogels at lower concentration of ACP_CIT (0.75 % w/v) in DN3 hydrogels (DN3-ACP0.75), reveals the G' of 9141 ± 2545 Pa and G" of 341.3 ± 134.8 Pa. The incorporation of ACP_CIT (0.75 % w/v) decreases G' and G" values, however the reduction in the G' was marginal while G" values drastically decreased, which may be responsible for

enhancing elastic property. However, as the concentration of ACP_CIT (1.5 % w/v) increased in DN3 hydrogels (DN3-ACP1.5) drastically increased values of G' (17766.6 ± 2689.4 Pa) and G" of (1034.9 ± 290.2 Pa) imparting rigidity to the hydrogel. A further increase in ACP_CIT concentration (3 % w/v) in DN3 hydrogels (DN3-ACP3) shows extreme enhancement on G' (22523.3 ± 6950 Pa) and G" of (1422.6 ± 47.6 Pa), which may be responsible for compromising the mechanical properties [61], [62].

The tan δ analysis of all the synthesized hydrogels is shown in Fig. 20 C. Tan δ is the ratio of G" to G' of viscoelastic material often used to analyze the damping properties of the material. It quantifies the ratio of energy dissipated as heat. In viscoelastic material, a higher tan δ value (close to 1) indicates a higher proportion of energies dissipated as heat relative to the energy stored elastically. On the other hand, a lower tan δ value indicates that more energy is elastically stored compared to dissipated energy [47].

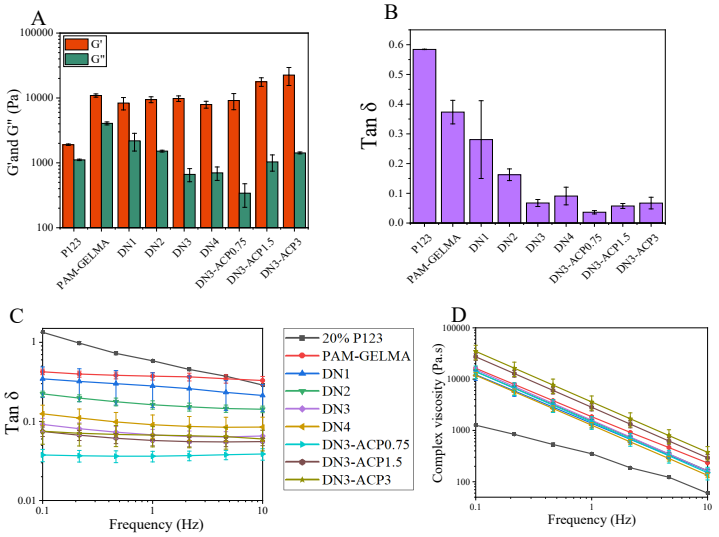

Fig. 20. A – Analyzing storage (G') loss modulus (G") at the frequency of 1 Hz. B – Evaluation of the tan δ at 1 Hz. C – Tan δ analyzed all synthesized hydrogels at varying frequencies. D – Complex viscosity.

The tan δ of PAM-GELMA hydrogel was 0.37±0.03 when analyzed at a frequency of 1 Hz, shown in Fig. 20 D. Increasing P123 concentration in PAM-GELMA hydrogels shows tan δ of 0.28±0.13 (DN1), 0.16 ± 0.01 (DN2), 0.067 ± 0.01 (DN3) and 0.09 ± 0.02 (DN4), respectively. This analysis revealed that tan δ values decreased till the P123 concentration was 7.5 % w/v in PAM-GELMA (DN3), which can be attributed to increased flexibility [63]. However, when the P123 concentration was increased to 10 % w/v in PAM-GELMA (DN4), the tan δ value increased, thus hindering the damping properties and reducing flexibility.

In the nanocomposite hydrogels, the tan δ values were 0.036 ± 0.05 (DN3-ACP0.75), 0.057 ± 0.008 (DN3-ACP1.5), and 0.067 ± 0.02 (DN3-ACP3). The tan δ value of DN3-ACP0.75 was the lowest, which can be attributed to the highest elasticity. Increasing the concentration of ACP_CIT in DN3 hydrogels to 1.5 % w/v (DN3-ACP1.5) and 3 % w/v (DN3-ACP3) increases the tan δ value, which can be attributed to the reduction in the damping properties. With the increase in the ACP_CIT concentration, the tan δ value starts to increase, which can alter the

crosslinking density and polymer chain mobility within the hydrogel, thus affecting the hydrogel's overall mechanical properties.

The complex viscosity of all the synthesized hydrogel decreased with an increase in frequency, demonstrating shear thinning behavior. Variations in the complex viscosities were observed with different concentrations of P123 and ACP_CIT in PAM-GELMA hydrogel [64]. As shown in Fig. 20 D, an increase in P123 concentration in PAM-GELMA hydrogel led to a notable reduction in complex viscosity.

The results from tensile strength analysis go hand in hand with the oscillatory shear tests, confirming that blending of P123 enhances the elasticity and mechanical properties of PAM-GELMA hydrogels. However, the performance of P123 was concentration-dependent. In addition, the performance of ACP_CIT was also concentration-dependent. At deficient concentrations, enhancement in elasticity was observed, which may be due to pseudo crosslinking of citrate in ACP_CIT with GELMA. However, more advanced analyses are required to confirm the ACP_CIT-GELMA interaction. The DN3 and its nanocomposite DN3-ACP0.75 hydrogel have the highest mechanical properties. Therefore, further analysis was performed on these two hydrogels.

Creep and recovery behavior help reflect the interaction of polymeric chains of the viscoelastic material, which helps to understand and analyze the deformation mechanism of the hydrogels. Therefore, the creep recovery analysis was performed to evaluate the interaction change among the polymer chain of the one DN3 and nanocomposite DN3-ACP0.75 hydrogels, as shown in Fig. 21 A. The incorporation of ACP_CIT in DN3 hydrogel (DN3-ACP0.75) shows a positive effect on decreasing creep strain. This can be due to restricted polymer chain movements by adding ACP_CIT nanoparticles [65]. The stress relaxation curves are presented in Fig. 21 B. The DN3 and nanocomposite DN3-ACP0.75 hydrogels show rapid stress relaxations.

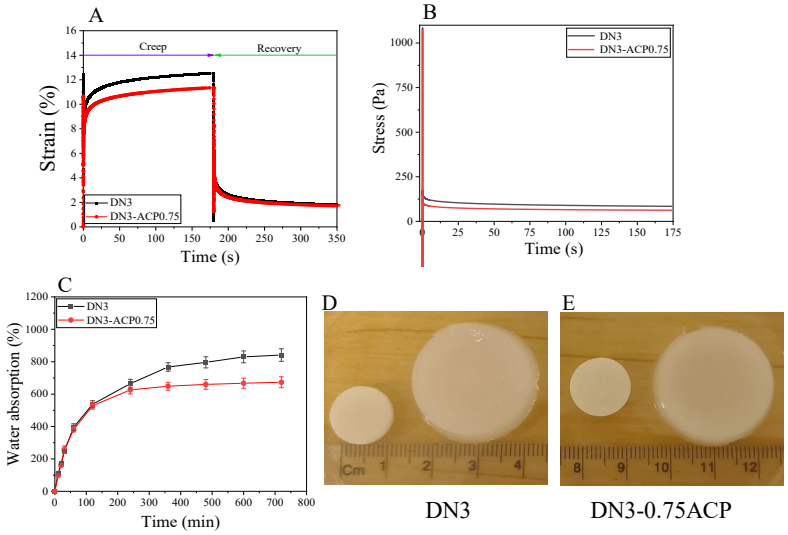

Fig. 21. Analyzing creep-recovery (A), stress relaxation (B), water uptake capacity (C), and photographs of dried and swelled DN3 and DN3-ACP0.75 hydrogels (D and E).

The water uptake capacity of DN3 hydrogel and its composite DN3-ACP0.75 is presented in Fig. 21 C. Both the DN3 and DN3-ACP0.75 hydrogels grow double in size after swelling, as observed in Fig. 21 D and E. The incorporation of ACP_CIT in the DN3 hydrogel affects the

swelling kinetics. A reduction in the water uptake capacity of DN3-ACP0.75 hydrogels can be due to the hindrance of the free polymer chain movement by the addition of ACP_CIT [66].

The shape memory hydrogel possesses two different types of crosslinks. One of the crosslinks is composed of a covalent network, which is essential to maintaining the structural integrity of the hydrogel. On the other hand, the second crosslink is composed of a physical reversible network responsible for fixing the temporary shape. In this investigation, PAM-GELMA forms the covalently crosslinked network [67]. The thermosensitive P123 forms reverse physical crosslinking when exposed to high temperature (70 °C), triggering the temporary shape formation when exposed to (4 °C), thus providing shape memory and recovery properties, as shown in Fig. 22.

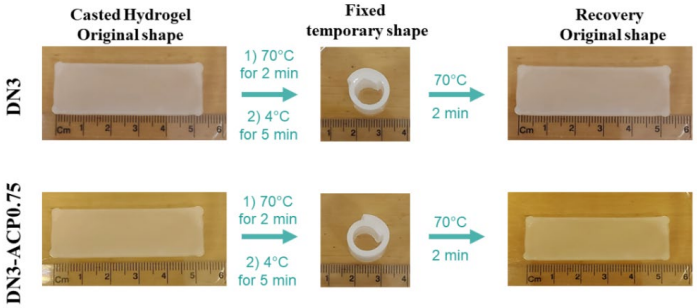

Fig. 22. Temperature-induced shape memory behavior of DN3 and DN3-ACP0.75 hydrogels.

In vitro analysis of the fabricated hydrogel was evaluated using rhodamine phalloidin and DAPI staining, as shown in Fig. 23. The cell attachment on the hydrogel was observed on day 1. On day 3, the cells spread well and were distributed on both hydrogels. On day 7, the scaffold was densely populated with cells, confirming the cytocompatibility of developed DN3 and DN3-ACP0.75 hydrogels.

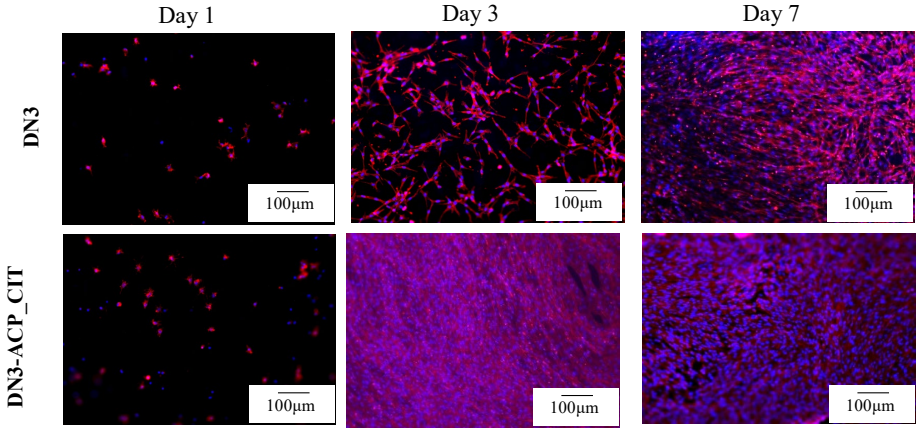

Fig. 23. Fluorescent microscopy of rhodamine-phalloidin (red) and DAPI (blue) staining of MC3T3-E1 cells in DN3 and DN3-ACP0.75 hydrogels.

CONCLUSIONS

1. The variation in the negative charge within the side chain of SOMs influences the interaction of SOMs with ACP, consequently impacting the physiological properties of ACP.

2. Solution-mediated transformation kinetics of ACP to Ap is affected by the media composition. However, the transformation order remains consistent across different media compositions: ACP_ACE>>pure ACP=ACP_ITN=ACP_GLU>>ACP_ASC>>ACP_CIT. In PBS, all the synthesized ACPs showed accelerated transformation to Ap compared to DI water. The presence of phosphate ions in PBS reduces the ACP stability, thus accelerating Ap formation. α-MEM shows slower transformation kinetics than PBS, attributed to its lower concentration of phosphate ions.

3. The addition of 1 % w/v ACP_CIT and ACP_ACE to ADA-GEL hydrogel increases both the storage and loss modulus (G' = 142.6 ± 14.1 Pa and G" = 7.6 ± 1.2 Pa for ACP_CIT, G' = 134.9 ± 16.5 Pa and G" = 6.5 ± 0.5 Pa for ACP_ACE, and G' = 99.2 ± 9.3 Pa and G" = 9 ± 1.1 Pa for ADA-GEL hydrogel). Enhancements in the storage and loss modulus improved the printed scaffold's structural integrity. The enhancement can be attributed to the additional calcium ions provided by ACP for ADA crosslinking.

4. The GELMA hydrogel possesses G' (82.6 ± 13 Pa) and G" (2.28 ± 0.5 Pa) addition of 2 % w/v ACP_CIT to GELMA hydrogel enhanced G' (318.8 ± 6.5 Pa) and G" (11.3 ± 0.23 Pa) values, thus confirming reinforcement of GELMA hydrogel by addition of ACP_CIT.

5. The effect of ACP_CIT on the mechanical properties of DN3 hydrogel was concentration-dependent. Adding 0.75 % w/v ACP_CIT increases the flexibility of DN3 hydrogel, which can be attributed to the reduction in polymer chain entanglement by the small amount of ACP_CIT. However, as the concentration of ACP_CIT increased, the G' and G" values drastically increased, thus imparting rigidity to the hydrogel, resulting in compromised mechanical properties.

REFERENCES

[1]J. M. Grasman, M. J. Zayas, R. L. Page, and G. D. Pins, "Biomimetic Scaffolds for Regeneration of Volumetric Muscle Loss in Skeletal Muscle Injuries," *Acta Biomater.*, vol. 25, p. 2, Oct. 2015, doi: 10.1016/J.ACTBIO.2015.07.038.

[2]"Musculoskeletal health." Accessed: Dec. 13, 2023. [Online]. Available: https://www.who.int/news-room/fact-sheets/detail/musculoskeletal-conditions

[3]A. R. Amini, C. T. Laurencin, and S. P. Nukavarapu, "Bone Tissue Engineering: Recent Advances and Challenges," *Crit. Rev. Biomed. Eng.*, vol. 40, no. 5, p. 363, 2012, doi: 10.1615/CRITREVBIOMEDENG.V40.I5.10.

[4]A. H. Schmidt, "Autologous bone graft: Is it still the gold standard?," *Injury*, vol. 52, pp. S18–S22, Jun. 2021, doi: 10.1016/J.INJURY.2021.01.043.

[5]O. Petrauskaite *et al.*, "Biomimetic mineralization on a macroporous cellulose-based matrix for bone regeneration," *Biomed Res. Int.*, vol. 2013, 2013, doi: 10.1155/2013/452750.

[6]A. L. Lehninger, "Mitochondria and Calcium Ion Transport THE FIFTH JUBILEE LECTURE," *Biochem. J.*, vol. 119, no. 2, pp. 129–138, 1970.

[7]J. H. Bradt, M. Mertig, A. Teresiak, and W. Pompe, "Biomimetic Mineralization of Collagen by Combined Fibril Assembly and Calcium Phosphate Formation," *Chem. Mater.*, vol. 11, no. 10, pp. 2694–2701, 1999, doi: 10.1021/CM991002P.

[8]A. G. Walton, B. A. Friedman, and A. Schwartz, "Nucleation and mineralization of organic matrices," *J. Biomed. Mater. Res.*, vol. 1, no. 3, pp. 337–354, Sep. 1967, doi: 10.1002/JBM.820010305.

[9]"Biomedical Applications of Inorganic Materials," *Biomed. Appl. Inorg. Mater.*, Dec. 2021, doi: 10.1039/9781788019293.

[10] C. Drouet, "Apatite formation: Why it may not work as planned, and how to conclusively identify apatite compounds," *Biomed Res. Int.*, vol. 2013, 2013, doi: 10.1155/2013/490946.

[11] A. Indurkar, R. Choudhary, K. Rubenis, and J. Locs, "Advances in Sintering Techniques for Calcium Phosphates Ceramics," *Mater. 2021, Vol. 14, Page 6133*, vol. 14, no. 20, p. 6133, Oct. 2021, doi: 10.3390/MA14206133.

[12] H. C. W. Skinner and H. Ehrlich, "Biomineralization," *Treatise Geochemistry Second Ed.*, vol. 10, pp. 105–162, Jan. 2014, doi: 10.1016/B978-0-08-095975-7.00804-4.

[13] I. Cacciotti, "Cationic and anionic substitutions in hydroxyapatite," *Handb. Bioceram. Biocomposites*, pp. 145–211, Jan. 2016, doi: 10.1007/978-3-319-12460-5_7/FIGURES/6.

[14] A. Lotsari, A. K. Rajasekharan, M. Halvarsson, and M. Andersson, "Transformation of amorphous calcium phosphate to bone-like apatite," *Nat. Commun. 2018 91*, vol. 9, no. 1, pp. 1–11, Oct. 2018, doi: 10.1038/s41467-018-06570-x.

[15] A. Indurkar, R. Choudhary, K. Rubenis, and J. Locs, "Role of carboxylic organic molecules in interfibrillar collagen mineralization," *Front. Bioeng. Biotechnol.*, vol. 11, p. 439, Apr. 2023, doi: 10.3389/FBIOE.2023.1150037.

[16] W. J. Landis, F. H. Silver, and J. W. Freeman, "Collagen as a scaffold for biomimetic mineralization of vertebrate tissues," *J. Mater. Chem.*, vol. 16, no. 16, pp. 1495–1503, 2006, doi: 10.1039/B505706J.

[17] W. J. Landis and F. H. Silver, "Mineral Deposition in the Extracellular Matrices of Vertebrate Tissues: Identification of Possible Apatite Nucleation Sites on Type I Collagen," *Cells. Tissues. Organs*, vol. 189, no. 1–4, p. 20, Dec. 2008, doi: 10.1159/000151454.

[18] Y. K. Kim *et al.*, "Mineralisation of reconstituted collagen using polyvinylphosphonic acid/polyacrylic acid templating matrix protein analogues in the presence of calcium, phosphate and hydroxyl ions," *Biomaterials*, vol. 31, no. 25, p. 6618, Sep. 2010, doi: 10.1016/J.BIOMATERIALS.2010.04.060.
[19] A. Pouikli *et al.*, "Chromatin remodeling due to degradation of citrate carrier impairs osteogenesis of aged mesenchymal stem cells," *Nat. Aging 2021 19*, vol. 1, no. 9, pp. 810–825, Sep. 2021, doi: 10.1038/s43587-021-00105-8.
[20] Y. Wang *et al.*, "Aging Relevant Metabolite Itaconate Inhibits Inflammatory Bone Loss," *Front. Endocrinol. (Lausanne).*, vol. 13, Jul. 2022, doi: 10.3389/FENDO.2022.885879/FULL.
[21] K. S. Brakspear and D. J. Mason, "Glutamate signaling in bone," *Front. Endocrinol. (Lausanne).*, vol. 3, no. AUG, 2012, doi: 10.3389/FENDO.2012.00097.
[22] O. Polat, S. S. Kilicoglu, and E. Erdemli, "A controlled trial of glutamine effects on bone healing," *Adv. Ther.*, vol. 24, no. 1, pp. 154–160, May 2007, doi: 10.1007/BF02850003.
[23] F. Dickens, "The citric acid content of animal tissues, with reference to its occurrence in bone and tumour," *Biochem. J.*, vol. 35, no. 8–9, pp. 1011–1023, Sep. 1941, doi: 10.1042/BJ0351011.
[24] D. Granchi, N. Baldini, F. M. Ulivieri, and R. Caudarella, "Role of Citrate in Pathophysiology and Medical Management of Bone Diseases," *Nutrients*, vol. 11, no. 11, 2019, doi: 10.3390/NU11112576.
[25] E. Davies *et al.*, "Citrate bridges between mineral platelets in bone," *Proc. Natl. Acad. Sci. U. S. A.*, vol. 111, no. 14, 2014, doi: 10.1073/PNAS.1315080111/-/DCSUPPLEMENTAL/PNAS.201315080SI.PDF.
[26] B. Xie and G. H. Nancollas, "How to control the size and morphology of apatite nanocrystals in bone," *Proc. Natl. Acad. Sci. U. S. A.*, vol. 107, no. 52, p. 22369, Dec. 2010, doi: 10.1073/PNAS.1017493108.
[27] S. Murad, D. Grove, K. A. Lindberg, G. Reynolds, A. Sivarajah, and S. R. Pinnell, "Regulation of collagen synthesis by ascorbic acid.," *Proc. Natl. Acad. Sci. U. S. A.*, vol. 78, no. 5, p. 2879, 1981, doi: 10.1073/PNAS.78.5.2879.
[28] D. Gunson, K. E. Gropp, and A. Varela, "Bone and Joints," *Haschek Rousseaux's Handb. Toxicol. Pathol. Third Ed. Vol. 1-3*, vol. 1–3, pp. 2761–2858, Jan. 2013, doi: 10.1016/B978-0-12-415759-0.00063-7.
[29] R. Thaler *et al.*, "Vitamin C epigenetically controls osteogenesis and bone mineralization," *Nat. Commun. 2022 131*, vol. 13, no. 1, pp. 1–18, Oct. 2022, doi: 10.1038/s41467-022-32915-8.
[30] P. Aghajanian, S. Hall, M. D. Wongworawat, and S. Mohan, "The Roles and Mechanisms of Actions of Vitamin C in Bone: New Developments," *J. Bone Miner. Res.*, vol. 30, no. 11, p. 1945, Nov. 2015, doi: 10.1002/JBMR.2709.
[31] C. Combes and C. Rey, "Amorphous calcium phosphates: synthesis, properties and uses in biomaterials," *Acta Biomater.*, vol. 6, no. 9, pp. 3362–3378, 2010, doi: 10.1016/J.ACTBIO.2010.02.017.
[32] A. L. Boskey and A. S. Posner, "Conversion of amorphous calcium phosphate to microcrystalline hydroxyapatite. A pH-dependent, solution-mediated, solid-solid conversion," *J. Phys. Chem.*, vol. 77, no. 19, pp. 2313–2317, 1973, doi: 10.1021/J100638A011/SUPPL_FILE/J100638A011_SI_001.PDF.
[33] L. N. Niu *et al.*, "Biomimetic remineralization of dentin," *Dent. Mater.*, vol. 30, no. 1, pp. 77–96, Jan. 2014, doi: 10.1016/J.DENTAL.2013.07.013.

[34] A. J. Hoeher, S. T. Mergelsberg, O. J. Borkiewicz, and F. M. Michel, “Impacts of Initial Ca/P on Amorphous Calcium Phosphate,” 2023, doi: 10.1021/acs.cgd.1c00058.
[35] M. Iafisco *et al.*, “Fluoride-doped amorphous calcium phosphate nanoparticles as a promising biomimetic material for dental remineralization,” *Sci. Rep.*, vol. 8, no. 1, Dec. 2018, doi: 10.1038/S41598-018-35258-X.
[36] J. M. Ten Cate and J. D. B. Featherstone, “Mechanistic aspects of the interactions between fluoride and dental enamel,” *Crit. Rev. Oral Biol. Med.*, vol. 2, no. 3, pp. 283–296, 1991, doi: 10.1177/10454411910020030101.
[37] K. Chatzipanagis *et al.*, “Crystallization of citrate-stabilized amorphous calcium phosphate to nanocrystalline apatite: a surface-mediated transformation,” *CrystEngComm*, vol. 18, no. 18, pp. 3170–3173, May 2016, doi: 10.1039/C6CE00521G.
[38] S. Dominguez-Medina, S. McDonough, P. Swanglap, C. F. Landes, and S. Link, “In situ measurement of bovine serum albumin interaction with gold nanospheres,” *Langmuir*, vol. 28, no. 24, pp. 9131–9139, Jun. 2012, doi: 10.1021/LA3005213.
[39] G. P. Szekeres and J. Kneipp, “Different binding sites of serum albumins in the protein corona of gold nanoparticles,” *Analyst*, vol. 143, no. 24, pp. 6061–6068, Dec. 2018, doi: 10.1039/C8AN01321G.
[40] D. Schubert and D. Piasecki, “Oxidative Glutamate Toxicity Can Be a Component of the Excitotoxicity Cascade,” *J. Neurosci.*, vol. 21, no. 19, p. 7455, Oct. 2001, doi: 10.1523/JNEUROSCI.21-19-07455.2001.
[41] A. A. Kritis, E. G. Stamoula, K. A. Paniskaki, and T. D. Vavilis, “Researching glutamate – induced cytotoxicity in different cell lines: A comparative/collective analysis/study,” *Front. Cell. Neurosci.*, vol. 9, p. 131867, Mar. 2015, doi: 10.3389/FNCEL.2015.00091/BIBTEX.
[42] P. W. Hwang and J. A. Horton, “Variable osteogenic performance of MC3T3-E1 subclones impacts their utility as models of osteoblast biology,” *Sci. Reports 2019 91*, vol. 9, no. 1, pp. 1–9, Jun. 2019, doi: 10.1038/s41598-019-44575-8.
[43] S. N. Hadzir *et al.*, “Ascorbic acid induces osteoblast differentiation of human suspension mononuclear cells,” *Cytotherapy*, vol. 16, no. 5, pp. 674–682, May 2014, doi: 10.1016/J.JCYT.2013.07.013.
[44] T. Fukunishi, T. Shoji, and T. Shinoka, “Nanofiber composites in vascular tissue engineering,” *Nanofiber Compos. Biomed. Appl.*, pp. 455–481, Jan. 2017, doi: 10.1016/B978-0-08-100173-8.00018-1.
[45] M. B. Łabowska, K. Cierluk, A. M. Jankowska, J. Kulbacka, J. Detyna, and I. Michalak, “A Review on the Adaption of Alginate-Gelatin Hydrogels for 3D Cultures and Bioprinting,” *Materials (Basel).*, vol. 14, no. 4, pp. 1–28, Feb. 2021, doi: 10.3390/MA14040858.
[46] S. Heid *et al.*, “Bioprinting with bioactive alginate dialdehyde-gelatin (ADA-GEL) composite bioinks: Time-dependent in-situ crosslinking via addition of calcium-silicate particles tunes in vitro stability of 3D bioprinted constructs,” *Bioprinting*, vol. 26, p. e00200, Jun. 2022, doi: 10.1016/J.BPRINT.2022.E00200.
[47] A. Indurkar, P. Bangde, M. Gore, P. Reddy, R. Jain, and P. Dandekar, “Optimization of guar gum-gelatin bioink for 3D printing of mammalian cells,” *Bioprinting*, vol. 20, p. e00101, Dec. 2020, doi: 10.1016/J.BPRINT.2020.E00101.
[48] H. Jongprasitkul, S. Turunen, V. S. Parihar, and M. Kellomäki, “Two-step crosslinking to enhance the printability of methacrylated gellan gum biomaterial ink for extrusion-based 3D

bioprinting," *Bioprinting*, vol. 25, Mar. 2022, doi: 10.1016/J.BPRINT.2021.E00185.
[49] S. Kyle, Z. M. Jessop, A. Al-Sabah, and I. S. Whitaker, "'Printability'' of Candidate Biomaterials for Extrusion Based 3D Printing: State-of-the-Art,'" *Adv. Healthc. Mater.*, vol. 6, no. 16, Aug. 2017, doi: 10.1002/ADHM.201700264.
[50] L. Ouyang, "3D Bioprinting of Thermal-Sensitive Bioink," pp. 63–80, 2019, doi: 10.1007/978-981-13-9455-3_5.
[51] W. Rasband, "ImageJ, U.S. National Institutes of Health, Bethesda, Maryland, USA," 2011.
[52] X. Niu, S. Chen, F. Tian, L. Wang, Q. Feng, and Y. Fan, "Hydrolytic conversion of amorphous calcium phosphate into apatite accompanied by sustained calcium and orthophosphate ions release," *Mater. Sci. Eng. C*, vol. 70, pp. 1120–1124, Jan. 2017, doi: 10.1016/J.MSEC.2016.04.095.
[53] X. Niu *et al.*, "Sustained delivery of calcium and orthophosphate ions from amorphous calcium phosphate and poly(L-lactic acid)-based electrospinning nanofibrous scaffold," *Sci. Reports 2017 71*, vol. 7, no. 1, pp. 1–9, Mar. 2017, doi: 10.1038/srep45655.
[54] Y. Cai, S. Y. Chang, S. W. Gan, S. Ma, W. F. Lu, and C. C. Yen, "Nanocomposite bioinks for 3D bioprinting," *Acta Biomater.*, vol. 151, pp. 45–69, Oct. 2022, doi: 10.1016/J.ACTBIO.2022.08.014.
[55] M. Inoue, M. Sasaki, A. Nakasu, M. Takayanagi, and T. Taguchi, "An antithrombogenic citric acid-crosslinked gelatin with endothelialization activity," *Adv. Healthc. Mater.*, vol. 1, no. 5, pp. 573–581, Sep. 2012, doi: 10.1002/ADHM.201200001.
[56] S. Bupphathong, C. Quiroz, W. Huang, P. F. Chung, H. Y. Tao, and C. H. Lin, "Gelatin Methacrylate Hydrogel for Tissue Engineering Applications—A Review on Material Modifications," *Pharmaceuticals*, vol. 15, no. 2, Feb. 2022, doi: 10.3390/PH15020171.
[57] J. Zhang *et al.*, "Injectable In Situ Photocrosslinked Hydrogel Dressing for Infected Wound Healing," *ACS Appl. Bio Mater.*, vol. 6, no. 5, pp. 1992–2002, May 2023, doi: 10.1021/ACSABM.3C00205/SUPPL_FILE/MT3C00205_SI_001.PDF.
[58] Q. Ma, Y. Zhang, V. Launay, M. Le Dot, S. Liu, and J. Lalevée, "How to overcome the light penetration issue in photopolymerization? An example for the preparation of high content iron-containing opaque composites and application in 3D printing," *Eur. Polym. J.*, vol. 165, p. 111011, Feb. 2022, doi: 10.1016/J.EURPOLYMJ.2022.111011.
[59] Y. Stuart, F. Lauren, and A. Brian, "A mechanically robust injectable hydrogel scaffold for adipose-derived stem cell delivery for the treatment of peripheral arterial disease," *Front. Bioeng. Biotechnol.*, vol. 4, 2016, doi: 10.3389/CONF.FBIOE.2016.01.00861/EVENT_ABSTRACT.
[60] H. Chen, S. Hou, H. Ma, X. Li, and Y. Tan, "Controlled gelation kinetics of cucurbit[7]uril-adamantane cross-linked supramolecular hydrogels with competing guest molecules," *Sci. Reports 2016 61*, vol. 6, no. 1, pp. 1–10, Feb. 2016, doi: 10.1038/srep20722.
[61] J. Zaragoza, S. Fukuoka, M. Kraus, J. Thomin, and P. Asuri, "Exploring the Role of Nanoparticles in Enhancing Mechanical Properties of Hydrogel Nanocomposites," *Nanomater. 2018, Vol. 8, Page 882*, vol. 8, no. 11, p. 882, Oct. 2018, doi: 10.3390/NANO8110882.
[62] M. Levin, A. Sonn-Segev, and Y. Roichman, "Structural changes in nanoparticle-hydrogel composites at very low filler concentrations," *J. Chem. Phys.*, vol. 150, no. 6, Feb. 2019, doi: 10.1063/1.5053171/198966.
[63] Z. Jing *et al.*, "Tough, stretchable and compressive alginate-based hydrogels achieved by non-covalent interactions," *RSC Adv.*, vol. 10, no. 40, pp. 23592–23606, Jun. 2020, doi:

10.1039/D0RA03733H.
[64] G. Kaya and F. Oytun, “Rheological properties of İnjectable hyaluronic acid hydrogels for soft tissue engineering applications,” *Biointerface Res. Appl. Chem.*, vol. 11, no. 1, pp. 8424–8430, 2021, doi: 10.33263/BRIAC111.84248430.
[65] S. Shojaei, M. Nikuei, V. Goodarzi, M. Hakani, H. A. Khonakdar, and M. R. Saeb, “Disclosing the role of surface and bulk erosion on the viscoelastic behavior of biodegradable poly(ε-caprolactone)/poly(lactic acid)/hydroxyapatite nanocomposites,” *J. Appl. Polym. Sci.*, vol. 136, no. 10, p. 47151, Mar. 2019, doi: 10.1002/APP.47151.
[66] B. Y. S. Kumar, A. M. Isloor, G. C. M. Kumar, Inamuddin, and A. M. Asiri, “Nanohydroxyapatite Reinforced Chitosan Composite Hydrogel with Tunable Mechanical and Biological Properties for Cartilage Regeneration,” *Sci. Reports 2019 91*, vol. 9, no. 1, pp. 1–13, Nov. 2019, doi: 10.1038/s41598-019-52042-7.
[67] B. Maiti *et al.*, “Thermoresponsive Shape-Memory Hydrogel Actuators Made by Phototriggered Click Chemistry,” *Adv. Funct. Mater.*, vol. 30, no. 24, p. 2001683, Jun. 2020, doi: 10.1002/ADFM.202001683.

1. PIELIKUMS / APPENDIX 1

1. PUBLIKĀCIJA / PUBLICATION

Indurkar, A., Choudhary, R., Rubenis, K., & Locs, J. (2021). Advances in sintering techniques for calcium phosphates ceramics. Materials, 14(20), 6133. doi.org/10.3390/ma14206133.

Doi: 10.3390/ma14206133

materials

MDPI

Review

Advances in Sintering Techniques for Calcium Phosphates Ceramics

Abhishek Indurkar [1,2], Rajan Choudhary [1,2], Kristaps Rubenis [1,2] and Janis Locs [1,2,*]

[1] Rudolfs Cimdins Riga Biomaterials Innovations and Development Centre of RTU, Institute of General Chemical Engineering, Faculty of Materials Science and Applied Chemistry, Riga Technical University, Pulka Street 3, LV-1007 Riga, Latvia; Abhishek-Rajesh.Indurkar@rtu.lv (A.I.); Rajan.Choudhary@rtu.lv (R.C.); kristaps.rubenis@rtu.lv (K.R.)

[2] Baltic Biomaterials Centre of Excellence, Headquarters at Riga Technical University, Kalku Street 1, LV-1658 Riga, Latvia

* Correspondence: janis.locs@rtu.lv

Abstract: Calcium phosphate (CaP) biomaterials are extensively used to reconstruct bone defects. They resemble a chemical similarity to the inorganic mineral present in bones. Thus, they are termed as the key players in bone regeneration. Sintering is a heat treatment process applied to CaP powder compact or fabricated porous material to impart strength and integrity. Conventional sintering is the simplest sintering technique, but the processing of CaPs at a high temperature for a long time usually leads to the formation of secondary phases due to their thermal instability. Furthermore, it results in excessive grain growth that obstructs the densification process, limiting the application of CaP's ceramics in bone regeneration. This review focuses on advanced sintering techniques used for the densification of CaPs. These techniques utilize the synergy of temperature with one or more parameters such as external pressure, electromagnetic radiation, electric current, or the incorporation of transient liquid that boosts the mass transfer while lowering the sintering temperature and time.

Keywords: calcium phosphates; sintering; bioceramics; bone tissue engineering

Citation: Indurkar, A.; Choudhary, R.; Rubenis, K.; Locs, J. Advances in Sintering Techniques for Calcium Phosphates Ceramics. *Materials* **2021**, *14*, 6133. https://doi.org/10.3390/ma14206133

Academic Editor: Dariusz Kata

Received: 13 September 2021
Accepted: 10 October 2021
Published: 15 October 2021

1. Introduction

Sintering is a thermal process in which loosely bound particles are converted into a consistent solid mass under the influence of heat and/or pressure without melting the particles. During the process, the atoms in the material migrate towards the boundaries of particles either by diffusion or assimilation. This results in the fusion of particles which leads to the formation of one solid piece. Sintering is a traditional technique known since human civilization and which was extensively used to treat (fire) pottery and earthenware [1]. Theoretical and experimental evidence of sintering came in the early 1900s. It is defined as a "processing technique used to produce density-controlled materials by utilizing thermal energy". It is the most crucial step in ceramic manufacturing, wherein a green body is fired at a high temperature, below the melting point of the material. A green body is referred to as a self-supporting compact procured from powders that are compacted uniaxially or isostatically. During sintering, the raw material undergoes several physical and chemical transformations [2]. The sole aim of sintering is to enhance the product's mechanical properties by particle bonding, densification, or recrystallization. For the accomplishment of desired mechanical properties' materials, sintering is inevitable. Therefore, it is considered amongst the four essential components of material science and engineering [3].

CaP bioceramics belong to a resorbable and bioactive class of biomaterials and are widely used in bone regeneration and tissue engineering applications [4]. The specific formulation of CaP is illustrated in Table 1.

Table 1. Physical properties, synthesis, and application of various types of calcium phosphates. Adapt from references [5–14].

Commercial Products	Implant Form	Biological Occurrence	Synthesis	Density (g/cm^3)	$-\log K_{sp}$ at 25 °C	Melting Point (°C)	Ca/P Molar Ratio	Crystal Structure	Chemical Formula	Phase
Bone source (TTCaP and DCP)	Cement	-	Solid-state reaction at temperature 1450–1500 °C for 6–12 h.	3.05	38	Decomposes and transforms to HAp	2	Monoclinic	$Ca_4(PO_4)_2O$	Tetra-calcium phosphate (TTCaP)
Ostim (HA) Graftys HBS (HA and TCP) Graftys quickset (HA and TCP)	Coating or deposited with polymer	Soft tissue calcification, enamel, dentin, bone, tooth, and urinary calculus	Precipitation performed at pH 9.5–12 at 90 °C	3.16	58.4	1670	1.67	Pseudohexagonal	$Ca_{10}(PO_4)_6(OH)_2$	Hydroxyapatite (HAp)
Fracture grout (α-TCP and Calcium carbonate $CaCO_3$) Biopex (α-TCP, DCPD, HA, and TTCaP)	Block	Dental and urinary calculus, salivary stones, tissue calcification, and milk Magnesium substituted β-TCP is identified in soft tissue calcification and dental calculus	Thermal Decomposition of β-TCP above 1125 °C	2.86	25.5	1391	1.5	Monoclinic	$Ca_3(PO_4)_2$	Tricalcium phosphate (a-TCP)
ChronOS Inkjet (β-TCP and DCPD)	Granules or block		a. Solid-state reaction b. Decomposition of calcium-deficient HAp above 750 °C c. Precipitation in an organic solvent	3.08	28.9	Decomposes and transforms α-TCP	1.5	Rhombohedral	$Ca_3(PO_4)_2$	Tricalcium phosphate (β-TCP)
-	Granules	Dental and urinary calculus	Precipitation performed at pH 5.5–7.0	2.61	96.6	Decomposes and transforms to HAp	1.33	Triclinic	$Ca_8H_2(PO_4)_6{\cdot}5H_2O$	Octa-calcium phosphate (OCP)
Embarc (ACP and DCPD) α−BΣM (AXΠ αvδ ΔXΠΔ)	Coating or granules	Kidney stone and heart calcification in uremic patients and soft tissue calcification	Precipitation performed at pH 5.0–12.0	0.92–1.75	26–33	Transforms to a stable phase	1.2–2.2	Amorphous	$Ca_3(PO_4)_2$	Amorphous calcium phosphate (ACP)
Eurobone (DCPD and TCP) Calcibon (DCPD, α-TCP, $CaCO_3$ and HA)	Powder	Dental calculi, chondrocalcinosis, crystalluria, and carious lesions	Precipitation performed below 80 °C under pH 2.0–6.5	2.32	6.59	Decomposes and transforms to a stable phase	1	Monoclinic	$CaHPO_4{\cdot}2H_2O$	Dicalcium phosphate dihydrate (DCPD)

CaP has a chemical similarity to bones and teeth; therefore, it possesses inherent properties that support osteoblast adhesion and proliferation, and new bone formation [15]. As a result, they are employed in damaged or diseased mineralized tissue to reduce pain and restore function. The biomedical application includes the healing of bone defects, bone augmentation, fracture treatment, joint replacement, craniomaxillofacial reconstruction, orthopedics, spinal injury, ophthalmology, percutaneous devices, dental fillings, periodontal treatment, and dental implants [16]. The aim of tissue engineering is the de novo formation of tissues and organs. Significant efforts are taken in the development of 3D supports for cells that can stimulate the formation of an extracellular matrix [17]. The progress of calcium phosphate biomaterials in bone regeneration is elaborated elsewhere [18].

Although CaP bioceramics have excellent biocompatibility, low mechanical strength is a major hurdle for load-bearing applications. Therefore, for such applications, CaP must be consolidated at elevated temperatures. However, due to narrow temperature ranges of respective calcium phosphate consolidation at high temperatures, this leads to thermal instabilities which give rise to different phases. For example, tricalcium phosphate (TCP) is a well-known bioresorbable ceramic [19] that exists in four polymorphs, α, α′, β, and γ, that are stable at different temperatures. For instance, the α′-phase is stable at temperatures above 1470 °C whereas the α-phase is stable at temperatures ranging from 1125 to 1420 °C [20]. On the contrary, the β-phase is stable at lower temperatures (less than 1125 °C). The conversion of β→α→α′-TCP occurs when heat treatment is beyond the respective stability temperature. On the other hand, under the application of high pressure (4 GPa) and a high temperature (950 °C), β-TCP is converted to γ-TCP [21]. Among the polymorphs of TCP, α′ and γ phases are difficult to synthesize because of their high temperature and pressure requirements [22]. Due to the very narrow temperature range of the polymorphs, it is crucial to control the sintering temperature to obtain a pure phase of TCP.

Moreover, the amorphous TCP (also known as amorphous calcium phosphate (ACP)) converts rapidly to TCP at elevated temperatures (above 600 °C) [23]. Another form of CaP is stoichiometric hydroxyapatite (HA) which is stable at a temperature range from 1300 to 1550 °C. Exposure to higher temperatures leads to its conversion to α′-TCP and tetra-calcium phosphate [24]. In addition, a high sintering temperature and long holding time that is characteristic of conventional sintering lead to the coarsening of grains and surface contamination which deteriorates the mechanical properties of CaPs [25]. To overcome these drawbacks, advanced sintering techniques are developed that utilize either external pressure, electromagnetic radiations, electric current, or the incorporation of transient liquids that boost up the mass transfer while lowering the time and temperature. This review is focused on such advanced sintering techniques that have potential in the development of single-phase CaPs under lower temperatures than conventional sintering.

2. Sintering Process

The sintering process has three stages: initial, intermediate, and final. The powder characteristics are governing the parameters of the compact. The uniform arrangement of powders without flaws or defects gives rise to an ideal compact [26]. In the sintering process, the expression of changes in the connectivity of the particle within the ideal compact is shown in Table 2 [27]. Sintering is an irreversible process that takes place due to a reduction in Gibbs's free energy. The three driving forces responsible for this reduction are: (i) surface curvature, (ii) external pressure, and (iii) chemical reaction [3]. Surface curvature is always the primary driving force of sintering. It is always present with or without the influence of pressure or a chemical reaction.

Table 2. Stages in the sintering process.

Stage	Process	Densification	Coarsening	Loss in Total Specific Surface Area (SSA)
Initial	Neck growth formation	Trivial	Negligible	50%
Intermediate	Elongation and rounding of pores	Substantial	Increase in grain and pore size	Complete loss of open porosity
Final	Closure of pores with final densification	Slow and minor change in density	Enormous pore and grain growth	Negligible

The addition of external pressure induces work conducted on the compact, which increases the driving force that aids the sintering process. The densification of a sample by a chemical reaction is the highest driving force compared to external pressure [28]. The detailed sintering behavior of these ceramics is illustrated elsewhere [29].

Densification and coarsening are two competitive mechanisms. Densification leads to shrinkage due to the grain boundary migration of the sintered object, while coarsening increases the particle size by interparticle mass transport, as shown in Figure 1. The reduction in surface or interface energy is the fundamental driving force of the sintering process indicated in Equation (1). γA stands for the total interfacial energy of the powder compact; γ is the specific surface area; and A is total surface area. In the equation, one $\Delta\gamma$ is a change in interfacial energy, which leads to densification, while ΔA states a change in the interfacial area due to grain coarsening [30].

$$\Delta(\gamma A) = (\Delta\gamma)A + \gamma(\Delta A) \quad (1)$$

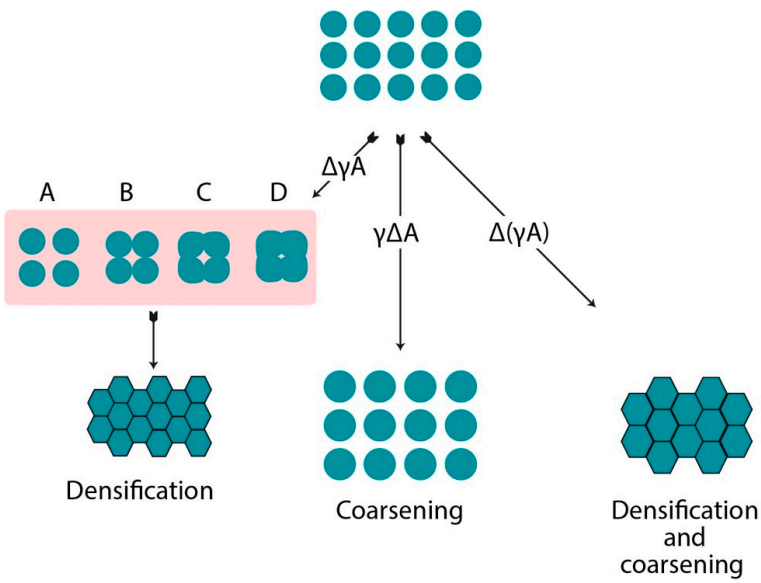

Figure 1. A basic phenomenon occurring during the sintering process.

3. Conventional Sintering

Conventional sintering is the simplest technique by which the green body is heated up to a defined temperature without applying any external pressure, as represented in Figure 2A. It is also known as the "pressure-less sintering" technique [31]. Considering the thermal instabilities of CaPs, conventional sintering possesses a major drawback in fabricating pure phases of CaPs. In addition to this, treatment at high temperatures for longer times makes the process expensive and energy intensive. Grain growth occurs simultaneously with the densification process. This takes place actively during the final stage of sintering and is promoted at elevated temperatures. In conventional sintering, extensive grain growth at higher temperatures compromises the mechanical properties and densification. Therefore, it has become the major hurdle in the development of CaP materials for bone tissue engineering applications. Significant efforts in the development of advanced sintering techniques to achieve phase purity and dense materials are elaborated in the following sections.

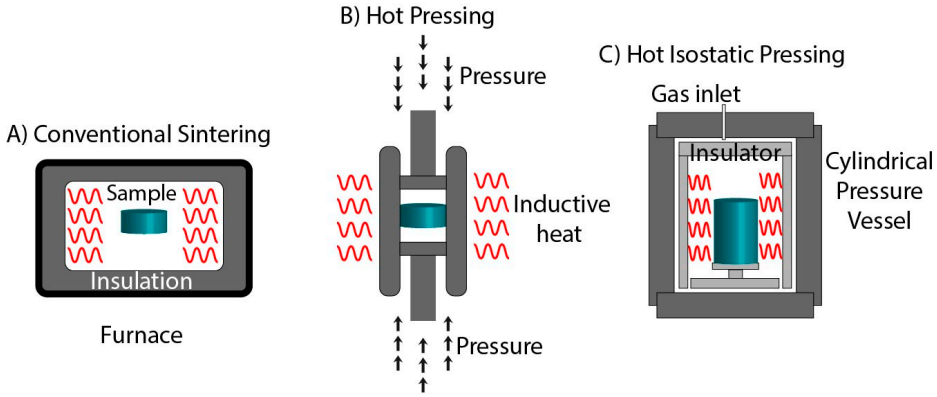

Figure 2. Schematic representation of (**A**) Conventional sintering, (**B**) Hot pressing, and (**C**) Hot Isostatic pressing.

3.1. Hot Pressing

Hot pressing (HP) is a sintering technique performed under the simultaneous application of heat and pressure [32]. As shown in Figure 2B, HP is committed to rigid graphite die by applying uniaxial pressure. The process is operated under a vacuum or protective atmosphere to avoid damage to the die. The uniaxial pressure delivers an extra driving force that elevates the sintering process by (a) increasing particle rearrangement in the initial stage, (b) accelerating the grain boundary sliding and diffusional creep in the intermediate and final stage, and (c) generating a surplus chemical potential and vacancy concentration gradient that promote mass transfer in the final stage [33]. Moreover, the friction resistance between the particles is reduced under heating and applied pressure to achieve dense packing. An external hydraulic system generates uniaxial pressure and radial pressure against the walls of the die [34]. The radial stress generated by applying pressure is given by the formula $(v/1-v)$, in which v is the effective Poisson's ratio. In the final stage of sintering, for nearly dense ceramics, v is equal to $1/2$, where the radial stress comes close to the applied pressure. These radial stresses result in the acceleration of an interparticle shear leading to the particle rearrangement and collapse of the large pores. Therefore, acceleration in the initial stage of sintering is due to the creation of more particle contact. Grain boundary sliding can be accomplished by viscous flow in liquid or creep flow in solid-state sintering assisted by hot pressing. In dense ceramics' gain, boundary sliding contributes to diffusional creep, assisting the pressure-aided sintering in the intermediate and final stages. Compared to conventional sintering, the consolidation of hydroxyapatite (HAp) by HP reveals a reduction in the temperature and holding time to

1100 °C and 30 min, respectively, under the pressure of 30 MPa [35]. Moreover, the addition of a sintering aid further reduces the requirement of a high temperature. Halouani et al. studied the effect of Na_3PO_4 on the densification of HAp by HP [36]. Results indicated that treatment at a temperature of 1000 °C within 30 min at a 20 MPa pressure results in a ceramic with a relative density of 97.5%. Compared to HP, in the absence of a sintering aid, the temperature requirement was increased to 1100 °C. Moreover, a drastic reduction in temperature was observed by combining hydrothermal synthesis with HP. HAp synthesized by hot hydrothermal pressing (HHP) required a temperature and pressure of 150 °C and 40 MPa, respectively, with a holding time of 6 h [37]. Moreover, a reduction in holding time to 3 h requires an increase in the pressure and temperature conditions up to 60 MPa and 200 °C, respectively [38].

3.2. Hot Isostatic Pressing

The hot isostatic pressing (HIP) technique utilizes the simultaneous application of isostatic pressure and heat for consolidation ceramics, as shown in Figure 2C. The primary factor that distinguishes HIP from other sintering techniques is the gas used for applying pressure in three dimensions to the material it surrounds [39]. For example, Argon gas heated to 1000 °C with 98 MPa of applied pressure results in higher heat transfer coefficients than conventional sintering. In HIP treatment, pressure, temperature, and time are the essential parameters that decide the density and mechanical properties of the product. The critical aspect of HIP is the isolation of the interface from applying pressure [40]. For sealing the contact area, the green body is encapsulated with thermally stable material. In HIP, heat is transferred through convection, and densification of the material occurs through particle rearrangement and plastic flow at the particle contact. This technique can work with up to 3000 °C and 200 MPa as the maximum temperature and pressure conditions [40]. Compared to uniaxial pressure in HP, isostatic pressure in HIP has flexibility in sintering samples having different shapes. One of the examples for the application of HIP is in the development of orthopedic implants, where fretting is observed due to potential degradation failure of the material [41]. Due to significant differences in the elastic modulus of two materials in contact, the shearing microenvironment occurs between the interface of the bone and implant. Fretting induces small groves and microgrooves in which the body fluid gets entrapped, leading to the corrosion of an implant. The oscillatory microenvironment at contact results in fatigue crack and wear, which cause early failure of the joint prosthesis [42]. Titanium (Ti) alloys are used as implants, but their biocompatibility and bioactivity are less than HAp. However, HAp is mechanically weak and cannot be used alone in load-bearing activities. Therefore, to overcome the drawback, HAp is coated on the implant surface [43]. HIP is extensively used for this process as it reduces the porosity and enhances ceramics' physical and mechanical properties while maintaining the shape of the implant. In 1994, Hero developed HP coating on titanium alloys. Consolidation of the coating by HIP at a temperature of 700–850 °C and pressure of 1000 bars for 35 min was conducted [44]. Furthermore, Fu and co-workers successfully developed HP-coated titanium implants. Results indicate that HIP treatment leads to the densification of ceramics while decreasing the fretting wear [42].

3.3. Spark Plasma Sintering

Spark Plasma sintering (SPS) is also known as pulsed electric current sintering (PECS) or the Field-assisted sintering technique (FAST). It utilizes uniaxial pressure and pulsed direct electric current (DC) under low atmospheric pressure or inert gases to densify ceramics [45]. In general, SPS consists of a mechanical loading system, an electric current generator, a water-cooling system, and a vacuum apparatus which allow rapid heating and cooling rates. The rapid heating rates favor particles' rearrangement, thus reducing the grain coarsening [46]. As shown in Figure 3A, SPS is a modification of the HP technique in which the application of the DC leads to Joule heating, achieving high heating rates of 1000 °C/min. The SPS system synchronizes both uniaxial pressure and the electric current

to consolidate the sample [47]. Moreover, the consolidation of materials is accelerated by the application of pressure [48]. SPS takes place in four stages. Initially, the powder compact is between the graphite die, and a vacuum is generated by removing the gas. Then, uniaxial pressure is applied to the die which contains the powder, followed by resistant heating of the die and finally cooling [49]. This results in the heating of the sample from outside and inside, leading to self-heating. This rapid increase in the temperature is governed by self-heating and does not rely on the external heating source [50]. This enables the processing of compacts without degrading their inherent properties. Grain coarsening can be prohibited by SPS more than conventional powder sintering [51]. SPS provides an advantage in processing materials with thermal instabilities such as calcium phosphates. Gu and co-workers utilized the advantage of SPS and successfully demonstrated the sintering of pure HAp. The consolidation was performed at a temperature and pressure of 950 °C and 30 MPa, respectively. Further, a pulsed electric discharge was applied at 25 V and 750 A for 30 s. The actual densification took place when DC was used. After holding the sample for 5 min at the desired temperature, the pressure was released, and the electric current was terminated; further cooling was performed at 100 °C/min. The XRD analysis showed no phase difference between pre-sintered and sintered samples, which states that the consolidation by SPS preserved the intrinsic nature of the material. The relative density of the sintered HAp was 99.6%, which resembled HAp ceramics that were conventionally sintered at 1100 °C for 1 h [25,52]. In another study, Kawagoe et al. utilized SPS for the fabrication of dense β-TCP. This sintering was performed in 10 min at a temperature ranging from 800 to 900 °C, under a uniaxial pressure of 60 MPa and heating rate of 25 °C/min. The XRD analysis of the sintered product did not show any secondary phase, which states that the original properties of the materials were preserved after sintering. β-TCP prepared at 800 °C, 900 °C, and 1000 °C had 70, 95, and 99% relative densities, respectively. Moreover, treatment at 1000°C led to an improved transparency of β-TCP [53]. Compared to HIP and the conventional sintering of β-TCP, a reduction in temperature, pressure, and time was observed when the sintering was conducted by SPS. [49]. Nanocrystalline apatite with a preserved hydrated layer is tough to sinter by the conventional technique. The generation of higher pressure (100 MPa) is required to limit the water elimination from the structure. Furthermore, the application of a higher pressure limits the temperature requirement to 150–200 °C. SPS has the potential to develop biomimetic apatite with a preserved hydrated layer [54].

3.4. Flash Spark Plasma Sintering

Flash Sintering (FS) is a technique in which an electric field is applied to produce a dense product by decreasing the sintering temperature. This technique differs from SPS as it involves a high electric field, a shorter sintering period, direct current flow through the specimen, and a lower furnace temperature. Three mechanisms are proposed for FS: (a) grain boundary diffusion and electrical conductivity are enriched due to Joule heating at grain boundaries; (b) there is an increase in Frenkel pair nucleation due to the applied field; and (c) there is a change in self-diffusion at the grain boundaries due to the non-linear field applied [55]. FS is the latest technique employed in the fabrication of dense materials. This technique falls under the domain of field-assisted sintering techniques (FAST), which utilize the voltage and current of FS, and the cell design is similar to SPS [56]. FS is an energy-efficient process that involves a short time of 1–60 s. It operates in two steps; initially, the specimen is heated by a conventional sintering process, and then the current is applied over the heated sample to achieve rapid sintering. Figure 3B shows the graphical representation of flash spark plasma sintering. This thermal profile enables heating rates ranging from 250 to 9726 °C/min, completing the sintering in a fraction of seconds [57]. The FS starts with a fine powder with a density ranging from 10 to 50 mW/mm^3. This technique was first used by Raj and co-workers who reported that the electric field retards the grain growth, resulting in an accelerated rate of sintering [58]. The consolidation of HA by FS was studied by Hwang and Yun. The powder compact was prepared by applying

uniaxial pressure, followed by drilling two holes of a diameter of 1 mm. A platinum wire was hooked in the two holes, and contact resistance was avoided by sealing the holes by platinum paste. Further, the furnace was heated to 900 °C at a heating rate of 10 °C/min, followed by an application of an electric field over the heated sample. The occurrence of flash was detected in the range of a 925–1200 °C temperature and 500–1200 V/cm electric field. The XRD analysis of the sintered samples indicated the presence of pure HAp. The relative density of the FS samples that were sintered for 10 s at 1051 °C was compared with the samples that were conventionally sintered at 1192 °C for 5 min. The relative density of FS samples was superior to conventionally sintered samples. Studies also revealed that sintering in a vacuum was more beneficial than in air. At elevated temperatures, the dehydration of HAp leads to the generation of hydroxyl or hydrogen type defects, leading to an increase in the electric current during FS [59]. In conventional sintering, a higher temperature initiates the transition of the β phase to the α phase of TCP. This conversion follows first-order kinetics, which is controlled by a high activation energy. Therefore, the reconversion of α→β-TCP is kinetically inhibited on cooling, giving rise to a metastable α-TCP [60]. In conventional sintering, the conversion of β→α and α→α′ occurs at 1125 °C and 1470 °C, respectively [61]. To overcome this drawback, Frasnelli and Sglavo utilized FS for the consolidation of pure β-TCP without a transition to the α-TCP phase. The consolidation process was carried out in a horizontal loading dilatometer in which the axes of the green body were aligned to the Al_2O_3 boat with a constant heating rate of 20 °C/min. At the contact of the base surface of the sample, Pt-Rh electrodes were placed and connected to the DC supply. Further, the silver paste was applied to enhance electrical conductivity. The current was limited to 100 mA for less than 5 min. For comparison, the samples were also consolidated by conventional sintering at the same heating rate up to 1500 °C. Results suggested that FS requires less processing time as well as a lower temperature to achieve considerable shrinkage and avoid the β→α transition of TCP. Dense β-TCP was obtained at a temperature of 1000 °C in a few minutes [62].

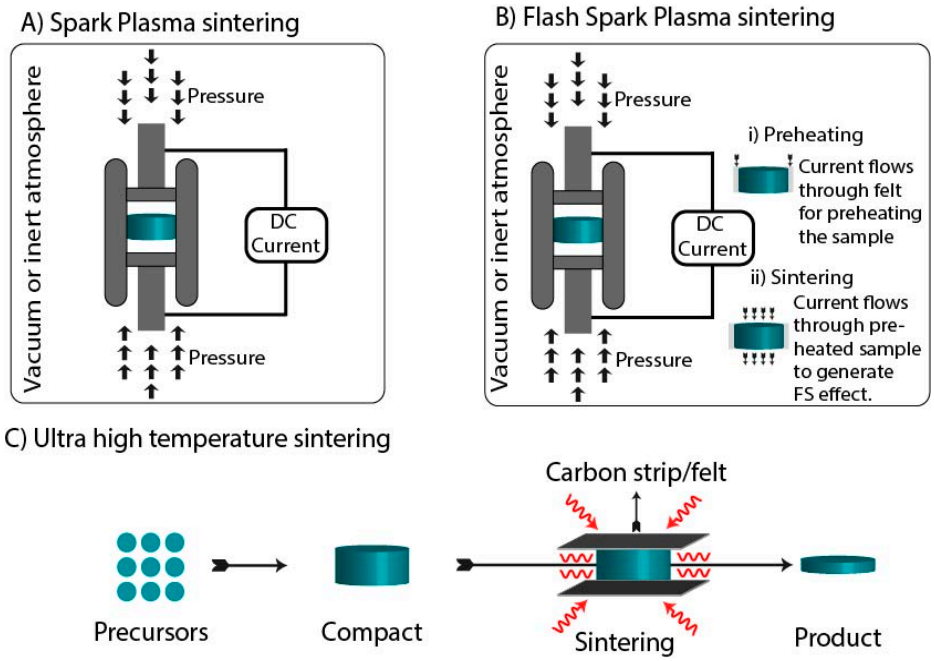

Figure 3. Schematic representation of (**A**) Spark Plasma sintering, (**B**) Flash spark plasma sintering, and (**C**) Ultrafast high-temperature sintering.

3.5. Ultrafast High-Temperature Sintering

Ultrafast high-temperature sintering (UHS) is performed under a uniform high sintering temperature (up to 3000 °C) under high heating (10^3–10^4 °C/min) and cooling rates (10^4 °C/min). The ultrafast temperature and heating rates enable rapid sintering (~10 s). UHS was first reported in 2020 by Wang et al., for the synthesis of Tantalum-doped $Li_{6.5}La_3Zr_{1.5}Ta_{0.5}O_{12}$. In this study, the green body was sandwiched between Joule-heating carbon strips, which were rapidly heated by conduction and radiation, forming a uniform heating environment shown in Figure 3C [63]. Compared to microwave and spark plasma sintering, UHS required a simple setup, allowing for the consolidation of complex geometries. Pure phase β or α-TCP are tough to synthesize due to their thermal instabilities [21]. Biesuz et al. reported the successful synthesis of pure phase TCP by sintering calcium deficient hydroxyapatite (CDHA). Results indicated that CDHA transforms to polymorphs of TCP depending on the application of the current. The sample treated with 20–25A converted to β-TCP, whereas α-TCP was formed when more than a 30A current was applied. Depending upon the current application, the temperature is influenced, leading to different polymorphs of TCP. These observations suggested that by the application of UHS, it is possible to fabricate a single phasic TCP [24].

3.6. Microwave Sintering

Electromagnetic radiation in the range of 300 MHz to 300 GHz is termed microwaves. They are mainly used for telecommunication and heating purposes [64]. Based on electrical and magnetic properties, materials are classified into transparent, opaque, and absorbing [65]. The most crucial parameter for any material to interact with microwaves is permittivity or permeability. Microwave sintering (MWS) is a relatively new approach to sintering which differs from conventional sintering by the nature of the heat transfer as shown in Figure 4A. In conventional sintering, the heat is transferred to materials from the surface to the core, while in MWS, the process occurs through several physical mechanisms such as resistive heating, bipolar rotation, and electromagnetic and dielectric heating. One or more mechanisms can be attributed to the response to the incoming radiation depending on the material [66]. When microwaves penetrate through the material, the electromagnetic waves stimulate motion in free and bound charges and dipoles. The natural equilibrium of the material resists the motion due to frictional, inertial, and elastic forces, which cause the dissipation of energies. This leads to an attenuation of the electric field associated with microwaves, and heating of the material occurs [67]. Therefore, MWS is categorized as a non-conventional technique of sintering. It is a fast, reliable, and user-friendly technique, with the significant advantage of higher heating rates, lower energy consumption, and lower cost. Hong Sung and associates studied the kinetic mechanism of MWS in ceramic materials and stated that the densification mechanism in MW is different from that of conventional sintering. Their model indicates that the MWS shrinkage rate is proportional to $t^{2/3}$, whereas the traditional shrinkage of the sintering rate is proportional to $t^{2/5}$, revealing that MWS is faster than conventional sintering [68]. Utilizing the advantages, Fang and co-workers studied the effect of MWS on the densification of hydroxyapatite (HAp). The experiment was performed in a 500 W microwave in which the specimen was sintered at temperatures ranging from 1200 to 1300 °C for different time points of 5, 10, and 20 min, respectively. The HAp pellets attained a density of 97% after sintering for 10 min. Compared to the convention sintering, MW consumed less energy and offered a dense structure, with a finer grain size and improved mechanical strength [69]. The consolidation of TCP by MWS was performed by Mirhadi. The green body was heated to the three different temperatures of 900 °C, 1000 °C, and 1100 °C, respectively, at a 20 °C/min heating rate. The XRD analysis of the sintered body revealed the presence of a pure β-TCP phase. The relative density of samples treated at 1100°C was found to be 98%, whereas the relative density of 81% was observed when samples were treated at the same temperature by conventional sintering for 2 h [70].

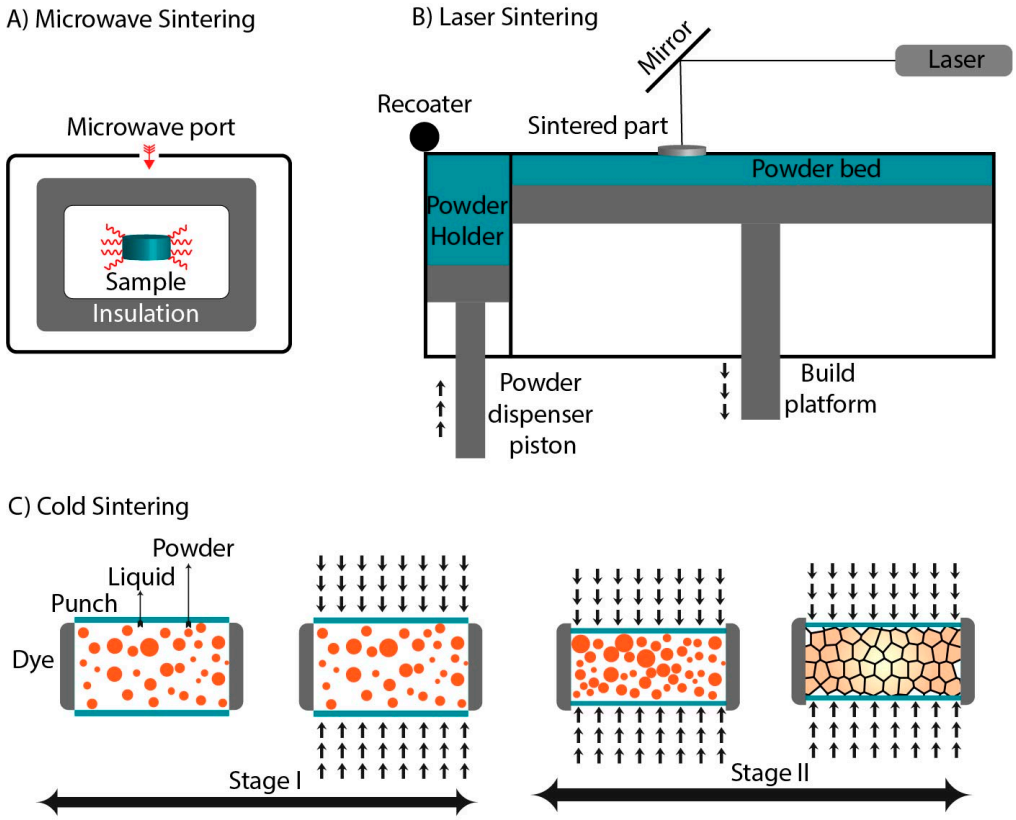

Figure 4. Schematic representation of (**A**) Microwave sintering, (**B**) Laser sintering, and (**C**) Cold sintering.

3.7. Laser Sintering

Laser sintering (LS), also known as selective laser sintering, was developed by Carl Deckard in 1980 [71]. It is an additive manufacturing technique that utilizes a high-power laser to fuse small particles of material layer-by-layer to form a component of a defined architecture. Industries widely accept this technique to fabricate complex parts in a single operation [72]. The LS system consists of a laser source, powder recharging system, building platform, and gas flow controller as shown in Figure 4B [73]. The process is governed by computer-aided manufacturing (CAM). Depending on the photon absorption characteristics of the materials, two types of lasers are used in LS, a continuous wave CO_2 laser (10.6 μm) and a yttrium fiber laser (1064 nm) [74]. The LS process begins with converting 3D CAD data into slices of STL files fed to the machine. Depending on the architecture of the STL file, the computer controls the scanning track of the laser. Subsequently, the sample is heated up just below the melting point of the material. The high-energy laser beam is guided by the CAD/CAM design to fuse the powder in a layer-by-layer pattern. After treating each layer, the powder bed is lowered by one layer of thickness, and fresh powder is rolled over the platform [75]. Both the rapid heating of the powder and cooling of melts occur when the laser moves quickly over the powder. Therefore, LS can be termed as a "high power density short interaction time" process. The melting/solidification approach is the mechanism of densification, following first-order kinetics. The laser energy input and powder characteristics play a significant role in densification kinetics. A higher sintering rate is observed in finer particles, as they possess

a higher surface area which provides more energy absorbed from the laser [76]. Ceramic compounds have very high melting points; therefore, the energy inputs are very high. A continuous-wave CO_2 laser has a high-energy beam that is absorbed by most of the ceramics [77]. LS can be performed directly. In this case, the laser is used to consolidate powder locally, and in the indirect mode, a sintering agent is deployed to enhance the densification. Qin and associates performed experiments for the development of tetra tricalcium phosphate (TTCaP) scaffold by selective LS. The parameters were as follows: laser power was varied from 6 to 10 W; the laser beam diameter was 1 mm; the line scanning speed was kept to 60 mm/s; the layer thickness was 0.1 mm; and the laser line thickness was 2 mm. Results indicate that only a few particles melted and fused at a laser power of 6 W due to insufficient energy. By increasing the laser power to 7 W and 8 W, more particles were fused, reducing the micro gaps. At a further increase in laser power to 9 W and 10 W, a compact structure was obtained without micro gaps. The XRD analysis of the sintered sample at a 9 W laser power shows a pure phase of TTCP without any impurities [78]. Bulina et al. studied the laser sintering of HAp, and a CO_2 laser was used at 4 W with a spot size of 0.2 mm and scanning speed of 640 mm/s. The fast-heating rates lead to the melting of HAp in the air without decomposition, which results in dense HAp with a preferential orientation in the c-axis. The XRD analysis showed a minor presence of β-TCP, which occurs because of very high heating [79]. Qingxi and co-workers attempted to sinter β-TCP by LS in which additives such as epoxy and nylon for the adhesion of β-TCP were used. The composite was formed by the physical mixing of additives with β-TCP. LS was performed at room temperature with a laser power of 11 W with a 0.15 focused diameter and scanning speed of 2400 mm/s, and a layer thickness of 0.1 mm. After that, the specimen was treated at 600 °C and further sintered at 1100 °C for 3 h to rid the specimen of binders. The XRD analysis of the treated samples matches with the standard β-TCP phase and shows the presence of HAp and α-TCP [80].

3.8. Cold Sintering

Cold sintering (CS) is a new technique that utilizes low temperatures (up to 300 °C) to consolidate ceramic powders. All the other densification techniques discussed above require higher temperatures for densification of the material. This not only reduces the energy needed but also allows for the consolidation of heat-sensitive materials and composites, which cannot be sintered using other techniques [81]. CS has opened new horizons for the sintering of hybrid materials such as organic/inorganic components. In 2016, Guo and co-workers demonstrated the CS process for the first time; since then, it has attracted many researchers [82]. CS is a pressure-assisted method carried out in the presence of a transient liquid. The process is performed either at room temperature or an elevated temperature up to 300 °C, depending on the boiling point of the liquid. Typically, in CS, uniaxial pressure is applied to powder/liquid mixtures [83]. Densification of the powder is driven by a dissolution and reprecipitation process coupled with Oswald ripening and a recrystallization phenomenon [84]. CS takes place in two stages, as shown in Figure 4C. In the first stage, the application of pressure to the liquid medium generates isostatic pressure (irrespective of the pressure applied uniaxially or isostatically), leading to four main phenomena: (a) initially, the material is partially dissolved in a liquid medium; (b) Ostwald ripening increases the average particle size; (c) recrystallization may occur (the formation of new crystals or phases in the liquid); and (d) drying is initiated. Based on drying, the uniaxial CS and isostatic CS are different. Dying in uniaxial CS takes place through the gap clearance; conversely, samples must be withdrawn from the press for drying in the isostatic CS. After that, the second stage starts, where solid particles make contact and give rise to a rigid framework. Three phenomena take place: (a) particle rearrangement, (b) solvent evaporation, and (c) precipitation. In addition to this, if pressure is maintained in stage II, the fourth phenomenon occurs; sintering leads to mass transfer and particle shape modification [85]. A recent development in CS occurred, resulting in the densification of materials which was not possible by other techniques. Amorphous calcium phosphate

(ACP) is challenging to sinter because of its unique hydrated structure and conversion to TCP or HAp at higher temperatures. Owing to the advantage of sintering samples at low temperatures, Rubenis et al. employed CS to densify ACP. The powder (ACP) was moistened with 0.1 mL of deionized water before pressing to study the effect of the transient liquid on CS. Further, a uniaxial pressure of 500 MPa was applied to the powder and sintered at room temperature, 100 °C, 120 °C, and 150 °C, respectively, with a holding time of 30 min. The XRD analysis revealed that the amorphous state was retained at room temperature, 100 °C, 120 °C when ACP was in a dry state. In contrast, in the moistened form, only treatment at room temperature retained the amorphous state. A further increase in temperature leads to the conversion of the amorphous state to crystalline. A relative density of ~76%, ~79%, ~76%, and ~85% was obtained when the sintering was performed at room temperature, 100 °C, 120 °C, and 150 °C, respectively [86]. Hassan, Akmal, and Ryu investigated the effect of vacuum-oven-dried HAp (110 °C) and calcinated HAp powder (1000 °C) on CS. The experiment was performed at a pressure of 500 MPa at 200 °C. Post sintering, the relative density of 98.8% was achieved, and the XRD analysis revealed a pure phase of apatite. The chemical-mechanical phenomenon drives low-temperature sintering. Therefore, the stoichiometry and the mechanical properties were not influenced by CS [87]. Owing to the advantage of the low-temperature processing of CS, it can effectively be used in the fabrication of organic/inorganic composites for bone tissue engineering.

4. Discussion

CaPs are the integral component of tissue engineering. The sintering of CaPs is vital to achieve desired mechanical properties. However, CDHA transforms to β-TCP or a biphasic β-TCP/HAp mixture below 1000 °C, whereas β-TCP is converted to α-TCP around 1125 °C, and a further increase in temperature leads to the formation of α′-TCP (1470 °C). Similar effects are observed when ACP and HAp are treated at very high temperatures for a long time. Moreover, a transformation of β→α-TCP at a higher temperature and holding time leads to volume expansion, thus hampering the densification process. Innovative technologies utilized various parameters, shown in Table 3, to overcome the limitations of conventional sintering. These techniques include HP, HIP, CS, MW, SPS, LS, UHS, and FS. CS, SPS, and FS are not capable of sintering structures with complex architectures, whereas MW, LS, HIP allow the sintering of structures with complex architectures.

Table 3. Parameters of various sintering techniques.

Technique	Temperature	Pressure	Current	Electromagnetic Radiations
Conventional sintering	✓	x	x	x
Hot Pressing	✓	✓	x	x
Hot Isostatic Pressing	✓	✓	x	x
Spark Plasma sintering	✓	✓	✓	x
Flash Spark Plasma sintering	✓	✓	✓	x
Ultrafast high-temperature sintering	✓	x	✓	x
Microwave sintering	✓	x	x	✓
Laser Sintering	✓	x	x	✓
Cold sintering	✓	✓	x	x

The instrumental setup of conventional sintering is relatively simple and allows for the sintering of a large number of samples simultaneously. However, the high-temperature

requirement and long holding time make the operation very expensive and time-consuming. The major advantages of conventional sintering are scalability and the ability to process a large number of samples. The pressure-assisted sintering techniques reduce the sintering time by accelerating the rate of mass transfer. This approach differs in the stress state during density which influences particle sliding and the change in dimension. The rate of densification and shrinkage is governed by the application of pressure [88]. Moreover, grain growth is inhibited by decreasing diffusivity and thus grain boundary mobility. The applied pressure is independent of the particle size, whereas the intrinsic sintering pressure increases when the particle size is reduced [89]. The power creep law is an effective mechanism of densification in pressure-assisted sintering [90]. This confirms that with pressure, densification of the material requires a temperature and time lower than conventional sintering. The techniques falling under pressure-assisted sintering are HP, HIP, SPS, FS, and CS. This advancement enabled the fabrication of pure dense materials, for example, the fabrication of dense ACP by CS, pure β-TCP by SPS and FS, which is not possible by conventional sintering. In addition, this advancement led to this considerable reduction in sintering time from hours to minutes. A significant limitation of pressure-assisted sintering techniques is dealing with a sample of industrial-relevant sizes. As the sample size increases, the requirement for equipment size and electric consumption also increases, making the process expensive. Furthermore, in SPS and FS, increases in the sample diameter elevate the current requirement for a high heating rate beyond 100 °C/min. Moreover, the increased need for achieving a high temperature and high heating rates makes the process more expensive on an industrial scale [49].

Field-assisted sintering technologies (FAST) utilize an electric current with a synergy of temperature and pressure. The application of an electric current provides a uniform temperature gradient and additional mass transfer, reducing the time and temperature requirements. The techniques that fall under FAST are SPS, FS, and UHS. The sintering time by these techniques ranges from minutes to seconds. MW and LS are two classes of sintering that utilize electromagnetic radiation for heat transfers. This creates higher heating rates and a uniform heat distribution that accelerates the densification process. They also have the potential to consolidate materials with complex architectures. Due to the non-uniformity of the laser route, the heat formation is non-homogenous, and the limitation of the laser diameter does not allow for the fabrication of objects with exemplary architectures. Compared to conventional sintering, MW and LS have very sophisticated instrumentation, which makes the entire process expensive. Though there are few limitations to the advanced sintering techniques, they can potentially sinter pure CaP compounds that can be effectively incorporated in tissue engineering applications.

5. Summary and Concluding Remarks

Sintering is a thermal process in which loosely bound particles are converted into a consistent solid mass under the influence of heat and/or pressure without melting the particles. During this process, grain growth and densification occur simultaneously. Typically, this is observed in the last stage of the sintering process and is promoted by high temperatures. Densification of CaP ceramics by conventional sintering is an energy-intensive and time-consuming operation. Due to the thermal instability of CaP, treatment at a high temperature for a long time leads to the formation of secondary phases. Furthermore, it also results in excessive grain growth that obstructs the densification process. To overcome these drawbacks, substantial efforts have been dedicated to developing innovative sintering techniques. These techniques utilize temperature in synergy with one or more parameters such as external pressure, radiation, electric current, the incorporation of transient liquid, etc. This accelerates the mass transfer, and therefore a considerable reduction in temperature and time is observed. A comparative analysis of the time and temperature required by advanced sintering techniques and conventional sintering is shown in Figure 5. This indicates that advanced sintering techniques considerably reduce temperature and time requirements. These techniques perform exceptionally well on a small scale, but the translation

to the industrial scale remains a challenge. Apart from these minor limitations, advanced sintering techniques have potential in the development of organic/inorganic composites and pure phases of CaP that was not possible by conventional sintering. This advancement has opened new doors in the development of pure materials for bone tissue regeneration.

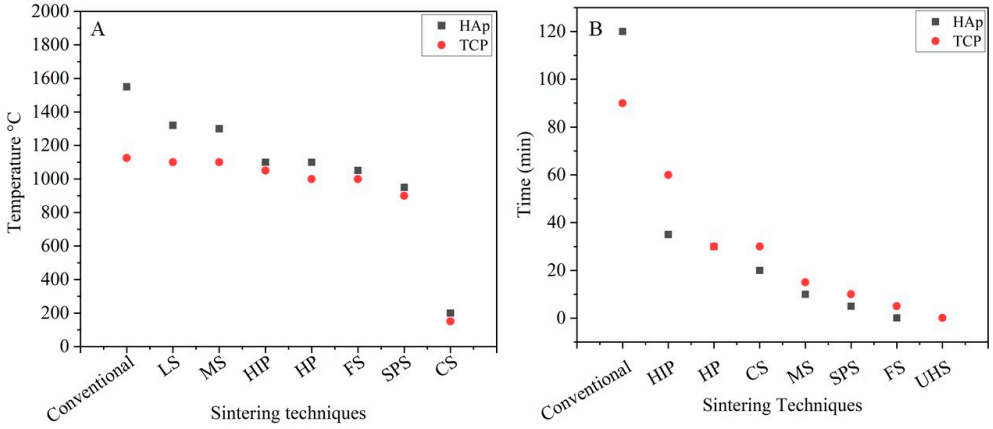

Figure 5. Comparison of sintering (**A**) temperature and (**B**) time required for conventional and advanced sintering techniques.

Author Contributions: Conceptualization and methodology, A.I. and J.L.; writing—original draft preparation, A.I. and R.C.; Images, A.I.; supervision, R.C., K.R. and J.L.; review and editing, K.R. and J.L. All authors have read and agreed to the published version of the manuscript.

Funding: This research was funded by the European Union's Horizon 2020 research and innovation program under grant agreement No 857287 and the European Regional Development Fund within the Activity 1.1.1.2 "Post-doctoral Research Aid" of the Specific Aid Objective 1.1.1 "To increase the research and innovative capacity of scientific institutions of Latvia and the ability to attract external financing, investing in human resources and infrastructure" of the Operational Program "Growth and Employment" (No.1.1.1.2/VIAA/2/18/318).

Conflicts of Interest: The authors declare no conflict of interest.

Abbreviations

CaP	Calcium Phosphate
HAp	Hydroxyapatite
TTCaP	Tetra-calcium phosphate
α-TCP	Alpha-tricalcium phosphate
β-TCP	Beta-tricalcium phosphate
OCP	Octa-calcium Phosphate
ACP	Amorphous calcium phosphate
DCPD	Dicalcium Phosphate dihydrate
CDHA	Calcium deficient hydroxyapatite
XRD	X-ray diffraction
SSA	Specific surface area
MPa	Mega Pascal
HP	Hot pressing
HIP	Hot isostatic pressing
SPS	Spark Plasma sintering
PECS	Pulsed electric current sintering
FAST	Field-assisted sintering technique

DC	Direct current
FS	Flash sintering
UHS	Ultrafast high-temperature sintering
MW	Microwave
MWS	Microwave sintering
LS	Laser sintering
CAM	Computer-aided manufacturing
CAD	Computer-aided design
3D	Three dimension
CS	Cold sintering

References

1. German, R.M. The Emergence of Quantitative Sintering Theory from 1945 to 1955. *JOM* **2017**, *69*, 630–634. [CrossRef]
2. Exner, H.; Arzt, E. Sintering Processes. In *Physical Metallurgy*; Elsevier: North Holland, The Netherlands, 1996; pp. 2627–2662. ISBN 9780444898753. [CrossRef]
3. Kang, S.-J.L. Sintering Processes: Densification, Grain Growth and Microstructure. In *Sintering*; Butterworth-Heinemann: Oxford, UK, 2005; pp. 3–8. [CrossRef]
4. Zimina, A.; Senatov, F.; Choudhary, R.; Kolesnikov, E.; Anisimova, N.; Kiselevskiy, M.; Orlova, P.; Strukova, N.; Generalova, M.; Manskikh, V.; et al. Biocompatibility and Physico-Chemical Properties of Highly Porous PLA/HA Scaffolds for Bone Reconstruction. *Polymers* **2020**, *12*, 2938. [CrossRef]
5. He, Z.; Zhai, Q.; Hu, M.; Cao, C.; Wang, J.; Yang, H.; Li, B. Bone cements for percutaneous vertebroplasty and balloon kyphoplasty: Current status and future developments. *J. Orthop. Transl.* **2015**, *3*, 1–11. [CrossRef]
6. LeGeros, R.Z. Calcium Phosphate-Based Osteoinductive Materials. *Chem. Rev.* **2008**, *108*, 4742–4753. [CrossRef]
7. De Sant'Anna, G.R.; Dos Santos, E.A.P.; Soares, L.E.S.; Santo, A.M.D.E.; Martin, A.; Duarte, D.A.; Pacheco-Soares, C.; Brugnera, A. Dental Enamel Irradiated with Infrared Diode Laser and Photo-Absorbing Cream: Part 2—EDX Study. *Photomed. Laser Surg.* **2009**, *27*, 771–782. [CrossRef]
8. Dorozhkin, S.V. Calcium orthophosphates ($CaPO_4$): Occurrence and properties. *Prog. Biomater.* **2016**, *5*, 9–70. [CrossRef]
9. Chow, L.C. Next generation calcium phosphate-based biomaterials. *Dent. Mater. J.* **2009**, *28*, 1–10. [CrossRef]
10. Thomas, S.; Harshita; Mishra, P.K.; Talegaonkar, S. Ceramic Nanoparticles: Fabrication Methods and Applications in Drug Delivery. *Curr. Pharm. Des.* **2015**, *21*, 6165–6188. [CrossRef]
11. Nikolenko, M.V.; Vasylenko, K.V.; Myrhorodska, V.D.; Kostyniuk, A.; Likozar, B. Synthesis of Calcium Orthophosphates by Chemical Precipitation in Aqueous Solutions: The Effect of the Acidity, Ca/P Molar Ratio, and Temperature on the Phase Composition and Solubility of Precipitates. *Processes* **2020**, *8*, 1009. [CrossRef]
12. Tung, M.S. Calcium Phosphates: Structure, Composition, Solubility, and Stability. In *Calcium Phosphates in Biological and Industrial Systems*; Springer: Boston, MA, USA, 1998; pp. 1–19. [CrossRef]
13. Dorozhkin, S.V. Calcium Orthophosphates in Nature, Biology and Medicine. *Materials* **2009**, *2*, 399–498. [CrossRef]
14. Moseke, C.; Gbureck, U. Tetracalcium phosphate: Synthesis, properties and biomedical applications. *Acta Biomater.* **2010**, *6*, 3815–3823. [CrossRef]
15. Samavedi, S.; Whittington, A.; Goldstein, A.S. Calcium phosphate ceramics in bone tissue engineering: A review of properties and their influence on cell behavior. *Acta Biomater.* **2013**, *9*, 8037–8045. [CrossRef]
16. Graça, M.P.F.; Gavinho, S.R. Calcium Phosphate Cements in Tissue Engineering. In *Contemporary Topics about Phosphorus in Biology and Materials*; IntechOpen: London, UK, 2020. [CrossRef]
17. Canillas, M.; Pena, P.; de Aza, A.H.; Rodríguez, M.A. Calcium phosphates for biomedical applications. *Boletín Soc. Española Cerámica y Vidr.* **2017**, *56*, 91–112. [CrossRef]
18. Jeong, J.; Kim, J.H.; Shim, J.H.; Hwang, N.S.; Heo, C.Y. Bioactive calcium phosphate materials and applications in bone regeneration. *Biomater. Res.* **2019**, *23*, 4. [CrossRef]
19. Lane, J.M.; Mait, J.E.; Unnanuntana, A.; Hirsch, B.P.; Shaffer, A.D.; Shonuga, O.A. Materials in Fracture Fixation. *Compr. Biomater.* **2011**, *6*, 219–235. [CrossRef]
20. Huang, J. Design and Development of Ceramics and Glasses. In *Biology and Engineering of Stem Cell Niches*; Elsevier: Cambridge, MA, USA, 2017; pp. 315–329. [CrossRef]
21. Ryu, H.-S.; Hong, K.S.; Lee, J.-K.; Kim, D.J.; Lee, J.H.; Chang, B.-S.; Lee, D.-H.; Lee, C.-K.; Chung, S.-S. Magnesia-doped HA/β-TCP ceramics and evaluation of their biocompatibility. *Biomaterials* **2004**, *25*, 393–401. [CrossRef]
22. Duncan, J.; Macdonald, J.F.; Hanna, J.V.; Shirosaki, Y.; Hayakawa, S.; Osaka, A.; Skakle, J.M.; Gibson, I. The role of the chemical composition of monetite on the synthesis and properties of α-tricalcium phosphate. *Mater. Sci. Eng. C* **2014**, *34*, 123–129. [CrossRef] [PubMed]
23. Eanes, E.D. Thermochemical studies on amorphous calcium phosphate. *Calcif. Tissue Int.* **1970**, *5*, 133–145. [CrossRef]
24. Biesuz, M.; Galotta, A.; Motta, A.; Kermani, M.; Grasso, S.; Vontorová, J.; Tyrpekl, V.; Vilémová, M.; Sglavo, V.M. Speedy bioceramics: Rapid densification of tricalcium phosphate by ultrafast high-temperature sintering. *Mater. Sci. Eng. C* **2021**, *127*, 112246. [CrossRef] [PubMed]

25. Gu, Y.; Loh, N.; Khor, K.; Tor, S.; Cheang, P. Spark plasma sintering of hydroxyapatite powders. *Biomaterials* **2002**, *23*, 37–43. [CrossRef]
26. Walker, P.; Tarn, W.H. *Handbook of Metal Etchants*; CRC Press: Boca Raton, FL, USA, 1990.
27. German, R. Sintering. In *Encyclopedia of Materials: Science and Technology*; Elsevier: Oxford, UK, 2001; pp. 8641–8643. [CrossRef]
28. Pask, J.A. Thermodynamics and Mechanisms of Sintering. Available online: https://escholarship.org/content/qt67t140k9/qt67t140k9.pdf (accessed on 29 September 2021).
29. Champion, E. Sintering of calcium phosphate bioceramics. *Acta Biomater.* **2013**, *9*, 5855–5875. [CrossRef]
30. Salem, S.; Salem, A. Mechanisms of Momentum Transport in Viscous Flow Sintering. In *Sintering Applications*; IntechOpen: London, UK, 2013.
31. Terwilliger, G.R.; Lange, F.F. Pressureless sintering of Si_3N_4. *J. Mater. Sci.* **1975**, *10*, 1169–1174. [CrossRef]
32. Ramakumar, S.; Deviannapoorani, C.; Dhivya, L.; Shankar, L.S.; Murugan, R. Lithium garnets: Synthesis, structure, Li^+ conductivity, Li^+ dynamics and applications. *Prog. Mater. Sci.* **2017**, *88*, 325–411. [CrossRef]
33. Nygren, M.; Shen, Z. Hot Pressing and Spark Plasma Sintering. In *Ceramics Science and Technology*; Wiley-VCH: Weinheim, Germany, 2012; pp. 189–214. ISBN 9783527311576.
34. Hostaša, J. Ceramics for Laser Technologies. In *Encyclopedia of Materials: Technical Ceramics and Glasses*; Elsevier: Amsterdam, The Netherlands, 2021; pp. 110–124.
35. Petrakova, N.V.; Lysenkov, A.S.; Ashmarin, A.A.; Egorov, A.A.; Fedotov, A.Y.; Shvorneva, L.I.; Komlev, V.S.; Barinov, S.M. Effect of hot pressing temperature on the microstructure and strength of hydroxyapatite ceramic. *Inorg. Mater. Appl. Res.* **2013**, *4*, 362–367. [CrossRef]
36. Halouani, R.; Bernache-Assolant, D.; Champion, E.; Ababou, A. Microstructure and related mechanical properties of hot pressed hydroxyapatite ceramics. *J. Mater. Sci. Mater. Electron.* **1994**, *5*, 563–568. [CrossRef]
37. Hosoi, K.; Hashida, T.; Takahashi, H.; Yamasaki, N.; Korenaga, T. New Processing Technique for Hydroxyapatite Ceramics by the Hydrothermal Hot-Pressing Method. *J. Am. Ceram. Soc.* **2005**, *79*, 2771–2774. [CrossRef]
38. Yanagisawa, K.; Zhu, K.; Fujino, T.; Onda, A.; Kajiyoshi, K.; Ioku, K. Preparation of Hydroxyapatite Ceramics by Hydrothermal Hot-Pressing Technique. *Key Eng. Mater.* **2006**, *309–311*, 57–60. [CrossRef]
39. Brook, R.J.; Cahn, R.W.; Bever, M.B. *Concise Encyclopedia of Advanced Ceramic Materials*; Elsevier: Oxford, UK, 1991.
40. Technologies and Applications | | KOBE STEEL, Ltd. Available online: https://www.kobelco.co.jp/english/products/ip/technology/hip.html (accessed on 16 January 2021).
41. Olmedo, D.G.; Tasat, D.R.; Duffó, G.; Guglielmotti, M.B.; Cabrini, R.L. The issue of corrosion in dental implants: A review. *Acta Odontol Lat.* **2009**, *22*, 3–9.
42. Fu, Y.; Batchelor, A.W.; Khori, K.A. Hot Isostatic Pressing of Hydroxyapatite Coating for Improved Fretting Wear Resistance. *J. Mater. Sci. Lett.* **1998**, *17*, 1695–1696. [CrossRef]
43. Harun, W.S.W.; Asri, R.I.M.; Sulong, A.B.; Ghani, S.A.C.; Ghazalli, Z. Hydroxyapatite-Based Coating on Biomedical Implant. In *Hydroxyapatite-Advances in Composite Nanomaterials, Biomedical Applications and Its Technological Facets*; IntechOpen: Rijeka, Croatia, 2018; pp. 69–88.
44. Bose, S.; Tarafder, S.; Bandyopadhyay, A. Hydroxyapatite coatings for metallic implants. In *Hydroxyapatite (HAp) for Biomedical Applications*; Woodhead Publishing: Cambridge, UK, 2015; pp. 143–157.
45. Suárez, M.; Fernández, A.; Menéndez, J.L.; Torrecillas, R.; Kessel, H.U.; Hennicke, J.; Kirchner, R.; Kessel, T. Challenges and Opportunities for Spark Plasma Sintering: A Key Technology for a New Generation of Materials. In *Sintering Applications*; IntechOpen: Rijeka, Croatia, 2013.
46. Wang, L.; Pouchly, V.; Maca, K.; Shen, Z.; Xiong, Y. Intensive particle rearrangement in the early stage of spark plasma sintering process. *J. Asian Ceram. Soc.* **2015**, *3*, 183–187. [CrossRef]
47. Hu, Z.-Y.; Zhang, Z.-H.; Cheng, X.-W.; Wang, F.-C.; Zhang, Y.-F.; Li, S.-L. A review of multi-physical fields induced phenomena and effects in spark plasma sintering: Fundamentals and applications. *Mater. Des.* **2020**, *191*, 108662. [CrossRef]
48. Zhou, M.; Ren, L.; Quan, G.; Gupta, M. Solid Phase Processing of Metal Matrix Composites. In *Encyclopedia of Materials: Composites*; Elsevier: Amsterdam, The Netherlands, 2021; pp. 173–196. [CrossRef]
49. Cavaliere, P.; Sadeghi, B.; Shabani, A. Spark Plasma Sintering: Process Fundamentals. In *Spark Plasma Sintering of Materials: Advances in Processing and Applications*; Cavaliere, P., Ed.; Springer: Cham, Switzerland, 2019; pp. 3–20. [CrossRef]
50. Leriche, A.; Cambier, F.; Hampshire, S. Sintering of Ceramics. In *Reference Module in Materials Science and Materials Engineering*; Elsevier: Amsterdam, The Netherlands, 2017. [CrossRef]
51. Pazhouhanfar, Y.; Delbari, S.A.; Asl, M.S.; Shaddel, S.; Pazhouhanfar, M.; Van Le, Q.; Shokouhimehr, M.; Mohammadi, M.; Namini, A.S. Characterization of spark plasma sintered TiC–Si3N4 ceramics. *Int. J. Refract. Met. Hard Mater.* **2021**, *95*, 105444. [CrossRef]
52. Jarcho, M.; Bolen, C.H.; Thomas, M.B.; Bobick, J.; Kay, J.F.; Doremus, R.H. Hydroxylapatite synthesis and characterization in dense polycrystalline form. *J. Mater. Sci.* **1976**, *11*, 2027–2035. [CrossRef]
53. Kawagoe, D.; Ioku, K.; Fujimori, H.; Goto, S. Transparent. BETA.-Tricalcium Phosphate Ceramics Prepared by Spark Plasma Sintering. *J. Ceram. Soc. Jpn.* **2004**, *112*, 462–463. [CrossRef]

54. Grossin, D.; Rollin-Martinet, S.; Estournès, C.; Rossignol, F.; Champion, E.; Combes, C.; Rey, C.; Geoffroy, C.; Drouet, C. Biomimetic apatite sintered at very low temperature by spark plasma sintering: Physico-chemistry and microstructure aspects. *Acta Biomater.* **2010**, *6*, 577–585. [CrossRef] [PubMed]
55. Luo, J. The scientific questions and technological opportunities of flash sintering: From a case study of ZnO to other ceramics. *Scr. Mater.* **2018**, *146*, 260–266. [CrossRef]
56. Du, B.; Gucci, F.; Porwal, H.; Grasso, S.; Mahajan, A.; Reece, M.J. Flash spark plasma sintering of magnesium silicide stannide with improved thermoelectric properties. *J. Mater. Chem. C* **2017**, *5*, 1514–1521. [CrossRef]
57. Manière, C.; Lee, G.; Olevsky, E.A. All-Materials-Inclusive Flash Spark Plasma Sintering. *Sci. Rep.* **2017**, *7*, 15071. [CrossRef]
58. Cologna, M.; Rashkova, B.; Raj, R. Flash Sintering of Nanograin Zirconia in <5 s at 850 °C. *J. Am. Ceram. Soc.* **2010**, *93*, 3556–3559. [CrossRef]
59. Hwang, C.; Yun, J. Flash sintering of hydroxyapatite ceramics. *J. Asian Ceram. Soc.* **2021**, *9*, 304–311. [CrossRef]
60. Carrodeguas, R.G.; De Aza, S. α-Tricalcium phosphate: Synthesis, properties and biomedical applications. *Acta Biomater.* **2011**, *7*, 3536–3546. [CrossRef]
61. Bohner, M.; Santoni, B.L.G.; Döbelin, N. β-tricalcium phosphate for bone substitution: Synthesis and properties. *Acta Biomater.* **2020**, *113*, 23–41. [CrossRef]
62. Frasnelli, M.; Sglavo, V.M. Flash sintering of tricalcium phosphate (TCP) bioceramics. *J. Eur. Ceram. Soc.* **2018**, *38*, 279–285. [CrossRef]
63. Wang, C.; Ping, W.; Bai, Q.; Cui, H.; Hensleigh, R.; Wang, R.; Brozena, A.H.; Xu, Z.; Dai, J.; Pei, Y.; et al. A general method to synthesize and sinter bulk ceramics in seconds. *Science* **2020**, *368*, 521–526. [CrossRef] [PubMed]
64. Zhang, Y. The Application of Microwave Technology in Chemistry and Chemical Engineering. In Proceedings of the Proceedings of the 2016 International Conference on Engineering Management (Iconf-EM 2016), Guangzhou, China, 26–27 November 2016.
65. Oghbaei, M.; Mirzaee, O. Microwave versus conventional sintering: A review of fundamentals, advantages and applications. *J. Alloys Compd.* **2010**, *494*, 175–189. [CrossRef]
66. Borrell, A.; Salvador, M.D. Advanced Ce ramic Materials Sintered by Microwave Technology. In *Sinter Technology Method and Application*; IntechOpen: London, UK, 2018. [CrossRef]
67. Chelladurai, S.J.S.; Mayilswamy, S.; Balakrishnan, A.S.; Gnanasekaran, S. *Green Materials and Advanced Manufacturing Technology: Concepts and Applications*; CRC Press: Boca Raton, FL, USA, 2020.
68. Hao, H.; Xu, L.; Huang, Y.; Zhang, X.; Xie, Z. Kinetics mechanism of microwave sintering in ceramic materials. *Sci. China Ser. E Technol. Sci.* **2008**, *52*, 2727–2731. [CrossRef]
69. Fang, Y.; Agrawal, D.K.; Roy, D.M.; Roy, R. Microwave sintering of hydroxyapatite ceramics. *J. Mater. Res.* **1994**, *9*, 180–187. [CrossRef]
70. Mirhadi, B. Microwave sintering of nano size powder β-TCP bioceramics. *Sci. Sinter.* **2014**, *46*, 185–193. [CrossRef]
71. Bourell, D.L. Sintering in Laser Sintering. *JOM* **2016**, *68*, 885–889. [CrossRef]
72. Dizon, J.R.C.; Espera, A.H.; Chen, Q.; Advincula, R.C. Mechanical characterization of 3D-printed polymers. *Addit. Manuf.* **2018**, *20*, 44–67. [CrossRef]
73. Kruth, J.; Mercelis, P.; Van Vaerenbergh, J.; Froyen, L.; Rombouts, M. Binding mechanisms in selective laser sintering and selective laser melting. *Rapid Prototyp. J.* **2005**, *11*, 26–36. [CrossRef]
74. Kruth, J.P.; Wang, X.; Laoui, T.; Froyen, L. Lasers and materials in selective laser sintering. *Assem. Autom.* **2003**, *23*, 357–371. [CrossRef]
75. Rho, J.-W.; Kim, J.-H.; Lee, C.-K. An Overview of Selective Laser Sintering. *J. Weld. Join.* **2008**, *26*, 34–37. [CrossRef]
76. Simchi, A. Direct laser sintering of metal powders: Mechanism, kinetics and microstructural features. *Mater. Sci. Eng. A* **2006**, *428*, 148–158. [CrossRef]
77. Qian, B.; Shen, Z. Laser sintering of ceramics. *J. Asian Ceram. Soc.* **2013**, *1*, 315–321. [CrossRef]
78. Qin, T.; Li, X.; Long, H.; Bin, S.; Xu, Y. Bioactive Tetracalcium Phosphate Scaffolds Fabricated by Selective Laser Sintering for Bone Regeneration Applications. *Materials* **2020**, *13*, 2268. [CrossRef] [PubMed]
79. Bulina, N.V.; Titkov, A.I.; Baev, S.G.; Makarova, S.V.; Khusnutdinov, V.R.; Bessmeltsev, V.P.; Lyakhov, N.Z. Laser sintering of hydroxyapatite for potential fabrication of bioceramic scaffolds. *Mater. Today Proc.* **2021**, *37*, 4022–4026. [CrossRef]
80. Qingxi, H.; Baigong, M.; Liulan, L.; Minglun, F. Selective laser sintering of -tricalcium phosphate for bionic scaffold. In Proceedings of the International Technology and Innovation Conference 2006 (ITIC 2006), Hangzhou, China, 6–7 November 2006; Institution of Engineering and Technology (IET): Zhejiang, China, 2006; pp. 2–7.
81. Grasso, S.; Biesuz, M.; Zoli, L.; Taveri, G.; Duff, A.I.; Ke, D.; Jiang, A.; Reece, M.J. A review of cold sintering processes. *Adv. Appl. Ceram.* **2020**, *119*, 115–143. [CrossRef]
82. Guo, J.; Guo, H.; Baker, A.L.; Lanagan, M.T.; Kupp, E.R.; Messing, G.L.; Randall, C.A. Cold Sintering: A Paradigm Shift for Processing and Integration of Ceramics. *Angew. Chem. Int. Ed.* **2016**, *55*, 11457–11461. [CrossRef]
83. Maria, J.-P.; Kang, X.; Floyd, R.; Dickey, E.; Guo, H.; Guo, J.; Baker, A.; Funihashi, S.; Randall, C.A. Cold sintering: Current status and prospects. *J. Mater. Res.* **2017**, *32*, 3205–3218. [CrossRef]
84. Riquet, G.; Marinel, S.; Bréard, Y.; Harnois, C. Sintering mechanism and grain growth in CaCu3Ti4O12 ceramics. *Ceram. Int.* **2019**, *45*, 9185–9191. [CrossRef]

85. Biesuz, M.; Taveri, G.; Duff, A.I.; Olevsky, E.; Zhu, D.; Hu, C.; Grasso, S. A theoretical analysis of cold sintering. *Adv. Appl. Ceram.* **2020**, *119*, 75–89. [CrossRef]
86. Rubenis, K.; Zemjane, S.; Vecstaudza, J.; Bitenieks, J.; Locs, J. Densification of amorphous calcium phosphate using principles of the cold sintering process. *J. Eur. Ceram. Soc.* **2021**, *41*, 912–919. [CrossRef]
87. Hassan, M.U.; Akmal, M.; Ryu, H.J. Cold sintering of as-dried nanostructured calcium hydroxyapatite without using additives. *J. Mater. Res. Technol.* **2021**, *11*, 811–822. [CrossRef]
88. German, R.M. Sintering With External Pressure. In *Sintering: From Empirical Observations to Scientific Principles*; Butterworth-Heinemann: Oxford, UK, 2014; pp. 305–354. [CrossRef]
89. Fang, Z.; Wang, H. Sintering of ultrafine and nanosized ceramic and metallic particles. *Ceramic Nanocomposites* **2013**, 431–473. [CrossRef]
90. Kang, S.-J.L. Intermediate and Final Stage Sintering. In *Sintering*; Elsevier: Oxford, UK, 2005; pp. 57–87.

2. PIELIKUMS / APPENDIX 2

2. PUBLIKĀCIJA / PUBLICATION

Rubenis, K., Zemjane, S., Vecstaudza, J., Lazdovica, K., Bitenieks, J., Wiecinski, P., **Indurkar, A.,** & Locs, J. (2022). Sintering of amorphous calcium phosphate to near-full density by uniaxial compaction at room temperature.

Doi: 10.1016/j.jeurceramsoc.2022.06.041

Journal of the European Ceramic Society 42 (2022) 6199–6205

Contents lists available at ScienceDirect

Journal of the European Ceramic Society

journal homepage: www.elsevier.com/locate/jeurceramsoc

Sintering of amorphous calcium phosphate to near-full density by uniaxial compaction at room temperature

Kristaps Rubenis [a,*], Signe Zemjane [a], Jana Vecstaudza [a], Kristine Lazdovica [b], Juris Bitenieks [c], Piotr Wiecinski [d], Abhishek Indurkar [a], Janis Locs [a,e]

[a] Rudolfs Cimdins Riga Biomaterials Innovations and Development Centre of RTU, Institute of General Chemical Engineering, Faculty of Materials Science and Applied Chemistry, Riga Technical University, Pulka St. 3/3, Riga LV-1007, Latvia
[b] Institute of Applied Chemistry, Faculty of Materials Science and Applied Chemistry, Riga Technical University, Paula Valdena St. 3/7, Riga LV-1048, Latvia
[c] Institute of Polymer Materials, Faculty of Materials Science and Applied Chemistry, Riga Technical University, Paula Valdena St. 3/7, Riga LV-1048, Latvia
[d] Faculty of Chemistry, Warsaw University of Technology, 3 Noakowskiego St., 00-664 Warsaw, Poland
[e] Baltic Biomaterials Centre of Excellence, Headquarters at Riga Technical University, Riga, Latvia

ARTICLE INFO

Keywords:
Amorphous calcium phosphate
Bioceramics
Uniaxial die pressing
Cold sintering
Near-full density

ABSTRACT

Amorphous calcium phosphate is a metastable phase with excellent biocompatibility and resorbability. Despite these characteristics, its use is currently limited to the powder and coating forms; only moderate success has been achieved in its densification, which has prevented its use in the bulk form. Here, we show that amorphous calcium phosphate can be sintered to near full density by simple uniaxial die pressing at 1250–1500 MPa at room temperature. The relative densities of the samples that were compacted at 1250 and 1500 MPa exceeded 95 %. Their specific surface area was more than 1000 times smaller than that of the starting powder and their Vickers hardness exceeded 1.90 GPa. The microstructures of the samples consisted of a grain-like structure with grain sizes below 100 nm. These results could inspire new applications for amorphous calcium phosphate in the form of bulk ceramics.

1. Introduction

The amorphous calcium phosphate (ACP) structure has been characterized by the presence of $Ca_9(PO_4)_6$ Posner's clusters. During the synthesis of ACP in aqueous solutions, the formed Posner's clusters aggregate and form spherical ACP particles (20–300 nm), with water molecules filling the inter-cluster space [1,2]. When heated, ACP loses structural water and, at approximately 600 °C, transforms into other calcium phosphate phases. This limits the possibility of using the pressureless sintering technique for ACP densification because temperatures above 1000 °C are necessary to obtain dense calcium phosphate ceramics [3]. Promising results on the densification of ACP have been obtained by pressure-assisted techniques, such as spark plasma sintering, however, only partially densified ACP ceramics have been obtained [4–6].

To date, the highest densification degree (relative density of ~75 %) of ACP was achieved in our previous study where we used principles of the cold sintering process for densification [5,7]. In that study, we observed that the use of a transient liquid phase (water) had no substantial effect on densification. Similar observations have also been made in the case of low crystalline apatite; if it has a hydrated surface layer, it can be sintered to near-full density by applying only heat (150–200 °C) and a uniaxial force [8–10]. However, in the case of ACP, we observed that heating (up to 120 °C) during the compaction process had no significant effect on densification. The relative density (~75 %) of the samples that were produced at room temperature was comparable to those that were produced at 100 or 120 °C (the samples produced at 150 °C were transformed to the low-crystalline apatite phase). The results indicated that the pressure applied to ACP was the driving force for its densification. In this study, we used a uniaxial pressure of 500 MPa for sample preparation. It remains unclear how uniaxial compaction at pressures higher than 500 MPa affects the densification and structure of ACP. Additionally, it is unclear if fully dense ACP ceramics will be obtained or if a phase transition will be induced at a certain critical pressure before full density is reached.

Few studies on the densification of ceramic materials to near-full density, by compaction at room temperature, have been reported. Sodium chloride (NaCl) can be densified to a relative density of 98.5–99.3

* Corresponding author.
E-mail address: kristaps.rubenis@rtu.lv (K. Rubenis).

https://doi.org/10.1016/j.jeurceramsoc.2022.06.041
Received 28 September 2021; Received in revised form 8 June 2022; Accepted 13 June 2022
Available online 16 June 2022

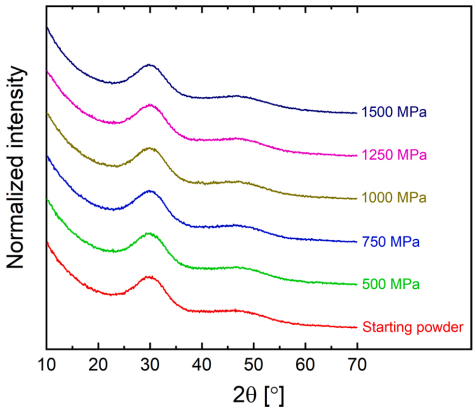

Fig. 1. XRD patterns of the starting ACP powder and the samples obtained at different uniaxial pressures.

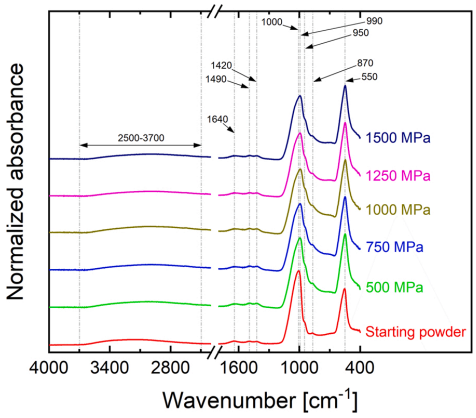

Fig. 2. ATR-FTIR spectra of the starting ACP powder and the compacted samples obtained at different uniaxial pressures.

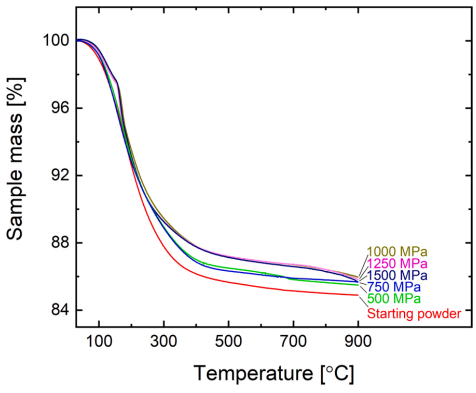

Fig. 3. Mass loss as a function of temperature for the samples obtained at different uniaxial pressures and the starting ACP powder.

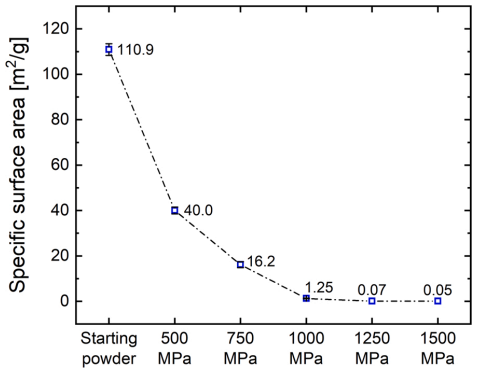

Fig. 4. SSA of the samples obtained at different uniaxial pressures and the starting ACP powder.

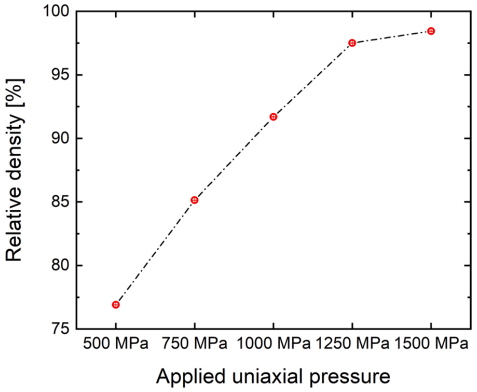

Fig. 5. Relative densities of the samples obtained at different uniaxial pressures.

% by dry pressing at 200–300 MPa, while alpha-aluminum oxide (α-Al_2O_3) to ~98.9 % by cold compression at 18 GPa [11,12]. In these example cases, plastic deformation was considered to be the dominant densification mechanism.

In the present study, we investigated the effect of uniaxial die pressing, at 500–1500 MPa and room temperature, on the structure and densification of ACP. The compacted samples were characterized by attenuated total reflectance-Fourier transform infrared spectroscopy (ATR-FTIR), scanning electron microscopy (SEM), nitrogen sorptometry, X-ray diffraction (XRD), and thermogravimetry-Fourier transform infrared spectroscopy (TG/FTIR). In addition, the bulk, true, and relative densities were determined and the Vickers hardness was determined for the samples obtained at 1250 and 1500 MPa.

2. Materials and methods

2.1. Synthesis of amorphous calcium phosphate

The dissolution-precipitation method was used to synthesize ACP [13]. First, a suspension of hydroxyapatite in water was prepared by adding hydroxyapatite powder (10 g, #289396; Sigma-Aldrich, USA) to deionized water (600 mL, stirred at 200 rpm). After 10 min of stirring, a 3 M HCl solution (64.46 mL) was added to the suspension to dissolve the hydroxyapatite. After an additional 10 min, the stirring rate of the

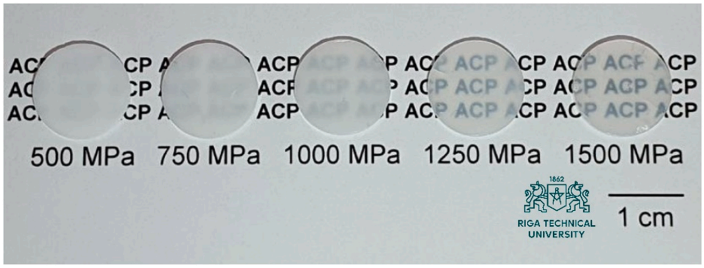

Fig. 6. Photograph illustrating the translucency of the samples obtained at different uniaxial pressures.

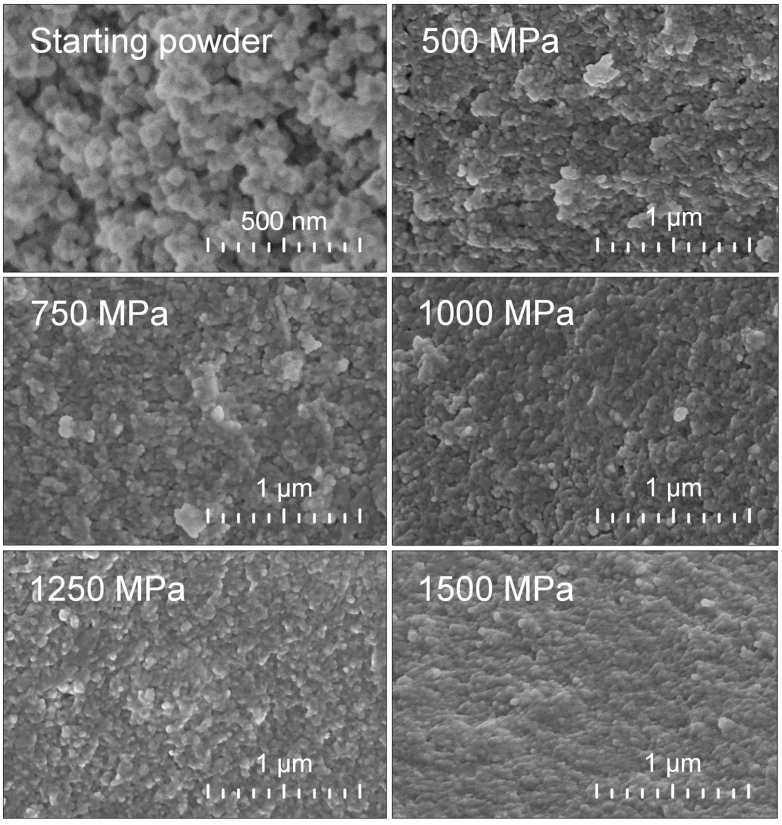

Fig. 7. SEM images of the surface morphology of the starting ACP powder and fracture surface morphology of the samples obtained at different uniaxial pressures.

obtained solution was increased (from 200 to 600 rpm), and a 2 M NaOH aqueous solution (91.5 mL) was rapidly added. This increased the pH of the synthesis solution to approximately 11.0, leading to the formation of a white precipitate. After stirring for 5 min, the precipitate was filtered and washed on the filter paper with deionized water. The filtered precipitate was transferred to a plastic container. The containers were then immersed in liquid nitrogen to freeze the precipitate. Freeze-drying was performed to remove excess water from the frozen precipitate. Freeze-drying was performed in a Beta 2–8 LSCplus freeze-dryer (Martin Christ Gefriertrocknungsanlagen, Germany) for 72 h. To produce sufficient ACP powder for the study, the synthesis was performed multiple times.

2.2. Uniaxial die pressing

Approximately 0.5 g of the synthesized ACP powder was used to prepare one sample. After weighing, the powder was transferred to a 13 mm inner-diameter split-sleeve pressing die made of W18Cr4V hardened carbon tool steel (Across International, USA). To prevent sample contamination, the surfaces of the core dies that were in contact with the powder were covered with a 125 μm thick Kapton® polyimide film (DuPont, USA). A PW 100 ES two-column electrohydraulic lab press (P/

O/WEBER, Germany) was used to apply uniaxial pressures of 500, 750, 1000, 1250, and 1500 MPa to the powder within the die. The pressure was increased at a rate of ~15 MPa/s. The powder was held under pressure for 10 min. Subsequently, the pressure was slowly released, and the compacted sample was removed from the die. During the sample preparation, the temperature in the laboratory was between 18 and 20 °C.

2.3. X-ray diffraction

The XRD patterns of the compacted samples and the synthesized ACP powder were collected on a PANalytical X-Pert PRO MPD diffractometer (PANalytical, Netherlands) operated at 40 kV and 30 mA (Cu tube). Diffraction data were collected over a 10–70° 2θ range, with a step size of 0.05° 2θ and time per step of 3.2 s. For X-ray diffraction data collection, the compacted samples were milled into a powder.

2.4. Attenuated total reflectance - Fourier transform infrared spectroscopy

A Varian FTS 800 Scimitar Series FT-IR spectrometer (Varian, Inc., USA) equipped with GladiATR™ ATR (PIKE Technologies, USA) was used to acquire the ATR-FTIR spectra of the compacted samples and the synthesized ACP powder. All spectra were acquired in the range 400–4000 cm^{-1} by co-adding 50 scans (resolution of 4 cm^{-1}). Before acquisition of the sample spectrum, a background spectrum was collected, which was subtracted from the spectra of the samples. For spectral collection, compacted samples were milled into a powder.

2.5. Scanning electron microscopy

The surface morphology of the starting ACP powder and the fracture surface morphology of the compacted samples were visualized using S-5500 and SU8000 scanning electron microscopes (Hitachi, Japan). For microscopy, the samples were attached to SEM specimen stubs with electrically conductive carbon tape or graphite base adhesive. Before the examination, the compacted samples (fractured) were sputter-coated with Cr-Ni using a precision etching coating system (Gatan, Inc., USA). The starting ACP powder was not coated with the conductive layer. For the SEM image acquisition, secondary electrons were used, and the applied acceleration voltage was 1.5 kV and 3–5 kV for the ACP powder and bulk samples, respectively.

2.6. Specific surface area

A Quadrasorb™ *SI* surface area and pore size analyzer (Quantachrome Instruments, USA) was used to generate N_2 adsorption-desorption isotherms of the compacted samples and the synthesized ACP powder at − 196 °C. Before the adsorption–desorption isotherms were generated, the samples were degassed in an AUTOSORB degasser (Quantachrome Instruments, USA) for 24 h under vacuum at room temperature. The Brunauer–Emmett–Teller model was used to determine the specific surface area (SSA) of the compacted samples and starting powder based on their adsorption isotherms in the P/P_0 range of 0.05–0.3 [14].

2.7. Thermogravimetry-Fourier transform infrared spectroscopy

An STA 6000 Simultaneous Thermal Analyzer (PerkinElmer Inc., USA) coupled to a Spectrum 100 FTIR spectrometer (PerkinElmer Inc., USA) via a TL 8000 transfer line (PerkinElmer Inc., USA) was used for TG/FTIR analyses of the compacted samples and the synthesized ACP powder. Before the analysis, the compacted samples were milled into a powder. During the analysis, the sample was heated at a rate of 100 °C/min to 900 °C under flowing N_2 gas (20 mL/min). The FTIR spectrum was collected every 9 s in the range 650–4000 cm^{-1} (resolution of 4 cm^{-1}). During the analysis, the gas cell and transfer line were maintained at 230 °C. Spectrum Search Plus Software (PerkinElmer Inc., USA) and Spectrum Timebase Software (PerkinElmer Inc., USA) were used to identify volatile products. The carbon dioxide (CO_2) relative yield (wt%) was assumed as the integrated intensity of the absorbance-temperature curve and calculated according to the Eq. (1):

$$S = \sum_{n=30}^{n=final} \sum^{temperature} 0.5 \times (A_n + A_{n-1}) \times (T_n - T_{n-1}) \quad (1)$$

where S is the relative yield, A is the absorbance at a specific wavenumber, at the experimental temperatures T_n and T_{n-1}, and n is the point of measurement [15].

Calcium oxalate was used as the reference material to determine the CO_2 yield. Analysis of calcium oxalate was performed at a heating rate of 100 °C/min to 1000 °C under flowing N_2 gas (20 mL/min). The evolution profile of CO_2 from calcium oxalate was obtained by processing the FTIR data. The linearity between the relative yield of CO_2 and mass loss of calcium oxalate was evaluated in the temperature range of 700–1000 °C (Supplementary Fig. 1) [16]. The precision of the TG measurements was estimated to be ± 0.1 %.

2.8. Helium pycnometry

A Micro UltraPyc™ 1200e helium pycnometer (Quantachrome Instruments, USA) was used to determine the true density of the compacted samples and synthesized ACP powder. To limit the impact of the closed porosity on the measurement accuracy, the compacted samples were milled into powders before the measurements. The pycnometer was first calibrated using stainless steel calibration spheres of known volumes. The volume of the sample was determined by pressurizing the powder-containing sample cell to a target pressure of 10 psig. The measurement was repeated until the percentage deviation of five consecutive measurements was ≤ 0.1 %. The true density of the sample was calculated by dividing its weight by its measured volume.

2.9. Bulk density

The bulk density of each sample was calculated by dividing the mass of the compacted sample by its bulk volume. An analytical balance was used to determine the mass of each sample. The bulk volume V_{bulk} of the sample was determined using the following Eq. (2):

$$V_{bulk} = \pi d^2 h/4 \quad (2)$$

where h and d are the height and diameter of the sample, respectively. The diameter and height of the samples were measured using digital calipers at five different positions around the sample, and the measured values were subsequently averaged.

2.10. Relative density

The relative density value of the sample was determined by dividing the bulk density value of the compacted sample by its true density value and multiplying by 100 %.

2.11. Vickers hardness

A HM-210D micro-Vickers hardness tester (Mitutoyo Corporation, Kanagawa, Japan) was used to determine the hardness of the uniaxially compacted samples. Before the measurements, the surfaces of the samples were polished to a mirror finish. The measurements were performed under a load of 0.05 gf (held for 10 s). At least seven measurements were performed for each sample compacted at a specific uniaxial pressure.

3. Results and discussion

3.1. Phase composition

XRD was used to determine the effect of the compaction pressure on the stability of the ACP phase. The XRD patterns of all the compacted samples were identical to those of the starting ACP powder (Fig. 1). Only two diffuse humps were observed in the diffraction patterns, indicating that the amorphous phase was retained at all compaction pressures.

3.2. Local structure

ATR-FTIR spectroscopy was used to evaluate the effect of compaction pressure on the local structure of ACP. Although the infrared absorption spectra of the starting powder and compacted samples were similar, there were some differences (Fig. 2). All spectra contained similar broad and relatively weak absorption bands at approximately 2500–3700 cm^{-1}, and narrower bands at approximately 1640, 1490, and 1420 cm^{-1}. In contrast, the band observed at 1000 cm^{-1} in the spectrum of the starting powder shifted to ~990 cm^{-1} in the spectra of the uniaxially compacted samples. Furthermore, the intensities of the bands at 950, 870, and 550 cm^{-1} were significantly higher in the spectra of the compacted samples.

The superimposed absorption bands at approximately 1000 and 950 cm^{-1}, and the band at 550 cm^{-1}, are characteristic of ACP and are assigned to ν_3 PO_4^{3-}, ν_1 PO_4^{3-}, and ν_4 PO_4^{3-} group vibrations, respectively [17]. The bands in the range of 2500–3700 cm^{-1} and around 1640 cm^{-1} are associated with the O–H stretching and bending vibrational modes of the water molecules, respectively [18]. Water in ACP, which is synthesized by wet-chemical synthesis routes, can be present in large amounts and is predominantly tightly bound in the inter-cluster space [17]. The doublet bands at 1420 and 1490 cm^{-1} are attributed to ν_3 CO_3^{2-} vibrations, while the band at 870 cm^{-1} is attributed to ν_2 CO_3^{2-} and/or HPO_4^{2-} vibrations [19,20]. Carbonate ions were incorporated into the ACP structure from the synthesis medium (i.e., water). Although ultrapure water was used, ACP could quickly absorb CO_2 from the air because the synthesis was performed under ambient conditions. Another source of carbonate ions could be the hydroxyapatite that was used for the synthesis of ACP; the presence of carbonates was detected in its structure (Supplementary Fig. 2), along with HPO_4^{2-} ions [21]. The differences observed between the FTIR spectra of ACP before and after its compaction (i.e., the changes in intensity of the bands at 950, 870, and 550 cm^{-1} (Fig. 2)) indicate that the application of a relatively high pressure induced changes in the local structure. The applied pressure can affect the bond parameters and short-range order present in ACP [17,22,23] Additionally, applied pressure can partly dehydrate ACP and thus make its structure more compact [5,24].

3.3. Water and carbonate content

TG-FTIR was used to determine the effect of compaction on the carbonate and water contents of the starting powder. TG analysis showed that the compacted samples lost less mass compared to the starting powder when heated to 900 °C (Fig. 3). The mass loss for the compacted samples and starting powder at 900 °C reached 14.0–14.5 % and 15.1 %, respectively. The samples compacted at 500 and 750 MPa had almost identical mass losses over the investigated temperature range and most of the mass loss occurred in the temperature range of 100–300 °C. Subsequently, the mass loss gradually decreased and the TG curves became almost flat. The TG curves for the samples compacted at 1000, 1250, and 1500 MPa were largely similar to those of the samples compacted at 500 and 750 MPa. Initially, the mass loss rates for the samples compacted at 1000, 1250, and 1500 MPa were lower than those of the samples compacted at 500 and 750 MPa. From 160 °C, the mass loss rate greatly increased but slowed down at approximately 180 °C, and up to 250 °C, the rate was similar to those of the samples compacted at 500 and 750 MPa. Over the temperature range of 400–750 °C, mass loss for the samples compacted at 1000, 1250, and 1500 MPa was approximately 0.7 % lower than of the samples compacted at 500 and 750 MPa. This difference decreased when the temperature exceeded 750 °C.

Only absorption bands characteristic of water and CO_2 were observed in the FTIR spectra of the volatiles released from the ACP powder and the uniaxially compacted samples during heating (Supplementary Fig. 3). Water was released from room temperature to ~550 °C, while CO_2 over ~100–900 °C. The CO_2 release profiles for the synthesized ACP powder and samples compacted at different uniaxial pressures differed from each other (Supplementary Fig. 4). The estimated CO_2 yield from the starting powder was 1.5 wt% (corresponding to a carbonate content of 2.0 wt%). The estimated CO_2 yields from the samples that were compacted at 500, 750, 1000, 1250, and 1500 MPa were 1.1, 1.0, 0.9, 0.9, and 0.9 wt%, respectively (corresponding to carbonate contents of 1.5, 1.4, 1.2, 1.2, and 1.2 wt%, respectively).

TG-FTIR analysis indicated that the compacted samples contained less carbonate and water than the starting powder. Previous studies on the consolidation of carbonated ACP and nanocrystalline apatite using the spark plasma sintering technique have reported a loss of carbonates from the structure of calcium phosphates during their consolidation. Since ACP can contain HPO_4^{2-} ions, carbonate loss may arise from the reaction between HPO_4^{2-} and carbonate ions (Eq. (3)), which could be favored by the pressure applied to ACP [25–27].

$$2HPO_4^{2-} + CO_3^{2-} \leftrightarrow 2PO_4^{3-} + CO_{2(gas)} + \quad H_2O \tag{3}$$

The differences between the TG curves of the samples compacted at 1000, 1250, and 1500 MPa and those of the samples compacted at 500 and 750 MPa can be partly related to the differences in their bulk densities and porosities. Because of the higher compaction pressure used, the samples compacted at 1000, 1250, and 1500 MPa had higher levels of closed porosity and bulk density than the samples compacted at 500 and 750 MPa. If the sample contained closed pores, part of the water released from its structure during heating could accumulate in the closed pores. This water can be rapidly released when the pressure inside the pore exceeds the tensile strength of the material [28].

3.4. Specific surface area

Nitrogen sorptometry was used to determine the effect of compaction pressure on the SSA of ACP. The SSA of ACP decreased with an increase in the pressure used for its compaction (Fig. 4). The SSA of the samples compacted at 500 MPa was less than half that of the starting powder (40.0 (± 1.5) m^2/g vs. 110.9 (± 2.6) m^2/g), while for the samples compacted at 1250 and 1500 MPa the SSA was more than 1000 times smaller than that of the starting powder (0.07 m^2/g and 0.05 m^2/g vs. 110.9 (± 2.6) m^2/g, respectively).

The smaller SSA of the compacted samples compared to the starting powder suggests that interparticle necks were formed between the ACP particles during the compaction process. With an increase in compaction pressure, the contact area between the particles increased, further reducing the SSA of the samples.

3.5. Relative density

The bulk, true, and relative densities of the compacted samples were determined to evaluate how the compaction pressure affected the densification of ACP. To determine the relative density of the compacted samples, their bulk density values were divided by the true density value of the starting powder (2.50 g/cm^3) instead of the true density values determined by He pycnometry. The true density values of the compacted samples (milled) were lower than those of the starting powder, indicating that closed porosity was not eliminated by milling (Supplementary Fig. 5). Actual true density values of the compacted samples could

be slightly higher than those of the starting powder, as they contained 0.6–1.1 % less water and carbonates than the starting powder (Fig. 3). The relative density of the compacted samples increased with increasing compaction pressure (Fig. 5). The relative density of the samples obtained at 1000 MPa already exceeded 90 %, and the relative density of the samples compacted at 1250 and 1500 MPa reached 97.51 (± 0.02) and 98.44 (± 0.02) %, respectively. The translucency of the samples increased with increasing relative density (Fig. 6). The text behind the samples compacted at 1250 and 1500 MPa became visible, which can be attributed to the reduced sample porosity.

The significant reduction in SSA (Fig. 4) and increase in the relative density of the samples, with an increase in the pressure used for their compaction, suggest that under the application of a relatively high pressure, the sintering process of ACP occurs at room temperature. Few ceramic materials have been sintered to a high relative density using only pressure for densification [12,29–32]. These materials possess a certain degree of plastic deformability or contain water in their structure, which promotes densification [28,30,33]. The large amount of water that is present in the ACP structure could play a significant role in the sintering process [34,35]. The water present in the ACP structure could help form bridges between the particles under the application of pressure and could provide high ion mobility, promoting diffusion processes [4,36]. More efforts are necessary to better understand the mechanisms that lead to the densification of ACP under an applied pressure.

3.6. Microstructure

SEM was used to characterize the surface morphology of the starting ACP powder and fracture surface morphology of the compacted samples (Fig. 7). The starting powder consisted of highly agglomerated spherical particles with sizes below 100 nm. The microstructure of all the compacted samples consisted of a grain-like structure with grain sizes below 100 nm. With an increase in the compaction pressure, the microstructure of the samples became more homogeneous, and their porosity decreased. An increase in the compaction pressure seemingly had no significant influence on the grain size and the application of pressure appeared to fuse the ACP particles (Supplementary Fig. 6).

3.7. Mechanical properties

The Vickers hardness of the samples compacted at 1250 and 1500 MPa reached 1.92 (± 0.04) and 2.02 (± 0.04) GPa, respectively. These values are comparable to those reported for low-crystalline hydroxyapatite ceramics sintered using the cold-sintering technique and indicate that strong bonding was formed between the ACP ceramic grains [37,38].

4. Conclusions

Uniaxial die pressing at 1250–1500 MPa at room temperature enabled ACP to be sintered to near-full density (relative density >95 %). Although the amorphous phase was retained, pressure-induced changes in the local structure of ACP were evident. During the compaction process, ACP loses part of its water and carbonate contents. The compaction process did not lead to substantial grain growth. The microstructure of the compacted samples consisted of a grain-like structure with grain sizes below 100 nm. It is possible that ACP could be sintered to full density at a lower pressure by optimizing the compaction parameters, and the technique used for the densification of ACP permits the co-sintering of ACP with temperature-sensitive substances.

Declaration of Competing Interest

The authors declare that they have no known competing financial interests or personal relationships that could have appeared to influence the work reported in this paper.

Data Availability

The data supporting the findings of this study are available from the corresponding author, K.R., upon reasonable request.

Acknowledgment

This work has been supported by the European Regional Development Fund within the Activity 1.1.1.2 “Post-doctoral Research Aid” of the Specific Aid Objective 1.1.1 “To increase the research and innovative capacity of scientific institutions of Latvia and the ability to attract external financing, investing in human resources and infrastructure” of the Operational Programme “Growth and Employment” (No.1.1.1.2/VIAA/2/18/318). The authors also acknowledge financial support for granting Open Access from the European Union’s Horizon 2020 Research and Innovation Programme under the grant agreement No. 857287. The authors also want to thank Mitutoyo Poland for providing the micro-Vickers hardness tester.

Appendix A. Supporting information

Supplementary data associated with this article can be found in the online version at doi:10.1016/j.jeurceramsoc.2022.06.041.

References

[1] F. Betts, A.S. Posner, An X-ray radial distribution study of amorphous calcium phosphate, Mater. Res. Bull. 9 (1974) 353–360, https://doi.org/10.1016/0025-5408(74)90087-7.
[2] J.C. Elliott, Structure and Chemistry of the Apatites and Other Calcium Orthophosphates, Volume 18 - 1st Edition, Elsevier Science, 1994. ⟨https://www.elsevier.com/books/structure-and-chemistry-of-the-apatites-and-other-calcium-orthophosphates/elliott/978-0-444-81582-8⟩ (Accessed 15 February 2021).
[3] A.L. Boskey, A.S. Posner, Conversion of amorphous calcium phosphate to microcrystalline hydroxyapatite. A pH-dependent, solution-mediated, solid-solid conversion, J. Phys. Chem. 77 (1973) 2313–2317, https://doi.org/10.1021/j100638a011.
[4] M. Luginina, R. Orru, G. Cao, D. Grossin, F. Brouillet, G. Chevallier, C. Thouron, C. Drouet, First successful stabilization of consolidated amorphous calcium phosphate (ACP) by cold sintering: toward highly-resorbable reactive bioceramics, J. Mater. Chem. B 8 (2020) 629–635, https://doi.org/10.1039/C9TB02121C.
[5] K. Rubenis, S. Zemjane, J. Vecstaudza, J. Bitenieks, J. Locs, Densification of amorphous calcium phosphate using principles of the cold sintering process, J. Eur. Ceram. Soc. 41 (2021) 912–919, https://doi.org/10.1016/j.jeurceramsoc.2020.08.074.
[6] A.A. Pudule, K.A. Gross, D. Ūbele, I. Jeränе, I. Šteins, Densification of amorphous calcium phosphate: a comparison of cold sintering processes, Key Eng. Mater. 903 (2021) 46–51, https://doi.org/10.4028/www.scientific.net/KEM.903.46.
[7] J. Guo, H. Guo, A.L. Baker, M.T. Lanagan, E.R. Kupp, G.L. Messing, C.A. Randall, Cold sintering: a paradigm shift for processing and integration of ceramics, Angew. Chem. Int. Ed. 55 (2016) 11457–11461, https://doi.org/10.1002/anie.201605443.
[8] M. ul Hassan, H.J. Ryu, Cold sintering and durability of iodate-substituted calcium hydroxyapatite (IO-HAp) for the immobilization of radioiodine, J. Nucl. Mater. 514 (2019) 84–89, https://doi.org/10.1016/j.jnucmat.2018.11.024.
[9] H.Z. Shen, N. Guo, L. Zhao, P. Shen, Role of ion substitution and lattice water in the densification of cold-sintered hydroxyapatite, Scr. Mater. 177 (2020) 141–145, https://doi.org/10.1016/j.scriptamat.2019.10.024.
[10] M.U. Hassan, M. Akmal, H.J. Ryu, Cold sintering of as-dried nanostructured calcium hydroxyapatite without using additives, J. Mater. Res. Technol. 11 (2021) 811–822, https://doi.org/10.1016/j.jmrt.2021.01.060.
[11] F. Liu, J. Zhang, P. Liu, Q. Deng, D. He, Strengthening of alumina ceramics under cold compression, Ceram. Int. 46 (2020) 3984–3988, https://doi.org/10.1016/j.ceramint.2019.09.257.
[12] W. Bin Hong, L. Li, M. Cao, X.M. Chen, Plastic deformation and effects of water in room-temperature cold sintering of NaCl microwave dielectric ceramics, J. Am. Ceram. Soc. 101 (2018) 4038–4043, https://doi.org/10.1111/jace.15572.
[13] J. Vecstaudza, J. Locs, Novel preparation route of stable amorphous calcium phosphate nanoparticles with high specific surface area, J. Alloy. Compd. 700 (2017) 215–222, https://doi.org/10.1016/j.jallcom.2017.01.038.
[14] S. Brunauer, P.H. Emmett, E. Teller, Adsorption of gases in multimolecular layers, J. Am. Chem. Soc. 60 (1938) 309–319, https://doi.org/10.1021/ja01269a023.
[15] K. Lazdovica, V. Kampars, L. Liepina, M. Vilka, Comparative study on thermal pyrolysis of buckwheat and wheat straws by using TGA-FTIR and Py-GC/MS

methods, J. Anal. Appl. Pyrolysis 124 (2017) 1–15, https://doi.org/10.1016/j.jaap.2017.03.010.
[16] K. Lazdovica, V. Kampars, J. Grabis, Effect of zinc-containing nanopowders on the catalytic intermediate pyrolysis of buckwheat straw by using TGA-FTIR method, J. Anal. Appl. Pyrolysis 152 (2020), 104882, https://doi.org/10.1016/j.jaap.2020.104882.
[17] C. Combes, C. Rey, Amorphous calcium phosphates: synthesis, properties and uses in biomaterials, Acta Biomater. 6 (2010) 3362–3378, https://doi.org/10.1016/j.actbio.2010.02.017.
[18] C. Mochales, R.M. Wilson, S.E.P. Dowker, M.-P. Ginebra, Dry mechanosynthesis of nanocrystalline calcium deficient hydroxyapatite: structural characterisation, J. Alloy. Compd. 509 (2011) 7389–7394, https://doi.org/10.1016/j.jallcom.2011.04.033.
[19] C. Su, In situ infrared speciation of adsorbed carbonate on aluminum and iron oxides, Clays Clay Min. 45 (1997) 814–825, https://doi.org/10.1346/CCMN.1997.0450605.
[20] C. Ortali, I. Julien, C. Drouet, E. Champion, Influence of carbonation on the low-temperature consolidation by Spark Plasma Sintering of carbonated calcium phosphate bioceramics, Ceram. Int. 46 (2020) 5799–5810, https://doi.org/10.1016/j.ceramint.2019.11.030.
[21] C. Holt, M.J.J.M. Van Kemenade, L.S. Nelson, D.W.L. Hukins, R.T. Bailey, J. E. Harries, S.S. Hasnain, P.L.De Bruyn, Amorphous calcium phosphates prepared at pH 6.5 and 6.0, Mater. Res. Bull. 24 (1989) 55–62, https://doi.org/10.1016/0025-5408(89)90008-1.
[22] J. Luo, Y. Zhou, S.T. Milner, C.G. Pantano, S.H. Kim, Molecular dynamics study of correlations between IR peak position and bond parameters of silica and silicate glasses: effects of temperature and stress, J. Am. Ceram. Soc. 101 (2018) 178–188, https://doi.org/10.1111/jace.15187.
[23] V. Uskoković, Visualizing different crystalline states during the infrared imaging of calcium phosphates, Vib. Spectrosc. 108 (2020), 103045, https://doi.org/10.1016/j.vibspec.2020.103045.
[24] V. Uskoković, Disordering the disorder as the route to a higher order: incoherent crystallization of calcium phosphate through amorphous precursors, Cryst. Growth Des. 19 (2019) 4340–4357, https://doi.org/10.1021/acs.cgd.9b00061.
[25] C. Ortali, I. Julien, M. Vandenhende, C. Drouet, E. Champion, Consolidation of bone-like apatite bioceramics by spark plasma sintering of amorphous carbonated calcium phosphate at very low temperature, J. Eur. Ceram. Soc. 38 (2018) 2098–2109, https://doi.org/10.1016/j.jeurceramsoc.2017.11.051.
[26] C. Ortali, I. Julien, C. Drouet, E. Champion, Influence of carbonation on the low-temperature consolidation by Spark Plasma Sintering of carbonated calcium phosphate bioceramics, Ceram. Int. 46 (2020) 5799–5810, https://doi.org/10.1016/j.ceramint.2019.11.030.
[27] Z. Mu, R. Tang, Z. Liu, Construction of inorganic bulks through coalescence of particle precursors, Nanomaterials 11 (2021) 241, https://doi.org/10.3390/nano11010241.
[28] T.M.H. Costa, M.R. Gallas, E.V. Benvenutti, J.A.H. da Jornada, Infrared and thermogravimetric study of high pressure consolidation in alkoxide silica gel powders, J. Non Cryst. Solids 220 (1997) 195–201, https://doi.org/10.1016/S0022-3093(97)00236-6.
[29] M.M. Stimson, M.J. O'Donnell, The infrared and ultraviolet absorption spectra of cytosine and isocytosine in the solid state, J. Am. Chem. Soc. 74 (1952) 1805–1808, https://doi.org/10.1021/ja01127a054.
[30] E.Y. Gutmanas, A. Rabinkin, M. Roitberg, Cold sintering under high pressure, Scr. Metall. 13 (1979) 11–15, https://doi.org/10.1016/0036-9748(79)90380-6.
[31] S. Grasso, M. Biesuz, L. Zoli, G. Taveri, A.I. Duff, D. Ke, A. Jiang, M.J. Reece, A review of cold sintering processes, Adv. Appl. Ceram. 119 (2020) 115–143, https://doi.org/10.1080/17436753.2019.1706825.
[32] L. Li, W. Bin Hong, S. Yang, H. Yan, X.M. Chen, Effects of water content during cold sintering process of NaCl ceramics, J. Alloy. Compd. 787 (2019) 352–357, https://doi.org/10.1016/j.jallcom.2019.02.112.
[33] M.R. Gallas, A.R. Rosa, T.H. Costa, J.A.H. da Jornada, High pressure compaction of nanosize ceramic powders, J. Mater. Res. 12 (1997) 764–768, https://doi.org/10.1557/JMR.1997.0111.
[34] E.D. Eanes, Thermochemical studies on amorphous calcium phosphate, Calcif. Tissue Res. 5 (1970) 133–145, https://doi.org/10.1007/BF02017543.
[35] J. Vecstaudza, M. Gasik, J. Locs, Amorphous calcium phosphate materials: formation, structure and thermal behaviour, J. Eur. Ceram. Soc. 39 (2019) 1642–1649, https://doi.org/10.1016/j.jeurceramsoc.2018.11.003.
[36] C. Drouet, F. Bosc, M. Banu, C. Largeot, C. Combes, G. Dechambre, C. Estournès, G. Raimbeaux, C. Rey, Nanocrystalline apatites: from powders to biomaterials, Powder Technol. 190 (2009) 118–122, https://doi.org/10.1016/j.powtec.2008.04.041.
[37] S. Venkatesan, M. ul Hassan, H.J. Ryu, Adsorption and immobilization of radioactive ionic-corrosion-products using magnetic hydroxyapatite and cold-sintering for nuclear waste management applications, J. Nucl. Mater. 514 (2019) 40–49, https://doi.org/10.1016/j.jnucmat.2018.11.026.
[38] M. Akmal, M. ul Hassan, M. Afzal, H.J. Ryu, , Novel approach to sintering hydroxyapatite-alumina nanocomposites at 300 °C, Mater. Chem. Phys. 260 (2021), 124187, https://doi.org/10.1016/j.matchemphys.2020.124187.

3. PIELIKUMS / APPENDIX 3

3. PUBLIKĀCIJA / PUBLICATION

Indurkar, A., Choudhary, R., Rubenis, K., & Locs, J. (2023). Role of carboxylic organic molecules in interfibrillar collagen mineralization.

Doi: 10.3389/fbioe.2023.1150037

frontiers | Frontiers in Bioengineering and Biotechnology

TYPE Review
PUBLISHED 05 April 2023
DOI 10.3389/fbioe.2023.1150037

OPEN ACCESS

EDITED BY
Jinhui Tao,
Pacific Northwest National Laboratory (DOE), United States

REVIEWED BY
Changyu Shao,
Zhejiang University, China
Arun Prabhu Rameshbabu,
Harvard Medical School, United States
Taifeng Wang,
Intel, United States

*CORRESPONDENCE
Janis Locs,
janis.locs@rtu.lv

SPECIALTY SECTION
This article was submitted to Biomaterials, a section of the journal Frontiers in Bioengineering and Biotechnology

RECEIVED 23 January 2023
ACCEPTED 20 March 2023
PUBLISHED 05 April 2023

CITATION
Indurkar A, Choudhary R, Rubenis K and Locs J (2023), Role of carboxylic organic molecules in interfibrillar collagen mineralization.
Front. Bioeng. Biotechnol. 11:1150037.
doi: 10.3389/fbioe.2023.1150037

Role of carboxylic organic molecules in interfibrillar collagen mineralization

Abhishek Indurkar[1,2], Rajan Choudhary[1,2], Kristaps Rubenis[1,2] and Janis Locs[1,2]*

[1]Rudolfs Cimdins Riga Biomaterials Innovations and Development Centre of RTU, Institute of General Chemical Engineering, Faculty of Materials Science and Applied Chemistry, Riga Technical University, Riga, Latvia, [2]Baltic Biomaterials Centre of Excellence, Headquarters at Riga Technical University, Riga, Latvia

Bone is a composite material made up of inorganic and organic counterparts. Most of the inorganic counterpart accounts for calcium phosphate (CaP) whereas the major organic part is composed of collagen. The interfibrillar mineralization of collagen is an important step in the biomineralization of bone and tooth. Studies have shown that synthetic CaP undergoes auto-transformation to apatite nanocrystals before entering the gap zone of collagen. Also, the synthetic amorphous calcium phosphate/collagen combination alone is not capable of initiating apatite nucleation rapidly. Therefore, it was understood that there is the presence of a nucleation catalyst obstructing the auto-transformation of CaP before entering the collagen gap zone and initiating rapid nucleation after entering the collagen gap zone. Therefore, studies were focused on finding the nucleation catalyst responsible for the regulation of interfibrillar collagen mineralization. Organic macromolecules and low-molecular-weight carboxylic compounds are predominantly present in the bone and tooth. These organic compounds can interact with both apatite and collagen. Adsorption of the organic compounds on the apatite nanocrystal governs the nucleation, crystal growth, lattice orientation, particle size, and distribution. Additionally, they prevent the auto-transformation of CaP into apatite before entering the interfibrillar compartment of the collagen fibril. Therefore, many carboxylic organic compounds have been utilized in developing CaP. In this review, we have covered different carboxylate organic compounds governing collagen interfibrillar mineralization.

KEYWORDS

carboxylate organic compound, calcium phosphate, bone, interfibrillar collagen, mineralization

Introduction

Bone is a heterogenous and anisotropic nanocomposite. The components are arranged hierarchically into several structural levels shown in Figure 1A. The macro-structure consists of cancellous and cortical bone which is divided into microstructure composed of the Haversian system and osteons. The microstructure is divided into sub-microstructures consisting of lamella that are further divided into fibrillar collagen and apatite nanocrystal nanostructure (Fratzl and Weinkamer, 2007). The final sub-nanostructure consists of elements such as minerals, collagen, non-collagenous proteins, and small organic moieties (Heikkilä, 2011). The remarkable mechanical and remodeling capabilities of

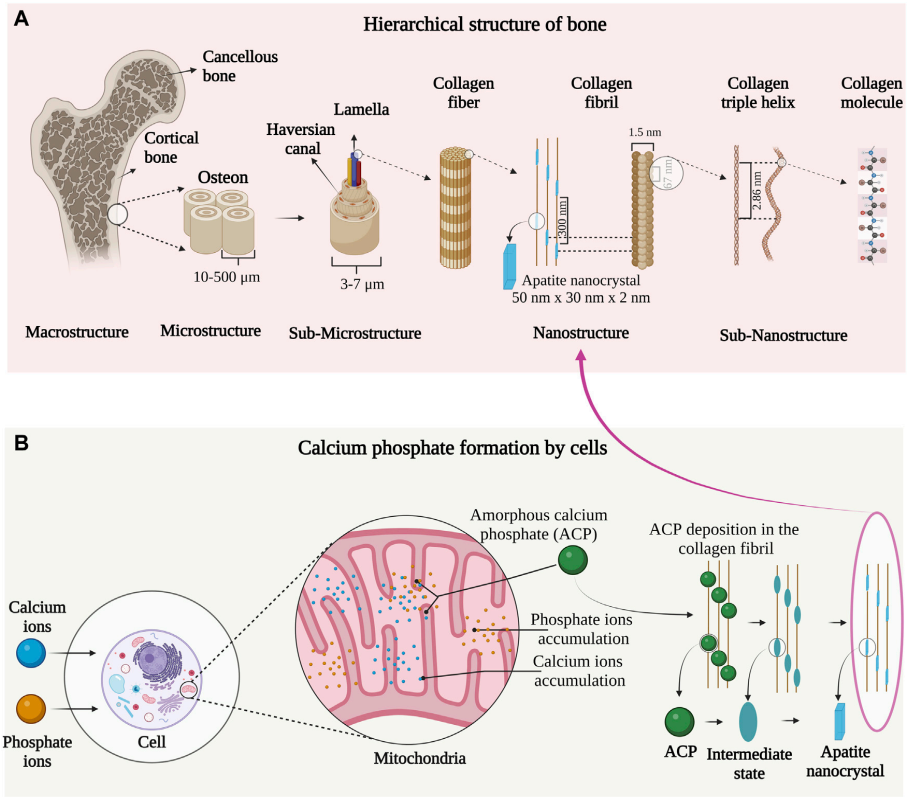

FIGURE 1
(A) Hierarchical organization of bone from macro to the nanoscale. Image inspired by the previous publication of (Rho et al., 1998). **(B)** Mitochondrial-dependent cellular mechanism of apatite nanocrystal formation. The image is inspired by the fifth jubilee lecture on mitochondria and calcium ion transport (Lehninger, 1970).

bone arise from the nanostructure level of collagen fibril and apatite nanocrystal (Liu et al., 2016).

The mineral component of bone is formed by a mitochondrial-dependent cellular process as indicated in Figure 1B. In the late '90s, Albert L. Leininger and coworkers first observed amorphous calcium phosphate (ACP) synthesis in the mitochondria of cells. According to their observations, Ca^{2+} and phosphate ions in blood plasma are transported into the cell cytoplasm and pumped into the inner wall of mitochondria on a specific carrier by energy-yielding electron transport (Rossi et al., 1967). The ions are accumulated in the mitochondria and once the solubility (concerning ACP) is exceeded, the precipitation occurs in the form of ACP micro-packets. These micro-packets are believed to be stabilized in the mitochondria by an organic moiety termed the "Howard factor."

In collagen, the charged amino acids are present in both the 67 nm overlap and 40 nm gap zone of collagen providing nucleation sites that regulate the conversion of ACP into an organized array of apatite nanocrystals (Nudelman et al., 2010). It is believed that the net positive charge on the C-terminal of the collagen molecule allows ACP to settle in the collagen fibril. However, auto-transformation of ACP into apatite nanocrystal before entering the interfibrillar compartment of the collagen fibril was observed. Studies have shown that organic carboxylic compounds regulate the conversion of ACP to apatite by hindering auto-transformation. Therefore, many carboxylic compounds have been utilized in developing calcium phosphates carboxylate (Xie and Nancollas, 2010; Yokoi et al., 2022).

Despite these discoveries, the complex process of collagen interfibrillar mineralization is not known completely understood. In the first section of this review, we have focused on the structural and chemical aspects of collagen. In the second half of this review, we have focused on the postulated mechanisms and role of the different carboxylic organic compounds responsible for interfibrillar collagen mineralization.

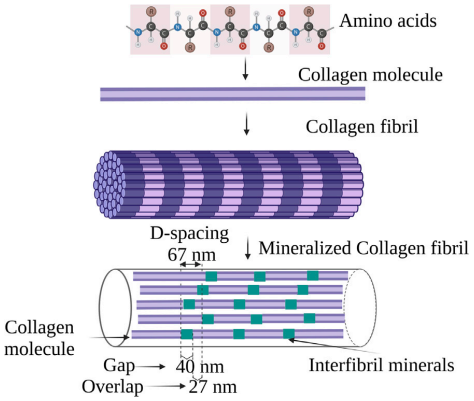

FIGURE 2
Schematic illustration of the hierarchical structure of collagen.

Structural and chemical properties of collagen

Collagen type I accounts for 90% of the total organic component of the bone (Fuchs et al., 2009). Structurally collagen consists of a subunit known as tropocollagen which is 300 nm long and 1.5 nm wide "rod" consisting of three polypeptide strands. Each polypeptide strand is a left-handed helix, and all three polypeptide strands are twisted to form a right-handed triple helix (Quan and Sone, 2013) as shown in Figure 2. The collagen fiber bends in a tube-like pattern indicating that the composition is not homogenous laterally, but consists of a hard shell and soft core (Gutsmann et al., 2003). In collagen, 64% of non-polar amino acids comprise glycine, proline, and alanine whereas the hydroxyl residue accounts for 16% and majorly consists of hydroxyproline and serine. The acidic, basic, and amide side chains account for the remaining 20% of the collagen structure. Collagen possesses two distinct hydration phenomena depending upon the pH 1) Swelling induced in the neutral salt solution, described as lyophilic or Hofmeister effect; 2) Swelling in acidic or basic solutions, described as the Donnan effect (Bear, 1952).

In bone, the collagen triple helix is arranged in a parallel staggered array in which collagen molecules are shifted by a distance D concerning their adjacent collagen molecule, after their self-assembly into collagen fibrils as indicated in Figure 2 (Glimcher et al., 1981). One D-repeat consists of a complete collagen sequence of 67 nm and the distance between two tropocollagen subunits measures 40 nm termed a gap zone (Landis et al., 2006). The nucleation site of apatite nanocrystal lies in the gap zone of collagen where it achieves the c-axis orientation parallel to the long axis of collagen (Parvizi and Kim, 2010). The intermediate state of CaP such as ACP and/or octa-calcium phosphates (OCP) (Lehninger, 1970; Brown et al., 1987) are presumed to be nucleated in the gap zone of collagen that results in apatite nanocrystal formation.

The remarkable mechanical property of bone arises from the complex association of the apatite nanocrystal and collagen nanocomposite. The initial studies of interfibrillar collagen mineralization were conducted by transmission electron microscopy (TEM) (Weiner and Traub, 1986) followed by electron tomography (ET) analysis (Landis et al., 1993; Landis et al., 1996). These studies revealed that the orientation of apatite nanocrystals may be regulated by confinement in the collagen fibrils forming a deck of card conformation. The cylindrical nanopores in the collagen can direct the oriented growth of apatite nanocrystals *in vivo* (Olszta et al., 2007). However, this suggestion cannot be considered without detailed ultrastructure of the collagen gap zone. Recently, the detailed model of interfibrillar collagen mineralization was presented by Xu and coworkers. The analysis was performed on the surgical waste material from the tibia fracture of a ten-year-old healthy female. X-ray diffraction (XRD), Electron microscopy and tomography analysis have revealed, the dimension (~65 nm × 20 nm × 3 nm) of the interfibrillar crystals that possess curved or propeller-like morphology. Extracellular apatite nanocrystals of similar dimensions were also observed which may potentially proliferate into the fibers. The charged amino acids in the collagen are considered to regulate and induce the nucleation of apatite nanocrystals. The study delivered three aspects a) Interfibrillar apatite nanocrystal orientation, b) structure of collagen gap zone, and c) apatite-collagen interaction (Xu et al., 2020).

Nucleation site in collagen

The ultrasound studies revealed that the apatite nanocrystal deposition in extracellular space and arrangement on collagen fibers was not random but aligned. The apatite nanocrystal was deposited specifically along the axial region of collagen fibers. Electron micrographs showed physiochemical interactions, organizing CaP in 700 Å axial repeat of the collagen fibers. Moreover, the c-axis of

apatite nanocrystals is aligned to the long axis of the collagen which may be responsible for the nucleation of apatite nanocrystals in c-axis orientation (Landis, 1986). This eliminates the possibility of orientation through mechanical pressure generated by the dense packing of many apatite nanocrystal crystals.

The charged amino acids such as glutamic acid, hydroxyl-serine, aspartic acid, lysine, arginine, and histidine were found in several two-dimension structure of type-I collagen molecular segment as well as in the adjacent segments of the triple helix chain. The charge distribution of the peptide in the collagen chain offers charged domain that serves as center for apatite formation (Landis and Silver, 2009). The locations containing these specific amino acids have stereochemical configurations that provided binding sites for calcium and phosphate ions. Moreover, the ions are sufficiently close to stimulating ion interaction and formation of apatite nucleation sites (Höhling et al., 1974). In the quasi-hexagonal model, the lysine (at residue 108) and the glutamic acid (at residue 110) in a segment I and the glutamic acid (at residue 815) and arginine (at residue 816) in segment 4 result in a pocket that can accommodate calcium and phosphate ions. The ion binding efficiency also increases in the same gap zone through interaction with glutamic acid (at residue 116) in segment 1, arginine (at residue 350) in segment 2, arginine/aspartic acid (at residue 581 and 582, respectively) and glutamic acid/arginine (at residue 815 and 816, respectively) in segment 4 (Hulmes and Miller, 1979). The stereochemical configuration of the amino acids present within or between the collagen segments provided calcium and phosphate binding sites that aid in the formation of nucleation centers. Recently Silver and Landis (2011) provided more consideration in collagen mineralization; a) orientation of charged side chain, b) collagen crosslinking, and c) impact of non-collagenous molecules.

Experimental studies have shown that the synthetic ACP/collagen combination alone is not capable of initiating the nucleation of apatite rapidly (Bradt et al., 1999). Therefore, it was understood that there is the presence of a nucleation catalyst governing the process (Wang and Nancollas, 2008). The nucleation catalyst was defined as an organized organic molecule, containing specific reactive side chains arranged in specific stereochemical and electrochemical arrays establishing a nucleation site as shown in Figure 3. This allows precise cellular control and molecular localization of the interfibrillar collagen mineralization process (Bonar and Glimcher, 1970; Glimcher, 1979).

ACP and role of Howard factor

Studies of infant rib bone revealed the presence of a non-crystalline phase before the initiation of the "interfibrillar collagen mineralization front" (Robinson and Watson, 1952). Following, in 1956, Jackson and Randall (2008) studied the periosteal bone growth in fowl embryos and discovered an electron-opaque substance in a newly formed fibrous matrix. This opaque substance was considered an amorphous phase of mineral. Further, in 1959, a similar finding was reported while investigating parietal bone in mice. They the provided first morphological evidence of the ACP (Molnar, 1959).

Finally, in 1966, the first experimental studies on ACP were demonstrated (Harper and Posner, 2016). They observed that the non-crystalline counterpart was evenly distributed in osseous tissue in several mammalian species. Further, they described that 40% of the bone mineral in the femur of adult humans, cows, and rats was comprised of the non-crystalline phase (Termine and Posner, 1966). Additionally, Posner (1969) confirmed bone mineral as poorly crystalline calcium phosphate (PCCP) which was not identical to the structure and composition of hydroxyapatite (HaP). They proved that bone consists of physically and chemically divergent phases of CaP. Further studies concluded that the bone consists of a large amount of non-crystalline or ACP apart from apatite nanocrystals.

Along with ACP, parallel studies were undergoing to understand the role of cells in the formation of CaP. In the fifth Jubilee lecture of Lehninger (1970), the role of mitochondria and the active Ca^{2+} ion transport was demonstrated in detail. The major topics such as Ca^{2+} ion a) specificity, b) tissue distribution, c) transport mechanism, d) affinity binding, e) relaxation cycle in muscle, f) formation of calcium phosphate granules, and g) role of mitochondria in interfibrillar collagen mineralization was thoroughly discussed. The key findings are highlighted in the following paragraph.

The rat kidney mitochondria can accumulate enormous quantities of Ca^{2+} depending on the presence of respiratory substances such as isocitrate, succinate, adenosine triphosphate (ATP), Mg^{2+}, and/or inorganic orthophosphate (Vasington and Murphy, 1962). In the following year, the relationship between the number of electrons flowing through the respiratory chain and the number of Ca^{2+} ion accumulation was identified. The stoichiometric uptake of both Ca^{2+} and phosphate ions was synergistic with electron transport in such a way that 1.7–2.0 Ca^{2+} ions and 1.0 phosphate ions accumulate per pair of electrons sloping each of three energy-conserving sites of the respiratory chain (Bielawski and Lehninger, 1966). Furthermore, it was also observed that the Ca^{2+} arouses respiration of mitochondria in such a way that two Ca^{2+} ions capitulate the same amount of oxygen as required by one Adenosine diphosphate (ADP) (Carafoli and Lehninger, 1964). The accumulation of Ca^{2+} ions is completed by the ejection of H^{+} ions (Rossi et al., 1966). This is one of the major findings of the relationship between Ca^{2+} and anion accumulation.

Mitochondria are accumulated with Ca^{2+} and diverse types of anions under different conditions. Thus, Ca^{2+} ions are bound to the inner membrane of mitochondria until a perfect anion is available and in the presence of the permanent anion, Ca^{2+} appears in the matrix. ATP or ADP is required in the formation of ACP that accumulates in the mitochondria. This leads to massive loading of mitochondria with ACP. However, the role of ATP in the process remains unknown (Lehninger, 1970).

Based on the experimental evidence of cellular machinery involved in CaP formation, Leininger and co-workers presented two theories on the formation of ACP and its conversion to apatite. According to the first theory, the formation of bone apatite in the presence of a biological inhibitor was presented as shown in Figure 4 (Scheme 1). The process is initiated in interstitial fluid, where the Ca^{2+} and phosphate ions in the presence of biological factor (presumed to be Howard factor) undergo localized concentration to exceed the solubility of ACP. The role of the Howard factor was crucial as it prevents the non-biological formation of apatite from free Ca^{2+} and phosphate ions.

10.3389/fbioe.2023.1150037

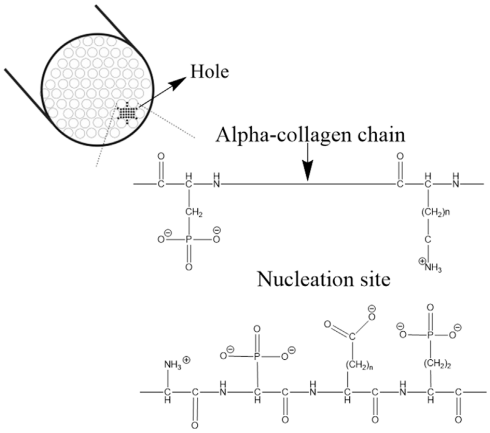

FIGURE 3
Nucleation sites in the hole zone of the alpha-collagen fibril. The image is inspired by the work of (Glimcher, 1984).

Further, the ACP micro-packets formed in association with the Howard factor undergo non-reversible hydrolysis followed by nucleation and are later converted to the apatite nanocrystal.

The Second hypothesis describes the mitochondrial-dependent cellular mechanism as shown in Figure 4 (Scheme 2). According to this theory, the Ca^{2+} and phosphates ions in blood plasma are transported into the cell cytoplasm. Further, the ions are pumped into the inner wall of mitochondria on specific carriers by energy-yielding electron transport (Rossi et al., 1967). When the solubility product of ACP is exceeded, precipitation of micro-packets occurs. The Adenosine triphosphate (ATP) dependent process continues resulting in electron opaque granules composed of many ACP micro-packets which are stabilized by the Howard factor. The micro-packet of ACP can transfer from the mitochondria in two ways; 1) Direct transfer through a mitochondrial membrane or 2) by reverse phagocytosis, leading to out pocketing of membrane vesicles containing two or more micro-packets. After ejecting these micro packets into the extracellular site, they attach to the epitaxial structure of collagen and become part of an amorphous bone mineral fraction. These micro-packets were identified as Posner clusters which possess a neutral ion cluster of 10Å in the longest dimension with a probable chemical structure $Ca_9(PO_4)_6$ (Betts et al., 1975).

In both, the hypothesis of the role of the Howard factor was crucial in stabilizing ACP. This Howard factor was discovered first, in urine samples (Howard and Thomas, 1968). It was classified as a small organic molecule synthesized by cells, organic in nature, highly acidic, chelating agent and its methylation causes loss of activity. Although there is no evidence about the exact chemical structure of the Howard factor in the literature. Further research was not performed to understand the exact chemical structure of the Howard factor.

Micro-vesicle theory

In 1967, Bonucci studied the early stage biomineralization in cartilage. The process was initiated by the formation of peri-circular, periodic acid-Schiff positive, osmiophilic, rounded bodies in which the nucleation of apatite nanocrystals was initiated. The crystallites were removed by decalcification leaving "ghost bodies," which were organic in nature like protein absorbed on the surface of the apatite nanocrystals. The formations of these bodies seem unclear but were believed that these bodies can be formed enzymatically or were secreted by cells. Electron microscopy analysis did not show any structure in these bodies until the initiation of biomineralization. However, these bodies were formed by a homogeneous substance that possesses variable electron density (Bonucci, 1967). In the same year, Anderson also studied the development of cartilage and biomineralization. The electron microscopy studies revealed that the culture of human amniotic cells (FL strain) induces the deposition of a radial cluster-like apatite nanocrystal in the cartilage matrix. This bears a resemblance to the native pattern observed at the epiphysis. Both these studies observed electron-dense "leaf-like" structures with needle-like projections attached to the collagen fibrils in ossifying cartilage matrix, which was then classified as matrix vesicles (MV) (Anderson, 1967).

The properties, function, biogenesis, and biological models of micro-vesicles from chondrocytes and osteoblasts are recently reported in the review presented by Bottini et al. (2018). They proposed that one or more annexin family proteins were responsible for the uptake of Ca^{2+} ion in the MV as shown in Figure 5. They assumed that AnxA5 may act as a carrier protein that will transport Ca^{2+} ions from mitochondria to the inner leaflet of the plasma membrane where it can bind to phosphatidylserine (PS). It was postulated that the lipid rafts in the microvilli membrane form a complex of PS, AnxA5, Ca^{2+}, and phosphate which accounts for the formation of the MV nucleation core. Further, it was speculated that

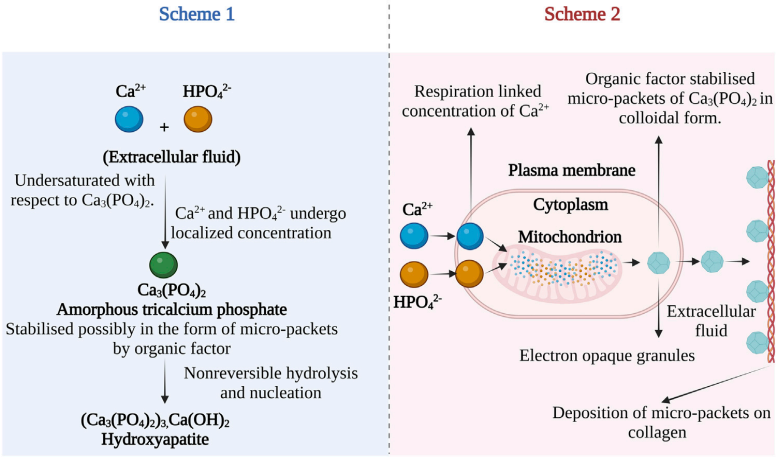

FIGURE 4
Possible mechanism of bone apatite formation from ACP in the presence of biological inhibitor. Scheme 1—apatite formation mechanism in extracellular fluid and Scheme 2—mitochondrial-dependent cellular mechanism of bone apatite formation. The images are inspired by the fifth jubilee lecture on mitochondria and calcium ion transport of (Lehninger, 1970).

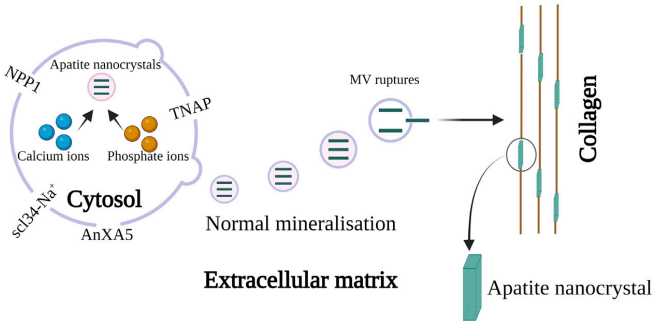

FIGURE 5
Schematic representation of MV in biomineralization. The biomineralization by MV occurs in two steps, in step 1 apatite nanocrystal is formed *via* the influx of calcium and phosphate ions through AnXA5. The hydrolytic action of the enzyme phospholipase and the protease leads to the penetration of apatite crystal inside MV. Once the MV is released into the extracellular matrix they bind to collagen. This initiates step 2 resulting in biomineralization in presence of collagen. The image is inspired by the artwork of (Bottini et al., 2018) and (Bommanavar et al., 2020).

the transport of Ca^{2+} and phosphate ions from mitochondria to intracellular vesicles (IV) towards the extracellular matrix may initiate biomineralization. The author also described another hypothesis in which empty MV budding from chondrocytes is released from the microvilli-like cell membrane. After they are released in the extracellular medium, Ca^{2+} and phosphate ions are accumulated following nucleation from apatite nanocrystal. Further, the MVs are ruptured by stress or by the activity of phospholipase and the apatite nanocrystals are released in the extracellular medium which mineralizes on collagen fibers (Bottini et al., 2018). Recently, Beck (2019) has described the role of scl34-Na^+ phosphate transporter in the biomineralization of bone

and tooth. The latest review covers the role of MV mediated mechanism with special reference to the crystal ghost in depth (Bommanavar et al., 2020).

Phosphoprotein

The phosphoproteins containing serine and threonine amino acids are believed to play a role in interfibrillar collagen mineralization. Organic phosphate and carboxylic side chain groups of serine and threonine account for half of all amino acid residues of phosphoprotein in bone (Spector and Glimcher, 1972). The Ca-binding ability is one of the essential requirements for initiating the nucleation of CaP from solution. The phosphate and the carboxylic side chains of phosphoproteins in dentine have shown remarkable Ca-binding ability (Lee et al., 1977). However, Seyer and Glimcher (1977) have mentioned that Ca-binding with phosphoproteins may decrease interfibrillar collagen mineralization because the electrochemical or stereochemical binding of calcium leads to the unavailability of Ca^{2+} ions to react with the inorganic phosphates. This results in preventing one or more physicochemical steps (nucleation, crystal growth, or crystal multiplication) in apatite deposition. Therefore, to understand the interaction of Ca-bonded phosphoprotein with organic phosphates; experiments and ^{31}P NMR analysis were performed.

Initially, the phosphoproteins were titrated with calcium chloride in presence of inorganic orthophosphates, and it was found that in the absence of calcium chloride, there was no shift in ^{31}P NMR signals but on the other hand phosphorous peak was observed with broadening or shifting in the presence of calcium chloride. This confirms the formation of a ternary complex between the orthophosphate ions and the proteins phosphomonoester group (Lee et al., 1983). The phosphoprotein-regulated interfibrillar collagen mineralization process is shown in Figure 6. In 1982, Lian and associates have revealed *in vivo* evidence of phosphoproteins in interfibrillar collagen mineralization (Kiebzak et al., 1988).

Non-collagenous proteins

Collagen account total of 90% organic part of the bone and the remaining part is non-collagenous proteins and low-molecular-weight organic compounds. The non-collagenous proteins are usually referred to as small-integrin binding ligand, N-linked glycoprotein (SIBLING) proteins which consist of osteopontin (OSP), dentin matrix protein (DMP), bone sialoprotein (BSP), dentin sailophosphoprotein (DSPP), and matrix extracellular phosphoglycolproteins (MEPE). These proteins possess the collagen-binding ability as well as RGD sequence for cell binding. Moreover, these proteins share common features of glycosylation, and phosphorylation and have similarities in genomic organization and localization (Huang et al., 2008). A detailed description of the proteins is presented elsewhere (Kalka et al., 2019). Moreover, albumin and α_2-HS-glycoproteins are present throughout the mineralized bone matrix (McKee et al., 1993). Studies have shown evidence of the involvement of these non-collagenous playing a vital role in interfibrillar collagen mineralization which is explained in the subsequent sections.

Albumin

Albumin is the major component of blood and one of the important non-collagenous proteins. It possesses a high affinity towards apatite surface inhibiting crystallization. Therefore, it is known as a factor regulation process of interfibrillar mineralization of collagen. Studies on the precipitation and growth mechanism of OCP in collagen, under the influence of serum albumin, revealed the inhibition capacity of albumin in two ways—the association of the carboxyl group of protein with the calcium of OCP and/or adsorption of albumin on the surface of OCP. There was electrostatic interaction between the positively charged OCP and collagen and negatively charged albumin at pH 6.5. The adsorption of albumin at the nucleation site of the collagen surfaces obstructs the nucleation sites of the substrate thus delaying the first nuclei formation. Crystallization of OCP is rapid on the collagen surface, therefore interfibrillar collagen mineralization is hampered. However, the addition of albumin would obstruct the nucleation sites leading to interfibrillar collagen mineralization (Combes et al., 1999).

α_2-HS-glycoproteins

In 1944, Fetuin was first isolated from bovine serum and since then most commonly known as Fetuin-A or α_2-HS-glycoprotein (Mori et al., 2012). α_2-HS-glycoproteins in the serum inhibit calcium precipitation thus hindering apatite formation. This inhibitory effect was governed by acidic amino acids modulating apatite formation and inhibiting phase separation in serum during the interfibrillar collagen mineralization (Schinke et al., 1996). Further electron microscopy studies have shown that α_2-HS-glycoproteins with ACP form soluble colloidal spheres. These spheres were termed calciprotein particles that are amorphous in nature with sizes ranging from 30 to 150 nm. The binding of acidic amino acid of α_2-HS-glycoproteins with ACP inhibits unwanted mineralization outside the interfibrillar collagen (Heiss et al., 2003).

Oesteopontin and osteocalcin

OCP-osteocalcin complex directs collagen interfibrillar collagen mineralization. Transmission electron microscopy (TEM) analysis revealed that the carboxylate groups in glutamic acid in osteocalcin (OSC) deliver attachment sites to OCP (Pompe et al., 2015). Further, the OSC attaches to collagen and interacts with the Ca-sites of apatite platelets with a Ca-Ca distance of 9.5 Å. Therefore, it was claimed that OSC governs the function of Ca^{2+} ion transport and acts as an intermediary molecule in the nucleation of OCP and apatite in the fibrillar space of collagen (Simon et al., 2018). Further studies revealed the interaction of OSP and OSC with calcium ions induces stability and delays nucleation, whereas interaction with

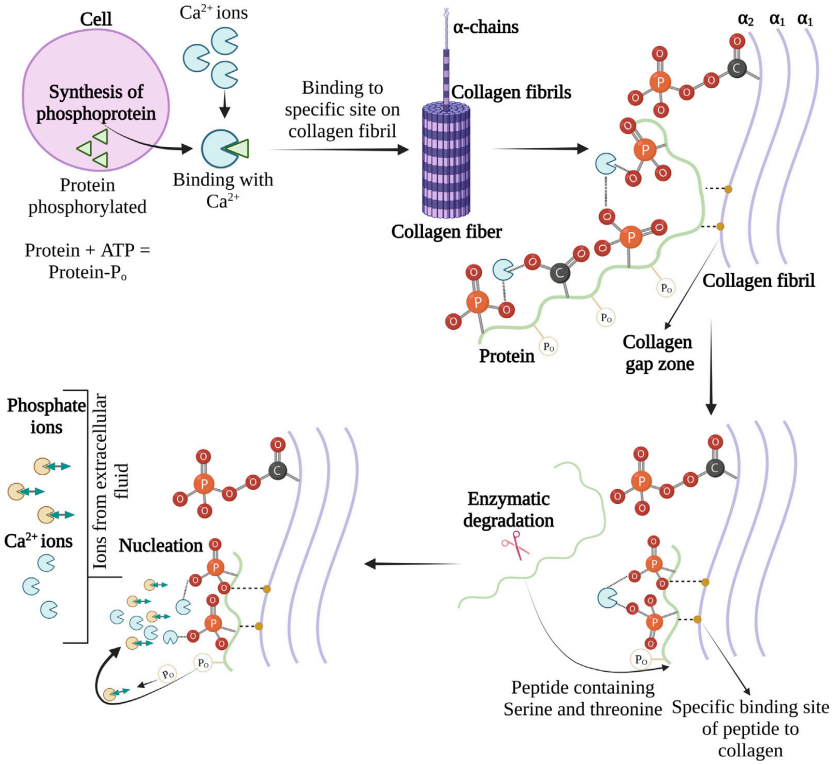

FIGURE 6
Schema for the role of phosphoproteins interfibrillar collagen mineralization. The image is inspired by the artwork of (Glimcher, 1984).

inorganic phosphates results in opposite effects. The study also indicates that OSC concentration negatively influences crystal size and rate of formation though OSC presence results in ordered apatite structures. On the contrary, OSP concentration promotes crystal formation and reduces the Ca:P ratio (Duman et al., 2019).

Dentin matrix protein

The carboxylic terminal present in the amino acids of the protein plays a crucial role in phosphorylation and binding with Ca^{2+} ions controlling interfibrillar collagen mineralization in dentin (George et al., 1993). Tsuji et al. (2008) synthesized artificial motifs analogous to dentin matrix protein. ACP in presence of these proteins increases the molecular mass and the fractal dimensions without affecting the gyration radii. The protein thus enables the conversion of ACP to apatite. The nucleation initiates at the small radius of the growing crystal till the crystal reaches a critical size (termed a critical radius), following rapid crystal growth. This critical radius can be expressed by the function of temperature, supersaturation, specific internal energies, and volume of growth units.

Low-molecular-weight organic compounds

Parathyroid hormone

The role of parathyroid hormone in calcium metabolism was discovered in 1909 (MacCallum and Voegtlin, 1909). The mechanism of action of the parathyroid hormone was well described in the previous review articles (Rasmussen, 1961; Potts et al., 1982). In 1956, Neuman et al. (1956) postulated a mechanism under the control of the parathyroid gland that was maintaining gradients of calcium ions between blood and bone. The cellular element in the bones secreted citrates in response to parathyroid activity. It was assumed that the citrates carrying calcium complex from serum to skeletal tissue get citrated and oxidized to form several calcium ions. If citrates were secreted in the form of citric acid, then due to the pH gradient ionized calcium ions will be transported to serum. The hypothesis was supported by the *in vitro* enzyme studies. It was found that the enzyme isocitrate

dehydrogenase, which is required for citrate utilisation was absent in mature bone. Moreover, the parathyroid hormone destroys the chromophore groups of Coenzyme II. Blocking Coenzyme II-linked reactions shuts glucose metabolism to citrate production. This provides a captivating biochemical mechanism governed by parathyroid hormone in regulating citrate gradient that is responsible for maintaining steady but supersaturated levels of calcium ions in serum.

Citrate

Citrates are small organic moieties that originate in the citric acid cycle and play a critical role in the human metabolic pathway. In 1941, the presence of citrate in bone was first identified (Dickens, 1941). Since then, it is known that citrate concentration in hard tissues is in the range of 20–80 μmole/g which is 100–400 folds higher than in most of the soft tissues. It should also be indicated that the bone consists of 1.6% of citrate and about 90% of total body citrates are found in human bone (Granchi et al., 2019). Such a high concentration of citrates in bone indicates their vital role in mineralization. Recent NMR studies have shown the presence of citrate in bone (Davies et al., 2014). The lattice orientation, particle size, and distribution of the apatite are regulated by the complex interaction of the citrate with the apatite. The long axis of the citrate molecule is parallel to the surface of the apatite. The three carboxylic groups of citrates are at 0.3–0.45 nm from the apatite surface. The spacing of the carboxylic groups matches with the calcium ion along the c-axis of the apatite. Therefore, the crystal growth is inhibited in the direction of thickness but continued in the longitudinal direction. This assists in the formation of a plate-like apatite structure analogous to natural bone (Xie and Nancollas, 2010).

The occurrence of citrate in bone and its relationship was well described by Costello et al. (2012). The author coined the term "citration" which describes the relationship between citrate-apatite nanocrystals. In further studies, the author also described the potential mechanism of how citrate is involved in interfibrillar collagen mineralization (Costello et al., 2015). The collagen/apatite structure incorporated with citrate in the apatite crystal was depicted as shown in Figure 7.

Succinate

Succinic acid (SA) is an intermediate of a citric acid cycle. It can be detected in the bones in exceedingly small concentrations. For instance, 1 g of bone consists of 3.6 mg of SA (Lees and Kuyper, 1957). Like citrates, the carboxylic groups in SA are chemisorbed on the apatite surface by coordinating with calcium ions and regulating the growth and morphology of the crystals. Studies on mineralization reported that SA binds to collagen by hydrogen bonding and encourages interfibrillar collagen mineralization. The interaction of SA with collagen improved the physicochemical properties of apatite and attract more calcium ions, thus leading to accelerated interfibrillar collagen mineralization. Moreover, the SA pre-treated demineralized dentin promoted dentin remineralization. The mechanical properties of the remineralized dentin were similar to natural dentin (Jin et al., 2022). Earlier efforts to synthesize OCP incorporated with SA have been commenced by Marković et al. (1994). They uncovered pH dependency on conversion from SA-OCP to apatite.

Amino acids

Apatite formation was observed near the crossband of collagen where basic and acidic amino acids are thought to be more concentrated (Robinson and Watson, 1955). Soon after this finding, Solomons and Irving (1958) studied the relationship of Ɛ-amino acid of lysine and hydroxylysine in mineralization. The Ɛ-amino acid may provide potential phosphate binding sites on the collagen, leading to its phosphorylation. This was assumed to be the first step in matrix interfibrillar collagen mineralization (Weidmann, 1963). Ikawa et al. (2009) have synthesized amino acid-containing ACP and investigated its transformation in a simulated body fluid. They found that the incorporation of amino acids enhanced the solubility of ACP and lead to faster conversion to apatite. The role of amino acids in mineralization is covered in-depth in a recent review by Tavafoghi and Cerruti (2016).

Pyrophosphate

Fleisch and Sylvia demonstrated *in vitro* nucleation and mineralization of apatite nanocrystals in presence of collagen (Herbert and Bisaz, 1962). They have proposed the role of pyrophosphate in regulating biomineralization. In the nucleating region of collagen, the precipitation of apatite nanocrystals occurs at the physiological concentration of the Ca^{2+} and phosphate ions. It was depicted that the inorganic pyrophosphates (PP_i) present in blood plasma protect the nucleation site in the collagen inhibiting growth of apatite nanocrystals. For the mineralization of collagen, the pyrophosphates must be inactivated by the enzyme pyrophosphatase which was found in mineralized tissue (Herbert And Bisaz, 1962). Further studies conducted by Moochhala et al. (2008) explored the role of proteins and genes in controlling biomineralization. The enzyme nucleoside pyrophosphatase phosphodiesterase (NPP1) acts on nucleoside triphosphate to generate extracellular PP_i. Harmey et al. (2004) have further demonstrated hyper-mineralization in *enpp1* (NPP1) knockout mice, resulting in peripheral joint hyperostosis intervertebral fusion. Moreover, the role of the *ank* gene (ANKH in humans) in exporting PP_i from cytoplasm to extracellular space was noticed. The *ank* protein was linked with tissue calcification in humans and mice. The third gene *akp2* encodes tissue non-specific alkaline phosphatase (TNAP) which hydrolyses PP_i, and polyphosphates to release inorganic phosphate. The TNAP activity promotes biomineralization by lowering PP_i levels and increasing levels of inorganic phosphate.

Polymer-induced liquid precursors

Polymer-induced liquid precursors (PILP) are amorphous mineral precursors stabilized by charged polymers. In the early 1990s, the role of acidic macromolecules in the biomineralization of bone and seashells was known. The acidic macromolecule was known to control the morphology of the inorganic crystal. However, the function of the acidic macromolecule was not clarified. In 1998, Gower and Tirrell (1998) have discovered that the addition of a small amount of polyaspartic acid (pAap) results in $CaCO_3$ helices and films. The polymer acts as a membrane and supports the deposition and growth of $CaCO_3$. The charge polymer ion inhibits crystal nucleation by inducing liquid-liquid phase separation in the crystallizing fluid. Droplets from the fluidic amorphous phase accumulate and combine resulting in mineral

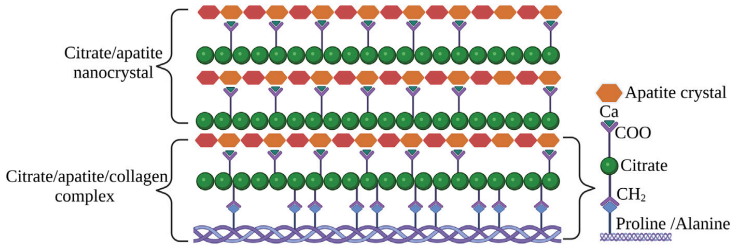

FIGURE 7
The status of citrate in apatite/collagen component of bone. The image is inspired by the artwork of (Costello et al., 2018).

films. Olszta et al. (2007) have postulated the role of PILP biomineralization of bone and teeth. They suggest that the apatite nanocrystal does not nucleate within the gap zone, rather a liquid amorphous phase is pulled into collagen fibers by capillary actions. Once the liquid precursor phase is converted to the solid amorphous phase, crystallization occurs resulting in mineralized collagen with apatite nanocrystals. A combination of polyanionic non-collagenous proteins was presumed to be analogous to PILP. This hypothesis was backed by cryo-TEM analysis by Nudelman et al. (2010). They discovered that the electrostatic interaction between pAap-ACP complex and the cationic amino acids in the gap zone of collagen assists infiltration of PILP. Citrate also plays a crucial role in PILP by enhancing the degree of collagen mineralization *in vitro*. The citrate reduces the interfacial energy between collagen and PILP leading to an increase in wettability (Shao et al., 2018). Polyacrylic acid (PAA) was also used successfully in PILP for the stabilization of ACP. PAA of various molecular weights was analyzed, and it was found that both low and high-concentration PAA stabilized ACP and allows infiltration in the collagen matrix. The unstable ACP results in extra fibrillar mineralization. On the contrary, extensively stabilized ACP did not initiate collagen mineralization. This suggests that the concentration of PAA plays a crucial role in regulating interfibrillar collagen mineralization (Shen et al., 2021).

Discussion

It is known that collagen plays a crucial role in the biomineralization process. The unique physiochemical properties of collagen offer this potential. Based on the physical characteristics of hydration a model of collagen interfibrillar biomineralization was demonstrated. Molecular dynamic studies have shown the balance between osmotic equilibrium and electroneutrality establishes Gibbs-Donnan equilibrium in a polyelectrolyte-directed system (Niu et al., 2017). Based on the chemical properties of collagen numerous models are presented. For instance, the amino acid residue in the two-dimension structure of type-I collagen molecular segment as well as in the adjacent segments of the triple helix chain. The charge distribution of the peptide in the collagen chain offers charged domain that serves as a center for apatite formation. However experimental studies have shown that the synthetic ACP/collagen combination alone is not capable of initiating the nucleation of apatite rapidly (Bradt et al., 1999). This indicates that collagen cannot initiate or regulate interfibrillar mineralization alone (Posner, 1969). Therefore, the role of non-collagenous proteins and other ECM molecules was considered to affect mineralization either by enhancing collagen mineral interaction or binding mineral ions. However, there are numerous postulations on this phenomenon, but the exact mechanism is poorly understood (Silver and Landis, 2011).

There are numerous mechanisms for how calcium phosphate is deposited on the collagen matrix. Different organic compounds are believed to regulate interfibrillar mineralization. Most of these compounds possess a carboxyl functional group. The carboxyl group is a combination of two functional groups in which a single carbon atom is attached to hydroxyl (−OH) and carbonate (=O) groups. This makes the carbonyl group polar, highly electronegative, and weakly acidic, capable of hydrogen bonding by accepting or donating proton (Klecker and Nair, 2017). The carboxylate anion has the capability of forming bonds with calcium by direct binding or by influencing electrostatic interactions away from the metal center (Chakrabarti, 1990). Moreover, the carboxylate ions also have the potential to react with phosphate *via* the formation of P-O-H-O-C bonding (Corbridge, 1971). Owing to these exclusive properties, carboxylate-incorporated calcium phosphate materials are gaining more interest.

In the past 20 years, the research is focused on finding the role of carboxylic compounds in interfibrillar collagen mineralization (Ikawa et al., 2008; Sakamoto et al., 2008; Ishikawa and Oaki, 2014; Josipović et al., 2020; Veiga et al., 2020; Wang et al., 2020). Recent studies have also provided new findings such as A) Influence of carboxylic ions in the conversion of ACP to OCP (Sugiura et al., 2015). B) The density of carboxylic ions plays a crucial role in controlling the growth and mineralization of calcium phosphates (Zhang et al., 2022). C) In the early nucleation, citrate binds to ACP and controls the size and morphology of apatite crystal (Xie and Nancollas, 2010). D) One-sixth of the available apatite surface area in bone is covered by citrate (Xie and Nancollas, 2010). E) Carboxylate ions can only be incorporated into the hydrated layer of CaP

(Yokoi et al., 2022). F) Collagen matrix is denser and irregularly distributed in the bone as compared to the majority of other soft tissues (Tzaphlidou, 2008).

Conclusion

Interfibrillar collagen mineralization has gained attention in the past 20 years, the major reason is the abundance of both apatite nanocrystals and collagen in bone. Studies have indicated the role of physiochemical properties of collagen as well as non-collagenous proteins and low molecular weight compounds regulating the process. New insights such as the role of genes and enzymes in this process are also discovered. Overall, the process of interfibrillar collagen mineralization is complex. However, advanced analysis techniques such as cryo-TEM, Cryo-scanning electron microscopy, X-Ray tomography, molecular dynamics, gene knockout, metabolomics, proteomics, DNA and RNA sequencing, etc. allow investigation of mechanism within nanometer resolution while maintaining the structure close to the native structure. These advanced analysis techniques with a combination of both *in vivo* and *in vitro* analysis potentially answer all the underlying questions in the future. However, the process is currently in the preliminary stage, but the technological advancement will soon decode the process of interfibrillar collagen mineralization.

Author contributions

AI: Conceptualisation, literature review, writing-original draft preparation. RC: Writing-review and editing. KR: Writing-review and editing. JL: Conceptualisation, writing-review, and editing. All authors provided critical feedback and helped to shape the research, analysis, and manuscript.

Acknowledgments

The authors acknowledge financial support from the European Union's Horizon 2020 research and innovation programme under the grant agreement No. 857287 (BBCE – Baltic Biomaterials Centre of Excellence) and the Baltic Research Programme project No. EEA-RESEARCH-85 "Waste-to-resource: eggshells as a source for next generation biomaterials for bone regeneration (EGGSHELL)" under the EEA Grant of Iceland, Liechtenstein, and Norway No. EEZ/BPP/VIAA/2021/1.

Conflict of interest

The authors declare that the research was conducted in the absence of any commercial or financial relationships that could be construed as a potential conflict of interest.

Publisher's note

References

Anderson, H. C. (1967). Electron microscopic studies of induced cartilage development and calcification. *J. Cell. Biol.* 35, 81–101. doi:10.1083/JCB.35.1.81

Bear, R. S. (1952). The structure of collagen fibrils. *Adv. Protein Chem.* 7, 69–160. doi:10.1016/S0065-3233(08)60018-2

Beck, L. (2019). Expression and function of Slc34 sodium–phosphate co-transporters in skeleton and teeth. *Pflugers Arch. Eur. J. Physiol.* 471, 175–184. doi:10.1007/S00424-018-2240-Y

Betts, F., Blumenthal, N. C., Posner, A. S., Beckert, G. L., and Lehningert, A. L. (1975). Atomic Structure of Intracellular Amorphous Calcium Phosphate Deposits (x-ray diffraction/radial distribution analysis/ion clusters/soft-tissue calcification/micropackets). 72, 2088–2090. Available at: https://www.pnas.org (Accessed June 7, 2022).

Bielawski, J., and Lehninger, A. L. (1966). Stoichiometric relationships in mitochondrial accumulation of calcium and phosphate supported by hydrolysis of adenosine triphosphate. *J. Biol. Chem.* 241, 4316–4322. doi:10.1016/S0021-9258(18)99724-3

Bommanavar, S., Hosmani, J., Togoo, R. A., Baeshen, H. A., Raj, A. T., Patil, S., et al. (2020). Role of matrix vesicles and crystal ghosts in bio-mineralization. *J. Bone Min. Metab.* 38, 759–764. doi:10.1007/S00774-020-01125-X

Bonar, L. C., and Glimcher, M. J. (1970). Thermal denaturation of mineralized and demineralized bone collagens. *J. Ultrasructure Res.* 32, 545–557. doi:10.1016/S0022-5320(70)80027-2

Bonucci, E. (1967). Fine structure of early cartilage calcification. *J. Ultrasructure Res.* 20, 33–50. doi:10.1016/S0022-5320(67)80034-0

Bottini, M., Mebarek, S., Anderson, K. L., Strzelecka-Kiliszek, A., Bozycki, L., Simão, A. M. S., et al. (2018). Matrix vesicles from chondrocytes and osteoblasts: Their biogenesis, properties, functions and biomimetic models. *Biochim. Biophys. Acta - Gen. Subj.* 1862, 532–546. doi:10.1016/J.BBAGEN.2017.11.005

Bradt, J. H., Mertig, M., Teresiak, A., and Pompe, W. (1999). Biomimetic mineralization of collagen by combined fibril assembly and calcium phosphate formation. *Chem. Mat.* 11, 2694–2701. doi:10.1021/CM991002P

Brown, W., Eidelman, N., and Tomazic, B. (1987). Octacalcium phosphate as a precursor in biomineral formation. *Adv. Dent. Res.* 1 (2), 306–313. doi:10.1177/08959374870010022201

Carafoli, E., and Lehninger, A. L. (1964). Binding of adenine nucleotides by mitochondria during active uptake of Ca++. *Biochem. Biophys. Res. Commun.* 16, 66–70. doi:10.1016/0006-291X(64)90212-8

Chakrabarti, P. (1990). Interaction of metal ions with carboxylic and carboxamide groups in protein structures. *Protein Eng. Des. Sel.* 4, 49–56. doi:10.1093/PROTEIN/4.1.49

Combes, C., Rey, C., and Freche, M. (1999). *In vitro* crystallization of octacalcium phosphate on type I collagen: Influence of serum albumin. *J. Mat. Sci. Mat. Med.* 10, 153–160. doi:10.1023/A:1008933406806

Corbridge, D. E. C. (1971). The structural chemistry of phosphates. *Bull. Minéralogie* 94, 271–299. doi:10.3406/BULMI.1971.6534

Costello, L. C., Chellaiah, M. A., Zou, J., Reynolds, M. A., and Franklin, R. B. (2015). *In vitro* BMP2 stimulation of osteoblast citrate production in concert with mineralized bone nodule formation. *J. Regen. Med. Tissue Eng.* 4, 2. doi:10.7243/2050-1218-4-2

Costello, L. C., Franklin, R. B., Reynolds, M. A., and Chellaiah, M. (2012). The important role of osteoblasts and citrate production in bone formation: "Osteoblast citration" as a new concept for an old relationship. *Open Bone J.* 4, 27–34. doi:10.2174/1876525401204010027

Costello, L. C., Franklin, R. B., and Reynolds, M. A. (2018). The important role and implications of citrate in the composition, structure, and function of oral/periodontal/craniofacial tissues. *Madridge J. Dent. Oral Surg.* 3, 85–90. doi:10.18689/MJDL-1000120

Davies, E., Müller, K. H., Wong, W. C., Pickard, C. J., Reid, D. G., Skepper, J. N., et al. (2014). Citrate bridges between mineral platelets in bone. *Proc. Natl. Acad. Sci. U. S. A.* 111. doi:10.1073/PNAS.1315080111/-/DCSUPPLEMENTAL/PNAS.201315080SI

Dickens, F. (1941). The citric acid content of animal tissues, with reference to its occurrence in bone and tumour. *Biochem. J.* 35, 1011–1023. doi:10.1042/BJ0351011

Duman, E., Şahin Kehribar, E., Ahan, R. E., Yuca, E., and Şeker, U. Ö. Ş. (2019). Biomineralization of calcium phosphate crystals controlled by protein-protein interactions. *ACS Biomater. Sci. Eng.* 5, 4750–4763. doi:10.1021/acsbiomaterials.9b00649

Fratzl, P., and Weinkamer, R. (2007). Hierarchical structure and repair of bone: Deformation, remodelling, healing. *Springer Ser. Mat. Sci.* 100, 323–335. doi:10.1007/978-1-4020-6250-6_15/COVER

Fuchs, R. K., Warden, S. J., and Turner, C. H. (2009). Bone anatomy, physiology and adaptation to mechanical loading. *Bone Repair Biomater.* 25–68. doi:10.1533/9781845696610.1.25

George, A., Sabsay, B., Simonian, P. A. L., and Veis, A. (1993). Characterization of a novel dentin matrix acidic phosphoprotein. Implications for induction of biomineralization. *J. Biol. Chem.* 268, 12624–12630. doi:10.1016/S0021-9258(18)31434-0

Glimcher, M. J. (1979). Phosphopeptides of enamel matrix. *J. Dent. Res.* 58, 790–809. doi:10.1177/00220345790580023101

Glimcher, M. J., Bonar, L. C., Grynpas, M. D., Landis, W. J., and Roufosse, A. H. (1981). Recent studies of bone mineral: Is the amorphous calcium phosphate theory valid? *J. Cryst. Growth* 53, 100–119. doi:10.1016/0022-0248(81)90058-0

Glimcher, M. J. (1984). Recent studies of the mineral phase in bone and its possible linkage to the organic matrix by protein-bound phosphate bonds. *Philos. Trans. R. Soc. Lond. Ser. B* 304, 479–508. doi:10.1098/rstb.1984.0041

Gower, L. A., and Tirrell, D. A. (1998). Calcium carbonate films and helices grown in solutions of poly(aspartate). *J. Cryst. Growth* 191, 153–160. doi:10.1016/S0022-0248(98)00002-5

Granchi, D., Baldini, N., Ulivieri, F. M., and Caudarella, R. (2019). Role of citrate in pathophysiology and medical management of bone diseases. *Nutrients* 11, 2576. doi:10.3390/NU11112576

Gutsmann, T., Fantner, G. E., Venturoni, M., Ekani-Nkodo, A., Thompson, J. B., Kindt, J. H., et al. (2003). Evidence that collagen fibrils in tendons are inhomogeneously structured in a tubelike manner. *Biophys. J.* 84, 2593–2598. doi:10.1016/S0006-3495(03)75064-4

Harmey, D., Hessle, L., Narisawa, S., Johnson, K. A., Terkeltaub, R., and Millán, J. L. (2004). Concerted regulation of inorganic pyrophosphate and osteopontin by Akp2, Enpp1, and ank: An integrated model of the pathogenesis of mineralization disorders. *Am. J. Pathol.* 164, 1199–1209. doi:10.1016/S0002-9440(10)63208-7

Harper, R. A., and Posner, A. S. (2016). Measurement of non-crystalline calcium phosphate in bone mineral. *Proc. Soc. Exp. Biol. Med.* 122 (1), 137–142. doi:10.3181/00379727-122-31073

Heikkilä, J. (2011). Use of bioactive glasses as bone substitutes in orthopaedics and traumatology. *Bioact. Glas. Mat. Prop. Appl.* 189–208. doi:10.1533/9780857093318.2.189

Heiss, A., DuChesne, A., Denecke, B., Grötzinger, J., Yamamoto, K., Renneé, T., et al. (2003). Structural basis of calcification inhibition by α2-HS glycoprotein/fetuin-A: Formation of colloidal calciprotein particles. *J. Biol. Chem.* 278, 13333–13341. doi:10.1074/JBC.M210868200

Herbert, F., and Bisaz, S. (1962). Mechanism of calcification: Inhibitory role of pyrophosphate. *Nat* 195, 911. doi:10.1038/195911a0

Höhling, H. J., Ashton, B. A., and Köster, H. D. (1974). Quantitative electron microscopic investigations of mineral nucleation in collagen. *Cell. Tissue Res.* 148, 11–26. doi:10.1007/BF00224315

Howard, J. E., and Thomas, W. C. (1968). Control of crystallization in urine. *Am. J. Med.* 45, 693–699. doi:10.1016/0002-9343(68)90205-2

Huang, B., Sun, Y., MacIejewska, I., Qin, D., Peng, T., McIntyre, B., et al. (2008). Distribution of SIBLING proteins in the organic and inorganic phases of rat dentin and bone. *Eur. J. Oral Sci.* 116, 104–112. doi:10.1111/J.1600-0722.2008.00522.X

Hulmes, D. J. S., and Miller, A. (1979). Quasi-hexagonal molecular packing in collagen fibrils. *Nature* 282, 878–880. doi:10.1038/282878A0

Ikawa, N., Hori, H., Kimura, T., Oumi, Y., and Sano, T. (2008). Templating route for mesostructured calcium phosphates with carboxylic acid- and amine-type surfactants. *Langmuir* 24, 13113–13120. doi:10.1021/la8008859

Ikawa, N., Kimura, T., Oumi, Y., and Sano, T. (2009). Amino acid containing amorphous calcium phosphates and the rapid transformation into apatite. *J. Mat. Chem.* 19, 4906–4913. doi:10.1039/B815154G

Ishikawa, M., and Oaki, Y. (2014). Synthesis of Hydroxyapatite/Nanocellulose Composites.

Jackson, S. F., and Randall, J. T. (2008). "*Fibrogenesis and the Formation of Matrix in Developing Bone*," in *John Wiley & Sons*. 47–64. doi:10.1002/9780470715222.CH5

Jin, W., Jin, Y., Duan, P., Wu, H., Zhang, L., Du, Q., et al. (2022). Promotion of collagen mineralization and dentin repair by succinates. *J. Mat. Chem. B* 10, 5826–5834. doi:10.1039/D2TB01005D

Josipović, T. M., Kovačević, M., Mateša, S., Kostešić, M., Matijaković, N., Radatović, B., et al. (2020). The influence of different classes of amino acids on calcium phosphates seeded growth. *Mater. (Basel)* 13, 4798. doi:10.3390/MA13214798

Kalka, M., Zoglowek, A., Ożyhar, A., and Dobryczycki, P. (2019). Proteins in Calcium Phosphates Biomineralization. *Contemp. Top. about Phosphorus Biol. Mater*. doi:10.5772/INTECHOPEN.86718

Kiebzak, G. M., Smith, R., Gundberg, C. C., Howe, J. C., and Sacktor, B. (1988). Bone status of senescent male rats: Chemical, morphometric, and mechanical analysis. *J. Bone Min. Res.* 3, 37–45. doi:10.1002/jbmr.5650030107

Klecker, C., and Nair, L. S. (2017). Matrix chemistry controlling stem cell behavior. *Biol. Eng. Stem Cell. Niches*, 195–213. doi:10.1016/B978-0-12-802734-9.00013-5

Landis, W. J. (1986). A study of calcification in the leg tendons from the domestic Turkey. *J. Ultrastruct. Mol. Struct. Res.* 94, 217–238. doi:10.1016/0889-1605(86)90069-8

Landis, W. J., Hodgens, K. J., A Song, M. J., and McEWEN, B. F. (1996). Structural relations between bone as determined by high microscopic tomography collagen and mineral in voltage electron. *Microsc. Res. Tech.* 33–192. doi:10.1002/(SICI)1097-0029(19960201)33:2

Landis, W. J., Silver, F. H., and Freeman, J. W. (2006). Collagen as a scaffold for biomimetic mineralization of vertebrate tissues. *J. Mat. Chem.* 16, 1495–1503. doi:10.1039/B505706J

Landis, W. J., and Silver, F. H. (2009). Mineral deposition in the extracellular matrices of vertebrate tissues: Identification of possible apatite nucleation sites on type I collagen. *Cells Tissues Organs* 189, 20–24. doi:10.1159/000151454

Landis, W. J., Song, M. J., Leith, A., McEwen, L., and McEwen, B. F. (1993). Mineral and organic matrix interaction in normally calcifying tendon visualized in three dimensions by high-voltage electron microscopic tomography and graphic image reconstruction. *J. Struct. Biol.* 110, 39–54. doi:10.1006/JSBI.1993.1003

Lee, S. L., Glonek, T., and Glimcher, M. J. (1983). 31P nuclear magnetic resonance spectroscopic evidence for ternary complex formation of fetal dentin phosphoprotein with calcium and inorganic orthophosphate ions. *Calcif. Tissue Int.* 35, 815–818. doi:10.1007/BF02405129

Lee, S. L., Veis, A., and Glonek, T. (1977). Dentin phosphoprotein: An extracellular calcium-binding protein. *Biochemistry* 16, 2971–2979. doi:10.1021/BI00632A026

Lees, H., and Kuyper, A. C. (1957). The organic acids of bone. *J. Biol. Chem.* 225, 641–649. doi:10.1016/S0021-9258(18)64863-X

Lehninger, A. L. (1970). Mitochondria and calcium ion transport. *Biochem. J.* 119, 129–138. doi:10.1042/bj1190129

Liu, Y., Luo, D., and Wang, T. (2016). Hierarchical structures of bone and bioinspired bone tissue engineering. *Small* 12, 4611–4632. doi:10.1002/SMLL.201600626

MacCallum, W. G., and Voegtlin, C. (1909). On the relation of tetany to the parathyroid glands and to calcium metabolism. *J. Exp. Med.* 11, 118–151. doi:10.1084/JEM.11.1.118

Marković, M., Fowler, B. O., and Brown, W. E. (1994). Octacalcium phosphate carboxylates: IV. Kinetics of formation and solubility of octacalcium phosphate succinate. *J. Cryst. Growth* 135, 533–538. doi:10.1016/0022-0248(94)90144-9

McKee, M. D., Farach-Carson, M. C., Butler, W. T., Hauschka, P. V., and Nanci, A. (1993). Ultrastructural immunolocalization of noncollagenous (osteopontin and osteocalcin) and plasma (albumin and α2HS-glycoprotein) proteins in rat bone. *J. Bone Min. Res.* 8, 485–496. doi:10.1002/JBMR.5650080413

Molnar, Z. (1959). Development of the parietal bone of young mice. *J. Ultrastruct. Res.* 3, 39–45. doi:10.1016/s0022-5320(59)80012-5

Moochhala, S. H., Sayer, J. A., Carr, G., and Simmons, N. L. (2008). Renal calcium stones: Insights from the control of bone mineralization. *Exp. Physiol.* 93, 43–49. doi:10.1113/EXPPHYSIOL.2007.040790

Mori, K., Emoto, M., and Inaba, M. (2012). Fetuin-A and the cardiovascular system. *Adv. Clin. Chem.* 56, 175–195. doi:10.1016/B978-0-12-394317-0.00010-8

Neuman, W. F., Firschein, H., Chen, P. S., Mulryan, B. J., and DiStefano, V. (1956). On the mechanism of action of parathormone. *J. Am. Chem. Soc.* 78, 3863–3864. doi:10.1021/ja01596a089

Niu, L. N., Jee, S. E., Jiao, K., Tonggu, L., Li, M., Wang, L., et al. (2017). Collagen intrafibrillar mineralization as a result of the balance between osmotic equilibrium and electroneutrality. *Nat. Mat.* 16, 370–378. doi:10.1038/NMAT4789

Nudelman, F., Pieterse, K., George, A., Bomans, P. H. H., Friedrich, H., Brylka, L. J., et al. (2010). The role of collagen in bone apatite formation in the presence of hydroxyapatite nucleation inhibitors. *Nat. Mat.* 9, 1004–1009. doi:10.1038/NMAT2875

Olszta, M. J., Cheng, X., Jee, S. S., Kumar, R., Kim, Y. Y., Kaufman, M. J., et al. (2007). Bone structure and formation: A new perspective. *Mat. Sci. Eng. R. Rep.* 58, 77–116. doi:10.1016/J.MSER.2007.05.001

Parvizi, J., and Kim, G. K. (2010). Collagen. *High. Yield Orthop.* 107–109. doi:10.1016/B978-1-4160-0236-9.00064-X

Pompe, W., Worch, H., Habraken, W. J. E. M., Simon, P., Kniep, R., Ehrlich, H., et al. (2015). Octacalcium phosphate – A metastable mineral phase controls the evolution of scaffold forming proteins. *J. Mat. Chem. B* 3, 5318–5329. doi:10.1039/C5TB00673B

Posner, A. S. (1969). Crystal chemistry of bone mineral. *Physiol. Rev.* 49, 760–792. doi:10.1152/PHYSREV.1969.49.4.760

Potts, J. T., Kronenberg, H. M., and Rosenblatt, M. (1982). Parathyroid hormone: Chemistry, biosynthesis, and mode of action. *Adv. Protein Chem.* 35, 323–396. doi:10.1016/S0065-3233(08)60471-4

Quan, B. D., and Sone, E. D. (2013). Cryo-TEM analysis of collagen fibrillar structure. *Methods Enzymol.* 532, 189–205. doi:10.1016/B978-0-12-416617-2.00009-6

Rasmussen, H. (1961). Parathyroid hormone: Nature and mechanism of action. *Am. J. Med.* 30, 112–128. doi:10.1016/0002-9343(61)90068-7

Rho, J. Y., Kuhn-Spearing, L., and Zioupos, P. (1998). Mechanical properties and the hierarchical structure of bone. *Med. Eng. Phys.* 20, 92–102. doi:10.1016/S1350-4533(98)00007-1

Robinson, R. A., and Watson, M. L. (1952). Collagen-crystal relationships in bone as seen in the electron microscope. *Anat. Rec.* 114, 383–409. doi:10.1002/AR.1091140302

Robinson, R. A., and Watson, M. L. (1955). Crystalcollagen relationships in bone as observed in the electron microscope. III. Crystal and collagen morphology as a function of age. *Ann. N. Y. Acad. Sci.* 60, 596–630. doi:10.1111/J.1749-6632.1955.TB40054.X

Rossi, C. S., Carafoli, E., and Lehninger, A. L. (1967). Active ion transport by mitochondria. *Symp. Biophys. Physiol. Biol. Transp.* 63, 90–94. doi:10.1007/978-3-7091-5577-6_20

Rossi, C. S., Bielawski, J., Carafoli, E., and Lehninger, A. L. (1966). The relationship of the Ca++ efflux rate to the "super-stoichiometry" of respiration-linked Ca++ accumulation by mitochondria. *Biochem. Biophys. Res. Commun.* 22, 206–210. doi:10.1016/0006-291X(66)90433-5

Sakamoto, K., Yamaguchi, S., Kaneno, M., Fujihara, I., Satoh, K., and Tsunawaki, Y. (2008). Synthesis and thermal decomposition of layered calcium phosphates including carboxylate ions. *Thin Solid Films* 517, 1354–1357. doi:10.1016/J.TSF.2008.09.050

Schinke, T., Amendt, C., Trindl, A., Pöschke, O., Müller-Esterl, W., and Jahnen-Dechent, W. (1996). The serum protein α2-HS glycoprotein/fetuin inhibits apatite formation *in vitro* and in mineralizing calvaria cells: A possible role in mineralization and calcium homeostasis. *J. Biol. Chem.* 271, 20789–20796. doi:10.1074/JBC.271.34.20789

Seyer, J. M., and Glimcher, M. J. (1977). Isolation, characterization and partial amino acid sequence of a phosphorylated polypeptide (E4) from bovine embryonic dental enamel. *Biochim. Biophys. Acta - Protein Struct.* 493, 441–451. doi:10.1016/0005-2795(77)90200-8

Shao, C., Zhao, R., Jiang, S., Yao, S., Wu, Z., Jin, B., et al. (2018). Citrate improves collagen mineralization via interface wetting: A physicochemical understanding of biomineralization control. *Adv. Mat.* 30, 1704876. doi:10.1002/ADMA.201704876

Shen, L., Bu, H., Zhang, Y., Tang, P., and Li, G. (2021). Molecular weight and concentration of poly (acrylic acid) dual-responsive homogeneous and intrafibrillar collagen mineralization using an *in situ* co-organization strategy. *Polym. Compos.* 42, 4448–4460. doi:10.1002/PC.26161

Silver, F. H., and Landis, W. J. (2011). Deposition of apatite in mineralizing vertebrate extracellular matrices: A model of possible nucleation sites on type I collagen. *Connect. Tissue Res.* 52, 242–254. doi:10.3109/03008207.2010.551567

Simon, P., Grüner, D., Worch, H., Pompe, W., Lichte, H., El Khassawna, T., et al. (2018). First evidence of octacalcium phosphate@osteocalcin nanocomplex as skeletal bone component directing collagen triple–helix nanofibril mineralization. *Sci. Rep.* 81 (8), 13696. doi:10.1038/s41598-018-31983-5

Solomons, C. C., and Irving, J. T. (1958). Studies in calcification the reaction of some hard- and soft-tissue collagens with 1-fluoro-2:4-dinitrobenzene. *Biochem. J.* 68, 499–503. doi:10.1042/BJ0680499

Spector, A. R., and Glimcher, M. J. (1972). The extraction and characterization of soluble anionic phosphoproteins from bone. *Biochim. Biophys. Acta - Protein Struct.* 263, 593–603. doi:10.1016/0005-2795(72)90040-2

Sugiura, Y., Onuma, K., Nagao, M., and Yamazaki, A. (2015). The effects of immobilized carboxylic-functional groups on the dynamics of phase transformation from amorphous to octacalcium phosphate. *Am. Mineral.* 100, 1624–1632. doi:10.2138/AM-2015-5179

Tavafoghi, M., and Cerruti, M. (2016). The role of amino acids in hydroxyapatite mineralization. *J. R. Soc. Interface* 13, 20160462. doi:10.1098/RSIF.2016.0462

Termine, J. D., and Posner, A. S. (1966). Infrared analysis of rat bone: Age dependency of amorphous and crystalline mineral fractions. *Science* 153, 1523–1525. doi:10.1126/SCIENCE.153.3743.1523

Tsuji, T., Onuma, K., Yamamoto, A., Iijima, M., and Shiba, K. (2008). Direct transformation from amorphous to crystalline calcium phosphate facilitated by motif-programmed artificial proteins. *Proc. Natl. Acad. Sci. U. S. A.* 105, 16866–16870. doi:10.1073/PNAS.0804277105/SUPPL_FILE/0804277105SI

Tzaphlidou, M. (2008). Bone architecture: Collagen structure and calcium/phosphorus maps. *J. Biol. Phys.* 34, 39–49. doi:10.1007/S10867-008-9115-Y

Vasington, F. D., and Murphy, J. V. (1962). Ca++ uptake by rat kidney mitochondria and its dependence on respiration and phosphorylation. *J. Biol. Chem.* 237, 2670–2677. doi:10.1016/S0021-9258(19)73805-8

Veiga, A., Castro, F., Rocha, F., and Oliveira, A. L. (2020). Recent advances in silk sericin/calcium phosphate biomaterials. *Front. Mat.* 7, 24. doi:10.3389/fmats.2020.00024

Wang, L., and Nancollas, G. H. (2008). Calcium orthophosphates: Crystallization and dissolution. *Chem. Rev.* 108, 4628–4669. doi:10.1021/CR0782574

Wang, S., Yang, Y., Wang, R., Kong, X., and Wang, X. (2020). Mineralization of calcium phosphate controlled by biomimetic self-assembled peptide monolayers via surface electrostatic potentials. *Bioact. Mat.* 5, 387–397. doi:10.1016/J.BIOACTMAT.2020.03.003

Weidmann, S. M. (1963). Calcification of skeletal tissues. *Int. Rev. Connect. Tissue Res.* 1, 339–377. doi:10.1016/B978-1-4831-6755-8.50013-9

Weiner, S., and Traub, W. (1986). Organization of hydroxyapatite crystals within collagen fibrils. *FEBS Lett.* 206, 262–266. doi:10.1016/0014-5793(86)80993-0

Xie, B., and Nancollas, G. H. (2010). How to control the size and morphology of apatite nanocrystals in bone. *Proc. Natl. Acad. Sci. U. S. A.* 107, 22369–22370. doi:10.1073/PNAS.1017493108

Xu, Y. F., Nudelman, F., Eren, E. D., Wirix, M. J. M., Cantaert, B., Nijhuis, W. H., et al. (2020). Intermolecular channels direct crystal orientation in mineralized collagen. *Nat. Commun.* 111, 5068. doi:10.1038/s41467-020-18846-2

Yokoi, T., Shimabukuro, M., and Kawashita, M. (2022). Octacalcium phosphate with incorporated carboxylate ions: A review. *Sci. Technol. Adv. Mat.* 23, 434–445. doi:10.1080/14686996.2022.2094728

Zhang, X., Wu, L., Feng, G., and Lei, S. (2022). Mineralization of calcium phosphate on two-dimensional polymer films with controllable density of carboxyl groups. *J. Mat. Chem. B* 10, 3793–3797. doi:10.1039/D2TB00195K

4. PIELIKUMS / APPENDIX 4

4. PUBLIKĀCIJA / PUBLICATION

Indurkar, A., Choudhary, R., Rubenis, K., Nimbalkar, M., Sarakovskis, A., Boccaccini, A. R., & Locs, J. (2023). Amorphous calcium phosphate and amorphous calcium phosphate carboxylate: Synthesis and characterization.

Doi: 10.1021/acsomega.3c00796

ACS OMEGA

http://pubs.acs.org/journal/acsodf

Article

Amorphous Calcium Phosphate and Amorphous Calcium Phosphate Carboxylate: Synthesis and Characterization

Abhishek Indurkar, Rajan Choudhary, Kristaps Rubenis, Mansingraj Nimbalkar, Anatolijs Sarakovskis, Aldo R. Boccaccini, and Janis Locs*

Cite This: *ACS Omega* 2023, 8, 26782−26792

Read Online

ACCESS | Metrics & More | Article Recommendations | Supporting Information

ABSTRACT: Amorphous calcium phosphate (ACP) is the first solid phase precipitated from a supersaturated calcium phosphate solution. Naturally, ACP is formed during the initial stages of biomineralization and stabilized by an organic compound. Carboxylic groups containing organic compounds are known to regulate the nucleation and crystallization of hydroxyapatite. Therefore, from a biomimetic point of view, the synthesis of carboxylate ions containing ACP (ACPC) is valuable. Usually, ACP is synthesized with fewer steps than ACPC. The precipitation reaction of ACP is rapid and influenced by pH, temperature, precursor concentration, stirring conditions, and reaction time. Due to phosphates triprotic nature, controlling pH in a multistep approach becomes tedious. Here, we developed a new ACP and ACPC synthesis approach and thoroughly characterized the obtained materials. Results from vibration spectroscopy, nuclear magnetic resonance (NMR), X-ray photoelectron spectroscopy (XPS), true density, specific surface area, and ion release studies have shown a difference in the physiochemical properties of the ACP and ACPC. Additionally, the effect of a carboxylic ion type on the physiochemical properties of ACPC was characterized. All of the ACPs and ACPCs were synthesized in sterile conditions, and in vitro analysis was performed using MC-3T3E1 cells, revealing the cytocompatibility of the synthesized ACPs and ACPCs, of which the ACPC synthesized with citrate showed the highest cell viability.

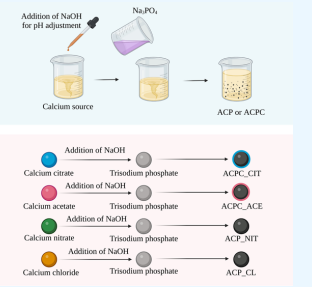

1. INTRODUCTION

ACP is the first solid phase precipitated from a supersaturated calcium phosphate solution.[1] Naturally, ACP is synthesized and stabilized by an organic compound (termed the "Howard factor") in mitochondria of cells.[2] It is known that the carboxyl group-containing organic compound provides a nucleation site, and the hydrocarbon chain provides an orientation to hydroxyapatite.[3] Synthetic precipitation reactions of ACP are rapid and highly influenced by the temperature, pH, and concentration of calcium and phosphate precursors.[4] Due to the triprotic nature of phosphates, variation in pH alters the relative concentration of four protonated forms of phosphoric acid such as H_3PO_4 (phosphoric acid), $H_2PO_4^-$ (dihydrogen phosphate), HPO_4^{2-} (hydrogen phosphate), and PO_4^{3-} (phosphates). This leads to variations in chemical composition and the amount of synthesized ACP, thus resulting in difficulties in controlling the formation of ACP.[5]

The interaction of different organic groups with inorganic materials has been a focus of biomineralization and biomaterials research. The role of macromolecules such as collagen, protein, and polymers in nucleation, crystallization, aggregation, and phase transformation of different calcium phosphates in biomineralization has been of particular interest for the last two decades.[6] Compared to noncollagenous proteins, small organic molecules such as citrate provide more carboxylic for calcium binding.[7] However, less consideration has been given to incorporating COO^--containing small organic molecules in calcium phosphate (CaP), although their role was indicated in numerous postulated biomineralization.[8] ACP and octa-calcium phosphate (OCP) are precursor phases that gradually crystallize to apatite.[9] Therefore, crystal growth, nucleation, and stabilization of apatite may be regulated by incorporating COO^- in ACP or OCP.[10] Usually, OCP is synthesized by hydrolysis of tricalcium phosphate (TCP), where the reaction is time-consuming and pH variations are controllable. The reaction parameter permits the addition of carboxylic compounds in developing octa-calcium phosphate carboxylate (OCPC).[11] In this manner, a series of COO^--containing small organic molecules were successfully integrated into OCPC.[12] On the contrary, ACP was synthesized by a precipitation reaction, and the direct addition of carboxylic acids leads to pH fluctuations affecting the physiochemical properties of the final product.[13] Due to the synthesis limitations of ACP, less attention has

Received: February 7, 2023
Accepted: June 27, 2023
Published: July 17, 2023

SCHEME 1

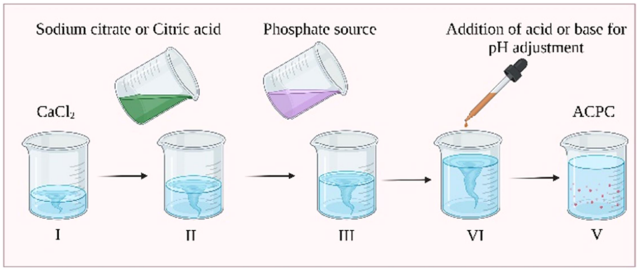

SCHEME 2

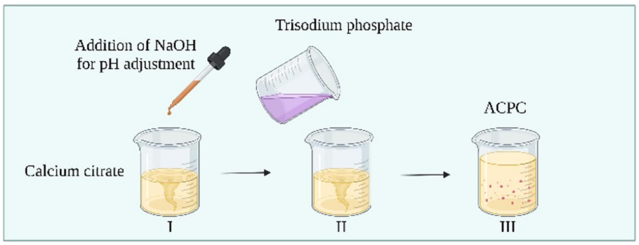

Figure 1. Synthesis mechanism of ACPC. Scheme 1 represents the traditional synthesis approach in which citrate is used as an acid or a base.[20−26] The reaction of ACPC synthesis is rapid, and due to the triprotic nature of phosphate, fluctuation in pH disturbs the protonated forms of phosphates, which can affect the final product. Scheme 2 represents our synthesis approach in which citrate was used as a calcium salt, and pH adjustments were made before mixing of calcium and phosphate sources. Therefore, the pH is maintained during the reaction.

been paid to the development of amorphous calcium phosphate carboxylate (ACPC).

The development of ACPC is a favorable option from the biomimetic point of view. For instance, citrate is a tricarboxylic compound synthesized in mitochondria and present in bone and teeth.[14] Recent nuclear magnetic resonance (NMR) studies have revealed the presence of citrate bridges between the mineral platelets of bone.[15,16] Moreover, one-sixth of the available surface area of apatite is covered by citrate.[15,17] The adsorbed citrate on the surface of apatite offers more COO^- groups for collagen binding compared to noncollagenous proteins. The bonded citrate on CaP reduces the hydrophilicity of the surface, making it favorable for binding with nonpolar amino acids such as alanine and proline in the collagen matrix.[18] In this study, citrate was utilized to develop one of the ACPCs. The literature shows that the OCPC possesses different properties depending upon the type of the incorporated COO^- ion.[19] Unfortunately, such data are not available for carboxylate ions containing ACP. To investigate the effect of carboxylic ion type on the properties of ACPC, we also utilized acetate as a source of the mono-carboxyl compound for the synthesis of ACPC.

In the scientific literature, the synthesis of ACP is usually described as a simple one-step process;[4] on the contrary, ACPC is synthesized by a multistep process.[20−26] As shown in Figure 1, Scheme 1, the precursor of COO^--containing small organic molecules is either used in the acidic or basic form, which can lead to variation in pH, making the reaction tedious, expensive, and affecting the final product. Moreover, ACP/ACPC reactions are rapidly performed at alkaline pH. Therefore, the addition of small organic molecules in the reaction leads to pH fluctuation affecting the reaction's phosphate species, which can influence the final product. We have developed a simplified one-step synthesis of ACPC, as shown in Scheme 2. This simple approach utilizes calcium salt of COO^--containing small organic molecules, resulting in marginal pH variations, and provides a rapid and cost-effective approach. The approach developed was used to synthesize ACPC from calcium citrate (ACPC_CIT), calcium acetate (ACPC_ACE), and ACP from calcium chloride (ACP_CL) and calcium nitrate (ACP_NIT).

ACP is a metastable compound. Therefore, sterilization and long-term stability are addressed in the current research. The major focus of this study was developing a simplified ACPC synthesis method and comparison of the physiochemical properties of the final products (ACP and ACPC).

2. MATERIALS AND METHODS

Calcium citrate tetrahydrate, calcium chloride, trisodium phosphate, and sodium hydroxide were procured from Sigma Aldrich. Calcium acetate monohydrate and calcium nitrate tetrahydrate were procured from Honeywell, Fluka, and VWR chemicals BDH.

2.1. Synthesis of ACP and ACPC. The synthesis of ACP and ACPC were performed at an ambient temperature (around 20 to 22 °C) and pH close to 11.5. For ACP_CL, ACP_NIT, ACPC_ACE, and ACPC_CIT, calcium chloride, calcium nitrate, calcium acetate, and calcium citrate were utilized, respectively, as calcium sources. For ACP_CL, ACP_NIT, and ACPC_ACE, the concentration of the calcium source was 150 mM, whereas, for ACPC_CIT, the concentration of the calcium source was 50 mM, and for all of the reactions, the concentration of trisodium phosphate was set to 100 mM. Both calcium and phosphate salt solutions were prepared in Milli-Q water and kept on separate magnetic stirrers at 500 rpm. To adjust the pH to 11.5, a few drops of 3

https://doi.org/10.1021/acsomega.3c00796
ACS Omega 2023, 8, 26782−26792

M sodium hydroxide were added to the beaker containing respective calcium salts. Further, a trisodium phosphate solution was rapidly added to the stirred calcium salt solution, and the reaction was performed at a pH of 11.5. Immediately after the precipitation, the suspension was centrifuged at 3000 rpm for 5 min and washed thrice with Milli-Q water. The reaction was stopped by immersing centrifuge tubes containing the precipitated ACPs and ACPCs in liquid nitrogen for 15 min. Excess water from the frozen precipitates was removed by freeze-drying (72 h). The obtained powder was preserved in airtight containers for further characterization.

2.2. Characterization of ACP and ACPC. An X-ray diffractometer (PANalytical X'Pert PRO MPD) equipped with a Cu tube (Cu Kα = 1.54 Å) was used to record the diffraction patterns of the synthesized powders. Diffraction data were collected at 40 kV and 30 mA in a step mode with a step size of 0.04°, in the 2θ range from 10° to 70°. Samples were prepared by gently packing the powder on a zero-background sample holder.

Fourier-transform infrared (FTIR) spectroscopy was performed in transmission mode from the wavenumber ranging from 4000 to 400 cm^{-1} with a resolution of 4 cm^{-1} (64 scans) using a Thermo Scientific Nicolet iS50 FT-IR spectrometer.

Raman spectral acquisition was recorded using a confocal Raman microscope (Renishaw plc) equipped with a 514 nm laser. The analysis was performed using a 50x objective to focus the excitation beam and collect the backscattered signals from the samples. The spectral scan was analyzed from 350 to 2000 cm^{-1} with three-time accumulation and an exposure time of 20 s. The system was calibrated at 520 cm^{-1} against a silicon wafer and periodically checked during the experiments to ensure the accuracy of the Raman shifts.

Solid-state ^{31}P NMR analysis was recorded by a JOEL, ECZR 600 MHz NMR spectrophotometer. The experiment was performed with a single 90° pulse at a mass frequency of 10 kHz. The number of scans was 338, and the relaxation delay was 5 s. Solid-state ^{13}C NMR spectra was recorded by a Bruker 18.8 T, 800 MHz NMR spectrophotometer. ^{13}C spectroscopy was performed with a single 90° pulse at a mass frequency of 10 kHz with 2048 scans, and the relaxation delay was 3 s.

X-ray photoelectron spectroscopy (XPS) was used to analyze the chemical composition of the samples. The spectrometer was of ThermoFisher Escalab 250xi. The pressure during spectra acquisition with the charge neutralizer switched on was 10^{-7} mbar. The calibration and linearity of the binding energy scale were confirmed by measuring the positions of Ag $3d_{5/2}$, Au $4f_{7/2}$, and Cu $2p_3$ to be at 368.21, 83.93, and 932.58 eV, respectively. The full-width at half-maximum (FWHM) of the Au $4f_{7/2}$ peak was better than 0.58 eV. The size of the analyzed sample was 650 mm × 100 mm.

The true density of ACP and ACPC was measured by a helium pycnometer Micro UltraPyc 1200e (Quantachrome instruments). Before measurement, calibration was performed by using a stainless steel calibration sphere. After calibration, a known amount of ACP or ACPC powder was added to the sample holder and purged with helium gas in pulse mode (30 pulses). Further, the volume was analyzed by pressurizing the sample with helium gas at a 10 psi pressure. The sample weight with the analyzed sample volume was used to calculate the true density. The analysis of each ACP and ACPC was performed in triplicate.

A nitrogen adsorption system Quadrasorb S1 (Quantachrome instruments) was used to determine the specific surface area (SSA) of the synthesized ACP and ACPC powder by the Brunauer–Emmett–Teller (BET) method. For removal of moisture, degassing of samples was performed for 24 h at room temperature before the analysis.

The morphology and particle size of synthesized ACP and ACPC were evaluated by a FEG-TEM (Tecnai G2 F30) operated at 300 kV. The sample preparation was as follows: a small amount of powder was dispersed in isopropyl alcohol and sonicated in an ultrasonic bath. Further, the samples were placed on a carbon-coated grid and dried before analysis.

2.3. Ion Release. Sample preparation for ion release studies was as follows: 50 mL of a 1% w/v ACP or ACPC suspension was prepared in Milli-Q water and incubated at 37 °C under constant stirring (250 rpm). Before analysis, the suspension was centrifuged at 3000 rpm for 5 min, and 750 μL of the supernatant was removed. The ACPs and ACPCs were further incubated in water at 37 °C under constant stirring until the next time point. The study was conducted for 7 days, and time points were recorded at 1, 24, 72, 120, and 168 h, respectively.

Calcium ion release was determined by a colorimetric calcium kit (Sigma Aldrich). The concentration of calcium ions was measured by the chromogenic complex between calcium ions and *o*-cresol phthalein, which is proportional to calcium ion concentration. Then, 50 μL of the supernatant was added to 96-well plates, in which 90 μL of chromogenic reagents and 60 μL of calcium assay buffer were added and gently mixed. The reaction was conducted for 5 min at room temperature in the dark, and further absorbance of the sample was recorded at 575 nm using a microplate reader (PHOmo, Anthos Mikro Systeme GmbH).

Orthophosphate ion release was evaluated by an orthophosphate calorimetric kit (Sigma Aldrich). Orthophosphate reacts with a chromogenic complex and produces a calorimetric product proportional to the orthophosphate concentration. Two hundred microliters of the supernatant was added to 96-well plates, in which 30 μL of the phosphate reagent was added and gently mixed. The reaction was conducted for 30 min at room temperature in the dark, and further absorbance was recorded at 650 nm using a microplate reader (PHOmo, Anthos Mikro Systeme GmbH).

2.4. In Vitro Biocompatibility Assay. An osteoblast precursor cell line derived from mouse (*Mus musculus*) calvaria (MC3T3-E1) was employed for cellular analysis after 10 passages. MC3T3-E1 cells were maintained in an α-MEM medium containing 10 vol % fetal bovine serum (Gibco Life Science) and 10 vol % penicillium–streptomycin at 37 °C in a humidified atmosphere of 95% air and 5% CO_2. The cultures of MC3T3-E1 cells were trypsinized, counted, and 1×10^5 cells/mL were inoculated into a 24-well plate followed by incubation at 37 °C in a humidified atmosphere of 95% air and 5% CO_2 for 24 h.

Due to the metastable properties of ACP, heat sterilization was not possible. Therefore, a sterile synthesis approach was developed and utilized in this study. Solutions of 150 mM calcium acetate, calcium chloride, and calcium nitrate, 100 mM trisodium phosphate, and 3 M sodium hydroxide were sterile filtered through 0.22 μm pore size filters. Then, 50 mM calcium citrate powder and 500 mL of Milli-Q water were sterilized by autoclaving at 121 °C at 15 psi for 30 min. Under the flow cabinet, the synthesis of ACP and ACPC was performed by the procedure described in Section 2.1 with all of the sterile precursors.

https://doi.org/10.1021/acsomega.3c00796
ACS Omega 2023, 8, 26782−26792

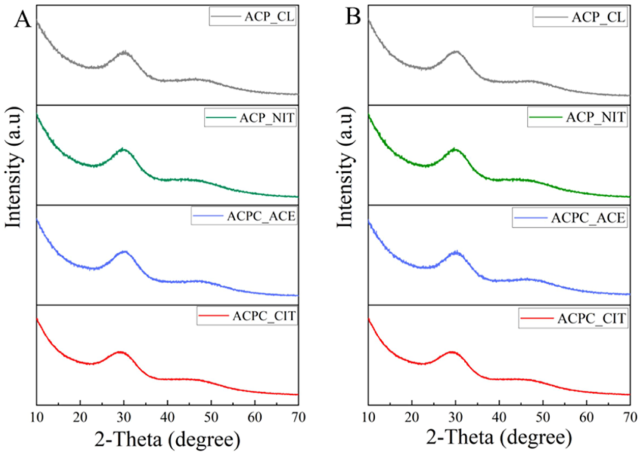

Figure 2. X-ray diffraction pattern of the synthesized ACPs and ACPCs. (A) Freshly prepared powder samples and (B) after 1 year of storage.

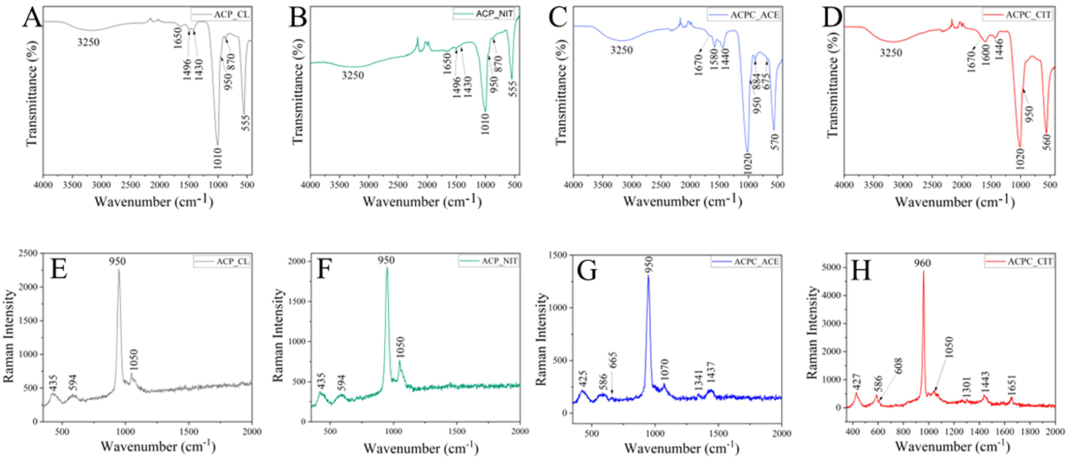

Figure 3. (A–D) FTIR spectra of all of the synthesized ACPs and ACPCs. (E–H) Raman spectra of all of the synthesized ACPs and ACPCs.

For cellular analysis, suspensions were prepared by adding a 10 w/v% ACP or ACPC precipitate in an α-MEM medium and incubating at 37 °C in a humidified atmosphere of 95% air and 5% CO_2 for 24 h. The extracts were collected by centrifugation and filtered to eliminate solid particles. The extracts were further diluted with the α-MEM medium to get the desired concentrations of 1 and 0.1 w/v%. Therefore, the total sample concentration comprises 10, 1, and 0.1 w/v% each ACP and ACPC. The extracts were then added to MC3T3-E1-containing well plates and incubated for 48 h. The α-MEM medium was added as a positive control, whereas the α-MEM medium with 6 vol % DMSO (dimethyl sulfoxide) was utilized as a negative control. Each sample was prepared in triplicate, and the same procedure was performed for all ACPs and ACPCs.

A WST-8 (CCK-8, Sigma Aldrich) kit was used to analyze the cell viability. In a colorless α-MEM medium, 1 v/v% WST was prepared. To each well, 400 μL of the 1 v/v% WST mixture was added and incubated for 3 h. The WST solution was used as a blank. Further, 100 μL of an aliquot from each 24-well plate was transferred to a 96-well plate. For spectrophotometric analysis, a 96-well plate was assigned in a microplate reader (PHOmo, Anthos Mikro Systeme GmbH), and absorbance was recorded at 450 nm. The experiments were performed in triplicate and cell viability was calculated from eq 1

$$\text{cell viability (\%)} = \frac{(\text{absorbance of sample} - \text{absorbance of blank})}{(\text{absorbance of positive control} - \text{absorbance of blank})} \times 100 \quad (1)$$

2.5. Cell Morphology. The cellular morphology of MC3T3-E1 was analyzed by hematoxylin and eosin (H&E) staining. After removing the WST solution from the 24-well plate, wells were washed with phosphate saline buffer (PBS) and fixed with 4% paraformaldehyde in PBS for 15 min.

https://doi.org/10.1021/acsomega.3c00796
ACS Omega 2023, 8, 26782−26792

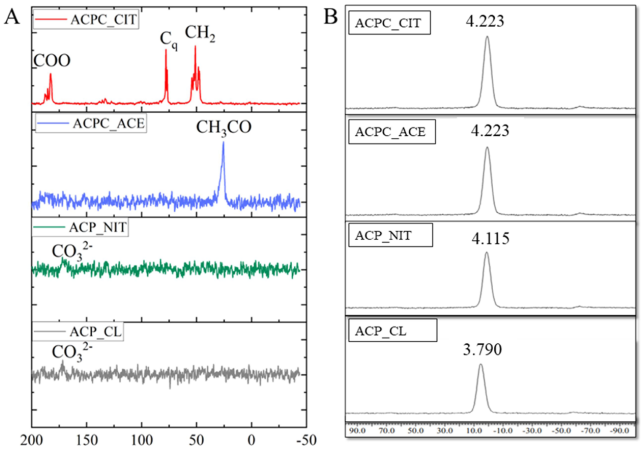

Figure 4. Solid-state NMR analysis of synthesized ACPs and ACPCs: (A) solid-state ^{13}C NMR spectra and (B) solid-state ^{31}P NMR spectra.

Further, it was washed with PBS and stained for 10 min with hematoxylin. Subsequently, samples were washed with tap water and then with Scott's water, followed by washing with deionized water for 5 min. Later, samples were stained with eosin (0.1 wt/v % eosin, 5% v/v% acetic acid, 60 v/v% ethanol, and 35 v/v% ultrapure water) for 5 min. Afterward, samples were washed with 95 v/v% ethanol and 99.5 v/v% ethanol and dried at room temperature. The cell morphology was analyzed using an optical microscope (Primo Vert, Carl Zeiss).

2.6. Statistical Analysis. Origin 2020 (Origin Lab, Northampton, MA) was utilized to perform statistical analysis by one-way ANOVA and Bonferroni's test. Probability (P) values $p < 0.05$ were considered the statistically significant differences. The results are expressed in mean ± standard deviation (S.D)

3. RESULTS AND DISCUSSION

3.1. Characterization of ACP and ACPC. *3.1.1. XRD.* The feature that differentiates ACP from other calcium phosphates is the lack of crystalline order.[27] As shown in Figure 2A, the XRD patterns of all of the synthesized ACPs and ACPCs were similar. As a metastable compound, ACP tends to convert into a crystalline phase; therefore, analyzing the stability of ACP is paramount. After initial characterization, the synthesized ACP and ACPC powders were stored in airtight containers, and the XRD analysis were performed after 1 year. As shown in Figure 2B, after 1 year of storage, all samples were still X-ray amorphous, thus confirming the long-term stability of all of the synthesized materials.

3.1.2. Vibrational Spectroscopies. The characteristic IR and Raman absorption bands of all of the synthesized ACPs and ACPCs are displayed in Figure 3A–H. Water molecules have three vibration modes: asymmetric and symmetric stretching modes have very close energies, making distinguishing difficult. Therefore, a broad band of water was observed at around 3000–3700 cm^{-1}. The bending mode of water was observed as a narrow band at around 1680–1640 cm^{-1}.[28,29] These bands were observed in all of the synthesized samples. In IR and Raman analyses, the PO_4^{3-} group possesses four vibration domains: ν_1 at around 950 cm^{-1}, ν_2 at 400–470 cm^{-1}, ν_3 at 1000–1150 cm^{-1}, and ν_4 at 500–620 cm^{-1}. In IR analysis, the phosphate ν_1, ν_2, and ν_3 vibrations are observed, whereas in Raman, all four PO_4^{3-} vibrations are detected in all of the synthesized ACPs and ACPCs.

Bands associated with C–O stretches have high intensity in IR spectra, whereas those associated with C–C stretches have high intensities in Raman spectra. Moreover, the bands associated with the bending modes have moderate intensities in both IR and Raman spectra.[30] Like phosphate, carbonate ions also possess four vibrational domains: ν_1 at around 1050 cm^{-1}, ν_2 at 820–900 cm^{-1}, ν_3 at 1400–1550 cm^{-1}, and ν_4 at 650–750 cm^{-1}. In IR spectra of ACP_CL and ACP_NIT, the stretching doublet was observed at around the 1400–1550 cm^{-1} region, corresponding to the asymmetric stretching of ν_3 CO_3^{2-} anions. Furthermore, the peak observed at ∼875 cm^{-1} represents the out-of-plane bending of the ν_2 CO_3^{2-} group. However, in the similar range at ∼875 cm^{-1}, the P–OH stretching mode overlaps heavily with ν_2 CO_3^{2-}.[31] The peak at ∼875 cm^{-1} was absent in ACPC_CIT, which indicates the incorporation of COO^- in the ACP.[32] Additionally, the bands observed at 1600 and 1432 cm^{-1} represent the COO^- bending and COH stretching of the carboxylic group in citrates.[30] Likewise, in ACPC_ACE, the band revealed at 675 and 1550 cm^{-1} corresponds to COO^- bending and stretching, and 1440 cm^{-1} represents COH stretching of the acetate carboxylic group.[33] The band observed at 884 cm^{-1} indicates shifting of the HPO_4^{2-} group, which may be due to the association of the carboxylic group.[32]

In the Raman spectra of ACPC_ACE, the bands observed at 1341 and 1437 cm^{-1} indicate H–C–H deformation and COO^- stretching of acetate. The O–C–O bending of acetate is observed in the region of 600–680 cm^{-1}.[34] Acetate is a mono-carboxylic anion, whereas citrate is a tricarboxylic anion; therefore, the Raman spectra of ACPC_CIT were more complex. In ACPC_CIT, the sharp peak observed at 960 cm^{-1} may represent two functional groups: ν_1 PO_4^{3-} and/or the CH_2 rocking vibration of citrate.[22,30] This might be a reason for shifting of the ν_1 PO_4^{3-} band from 950 to 960 cm^{-1}. The characteristic carboxylic band was observed at 1443 cm^{-1}, and the band at 1651 cm^{-1} represents COO^- vibration coupled with CH_2 bending vibration observed at 1301 cm^{-1}. The out-of-plane COO^- modes can be assigned to the region 500–800

https://doi.org/10.1021/acsomega.3c00796
ACS Omega 2023, 8, 26782–26792

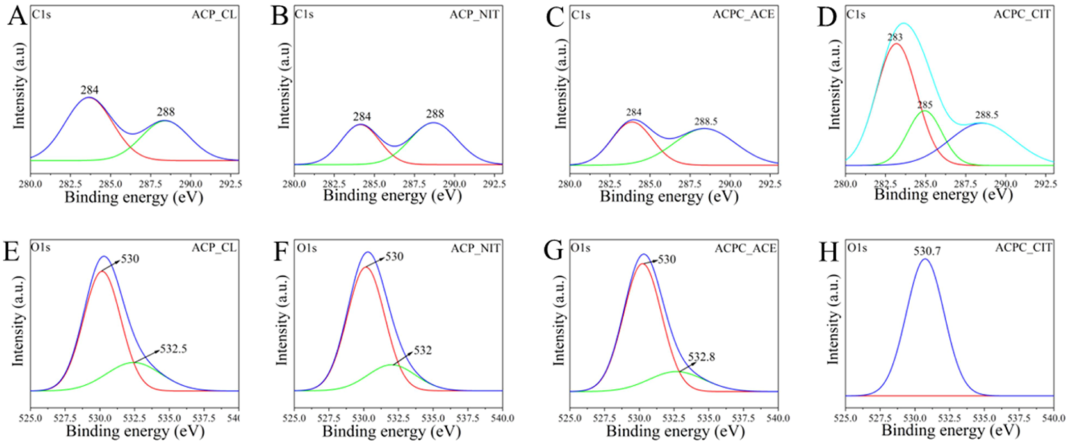

Figure 5. XPS of all of the synthesized ACPs and ACPCs (A–D) focuses on C1s spectra in the binding energy range of 280–292.5 eV and (E–H) focuses on O1s spectra in the 525–540 eV binding energy range. Spectral lines are represented as smoothened, normalized to their maxima, and deconvoluted.

cm^{-1}, which can be attributed to the peaks observed at 586 and 608 cm^{-1}, respectively.[30] Solid-state NMR analysis was performed to confirm the presence of acetate and citrate in ACPC_ACE and ACPC_CIT.

3.1.3. NMR Analysis. The ^{13}C and ^{31}P NMR spectra of the synthesized ACPs and ACPCs are presented in Figure 4A,B, respectively. In the ACPC_CIT samples, three carboxylate signals were observed; COO(1) corresponds to a strong signal at 182 ppm, and COO(2) and COO(3) are represented by 183 and 185 ppm, respectively. The signal at 77 ppm represents the quaternary carbon Cq and the second signal at 76 ppm indicates the association of the Ca^{2+} ion with −OH of the Cq in citrate.[35] The methylene groups $CH_2(1)$ and $CH_2(2)$ are represented at 51 and 47 ppm, respectively. This indicates the incorporation of citrate in ACP.[15,16,18] The signal observed at 26 ppm in ACP-ACE corresponds to the acetyl (CH_3CO-) group of acetate.[36,37] The ^{13}C NMR analysis confirmed the retention of citrate and acetate in the ACPC_CIT and ACPC_ACE, respectively. For samples ACP_NIT and ACP_CL, a small signal was observed at 170 ppm, which corresponds to the CO_3^{2-} group.[38]

The ^{31}P spectra of ACPs and ACPCs are shown in Figure 4B. The characteristic broad Gaussian-shaped signal is between −15 and 15 ppm, centered from 2.2 to 6.5 ppm.[39−42] This area represents the PO_4^{3-} a resonance observed in all of the synthesized ACPs and ACPCs. The signal observed at 4.223 ppm in ACPC_CIT and ACP-ACE was identical; this can be due to the association of the COO^- group. On the other hand, ACP_NIT and ACP_CL show a broad peak at around 4.1 and 3.7 ppm, respectively.

3.1.4. XPS. The fingerprint region of all of the ACP and ACPC samples is presented in Figure S1 provided in supplementary data. The obtained peaks were deconvoluted using Origin 2020 software and presented in Figure 5. The sample prepared for XPS analysis was in the form of pellets. As shown in Figure 5A–B ACP_CL and ACP_NIT, peaks at around 284 eV and 288 eV denote C–C and O–C=O of carbonates.[43] On the contrary, the ACPC_CIT and ACPC_ACE show the presence of COO^- groups. Therefore, in Figure 5C, ACPC_ACE shows the absorption band at 284 eV and 288.5 eV represents the acetyl group.[44] Typically citrate-containing compounds show three peaks at around 283, 285, and 288.5 eV. The peak at 283 eV represents the C–C and $(CH_2)_n$ bonds, the peak at around 285 eV indicates C=O, and the third peak at around 288.5 eV accounts for COO.[45,46] As shown in Figure 5D, these three signature carboxylate peaks were observed in ACPC_CIT samples.

The O1s spectra shown in Figure 5E–H were used to detect the presence of the HPO_4^{2-} group. The O1s spectrum was dissymmetrical in the presence of HPO_4^{2-} and symmetrical in the case of PO_4^{3-}. In Figure 5H, ACPC_CIT shows a symmetrical peak representing PO_4^{3-}. On the other hand, in Figure 5E–G, dissymmetry was observed in ACPC_CL, ACP_NIT, and ACP_ACE samples, confirming the presence of both PO_4^{3-} and HPO_4^{2-} groups.[47]

3.1.5. Density and Brunauer–Emmett–Teller (BET) Analysis. The data shown in Table 1 reveals the specific surface area and density of synthesized ACPs and ACPCs. The specific surface area of the ACP_NIT and ACP_CL was the same, but a difference was observed in ACPC_CIT and ACPC_ACE. This might be due to the association of the COO^- group. On the contrary, there were differences in the densities of the synthesized ACPs and ACPCs. This shows that the nature of COO^- ions affects the properties of ACP.

Table 1. Density, BET, and Average Particle Size of the Synthesized ACPs and ACPCs from Different Calcium Sources

sample	density (g/cm^3)	BET (m^2/g)
ACP_CL	2.62	105
ACP_NIT	2.58	105
ACPC_ACE	2.47	118
ACPC_CIT	2.57	62

3.1.6. FEG_TEM Analysis. The morphology of the synthesized ACPs and ACPCs was evaluated by FEG-TEM, as shown in Figure 6A–D. The sample ACPC_ACE, ACP_CL, and ACP_NIT showed porous spherical particles

https://doi.org/10.1021/acsomega.3c00796
ACS Omega 2023, 8, 26782−26792

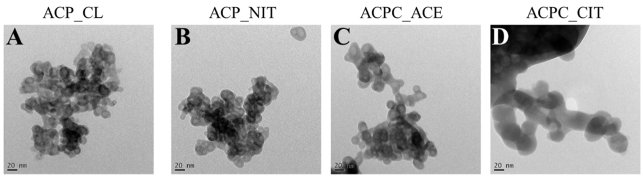

Figure 6. Morphological evaluation of ACP and ACPC synthesized from different calcium precursors. The effect of different calcium precursors was observed on the particle size of ACP. The samples are represented as (A) ACP_CL, (B) ACP_NIT, (C) ACPC_ACE, and (D) ACPC_CIT. Scale bar: 20 nm.

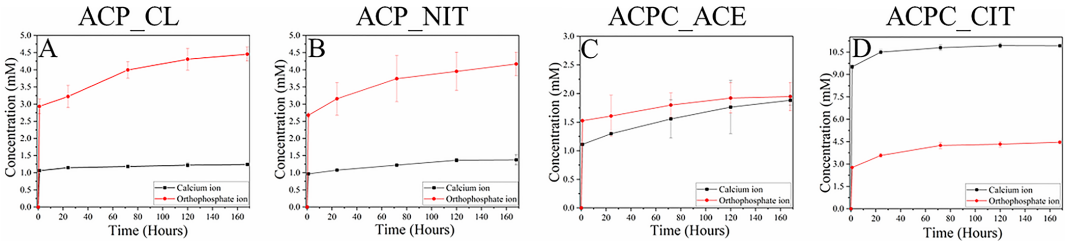

Figure 7. Kinetic release of phosphate and calcium ions in (A) ACP_CL, (B) ACP_NIT, (C) ACPC_ACE, and (D) ACPC_CIT was performed for 168 h (7 days).

of a size less than 20 nm. On the contrary, ACPC_CIT reveals solid particles of size ∼40 nm. Previous studies have reported that ACP nanoparticles had maximum stability with a diameter of 30−50 nm.[48] Naturally, ACP is synthesized and stabilized in mitochondria, nucleates in the 40 nm collagen gap zone, and converts to apatite.[49] The elongated plate-like geometry of apatite has a length between 30 and 50 nm and a width between 15 and 30 nm while maintaining a thickness of 2−10 nm.[50] Therefore, the ∼40 nm particle size of ACPC_CIT is in the size range to fit in the gap zone of collagen. Moreover, the association of citrate provides sites ($-CH_2$) for binding with nonpolar amino acids such as alanine and proline in the collagen matrix. ACPs are highly sensitive to the electron beam and crystallize rapidly under high-energy electron irradiation exposure.[49] The crystallization of both ACP and ACPC particles under a high-energy electron beam was observed and can be seen in Figure S2 in the supplementary data.

3.1.7. Ion Release. The kinetics of ion release from the ACPs and ACPCs is shown in Figure 7A−D. The ion release was studied for 168 h (7 days) to analyze Ca^{2+} and phosphate ion release. A burst release was initially observed within the first hour, gradually reducing over time.[51,52] The highest ion release was observed in ACPC_CIT, followed by ACP_NIT and ACP_CL, and the least was in ACPC_ACE. Moreover, the release of Ca^{2+} ions was more than the phosphate ions in ACPC_CIT, whereas the opposite scenario was observed in all other ACPs. In Figure 7A,B, in ACP_NIT and ACP_CL, the phosphate ion release was between 3 and 4 mM, whereas the calcium release was between 1 and 2 mM. Comparatively, the Ca^{2+} and phosphate ions released in ACPC_ACE ranged between 1 and 1.5 mM. Acetate possesses fewer COO^- groups than citrate, so the ion release might differ from ACPC_CIT. From these studies, it can be determined that ACP and ACPC possess different ion release profiles. Additionally, different COO− groups have a considerable effect on the ion release profiles of ACPC.

3.2. Cellular Analysis. *3.2.1. In Vitro Cytotoxicity.* The cell viability of MC-3T3E1 cells in the presence of extracts of ACPs and ACPCs is shown in Figure 8. The absorbance

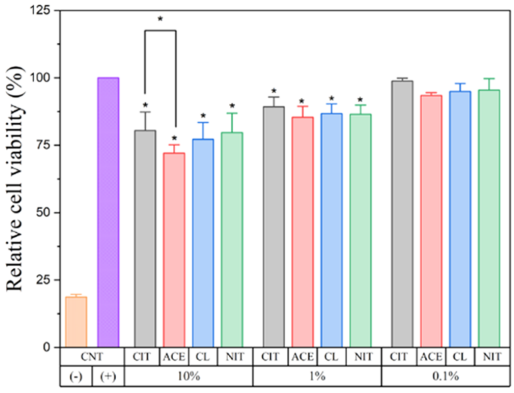

Figure 8. Relative viabilities of MC-3T3E1 cells cultured with the extract of different ACPs and ACPCs in 10%, 1%, and 0.1% w/v cell culture media dilutions (n = 12, CNT = control, samples in triplicate, *p < 0.05). CIT, ACE, CL, and NIT represent the ACP samples ACPC_CIT, ACPC_ACE, ACP_CL, and ACP_NIT, respectively.

recorded from the positive control cells cultured in the only medium was normalized as 100%. The cells cultured with a 10 w/v% extract of ACPC_ACE showed the lowest cell viability, whereas the highest cell viability was observed in a 0.1 w/v% extract of ACPC_CIT. In the group of 10 w/v%, ACPC_CIT possesses the highest cell viability, followed by ACP_CL, ACP_NIT, and ACPC_ACE. A similar trend was observed in 1 and 0.1 w/v% ACP extracts. The extract of 10 w/v% ACP_CL, ACP_NIT, and ACPC_ACE maintained a cell viability of ∼80%, whereas for ACPC_ACE, it was close to

https://doi.org/10.1021/acsomega.3c00796
ACS Omega 2023, 8, 26782−26792

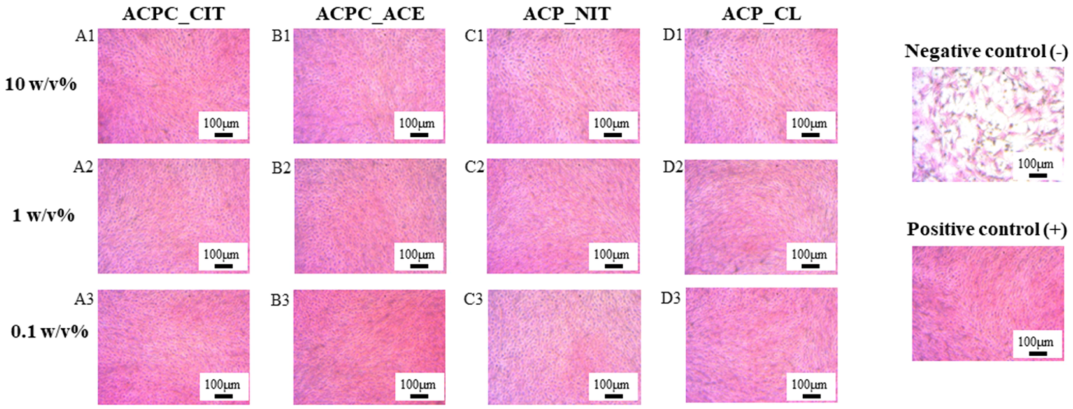

Figure 9. Optical microscopy was performed on H&E-stained MC-3T3E1 cells cultured with the extract of different ACP and ACPC. Cells treated with 10 wt % extracts of ACPC_CIT, ACPC_ACE, ACP_NIT, and ACP_CL are displayed from A1 to D1, respectively. Panels from A2 to D2 indicate cells treated with 1 wt % extracts of ACPC_CIT, ACPC_ACE, ACP_NIT, and ACP_CL, respectively. Panels from A3 to D3 denote the cells treated with 0.1 wt % extracts of ACPC_CIT, ACPC_ACE, ACP_NIT, and ACP_CL, respectively.

∼72%. However, extracts of respective ACP and ACPC with 1 and 0.1 w/v% extracts show cell viabilities of ∼90 and ∼95%, respectively. It can be concluded that ACPC_CIT has more cell viability in all of the respective groups. Overall, after 48 h of cell culture, the cell viability increased gradually with a higher dilution of ACP and ACPC. Since all of the ACP and ACPC samples show cell viability of more than ∼70%, it can be inferred that all of the samples were cytocompatible. In vitro analysis indicates that ACPC_CIT possesses maximum cell viability compared to other ACP and ACPC samples, indicating that the association of citrates enhanced the cell viability of ACP.

3.2.2. Cell Morphology. Optical microscopy images of H&E-stained MC-3T3E1 cells cultured with 0.1, 1, and 10% w/v extracts of synthesized ACPs and ACPCs are shown in Figure 9. The shape and size of the cells were not affected in the presence of ACP and ACPC extracts; thus, the cytocompatibility was not affected. Moreover, the results were correlated with the cell viability measured by the WST-8 assay, which confirms the biocompatibility of all of the synthesized samples. The image of H&E staining at lower magnification is displayed in Figure S3 provided in supplementary data.

4. DISCUSSION

Citrate is tricarboxylic acid naturally associated with bone.[15,16,53−56] Moreover, citrate is also known to stabilize ACP.[57,58] Therefore, citrate is a natural candidate in the development of ACPC. From the biomimetic perspective, the particle size of ACP is a crucial parameter as it needs to ft in the 40 nm gap zone of collagen. Studies in zebrafish, developing mouse calvaria, and chicken long bone have shown the presence of ACP in the size range of 50−80 nm.[49] However, synthesizing ACPs in this range is challenging.

In the literature, synthetic ACPs show size variations ranging from several nanometers to micrometers. The synthetic reactions of ACPs are highly sensitive to pH, temperature, and precursor concentration, affecting particle size. A brief literature review in Table S1 in supplementary data shows variations in particle sizes and synthesis pH of ACP. Moreover, most previous studies utilized calcium chloride and calcium nitrate as starting materials; however, different particle sizes were obtained. In wet synthesis, calcium chloride and calcium nitrate undergo complete dissociation. On the contrary, calcium acetate and calcium citrate undergo partial dissociation.[59] Therefore, the mechanism of ACP formation is simple in the case of calcium chloride and calcium nitrate, whereas complex in the case of calcium acetate and calcium citrate. This partial dissociation of calcium acetate and calcium citrate may be responsible for the complex ternary formation of ACPC with functional groups of citrate and acetate.[60,61] The association of the carboxylic group in ACP affects the physiochemical properties such as the surface area, particle size, and ion release kinetics. Moreover, citrate-associated ACP possesses biomimetic particle size.

Comparative analysis of ACP and ACPC provided new insights. First, the presence of both CO_3^{2-} and HPO_4^{2-} in ACP_CL and ACP_NIT. Second, the incorporation of COO^- ions in ACP was concluded from missing and shifting of the HPO_4^{2-} peak at 875 cm^{-1} in IR spectra of ACPC_CIT and ACPC_ACE, respectively. Further, incorporating COO^- ions restricted the incorporation of the CO_3^{2-} group, which was discovered from ACPC_CIT and ACPC_ACE, respectively. Lastly, acetate is a mono-carboxylic ion, whereas citrate is a tricarboxylic ion that greatly affects the physiochemical properties of ACP.

There are four interpretations for the interaction of citrate with calcium phosphate. The first most accepted interpretation is the interaction of Ca^{2+} with the COO^- group of citrates.[62] The second interpretation is the interaction of OH^- of citrate with the phosphate ions.[63] The third possibility occurs by substituting the phosphate group with a citrate anion.[64] At the synthesis pH above 11, citrates are present in the form of $Hcit^{3-}$ ions, which can potentially substitute PO_4^{3-} ions as they share the same charge. The fourth prediction is the interaction of carboxylic groups with phosphate ions.[65] Focusing on the fourth prediction, carboxylates and phosphate are Lewis acids with a common preferential stereochemistry.[66] The syn or antistereochemistry is observed in carboxylate−Lewis acid interactions. The syn interaction is preferred by carboxylate

https://doi.org/10.1021/acsomega.3c00796
ACS Omega 2023, 8, 26782−26792

with a covalently bonded proton, metal ion, or hydrogen bond donor. The preferential reaction occurs in the plane of carboxylate to complex sp^2 oxygen lone pair.[67] Phosphates can react with other phosphate groups by forming P−O−H−O−P, whereas carboxylate can react with other carboxylates by C−O−H−O−C. Similar phosphate and carbonates can react with each other via P−O−H−O−C bonding, though the bond length of P−O−H−O−C is greater than that of P−O−H−O−P, indicating a slightly weaker bond. The polar nature of C−O is less than the P−O linkage, which signifies that C−O−H−O−C is even weaker.[68] Therefore, the carboxylic groups of citrates can interact with phosphate via P−O−H−O−C bonding.

On the contrary, the mechanism of ACPC_ACE formation differs from that of ACPC_CIT. One of the main reasons is the incompatible negative charge of −1 and the lack of a secondary carboxylic group in acetate.[69] Therefore, the association of the acetyl group with ACP can be in two different ways, either by adsorption on the ACP surface[70] or by the formation of calcium acetyl phosphate.[71] However, more advanced analysis is required to understand the exact interaction of ACP with carboxylates.

5. CONCLUSIONS

A simplified synthesis approach was developed for the synthesis of ACP and ACPC. Characterization of the synthesized materials by vibration spectroscopy, NMR, FTIR, and XPS analyses confirmed the formation of ACP and ACPC. The particle size, specific surface area, and ion release profile of the synthesized ACPs and ACPCs depend on the calcium source used. A sterile synthesis method was developed and utilized for ACP and ACPC analysis in vitro. In vitro results confirmed the biocompatibility of all of the synthesized ACPs and ACPCs. ACPC_ACE shows relatively less cell viability at a 10 w/v% concentration, whereas ACPC_CIT shows higher cell viability than other of the synthesized ACP/ACPC. The association of ACP with acetate and citrate is a complex process, and more advanced analysis is required to depict the exact interaction. All of the analyses in this study indicated the difference in the physiochemical properties of ACP and ACPC. Additionally, the physiochemical properties of ACP are affected by the incorporated carboxylic group.

■ ASSOCIATED CONTENT

Supporting Information

The Supporting Information is available free of charge at https://pubs.acs.org/doi/10.1021/acsomega.3c00796.

XPS survey spectra and TEM images of ACPC_CIT, ACPC_ACE, ACP_CL, and ACP_NIT; optical microscopy of H&E-stained MC-3T3E1 cells cultured with the extract of different ACPs; and table of literature survey on the synthesis of ACP by precipitation (PDF)

■ AUTHOR INFORMATION

Corresponding Author

Janis Locs − *Rudolfs Cimdins Riga Biomaterials Innovations and Development Centre of RTU, Institute of General Chemical Engineering, Faculty of Materials Science and Applied Chemistry, Riga Technical University, LV-1007 Riga, Latvia; Baltic Biomaterials Centre of Excellence, Headquarters at Riga Technical University, LV-1048 Riga, Latvia;* orcid.org/0000-0003-3162-7431; Email: Janis.Locs@rtu.lv

Authors

Abhishek Indurkar − *Rudolfs Cimdins Riga Biomaterials Innovations and Development Centre of RTU, Institute of General Chemical Engineering, Faculty of Materials Science and Applied Chemistry, Riga Technical University, LV-1007 Riga, Latvia; Baltic Biomaterials Centre of Excellence, Headquarters at Riga Technical University, LV-1048 Riga, Latvia*

Rajan Choudhary − *Rudolfs Cimdins Riga Biomaterials Innovations and Development Centre of RTU, Institute of General Chemical Engineering, Faculty of Materials Science and Applied Chemistry, Riga Technical University, LV-1007 Riga, Latvia; Baltic Biomaterials Centre of Excellence, Headquarters at Riga Technical University, LV-1048 Riga, Latvia*

Kristaps Rubenis − *Rudolfs Cimdins Riga Biomaterials Innovations and Development Centre of RTU, Institute of General Chemical Engineering, Faculty of Materials Science and Applied Chemistry, Riga Technical University, LV-1007 Riga, Latvia; Baltic Biomaterials Centre of Excellence, Headquarters at Riga Technical University, LV-1048 Riga, Latvia;* orcid.org/0000-0002-9044-8479

Mansingraj Nimbalkar − *Department of Botany, Shivaji University, Kolhapur 416004 Maharashtra, India*

Anatolijs Sarakovskis − *Institute of Solid State Physics, University of Latvia, LV-1063 Riga, Latvia*

Aldo R. Boccaccini − *Institute of Biomaterials, Department of Material Science and Engineering, University of Erlangen-Nuremberg, 91085 Erlangen, Germany;* orcid.org/0000-0002-7377-2955

Complete contact information is available at: https://pubs.acs.org/10.1021/acsomega.3c00796

Author Contributions

A.I. contributed to conceptualization, literature review, methodology, investigation, data curation, and writing—original draft preparation. R.C. contributed to the literature review and writing-reviewing and editing. K.R. contributed to data curation, writing and editing, and helium pycnometer analysis. M.N. contributed to NMR and FEG-TEM analyses. A.S. contributed to XPS analysis. A.R.B. contributed to supervision, writing- reviewing and editing. J.L. contributed to conceptualization, supervision, writing—reviewing and editing. All authors provided critical feedback and helped to shape the research, analysis, and manuscript.

Notes

The authors declare no competing financial interest.

■ ACKNOWLEDGMENTS

The authors acknowledge financial support from the European Union's Horizon 2020 Research and Innovation Program under grant agreement no. 857287 and Baltic Research Programme Project No. EEA-RESEARCH-85 "Waste-to-resource: eggshells as a source for next generation biomaterials for bone regeneration (EGGSHELL)" under the EEA Grant of Iceland, Liechtenstein and Norway No. EEZ/BPP/VIAA/2021/1. Institute of Solid State Physics, University of Latvia, received funding from the European Union's Horizon 2020 Framework Programme H2020-WIDESPREAD-01-2016-

2017-TeamingPhase2 under grant agreement No. 739508, project CAMART^2.

REFERENCES

(1) Urello, M. A.; Luo, T.; Fang, B.; Kiick, K. L.; Sullivan, M. O. Drug and Gene Delivery for Regenerative Engineering. *Encycl. Biomed. Eng.* **2019**, *1*−*3*, 565−583.

(2) Lehninger, A. L. Mitochondria and Calcium Ion Transport THE FIFTH JUBILEE LECTURE. *Biochem. J.* **1970**, *119*, 129−138.

(3) In, Y.; Amornkitbamrung, U.; Hong, M.-H.; Shin, H. On the Crystallization of Hydroxyapatite under Hydrothermal Conditions: Role of Sebacic Acid as an Additive. *ACS Omega* **2020**, 27204−27210.

(4) Combes, C.; Rey, C. Amorphous calcium phosphates: synthesis, properties and uses in biomaterials. *Acta Biomater.* **2010**, *6*, 3362−3378.

(5) Wang, L.; Nancollas, G. H. Calcium orthophosphates: Crystallization and Dissolution. *Chem. Rev.* **2008**, *108*, 4628−4669.

(6) Markovic, M. Octacalcium Phosphate Carboxylates. *Monogr. Oral Sci.* **2001**, *18*, 77−93.

(7) C Costello, L.; Franklin, R. B.; Reynolds, M. A.; Chellaiah, M. The Important Role of Osteoblasts and Citrate Production in Bone Formation: "Osteoblast Citration" as a New Concept for an Old Relationship. *Open Bone J* **2012**, *4*, 27−34.

(8) Indurkar, A.; Choudhary, R.; Rubenis, K.; Locs, J. Role of carboxylic organic molecules in interfibrillar collagen mineralization. *Front. Bioeng. Biotechnol.* **2023**, *11*, No. 439.

(9) Christoffersen, M. R.; Christoffersen, J.; Kibalczyc, W. Apparent solubilities of two amorphous calcium phosphates and of octacalcium phosphate in the temperature range 30−42 °C. *J. Cryst. Growth* **1990**, *106*, 349−354.

(10) Yokoi, T.; Shimabukuro, M.; Kawashita, M. Octacalcium phosphate with incorporated carboxylate ions: a review. *Sci. Technol. Adv. Mater.* **2022**, 434−445.

(11) Bigi, A.; Boanini, E.Functionalization of octacalcium phosphate for bone replacement. In *Octacalcium Phosphate Biomaterials: Understanding of Bioactive Properties and Application*; Woodhead Publishing, 2020; pp 37−54.

(12) Yokoi, T.; Shimabukuro, M.; Kawashita, M. Octacalcium phosphate with incorporated carboxylate ions: a review. *Sci. Technol. Adv. Mater.* **2022**, *23*, 434−445.

(13) Vecstaudza, J.; Locs, J. Novel preparation route of stable amorphous calcium phosphate nanoparticles with high specific surface area. *J. Alloys Compd.* **2017**, *700*, 215−222.

(14) Martínez-Reyes, I.; Chandel, N. S. Mitochondrial TCA cycle metabolites control physiology and disease. *Nat. Commun.* **2020**, *11*, No. 102.

(15) Hu, Y. Y.; Rawal, A.; Schmidt-Rohr, K. Strongly bound citrate stabilizes the apatite nanocrystals in bone. *Proc. Natl. Acad. Sci. U.S.A.* **2010**, *107*, 22425−22429.

(16) Davies, E.; Müller, K. H.; Wong, W. C.; Pickard, C. J.; Reid, D. G.; Skepper, J. N.; et al. Citrate bridges between mineral platelets in bone. *Proc. Natl. Acad. Sci. U.S.A.* **2014**, E1354−E1363.

(17) Wang, Z.; Xu, Z.; Zhao, W.; Chen, W.; Miyoshi, T.; Sahai, N. Isoexergonic Conformations of Surface-Bound Citrate Regulated Bioinspired Apatite Nanocrystal Growth. *ACS Appl. Mater. Interfaces* **2016**, *8*, 28116−28123.

(18) Xie, B.; Nancollas, G. H. How to control the size and morphology of apatite nanocrystals in bone. *Proc. Natl. Acad. Sci. U.S.A.* **2010**, *107*, 22369.

(19) Yokoi, T.; Kamitakahara, M.; Kawashita, M.; Ohtsuki, C. Formation of organically modified octacalcium phosphate in solutions containing various amounts of benzenedicarboxylic acids. *J. Ceram. Soc. Jpn.* **2013**, *121*, 219−225.

(20) Iafisco, M.; Degli Esposti, L.; Ramírez-Rodríguez, G. B.; Carella, F.; Gómez-Morales, J.; Ionescu, A. C.; et al. Fluoride-doped amorphous calcium phosphate nanoparticles as a promising biomimetic material for dental remineralization. *Sci. Rep.* **2018**, *8*, No. 17016.

(21) Degli Esposti, L.; Markovic, S.; Ignjatovic, N.; Panseri, S.; Montesi, M.; Adamiano, A.; et al. Thermal crystallization of amorphous calcium phosphate combined with citrate and fluoride doping: a novel route to produce hydroxyapatite bioceramics. *J. Mater. Chem. B* **2021**, *9*, 4832−4845.

(22) Carella, F.; Degli Esposti, L.; Barreca, D.; Rizzi, G. A.; Martra, G.; Ivanchenko, P.; et al. Role of citrate in the formation of enamel-like calcium phosphate oriented nanorod arrays. *CrystEngComm* **2019**, *21*, 4684−4689.

(23) Delgado-López, J. M.; Frison, R.; Cervellino, A.; Gõmez-Morales, J.; Guagliardi, A.; Masciocchi, N. Crystal Size, Morphology, and Growth Mechanism in Bio-Inspired Apatite Nanocrystals. *Adv. Funct. Mater.* **2014**, *24*, 1090−1099.

(24) Chatzipanagis, K.; Iafisco, M.; Roncal-Herrero, T.; Bilton, M.; Tampieri, A.; Kröger, R.; Delgado-López, J. M. Crystallization of citrate-stabilized amorphous calcium phosphate to nanocrystalline apatite: a surface-mediated transformation. *CrystEngComm* **2016**, *18*, 3170−3173.

(25) Wang, X. M.; Yan, Y.; Ren, H. H.; Li, S. Y. Nano-amorphous calcium phosphate doped with citrate: Fabrication, structure, and evaluation of the biological performance. *J. Biomater. Appl.* **2019**, 273−283.

(26) Anabel López-Macipe, B.; Gómez-Morales, J.; Rodríguez-Clemente, R. Nanosized Hydroxyapatite Precipitation from Homogeneous Calcium/Citrate/Phosphate Solutions Using Microwave and Conventional Heating. *J. Chem. Soc., Faraday Trans.* **1989**, *218*, 291.

(27) Boskey, A. L. Amorphous calcium phosphate: The contention of bone. *J. Dent. Res.* **1997**, *76*, 1433−1436.

(28) Rey, C.; Combes, C.; Drouet, C.; Grossin, D.; Bertrand, G.; Soulié, J. 1.11 Bioactive Calcium Phosphate Compounds: Physical Chemistry. *Compr. Biomater. II* **2017**, 244−290.

(29) Palencia, M. Functional transformation of Fourier-transform mid-infrared spectrum for improving spectral specificity by simple algorithm based on wavelet-like functions. *J. Adv. Res.* **2018**, *14*, 53−62.

(30) Tarakeshwar, P.; Manogaran, S. Ground state vibrations of citric acid and the citrate trianion—an ab initio study. *Spectrochim. Acta, Part A* **1994**, *50*, 2327−2343.

(31) Yasar, O. F.; Liao, W. C.; Stevensson, B.; Edén, M. Structural Role and Spatial Distribution of Carbonate Ions in Amorphous Calcium Phosphate. *J. Phys. Chem. C* **2021**, *125*, 4675−4693.

(32) Marković, M.; Brown, W. E.; Fowler, B. O. Octacalcium Phosphate Carboxylates. 2. Characterization and Structural Considerations. *Chem. Mater.* **1993**, *5*, 1406−1416.

(33) Safronova, T. V.; Mukhin, E. A.; Putlyaev, V. I.; Knotko, A. V.; Evdokimov, P. V.; Shatalova, T. B.; et al. Amorphous calcium phosphate powder synthesized from calcium acetate and polyphosphoric acid for bioceramics application. *Ceram. Int.* **2017**, *43*, 1310−1317.

(34) Frost, R. L.; Kloprogge, J. T. Raman spectroscopy of the acetates of sodium, potassium and magnesium at liquid nitrogen temperature. *J. Mol. Struct.* **2000**, *526*, 131−141.

(35) Wu, Y. J.; Tsai, T. W. T.; Huang, S. J.; Mou, Y.; Lin, C. J.; Chan, J. C. C. Hydrogen bond formation between citrate and phosphate ions in spherulites of fluorapatite. *Langmuir* **2013**, *29*, 11681−11686.

(36) Interpreting C-13 NMR spectra n.d. https://www.chemguide.co.uk/analysis/nmr/interpretc13.html (accessed July 5, 2022).

(37) Xu, W. J.; Wen, H.; Kim, H. S.; Ko, Y. J.; Dong, S. M.; Park, I. S.; et al. Observation of acetyl phosphate formation in mammalian mitochondria using real-time in-organelle NMR metabolomics. *Proc. Natl. Acad. Sci. U.S.A.* **2018**, *115*, 4152−4157.

(38) Sen, S.; Kaseman, D. C.; Colas, B.; Jacob, D. E.; Clark, S. M. Hydrogen bonding induced distortion of CO3 units and kinetic stabilization of amorphous calcium carbonate: Results from 2D 13C NMR spectroscopy. *Phys. Chem. Chem. Phys.* **2016**, *18*, 20330−20337.

(39) Lu, B. Q.; Garcia, N. A.; Chevrier, D. M.; Zhang, P.; Raiteri, P.; Gale, J. D.; Gebauer, D. Short-Range Structure of Amorphous

https://doi.org/10.1021/acsomega.3c00796
ACS Omega 2023, 8, 26782−26792

Calcium Hydrogen Phosphate. *Cryst. Growth Des.* **2019**, *19*, 3030−3038.
(40) Ajili, W.; Tovani, C. B.; Fouassier, J.; de Frutos, M.; Laurent, G. P.; Bertani, P.; et al. Inorganic phosphate in growing calcium carbonate abalone shell suggests a shared mineral ancestral precursor. *Nat. Commun.* **2022**, *13*, No. 1496.
(41) Vyalikh, A.; Elschner, C.; Schulz, M.; Mai, R.; Scheler, U. Early Stages of Biomineral Formation-A Solid-State NMR Investigation of the Mandibles of Minipigs. *Magnetochemistry* **2017**, No. 39.
(42) Belton, P. S.; Harris, R. K.; Wilkes, P. J. Solid-state phosphorus-31 NMR studies of synthetic inorganic calcium phosphates. *J. Phys. Chem. Solids* **1988**, *49*, 21−27.
(43) Xu, Y.; Zhong, X.; Li, Y.; Liu, J. Morphology-controllable self-assembly of strontium carbonate (SrCO3) crystals under the action of different regulators. *J. Mater. Sci. Mater. Electron.* **2019**, *30*, 21150−21159.
(44) Mudiyanselage, K.; Burrell, A. K.; Senanayake, S. D.; Idriss, H. XPS and NEXAFS study of the reactions of acetic acid and acetaldehyde over UO2(100) thin film. *Surf. Sci.* **2019**, *680*, 107−112.
(45) Schmidt, M.; Steinemann, S. G. XPS studies of amino acids adsorbed on titanium dioxide surfaces. *Fresenius' J. Anal. Chem.* **1991**, *341*, 412−415.
(46) Mai, T.; Wolski, K.; Puciul-Malinowska, A.; Kopyshev, A.; Gräf, R.; Bruns, M.; et al. Anionic polymer brushes for biomimetic calcium phosphate mineralization — a surface with application potential in biomaterials. *Polymers* **2018**, No. 1165.
(47) Yoshimura, M.; Suda, H. Hydrothermal Processing of Hydroxyapatite: Past, Present and Future. In *Hydroxyapatite and Related Materials*; CRC Press, 1994.
(48) Dey, A.; Bomans, P. H. H.; Müller, F. A.; Will, J.; Frederik, P. M.; de With, G.; De With, G. The role of prenucleation clusters in surface-induced calcium phosphate crystallization. *Nat. Mater.* **2010**, *9*, 1010−1014.
(49) Lotsari, A.; Rajasekharan, A. K.; Halvarsson, M.; Andersson, M. Transformation of amorphous calcium phosphate to bone-like apatite. *Nat. Commun.* **2018**, *9*, No. 4170.
(50) Edén, M. Structure and formation of amorphous calcium phosphate and its role as surface layer of nanocrystalline apatite: Implications for bone mineralization. *Materialia* **2021**, *17*, No. 101107.
(51) Niu, X.; Chen, S.; Tian, F.; Wang, L.; Feng, Q.; Fan, Y. Hydrolytic conversion of amorphous calcium phosphate into apatite accompanied by sustained calcium and orthophosphate ions release. *Mater. Sci. Eng., C* **2017**, *70*, 1120−1124.
(52) Niu, X.; Liu, Z.; Tian, F.; Chen, S.; Lei, L.; Jiang, T.; et al. Sustained delivery of calcium and orthophosphate ions from amorphous calcium phosphate and poly(L-lactic acid)-based electrospinning nanofibrous scaffold. *Sci. Rep.* **2017**, *7*, No. 45655.
(53) Costello, L. C.; Chellaiah, M.; Zou, J.; Franklin, R. B.; Reynolds, M. A. The status of citrate in the hydroxyapatite/collagen complex of bone; and Its role in bone formation. *J. Regen. Med. Tissue Eng.* **2014**, *3*, No. 4.
(54) Costello, L. C.; Franklin, R. B.; Reynolds, M. A. The Important Role and Implications of Citrate in the Composition, Structure, and Function of Oral/Periodontal/Craniofacial Tissues. *Madridge J. Dent. Oral Surg.* **2018**, *3*, 85−90.
(55) Granchi, D.; Baldini, N.; Ulivieri, F. M.; Caudarella, R. Role of Citrate in Pathophysiology and Medical Management of Bone Diseases. *Nutrients* **2019**, *11*, No. 2576.
(56) Chen, H.; Wang, Y.; Dai, H.; Tian, X.; Cui, Z.-K.; Chen, Z.; et al. Bone and plasma citrate is reduced in osteoporosis. *Bone* **2018**, *114*, 189−197.
(57) Chen, Y.; Gu, W.; Pan, H.; Jiang, S.; Tang, R. Stabilizing amorphous calcium phosphate phase by citrate adsorption. *CrystEngComm* **2014**, *16*, 1864−1867.
(58) Ruiz-Agudo, E.; Ruiz-Agudo, C.; Di Lorenzo, F.; Alvarez-Lloret, P.; Ibañez-Velasco, A.; Rodriguez-Navarro, C. Citrate Stabilizes Hydroxylapatite Precursors: Implications for Bone Mineralization. *ACS Biomater. Sci. Eng.* **2021**, *7*, 2346−2357.
(59) Greenwald, I. THE DISSOCIATION OF SOME CALCIUM SALTS. *J. Biol. Chem.* **1938**, *124*, 437−452.
(60) Dziuba, N.; Hardy, J.; Lindahl, P. A. Low-Molecular-Mass Iron in Healthy Blood Plasma is not Predominately Ferric Citrate. *Metallomics* **2018**, *10*, 802.
(61) Boehm, A. V.; Meininger, S.; Tesch, A.; Gbureck, U.; Müller, F. A. The Mechanical Properties of Biocompatible Apatite Bone Cement Reinforced with Chemically Activated Carbon Fibers. *Materials* **2018**, *11*, No. 192.
(62) Degli Esposti, L.; Adamiano, A.; Siliqi, D.; Giannini, C.; Iafisco, M. The effect of chemical structure of carboxylate molecules on hydroxyapatite nanoparticles. A structural and morphological study. *Bioact. Mater.* **2021**, *6*, 2360−2371.
(63) Wu, Y. J.; Tsai, T. W. T.; Huang, S. J.; Mou, Y.; Lin, C. J.; Chan, J. C. C. Hydrogen bond formation between citrate and phosphate ions in spherulites of fluorapatite. *Langmuir* **2013**, *29*, 11681−11686.
(64) Skwarek, E.; Janusz, W.; Sternik, D. Adsorption of citrate ions on hydroxyapatite synthetized by various methods. *J. Radioanal. Nucl. Chem.* **2014**, *299*, 2027−2036.
(65) Vega, E. D.; Narda, G. E.; Ferretti, F. H. Adsorption of citric acid from dilute aqueous solutions by hydroxyapatite. *J. Colloid Interface Sci.* **2003**, *268*, 37−42.
(66) Alahiane, A.; Rochdi, A.; Taourirte, M.; Redwane, N.; Sebti, S.; Lazrek, H. B. Natural phosphate as Lewis acid catalyst: A simple and convenient method for acyclonucleoside synthesis. *Tetrahedron Lett.* **2001**, *42*, 3579−3581.
(67) Alexander, R. S.; Kanyo, Z. F.; Chirlian, L. E.; Christianson, D. W. Stereochemistry of Phosphate-Lewis Acid Interactions: Implications for Nucleic Acid Structure and Recognition. *J. Am. Chem. Soc.* **1990**, *112*, 933−937.
(68) Corbridge, D. E. C. The structural chemistry of phosphates. *Bull. Mineral.* **1971**, *94*, 271−299.
(69) Marković, M.; Fowler, B. O.; Brown, W. E. Octacalcium Phosphate Carboxylates. 1. Preparation and Identification. *Chem. Mater.* **1993**, *5*, 1401−1405.
(70) Xin, Y.; Shirai, T.Noble-metal-free hydroxyapatite activated by facile mechanochemical treatment towards highly-efficient catalytic oxidation of volatile organic compound. *Sci. Rep.* 123AD; 11: 7512 DOI: 10.1038/s41598-021-86992-8.
(71) Calcium;acetyl phosphate | C2H3CaO5P - PubChem. https://pubchem.ncbi.nlm.nih.gov/compound/15846981#section=3D-Conformer (accessed October 3, 2022).

https://doi.org/10.1021/acsomega.3c00796
ACS Omega 2023, 8, 26782−26792

Amorphous calcium phosphate and amorphous calcium phosphate carboxylate: synthesis and characterization

Abhishek Indurkar[1,2], Rajan Choudhary[1,2], Kristaps Rubenis[1,2], Mansingraj Nimbalkar[3], Anatolijs Sarakovskis[4], Aldo R. Boccaccini[5,] and Janis Locs[1,2*]

[1] Rudolfs Cimdins Riga Biomaterials Innovations and Development Centre of RTU, Institute of General Chemical Engineering, Faculty of Materials Science and Applied Chemistry, Riga Technical University, Pulka Street 3, LV-1007 Riga, Latvia

[2] Baltic Biomaterials Centre of Excellence, Headquarters at Riga Technical University, Kipsalas Street 6A, LV-1048 Riga, Latvia

[3] Department of Botany, Shivaji University, Kolhapur – 416 004 (MS), India

[4] Institute of Solid State Physics, University of Latvia, 8 Kengaraga Str., LV-1063 Riga, Latvia

[5] Institute of Biomaterials, Department of Material Science and Engineering, University of Erlangen-Nuremberg, 91085, Erlangen, Germany.

*Corresponding author - Janis.Locs@rtu.lv

Content

Figure S1. XPS survey spectra of ACPC_CIT, ACPC_ACE, ACP_CL and ACP_NIT

Figure S2. The crystallization of ACP under a high electron beam. The sample represented as A) ACP_CL, B) ACP_NIT, C) ACPC_ACE and D) ACPC_CIT.

Figure S3. Optical microscopy of H&E-stained MC-3T3E1 cells cultured with extract of different ACPs. Cells treated with 10 wt% extracts of ACPC_CIT, ACPC_ACE, ACP_NIT, and ACP_CL are displayed from A1 to D1 respectively. Figures from A2 to D2 indicate cells treated with 1 wt% extracts of ACPC_CIT, ACPC_ACE, ACP_NIT, and ACP_CL are displayed respectively. Finally, the cells treated with 0.1 wt% extracts of ACPC_CIT, ACPC_ACE, ACP_NIT, and ACP_CL are displayed from A3 to D3 respectively.

Table S1 - Literature survey on the synthesis of ACP by precipitation.

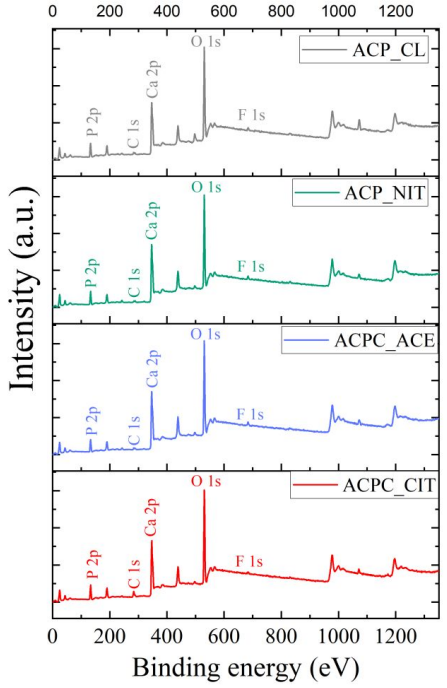

Figure S1. XPS survey spectra of ACPC_CIT, ACPC_ACE, ACP_CL and ACP_NIT

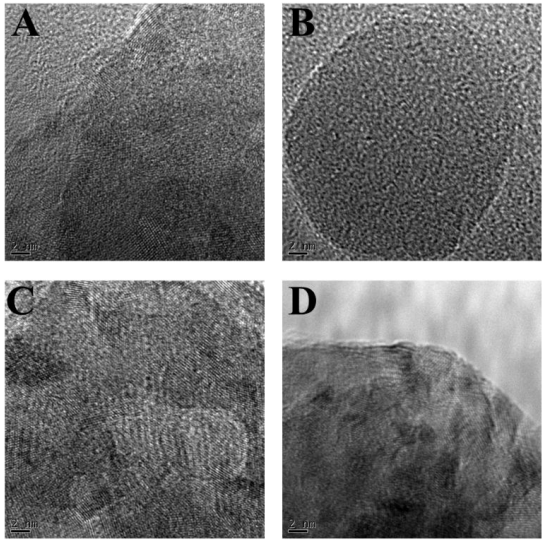

Figure S2. The crystallization of ACP under a high electron beam. The sample represented as A) ACP_CL, B) ACP_NIT, C) ACPC_ACE and D) ACPC_CIT.

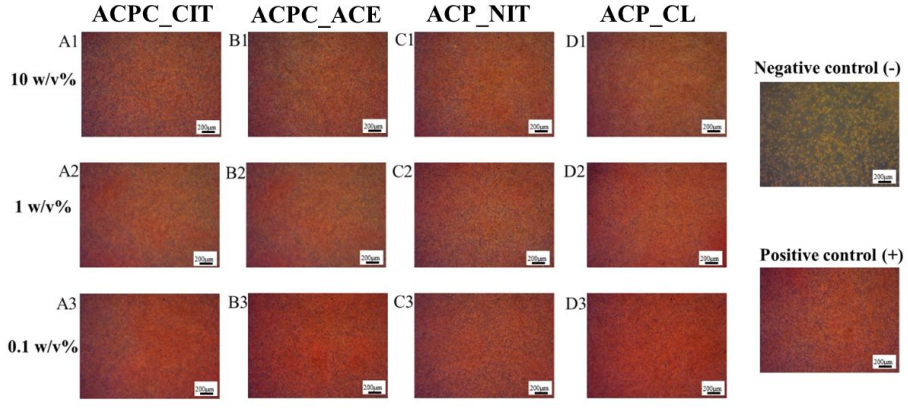

Figure S3. Optical microscopy of H&E-stained MC-3T3E1 cells cultured with extract of different ACPs. Cells treated with 10 wt% extracts of ACPC_CIT, ACPC_ACE, ACP_NIT, and ACP_CL are displayed from A1 to D1 respectively. Figures from A2 to D2 indicate cells treated with 1 wt% extracts of ACPC_CIT, ACPC_ACE, ACP_NIT, and ACP_CL are displayed respectively. Finally, the cells treated with 0.1 wt% extracts of ACPC_CIT, ACPC_ACE, ACP_NIT, and ACP_CL are displayed from A3 to D3 respectively.

Table S1 - Literature survey on the synthesis of ACP by precipitation.

Sr no.	Year	Calcium source	Phosphate source	Additive to achieving the desired pH	pH	Post treatments	Particle size	Cellular studies	Product

1.	2012	a. Calcium metal b. $Ca(NO_3)_2.4H_2O$ c. $CaCl_2.2H_2O$ d. $Ca(OH)_2$ e. $Ca(CH_3COO)_2$	a. Na_2HPO_4 b. $(NH_4)_2HPO_4$		9.2 - 11.3	N.A.	< 70nm	N.A.	ACP [1]
2.	2017	$Ca(CH_3COO)_2$	H_3PO_4	$NH_3.H_2O$	9	Filtration and Air drying	The size reported in μm of heat-treated samples	N.A.	ACP [2]
3.	2012	$CaCl_2.2H_2O$	KH_2PO_4	-	6.76	Centrifuge and Oven-dried at 37°C	Scale bar in TEM reveals size in nm. But the exact size is not indicated.	7F2 Mouse osteoblasts	ACP [3]
4.	2019	Hydroxyapatite suspension in HCl		NH_4OH	8 - 11	Centrifuge and washed with distilled water. Freeze drying or oven drying at 80°C	14 - 18 nm	N.A.	ACP [4]
5.	2018	$CaCl_2.2H_2O$	Na_2HPO_4	HCl	7.4	N.A.	56 - 85 nm	N.A.	ACP [5]
6.	2014	$Ca(NO_3)_2.4H_2O$	$(NH_4)_2HPO_4$	Ammonia	10.5 - 12	Filtration and drying at room temperature	Scale bar in TEM reveals size in nm.	N.A.	ACP [6]

							But the exact size is not indicated.		
7.	2019	Hydroxyapatite suspension in HCl		NH_4OH	8 - 11	Centrifuge and washed with distilled water. Oven drying at 80°C	11 - 30 nm	N.A.	ACP [7]
8.	2014	$CaCl_2.2H_2O$	Na_2HPO_4	-	7.4	Aging at 55°C, 65°C, and 70°C for 15 mins. Further centrifugation or filtration and drying at room temperature.	245 ± 20 nm	N.A.	ACP [8]
9.	2010	$CaCl_2.2H_2O$	$Na_3PO_4.H_2O$	NaOH	N.A.	Centrifuge and washed with distilled water. Oven drying at 60°C	10 – 50 nm	N.A.	Mg Substituted ACP [9]
10.	2017	$Ca(NO_3)_2.4H_2O$	$(NH_4)_2HPO_4$	Tris buffer	9.5	Filtration and freeze drying	260 – 300 nm	G-292 Human osteosarcoma cell line	Mg-doped ACP [10]
11.	2015	$Ca(NO_3)_2.4H_2O$	$(NH_4)_2HPO_4$	Ammonia	9.6 – 9.8	Centrifuge and washed with distilled water. Freeze drying or Oven drying at 80°C or drying at room temperature.	Scale bar in TEM reveals size in nm. But the exact size is not indicated.	MC-3T3E1 preosteoblasts	Amorphous calcium magnesium phosphate [11]

12.	2020	$CaCl_2$	$(NH_4)_2HPO_4$	NaOH	10	Filtration, washing, and drying at 60°C	< 500nm	1. SaOS-2 human osteosarcoma cell line 2. HUVEC human umbilical vein endothelial cells	Polyphosphate stabilized ACP [12]
13.	2016	$CaCl_2$	$Na_2HPO_4.12H_2O$	$NaBH_4$	Information not given	Hydrothermal synthesis, then the precipitate was filtered, washed and oven dried at 60°C	The doped ACP shell size was 14 nm	-	CdTe quantum dots of zerovalent iron/ACP composite [13]
14.	2016	$CaCl_2$ or $Ca(NO_3)_2.4H_2O$	$(NH_4)_2HPO_4$ or K_2HPO_4	CH_4N_2O	Information not given	Filtration washing and freeze drying	30nm	-	ACP [14]
15.	2010	$CaCl_2$	K_2HPO_4	KOH	11.5	Filtration washing and freeze drying	-	-	ACP [15]
16.	2021	$CaCl_2.2H_2O$	Na_2HPO_4	NaOH	7.8 - 11	-	-	-	ACP [16]
17.	2016	$CaCl_2$	K_2HPO_4	KOH	8	Washing and freeze drying	100nm	-	ACP [17]
18.	2021	$CaCl_2$	Na_2HPO_4	HCl	7.4	Dried in desiccator	99.5 ± 29.4nm	-	ACP [18]
19.	2022	$Ca(NO_3)_2.4H_2O$	$(NH_4)_2HPO_4$	NH_4OH	10	Filtered and washed with distilled water. Oven drying at 80°C or drying at room temperature.	Scale bar in SEM reveals size in µm. But the exact size was not indicated.	-	Zn constating ACP [19]

20.	2014	$Ca(NO_3)_2.4H_2O$	$Na_2HPO_4.12H_2O$	-	-	Centrifuge, Freeze drying, and ball milling	Scale bar in SEM reveals size in µm. But the exact size is not indicated.	-	Silver substituted ACP [20]
21.	2021	$CaCl_2.2H_2O$	Na_2HPO_4	HCl	7.4	Filtration, washing, and drying in a stream of nitrogen	64.5 ± 9.9nm to 143.5 ± 24.8 nm	-	Effect of amino acids on ACP [21]
22.	2010	$Ca(NO_3)_2.4H_2O$	$(NH_4)_2HPO_4$	NH_4OH	12	Frozen and refrozen to obtain precipitate followed by freezing and freeze drying	-	-	ACP [22]
23.	2006	$Ca(NO_3)_2.4H_2O$	H_3PO_4	-	-	-	-	Animal studies	Electro-sprayed calcium phosphate coatings [23]
24.	2014	$CaCl_2.2H_2O$	$HPO_4.3H_2O$	Tris hydroxymethyl aminomethane and HCl	7.4	Rinsed with distilled water and air dried	Particle size not given	-	Calcium phosphate on bacterial cellulose nanofibers [24]
25.	2016	$Ca(NO_3)_2.4H_2O$	Na_3PO_3S	Ammonia	10.5	Centrifuged, washed, and freeze-dried	60 – 100nm	-	Sulfur containing ACP [25]
26.	2000	$Ca(NO_3)_2$	$(NH_4)_2HPO_4$	NH_4OH	10	Washed with acetone	-	-	Effect of nickel on ACP [26]
27	2021	$CaCl_2$	H_3PO_4	-	6 to 8	-	60 and more than 500 nm	-	ACP synthesized by Epoxide Route [27]

28	2022	$CaCl_2$	NaH_2PO_4 Na_2HPO_4	NaOH	7.40	Filtered, frozen in liquid nitrogen, and freeze-dried	40 to 80 nm	-	Magnesium-doped ACP [28]
29	2021	$CaCl_2$	$(NH_4)_2HPO_4$	NaOH	8	Centrifuged, and freeze-dried	-	1. A549 cells 2. MG63 cells	Composite: Hyaluronic acid fluorescent carbon/amorphous calcium phosphate [29]
30	2019	$CaCl_2$	H_3PO_4	-	8	Filtration, washing, and drying in a vacuum oven at 50 °C	20 to 100 nm	Mouse Bone Marrow Stem Cells	ACP synthesis [30]
31	2021	$CaCl_2$	H_3PO_4	-	8	Filtration, washing, and drying in a vacuum oven at 50°C	-	1. Mouse Bone Marrow Stem Cells 2. New Zealand white Rabbit	Composite: ACP doped with citrate/poly-amino acid [31]
32	2020	$CaCl_2.2H_2O$	Potassium Phosphate dibasic	KOH	12	Centrifuged, washed, and stored at 4°C	Below 10 nm	-	Europium doped ACP [32]
33	2013	Biomineralization medium			7.45	Centrifugation or filtration washed and dried at room temperature	20 nm	-	ACP [33]
34	1998	$Ca(NO_3)_2.4H_2O$	$(NH_4)_2HPO_4$	Ammonia	9.8	Filtered, washed, and freeze-dried	-	-	Synthesis in alcohol medium [34]
35	2020	$Ca(CH_3COO)_2.H_2O$	H_3PO_4	-	-	Spray drying	100 nm	-	ACP [35]

36	1999	$CaCl_2$	KH_2PO_4, K_2HPO_4	Tris(hydroxymethyl)aminomethane	6.8	-	-	-	ACP [36]
37	2005	$Ca(NO_3)_2.4H_2O$	$(NH_4)H_2PO_4$ $(NH_4)_2HPO_4$	Ammonia	10	Filtered, washed, and air-dried	-	-	ACP [37]
38	2009	$CaCl_2.2H_2O$	Na_2HPO_4	NaOH	-	Centrifuged and washed	-	-	ACP [38]
39	2017	$CaCl_2$	K_2HPO_4	-	-	Filtered, washed, and freeze-dried	29-98 nm	-	ACP [39]
40	2008	$Ca_5(PO_4)_3OH$	-	NaOH	6.5	Centrifuged and washed	30-50 nm	-	ACP-chitosan [40]
41	2019	$Ca(NO_3)_2.4H_2O$	$(NH_4)_2HPO_4$	Ammonia	10	Filtered, washed, and dried at 50°C	-	-	Mn-ACP [41]
42	2013	$Ca(NO_3)_2.4H_2O$	$(NH_4)_2HPO_4$	NH_4OH	10	Centrifuged and dried at 70°C	-	-	ACP [42]
43	2011	$CaCl_2$	H_3PO_4	pH not adjusted	-	-	-	-	ACP [43]
44	2014	$Ca(NO_3)_2.4H_2O$	$(NH_4)_2HPO_4$	-	-	washed and freeze-dried	40 nm	-	ACP [44]
45	2004	$CaCl_2$	$(NH_4)H_2PO_4$	NaOH	7.1	washed and dried	-	-	ACP [45]
46	2018	$Ca(NO_3)_2$	$(NH_4)_2HPO_4$	Ammonia	10	washed and dried at 25 °Cs	34.4 nm	-	Polyacrylic acid nano Hap [46]
47	1999	$Ca(NO_3)_2$	diammonium phosphate	NH_4OH	8.5 to 9	Filter washed and dried	submicron	-	ACP to HaP [47]

References

[1] Tas AC. Calcium metal to synthesize amorphous or cryptocrystalline calcium phosphates ☆ 2012. https://doi.org/10.1016/j.msec.2012.01.024.

[2] Safronova T V., Mukhin EA, Putlyaev VI, Knotko A V., Evdokimov P V., Shatalova TB, et al. Amorphous calcium phosphate powder synthesized from calcium acetate and polyphosphoric acid for bioceramics application. Ceram Int 2017;43:1310–7. https://doi.org/10.1016/J.CERAMINT.2016.10.085.

[3] Zhou H, Bhaduri S. Novel microwave synthesis of amorphous calcium phosphate nanospheres. J Biomed Mater Res Part B Appl Biomater 2012;100B:1142–50. https://doi.org/10.1002/JBM.B.32681.

[4] Vecstaudza J, Gasik M, Locs J. Amorphous calcium phosphate materials: Formation, structure and thermal behaviour. J Eur Ceram Soc 2019;39:1642–9. https://doi.org/10.1016/J.JEURCERAMSOC.2018.11.003.

[5] Čadež V, Erceg I, Selmani A, Jurašin DD, Šegota S, Lyons DM, et al. Amorphous Calcium Phosphate Formation and Aggregation Process Revealed by Light Scattering Techniques. Cryst 2018, Vol 8, Page 254 2018;8:254. https://doi.org/10.3390/CRYST8060254.

[6] He K, Xiao GY, Xu WH, Zhu RF, Lu YP. Ultrasonic enhancing amorphization during synthesis of calcium phosphate. Ultrason Sonochem 2014;21:499–504. https://doi.org/10.1016/J.ULTSONCH.2013.08.011.

[7] Vecstaudza J, Locs J. Novel preparation route of stable amorphous calcium phosphate nanoparticles with high specific surface area. J Alloys Compd 2017;700:215–22. https://doi.org/10.1016/J.JALLCOM.2017.01.038.

[8] Cuneyt Tas A. Submicron spheres of amorphous calcium phosphate forming in a stirred SBF solution at 55 °C. J Non Cryst Solids 2014;400:27–32. https://doi.org/10.1016/J.JNONCRYSOL.2014.04.031.

[9] Lee D, Kumta PN. Chemical synthesis and characterization of magnesium substituted amorphous calcium phosphate (MG-ACP). Mater Sci Eng C 2010;30:1313–7. https://doi.org/10.1016/J.MSEC.2010.05.009.

[10] Shahrezaee M, Raz M, Shishehbor S, Moztarzadeh F, Baghbani F, Sadeghi A, et al. Synthesis of Magnesium Doped Amorphous Calcium Phosphate as a Bioceramic for Biomedical Application: In Vitro Study. Silicon 2018;10:1171–9. https://doi.org/10.1007/S12633-017-9589-Y.

[11] Babaie E, Zhou H, Lin B, Bhaduri SB. Influence of ethanol content in the precipitation medium on the composition, structure and reactivity of magnesium-calcium

phosphate. Mater Sci Eng C 2015;53:204–11. https://doi.org/10.1016/J.MSEC.2015.04.011.

[12] Müller WEG, Ackermann M, Al-Nawas B, Righesso LAR, Muñoz-Espí R, Tolba E, et al. Amplified morphogenetic and bone forming activity of amorphous versus crystalline calcium phosphate/polyphosphate. Acta Biomater 2020;118:233–47. https://doi.org/10.1016/J.ACTBIO.2020.10.023.

[13] Jin L, Na LH, Liu FT, Gong LY, Lou DW, Zhang JP. Synthesis and adsorption properties for CdTe quantum dots of zero-valent iron/amorphous calcium phosphate composites. Chinese J Inorg Chem 2016;32:2025–33. https://doi.org/10.11862/CJIC.2016.251.

[14] Karimi M, Hesaraki S, Alizadeh M, Kazemzadeh A. A facile and sustainable method based on deep eutectic solvents toward synthesis of amorphous calcium phosphate nanoparticles: The effect of using various solvents and precursors on physical characteristics. J Non Cryst Solids 2016;443:59–64. https://doi.org/10.1016/J.JNONCRYSOL.2016.04.026.

[15] Rabadjieva D, Gergulova R, Titorenkova R, Tepavitcharova S, Dyulgerova E, Balarew C, et al. Biomimetic transformations of amorphous calcium phosphate: kinetic and thermodynamic studies. J Mater Sci Mater Med 2010;21:2501–9. https://doi.org/10.1007/S10856-010-4103-8.

[16] Hoeher AJ, Mergelsberg ST, Borkiewicz OJ, Michel FM. Impacts of initial Ca/P on amorphous calcium phosphate. Cryst Growth Des 2021;21:3736–45. https://doi.org/10.1021/ACS.CGD.1C00058/ASSET/IMAGES/LARGE/CG1C00058_0007.JPEG.

[17] Rabadjieva D, Tepavitcharova S, Sezanova K, Gergulova R. Chemical Equilibria Modeling of Calcium Phosphate Precipitation and Transformation in Simulated Physiological Solutions. J Solution Chem 2016;45:1620–33. https://doi.org/10.1007/S10953-016-0528-0.

[18] Erceg I, Selmani A da, Gajović A, Radatović B, Šegota S, Ćurlin M, et al. Precipitation at room temperature as a fast and versatile method for calcium phosphate/tio2 nanocomposites synthesis. Nanomaterials 2021;11. https://doi.org/10.3390/NANO11061523/S1.

[19] Chaudhry AA, Khalid H, Zahid M, Ijaz K, Akhtar H, Younas B, et al. Zinc containing calcium phosphates obtained via microwave irradiation of suspensions. Mater Chem Phys 2022;276:124921. https://doi.org/10.1016/J.MATCHEMPHYS.2021.124921.

[20] Yu T, Gao C, Ye J, Zhang M. Synthesis and Characterization of a Novel Silver-Substituted Calcium Phosphate Cement. J Mater Sci Technol 2014;30:686–91. https://doi.org/10.1016/J.JMST.2014.03.005.

[21] Erceg I, Maltar-Strmečki N, Domazet Jurašin D, Strasser V, Curlin M, Lyons DM, et al. Comparison of the Effect of the Amino Acids on Spontaneous Formation and

Transformation of Calcium Phosphates. Cryst 2021, Vol 11, Page 792 2021;11:792. https://doi.org/10.3390/CRYST11070792.

[22] Zyman ZZ, Rokhmistrov D V., Glushko VI. Structural and compositional features of amorphous calcium phosphate at the early stage of precipitation. J Mater Sci Mater Med 2010;21:123–30. https://doi.org/10.1007/S10856-009-3856-4.

[23] Leeuwenburgh SCG, Wolke JGC, Siebers MC, Schoonman J, Jansen JA. In vitro and in vivo reactivity of porous, electrosprayed calcium phosphate coatings. Biomaterials 2006;27:3368–78. https://doi.org/10.1016/J.BIOMATERIALS.2006.01.052.

[24] Luo H, Xiong G, Wan Y. In situ phosphorus K-edge X-ray absorption spectroscopy studies of calcium-phosphate formation and transformation on the surface of bacterial cellulose nanofibers. Cellulose 2014;21:3303–9. https://doi.org/10.1007/S10570-014-0359-3/FIGURES/4.

[25] Gong CY, Geng ZG, Dong A Le, Ye XX, Wang GZ, Zhang YX. Highly Efficient and Selective Removal of Pb(II) ions by Sulfur-Containing Calcium Phosphate Nanoparticles. Chinese J Chem Phys 2016;29:607. https://doi.org/10.1063/1674-0068/29/CJCP1603045.

[26] Guerra-López J, González R, Gómez A, Pomés R, Punte G, Della Védova CO. Effects of Nickel on Calcium Phosphate Formation. J Solid State Chem 2000;151:163–9. https://doi.org/10.1006/JSSC.1999.8615.

[27] Borovik P, Oestreicher V, Huck-Iriart C, Jobbágy M. Amorphous Calcium Phosphates: Solvent-Controlled Growth and Stabilization through the Epoxide Route. Chem – A Eur J 2021;27:10077–86. https://doi.org/10.1002/CHEM.202005483.

[28] Gelli R, Briccolani-Bandini L, Pagliai M, Cardini G, Ridi F, Baglioni P. Exploring the effect of Mg2+ substitution on amorphous calcium phosphate nanoparticles. J Colloid Interface Sci 2022;606:444–53. https://doi.org/10.1016/J.JCIS.2021.08.033.

[29] Gang X, Wang L, Jia J, Wang H, Lian X, Gao X, et al. Synthesis and biological evaluation of fluorescent hyaluronic acid modified amorphous calcium phosphate drug carriers for tumor-targeting. Int J Biol Macromol 2021;182:1445–54. https://doi.org/10.1016/J.IJBIOMAC.2021.05.068.

[30] Wang XM, Yan Y, Ren HH, Li SY. Nano-amorphous calcium phosphate doped with citrate: Fabrication, structure, and evaluation of the biological performance. Https://DoiOrg/101177/0885328219845969 2019;34:273–83. https://doi.org/10.1177/0885328219845969.

[31] Wang X, Zhao D, Ren H, Yan Y, Li S. Biological evaluation of the modified nano-amorphous phosphate calcium doped with citrate/poly-amino acid composite as a potential candidate for bone repair and reconstruction. J Mater Sci Mater Med 2021;32:1–18. https://doi.org/10.1007/S10856-020-06482-7/TABLES/2.

[32] Ortiz-Gómez I, Ramírez-Rodríguez GB, Capitán-Vallvey LF, Salinas-Castillo A, Delgado-López JM. Highly stable luminescent europium-doped calcium phosphate nanoparticles for creatinine quantification. Colloids Surfaces B Biointerfaces 2020;196:111337. https://doi.org/10.1016/J.COLSURFB.2020.111337.

[33] Tas AC. X-ray-amorphous calcium phosphate (ACP) synthesis in a simple biomineralization medium. J Mater Chem B 2013;1:4511–20. https://doi.org/10.1039/C3TB20854K.

[34] Rodrigues A, Lebugle A. Influence of ethanol in the precipitation medium on the composition, structure and reactivity of tricalcium phosphate. Colloids Surfaces A Physicochem Eng Asp 1998;145:191–204. https://doi.org/10.1016/S0927-7757(98)00660-8.

[35] Le Grill S, Soulie J, Coppel Y, Roblin P, Lecante P, Marsan O, et al. Spray-drying-derived amorphous calcium phosphate: a multi-scale characterization. J Mater Sci 2020 562 2020;56:1189–202. https://doi.org/10.1007/S10853-020-05396-7.

[36] Bradt JH, Mertig M, Teresiak A, Pompe W. Biomimetic Mineralization of Collagen by Combined Fibril Assembly and Calcium Phosphate Formation. Chem Mater 1999;11:2694–701. https://doi.org/10.1021/CM991002P.

[37] Hakimimehr D, Liu DM, Troczynski T. In-situ preparation of poly(propylene fumarate)—hydroxyapatite composite. Biomaterials 2005;26:7297–303. https://doi.org/10.1016/J.BIOMATERIALS.2005.05.065.

[38] Tao J, Pan H, Zhai H, Wang J, Li L, Wu J, et al. Controls of tricalcium phosphate single-crystal formation from its amorphous precursor by interfacial energy. Cryst Growth Des 2009;9:3154–60. https://doi.org/10.1021/CG801130W/SUPPL_FILE/CG801130W_SI_001.PDF.

[39] Karimi M, Hesaraki S, Alizadeh M, Kazemzadeh A. Time and temperature mediated evolution of CDHA from ACP nanoparticles in deep eutectic solvents: Kinetic and thermodynamic considerations. Mater Des 2017;122:1–10. https://doi.org/10.1016/J.MATDES.2017.02.076.

[40] Gutiérrez MC, Jobbágy M, Ferrer ML, Del Monte F. Enzymatic synthesis of amorphous calcium phosphate-chitosan nanocomposites and their processing into hierarchical structures. Chem Mater 2008;20:11–3. https://doi.org/10.1021/CM7020164/SUPPL_FILE/CM7020164.PDF.

[41] Sinusaite L, Renner AM, Schütz MB, Antuzevics A, Rogulis U, Grigoraviciute-Puroniene I, et al. Effect of Mn doping on the low-temperature synthesis of tricalcium phosphate (TCP) polymorphs. J Eur Ceram Soc 2019;39:3257–63. https://doi.org/10.1016/J.JEURCERAMSOC.2019.03.057.

[42] Salahi E, Heinrich JG. Synthesis and thermal behaviour of β tricalcium phosphate precipitated from aqueous solutions. Http://DxDoiOrg/101179/096797803225001597

2013;102:79–83. https://doi.org/10.1179/096797803225001597.

[43] Bucur AI, Bucur R, Vlase T, Doca N. Thermal analysis and high-temperature X-ray diffraction of nano-tricalcium phosphate crystallization. J Therm Anal Calorim 2011 1071 2011;107:249–55. https://doi.org/10.1007/S10973-011-1753-9.

[44] Garskaite E, Gross KA, Yang SW, Yang TCK, Yang JC, Kareiva A. Effect of processing conditions on the crystallinity and structure of carbonated calcium hydroxyapatite (CHAp). CrystEngComm 2014;16:3950–9. https://doi.org/10.1039/C4CE00119B.

[45] Arifuzzaman SM, Rohani S. Experimental study of brushite precipitation. J Cryst Growth 2004;267:624–34. https://doi.org/10.1016/J.JCRYSGRO.2004.04.024.

[46] Yan D, Lou Y, Han Y, Wickramaratne MN, Dai H, Wang X. Controllable synthesis of poly(acrylic acid)-stabilized nano-hydroxyapatite suspension by an ultrasound-assisted precipitation method. Mater Lett 2018;227:9–12. https://doi.org/10.1016/J.MATLET.2018.04.124.

[47] Seckler MM, Danese M, Derenzo S, Valarelli J V, Giulietti M, Rodríguez-Clemente R. Influence of Process Conditions on Hydroxyapatite Crystallinity Obtained by Direct Crystallization 1999.

5. PIELIKUMS / APPENDIX 5

5. PUBLIKĀCIJA / PUBLICATION

Indurkar, A., Kudale, P., Rjabovs, K., Heinmaa, I,. Demir, O., Kirejevs, M., Rubenis, K., Chaturbhuj, G., Turka, M,. & Locs, J. (2023). Small Organic Molecules Containing Amorphous Calcium Phosphate: Synthesis, Characterization and Transformation.

Doi: 10.3389/fbioe.2023.1329752

frontiers | Frontiers in Bioengineering and Biotechnology

TYPE Original Research
PUBLISHED 12 January 2024
DOI 10.3389/fbioe.2023.1329752

OPEN ACCESS

EDITED BY
Jian Yu,
University of British Columbia, Canada

REVIEWED BY
Xiaopei Wu,
Wuhan University of Technology, China
Milad Fathi,
Middle East Technical University, Türkiye

*CORRESPONDENCE
Janis Locs,
Janis.Locs@rtu.lv

RECEIVED 29 October 2023
ACCEPTED 13 December 2023
PUBLISHED 12 January 2024

CITATION
Indurkar A, Kudale P, Rjabovs V, Heinmaa I, Demir Ö, Kirejevs M, Rubenis K, Chaturbhuj G, Turks M and Locs J (2024), Small organic molecules containing amorphous calcium phosphate: synthesis, characterization and transformation.
Front. Bioeng. Biotechnol. 11:1329752.
doi: 10.3389/fbioe.2023.1329752

Small organic molecules containing amorphous calcium phosphate: synthesis, characterization and transformation

Abhishek Indurkar[1,2], Pawan Kudale[3], Vitālijs Rjabovs[4], Ivo Heinmaa[5], Öznur Demir[1,2], Matvejs Kirejevs[1], Kristaps Rubenis[1,2], Ganesh Chaturbhuj[3], Māris Turks[4] and Janis Locs[1,2]*

[1]Rudolfs Cimdins Riga Biomaterials Innovations and Development Centre of RTU, Institute of General Chemical Engineering, Faculty of Materials Science and Applied Chemistry, Riga Technical University, Riga, Latvia, [2]Baltic Biomaterials Centre of Excellence, Headquarters at Riga Technical University, Riga, Latvia, [3]Department of Pharmaceutical Sciences and Technology, Institute of Chemical Technology, Mumbai, India, [4]Institute of Technology of Organic Chemistry, Faculty of Materials Science and Applied Chemistry, Riga Technical University, Riga, Latvia, [5]National Institute of Chemical Physics and Biophysics, Tallinn, Estonia

As the primary solid phase, amorphous calcium phosphate (ACP) is a pivotal precursor in cellular biomineralization. The intrinsic interplay between ACP and Howard factor underscores the significance of understanding their association for advancing biomimetic ACP development. While organic compounds play established roles in biomineralization, this study presents the synthesis of ACP with naturally occurring organic compounds (ascorbate, glutamate, and itaconate) ubiquitously found in mitochondria and vital for bone remodeling and healing. The developed ACP with organic compounds was meticulously characterized using XRD, FTIR, and solid-state ^{13}C and ^{31}P NMR. The morphological analysis revealed the characteristic spherical morphology with particle size close to 20 nm of all synthesized ACP variants. Notably, the type of organic compound strongly influences true density, specific surface area, particle size, and transformation. The *in vitro* analysis was performed with MC3T3-E1 cells, indicating the highest cell viability with ACP_ASC (ascorbate), followed by ACP_ITA (itaconate). The lowest cell viability was observed with 10 %w/v of ACP_GLU (glutamate); however, 1 %w/v of ACP_GLU was cytocompatible. Further, the effect of small organic molecules on the transformation of ACP to low crystalline apatite (Ap) was examined in Milli-Q® water, PBS, and α-MEM.

KEYWORDS

amorphous calcium phosphate, organic compounds, ascorbate, itaconate, glutamate, biomaterials, bone tissue engineering, biomimetics

1 Introduction

Amorphous calcium phosphate (ACP) has attracted much attention since it is the first calcium phosphate (CaP) phase synthesized and stabilized by cells and acts as a precursor of hydroxyapatite (HAp) (Combes and Rey, 2010). ACP provides a reservoir of calcium and phosphate ions that can be utilized for bone growth and regeneration. It is formed in the early stages of mineralization, which gradually crystallizes to HAp (Barrère et al., 2006). Naturally, ACP is stabilized by an organic compound known as the "Howard factor," whose exact chemical properties are unknown (Howard and Thomas, 1968; Lehninger, 1970). The association of Howard factor with ACP occurs in mitochondria, indicating that ACP forms a complex natural composite of inorganic CaP associated with an organic compound. In literature, synthetic ACP was prepared via numerous routes; however, the biogenic organic additives were not considered (Combes and Rey, 2010). The prerequisite for developing biomimetic ACP is the association of organic compounds present in mitochondria.

Considering this, numerous attempts have been undertaken in the development of ACP composite materials using macromolecules such as osteopontin, osteocalcin, dentin matrix protein, bone sialoprotein, dentin phosphoprotein, matrix extracellular protein, connexin 43, casein phospho-peptide, α_2HS-glycoproteins, fibrin, and albumin (Reynolds, 1998; Makowski and Ramsby, 2001; Gajjeraman et al., 2007; Yang et al., 2010; Yarbrough et al., 2010; Syed-Picard et al., 2013; Padovano et al., 2015; Zhao et al., 2018; Iline-Vul et al., 2020; Erceg and Dutour Sikirić, 2022; Nakamura et al., 2022; Indurkar et al., 2023a). However, *Becher et al.* have identified that many biological ubiquitous small organic molecules can inhibit the conversion of ACP to HAp at their respective tissue concentration (Becker, 1977). Considering these findings, ACP composites were developed using small organic molecules of polycarboxylate (such as citrate, succinate, acetate, and several amino acids), pyrophosphate, phosphocitric acid, polyphosphates as well as di-and-triphosphate nucleotide (Ikawa et al., 2009; Chinopoulos and Adam-Vizi, 2010; Grover et al., 2013; Stipniece et al., 2016; Feng et al., 2020; Indurkar et al., 2023b).

Mitochondria, which is the epicenter of numerous biochemical cycles, result in the formation of many small organic molecules (Scheffler, 2002; Osellame et al., 2012). Considering that ACP was associated with organic compounds in mitochondria, we have screened molecules based on their functions in bone remodeling and regeneration, such as ascorbate, glutamate, and itaconate, as shown in Figure 1.

Ascorbate (ascorbic acid or vitamin C) is crucial in collagen synthesis and is a vital organic compound in connective tissues and bone (Murad et al., 1981). Collagen provides structure and flexibility to the bone, enabling it to withstand mechanical stress. Without sufficient ascorbate, collagen synthesis is impaired, weakening the bone structure and increasing susceptibility to bone fractures (Gunson et al., 2013). Furthermore, osteogenic cell differentiation depends on ascorbate (Aghajanian et al., 2015; Thaler et al., 2022). Despite human's incapability of ascorbate synthesis, a specific mitochondrial uptake mechanism obtains vitamins from the diet. The vitamin carrier dehydroascorbic acid enters the mitochondria, where it is reduced and accumulated as ascorbic acid (Chen et al., 2022). Human studies have shown a positive relationship between ascorbic acid and biomineralization, emphasizing its importance in maintaining bone health (Chin and Ima-Nirwana, 2018).

Glutamate is an amino acid that plays a significant role in bone remodeling and healing processes. The glutamate receptors are expressed on the osteoblasts, osteoclasts, and bone marrow cells.

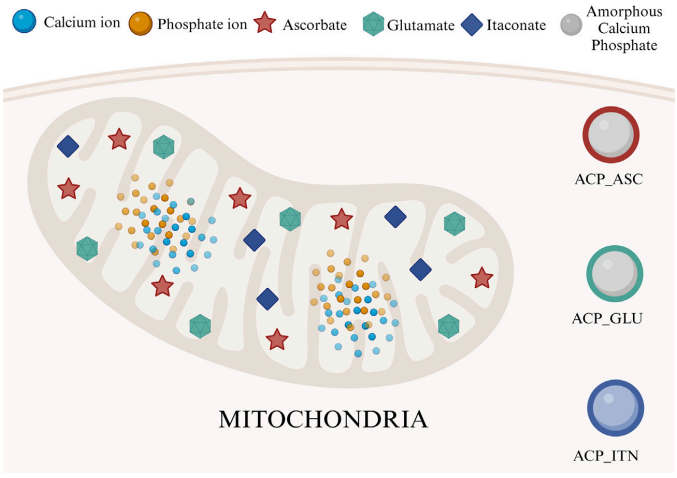

FIGURE 1
Mitochondria is an epicenter of various small organic compounds and ACP synthesis. In this study, we have utilized ascorbate, glutamate, and itaconate to develop composite ACP nanoparticles.

Activation of glutamate receptors controls the phenotype of osteoblasts and osteoclasts *in vitro* and bone mass *in vivo* (Brakspear and Mason, 2012). Moreover, glutamate has attained the nitrogen balance in a fractured bone, thus accelerating the bone healing process (Polat et al., 2007).

Itaconate is a metabolite that has gained much attention in recent years due to its role in immune regulation and inhibiting the production of proinflammatory molecules (Wang et al., 2022). Inflammation occurs in various bone disorders, such as rheumatoid arthritis and osteoporosis (Shi et al., 2022). Itaconate controls the immune response, thus indirectly controlling bone health. It also affects the function of macrophages, impacting the bone remodeling process (Peace and O'Neill, 2022). Itaconate interferes with the Krebs cycle, and changes in metabolism influences cell function and overall bone health (Yang et al., 2020).

Mitochondrial molecules such as acetate, citrate, ascorbate, glutamate, and itaconate play a major role in bone regeneration and are linked closely to mitochondrial function. As mitochondria are abundant in bone cells, the dysfunction of these organelles can lead to bone-related disorders (Kalani et al., 2014). The novel direction of incorporation of mitochondrial organic molecules in ACP offers a unique strategy to address bone-related disorders, potentially leading to innovative therapeutic interventions. Previously, we have developed ACP and its composite with citrate (ACP_CIT) and acetate (ACP_ACE) (Indurkar et al., 2023b). In this study, the ACP was synthesized with ascorbate (ACP_ASC), glutamate (ACP_GLU), and itaconate (ACP_ITN), were thoroughly characterized, and their cytocompatibility was evaluated. Additionally, transformation rate of ACP containing small organic molecules in different media were assessed.

The mechanism behind the transformation of ACP to low crystalline apatite (Ap) is a subject of ongoing debate. Several proposed mechanisms include dissolution reprecipitation, cluster reorganization, and solution-mediated solid-solid transformation. It is plausible that multiple processes may coincide during transformation (Jin et al., 2021). Previous studies have explored the transformation of ACP in aqueous solutions and have revealed the influence of factors such as pH, temperature, presence of foreign ions, and additives (polyelectrolyte, phospholipids, polyglycols, proteins, etc.), all of which can affect the transformation rate of ACP (Chatzipanagis et al., 2016). In this context, the role of small organic molecules containing ACP has received relatively less attention, with only a few reports available in the literature (Tsuji et al., 2008; Ikawa et al., 2009; Chatzipanagis et al., 2016; Sun et al., 2020).

In this study, we have also explored the transformation of ACP containing small organic molecules (acetate, glutamate, itaconate, ascorbate, and citrate) in three different mediums: Milli-Q® water, phosphate buffer saline (PBS), and alpha-modified minimum essential eagle medium with 10% fetal bovine serum (FBS) and 1% penicillin and streptomycin (α-MEM). The transformation of ACP was studied using X-ray diffraction (XRD) and Fourier-transformed infrared spectroscopy (FTIR) analysis performed at various time points. The results uncover how incorporation of small organic molecules into the ACP affects its crystallization rate in different media.

2 Material and methods

Calcium chloride (CAS 10043-52-4), trisodium phosphate (CAS 7601-54-9), sodium hydroxide (CAS 1301-73-2), and itaconic anhydride (CAS 2170-03-8) were procured from Sigma Aldrich, Germany. Calcium glutamate (CAS 19238-49-4) was obtained from BenchChem, United States, and ascorbic acid (CAS 50-81-7) was procured from Enola, Latvia.

2.1 Synthesis

To synthesize ACP_GLU, 150 mM calcium glutamate solution was prepared in Milli-Q® water. For the synthesis of ACP_ITN and ACP_ASC, a similar procedure was followed, starting with the preparation of 150 mM calcium chloride was prepared in Milli-Q® water, followed by the addition of 150 mM itaconic acid (ACP_ITN) and ascorbic acid (ACP_ASC) respectively. Afterwards, the pH of the calcium precursor solution was carefully adjusted to 11.5 using 3 M NaOH solution.

Following the pH adjustment, an equal amount (150 mL) of 100 mM of trisodium phosphate solution was added rapidly to the respective calcium salt solution (total volume 300 mL). Throughout the process, continuous stirring was maintained. Immediately after precipitation, the suspension underwent centrifugation at 3,000 rpm for 5 min, and the resulting precipitate was washed thrice with Milli-Q® water. Later, the centrifuge tube containing the precipitate was immersed in liquid nitrogen for 15 min, followed by freeze-drying for 72 h. The obtained power was stored in airtight containers until further characterization. Similarly, pure ACP, ACP_ACE and ACP_CIT were synthesized and characterized previously (Indurkar et al., 2023b).

2.2 Characterization

The phase composition of synthesized ACP variants were determined using X-ray diffraction, performed with a PANalytical Aeris diffractometer (Netherlands). The diffraction data were collected at 40 kV and 15 mA in a step mode with a step size of 0.04°, in the 2θ range from 10° to 60°.

The Fourier-transformed infrared spectroscopy (FTIR) analysis was performed using a Nicolet iS50 FT-IR spectrometer (Thermo Scientific, Waltham, MA, United States). Experiments were performed in transmission mode from the wavenumber ranging from 4,000 to 400 cm^{-1} with a resolution of 4 cm^{-1} (64 scans).

Solid-state CP MAS ^{13}C NMR spectra were recorded on Bruker AVANCE-II spectrometer at 14.1 T magnetic field using a home-built double resonance magic-angle-spinning probe for 4 x 25 mm Si_3N_4 rotors. The spinning speed of the sample was 12.5 kHz, the duration of the ramped polarization transfer pulse was 1 ms, and the relaxation delay between accumulations was 5 s. From 15,000 to 32,000, scans were accumulated for the spectra. The intensities were normalized to the number of scans and the sample's weight. Solid-state ^{31}P NMR spectra were recorded on JOEL, ECZR 600 NMR spectrometer. The experiment was performed with a 90° single pulse at a MAS frequency of 10 Hz with 2048 scans and a relaxation delay of 3 s.

The morphology and particle size of synthesized ACPs were evaluated by FEG-TEM (Tecnai G2 F30, United States) operated at 300 kV. The sample preparation was as follows: a small amount of powder was dispersed in isopropyl alcohol and sonicated in an ultrasonic bath. Further, the samples were placed on a carbon-coated grid and dried before analysis.

The true density of ACPs was analyzed by a helium pycnometer Micro UltraPyc 1200e (Quantachrome instruments, Boynton, FL, United States). Initially, the calibration was performed using a stainless-steel calibration sphere. It was followed by adding a known amount of ACP powder into the sample holder and purging it with helium gas in pulse mode (30 pulses). Subsequently, the sample volume was analyzed by pressurizing it at 10 psi with helium gas. The true density was calculated using sample weight and the analyzed sample volume. The analysis of each ACP was performed in triplicate.

The specific surface area (SSA) of the synthesized powder was analyzed using a nitrogen adsorption system Quadrasorb S1 (Quantachrome instruments, Boynton, FL, United States) by Brunauer-Emmett-Taylor (BET) method. Before analysis, the samples were degassed at room temperature for 24 h.

2.3 *In vitro* cytocompatibility

The preosteoblast (MC3T3-E1) cell line, obtained from ATCC, United States, was used in this study. Cells were grown in α-MEM (alpha-modified minimum essential medium eagle) with 10% fetal bovine serum (FBS) and 1% penicillin and streptomycin (pen-strep). The cells were cultured in 75 cm^2 flasks and maintained under 5% CO_2 at 37°C until the cell confluency reached 70%. The medium was replaced every 2 days.

For cellular analysis, suspensions were prepared by adding 10 %w/v ACP precipitate in α-MEM medium and incubated at 37°C in a humidified atmosphere of 95% air and 5% CO_2 for 24 h. The extracts were collected by centrifugation at 350 rpm for 5 min and filtered to eliminate solid particles. The extracts were diluted with α-MEM medium to get the desired concentration of 1 %w/v. Therefore, the total sample concentration comprises 10 %w/v and 1 %w/v of each ACP. The extracts were then added to MC3T3-E1 cells containing well plates and incubated for 48 h. The α-MEM medium was added as a positive control, whereas the α-MEM medium with 6 %vol DMSO (dimethyl sulfoxide) was utilized as a negative control. Each sample was prepared in triplicate, and the same procedure was performed for all ACP variants.

Cell viability was measured by Cell counting kit-8 (CCK-8) (Sigma Aldrich, United States). Briefly, cells at a density of 1×10^4 per well were seeded in a 96-well plate and pre-incubated at 37°C under 5% CO_2 for 24 h. After 24 h, the cell culture medium was replaced with various concentrations of ACP extracted medium [0 (as positive control), 10 %w/v, and 1 %w/v] and was further incubated for 48 h. CCK-8 was performed following the manufacturer's protocol to determine cell viability. Cell viability (in percent) was determined as the absorbance ratio between cells grown in the presence and absence of extracted solutions. The average values and standard deviations were calculated from six replicate samples. 6 %v/v DMSO was used as a negative control. The experiments were performed in triplicate, and cytocompatibility was evaluated by calculating cell viability using Eq. 1:

$$Cell\ viability\ (\%) = \frac{(Absorbance\ of\ sample - Absorbance\ of\ blank)}{(Absorbance\ of\ positive\ control - Absorbance\ of\ blank)} \times 100 \quad (1)$$

2.4 *In vitro* biomineralization

The *invitro* biomineralization experiments were performed with six types of ACP (pure ACP, ACP_ACE, ACP_GLU, ACP_ITN, ACP_ASC, and ACP_CIT). The ACP variants, such as pure ACP, ACP with citrate (ACP_CIT), and acetate (ACP_ACE), were synthesized, and characterization was reported in our previous study (Indurkar et al., 2023b). On the other hand, ACP variants such as ACP_GLU, ACP_ITN, and ACP_ASC were synthesized and characterized in the current study.

Experiments were performed in batch mode. To analyze the effect of small organic molecules containing ACP on transformation to Ap, 100 mg of ACP was added into 5 mL of media (Milli-Q® water, PBS, and α-MEM) preheated at 37°C. Further, the samples were incubated at 37°C and removed after specific time points (15, 30, 60, 120, 240, 1,440, 2,880, and 4,320 min) followed by centrifugation, freezing in liquid nitrogen for 15 min and freeze-drying for 72 h. The obtained powders were used for characterization as shown in Figure 2.

The obtained powders after freeze drying were analyzed using X-ray diffraction, performed with a Malvern Panalytical Aeris diffractometer (Netherlands). The diffraction data were collected at 40 kV and 15 mA in a step mode with a step size of 0.04°, in the 2θ range from 10° to 60°. This was followed by Fourier-transformed infrared spectroscopy (FTIR) analysis performed using a Nicolet iS50 FT-IR spectrometer (Thermo Scientific, Waltham, MA, United States). Experiments were performed in transmission mode in the range from 4,000 to 400 cm^{-1} with a resolution of 4 cm^{-1} (64 scans).

2.5 Statistical analysis

GraphPad Prism (GraphPad Software, San Diego, United States) was utilized to perform statistical analysis by two-way ANOVA and Tukey's multiple comparisons. Probability (P) values $*p < 0.05$ $**p < 0.01$ were considered the statistically significant differences. The results were expressed in mean ± standard deviation (S.D.).

3 Results and discussion

3.1 Synthesis and characterization

The synthesis of ACP_ASC and ACP_ITN showed color changes during the reaction. For instance, a colorless solution was formed when ascorbic acid was added to calcium chloride. However, as the pH of the solution increased to 11.5 using 3 M NaOH, a light-yellow solution was obtained. Therefore, the resultant ACP_ASC powder was light-yellow. Similarly, the color change was observed during the synthesis of ACP_ITN; when the itaconic anhydride was added to the calcium chloride, a colorless solution was formed, which changes to light brown when pH was increased to

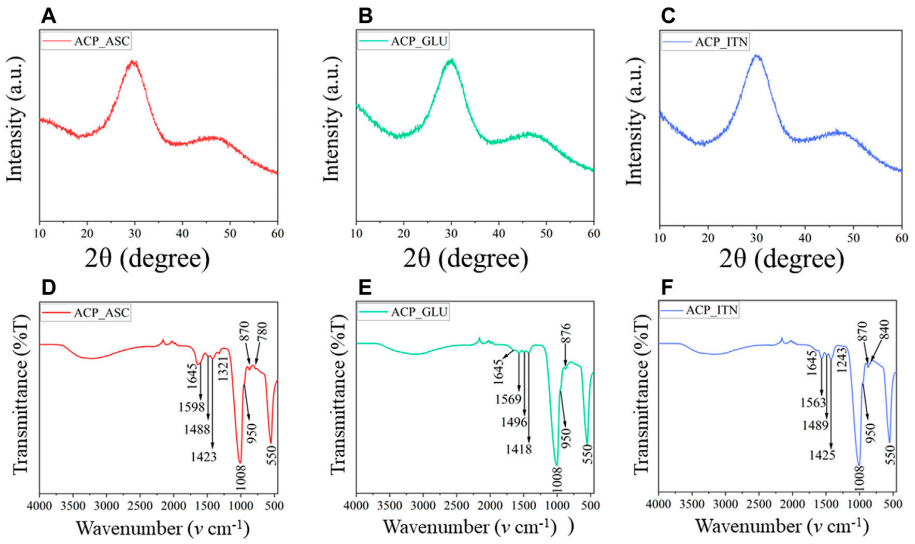

FIGURE 2
XRD **(A–C)** analysis confirms the amorphous nature of synthesized ACP with respective small compounds. The functional groups of ACP and the small compounds were revealed by FTIR **(D–F)** analysis.

11.5 using 3 M NaOH. Therefore, the resultant ACP_ITN powder had a brownish tinge. No color change was observed during the synthesis of ACP_GLU; therefore, a white powder was obtained.

3.1.1 XRD and FTIR analysis

The lack of crystalline order was observed in Figures 2A–C, confirming the formation of X-ray amorphous ACP. The FTIR spectra are shown in Figures 2D–F. The broad band of water observed between 3,000 cm^{-1} and 3,700 cm^{-1} corresponds to asymmetric and symmetric vibrations, and the band detected at 1,645 cm^{-1} represents the bending mode of water. These bands were observed in all the synthesized ACPs. In FTIR, the phosphate group shows four vibrational domains: *v1* (~950 cm^{-1}), *v2* (400–470 cm^{-1}), *v3* (1,000–1,150 cm^{-1}), and *v4* (500–620 cm^{-1}). The phosphate vibrational peaks at *v1, v3,* and *v4* were observed in all the synthesized ACP variants (Indurkar et al., 2023a).

The ascorbate bands in ACP_ASC were observed at ~3,000 cm^{-1} attributed to C-H vibrations. The bands between 1,500 cm^{-1} and 1,660 cm^{-1} indicate the presence of C=O and C-O vibrations (Williams and Rogers, 1937). The band at 1,488 cm^{-1} represents the CH bending, 1,423 cm^{-1} (CH_2 scissoring), 1,321 cm^{-1} (CH bending), 871 cm^{-1} (C-C ring stretching), and 780 cm^{-1} (OH out of plane deformation) (Yohannan Panicker et al., 2006; Bichara et al., 2010; Dabbagh et al., 2014).

The glutamate bands in ACP_GLU were observed between 3,000 cm^{-1} and 3,700 cm^{-1}, which also corresponds to -NH_2 vibrations (Cárdenas-Triviño et al., 2020). The bands at 1,569 cm^{-1} and 1,418 cm^{-1} correspond to the asymmetric and symmetric vibration of C=O (Barth, 2000). The bands observed in 1,496 cm^{-1} were attributed to symmetric and asymmetric stretching of C-O of carboxylate ion (De Castro and Cassella, 2016). The band observed at 876 cm^{-1} represents C-C vibration of glutamate (Sumayya et al., 2008).

The itaconate bands in ACP_ITN were observed at 1,645 cm^{-1} and attributed to C=C vibrations. The band at 1,563 and 1,425 cm^{-1} corresponds to the asymmetric and symmetric vibration of C=O (Damilola Olawale et al., 2020). Moreover, the band observed at 1,489 cm^{-1} and 1,243 cm^{-1} corresponds to O-C-O and C-O stretching (Loginova et al., 2016; Wibowo et al., 2018). The band observed at 870 cm^{-1} and 840 cm^{-1} indicates CH stretching vibrations (Uhanov et al., 2020).

3.1.2 NMR analysis

The solid-state ^{13}C and ^{31}P NMR analysis of synthesized ACPs is shown in Figures 3A, B. The ascorbate signals in ^{13}C NMR analysis of ACP_ASC show the lactone ring and β-carbon carbonyl groups in the range of 170–180 ppm, corresponding to C=O of the carbonyl group. The carbon atoms at γ-,δ-, and ε-positions of ascorbate appeared at 72 and 64 ppm (Tajmir-Riahi, 1991). The interaction of ACP resulted in the shifted peaks of ascorbate.

Glutamate signals in ^{13}C NMR analysis of ACP_GLU were observed at 183 and 169 ppm correspond to the carboxylate signals. The signal observed at 58 and 36 ppm was assigned to the carbon atom of the methine group bonded to the amino and carboxyl group (C2) and those branches in the alkyl chain (C3 and C4), respectively. The peak of the C4 carbon was shifted by the disordered conformation of the methylene group due to the association of ACP (Ikawa et al., 2009; Sannelli et al., 2023).

Itaconate signals in ^{13}C NMR analysis of ACP_ITN were observed at 183 and 163 ppm, corresponding to the carboxyl

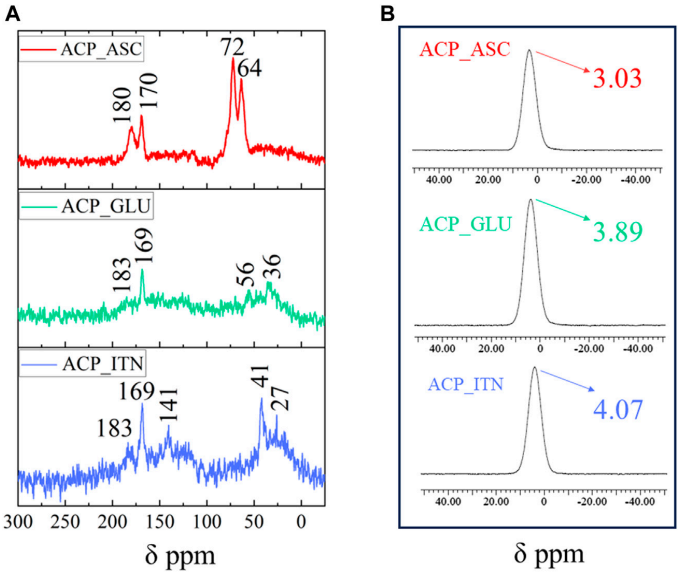

FIGURE 3
Solid-state NMR analysis of synthesized ACP with respective organic compounds **(A)** ^{13}C NMR and **(B)** ^{31}P NMR.

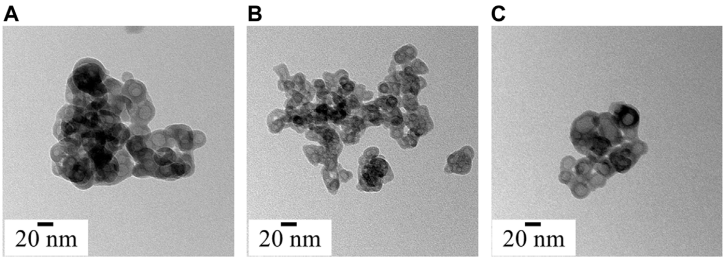

FIGURE 4
Morphology and particle size analysis of synthesized ACP variants **(A)** ACP_ASC, **(B)** ACP_GLU and **(C)** ACP_ITN.

group. The double bond signals were observed at 141 ppm. The carbon atom at the gamma position relative to the carboxyl group in the side chain appeared at 42 ppm, and the carbon atom of the methylene group was observed at 27 ppm (C3) (Strelko et al., 2011; Jahandideh et al., 2018; Vettori et al., 2022). The association with ACP resulted in peaks shifting in all the organic compounds.

The ^{31}P NMR spectra of ACP show characteristic broad Gaussian peaks between −15 and 15 ppm centered from 2.2 to 6.5 ppm (Indurkar et al., 2023b). As shown in Figure 4B, the broad peak was observed in all the synthesized ACPs centered at 3.03 ppm (ASP_ASC), 3.89 ppm (ACP_GLU), and 4.07 ppm (ACP_ITN) respectively. The NMR analysis has confirmed the formation of ACP in the presence of the respective organic compounds (ascorbate, glutamate, and itaconate).

3.1.3 Density and Brauner-Emmette-Teller (B.E.T.) analysis

The density and the specific surface area (SSA) of the synthesized ACP are shown in Table 1. The difference in density and SSA was observed, indicating the effect of the type of carboxyl ions on the synthesized ACP. One or several of the possible mechanisms can facilitate the interaction of ACP with organic compounds: 1) surface adsorption of organic compounds by chelating action of calcium ions of ACP and the carboxyl groups

TABLE 1 The density and specific surface area of the synthesized ACP.

Sample	Density (g/cm^3)	SSA (m^2/g)
ACP_ASC	2.82	115.2
ACP_GLU	2.64	92.4
ACP_ITN	2.43	130.3

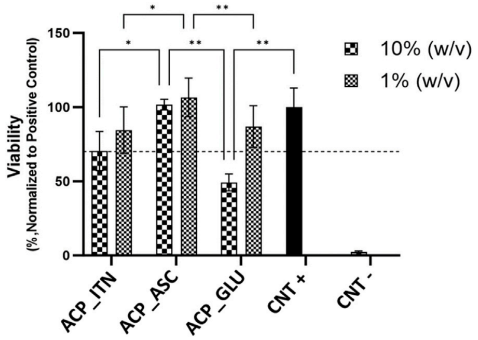

FIGURE 5
Relative cell viabilities of MC3T3-E1 cells cultured with extracts of ACP variants (10% and 1% w/v) prepared in α-MEM medium. All the samples were analyzed in triplicate, and data is presented in average and standard deviation. The CNT + and CNT−were positive and negative controls.

of organic compounds (Gorbunoff, 1984; Zong et al., 2023); 2) Organic compounds bearing two carboxylate ions ($^-$O(O)C-R-C(O)O$^-$) can substitute the hydrogen phosphate ion (HPO_4^{2-}) during the precipitation of ACP (Yokoi et al., 2022); 3) interaction between phosphates and carboxylates groups (P-O···H-O-C or P-O-H···O-C) (Corbridge, 1971). 4) Interaction of ascorbate anion can interact with calcium and/or phosphate group (Xu et al., 2019). However, more advanced analysis is required to evaluate the exact interaction of ACP with the organic compound.

3.1.4 Morphological analysis

Under electron microscopy, the morphological appearance of ACP shows spherical particles of a few tenths of the nanometre scale (Zhao et al., 2012). All the synthesized ACPs show the characteristic spherical morphology, as shown in Figure 4. Numerous research groups have consistently identified the biomimetic size range of ACP, typically falling between 10 and 50 nm (Niu et al., 2014; Hoeher et al., 2023). Interestingly, the ascorbate, glutamate, and itaconate ACP variants show spherical hollow particles that align with the biomimetic size range. Moreover, ACP is highly sensitive to the electron beam and crystalizes on high electron beam exposure (Lotsari et al., 2018). The crystallization of synthesized ACP under a high electron beam is presented in Supplementary Figure S1.

3.1.5 Cell culture analysis

The cytocompatibility was evaluated by analyzing the cell viability of MC3T3-E1 cells in the presence of synthesized ACP extracts (10% and 1% w/v) prepared in α-MEM medium, as shown in Figure 5. The absorbance recorded for the cells cultured in the plain cell culture medium was normalized to 100% and termed positive control (CNT+). The cells cultured in 10% w/v ACP_GLU showed the lowest cell viability compared to other groups. The higher glutamate concentration can lead to excitotoxicity and or oxidative glutamate toxicity (Schubert and Piasecki, 2001; Kritis et al., 2015). However, reducing the concentration to 1% w/v, ACP_GLU enhanced the cell viability. The concentration of 10% w/v ACP_ITN and 10% w/v ACP_ASC was better than 10% w/v ACP_GLU. A similar trend was found in 1% w/v ACP_ITN and 1% w/v ACP_ASC. The cell viability of 10% and 1% w/v ACP_ASC was better than CNT+. Ascorbate is critical for the differentiation of the preosteoblast, and this may be the reason for the higher cell viability (Hadzir et al., 2014; Hwang and Horton, 2019). The preliminary analysis has confirmed the cytocompatibility of ACP_ASC (10% and 1% w/v), ACP_ITN (10% and 1% w/v), and ACP_GLU (1% w/v).

3.1.6 *In vitro* biomineralization

The first *in vitro* biomineralization was investigated by Boskey and Posner by examining the impact of pH on the conversion of ACP to Ap. Their finding has provided critical insights revealing that transformation rate increases with higher pH levels. Furthermore, it was also discovered that the conversion pathways remain unaffected by the following factors: a) the nature of the buffer system used, b) the presence of a different type of univalent ions, and c) whether the material was in contact with mother liquor or filtered, dried, or added to the fresh buffer. Additionally, the transformation rate exhibited dependency on several factors, including smaller particle size, faster stirring rate, and higher ACP concentration (Boskey and Posner, 1973). Temperature also emerged as a significant variable affecting the conversion of ACP. For instance, at pH of 7.5, ACP converts five times more rapidly at 37°C than at 25°C. The synthesis condition of ACP was also found to influence the transformation rate (Eanes, 1998). Given the focus of our study on the application of ACP and its variants in tissue engineering, we consistently maintained 37°C in all the transformation experiments.

XRD analysis was employed to track alteration in long-range structural order as samples underwent successive progressive crystallization in different solvents, as shown in Supplementary Figure S2. In the analysis of CaP material, it is conventionally assumed that any part of the diffractogram not corresponding to the crystalline phase is amorphous. Nonetheless, there is ambiguity between non-coherent diffraction domains and genuinely separated amorphous phases. In the case of CaP (except hydroxyapatite), various ionic substitutions, defects, and vacancies can disrupt the regularity of the atomic array. This can significantly increase background diffraction patterns without necessarily implying the presence of any amorphous phase or domain (Combes and Rey, 2010). Therefore, FTIR analysis was also employed to provide additional insights. The FTIR spectra of all the ACP variants are shown in Supplementary Figure S3. The characteristic bands of ACP and the respective small organic molecules are shown in Supplementary Table S1).

FTIR spectral examination of ACP variants exhibits a distinct short order evident through absorbance band related to phosphate absorption bands. Notably, the ACP spectrum displays a broader band with no evident splitting in the ν_4 PO_4^{3-} vibration region. The highlights distinction between XRD, which primarily detects specific

10.3389/fbioe.2023.1329752

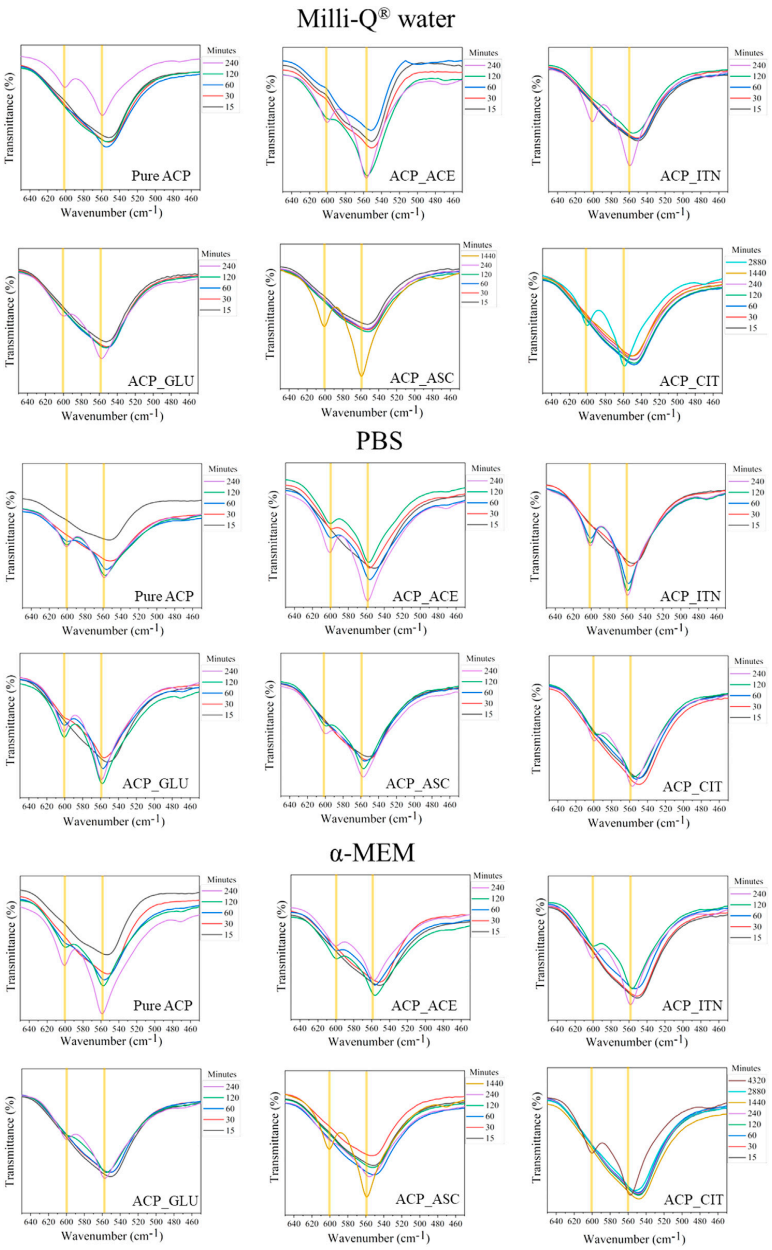

FIGURE 6
The stability of ACP in the different mediums was evaluated based on $v_4\ PO_4^{3-}$ vibration region. The samples that did not show evident splitting in the $v_4\ PO_4^{3-}$ vibration region was termed amorphous; on the contrary, the samples that showed splitting of $v_4\ PO_4^{3-}$ vibration region were termed crystalline.

TABLE 2 Time required for transformation of ACP to Ap evaluated from peak formation in XRD and splitting of the v_4 PO_4^{3-} vibration observed in FTIR spectra.

Samples	Milli-Q® water (min)	PBS (min)	α-MEM (min)
Pure ACP	120	30	60
ACP_ACE	60	15	30
ACP_ITN	120	30	60
ACP_GLU	120	30	60
ACP_ASC	240	60	120
ACP_CIT	1,440	120	2,880

peaks associated with crystalline phases, and FTIR, which detects absorbances originating from both amorphous and crystalline components (Querido et al., 2020). The splitting of the v_4 PO_4^{3-} vibration region confirms the crystallization of ACP, as shown in Figure 6. XRD analysis was utilized to complement the data obtained from FTIR analysis, and the stability time of the ACP variant in the respective medium is presented in Table 2.

The inorganic contentment in the respective solvents is presented in Supplementary Table S2. The inorganic ions were absent in Milli-Q® water; therefore, the transformation rates of ACP variants (except ACP_CIT) were slower compared to PBS and α-MEM medium. In PBS, all the synthesized ACP variants underwent a rapid transformation, aligning perfectly with findings from the literature (Zhao et al., 2012).

Previous studies have revealed that in the presence of PBS solution, the organic molecules are released from the surface of ACP, likely due to ionic exchange with the phosphate groups in the medium. This leads to an elevated concentration of phosphate in ACP, thus reducing stability and resulting in rapid transformation to low crystalline apatite (Chatzipanagis et al., 2016). This outcome was consistently observed for all the synthesized ACP variants. The phosphate content in α-MEM medium was less compared to PBS; therefore, the transformation rates were slower (except ACP_CIT). In the case of ACP_CIT, the highest stability of 2,880 min was observed in α-MEM medium. Previous studies have shown the interaction of serum albumin with citrate-stabilized gold nanoparticles forming protein corona (Dominguez-Medina et al., 2012; Zhang et al., 2014; Szekeres and Kneipp, 2018). Similarly, the delayed transformation of ACP_CIT may be due to the interaction of negatively charged citrate with FBS present in α-MEM medium. However, in-depth analysis is required to confirm this phenomenon.

The organic molecules such as acetate, itaconate, glutamate, and citrate contain carboxyl groups, as shown in Figure 7. Both the carboxyl and ascorbate anion have the potential to interact with both calcium and phosphate ions present in ACP (Winand et al., 1961; Corbridge, 1971; Ancillotti et al., 1977; Chatzipanagis et al., 2016). Due to the combination of these factors, the interaction between these organic compounds and ACP is complex and demands a sophisticated analysis to fully comprehend the precise nature of these interactions.

To investigate the effect of small organic molecules on transformation rate, pure ACP was used for comparison as shown in Figure 8. The variations in the transformation rate can be attributed to the changes in the physiochemical properties of ACP, such as particle size, morphology, specific surface area (SSA), and density induced by different functional groups from the respective small organic molecules, as illustrated in Supplementary Table S3.

The fastest conversion rate was observed in ACP_ACE in all the respective mediums compared to other ACP variants. Acetate consists of one carboxyl group (COO^-) representing a negative charge of −1. Monocarboxylic ions can interact with calcium ions but are not capable of bridging two calcium ions. The incompatible charge of −1 promotes the formation of HAp (Yamada et al., 2021). A similar phenomenon is observed in the case of fluoride-doped ACP. Fluoride ions also have a negative charge of −1; therefore, the transformation of ACP to Ap was faster in the presence of fluoride-doped ACP than in pure ACP (Ten Cate and Featherstone, 1991; Iafisco et al., 2018).

Pure ACP, ACP_GLU, and ACP_ITN represent similar conversion rates in respective medium. Our previous study observed presence of carbonate (CO_3^{2-}) in pure ACP. The presence of carbonate ions in ACP is known to retard its conversion to Ap (Combes and Rey, 2010; Edén, 2021). Similarly, itaconate and

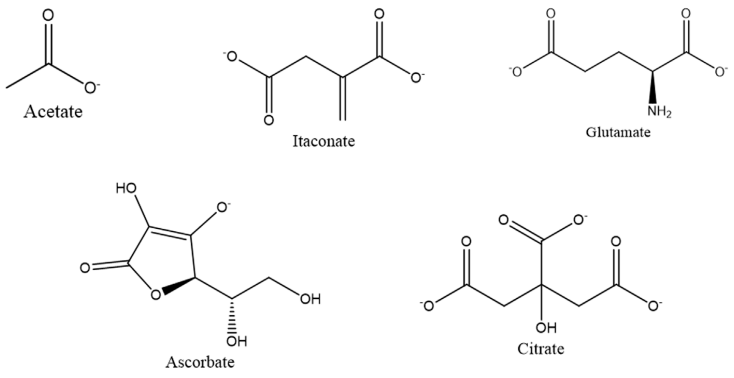

FIGURE 7
Small organic compounds are utilized for the synthesis of ACP variants.

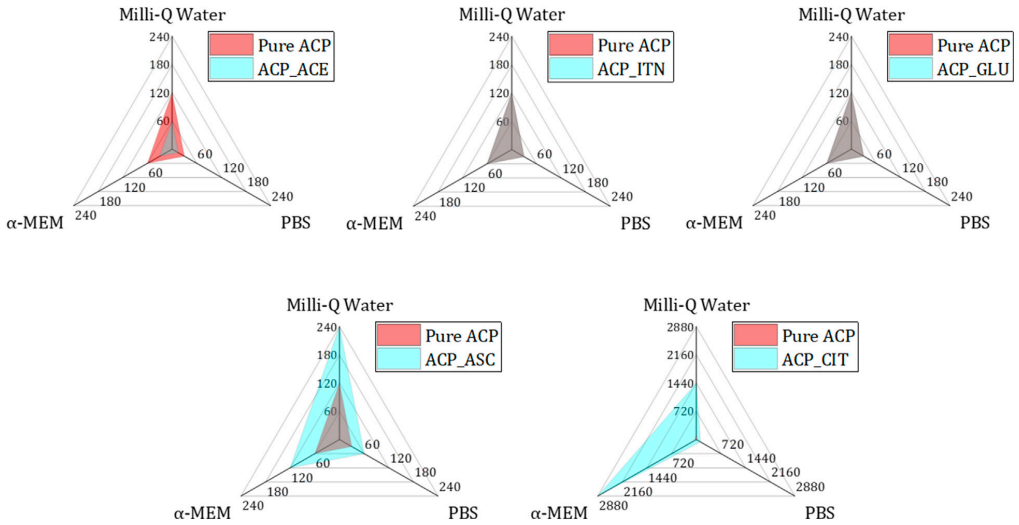

FIGURE 8
Analysing the transformation rates of small organic molecules containing ACP (blue) in comparison to pure ACP (red) across different mediums (Milli-Q® water, PBS, and α-MEM) reveals distinct patterns. Specifically, ACP_ACE exhibited accelerated transformation rates in all mediums compared to pure ACP (both represented in grey colour by combination of blue and red). Conversely, ACP_ITN and ACP_GLU demonstrated similar transformation rates to pure ACP. Notably, ACP_GLU and ACP_CIT displayed slower transformation rates compared to their pure ACP counterpart.

glutamate are dicarboxylic compounds with a negative charge of −2 and may behave similarly to carbonate-substituted ACP. Therefore, the transformation rate of pure ACP, ACP_ITN and ACP_GLU was the same.

In the case of ascorbate containing ACP, the conversion was slower than that of other ACP variants (except ACP_CIT). The presence of the ascorbate anion can interact with ACP, thus retarding its conversion to Ap. Previous studies have shown delayed struvite crystallization in the presence of ascorbate due to a decrease in pH (Manzoor et al., 2018). Additionally, ascorbate in the bloodstream has been shown to prevent struvite stone formation in urine (Flannigan et al., 2014). Similarly, delayed sugar crystallization was observed in the presence of ascorbic acid (Zhou and Roos, 2012). Likewise, a delayed transformation was observed in ACP_ASC despite its higher surface area (115.2 m^2/g). However, a more comprehensive analysis is required to confirm the exact behavior.

The highest stability was observed in ACP_CIT. Citrate is a tricarboxylic acid that can interact in four ways with ACP: a). The carboxyl group can interact with calcium ions of ACP. B) $HCit^{3-}$ can substitute PO_4^{3-} of ACP. c) The hydroxy group of citrates can interact with phosphate ions and/or d) The phosphate ions can interact with the carboxyl group of citrates (Indurkar et al., 2023b). Previous reports have also shown citrate's efficacy in stabilizing ACP (Chen et al., 2014; Sakhno et al., 2023).

The ACP variants displayed a generally spherical and hollow morphology, except for ACP citrate, which exhibited a dense spherical structure. Differences in the morphologies may also contribute to the transformation rate. However, more detailed analysis is required to confirm this phenomenon.

4 Discussion

The synthesis reactions of ACP are known for their rapid nature and are typically performed under alkaline conditions. However, owing to the triprotic nature of phosphate ions, fluctuations in pH, temperature, and precursor concentration play a crucial role in determining the efficiency of precipitation and particle size of the synthesized product (ACP) (Mekmene et al., 2009).

To address these inherent challenges, we have devised a straightforward and effective method to synthesize ACP, aiming to minimize pH variations. Based on this approach, we have previously achieved successful ACP synthesis with citrate and acetate (Indurkar et al., 2023b). Inspired by this successful strategy, we have extended our efforts to synthesize ACP with other organic compounds such as ascorbate, glutamate, and itaconate. The schematic representation of our synthesis method is outlined in Figure 9. These methods have broadened the scope of ACP synthesized by incorporating diverse organic compounds, thus showcasing its versatility and potential for further exploration in developing novel ACP composites.

Our prior study also synthesized two pristine ACPs devoid of organic compounds (Indurkar et al., 2023b). The ACP particles exhibited an SSA of 105 m^2/g and particle size of less than 20 nm. In that investigation, acetate and citrate have shown distinct effects on the properties of ACP. The surface area and particle size were affected when ACP was linked with acetate and citrate. Building on these findings, our current study investigated the effect of other organic compounds, ascorbate, glutamate, and

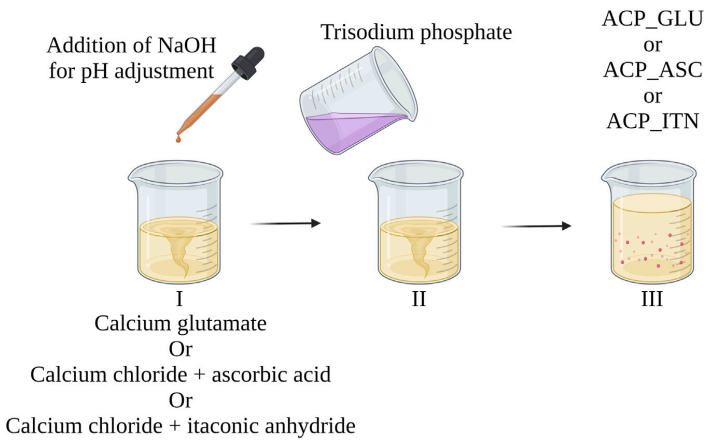

FIGURE 9
Illustrating the systematic approach to achieve controlled ACP (with organic compounds) synthesis with minimal pH variations. The approach was previously reported in developing pure ACP and ACP with citrate and acetate (Indurkar et al., 2023b).

itaconate, on the properties of ACP. Interestingly, introducing these compounds impacted the SSA and particle size. Moreover, an effect on cytocompatibility was also observed, wherein the 10% w/v ACP_GLU represented a toxic effect on MC3T3-E1 cells.

Glutamate is a versatile molecule with a potential role in influencing cellular processes and viability in bone tissue (Skerry and Taylor, 2005). It has been suggested that glutamate can impact cell proliferation and differentiation through group III metabotropic glutamate receptors expressed in mouse calvaria osteoblasts. Furthermore, previous investigations have revealed that specific concentrations within 50 μM to 1 mM enhance survival rates of human primary osteoblasts when exposed to tumor necrosis factor-α and interferon-γ. However, it is essential to note that a cytotoxic effect was observed when glutamate concentration exceeded 10 mM (Genever and Skerry, 2001).

The cytotoxicity resulting from elevated glutamate levels is attributed to the induction of oxidative stress. This occurs because of triggering the release of reactive oxygen species and nitric oxide. Consequently, excess glutamate concentration leads to oxidative damage to MC3T3-E1 cells, resulting in apoptosis (Fatokun et al., 2006). A similar behavior may be responsible for 10% w/v ACP_GLU samples resulting in cell death. However, further advanced analysis and experiments are required to confirm this phenomenon and gain a deeper understanding of the underlying mechanism.

Examination into *in vitro* biomineralization has revealed a significant influence of small organic molecules on the transformation rate of ACP. By aligning ACP with small organic molecules and solvents, transformation necessities can be tuned based on the applications. FTIR analysis has confirmed that the resulting Ap retained characteristics of the respective small organic molecules. This observation suggests the potential utilization of transformed Ap as an advanced bone substitute material.

5 Conclusion

The study introduces a promising avenue for biomimetic ACP developed by leveraging mitochondrial (ascorbate, glutamate, and itaconate) small organic molecules. Synthesized ACP variants were characterized using XRD, FTIR, and NMR, which confirmed the presence of respective organic compounds and the amorphous nature of ACP. Advanced analysis is required to understand the exact interaction of the organic compounds with ACP. *In vitro* analysis using MC3T3-E1 cells has provided primary evidence of cytocompatibility of compositions obtained. *In vitro* biomineralization studies have shown differences in the transformation rate of small organic molecules containing ACP. The variations in the transformation rate can be induced by different functional groups from the respective small organic molecules. The research contributes to the expanding field of biomaterial science by bridging the gap between the biomineralization process and synthetic material, thus opening the door to innovative tissue engineering strategies and bone therapeutic interventions.

Data availability statement

The raw data supporting the conclusion of this article will be made available by the authors, without undue reservation.

Author contributions

AI: Conceptualization, Data curation, Formal Analysis, Investigation, Methodology, Writing–original draft. PK: Data curation, Validation, Writing–review and editing. VR: Software, Validation, Writing–review and editing. IH: Resources, Writing–review and editing. ÖD: Data curation, Formal Analysis,

Writing–review and editing. MK: Data curation, Writing–review and editing. KR: Formal Analysis, Validation, Writing–review and editing. GC: Formal Analysis, Investigation, Resources, Software, Validation, Writing–review and editing. MT: Formal Analysis, Resources, Validation, Writing–review and editing. JL: Formal Analysis, Funding acquisition, Project administration, Resources, Supervision, Validation, Writing–review and editing.

Funding

The author(s) declare financial support was received for the research, authorship, and/or publication of this article. The authors acknowledge financial support from the European Union' Horizon 2020 research and innovation program under grant agreement No. 857287 (BBCE) and Baltic Research Programme Project No. EEA-RESEARCH-85"Waste-to-resource: eggshells as a source for next-generation biomaterials for bone regeneration (EGGSHELL)" under the EEA Grant of Iceland, Liechtenstein and Norway No. EEZ/BPP/VIAA/2021/1. The authors are grateful for generous funding from the Mahatma Jyotiba Phule Research Fellowship, Govt. of Maharashtra, India (MAHAJYOTI/2022/PhD Fellowship/1002(624)).

Conflict of interest

The authors declare that the research was conducted in the absence of any commercial or financial relationships that could be construed as a potential conflict of interest.

Publisher's note

All claims expressed in this article are solely those of the authors and do not necessarily represent those of their affiliated organizations, or those of the publisher, the editors and the reviewers. Any product that may be evaluated in this article, or claim that may be made by its manufacturer, is not guaranteed or endorsed by the publisher.

Supplementary material

The Supplementary Material for this article can be found online at: https://www.frontiersin.org/articles/10.3389/fbioe.2023.1329752/full#supplementary-material

References

Aghajanian, P., Hall, S., Wongworawat, M. D., and Mohan, S. (2015). The roles and mechanisms of actions of vitamin C in bone: new developments. *J. Bone Min. Res.* 30, 1945–1955. doi:10.1002/JBMR.2709

Ancillotti, F., Boschi, G., Perego, G., and Zazzetta, A. (1977). Calcium binding capacity of carboxylic acids with an ethereal function. Crystal and molecular structure of calcium ethylenedioxydiacetate. *J. Chem. Soc. Dalt. Trans.* 1977, 901–905. doi:10.1039/DT9770000901

Barrère, F., van Blitterswijk, C. A., and de Groot, K. (2006). Bone regeneration: molecular and cellular interactions with calcium phosphate ceramics. *Int. J. Nanomedicine* 1, 317–332.

Barth, A. (2000). The infrared absorption of amino acid side chains. *Prog. Biophys. Mol. Biol.* 74, 141–173. doi:10.1016/S0079-6107(00)00021-3

Becker, G. L. (1977). Calcification mechanisms: roles for cells and mineral. *J. Oral Pathol.* 6, 307–315. doi:10.1111/J.1600-0714.1977.TB01653.X

Bichara, L. C., Lanús, H. E., Nieto, C. G., and Brandán, S. A. (2010). Density functional theory calculations of the molecular force field of L -ascorbic acid, vitamin C. *J. Phys. Chem. A* 114, 4997–5004. doi:10.1021/jp912251g

Boskey, A. L., and Posner, A. S. (1973). Conversion of amorphous calcium phosphate to microcrystalline hydroxyapatite. A pH-dependent, solution-mediated, solid-solid conversion. *J. Phys. Chem.* 77, 2313–2317. doi:10.1021/j100638a011

Brakspear, K. S., and Mason, D. J. (2012). Glutamate signaling in bone. *Front. Endocrinol. (Lausanne).* 3, 97. doi:10.3389/FENDO.2012.00097

Cárdenas-Triviño, G., Soto-Seguel, R., Cárdenas-Triviño, G., and Soto-Seguel, R. (2020). CHITOSAN COMPOSITES PREPARATION AND CHARACTERIZATION OF GUIDE TUBES FOR NERVE REPAIR. *J. Chil. Chem. Soc.* 65, 4870–4878. doi:10.4067/S0717-97072020000204870

Chatzipanagis, K., Iafisco, M., Roncal-Herrero, T., Bilton, M., Tampieri, A., Kröger, R., et al. (2016). Crystallization of citrate-stabilized amorphous calcium phosphate to nanocrystalline apatite: a surface-mediated transformation. *CrystEngComm* 18, 3170–3173. doi:10.1039/C6CE00521G

Chen, M. M., Li, Y., Deng, S. L., Zhao, Y., Lian, Z. X., and Yu, K. (2022). Mitochondrial function and reactive oxygen/nitrogen species in skeletal muscle. *Front. Cell Dev. Biol.* 10, 826981. doi:10.3389/fcell.2022.826981

Chen, Y., Gu, W., Pan, H., Jiang, S., and Tang, R. (2014). Stabilizing amorphous calcium phosphate phase by citrate adsorption. *CrystEngComm* 16, 1864–1867. doi:10.1039/C3CE42274G

Chin, K.-Y., and Ima-Nirwana, S. (2018). Vitamin C and bone health: evidence from cell, animal and human studies. *Curr. Drug Targets* 19, 439–450. doi:10.2174/1389450116666150907100838

Chinopoulos, C., and Adam-Vizi, V. (2010). Mitochondrial Ca2+ sequestration and precipitation revisited. *FEBS J.* 277, 3637–3651. doi:10.1111/J.1742-4658.2010.07755.X

Combes, C., and Rey, C. (2010). Amorphous calcium phosphates: synthesis, properties and uses in biomaterials. *Acta Biomater.* 6, 3362–3378. doi:10.1016/J.ACTBIO.2010.02.017

Corbridge, D. E. C. (1971). The structural chemistry of phosphates. *Bull. Minéralogie* 94, 271–299. doi:10.3406/BULMI.1971.6534

Dabbagh, H. A., Azami, F., Farrokhpour, H., and Chermahini, A. N. (2014). UV-VIS, NMR AND FT-IR SPECTRA OF TAUTOMERS OF VITAMIN C. EXPERIMENTAL AND DFT CALCULATIONS. *J. Chil. Chem. Soc.* 59, 2588–2594. doi:10.4067/S0717-97072014000300013

Damilola Olawale, M., Obaleye, J., Olawale, M. D., Obaleye, J. A., and Oladele, E. O. (2020). ITACONIC ACID BASED COORDINATION POLYMER: MECHANOCHEMICAL SYNTHESIS, CHARACTERIZATION AND VAPOCHROMIC STUDY. *Niger. Res. J. Chem. Sci.* 8, 2020. Available at: http://repository.elizadeuniversity.edu.ng/jspui/handle/20.500.12398/887 (Accessed August 15, 2023).

De Castro, E. D. S. G., and Cassella, R. J. (2016). Direct determination of sorbitol and sodium glutamate by attenuated total reflectance Fourier transform infrared spectroscopy (ATR-FTIR) in the thermostabilizer employed in the production of yellow-fever vaccine. *Talanta* 152, 33–38. doi:10.1016/J.TALANTA.2016.01.054

Dominguez-Medina, S., McDonough, S., Swanglap, P., Landes, C. F., and Link, S. (2012). *In situ* measurement of bovine serum albumin interaction with gold nanospheres. *Langmuir* 28, 9131–9139. doi:10.1021/LA3005213

Eanes, E. D. (1998). Amorphous calcium phosphate: thermodynamic and kinetic considerations. *Calcium Phosphates Biol. Ind. Syst.* 1998, 21–39. doi:10.1007/978-1-4615-5517-9_2

Edén, M. (2021). Structure and formation of amorphous calcium phosphate and its role as surface layer of nanocrystalline apatite: implications for bone mineralization. *Materialia* 17, 101107. doi:10.1016/J.MTLA.2021.101107

Erceg, I., and Dutour Sikirić, M. (2022). Influence of biomacromolecules on calcium phosphate formation on TiO2 nanomaterials. *Minerals* 12, 1557. doi:10.3390/min12121557

Fatokun, A. A., Stone, T. W., and Smith, R. A. (2006). Hydrogen peroxide-induced oxidative stress in MC3T3-E1 cells: the effects of glutamate and protection by purines. *Bone* 39, 542–551. doi:10.1016/J.BONE.2006.02.062

Feng, W., Feng, C., Wang, B., Jing, A., Li, G., Xia, X., et al. (2020). An amorphous calcium phosphate for drug delivery: ATP provides a phosphorus source and microwave-assisted hydrothermal synthesis. *Mat. Today Commun.* 25, 101455. doi:10.1016/J.MTCOMM.2020.101455

Flannigan, R., Choy, W. H., Chew, B., and Lange, D. (2014). Renal struvite stones-pathogenesis, microbiology, and management strategies. *Nat. Rev. | Urol.* 11, 333–341. doi:10.1038/nrurol.2014.99

Gajjeraman, S., Narayanan, K., Hao, J., Qin, C., and George, A. (2007). Matrix macromolecules in hard tissues control the nucleation and hierarchical assembly of hydroxyapatite. *J. Biol. Chem.* 282, 1193–1204. doi:10.1074/JBC.M604732200

Genever, P. G., and Skerry, T. M. (2001). Regulation of spontaneous glutamate release activity in osteoblastic cells and its role in differentiation and survival: evidence for intrinsic glutamatergic signaling in bone. *FASEB J.* 15, 1586–1588. doi:10.1096/FJ.00-0594FJE

Gorbunoff, M. J. (1984). The interaction of proteins with hydroxyapatite. *Anal. Biochem.* 136, 433–439. doi:10.1016/0003-2697(84)90240-9

Grover, L. M., Wright, A. J., Gbureck, U., Bolarinwa, A., Song, J., Liu, Y., et al. (2013). The effect of amorphous pyrophosphate on calcium phosphate cement resorption and bone generation. *Biomaterials* 34, 6631–6637. doi:10.1016/J.BIOMATERIALS.2013.05.001

Gunson, D., Gropp, K. E., and Varela, A. (2013). Bone and joints. *Haschek Rousseaux's Handb. Toxicol. Pathol.* 1-3, 2761–2858. doi:10.1016/B978-0-12-415759-0.00063-7

Hadzir, S. N., Ibrahim, S. N., Abdul Wahab, R. M., Zainol Abidin, I. Z., Senafi, S., Ariffin, Z. Z., et al. (2014). Ascorbic acid induces osteoblast differentiation of human suspension mononuclear cells. *Cytotherapy* 16, 674–682. doi:10.1016/J.JCYT.2013.07.013

Hoeher, A. J., Mergelsberg, S. T., Borkiewicz, O. J., and Michel, F. M. (2023). Impacts of initial Ca/P on amorphous calcium phosphate. *Cryst. Growth Des.* 7, 3736–3745. doi:10.1021/acs.cgd.1c00058

Howard, J. E., and Thomas, W. C. (1968). Control of crystallization in urine. *Am. J. Med.* 45, 693–699. doi:10.1016/0002-9343(68)90205-2

Hwang, P. W., and Horton, J. A. (2019). Variable osteogenic performance of MC3T3-E1 subclones impacts their utility as models of osteoblast biology. *Sci. Rep.* 9, 8299. doi:10.1038/s41598-019-44575-8

Iafisco, M., Degli Esposti, L., Ramírez-Rodríguez, G. B., Carella, F., Gómez-Morales, J., Ionescu, A. C., et al. (2018). Fluoride-doped amorphous calcium phosphate nanoparticles as a promising biomimetic material for dental remineralization. *Sci. Rep.* 8, 17016. doi:10.1038/S41598-018-35258-X

Ikawa, N., Kimura, T., Oumi, Y., and Sano, T. (2009). Amino acid containing amorphous calcium phosphates and the rapid transformation into apatite. *J. Mat. Chem.* 19, 4906–4913. doi:10.1039/B815154G

Iline-Vul, T., Nanda, R., Mateos, B., Hazan, S., Matlahov, I., Perelshtein, I., et al. (2020). Osteopontin regulates biomimetic calcium phosphate crystallization from disordered mineral layers covering apatite crystallites. *Sci. Rep.* 101 (10), 15722–15816. doi:10.1038/s41598-020-72786-x

Indurkar, A., Choudhary, R., Rubenis, K., and Locs, J. (2023a). Role of carboxylic organic molecules in interfibrillar collagen mineralization. *Front. Bioeng. Biotechnol.* 11, 1150037. doi:10.3389/FBIOE.2023.1150037

Indurkar, A., Choudhary, R., Rubenis, K., Nimbalkar, M., Sarakovskis, A., Boccaccini, A. R., et al. (2023b). Amorphous calcium phosphate and amorphous calcium phosphate carboxylate: synthesis and characterization. *ACS Omega* 8, 26782–26792. doi:10.1021/ACSOMEGA.3C00796

Jahandideh, A., Esmaeili, N., and Muthukumarappan, K. (2018). Facile synthesis and characterization of activated star-shaped itaconic acid based thermosetting resins. *Polym. Degrad. Stab.* 153, 201–209. doi:10.1016/J.POLYMDEGRADSTAB.2018.04.035

Jin, B., Liu, Z., Shao, C., Chen, J., Liu, L., Tang, R., et al. (2021). Phase transformation mechanism of amorphous calcium phosphate to hydroxyapatite investigated by liquid-cell transmission electron microscopy. *Cryst. Growth Des.* 21, 5126–5134. doi:10.1021/acs.cgd.1c00503

Kalani, A., Kamat, P. K., Voor, M. J., Tyagi, S. C., and Tyagi, N. (2014). Mitochondrial epigenetics in bone remodeling during hyperhomocysteinemia. *Mol. Cell. Biochem.* 395, 89–98. doi:10.1007/S11010-014-2114-3

Kritis, A. A., Stamoula, E. G., Paniskaki, K. A., and Vavilis, T. D. (2015). Researching glutamate – induced cytotoxicity in different cell lines: a comparative/collective analysis/study. *Front. Cell. Neurosci.* 9, 91. doi:10.3389/fncel.2015.00091

Lehninger, A. L. (1970). Mitochondria and calcium ion transport. *Biochem. J.* 119, 129–138. doi:10.1042/bj1190129

Loginova, E. V., Mikheev, I. V., Volkov, D. S., and Proskurnin, M. A. (2016). Quantification of copolymer composition (methyl acrylate and itaconic acid) in polyacrylonitrile carbon-fiber precursors by FTIR-spectroscopy. *Anal. Methods* 8, 371–380. doi:10.1039/C5AY02264A

Lotsari, A., Rajasekharan, A. K., Halvarsson, M., and Andersson, M. (2018). Transformation of amorphous calcium phosphate to bone-like apatite. *Nat. Commun.* 91 (9), 4170–4211. doi:10.1038/s41467-018-06570-x

Makowski, G. S., and Ramsby, M. L. (2001). Interaction of amorphous calcium phosphate with fibrin *in vitro* causes decreased fibrinolysis and altered protease profiles: implications for atherosclerotic disease. *Inflammation* 25, 319–329. doi:10.1023/a:1012831900153

Manzoor, M. A. P., Duwal, S. R., Mujeeburahiman, M., and Rekha, P. D. (2018). Vitamin C inhibits crystallization of struvite from artificial urine in the presence of *Pseudomonas aeruginosa*. *Int. Braz. J. Urol. Off. J. Braz. Soc. Urol.* 44, 1234–1242. doi:10.1590/S1677-5538.IBJU.2017.0656

Mekmene, O., Quillard, S., Rouillon, T., Bouler, J. M., Piot, M., and Gaucheron, F. (2009). Effects of pH and Ca/P molar ratio on the quantity and crystalline structure of calcium phosphates obtained from aqueous solutions. *Dairy Sci. Technol.* 89, 301–316. doi:10.1051/DST/2009019

Murad, S., Grove, D., Lindberg, K. A., Reynolds, G., Sivarajah, A., and Pinnell, S. R. (1981). Regulation of collagen synthesis by ascorbic acid. *Proc. Natl. Acad. Sci. U. S. A.* 78, 2879–2882. doi:10.1073/PNAS.78.5.2879

Nakamura, K., Isoyama, N., Nakayama, Y., Hiroyoshi, T., Fujikawa, K., Miura, Y., et al. (2022). Association between amorphous calcium-phosphate ratios in circulating calciprotein particles and prognostic biomarkers in hemodialysis patients. *Sci. Rep.* 121 (12), 13030–13038. doi:10.1038/s41598-022-17405-7

Niu, L. N., Zhang, W., Pashley, D. H., Breschi, L., Mao, J., Chen, J. H., et al. (2014). Biomimetic remineralization of dentin. *Dent. Mat.* 30, 77–96. doi:10.1016/J.DENTAL.2013.07.013

Osellame, L. D., Blacker, T. S., and Duchen, M. R. (2012). Cellular and molecular mechanisms of mitochondrial function. *Best. Pract. Res. Clin. Endocrinol. Metab.* 26, 711–723. doi:10.1016/J.BEEM.2012.05.003

Padovano, J. D., Ravindran, S., Snee, P. T., Ramachandran, A., Bedran-Russo, A. K., and George, A. (2015). DMP1-derived peptides promote remineralization of human dentin. *J. Dent. Res.* 94, 608–614. doi:10.1177/0022034515572441

Peace, C. G., and O'Neill, L. A. J. (2022). The role of itaconate in host defense and inflammation. *J. Clin. Invest.* 132, e148548. doi:10.1172/JCI148548

Polat, O., Kilicoglu, S. S., and Erdemli, E. (2007). A controlled trial of glutamine effects on bone healing. *Adv. Ther.* 24, 154–160. doi:10.1007/BF02850003

Querido, W., Shanas, N., Bookbinder, S., Oliveira-Nunes, M. C., Krynska, B., and Pleshko, N. (2020). Fourier transform infrared spectroscopy of developing bone mineral: from amorphous precursor to mature crystal. *Analyst* 145, 764–776. doi:10.1039/C9AN01588D

Reynolds, E. C. (1998). Anticariogenic complexes of amorphous calcium phosphate stabilized by casein phosphopeptides: a review. *Spec. Care Dent.* 18, 8–16. doi:10.1111/j.1754-4505.1998.tb01353.x

Sakhno, Y., Degli Esposti, L., Adamiano, A., Borgatta, J., Cahill, M., Vaidya, S., et al. (2023). Citrate-stabilized amorphous calcium phosphate nanoparticles doped with micronutrients as a highly efficient nanofertilizer for environmental sustainability. *ACS Agric. Sci. Technol.* 3, 845–854. doi:10.1021/acsagscitech.3c00117

Sannelli, F., Jensen, P. R., and Meier, S. (2023). In-cell NMR approach for real-time exploration of pathway versatility: substrate mixtures in nonengineered yeast. *Anal. Chem.* 95, 7262–7270. doi:10.1021/acs.analchem.3c00225

Scheffler, I. E. (2002). Metabolic pathways inside mitochondria. *Mitochondria* 2002, 246–272. doi:10.1002/0471223891.CH6

Schubert, D., and Piasecki, D. (2001). Oxidative glutamate toxicity can Be a component of the excitotoxicity cascade. *J. Neurosci.* 21, 7455–7462. doi:10.1523/JNEUROSCI.21-19-07455.2001

Shi, X., Zhou, H., Wei, J., Mo, W., Li, Q., and Lv, X. (2022). The signaling pathways and therapeutic potential of itaconate to alleviate inflammation and oxidative stress in inflammatory diseases. *Redox Biol.* 58, 102553. doi:10.1016/J.REDOX.2022.102553

Skerry, T., and Taylor, A. (2005). Glutamate signalling in bone. *Curr. Pharm. Des.* 7, 737–750. doi:10.2174/1381612013397771

Stipniece, L., Salma-Ancane, K., Rjabovs, V., Juhnevica, I., Turks, M., Narkevica, I., et al. (2016). Development of functionalized hydroxyapatite/poly(vinyl alcohol) composites. *J. Cryst. Growth* 444, 14–20. doi:10.1016/J.JCRYSGRO.2016.03.029

Strelko, C. L., Lu, W., Dufort, F. J., Seyfried, T. N., Chiles, T. C., Rabinowitz, J. D., et al. (2011). Itaconic acid is a mammalian metabolite induced during macrophage activation. *J. Am. Chem. Soc.* 133, 16386–16389. doi:10.1021/ja2070889

Sumayya, A., Panicker, Cy., and Tresa Varghese, H. (2008). VIBRATIONAL SPECTROSCOPIC STUDIES AND *ab initio* CALCULATIONS OF L-GLUTAMIC ACID 5-AMIDE. *Rasayan J. Chem.* 1, 548–555.

Sun, R., Åhlén, M., Tai, C. W., Bajnóczi, É. G., de Kleijne, F., Ferraz, N., et al. (2020). Highly porous amorphous calcium phosphate for drug delivery and bio-medical applications. *Nanomaterials* 10, 20. doi:10.3390/NANO10010020

Syed-Picard, F. N., Jayaraman, T., Lam, R. S. K., Beniash, E., and Sfeir, C. (2013). Osteoinductivity of calcium phosphate mediated by connexin 43. *Biomaterials* 34, 3763–3774. doi:10.1016/J.BIOMATERIALS.2013.01.095

Szekeres, G. P., and Kneipp, J. (2018). Different binding sites of serum albumins in the protein corona of gold nanoparticles. *Analyst* 143, 6061–6068. doi:10.1039/C8AN01321G

Tajmir-Riahi, H. A. (1991). Coordination chemistry of vitamin C. Part II. Interaction of L-ascorbic acid with Zn(II), Cd(II), Hg(II), and Mn(II) ions in the solid state and in aqueous solution. *J. Inorg. Biochem.* 42, 47–55. doi:10.1016/0162-0134(91)80031-C

Ten Cate, J. M., and Featherstone, J. D. B. (1991). Mechanistic aspects of the interactions between fluoride and dental enamel. *Crit. Rev. Oral Biol. Med.* 2, 283–296. doi:10.1177/10454411910020030101

Thaler, R., Khani, F., Sturmlechner, I., Dehghani, S. S., Denbeigh, J. M., Zhou, X., et al. (2022). Vitamin C epigenetically controls osteogenesis and bone mineralization. *Nat. Commun.* 131 (13), 5883–5918. doi:10.1038/s41467-022-32915-8

Tsuji, T., Onuma, K., Yamamoto, A., Iijima, M., and Shiba, K. (2008). Direct transformation from amorphous to crystalline calcium phosphate facilitated by

motif-programmed artificial proteins. *Proc. Natl. Acad. Sci. U. S. A.* 105, 16866–16870. doi:10.1073/PNAS.0804277105

Uhanov, A. S., Klepov, V. V., Vologzhanina, A. V., Zubavichus, Y. V., Savchenkov, A. V., Pushkin, D. V., et al. (2020). New itaconate-containing uranyl complex unit and coordination modes of itaconate ions. *Comptes Rendus Chim.* 23, 117–126. doi:10.5802/crchim.8

Vettori, I., Macchiagodena, M., Pagliai, M., Bassu, G., Fratini, E., and Baglioni, P. (2022). Conformational and solvent effects in structural and spectroscopic properties of 2-hydroxyethyl methacrylate and acrylic acid. *J. Mol. Liq.* 360, 119428. doi:10.1016/j.molliq.2022.119428

Wang, Y., Li, S., Zhao, L., Cheng, P., Liu, J., Guo, F., et al. (2022). Aging relevant metabolite itaconate inhibits inflammatory bone loss. *Front. Endocrinol. (Lausanne)* 13, 885879. doi:10.3389/fendo.2022.885879

Wibowo, A. H., Hasanah, Y. I. F., Firdaus, M., Widjonarko, D. M., and Cepeda, J. (2018). Efficient CO2 adsorption by Cu(II) acetate and itaconate bioproduct based MOF. *J. Environ. Chem. Eng.* 6, 2910–2917. doi:10.1016/J.JECE.2018.04.031

Williams, D., and Rogers, L. H. (1937). The infrared absorption spectrum of vitamin C. *J. Am. Chem. Soc.* 59, 1422–1423. doi:10.1021/ja01287a005

Winand, L., Dallemagne, M. J., and Duyckaerts, G. (1961). Hydrogen bonding in apatitic calcium phosphates. *Nat* 190, 164–165. doi:10.1038/190164a0

Xu, X., Urlaub, J., Woźniczka, M., Wynendaele, E., Herman, K., Schollmayer, C., et al. (2019). Zwitterionic-hydrophilic interaction liquid chromatography for l-ascorbic acid 2-phosphate magnesium, a raw material in cell therapy. *J. Pharm. Biomed. Anal.* 165, 338–345. doi:10.1016/J.JPBA.2018.12.010

Yamada, I., Galindo, T. G. P., Noda, D., and Tagaya, M. (2021). Effect of orotic acid addition on hydrolysis conversion of α-tricalcium phosphate to hydroxyapatite. *Int. J. Ceram. Eng. Sci.* 3, 267–271. doi:10.1002/CES2.10109

Yang, C., Liu, T., and Shi, G. P. (2020). Therapeutic potential of tricarboxylic acid cycle metabolite itaconate in cardiovascular diseases. *EBioMedicine* 59, 102938. doi:10.1016/j.ebiom.2020.102938

Yang, Y., Cui, Q., and Sahai, N. (2010). How does bone sialoprotein promote the nucleation of hydroxyapatite? A molecular dynamics study using model peptides of different conformations. *Langmuir* 26, 9848–9859. doi:10.1021/LA100192Z

Yarbrough, D. K., Hagerman, E., Eckert, R., He, J., Choi, H., Cao, N., et al. (2010). Specific binding and mineralization of calcified surfaces by small peptides. *Calcif. Tissue Int.* 86, 58–66. doi:10.1007/S00223-009-9312-0

Yohannan Panicker, C., Tresa Varghese, H., and Philip, D. (2006). FT-IR, FT-Raman and SERS spectra of Vitamin C. *Spectrochim. Acta Part A Mol. Biomol. Spectrosc.* 65, 802–804. doi:10.1016/J.SAA.2005.12.044

Yokoi, T., Shimabukuro, M., and Kawashita, M. (2022). Octacalcium phosphate with incorporated carboxylate ions: a review. *Sci. Technol. Adv. Mat.* 23, 434–445. doi:10.1080/14686996.2022.2094728

Zhang, S., Moustafa, Y., and Huo, Q. (2014). Different interaction modes of biomolecules with citrate-capped gold nanoparticles. *ACS Appl. Mat. Interfaces* 6, 21184–21192. doi:10.1021/am506112u

Zhao, J., Liu, Y., Sun, W. B., and Yang, X. (2012). First detection, characterization, and application of amorphous calcium phosphate in dentistry. *J. Dent. Sci.* 7, 316–323. doi:10.1016/J.JDS.2012.09.001

Zhao, W., Wang, Z., Xu, Z., and Sahai, N. (2018). Osteocalcin facilitates calcium phosphate ion complex growth as revealed by free energy calculation. *Phys. Chem. Chem. Phys.* 20, 13047–13056. doi:10.1039/C8CP01105B

Zhou, Y., and Roos, Y. H. (2012). Stability and plasticizing and crystallization effects of vitamins in amorphous sugar systems. *J. Agric. Food Chem.* 60, 1075–1083. doi:10.1021/JF204168F

Zong, C., Wang, Y., and Jiang, S. (2023). Toward the understanding of poly (Acrylic Acid) on amorphous calcium phosphate mediated collagen intrafibrillar Mineralization: surface adsorption versus bulk incorporation. *J. Cryst. Growth* 616, 127304. doi:10.1016/J.JCRYSGRO.2023.127304

Small Organic Molecules Containing Amorphous Calcium Phosphate: Synthesis, Characterization and Transformation

Abhishek Indurkar,[1,2] Pawan Kudale,[3] Vitālijs Rjabovs,[4] Ivo Heinmaa,[5] Öznur Demir,[1,2] Matvejs Kirejevs,[1] Kristaps Rubenis,[1,2] Ganesh Chaturbhuj,[3] Māris Turks,[4] and Janis Locs[1,2]*

[1]Rudolfs Cimdins Riga Biomaterials Innovations and Development Centre of RTU, Institute of General Chemical Engineering, Faculty of Materials Science and Applied Chemistry, Riga Technical University, Pulka Street 3, LV-1007 Riga, Latvia.

[2]Baltic Biomaterials Centre of Excellence, Headquarters at Riga Technical University, Kipsalas Street 6A, LV-1048 Riga, Latvia.

[3]Department of Pharmaceutical Sciences and Technology, Institute of Chemical Technology, Matunga, Mumbai, 400019, India.

[4]Institute of Technology of Organic Chemistry, Faculty of Materials Science and Applied Chemistry, Riga Technical University, P. Valdena 3, LV-1048, Riga, Latvia.

[5]National Institute of Chemical Physics and Biophysics, Akadeemia tee 23, 12618 Tallinn, Estonia.

*Corresponding author – Janis.Locs@rtu.lv

Supplementary data

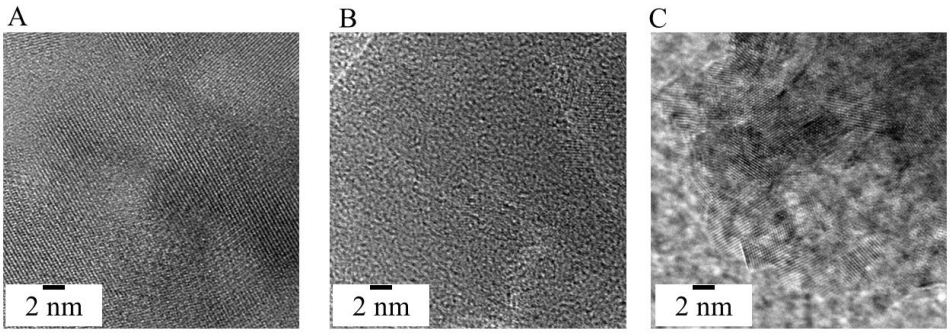

Figure S1. Crystallization of ACP variants under high electron beam A) ACP_ASC, B) ACP_GLU and C) ACP_ITN

Milli-Q® water

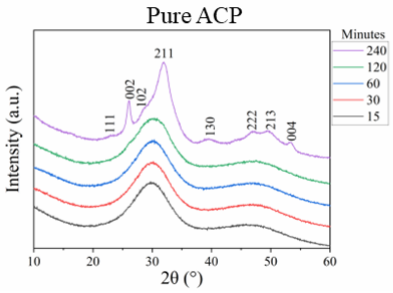

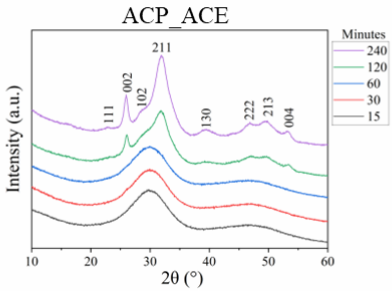

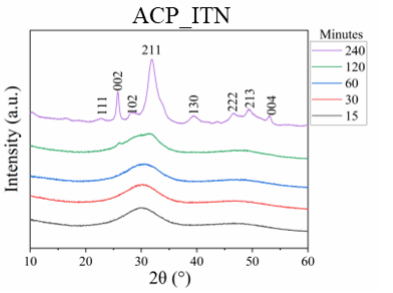

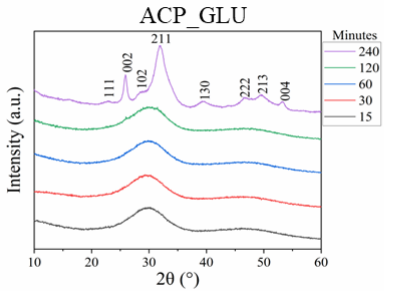

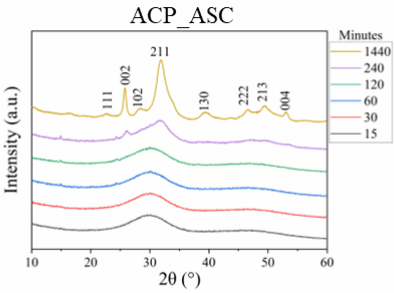

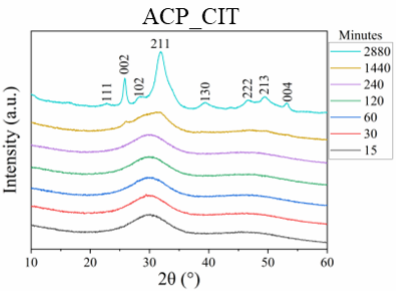

PBS

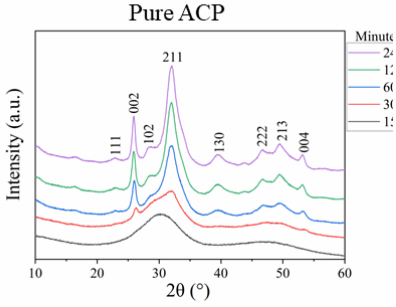

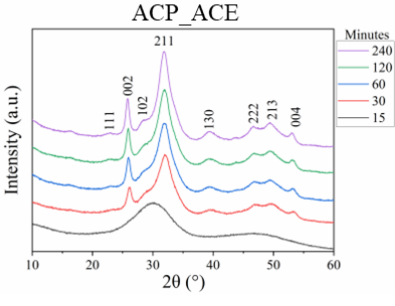

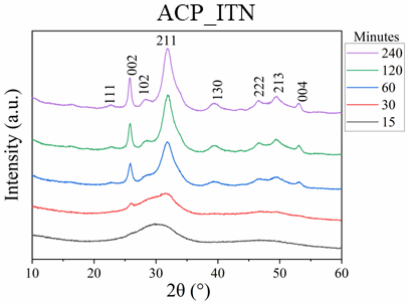

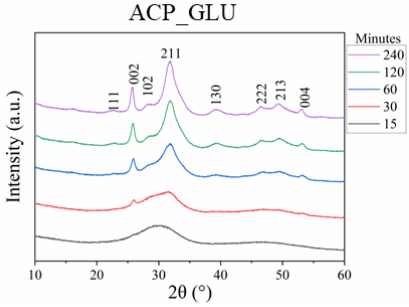

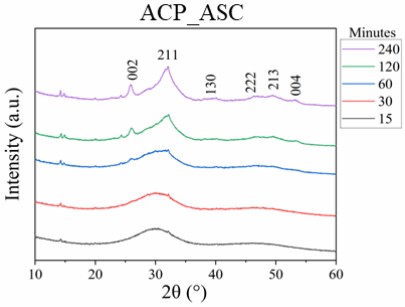

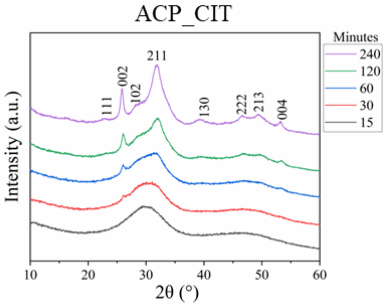

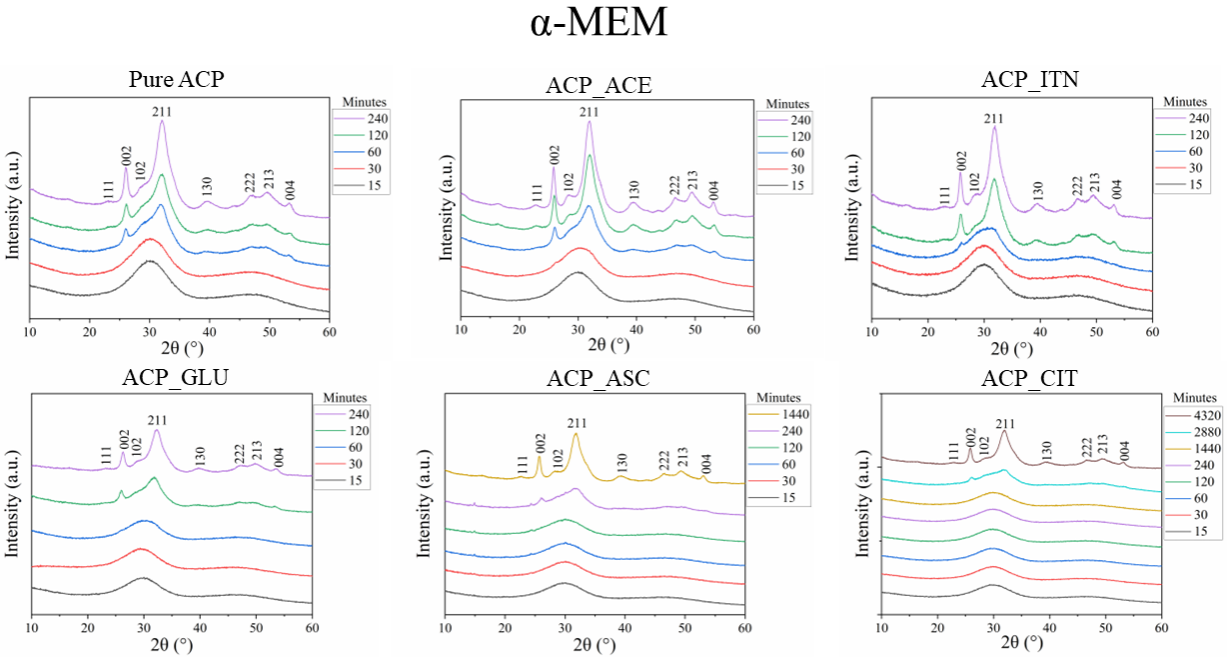

Figure S2. XRD analysis to track alteration and successive progression in crystallization of ACP in different solvents such as Milli-Q® water, PBS, and α-MEM medium. The peaks were matched with standard ICDD card no. 00-064-0738.

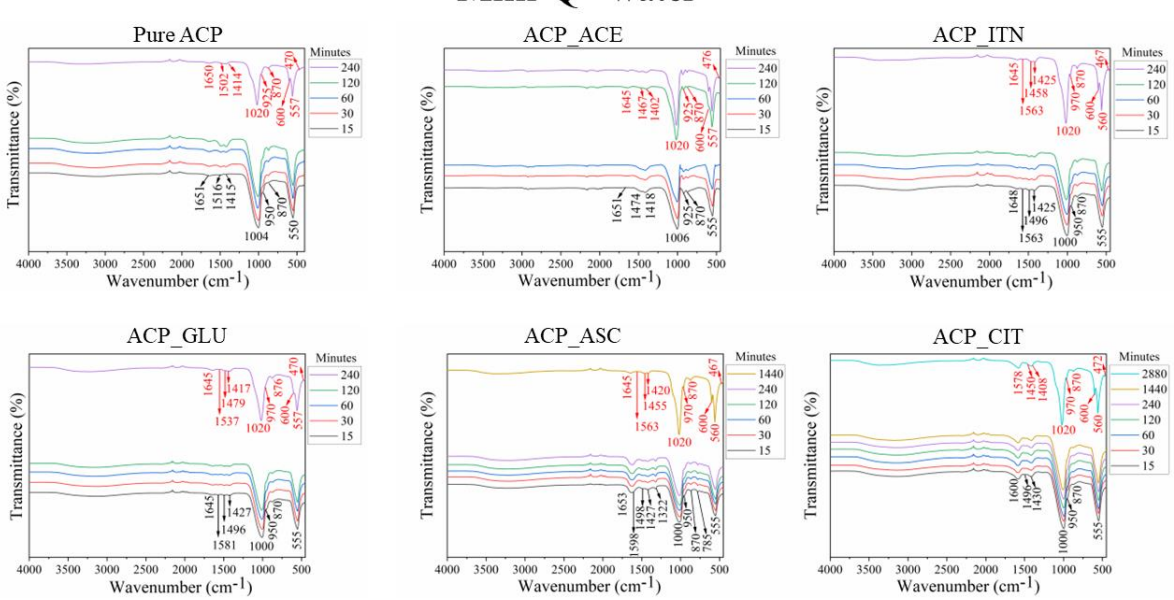

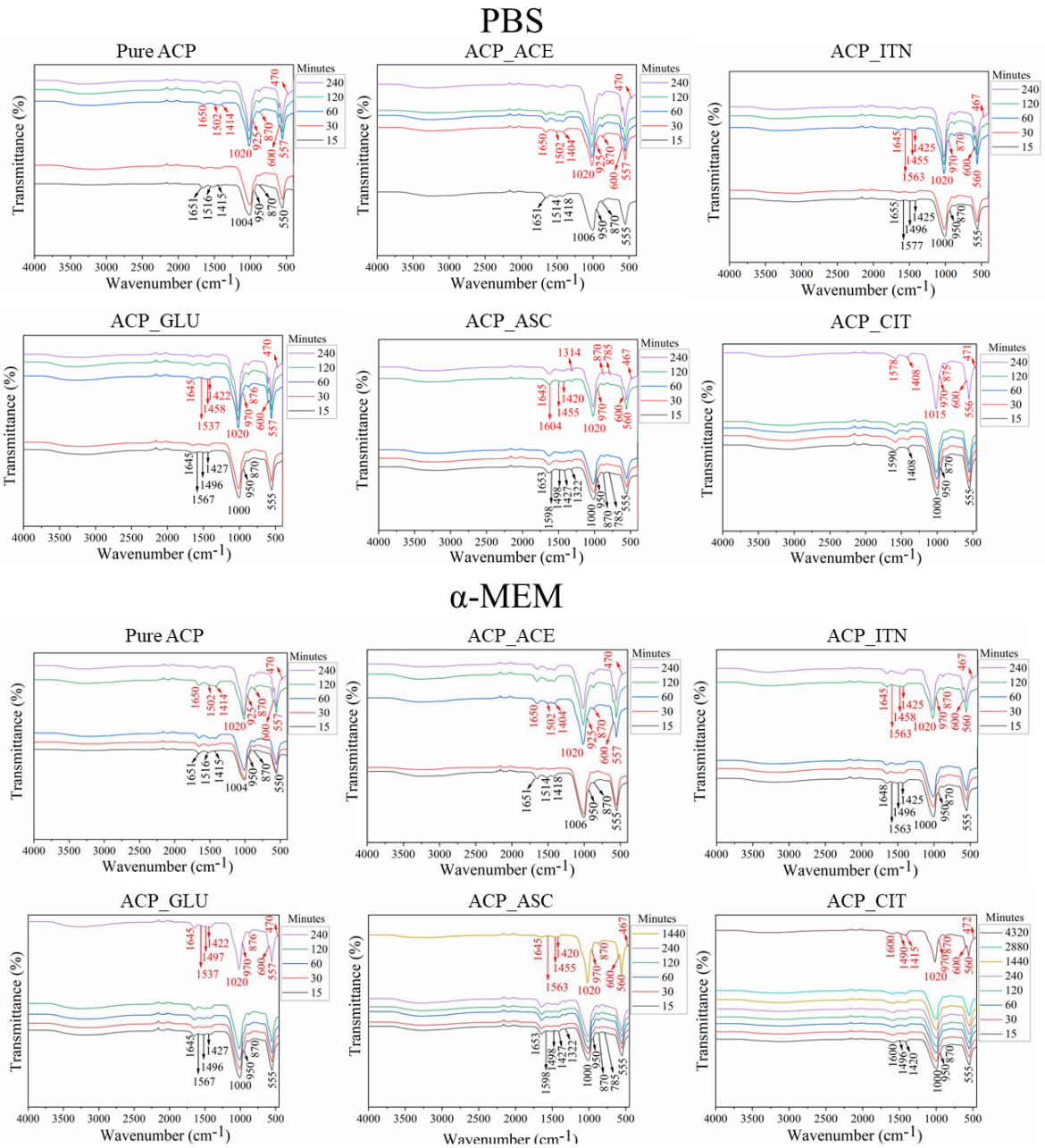

Figure S3. FTIR analysis to track alteration and successive progression in crystallization of ACP in different solvents such as Milli-Q® water, PBS, and α-MEM medium.

Table S1 – FTIR bands and corresponding functional groups of ACP and its variants.

Sample	Bands (cm^{-1})	Functional groups	Reference
Pure ACP_CL	3000 - 3700	OH asymmetric and symmetric stretching mode	(Indurkar et al., 2023)
	1680 - 1640	OH bending mode	
	1400 - 1550	$v_3CO_3^{2-}$	
	1000 - 1150	$v_3PO_4^{3-}$	
	950	$v_1PO_4^{3-}$	
	875	$v_2CO_3^{2-}$	
	500 - 620	$v_4PO_4^{3-}$	
ACP_ACE	3000 - 3700	OH asymmetric and symmetric stretching mode	(Indurkar et al., 2023)
	1680 - 1640	OH bending mode	
	1550	COO^- bending	
	1440	COH stretching.	
	1000 - 1150	$v_3PO_4^{3-}$	
	950	$v_1PO_4^{3-}$	
	600 - 680	COO^- bending	
	500 - 620	$v_4PO_4^{3-}$	
ACP_ITN	3000 - 3700	OH asymmetric and symmetric stretching mode	Reported in the current study
	1680 - 1640	OH bending mode and/or C=C vibrations	
	1563	asymmetric C=O vibration	
	1489	O-C-O stretching	
	1425	symmetric C=O vibration	
	1243	C-O stretching	
	1000 - 1150	$v_3PO_4^{3-}$	
	950	$v_1PO_4^{3-}$	
	870 and 840	CH stretching vibrations	
	500 - 620	$v_4PO_4^{3-}$	
ACP_GLU	3000 - 3700	NH_2 vibrations and OH asymmetric and symmetric stretching mode	Reported in the current study
	1680 - 1640	OH bending mode	
	1569	asymmetric C=O vibration	
	1496	symmetric and asymmetric stretching of C-O	
	1418	symmetric C=O vibration	
	1117 - 870	C-C bending mode	
	1000 - 1150	$v_3PO_4^{3-}$	
	950	$v_1PO_4^{3-}$	
	500 - 620	$v_4PO_4^{3-}$	
ACP_ASC	3000 - 3700	OH asymmetric and symmetric stretching mode	Reported in the current study
	~3000	C-H vibrations	
	1500 - 1660	C=O and C-O vibrations of carboxylate ions	
	1488	CH bending	
	1423	CH_2 scissoring	
	1321	CH bending	
	1000 - 1150	$v_3PO_4^{3-}$	
	950	$v_1PO_4^{3-}$	
	871	C-C ring stretching	
	780	OH out of plane deformation	
	500 - 620	$v_4PO_4^{3-}$	
ACP_CIT	3000 - 3700	OH asymmetric and symmetric stretching mode	(Indurkar et al., 2023)
	1680 - 1640	OH bending mode	
	1600	COO^- bending	
	1446	COH stretching	
	1000 - 1150	$v_3PO_4^{3-}$	
	950	$v_1PO_4^{3-}$	
	500 - 620	$v_4PO_4^{3-}$	

Table S2 – Inorganic compounds present in the respective mediums

Solvents	Milli-Q® water	PBS pH – 7.4	α-MEM pH – 7.4
Sodium chloride	-	8 g	6.8 g
Potassium chloride	-	0.2 g	0.4 g
Sodium phosphate	-	1.44 g	0.014 g
Potassium phosphate monobasic	-	0.245 g	-
Calcium chloride	-	-	0.2 g
Magnesium chloride	-	-	-
Magnesium sulphate	-	-	0.097 g
Sodium bicarbonate	-	-	2.2 g
Dextrose	-	-	1 g
Dipotassium phosphate	-	-	-
1M HCl	-	-	-
Sodium sulphate	-	-	-
Tris(hydroxymethyl)aminomethane	-	-	-

Table S3 – Physiochemical properties of synthesised ACP and its composites

Sample	**Density (g/cm^3)**	**BET (m^2/g)**	**Morphology**
Pure ACP_CL	2.62	105	Spherical hollow (Indurkar et al., 2023)
ACP_ACE	2.47	118	Spherical hollow (Indurkar et al., 2023)
ACP_ITN	2.43	130.3	Spherical hollow (current study)
ACP_GLU	2.64	92.4	Spherical hollow (current study)
ACP_ASC	2.82	115.2	Spherical hollow (current study)
ACP_CIT	2.57	62	Spherical Dense (Indurkar et al., 2023)

References

Indurkar, A., Choudhary, R., Rubenis, K., Nimbalkar, M., Sarakovskis, A., R. Boccaccini, A., et al. (2023). Amorphous Calcium Phosphate and Amorphous Calcium Phosphate Carboxylate: Synthesis and Characterization. *ACS Omega* 8, 26782–26792. doi: 10.1021/acsomega.3c00796.

6. PIELIKUMS / APPENDIX 6

6. PUBLIKĀCIJA / PUBLICATION

Indurkar, A., Heid, S., Bauer, J., Rubenis, K., Friedrich, O., A., Locs, J., & Boccaccini, A. R. Amorphous Calcium Phosphate Reinforced Alginate-Dialdehyde-Gelatin (Ada-Gel) Bioinks for Biofabrication of Bone Tissue Scaffolds.

The article is currently uncer peer review in Scientific reports

Amorphous calcium phosphate reinforced alginate-dialdehyde-gelatin (ADA-GEL) bioinks for biofabrication of bone tissue scaffolds

Abhishek Indurkar[1,2], Susanne Heid[3], Julian Bauer[4,5], Kristaps Rubenis[1,2], Oliver Friedrich[4,5], Janis Locs[1,2], and Aldo R. Boccaccini[3*]

[1] Rudolfs Cimdins Riga Biomaterials Innovations and Development Centre of RTU, Institute of General Chemical Engineering, Faculty of Materials Science and Applied Chemistry, Riga Technical University, Pulka Street 3, LV-1007 Riga, Latvia

[2] Baltic Biomaterials Centre of Excellence, Headquarters at Riga Technical University, Kipsalas Street 6A, LV-1048 Riga, Latvia

[3] Institute of Biomaterials, Department of Material Science and Engineering, Friedrich-Alexander University Erlangen-Nürnberg, Cauerstraße 6, 91058 Erlangen, Germany.

[4] Institute of Medical Biotechnology, Friedrich-Alexander University Erlangen-Nürnberg, Paul-Gordan-Str. 3, 91052 Erlangen, Germany.

[5] Erlangen Graduate School in Advanced Optical Technologies (SAOT), Friedrich-Alexander University Erlangen-Nürnberg, 91052 Erlangen, Germany.

*Corresponding author: aldo.boccaccini@fau.de

Abstract

The aim of this study was to develop bioinks closely resembling the nanostructure of bone incorporating amorphous calcium phosphate (ACP) as inorganic counterpart; specifically citrate stabilized ACP (ACP_CIT) and non-stabilized ACP (ACP_ACE), in alginate dialdehyde-gelatin (ADA-GEL). Oscillatory shear tests were performed to understand the viscoelastic behavior of the hydrogels. G' and G" of ADA-GEL were 78 ± 8 Pa and 3.4 ± 0.4 Pa, respectively. By addition of ACP_ACE, G' and G" increased to 117 ± 15 Pa and 6.2 ± 0.4 Pa, while incorporation of ACP_CIT led to G' and G" values of 127 ± 14 Pa and 8 ± 1 Pa, respectively. The viscoelastic properties of ADA-GEL were enhanced by the reinforcement with ACP. ACP_CIT was more effective than ACP_ACE. Bioinks were formulated by embedding MC3T3-E1 cells in the hydrogels, followed by fabrication of constructs at 65 kPa and speed of 5 mm/s. Crosslinking was performed by immersing in $CaCl_2$ and microbial transglutaminase solution. Post-printing analysis was performed using printability index and average pore area analysis. The lowest structural stability was observed in ADA-GEL constructs and the highest was noted in ADA-GEL-ACP_CIT. Epifluorescence and two-photon microscopy of Rhodamine/Phalloidin stained constructs confirmed the cytocompatibility of the bioinks.

Graphical abstract

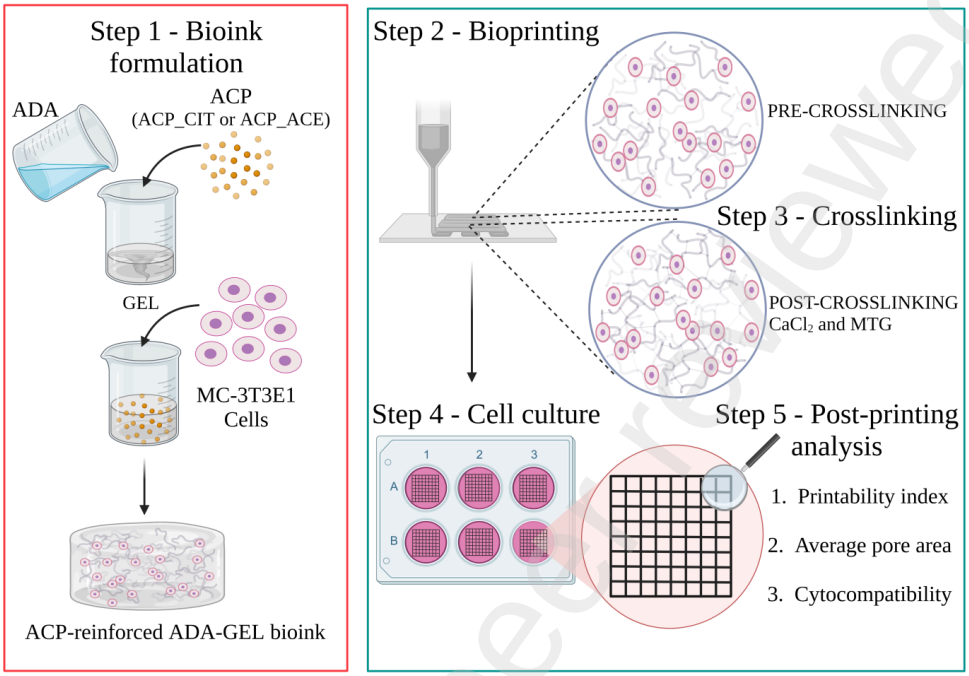

Keywords – Amorphous calcium phosphate; Alginate dialdehyde; Gelatin; Nanocomposite; Bioink, Bone tissue engineering

1. Introduction

Computer-aided deposition of cells and biomaterials using three-dimensional bioprinting is a promising approach to fabricate complex and hierarchically organized constructs with architecture closely resembling bone [1]. The printable material, called bioink, is a combination of cells and hydrogel that is a crucial component of bioprinting [2]. Composite bioinks incorporating inorganic fillers are also being increasingly investigated [3]. The biosynthesis of the inorganic component (calcium phosphate, bioactive glass) and its association with the organic counterpart must be considered to develop biomimetic nanocomposite bioinks [3, 4]. Amorphous calcium phosphate (ACP) is the first inorganic phase synthesized and stabilized in the mitochondria of cells. Further, ACP is embedded in the 40 nm gap zone of the collagen matrix, where it crystallizes to hydroxyapatite (HAp) [4,5]. Bone repair and reconstruction require innovative strategies that account for the nano to macroscale hierarchical assembly of bone tissue [6]. Therefore, in the current study, we have focused on developing nanocomposite bioinks reinforced with ACP.

Nanocomposite bioinks made up of inorganic and organic counterparts are expected to be more suitable than pure hydrogel bioinks for bone regeneration [3, 7,8]. Such nanocomposite bioinks have shown positive effects on adhesion, migration, genetic expression, proliferation and cell signaling capability in osteoblast and bone-derived stem cells [9].

Numerous inorganic nanomaterials such as HAp, tricalcium phosphate (TCP), octa-calcium phosphate (OCP), biphasic calcium phosphate, calcium metaphosphate, nano-silicates, bioactive glasses, graphene oxide, carbon nanotubes, titanium oxide, halloysite, zirconium oxide, etc. have been incorporated in polymer matrices to make nanocomposites [10]. Despite being the first calcium phosphate phase synthesized by cells, the application of ACP has been rather limited in tissue engineering. In previous studies, ACP was utilized to make nanocomposites, but the stabilization of ACP was not considered [11,12,21,22,13–20]. The stabilizing agent is essential in regulating collagen interfibrillar mineralization [23][24].

Various materials have been utilized to stabilize ACP by surface adsorption or ion substitution. Typical organic compounds stabilizing ACP by surface adsorption are adenosine triphosphate (ATP), polyelectrolyte, citrate, and polyethylene glycol [25–27]. Moreover, ions of magnesium, zinc, iron, carbonates, pyrophosphates, and fluorine can stabilize ACP by substituting calcium or phosphate ions [28–30].

Citrate is a favorable stabilizing agent as it is naturally synthesized through the Krebs cycle in mitochondria, which are also a site for ACP synthesis [31]. Recent findings revealed that one-sixth of the available surface area of HAp is covered by citrate, and NMR analysis also confirmed its presence in the bone [32,33]. Moreover, it has the inherent property of osteo-inductivity and enhances collagen mineralization through interface wetting [34–36]. Based on these findings, citrate-stabilized ACP was utilized in this study as an inorganic counterpart for the development of nanocomposite bioinks. For comparative analysis, a bioink reinforced with non-stabilized ACP (ACP_ACE) was also synthesized and tested.

Gelatin (GEL) and alginate dialdehyde (ADA) were used as the hydrogel components of the nanocomposite bioink. GEL is a single-stranded protein obtained from the hydrolytic degradation of collagen. It consists of a

large number of glycine, proline, and hydroxyproline residues that display similar biomechanical properties to collagen [37]. Alginate is a natural polymer obtained from brown seaweed consisting of β-(1-4) linked to d-mannouronic acid and β-(1-4) linked with I-glucuronic acid units. It lacks a cell attachment site and is often used with GEL to fabricate 3D scaffolds [38]. Alginate lacks binding properties with GEL; therefore, it is commonly modified to alginate dialdehyde (ADA), offering reactive groups for crosslinking with GEL by Schiff base formation, thus forming ADA-GEL [39].

Several nanocomposite bioinks have been formulated for bone tissue regeneration [3, 40]. Most bioinks employed HAp, TCP, OCP or bioactive glass particles as inorganic counterparts [3,41,42]. Even if ACP is the first naturally synthesized inorganic calcium phosphate phase, it has not been yet utilized in bioink formulations. Therefore, we have developed a new nanocomposite bioink based on citrate-stabilized ACP (ACP_CIT) and ADA-GEL. For comparison, another nanocomposite bioink consisting of non-stabilized ACP (ACP_ACE) and ADA-GEL was developed, and pure ADA-GEL was used as control. The bioinks were developed by embedding MC3T3-E1 cells, and cell-laden constructs were fabricated with the three mentioned hydrogels. Subsequently, preprinting and post-printing analyses were performed to evaluate the suitability of the new bioinks for bioprinting applications.

2. Materials and Methods

Calcium acetate monohydrate was procured from Honeywell, Fluka, USA (CAS 114460-21-8). Calcium citrate tetrahydrate (CAS 5785-44-4), trisodium phosphate (CAS 7601-54-9), sodium hydroxide (CAS 1301-73-2), and gelatin type-A from porcine skin (CAS 9000-70-8) were procured from Sigma Aldrich, Germany. Ethylene glycol (CAS 107-21-1) was obtained from VWR Chemical International (USA). Sodium meta periodate (CAS 7790-28-5) was procured from Bioultra, ≥ 99.5, Sigma Aldrich, Germany. Sodium alginate (CAS 9005-38-3) was obtained from VIVAPHARM®, JSR Pharma GmbH & Co, KG Rosenberg, Germany. The dialysis membrane with molecular cut-off 6-8 kDa was obtained from Spectrum lab™ USA.

2.1 Synthesis of ACP

ACP was synthesized by the protocol described in a previous publication [43]. Briefly, for the synthesis of ACP_CIT, 50 mM of calcium citrate tetrahydrate was added into Milli-Q® water. Moreover, for the synthesis of ACP_ACE, 150 mM calcium acetate was added to Milli-Q® water. The pH of the calcium citrate and calcium acetate solution was adjusted to 11.5 using 3 M NaOH. Further, an equal amount of 100 mM of trisodium phosphate solution was rapidly added to the beakers containing ACP_CIT and ACP_ACE solution, respectively. The precipitate was isolated by centrifugation and washed thrice with Milli-Q® water. The precipitates were frozen in liquid nitrogen, followed by lyophilization for 72 hr. The obtained powder was used for characterization and bioink formulation.

2.2 Synthesis of ADA

According to a slightly modified protocol presented by Sarker et al. [44], ADA was prepared by oxidation of sodium alginate. Briefly, in 50 ml ethanol, 10 g of sodium alginate was dispersed, and 2.67 g of sodium metaperiodate was dissolved in 50 ml of Milli-Q® water. An equal amount of sodium metaperiodate was added dropwise in the 50 ml sodium alginate dispersion under constant stirring. The entire reaction was performed in the dark. Further, the reaction was quenched after 6 h by adding 10 ml ethylene glycol to deactivate excess

periodate ions, and mixing continued for another 30 min. The mixtures were then collected into 50 ml Falcon tubes and centrifuged at 2,500 rpm for 5 min, and then the ethanol phase was decanted. The remaining ADA solution was dialyzed in Milli-Q® water for four days and replenished daily. The product was removed from the dialysis membrane, transferred to clean trays, and was frozen for at least 24 h before lyophilization (Christ Alpha, 1-4LD, Christ Gefriertrocknungsanlangen, Osterode am Harz, Germany) and subsequently harvested the final dry product.

2.3 Chemical characterization

2.3.1 X-ray powder diffraction (XRD)

XRD analysis was performed to examine the phase of ACP_ACE and ACP_CIT, using X-ray diffraction, performed with a PANalytical Aeris diffractometer (The Netherlands). The diffraction data were collected at 40 kV and 15 mA in a step mode with a step size of 0.04°, in the 2θ range from 10 to 70°.

2.3.2 Field-emission gun transmission electron microscopy (FEG-TEM)

The morphology and particle size of ACP_ACE and ACP_CIT were evaluated by FEG-TEM (FEI, Tecnai G2 F30, USA) operated at 300 kV. The sample preparation was as follows: a small amount of powder was dispersed in isopropyl alcohol and sonicated in an ultrasonic bath. Further, the samples were placed on a carbon-coated grid and dried before analysis.

2.3.3 Fourier-transformed infrared spectroscopy (FTIR)

FTIR analysis was performed to analyze the functional groups in ACP. Furthermore, FTIR analysis investigated ADA modification and the Schiff-base formation in ADA-GEL. Samples were analyzed in transmission mode from the wavenumber ranging from 4,000 to 400 cm^{-1} with a resolution of 4 cm^{-1} (64 scans) using an iS50 FT-IR spectrometer (Thermo Scientific Nicolet Waltham, MA, USA).

2.4 Hydrogel precursor solution

To prepare ADA-GEL bioink, 5% (w/v) GEL solution was prepared in Milli-Q® water at 37° C and filtered through 0.22µm Millipore filters (Rotilab-syringe filter, PVDF Carl Roth). 5% (w/v) ADA solution was prepared in Dulbecco's phosphate buffer saline (DPBS) at 37° C and filtered through 0.45µm Millipore filters (Rotilab-syringe filter, PVDF Carl Roth). The solutions of ADA and GEL were filtered only when sterile working conditions were required; otherwise, unfiltered solutions were used.

The following procedure was used to synthesize ACP-reinforced ADA-GEL hydrogels. Initially, sterile synthesis of ACP was performed in which 150 mM calcium acetate, 100 mM trisodium phosphate, and 3M NaOH solutions were filtered through 0.22µm Millipore filters. Moreover, 50 mM of calcium citrate was autoclaved at 121°C at 15 psi for 30 min. ACP synthesis was performed under sterile conditions by the procedure mentioned in section 2.1. Sterile ACP was only synthesized when such working conditions were required. For hydrogel synthesis, 2% (w/v) ACP was added to 5% (w/v) ADA solution and stirred for 5 min until a homogeneous suspension was formed. Further, 5% (w/v) GEL solution was added in a 1:1 ratio and allowed to stir for 10 min at 37°C for Schiff's base formation. The same procedure was utilized for both ACP_CIT and ACP_ACE. ADA-GEL hydrogel

was used as a control to allow for comparison with ACP-reinforced ADA-GEL hydrogels. The final concentration of the formulated hydrogel was 2.5% (w/v) ADA, 2.5% (w/v) GEL, and 1% (w/v) ACP.

2.5 Oscillatory shear tests

The printability of the hydrogel is regulated by the viscoelastic properties of the material that must be adjusted to create a construct with long-term shape fidelity. Every material has its unique viscoelastic properties; for instance, GEL has weak mechanical strength and, hence, cannot be used on its own in bioprinting [44,45]. Therefore, to impart mechanical strength, ADA was used in this study. Moreover, ACP was incorporated in ADA-GEL for the development of a nanocomposite bioink. When a new bioink is developed, the oscillator shear test of the hydrogels is the first step in understanding its viscoelastic behavior. The tests were performed using an HR20 rheometer (TA Instruments, New Castle, USA) with a 25 mm diameter parallel plate for analysis. Initially, the linear viscoelastic region (LVE) was analyzed using an amplitude sweep performed under a constant frequency of 1 Hz and shear stress ranging from 0.1 to 100%.

Hydrogels are divided into several categories according to their rheological properties, i.e., Newtonian, shear thinning, and shear thickening fluids [46]. Shear thinning is an essential property of the hydrogels that determines the resolution, printing pattern, and shape fidelity by preventing shear stress, clogging, and cellular damage [46,47]. Viscosity was measured at a shear rate of 0.1 to 10 s^{-1} to analyze the flow behavior of ADA-GEL and ACP-reinforced ADA-GEL hydrogels. To analyze the effect of ACP on the viscoelastic properties of ADA-GEL hydrogel, frequency sweep analysis was performed under frequencies ranging from 0.1 to 10 Hz to analyze loss modulus (G") and storage modulus (G').

2.6 Printing optimization

Once the bioink was formulated, printing conditions were optimized to maximize resolution and repeatability. A sequential optimization approach was utilized to optimize printing pressure by keeping a constant printing speed of 2 mm/s. Printing pressure resulting in intact struts and pores was selected. Afterward, the printing speed was adjusted at constant optimized pressure. The construct was printed at different printing speeds to obtain square-shaped pores. The printing optimization was performed using uncross-linked ADA-GEL hydrogel. A small 8 x 8 mm^2 dimension construct was printed to avoid wasting the biomaterials and was further analyzed using a stereo microscope (Carl Zeiss, Jena, Germany). This test was performed to visually assess optimum printing conditions for ADA-GEL hydrogels. The optimized printing parameters were further utilized in fabricating the ADA-GEL and ACP-reinforced ADA-GEL constructs.

2.7 Cell printing process

2.7.1 Cell Culture

An osteoblast precursor cell line derived from mouse (*Mus musculus*) calvaria (MC3T3-E1, Sigma Aldrich, Germany) was employed for cellular analysis after 10 passages. MC3T3-E1 cells were maintained in an α-MEM medium containing 10 vol% Fetal bovine serum (FBS; Sigma Aldrich, Germany) and 10 vol% penicillin-streptomycin at 37°C in a humidified atmosphere of 95% air and 5% CO_2. The cultures of MC3T3-E1 cells were trypsinized by adding 3 ml of trypsin-EDTA solution. When the cells detached, 9 ml of α-MEM medium was

added to the T75 flask. The cells were counted, and $1x10^5$ cells/ml were inoculated into fresh T75 flasks, followed by incubation at 37°C in a humidified atmosphere of 95% air and 5% CO_2 for 24 h.

2.7.2 Cell printing

For the development of bioinks, MC3T3-E1 cells were encapsulated in ADA-GEL and ACP-reinforced ADA-GEL hydrogels. Cells were detached and diluted to a concentration of 20,000 cells/ml, centrifuged at 300 g for 5 min. The supernatant was removed, and the obtained cell pellet was mixed with the respective bioinks with the help of positive displacement pipettes. Further, 2 ml of bioinks were transferred to the bioprinting cartridges, closed with a blind plug, and incubated for 10 min at 4°C. Five-layer grid structures without an outline and outer dimension of 15 x 15 mm^2 were then printed into a six-well plate using a Cellink BioX printer equipped with a cool printhead at 23°C. The printing speed was fixed to 5 mm/s, and 65 kPa pressure was applied. Thirty seconds after the print was completed, the constructs were crosslinked with 100 mM $CaCl_2$ and 1% w/v Microbial transglutaminase (MTG) solutions (filtered through 0.22µm Millipore filters). Further, the samples were washed with Hanks balanced salts solution (HBSS), and α-MEM medium was added, followed by incubation at 37°C in a humidified atmosphere of 95% air and 5% CO_2 for 24 h. The printability index, average pore area, and cytocompatibility analysis were performed on days 1, 3, 7, and 14.

2.8 post-printing analysis

2.8.1 Semi-quantification of printability index

Under the ideal gelation condition of the bioink, a regular grid structure with square pores is formed in the construct. On the other hand, when the bioink is under gelation, the extruded filament shows a liquid-like state wherein the upper layer fuses with the lower layer, creating circular pores. To analyze the pore geometry on the printed constructs, a printability index was evaluated [48]. The circularity (C) of an enclosed area is defined as follows:

$$C = \frac{4\pi A}{L^2} \quad (1)$$

where L is the perimeter, and A is the area of the pore. Circles have the highest circularity where C equals 1, whereas, for the square shape, circularity equals $\pi/4$. Therefore, previous studies have defined the bioink printability index (Pr) based on square shape using the following function [49]:

$$\mathrm{Pr} = \frac{\pi}{4} \cdot \frac{1}{C} = \frac{L^2}{16A} \quad (2)$$

For an ideal gelation condition, the interconnected channels of the constructs would display a square shape with a Pr value of 1. The Pr>1 shows irregular pore geometry, while Pr<1 signifies curved geometry [50]. Optical images of ADA-GEL and ACP-reinforced ADA-GEL constructs were obtained using a stereo microscope. The circularity of pores (n=16) of each construct was analyzed using Image-J software (National Institute of Health, Maryland, USA), and Pr values were calculated [51]. The data are presented as averages of Pr values with standard deviation.

2.8.2 Construct stability analysis

The printed constructs were incubated for 14 days in cell culture medium. Over time, the average pore area analysis was performed on different time points (days 1, 3, 7, and 14) to assess the conformational changes in the printed constructs. The printed constructs were visualized under a stereo microscope. The area of 16 pores was evaluated using ImageJ software. The average pore area and standard deviations were calculated and compared with the theoretical pore area of 2 mm^2 of the single pore. Initially, the average area of the pore was utilized to evaluate the effect of ACP in ADA-GEL bioink. The stability was also examined by comparing the average pore area at different time points (days 1, 3, 7, and 14).

2.8.3 Rhodamine phalloidin/DAPI staining

Cellular constructs were examined under an epifluorescence microscope (Axio, Carl Zeiss, Jena, Germany) to assess cell orientation. Samples (n=3) were treated with 4% formaldehyde solution for 5 min in the dark. Subsequently, the sample was treated with 0.1% Triton-X solution for permeation. Further, the samples were washed twice with HBSS. Afterward, the samples were stained with 5 µl/ml solution of Rhodamine-Phalloidin staining (Thermofisher Scientific, USA) for 1 h followed by 1 µl/ml DAPI (Thermofisher Scientific, USA) solution for 5 min in the dark. Further, the samples were washed, immersed in HBSS solution, and analyzed under an epifluorescence microscope.

2.8.4 Two-Photon microscopy

To allow for the analysis of time-based three-dimensional cell distribution and qualitative morphometry inside of the different hydrogel formulations, two-photon microscopy image XYZ stacks were recorded using an ultra-fast laser-scanning multiphoton microscope (*TriMScope II,* LaVision Biotech GmbH, Bielefeld, Germany) in conjunction with a high numerical aperture (NA = 0.95) water immersion objective, *Leica HC FLUOTAR L 25x/0.95 W VISIR* (Leica Microsystems, Wetzlar, Germany). The fluorophores (Rhodamine, DAPI) were excited at a laser wavelength of 810 nm, with a pulse frequency of 80 MHz and an exponentially increasing output power from 60 to 320 mW (first to last image plane). The backward emission signal was chromatically separated with two bandpass filters (Rhodamine: CHROMA ET 560/40x; DAPI: CHROMA ET 450/30x; Chroma, Olching, Germany) and one dichroic mirror (CHROMA T495lpxr; Chroma, Olching, Germany) before it was eventually detected by two ultrasensitive transmission photomultiplier tube (H 7422-40 LV 5M, Hamamatsu Photonics, Herrsching, Germany). As morphometric analysis requires relatively high resolution, the imaging parameters were set to 1,024 x 1,024 pixels with a corresponding image size of 436 x 436 µm and a laser scanning frequency of 800 Hz, which results in a lateral pixel size of 0.43 µm and a pixel dwell time of 0.91 µs. Given the adjusted step size in the axial direction of 2 µm, the resulting voxel size is 0.43 x 0.43 x 2 µm. The height of each image stack varied according to the thickness of the printed filaments, but it ranged from approximately 300 µm to 580 µm. Therefore, each measurement yielded an image stack with 150 to 290 consecutive images. The three-dimensional image analysis and reconstruction were performed in ImageJ/FIJI [52][53].

3. Results and discussion

3.1 Characterization of ACP

The XRD analysis shown in Fig 1(A) indicates the XRD amorphous nature of synthesized ACP [54]. The FTIR spectra of the hydrogels are presented in Fig 1(B). The PO_4^{3-} group in ACP_ACE and ACP_CIT shows four

different vibrations: v_1 (950 cm^{-1}), v_2 (400 – 470 cm^{-1}), v_3 (1,000 – 1,150 cm^{-1}), and v_4 (500 – 620 cm^{-1}) [55,56]. In Fig 1(B), the ACP_ACE and ACP_CIT show v_1, v_3, and v_4 PO_4^{3-} vibrations. In ACP_CIT, the bands were observed at 1,600 cm^{-1} and 1,446 cm^{-1}, representing COO^- bending and COH stretching, respectively, of the carboxylic group in citrates [57]. Moreover, the peak at ~875 cm^{-1} was absent, indicating the incorporation of the COO^- group [58]. Similarly, in ACP_ACE, the band revealed at 675 cm^{-1} and 1,580 cm^{-1} corresponds to COO^- bending and stretching, and 1,440 cm^{-1} represents COH stretching of the acetate group [59]. The band observed at 884 cm^{-1} shows shifting of the HPO_4^{2-} group, indicating a possible association of the carboxylic group [58]. The HR-TEM analysis illustrated in Fig 1 (C and D) reveals the particle size of ACPC_CIT (~40 nm) and ACPC_ACE (~20 nm). The detailed characteristics such as density, NMR, XPS, surface area, and ion release kinetics of both ACP_CIT and ACP_ACE were presented in our previous article [43].

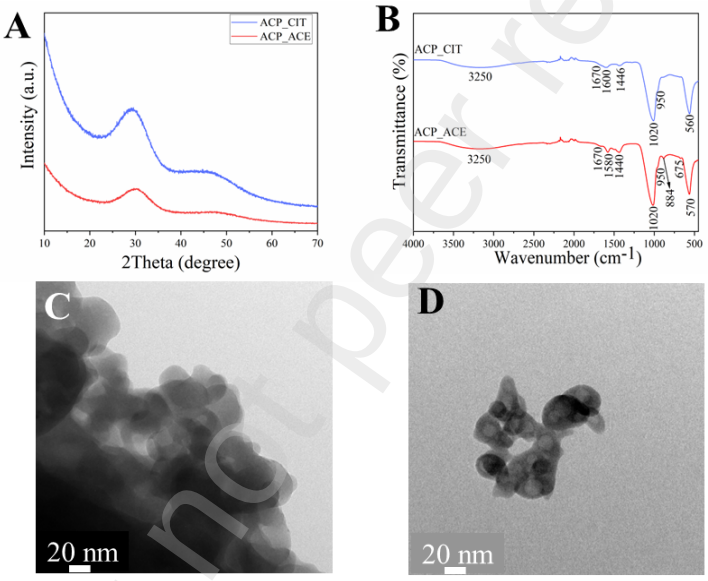

Figure 1. Characterization of synthesized ACPs. (A) X-Ray diffraction pattern showing amorphous ACP_ACE and ACP_CIT. (B) FTIR analysis confirming the presence of PO_4^{3-} and COO^- functional groups in ACP_CIT and ACP_ACE. (C and D) FEG-TEM micrographs revealing the morphology and particle size of the ACP_ACE (~20 nm) and ACP_CIT (~40 nm)

3.2 Fourier-transform infrared spectroscopy

In Fig 2 (A and B), Gelatin spectra show characteristic amide regions; the bands observed at wavenumbers 3,310 – 3,270 cm^{-1} (Amide A), 1,700 – 1,600 cm^{-1} (Amide I), 1,550 – 1,400 cm^{-1} (Amide II), and 1,240 - 670 cm^{-1} (Amide III) region of gelatin [60]. The characteristic polysaccharide structure of alginate was observed at 3,300 cm^{-1} (OH stretching), 2,900 cm^{-1} (-CH_2 stretching), 1,600 cm^{-1} (O-C-O asymmetric vibrations), 1,405 cm^{-1} (O-C-O symmetric vibrations and C-O-H bending), 1,084 cm^{-1} (C-O and C-C vibration arising from the pyranose

ring), 948 cm^{-1} (C-O vibrations from the uronic acid residue), 886 cm^{-1} and 809 cm^{-1} (in-plane bending of C1-H β-mannouronic residue) in all alginate and ADA containing samples [61].

In ADA-GEL, ADA-GEL-ACP_ACE, and ADA-GEL-ACP_CIT show peaks at 1,615 cm^{-1} (C=O vibrations) and 1,550 cm^{-1} (C=N vibrations), confirming crosslinking by the Schiff's base formation [62]. For ADA-GEL-ACPC_ACE and ADA-GEL-ACPC_CIT, the v_1 and v_3 of PO_4^{3-} fall within the range of ADA-GEL. Therefore, the analysis was complicated. However, the PO_4^{3-} v_2 vibrations were observed at 522 cm^{-1}in ADA-GEL-ACP_CIT and ADA-GEL-ACP_ACE.

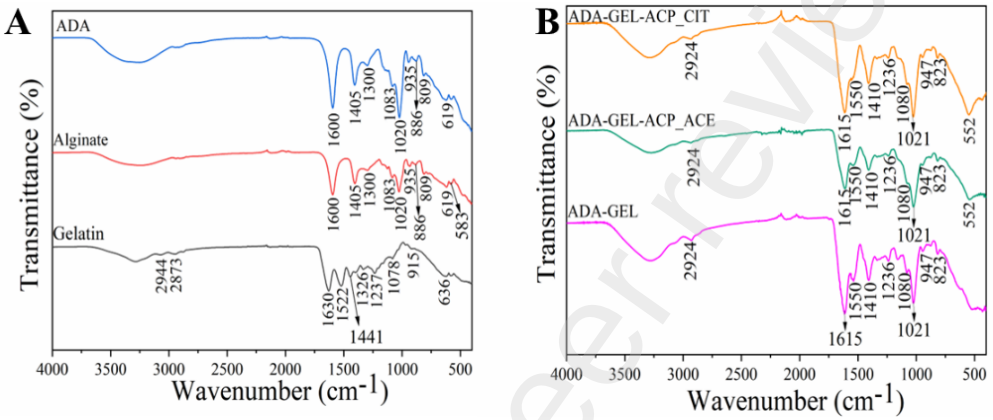

Figure 2. FTIR spectra of the A) precursor materials (gelatin, sodium alginate, and alginate dialdehyde) and B) of the composite materials (ADA-GEL, ADA-GEL-ACPC_ACE, and ADA-GEL-ACPC_CIT). The Schiff base formation in ADA-GEL hydrogel was confirmed from the peak observed at 1,615 cm^{-1} and 1,550 cm^{-1}. Moreover, the PO_4^{3-} band observed at 552 cm^{-1} in ADA-GEL-ACP_CIT and ADA-GEL-ACP_ACE samples confirmed the nanocomposite formation.

3.3 Oscillatory shear tests

The linear viscoelastic region (LVE) of the hydrogels provides an optimum range in which the oscillatory shear tests can be performed without harming the structural properties of the hydrogel. Therefore, amplitude sweep analysis is the first step in characterizing the viscoelastic behavior of hydrogels [44]. The LVE region of all the hydrogels falls within 20% of the strain, as shown in Fig 3 (A-C). Therefore, further analysis was performed under 1% strain.

The frequency sweep analysis was performed to analyze the storage moduli (G') and loss moduli (G") of the hydrogels as shown in Fig 3 (D-F). G' represents the solid-like while the G" corresponds to the liquid-like characteristics of the hydrogel. When G'>G", the hydrogel possesses gel-like behavior, termed a viscoelastic solid, and when G'<G", the hydrogel possesses liquid-like properties, termed a viscoelastic liquid [62]. For bioprinting applications, the hydrogel should possess G'>G" for filament formation and shape fidelity [63]. The formulated hydrogels of ADA-GEL and ACP reinforced ADA-GEL show G'>G", favorable for bioprinting of constructs. The G' and G" values of hydrogels were analyzed at the frequency of 0.01 Hz. The ADA-GEL hydrogel shows G' and G" of 78 ± 8 Pa and 3.4 ± 0.4 Pa, respectively. After reinforcement of ACP_ACE in ADA-

GEL hydrogel improved the G' and G" to 117 ± 15 Pa and 6.2 ± 0.4 Pa, respectively. On the other hand, reinforcement of ACP_CIT enhanced the G' and G" to 127 ± 14 Pa and 8 ± 1 Pa of ADA-GEL hydrogel.

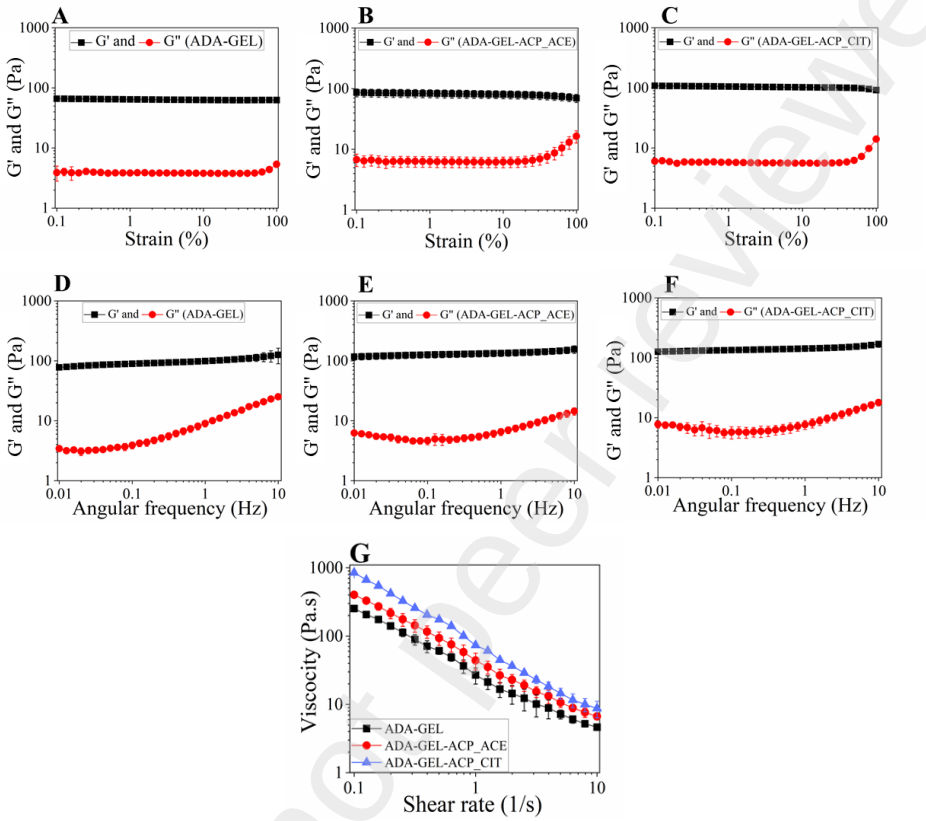

Figure 3. Oscillatory shear tests of ADA-GEL and ACP-reinforced ADA-GEL hydrogels. (A-C) Amplitude sweep analysis was performed to assess the LVE region of the hydrogel. (D-F) Frequency sweep analysis to examine (G') and loss moduli (G") of the hydrogels. Results indicate reinforcement of ACP in ADA-GEL enhances both G' and loss moduli G" of the ADA-GEL hydrogel. (G) Flow behavior analysis of hydrogels was performed by viscosity analysis against shear rate. An increase in the shear rate led to decreased viscosity, revealing the shear-thinning properties of hydrogels.

The flow behavior of hydrogels is an essential aspect of bioprinting. A hydrogel is a Newtonian fluid if the viscosity is independent of the shear rate, but cells will experience high shear on extrusion in this case. On the other hand, if a hydrogel is a non-Newtonian shear thinning fluid, a high shear will lower the viscosity of the hydrogel, resulting in the safe extrusion of cells [64]. The flow behavior of all formulated hydrogels possesses non-Newtonian shear thinning properties, as shown in Fig 3 (G).

3.4 Printing optimization

To find the printing window of the formulated bioinks, a trial-and-error method was performed. The crosslinking step was not performed in this analysis, and the construct was not immersed in any medium post-printing. Initially,

ADA-GEL hydrogel was utilized, and pressure was selected as a variable process parameter to keep the printing speed constant at 2 mm/sec. The printing was performed at different pressures, and the printed constructs were analyzed using stereo-electron microscopy, as shown in Fig 4(A). Printing below 45 kPa did not extrude as a filament; therefore, the construct was not deemed printable. The construct was formed at a printing pressure of 45 kPa; however, there were structural inconsistencies. The gaps in the struts are shown in Fig 4(A) with a red ellipse. These inconsistencies in the structures were due to non-uniform filament formation. On increasing the pressure, the inconsistencies within the construct were gradually reduced. The pressure of 65 kPa formed a construct without structural inconsistency, indicating uniform filament formation. However, the construct did not display square-shaped pore geometry; therefore, printing speed optimization was performed.

In the previous step, uniform filament formation was observed when the printing pressure was 65 kPa and the printing speed was 2 mm/s. The printing speed optimization shown in Fig 4(B) was performed by keeping constant a printing pressure of 65 kPa. Lowering the printing speed to 1 mm/s leads to over extrusion of materials observed from the reduced pore size. On the contrary, increasing speed to 3 mm/s showed minor changes in the pore geometry. The geometry of pores was gradually enhanced by increasing the printing speed. A squared-shaped pore geometry was formed at a printing speed of 5 mm/s. Further, increased printing speed enhanced the pore geometry; however, structural irregularities were observed. Therefore, a printing speed of 5 mm/s and 65 kPa pressure were used for cell printing experiments.

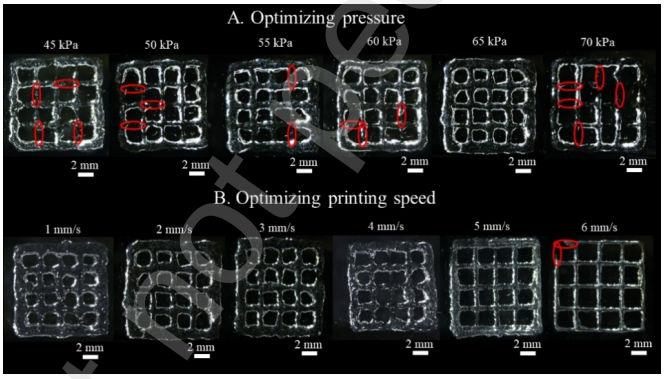

Figure 4. Trial-and-error approach for evaluating the optimum printing outcome for ADA-GEL hydrogels under different printing pressure and speed combinations. A) Initially, the printing pressure was assessed at a slow printing speed of 2 mm/s. B) To overcome this, printing was performed at different speeds, keeping the pressure at 65 kPa.

3.5 Post-printing analysis

The changes in the construct's pore geometry can be visually appreciated in Fig 5 (A-C). On day 1, the Pr value of ADA-GEL and ACP-reinforced ADA-GEL was close to 1, indicating the square shape geometry of pores. However, in ADA-GEL bioinks, a subsequent increase in the Pr value was observed on day 3 and day 7, signifying uneven pore geometry. By day 14, the Pr value of the construct dropped below 1, indicating circular porosity. In contrast, the ACP-reinforced bioinks showed decreasing Pr values, suggesting curved porosity. Notably,

compared to pristine ADA-GEL bioink, the Pr values of ACP-reinforced ADA_GEL bioinks remain relatively stable on days 3, 7, and 14.

Moreover, the changes of the construct pore area are presented in Fig 5 (D-F). On day 1 the average pore area of ADA-GEL- ACP_CIT construct was close to the calculated pore area of 2 mm^2. However, ADA-GEL- ACP_ACE and ADA-GEL construct exhibited reduced average pore area. Subsequently, a decrease in the average pore area was observed. In all the printed constructs after day 1, the reduction in the ADA-GEL bioink was rapid compared to ACP-reinforced ADA-GEL constructs. This analysis confirmed that ACP reinforcement in ADA-GEL hydrogel enhances the structural stability of the constructs. Notably, ACP_CIT was more effective in maintaining structural integrity compared to ACP_ACE.

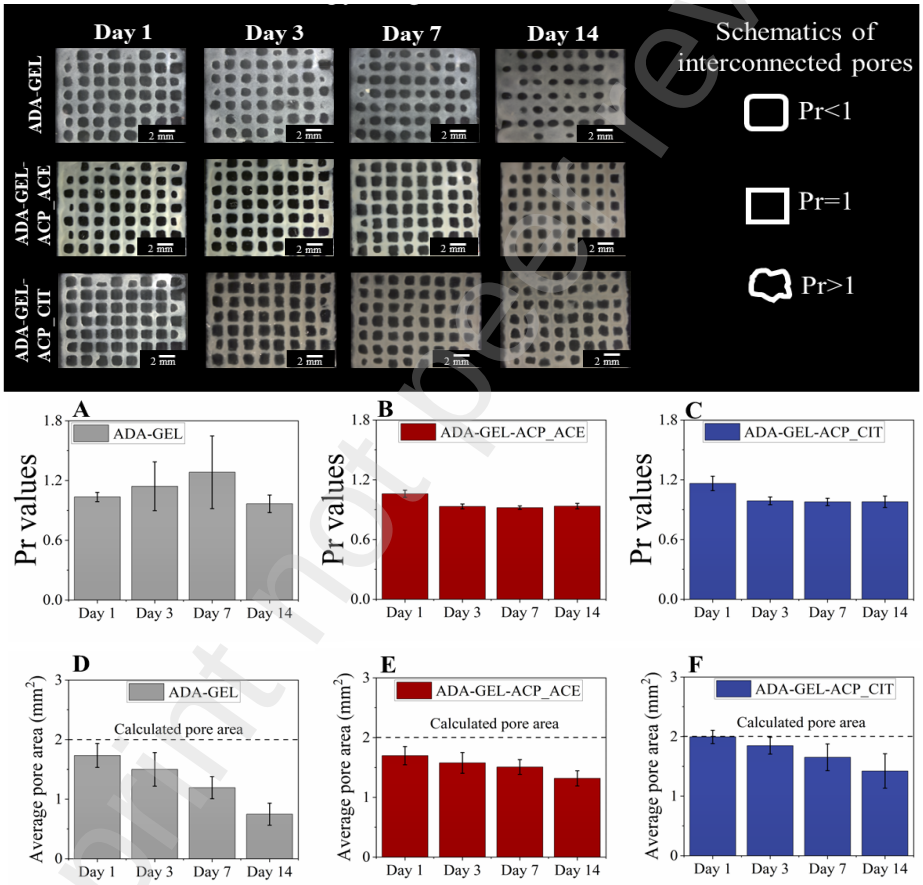

Figure 5. Post-printing analysis of the printed constructs of ADA-GEL and ACP reinforced ADA-GEL bioinks (ADA-GEL-ACP_ACE and ADA-GEL-ACP_CIT). Stereo microscopy image analysis was performed on days 1, 3, 7, and 14 (scale bar 2 mm). Printability index (Pr) and average pore area analysis were performed using image J analysis by selecting 16 pores. Pore geometry was evaluated by analyzing the Pr value; for instance, Pr<1 represents curved, Pr = 1 corresponds to square, and Pr>1 resembles variable pore geometry. (A-C) Pr values and

(D-F) average pore area. ADA-GEL bioinks show rapid conformational changes in pore geometry and reduction in the average pore area, indicating poor structural stability compared to ACP-reinforced ADA-GEL constructs.

3.6 Rhodamine phalloidin/DAPI staining

Rhodamine phalloidin staining was employed to stain F-actin (a structural and cytoskeletal protein), and DAPI was utilized to stain the nucleus of cells [65]. This staining allows for analyzing the morphology of the encapsulated MC3T3-E1 cells in the bioprinted constructs. ADA-GEL bioink was used as a positive control, and the effect of ACP_ACE and ACP_CIT on cells was analyzed. Fig 6 shows cellular attachment on day 1, followed by cell elongation, fusion, and network formation on the consecutive day points. The scaffold was entirely covered with cells on day 14, confirming the non-cytotoxic effect of ACP_ACE and ACP_CIT in the bioink.

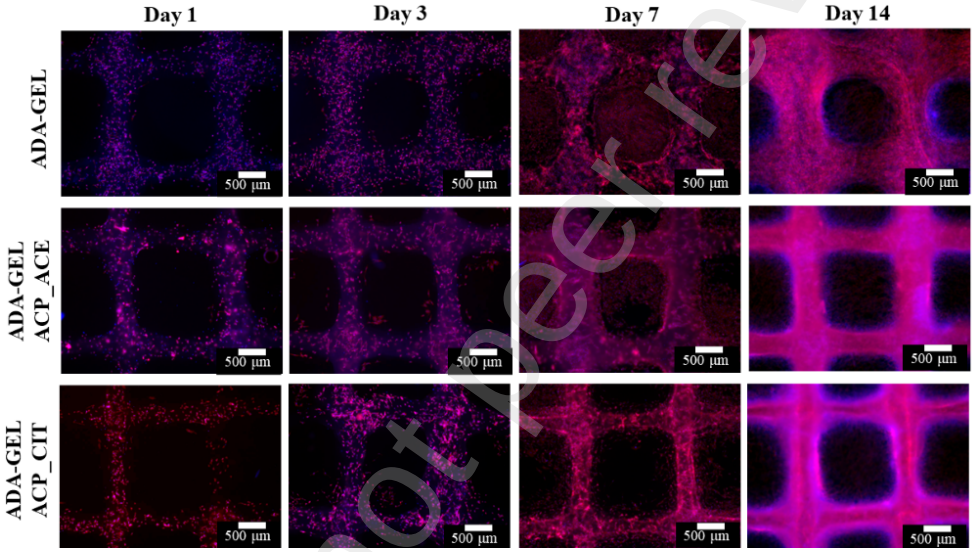

Figure 6. Epifluorescence microscopy of rhodamine-phalloidin (red) and DAPI (blue) staining of MC3T3-E1 cells embedded in ADA-GEL and ACP reinforced ADA-GEL constructs (ADA-GEL-ACP_ACE and ADA-GEL-ACP_ACE). (Scale bar 500µm).

3.7 Two-photon microscopy

The cytocompatibility analysis using an inverse epifluorescence microscope revealed the cytocompatibility of the constructs. Additionally, two-photon microscopy was performed to analyze the three-dimensional cell distribution within the biofabricated constructs at depth. This technique can resolve fluorescently labeled cells within thick, strongly scattering samples while reducing phototoxicity [66]. To provide a clear view of the cell distribution, the 3D reconstructions of the obtained two-photon microscopy image stacks are presented in Fig 7. The XY images (top-down view along the optical axis) indicate homogeneous distribution on the surface of the respective hydrogels. On the other hand, the YZ images (the stack was rotated by 90° around the Y axis) show how cells are colonized inside the respective bioinks. From the images, it can be concluded that the cell population gradually

grows over time in the constructs, supporting the results from the epifluorescence microscopy experiments. Moreover, the cells are well embedded into the constructs, confirming the fabricated bioinks' cytocompatibility.

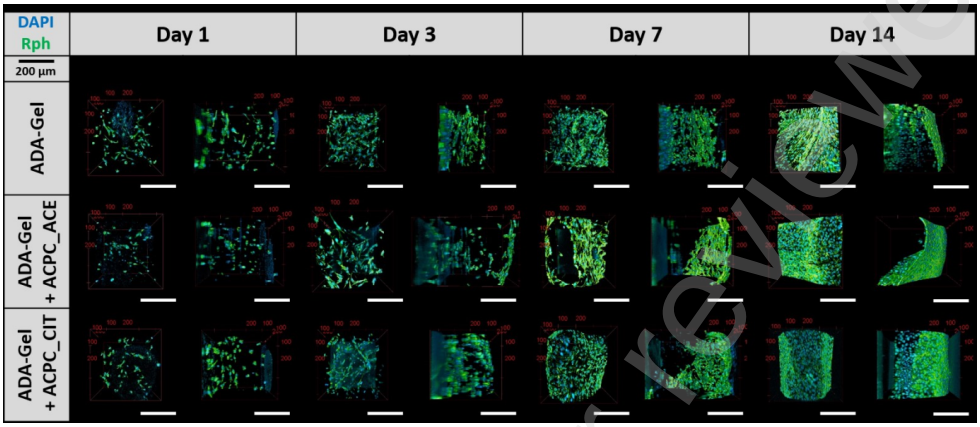

Figure 7. **Three-dimensionally reconstructed multiphoton microscopy images for qualitative morphometry and cell distribution analysis**.

Figure 7 shows two different viewing angles onto three-dimensionally reconstructed multiphoton image stacks. One representative image stack was chosen for each hydrogel composition, three-dimensionally reconstructed, and single images of the transversal (XY, top-down view along the optical axis) and the sagittal (YZ, rotated by 90 degrees) plane were taken. While the XY perspective allows for qualitative morphometry, the YZ perspective provides the opportunity to qualitatively determine the homogeneity of the cell distribution inside the hydrogel filament. The green Lookup-Table represents actin filaments stained with Rhodamine-Phalloidin, and the blue table shows the cell nuclei stained with DAPI.

4. Discussion

The study centers on developing ACP-reinforced ADA-GEL nanocomposite bioink for bone tissue regeneration using 3D printing technology. To create biomimetic nanocomposite bioinks, ACP was used as an inorganic component, inspired by its natural role in bone formation. Two types of ACP were used: ACP_CIT and ACP_ACE. These ACPs were combined with a hydrogel system made up of ADA-GEL. The goal was to evaluate the suitability of these bioinks for bone tissue engineering applications including characterization of bioink printability.

The rheological and post-printing analysis confirmed the reinforcement behavior of both ACP_CIT and ACP_ACE. Moreover, ACP_CIT offers better structural stability to the scaffold compared to ACP_ACE. The superior calcium and phosphate release of ACP_CIT (shown in Fig 8) may be responsible for this behavior [45]. The ion release kinetics is critical as calcium ions crosslink ADA. The higher release of calcium ions in ACP_CIT may help to enhance the crosslinking of ADA, thus contributing to the structural stability of the constructs [3,39].

Another mechanism that might be contributing to the mechanical behavior of the bioinks is citrate-GEL crosslinking [67]. The free carboxyl group of citrates in ACP_CIT can potentially react with the amine group of GEL to form amide bonds. ADA, GEL, or both can be crosslinked with ACP_CIT. However, more advanced analyses are required to confirm the exact mechanism.

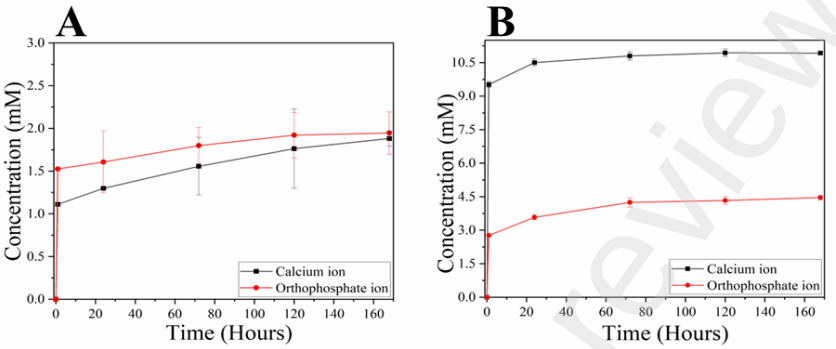

Figure 8. Ion release kinetics measured on (A) ACP_ACE and (B) ACP_CIT samples. The image is taken from "Amorphous calcium phosphate and amorphous calcium phosphate carboxylate: Synthesis and Characterization" (Indurkar et al., 2023) [43]. (Reproduced from the Open Access paper according to the license CC-BY 4.0)

Furthermore, particle size can also play a crucial role in maintaining the structural integrity of the constructs. ACP_ACE has a smaller particle size (~20 nm) than ACP_CIT (~40 nm). Smaller particle size provides higher surface area and a higher agglomeration tendency, thus affecting the structural integrity [68].

In summary, developing ADA-GEL nanocomposite bioinks reinforced with ACP_ACE or ACP_CIT is a promising approach for obtaining scaffolds for tissue regeneration application by bioprinting. These nanocomposite bioinks present a biomimetic approach and have shown enhanced mechanical stability and structural integrity compared to the pristine ADA-GEL hydrogels. This research contributes to the understanding of ACP-based bioink development and shows the importance of citrate in enhancing the structural stability of the printed constructs.

Moreover, the developed nanocomposite hydrogels can be considered for broader applications, including 3D printing of various cell types such as mesenchymal stem cells and primary osteoprogenitor cells. By harnessing the unique properties of ACP and the stabilizing agent citrate, the study contributes to the field of ADA-GEL composite bioinks with improved printability.

5. Conclusion

Intending to develop biomimetic nanocomposite bioinks, we have utilized citrate stabilized ACP (ACP_CIT) or non-stabilized ACP (ACP_ACE) as the inorganic component and ADA-GEL as the organic bioink component. The incorporation of ACP significantly improved the viscoelastic properties of the ADA-GEL hydrogel. The bioinks were developed by embedding MC3T3-E1 cells into the respective hydrogels. For imparting structural integrity, $CaCl_2$ and MTG were used as crosslinking agents. Post-printing analysis (printability index and average

pore size) was performed, and the stability of the constructs was analyzed. Results revealed that ADA-GEL-ACP_CIT constructs were the most stable compared to ADA-GEL-ACP_ACE, and minimum stability was observed in ADA-GEL constructs. The cellular analysis attested the cytocompatibility of the bioinks. Further research should delve deeper into the specific properties of these bioinks and their interaction with different cell types, ultimately advancing the prospects of personalized bone tissue regeneration and repair.

6. Acknowledgment

The authors acknowledge financial support from the European Union's Horizon 2020 research and innovation program under grant agreement No. 857287 (BBCE) and Baltic Research Programme Project No. EEA-RESEARCH-85 "Waste-to-resource: eggshells as a source for next generation biomaterials for bone regeneration (EGGSHELL)" under the EEA Grant of Iceland, Liechtenstein and Norway No. EEZ/BPP/VIAA/2021/1. J.B. and O.F. and S.H. were financially supported by Deutsche Forschungsgemeinschaft (DFG, German Research Foundation)—#326998133—TRR225 Biofabrication (subproject Z02 to OF and subproject BO3 to ARB).

7. CRediT authorship contribution statement

Abhishek Indurkar: Conceptualization, Literature review, Methodology, Investigation, Data curation, Writing-original draft preparation. **Susanne Heid:** Bioprinting Methodology, Investigation, writing and editing. **Julian Bauer:** Two-photon microscopy experiments and data curation, writing, and editing, **Kristaps Rubenis:** Methodology, Writing and editing, **Oliver Friedrich**: Supervision, Writing and editing. **Janis Locs:** Conceptualization, Supervision, Resources, Writing, and Editing. **Aldo R. Boccaccini:** Conceptualization, Supervision, Resources, Writing, and Editing. All authors provided critical feedback and helped to shape the research, analysis, and manuscript.

The raw/processed data required to reproduce these findings cannot be shared at this time due to technical limitations. However, the data can be requested from the corresponding author.

8. Reference

[1] D. Kim, J.U. Lee, G.H. Kim, Biomimetic gelatin/HA biocomposites with effective elastic properties and 3D-structural flexibility using a 3D-printing process, Addit. Manuf. 36 (2020) 101616. https://doi.org/10.1016/J.ADDMA.2020.101616.

[2] N. Li, R. Guo, Z.J. Zhang, Bioink Formulations for Bone Tissue Regeneration, Front. Bioeng. Biotechnol. 9 (2021) 630488. https://doi.org/10.3389/FBIOE.2021.630488/BIBTEX.

[3] S. Heid, K. Becker, J. Byun, I. Biermann, Z. Neščáková, H. Zhu, J. Groll, A.R. Boccaccini, Bioprinting with bioactive alginate dialdehyde-gelatin (ADA-GEL) composite bioinks: Time-dependent in-situ crosslinking via addition of calcium-silicate particles tunes in vitro stability of 3D bioprinted constructs, Bioprinting. 26 (2022) e00200. https://doi.org/10.1016/J.BPRINT.2022.E00200.

[4] A. Indurkar, R. Choudhary, K. Rubenis, J. Locs, Role of carboxylic organic molecules in interfibrillar collagen mineralization, Front. Bioeng. Biotechnol. 11 (2023) 439. https://doi.org/10.3389/FBIOE.2023.1150037.

[5] A.L. Lehninger, Mitochondria and Calcium Ion Transport THE FIFTH JUBILEE LECTURE, Biochem. J. 119 (1970) 129–138.

[6] L. Zhu, D. Luo, Y. Liu, Effect of the nano/microscale structure of biomaterial scaffolds on bone regeneration, Int. J. Oral Sci. 2020 121. 12 (2020) 1–15. https://doi.org/10.1038/s41368-020-0073-y.

[7] G. Cidonio, M. Cooke, M. Glinka, J.I. Dawson, L. Grover, R.O.C. Oreffo, Printing bone in a gel: using nanocomposite bioink to print functionalised bone scaffolds, Mater. Today Bio. 4 (2019) 100028. https://doi.org/10.1016/J.MTBIO.2019.100028.

[8] N. Masne, R. Ambade, K. Bhugaonkar, Use of Nanocomposites in Bone Regeneration, Cureus. 14 (2022). https://doi.org/10.7759/CUREUS.31346.

[9] Z. Yao, J. Xu, J. Shen, L. Qin, W. Yuan, Biomimetic Hierarchical Nanocomposite Hydrogels: From Design to Biomedical Applications, J. Compos. Sci. 2022, Vol. 6, Page 340. 6 (2022) 340. https://doi.org/10.3390/JCS6110340.

[10] S. Sagadevan, R. Schirhagl, M.Z. Rahman, M.F. Bin Ismail, J.A. Lett, I. Fatimah, N.H. Mohd Kaus, W.C. Oh, Recent advancements in polymer matrix nanocomposites for bone tissue engineering applications, J. Drug Deliv. Sci. Technol. 82 (2023) 104313. https://doi.org/10.1016/J.JDDST.2023.104313.

[11] H.H.K. Xu, J.L. Moreau, L. Sun, L.C. Chow, Nanocomposite containing amorphous calcium phosphate nanoparticles for caries inhibition, Dent. Mater. 27 (2011) 762–769. https://doi.org/10.1016/J.DENTAL.2011.03.016.

[12] F. Chen, B. Yang, C. Qi, T.W. Sun, Y.Y. Jiang, J. Wu, X. Chen, Y.J. Zhu, An amorphous calcium phosphate nanocomposite for storing and sustained release of IgY protein with antibacterial activity, RSC Adv. 5 (2015) 100682–100688. https://doi.org/10.1039/C5RA19065G.

[13] Y. Jiang, S. Tan, J. Hu, X. Chen, F. Chen, Q. Yao, Z. Zhou, X. Wang, Z. Zhou, Y. Fan, J. Liu, Y. Lin, L. Liu, S. He, Amorphous calcium magnesium phosphate nanocomposites with superior osteogenic activity for bone regeneration, Regen. Biomater. 8 (2021) 1–11. https://doi.org/10.1093/RB/RBAB068.

[14] R. Sun, M. Åhlén, C.W. Tai, É.G. Bajnóczi, F. de Kleijne, N. Ferraz, I. Persson, M. Strømme, O. Cheung, Highly Porous Amorphous Calcium Phosphate for Drug Delivery and Bio-Medical Applications, Nanomater. 2020, Vol. 10, Page 20. 10 (2019) 20. https://doi.org/10.3390/NANO10010020.

[15] M.D. Weir, L.C. Chow, H.H.K. Xu, Remineralization of Demineralized Enamel via Calcium Phosphate Nanocomposite, Http://Dx.Doi.Org/10.1177/0022034512458288. 91 (2012) 979–984. https://doi.org/10.1177/0022034512458288.

[16] E.T. Hwang, R. Tatavarty, J. Chung, M.B. Gu, New functional amorphous calcium phosphate nanocomposites by enzyme-assisted biomineralization, ACS Appl. Mater. Interfaces. 5 (2013) 532–537. https://doi.org/10.1021/AM302580P/ASSET/IMAGES/MEDIUM/AM-2012-02580P_0010.GIF.

[17] L. Cheng, M.D. Weir, H.H.K. Xu, J.M. Antonucci, N.J. Lin, S. Lin-Gibson, S.M. Xu, X. Zhou, Antibacterial nanocomposites containing amorphous calcium phosphate and silver nanoparticles with different filler levels, J. Biomed. Mater. Res. - Part B Appl. Biomater. 100 (2012) 1378–1386. https://doi.org/10.1002/JBM.B.32709.

[18] L. Cheng, M.D. Weir, H.H.K. Xu, J.M. Antonucci, A.M. Kraigsley, N.J. Lin, S. Lin-Gibson, X. Zhou, Antibacterial amorphous calcium phosphate nanocomposites with a quaternary ammonium dimethacrylate and silver nanoparticles., Dent. Mater. 28 (2012) 561–572. https://doi.org/10.1016/J.DENTAL.2012.01.005.

[19] J. Buschmann, L. Härter, S. Gao, S. Hemmi, M. Welti, N. Hild, O.D. Schneider, W.J. Stark, N. Lindenblatt, C.M.L. Werner, G.A. Wanner, M. Calcagni, Tissue engineered bone grafts based on biomimetic nanocomposite PLGA/amorphous calcium phosphate scaffold and human adipose-derived stem cells, Injury. 43 (2012) 1689–1697. https://doi.org/10.1016/J.INJURY.2012.06.004.

[20] P. Wolint, L. Näf, D. Schibler, N. Hild, W.J. Stark, P. Giovanoli, M. Calcagni, J. Buschmann, Suspension of amorphous calcium phosphate nanoparticles impact commitment of human adipose-derived stem cells in vitro, Biology (Basel). 10 (2021) 675. https://doi.org/10.3390/BIOLOGY10070675/S1.

[21] X. Hou, L. Zhang, Z. Zhou, X. Luo, T. Wang, X. Zhao, B. Lu, F. Chen, L. Zheng, Calcium Phosphate-Based Biomaterials for Bone Repair, J. Funct. Biomater. 13 (2022). https://doi.org/10.3390/JFB13040187.

[22] X. Niu, Z. Liu, F. Tian, S. Chen, L. Lei, T. Jiang, Q. Feng, Y. Fan, Sustained delivery of calcium and orthophosphate ions from amorphous calcium phosphate and poly(L-lactic acid)-based electrospinning nanofibrous scaffold, Sci. Reports 2017 71. 7 (2017) 1–9. https://doi.org/10.1038/srep45655.

[23] Y. Liu, N. Li, Y.P. Qi, L. Dai, T.E. Bryan, J. Mao, D.H. Pashley, F.R. Tay, Intrafibrillar Collagen Mineralization Produced by Biomimetic Hierarchical Nanoapatite Assembly, Adv. Mater. 23 (2011) 975. https://doi.org/10.1002/ADMA.201003882.

[24] F. Nudelman, A.J. Lausch, N.A.J.M. Sommerdijk, E.D. Sone, In vitro models of collagen biomineralization, J. Struct. Biol. 183 (2013) 258–269. https://doi.org/10.1016/J.JSB.2013.04.003.

[25] Y. Chen, W. Gu, H. Pan, S. Jiang, R. Tang, Stabilizing amorphous calcium phosphate phase by citrate adsorption, CrystEngComm. 16 (2014) 1864–1867. https://doi.org/10.1039/C3CE42274G.

[26] D. Krogstad, D. Wang, S. Lin-Gibson, The role of polyelectrolytes in the stabilization of calcium phosphate nanoparticles for the production of biomimetic materials, APS. 2014 (2014) W11.009. https://ui.adsabs.harvard.edu/abs/2014APS..MARW11009K/abstract (accessed July 2, 2023).

[27] M. Schweikle, S.H. Bjørnøy, A.T.J. van Helvoort, H.J. Haugen, P. Sikorski, H. Tiainen, Stabilisation of amorphous calcium phosphate in polyethylene glycol hydrogels, Acta Biomater. 90 (2019) 132–145. https://doi.org/10.1016/J.ACTBIO.2019.03.044.

[28] M. Schweikle, S.H. Bjørnøy, A.T.J. van Helvoort, H.J. Haugen, P. Sikorski, H. Tiainen, Stabilisation of amorphous calcium phosphate in polyethylene glycol hydrogels, Acta Biomater. 90 (2019) 132–145. https://doi.org/10.1016/J.ACTBIO.2019.03.044.

[29] S. Chen, D. Liu, L. Fu, B. Ni, Z. Chen, J. Knaus, E. V Sturm, B. Wang, H.J. Haugen, H. Yan, H. Cölfen, B. Li, Formation Of Amorphous Iron-Calcium Phosphate With High Stability, Adv. Mater. (2023) 2301422. https://doi.org/10.1002/ADMA.202301422.

[30] W. Jin, Z. Liu, Y. Wu, B. Jin, C. Shao, X. Xu, R. Tang, H. Pan, Synergic Effect of Sr2+ and Mg2+ on the Stabilization of Amorphous Calcium Phosphate, Cryst. Growth Des. 18 (2018) 6054–6060. https://doi.org/10.1021/ACS.CGD.8B00908.

[31] N.C. Williams, L.A.J. O'Neill, A Role for the Krebs Cycle Intermediate Citrate in Metabolic Reprogramming in Innate Immunity and Inflammation, Front. Immunol. 9 (2018) 1. https://doi.org/10.3389/FIMMU.2018.00141.

[32] B. Xie, G.H. Nancollas, How to control the size and morphology of apatite nanocrystals in bone, Proc. Natl. Acad. Sci. U. S. A. 107 (2010) 22369. https://doi.org/10.1073/PNAS.1017493108.

[33] Y.Y. Hu, A. Rawal, K. Schmidt-Rohr, Strongly bound citrate stabilizes the apatite nanocrystals in bone, Proc. Natl. Acad. Sci. U. S. A. 107 (2010) 22425–22429. https://doi.org/10.1073/PNAS.1009219107/ASSET/B53276B2-073E-40A7-B8F7-E28AC70040CD/ASSETS/GRAPHIC/PNAS.1009219107EQ8.GIF.

[34] D. Granchi, N. Baldini, F.M. Ulivieri, R. Caudarella, Role of Citrate in Pathophysiology and Medical Management of Bone Diseases, Nutrients. 11 (2019). https://doi.org/10.3390/NU11112576.

[35] L.C. Costello, R.B. Franklin, M.A. Reynolds, M. Chellaiah, The Important Role of Osteoblasts and Citrate Production in Bone Formation: "Osteoblast Citration" as a New Concept for an Old Relationship, Open Bone J. 4 (2012) 27–34. https://doi.org/10.2174/1876525401204010027.

[36] C. Shao, R. Zhao, S. Jiang, S. Yao, Z. Wu, B. Jin, Y. Yang, H. Pan, R. Tang, Citrate Improves Collagen Mineralization via Interface Wetting: A Physicochemical Understanding of Biomineralization Control, Adv. Mater. 30 (2018). https://doi.org/10.1002/ADMA.201704876.

[37] T. Fukunishi, T. Shoji, T. Shinoka, Nanofiber composites in vascular tissue engineering, Nanofiber Compos. Biomed. Appl. (2017) 455–481. https://doi.org/10.1016/B978-0-08-100173-8.00018-1.

[38] M.B. Łabowska, K. Cierluk, A.M. Jankowska, J. Kulbacka, J. Detyna, I. Michalak, A Review on the Adaption of Alginate-Gelatin Hydrogels for 3D Cultures and Bioprinting, Materials (Basel). 14 (2021) 1–28. https://doi.org/10.3390/MA14040858.

[39] S. Reakasame, A. R. Boccaccini, Oxidized Alginate-Based Hydrogels for Tissue Engineering Applications: A Review. Biomacromolecules 19 (2018) 3–21. https://doi.org/10.1021/acs.biomac.7b01331

[40] G. Gao, A.F. Schilling, T. Yonezawa, J. Wang, G. Dai, X. Cui, Bioactive nanoparticles stimulate bone

tissue formation in bioprinted three-dimensional scaffold and human mesenchymal stem cells, Biotechnol. J. 9 (2014) 1304–1311. https://doi.org/10.1002/biot.201400305.

[41] A. Habib, B. Khoda, Development of clay based novel hybrid bio-ink for 3D bio-printing process, J. Manuf. Process. 38 (2019) 76–87.

[42] W. Kim, G. Kim, Collagen/bioceramic-based composite bioink to fabricate a porous 3D hASCs-laden structure for bone tissue regeneration, Biofabrication. 12 (2020) 1–12. https://doi.org/10.1088/1758-5090/ab436d.

[43] A. Indurkar, R. Choudhary, K. Rubenis, M. Nimbalkar, A. Sarakovskis, A. R. Boccaccini, J. Locs, Amorphous Calcium Phosphate and Amorphous Calcium Phosphate Carboxylate: Synthesis and Characterization, ACS Omega. 8 (2023) 26782–26792. https://doi.org/10.1021/acsomega.3c00796.

[44] B. Sarker, D.G. Papageorgiou, R. Silva, T. Zehnder, F. Gul-E-Noor, M. Bertmer, J. Kaschta, K. Chrissafis, R. Detsch, A.R. Boccaccini, Fabrication of alginate-gelatin crosslinked hydrogel microcapsules and evaluation of the microstructure and physico-chemical properties, J. Mater. Chem. B. 2 (2014) 1470–1482. https://doi.org/10.1039/c3tb21509a.

[45] H. Mao, L. Yang, H. Zhu, L. Wu, P. Ji, J. Yang, Z. Gu, Recent advances and challenges in materials for 3D bioprinting, Prog. Nat. Sci. Mater. Int. 30 (2020) 618–634. https://doi.org/10.1016/J.PNSC.2020.09.015.

[46] B. Rehm, A. Haghshenas, Flow Drilling: Underbalance Drilling with Liquid Single-Phase Systems, Underbalanced Drill. Limits Extrem. (2012) 39–108. https://doi.org/10.1016/B978-1-933762-05-0.50009-7.

[47] Y. Wu, A. Wenger, H. Golzar, X. (Shirley) Tang, 3D bioprinting of bicellular liver lobule-mimetic structures via microextrusion of cellulose nanocrystal-incorporated shear-thinning bioink, Sci. Reports 2020 101. 10 (2020) 1–12. https://doi.org/10.1038/s41598-020-77146-3.

[48] H. Jongprasitkul, S. Turunen, V.S. Parihar, M. Kellomäki, Two-step crosslinking to enhance the printability of methacrylated gellan gum biomaterial ink for extrusion-based 3D bioprinting, Bioprinting. 25 (2022). https://doi.org/10.1016/J.BPRINT.2021.E00185.

[49] S. Kyle, Z.M. Jessop, A. Al-Sabah, I.S. Whitaker, 'Printability'' of Candidate Biomaterials for Extrusion Based 3D Printing: State-of-the-Art,' Adv. Healthc. Mater. 6 (2017). https://doi.org/10.1002/ADHM.201700264.

[50] L. Ouyang, 3D Bioprinting of Thermal-Sensitive Bioink, (2019) 63–80. https://doi.org/10.1007/978-981-13-9455-3_5.

[51] W. Rasband, ImageJ, U.S. National Institutes of Health, Bethesda, Maryland, USA, (2011).

[52] J. Schindelin, I. Arganda-Carreras, E. Frise, V. Kaynig, M. Longair, T. Pietzsch, S. Preibisch, C. Rueden, S. Saalfeld, B. Schmid, J.Y. Tinevez, D.J. White, V. Hartenstein, K. Eliceiri, P. Tomancak, A. Cardona, Fiji: an open-source platform for biological-image analysis, Nat. Methods 2012 97. 9 (2012)

676–682. https://doi.org/10.1038/nmeth.2019.

[53] J. Schindelin, I. Arganda-Carreras, E. Frise, V. Kaynig, M. Longair, T. Pietzsch, S. Preibisch, C. Rueden, S. Saalfeld, B. Schmid, J.Y. Tinevez, D.J. White, V. Hartenstein, K. Eliceiri, P. Tomancak, A. Cardona, Fiji: an open-source platform for biological-image analysis, Nat. Methods 2012 97. 9 (2012) 676–682. https://doi.org/10.1038/nmeth.2019.

[54] K. Rubenis, S. Zemjane, J. Vecstaudza, K. Lazdovica, J. Bitenieks, P. Wiecinski, A. Indurkar, J. Locs, Sintering of amorphous calcium phosphate to near-full density by uniaxial compaction at room temperature, J. Eur. Ceram. Soc. 42 (2022) 6199–6205. https://doi.org/10.1016/J.JEURCERAMSOC.2022.06.041.

[55] C. Rey, C. Combes, C. Drouet, D. Grossin, G. Bertrand, J. Soulié, 1.11 Bioactive Calcium Phosphate Compounds: Physical Chemistry, Compr. Biomater. II. (2017) 244–290. https://doi.org/10.1016/B978-0-12-803581-8.10171-7.

[56] M. Palencia, Functional transformation of Fourier-transform mid-infrared spectrum for improving spectral specificity by simple algorithm based on wavelet-like functions, J. Adv. Res. 14 (2018) 53–62. https://doi.org/10.1016/J.JARE.2018.05.009.

[57] P. Tarakeshwar, S. Manogaran, Ground state vibrations of citric acid and the citrate trianion—an ab initio study, Spectrochim. Acta Part A Mol. Spectrosc. 50 (1994) 2327–2343. https://doi.org/10.1016/0584-8539(94)E0017-5.

[58] M. Marković, W.E. Brown, B.O. Fowler, Octacalcium Phosphate Carboxylates. 2. Characterization and Structural Considerations, Chem. Mater. 5 (1993) 1406–1416. https://doi.org/10.1021/CM00034A008.

[59] T. V. Safronova, E.A. Mukhin, V.I. Putlyaev, A. V. Knotko, P. V. Evdokimov, T.B. Shatalova, Y.Y. Filippov, A. V. Sidorov, E.A. Karpushkin, Amorphous calcium phosphate powder synthesized from calcium acetate and polyphosphoric acid for bioceramics application, Ceram. Int. 43 (2017) 1310–1317. https://doi.org/10.1016/J.CERAMINT.2016.10.085.

[60] H.M. Elsayed, R.Z. Attia, O.A. Mohamed, N.H. El-Sayed, S.A. Ibrahim, High bloom gelatin strength from white leather shavings, Leather Footwear J. 18 (2018) 259–274. https://doi.org/10.24264/LFJ.18.4.2.

[61] A. Husni, S. Pawestri, A. Isnansetyo, Blood glucose level and lipid profile of alloxan–induced diabetic rats treated with na-alginate from seaweed turbinaria ornata (Turner) J.agardh, J. Teknol. 78 (2016) 7–14. https://doi.org/10.11113/JT.V78.8145.

[62] A. Indurkar, P. Bangde, M. Gore, A.K. Agrawal, R. Jain, P. Dandekar, Fabrication of guar gum-gelatin scaffold for soft tissue engineering, Carbohydr. Polym. Technol. Appl. 1 (2020) 100006. https://doi.org/10.1016/J.CARPTA.2020.100006.

[63] G. Kimbell, M.A. Azad, 3D printing: Bioinspired materials for drug delivery, Bioinspired Biomim. Mater. Drug Deliv. (2021) 295–318. https://doi.org/10.1016/B978-0-12-821352-0.00011-3.

[64] M.E. Cooke, D.H. Rosenzweig, The rheology of direct and suspended extrusion bioprinting, APL Bioeng. 5 (2021) 11502. https://doi.org/10.1063/5.0031475.

[65] K. Kapat, P.P. Maity, A.P. Rameshbabu, P.K. Srivas, P. Majumdar, S. Dhara, Simultaneous hydrothermal bioactivation with nano-topographic modulation of porous titanium alloys towards enhanced osteogenic and antimicrobial responses, J. Mater. Chem. B. 6 (2018) 2877–2893. https://doi.org/10.1039/C8TB00382C.

[66] B. O'rourke, M. Rubart, Two-Photon Microscopy of Cells and Tissue, Circ. Res. 95 (2004) 1154–1166. https://doi.org/10.1161/01.RES.0000150593.30324.42.

[67] M. Inoue, M. Sasaki, A. Nakasu, M. Takayanagi, T. Taguchi, An antithrombogenic citric acid-crosslinked gelatin with endothelialization activity, Adv. Healthc. Mater. 1 (2012) 573–581. https://doi.org/10.1002/ADHM.201200001.

[68] Y. Cai, S.Y. Chang, S.W. Gan, S. Ma, W.F. Lu, C.C. Yen, Nanocomposite bioinks for 3D bioprinting, Acta Biomater. 151 (2022) 45–69. https://doi.org/10.1016/J.ACTBIO.2022.08.014.

7. PIELIKUMS / APPENDIX 7

7. PUBLIKĀCIJA / PUBLICATION

Indurkar, A., Rubenis, K., A., Boccaccini, A. R., & Locs, J. Development of nanocomposite hydrogel using citrate-containing amorphous calcium phosphate and gelatin methacrylate.

The article is currently uncer peer review in Frontiers Bioengnieering and Biotechnology

Development of nanocomposite hydrogel using citrate-containing amorphous calcium phosphate and gelatin methacrylate

Abhishek Indurkar[1], Kristaps Rubenis[1], Aldo R. Boccaccini[2], Janis Locs[3, 1*]

[1]Institute of Biomaterials and Bioengineering, Faculty of Natural Sciences and Technology, Riga Technical University, Riga, Pulka 3, LV-1007, Latvia, Latvia, [2]Institute of Biomaterials, Department of Materials Science and Engineering, Faculty of Technology, Friedrich Alexander University Erlangen-Nuremberg, Germany, [3]Riga Technical University, Latvia

Submitted to Journal:
Frontiers in Bioengineering and Biotechnology

Specialty Section:
Biomaterials

Article type:
Brief Research Report Article

Manuscript ID:
1421415

Received on:
22 Apr 2024

Journal website link:
www.frontiersin.org

Scope Statement

Nanocomposite hydrogels have emerged as promising materials for biomedical applications, particularly in bone tissue engineering. Our manuscript focuses on developing nanocomposite GELMA hydrogels through a chemical crosslinking approach, incorporating citrate-containing amorphous calcium phosphate (ACP_CIT). Through experimentation, including oscillatory shear tests and in vitro cytocompatibility analysis, we have demonstrated that our approach overcomes the challenges associated with traditional photo-crosslinking methods, offering a viable alternative for fabricating thicker nanocomposite hydrogels.

Conflict of interest statement

The authors declare a potential conflict of interest and state it below

The author(s) declared that they were an editorial board member of Frontiers, at the time of submission. This had no impact on the peer review process and the final decision

CRediT Author Statement

Abhishek Indurkar: Conceptualization, Data curation, Investigation, Methodology, Software, Validation, Writing – original draft. Aldo R. Boccaccini: Funding acquisition, Resources, Supervision, Validation, Writing – review & editing. Janis Locs: Formal Analysis, Funding acquisition, Resources, Supervision, Writing – review & editing. Kristaps Rubenis: Formal Analysis, Supervision, Validation, Writing – review & editing.

Keywords

nanocomposite hydrogel, amorphous calcium phosphate, Citrate-containing amorphous calcium phosphate, Gelatin methacrylate, chemical crosslinking, Biomaterials, bone tissue engineering

Abstract

Word count: 199

Nanocomposite hydrogels are suitable in bone tissue engineering due to their resemblance with the extracellular matrix, ability to match complex geometries, and ability to provide a framework for cell attachment and proliferation. The nanocomposite hydrogel comprises organic and inorganic counterparts. Gelatin methacrylate (GELMA) is an extensively used organic counterpart in tissue engineering due to its excellent biocompatibility, biodegradability, and bioactivity. The photo-crosslinking of GELMA presents a challenge when aiming to create thicker nanocomposite hydrogels due to opacity induced by fillers, which obstructs the penetration of ultraviolet (UV) light. Therefore, using a chemical crosslinking approach, we have developed nanocomposite GELMA hydrogel in this study by incorporating citrate-containing amorphous calcium phosphate (ACP_CIT). Ammonium persulfate (APS) and N, N, N', N'-Tetramethylethylenediamine (TEMED) were deployed to crosslink the methacrylate group of GELMA. The oscillatory shear tests have confirmed that crosslinking enhances both storage (G') and loss modulus (G") of GELMA. Subsequently, incorporation of ACP_CIT in GELMA hydrogel shows further enhancement in G' and G" values. In vitro, analysis of the developed hydrogels revealed that chemical crosslinking and incorporation of ACP_CIT do not compromise the cytocompatibility of the GELMA.Hence, for developing nanocomposite GELMA hydrogels employing APS/TEMED crosslinking emerges as a promising alternative to photo-crosslinking.

Funding information

The authors acknowledge financial support from the European Union's Horizon 2020 research and innovation program under grant agreement No. 857287 and Baltic Research Programme Project No. EEA-RESEARCH-85 "Waste-to-resource: eggshells as a source for next generation biomaterials for bone regeneration (EGGSHELL)" under the EEA Grant of Iceland, Liechtenstein and Norway No. EEZ/BPP/VIAA/2021/1.

Funding statement

The author(s) declare that financial support was received for the research, authorship, and/or publication of this article.

Ethics statements

Studies involving animal subjects

Generated Statement: Ethical approval was not required for the studies on animals in accordance with the local legislation and institutional requirements because only commercially available established cell lines were used.

Studies involving human subjects

Generated Statement: No human studies are presented in the manuscript.

Inclusion of identifiable human data

Generated Statement: No potentially identifiable images or data are presented in this study.

Data availability statement

Generated Statement: The raw data supporting the conclusions of this article will be made available by the authors, without undue reservation.

Development of nanocomposite hydrogel using citrate-containing amorphous calcium phosphate and gelatin methacrylate

Abhishek Indurkar[1,2], Kristaps Rubenis[1,2], Aldo R. Boccaccini[3], and Janis Locs[1,2*]

[1]Institute of Biomaterials and Bioengineering, Faculty of Natural Sciences and Technology, Riga Technical University, Riga, Pulka 3, LV-1007, Latvia

[2] Baltic Biomaterials Centre of Excellence, Headquarters at Riga Technical University, Kipsalas Street 6A, LV-1048 Riga, Latvia

[3] Institute of Biomaterials, Department of Material Science and Engineering, University of Erlangen-Nuremberg, 91058, Erlangen, Germany

[*]Corresponding author - janis.locs@rtu.lv

Abstract

Nanocomposite hydrogels are suitable in bone tissue engineering due to their resemblance with the extracellular matrix, ability to match complex geometries, and ability to provide a framework for cell attachment and proliferation. The nanocomposite hydrogel comprises organic and inorganic counterparts. Gelatin methacrylate (GELMA) is an extensively used organic counterpart in tissue engineering due to its excellent biocompatibility, biodegradability, and bioactivity. The photo-crosslinking of GELMA presents a challenge when aiming to create thicker nanocomposite hydrogels due to opacity induced by fillers, which obstructs the penetration of ultraviolet (UV) light. Therefore, using a chemical crosslinking approach, we have developed nanocomposite GELMA hydrogel in this study by incorporating citrate-containing amorphous calcium phosphate (ACP_CIT). Ammonium persulfate (APS) and N, N, N', N'-Tetramethylethylenediamine (TEMED) were deployed to crosslink the methacrylate group of GELMA. The oscillatory shear tests have confirmed that crosslinking enhances both storage (G') and loss modulus (G") of GELMA. Subsequently, incorporation of ACP_CIT in GELMA hydrogel shows further enhancement in G' and G" values. *In vitro*, analysis of the developed hydrogels revealed that chemical crosslinking and incorporation of ACP_CIT do not compromise the cytocompatibility of the GELMA. Hence, for developing nanocomposite GELMA hydrogels employing APS/TEMED crosslinking emerges as a promising alternative to photo-crosslinking.

Graphical abstract

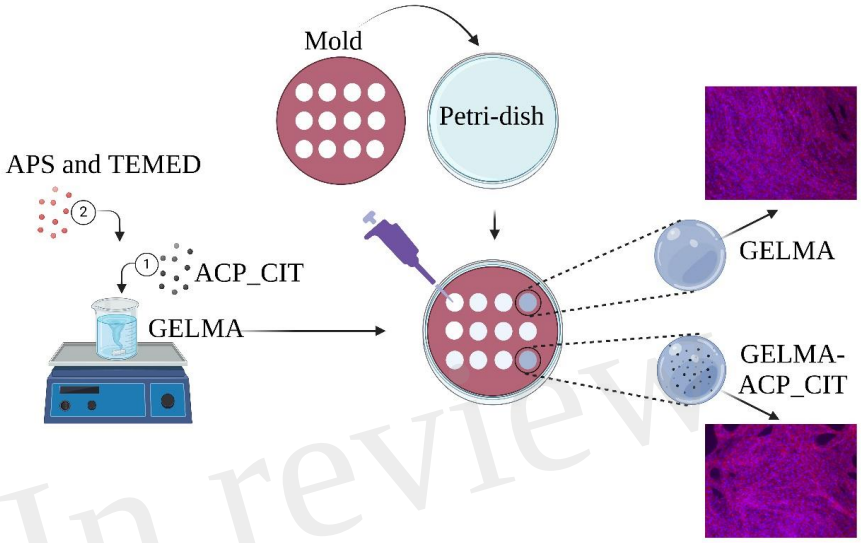

Keywords – Nanocomposite hydrogel, Amorphous calcium phosphate, Citrate-containing amorphous calcium phosphate, Gelatin methacrylate, Chemical crosslinking, Biomaterials, Bone Tissue Engineering

Introduction

The nanostructure arrangement of the extracellular matrix (ECM) provides appropriate physical and biological properties to bone. Nanocomposites are preferred for mimicking bone tissue as they provide an appropriate matrix environment and integrate desired biological properties (Sahoo et al., 2013). Nanocomposites comprise organic (hydrogel) and inorganic (nanofiller) components (Indurkar et al., 2023a). The organic component is conducive to cell proliferation, nutrient, and waste transport, while the nanofiller enhances mechanical properties by hydrogen bonding, hydrophobic interaction, or charge interactions with the hydrogel (Phogat et al., 2023). Nanocomposite hydrogels provide superior reinforcement potential, biomolecule delivery, and tunable degradability compared to pure hydrogel (Nallusamy and Das, 2021). Therefore, it can be considered a preferred strategy for bone tissue regeneration.

GELMA is an attractive material in tissue engineering due to its biocompatibility, biodegradability, bioactivity, and unique crosslinking properties in developing nanocomposite hydrogels. The versatile bio-functionality of GELMA arises from the arginine-lysine-aspartic acid (RGD) motifs essential for cell attachment (González-Gamboa et al., 2022). A commonly used method for crosslinking GELMA hydrogels is photo-crosslinking,

wherein ultraviolet (UV) light is used as a photoinitiator, which enters a high-energy radical state and acts on the reactive functional group of GELMA (Zhang et al., 2023). The major shortcoming of photo-crosslinking is limited light penetration depth caused by decreased light intensity along the height of the hydrogel to be cured. A 5 to 200 μm layer or up to a few millimeters can be cured effectively. However, as the height increases, the light intensity decreases, causing decaying light intensity within the material according to the Beer-Lambert law. The photoinitiator absorbs the incident light at the top of the hydrogel, leading to a top-to-bottom crosslinking gradient (Klikovits et al., 2022). Moreover, filler addition deteriorates hydrogel's transparency, further complicating the photo-crosslinking process. The incorporation of filler makes opaque hydrogels, which can reflect, refract, and absorb light, which decreases the intensity of penetration light (Gao et al., 2024).

A redox system that uses a chemical initiator (APS and TEMED) is relatively simple and effective in overcoming GELMA's shortcomings in developing nanocomposite hydrogels. Like photoinitiated crosslinking, the APS/TEMED crosslinking approach works on free radical polymerization. The addition of TEMED accelerates the scission of ammonium persulfate (APS), forming disulfide radicles and hydroxyl radicles (Seetharaman et al., 2017). These free radicles snatch one electron from the carbon-carbon double bonds in the methacrylate group of the GELMA monomer and later become free radicles, which binds the monomers together to form long aliphatic chains that are consequently crosslinked (Tsanaktsidou et al., 2019). The crosslinking mechanism is reported in previous studies (Park et al., 2018).

Amorphous calcium phosphate (ACP) is the precursor of hydroxyapatite (HAP) and possesses remineralization potential. However, due to ACP's metastability, it rapidly converts to HAP, resulting in a loss of remineralization activity (Yan et al., 2022). Various organic and inorganic stabilizing agents have been used previously to prolong the crystallization of ACP (Chen et al., 2014). In our previous study, we evaluated the effect of various small organic compounds on the transformation kinetics of ACP, wherein citrate has shown the most delayed transformation of ACP to apatite (Indurkar et al., 2023c). Therefore, in this study, we used citrate-containing ACP (ACP_CIT) as a nanofiller to develop nanocomposite GELMA hydrogels. The effect of ACP_CIT on the rheological properties of GELMA hydrogel was evaluated, and the *in vitro* analysis was performed using MC3T3-E1 cells to evaluate the effect of crosslinking and ACP_CIT.

2. Materials and methods

2.1 Materials

Calcium citrate tetrahydrate (CAS 5785-44-4), trisodium phosphate (CAS 7601-54-9), sodium hydroxide (CAS 1301-73-2), ammonium persulfate (CAS 7727-54-0), and N, N, N', N'-Tetramethylethylenediamine (CAS 110-18-9) were procured from Sigma Aldrich, Germany. Methacrylate gelatin (GELMA) with ~50 % degree of methacrylate was obtained from Cellink, Sweden. Hanks balanced salt solution (HBSS) was acquired from Gibco Life Technologies, Germany.

2.2 Synthesis of ACP_CIT

The synthesis of ACP_CIT was performed according to the previously reported procedure (Indurkar et al., 2023b). Briefly, the reaction was performed in a volume of 300 ml. Initially, 150 ml of 50 mM of calcium citrate solution was prepared in Milli-Q® water, followed by pH adjustment to 11.5 using 2M sodium hydroxide. Subsequently,

150 ml of 100 mM trisodium phosphate solution was rapidly added into 150 ml of 50 mM of calcium citrate solution. The precipitate was isolated by centrifuging at 3000 rpm for 5 min, and the precipitate was washed thrice with Milli-Q® water. Subsequently, the centrifuge tubes containing the precipitates were immersed in liquid nitrogen for 15 min, followed by freeze-drying for 72 h. The obtained powder was preserved in airtight containers for further characterization.

2.3 Characterization

The phase composition of synthesized ACP_CIT was determined using X-ray diffraction (XRD) and performed with a PANalytical Aeris diffractometer (The Netherlands). The diffraction data were collected at 40 kV and 15 mA in a step mode with a step size of 0.04°, in the 2θ range from 10 to 70°.

Fourier-transformed infrared spectroscopy (FTIR) analysis was performed using Nicolet iS50 FT-IR spectrometer (Thermo Scientific, Waltham, MA, USA). Experiments were performed in transmission mode from the wavenumber ranging from 4000 to 400 cm^{-1} with a resolution of 4 cm^{-1} (64 scans).

The morphology and particle size of ACP_CIT were evaluated by Field Emission Gun Transmission Electron Microscopy (FEG-TEM, Tecnai G2 F30, USA) operated at 300 kV. The sample preparation was as follows: a small amount of ACP-CIT powder was dispersed in isopropyl alcohol and sonicated in an ultrasonic bath. Further, the samples were placed on a carbon-coated grid and dried before analysis.

2.4 Synthesis of the hydrogels

Two sets of hydrogels were prepared: GELMA and nanocomposite GELMA-ACP_CIT. The GELMA hydrogel was prepared by dissolving 5 ml of (5% w/v) GELMA in Milli-Q® water at 50°C. Subsequently, the nanocomposite hydrogel was prepared by adding 100 mg of ACP_CIT (2% w/v) in 5 ml of (5% w/v) GELMA solution and stirred for 10 mins at 500 rpm. Subsequently, 100µl of APS (10 % w/v) and 10µl TEMED were added to GELMA and GELMA-ACP_CIT solution. After mixing, each hydrogel was poured into the 12 mm diameter and 2 mm height silicon molds using a displacement pipette. The hydrogels were allowed to crosslink for 30 min at 37°C.

2.5 Oscillatory shear tests

Oscillatory shear tests were performed with a TA HR20 rheometer (USA) to examine the hydrogels' viscoelastic properties. A 20 mm diameter parallel plate geometry with a solvent trap was used. Each sample was analyzed in triplicate, presenting average and standard deviation data. The linear viscoelastic region (LVE) was analyzed by amplitude sweep analysis, and complex viscosity was performed under a constant frequency of 1 Hz and shear stress ranging from 1–1000%. The loss moduli (G") and storage moduli (G') were characterized by the frequency sweep analysis performed under 1% strain under the frequency range from 0.1 to 10 Hz. All the analyses were performed at a constant temperature of 37°C in triplicate, and data is presented as average with standard deviation.

2.5 *In vitro* analysis

2.5.1 Cell culture maintenance

An osteoblast precursor cell line derived from mouse (Mus musculus) calvaria (MC3T3-E1, Sigma Aldrich, Germany) was employed for cellular analysis after 10 passages. MC3T3-E1 cells were maintained in an α-MEM medium containing 10 vol% Fetal bovine serum (Gibco Life Science, USA) and 10 vol % penicillium-streptomycin (Thermo Fisher Scientific, Waltham, MA, USA) at 37 °C in a humidified atmosphere of 95 % air and 5% CO_2. The cultures of MC3T3-E1 cells were trypsinized by adding 3 ml of trypsin-EDTA solution. When the cells were detached, 9 ml of α-MEM medium was added to the T75 flask. The cells were counted, and $1x10^5$ cells/ml were inoculated into fresh T-75 flasks, followed by incubation at 37 °C in a humidified atmosphere of 95% air and 5% CO_2.

2.5.2 Cell Harvesting

Cell culture media was removed from the T-75 flask, followed by adding 5 ml of sterile Dulbecco's phosphate buffer saline (DPBS) (Thermo Fisher Scientific, Waltham, MA, USA) to dislodge loosely attached cells and remove fractions. Then, the DPBS was discarded, followed by adding 3 ml of 0.25% Trypsin-EDTA (Thermo Fisher Scientific, Waltham, MA, USA) solution for 3-5 minutes and incubation at 37 °C for 3-5 min. After detachment of cells, 9 ml of α-MEM medium was added and mixed well and then transferred to a centrifuge tube at 350 rpm for 2 mins to acquire cell pellet, followed by redispersion in 3 ml of cell medium and mixed well. 100 µl of the cell suspension was transferred to 96-well plates, later 100 µl of trypan blue was added, and cells were further counted using a Neubauer chamber (Neubauer-improved, Paul Marienfeld Gmbh and Co.Kg, Germany). A solution containing 25,000 cells per ml was prepared and centrifuged at 350 rpm for 2 mins to acquire a cell pellet.

2.5.3 Cell encapsulation

For the cellular analysis, sterile synthesis of ACP_CIT and GELMA was performed. All the reagents were passed through 0.22µm Millipore filters, whereas calcium citrate and Milli-Q® water were autoclaved at 121 °C for 15 psi for 30 mins. The obtained cell pellet (section 2.5.2) was mixed in 5 % (w/v) GELMA solutions and crosslinked with sterile filtered 100 µl of APS (10 % w/v) and 10 µl TEMED. The hydrogel was poured into the silicon molds and allowed to crosslink for 30 min at room temperature. The same procedure was performed for encapsulation in ACP_CIT-GELMA hydrogels. The hydrogels were incubated in the α-MEM medium at 37 °C in a humidified atmosphere of 95 % air and 5 % CO_2. The cell culture analysis was performed for 7 days, and the medium was changed every 2 days.

2.5.4 Rhodamine phalloidin/DAPI staining

Cell orientation in hydrogels was examined under an fluorescence microscope (Axio, Carl Zeiss, Jena, Germany). Samples (n=3) were treated with 4 % formaldehyde solution for 5 min in the dark. Subsequently, the samples were treated with 0.1 % Triton-X solution for permeation. Further, the samples were washed twice with HBSS. Afterward, the samples were stained with 5µl/ml solution of Rhodamine-Phalloidin staining (Thermofisher Scientific, USA) for 1 h followed by 1 µl/ml DAPI (Thermofisher Scientific, USA) solution for 5 min in the dark. Further, the samples were washed, immersed in HBSS solution, and analyzed under an fluorescence microscope.

3. Result and discussion

3.1 Characterization

The lack of crystalline order confirms the formation of ACP_CIT, as shown in Figure 1 (A). Detailed characterization of ACP_CIT was reported in our previous publication (Indurkar et al., 2023b). The FEG-TEM analysis in Figure 1 (B) reveals the spherical morphology and particle size of ~40 nm of synthesized ACP_CIT.

The FTIR analysis of non-crosslinked GELMA and APS/TEMED crosslinked hydrogels (GELMA and GELMA-ACP_CIT) are shown in Figure 1(C). The characteristic peaks of O-H and N-H group stretching vibrations were observed at 3300 cm^{-1}. The peaks in the regions 3100-2800 cm^{-1} correspond to the CH_2 stretching vibrations. The characteristics of amide bands of gelatin were observed around i) 1632 cm^{-1} representing C=O stretching of amide I, ii) 1533 cm^{-1} representing N-H bending coupled with C-H stretching of amide II, iii) 1232 cm^{-1} was denoted to C-N stretching and N-H bending of amide III, iv) 922 cm^{-1} indicating -C-C- the skeletal stretch of amide IV and v) 615 cm^{-1} corresponds to the CH out-off plane skeletal stretch of amide V (Elsayed et al., 2018). The results indicate that all the amide bands of gelatin remain intact after crosslinking.

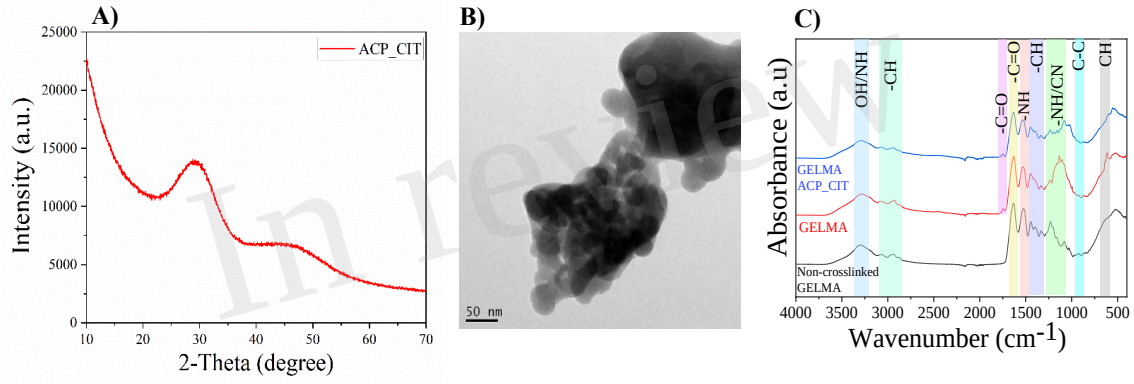

Figure 1. XRD (A), the morphology of synthesized ACP_CIT (B), and FTIR of Non-crosslinked GELMA, radically GELMA (non-crosslinked and crosslinked), and GELMA-ACP_CIT nanocomposite hydrogel (C).

3.2 Synthesized hydrogel

The synthesized hydrogels are shown in Figure 2. The GELMA forms transparent hydrogels, therefore making it suitable for photo-crosslinking. However, ACP_CIT was incorporated in GELMA, resulting in opaque hydrogels; hence, the photo-crosslinking potential of GELMA has deteriorated. In a recent study of developing nanocomposites, GELMA hydrogel containing nanohydroxyapatite (nHA) revealed incomplete crosslinking of GELMA/nHA inside a multilayer scaffold (Liu et al., 2019). Similarly, incorporating amorphous magnesium phosphate in GELMA leads to opaque hydrogels, making crosslinking difficult and affecting the hydrogels' stiffness (Dubey et al., 2020). Crosslinking is essential to the biofabrication technique to maintain the scaffold's structural integrity. Due to the limitation of photo-crosslinking, there is a pressing need to develop a chemical crosslinking approach for creating nanocomposite GELMA hydrogel. The APS/TEMED chemical crosslinking is a simple approach that results in quick crosslinking of nanocomposite GELMA hydrogel containing ACP_CIT, as shown in Figure 2B.

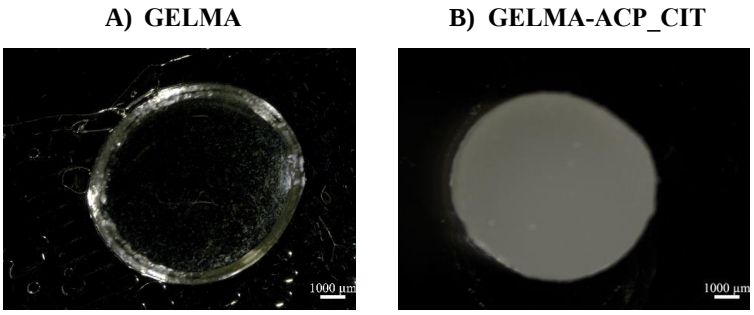

Figure 2. APS/TEMED crosslinked GELMA (A) and nanocomposite GELMA scaffolds containing ACP_CIT (B).

3.2 Oscillatory shear tests

Analyzing the linear viscoelastic region of the hydrogels (LVE) is the first step in evaluating the viscoelastic properties shown in Figure 3 (A-C). The storage modulus (G') represents the elastic property of viscoelastic material, indicating the stored deformation energy, while the loss modulus (G") corresponds to the viscous property of viscoelastic indicating deformation energy lost through internal friction when flowing. When G'>G" the material possesses viscoelastic solid-like properties on the other hand when G'<G" the material possesses viscoelastic fluid-like behavior (Indurkar et al., 2020). The GELMA (non-crosslinked), GELMA and GELMA-ACP_CIT exhibits G'>G" corresponding to viscoelastic gel-like behavior with LVE region falling within 10 % of strain. On increasing the strain, the crossover point is reached where G'=G" corresponds to the gel-sol transformation. After the crossover point, the three-dimensional network completely ruptures, and the material starts showing fluid-like characteristics (Pereira et al., 2022).

The polymeric chain in the non-crosslinked hydrogel is free and exhibits a high degree of freedom. Therefore, the ability to withstand irreversible strain-induced deformation is high, so the crossover point of GELMA was observed at 501% strain. However, after crosslinking with APS/TEMED, the polymeric chains are linked together, observed from enhancement in G' and G"; therefore, the ability to withstand irreversible strain-induced deformation is reduced. Incorporating ACP_CIT in GELMA hydrogel enhances the crossover point to 158%, imparting the ability to withstand higher stains.

The frequency sweep analysis was performed at a constant strain of 1% within the LVE region. The G' and G" were analyzed against frequency, as shown in Figure 3 (D-F). At lower frequencies, the G" of non-crosslinked GELMA hydrogel dominates over the G' value corresponding to the sol-gel behavior. With increased frequency, the G' drastically increases and takes over G" values. Conversely, the G' and G" of GELMA and GELMA-ACP_CIT were independent of frequency.

The G' and G" of each sample were analyzed at 1Hz frequency, which indicates the fragile nature of non-crosslinked GELMA with G' of 0.12 Pa and G" of 0.016 Pa. The moduli were enhanced by crosslinking the GELMA with APS/TEMED, showing the G' of 82.58 ± 13 Pa and G" of 2.25 ± 0.5 Pa. Moreover, incorporation of ACP_CIT in GELMA has shown further enhancement in G' of 318.8 ± 6.5 Pa and G" of 11.3 ± 0.2 Pa, thus confirming the reinforcement. The moduli of GELMA and GELMA-ACP_CIT were independent of frequency; therefore, further analysis was performed on these two samples.

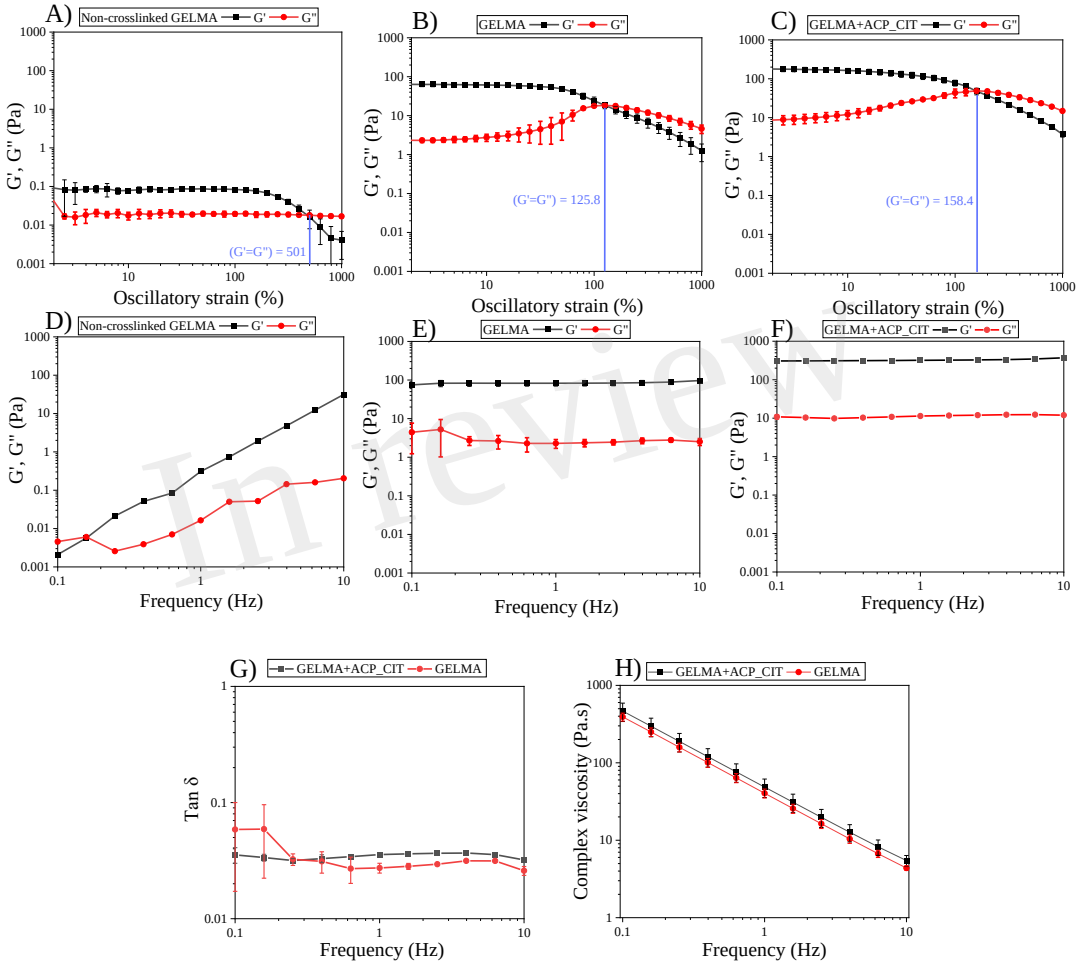

Figure 3. The viscoelastic properties of the hydrogels were analyzed using oscillatory shear tests: the LVE region of the hydrogel was analyzed by amplitude sweep (A-C). Investigation of storage and loss modulus of the hydrogels by frequency sweep (D-F). Tan δ analysis (G), and complex viscosity test analyzing the flow properties of the hydrogels (H).

Tan δ is the G" to G' ratio often used to analyze the damping factor of the hydrogels represented in Figure 3 (G). When the tan δ>1 sample behaves like a viscous liquid, whereas the tan δ<1 sample behaves more like an elastic solid (Yan and Pochan, 2010). At 1 Hz, the tan δ value of GELMA was 0.035 ± 0.0006. On incorporating

ACP_CIT, the tan δ value was reduced to 0.027 ± 0.002, enhancing the elastic solid-like behavior of GELMA. The flow behavior of hydrogel was analyzed by complex viscosity analysis, as shown in Figure 3 (H), revealing the shear-thinning behavior of the GELMA and GELMA-ACP_CIT hydrogels (Vlachopoulos and Strutt, 2016).

3.3 Rhodamine phalloidin and DAPI staining

In vitro analysis evaluated the effect of the APS/TEMED crosslinking and ACP_CIT incorporation in GELMA hydrogel. The fluorescent microscopy images are presented in Figure 4, which show the cytoskeleton (red) and the nucleus (blue) of MC3T3-E1 cells. Cell attachment was observed on the first day, and by the seventh day, the cells were spread and distributed well on the hydrogel, confirming the cytocompatibility of APS/TEMED crosslinking. The preliminary analysis indicates that APS/TEMED crosslinking and incorporation of ACP_CIT have not shown adverse effects on the cytocompatibility of GELMA.

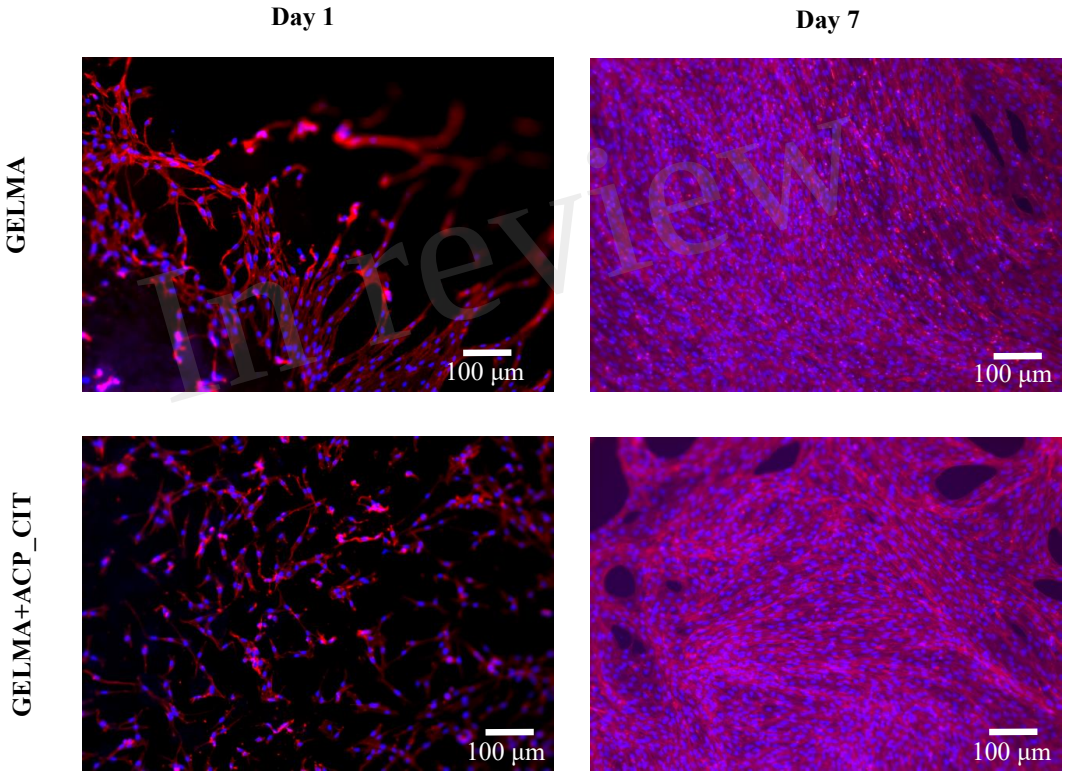

Figure 4. Fluorescent microscopy of rhodamine-phalloidin (red) and DAPI (blue) staining of MC3T3-E1 cells embedded in GELMA and GELMA-ACP_CIT hydrogels.

4. Conclusion

The nanocomposite hydrogels of GELMA containing ACP_CIT were developed successfully using chemical crosslinking. The FTIR analysis revealed that the APS/TEMED crosslinking did not alter the functional groups of GELMA. Subsequently, the oscillatory shear tests revealed that the non-crosslinked GELMA possesses very

low G' and G" values (less than 0.1 Pa). On crosslinking, G' (82.58 ± 13 Pa) and G" (2.25 ± 0.5 Pa) were significantly enhanced imparting structural integrity to the scaffold. On incorporation of ACP_CIT in GELMA, a further enhancement in G' (318.8 ± 6.5 Pa) and G" (11.3 ± 0.2 Pa) confirms the reinforcement potential. Finally, the *in vitro* analysis has concluded that APS/TEMED and ACP_CIT do not obstruct the growth of MC3T3-E1 cells. The preliminary analysis has shown the cytocompatibility of chemical crosslinking and ACP_CIT incorporation in GELMA hydrogel. Therefore, the APS/TEMED crosslinking can be further explored in various biofabrication approaches to develop GELMA-based nanocomposites.

6. Acknowledgment

The authors acknowledge financial support from the European Union's Horizon 2020 research and innovation program under grant agreement No. 857287 and Baltic Research Programme Project No. EEA-RESEARCH-85 "Waste-to-resource: eggshells as a source for next generation biomaterials for bone regeneration (EGGSHELL)" under the EEA Grant of Iceland, Liechtenstein and Norway No. EEZ/BPP/VIAA/2021/1.

7. CRediT authorship contribution statement

Abhishek Indurkar: Conceptualization, Literature review, Methodology, Investigation, Data curation, Writing-original draft preparation. **Kristaps Rubenis:** Writing-Review, and editing. **Aldo R. Boccaccini:** Supervision, Writing-Review, Resources and Editing. **Janis Locs:** Supervision, Writing-Review, and Editing. All authors provided critical feedback and helped to shape the research, analysis, and manuscript.

8. References

Chen, Y., Gu, W., Pan, H., Jiang, S., and Tang, R. (2014). Stabilizing amorphous calcium phosphate phase by citrate adsorption. *CrystEngComm* 16, 1864–1867. doi: 10.1039/C3CE42274G.

Dubey, N., Ferreira, J. A., Daghrery, A., Aytac, Z., Malda, J., Bhaduri, S. B., et al. (2020). Highly tunable bioactive fiber-reinforced hydrogel for guided bone regeneration. *Acta Biomater.* 113, 164–176. doi: 10.1016/J.ACTBIO.2020.06.011.

Elsayed, H. M., Attia, R. Z., Mohamed, O. A., El-Sayed, N. H., and Ibrahim, S. A. (2018). High bloom gelatin strength from white leather shavings. *Leather Footwear J.* 18, 259–274. doi: 10.24264/LFJ.18.4.2.

Gao, Y., Karatas, Y. D., Nouali, H., Salomon, J. P., Lalevée, J., and Simon-Masseron, A. (2024). Zeolite/Polymer Composites Prepared by Photopolymerization: Effect of Compensation Cations on Opacity and Gas Adsorption Applications. *Chem. – A Eur. J.* 30, e202302229. doi: 10.1002/CHEM.202302229.

González-Gamboa, I., Velázquez-Lam, E., Lobo-Zegers, M. J., Frías-Sánchez, A. I., Tavares-Negrete, J. A., Monroy-Borrego, A., et al. (2022). Gelatin-methacryloyl hydrogels containing turnip mosaic virus for fabrication of nanostructured materials for tissue engineering. *Front. Bioeng. Biotechnol.* 10, 907601. doi: 10.3389/FBIOE.2022.907601/BIBTEX.

Indurkar, A., Bangde, P., Gore, M., Reddy, P., Jain, R., and Dandekar, P. (2020). Optimization of guar gum-gelatin bioink for 3D printing of mammalian cells. *Bioprinting* 20, e00101. doi: 10.1016/J.BPRINT.2020.E00101.

Indurkar, A., Choudhary, R., Rubenis, K., and Locs, J. (2023a). Role of carboxylic organic molecules in interfibrillar collagen mineralization. *Front. Bioeng. Biotechnol.* 11, 439. doi: 10.3389/FBIOE.2023.1150037.

Indurkar, A., Choudhary, R., Rubenis, K., Nimbalkar, M., Sarakovskis, A., Boccaccini, A. R., et al. (2023b). Amorphous Calcium Phosphate and Amorphous Calcium Phosphate Carboxylate: Synthesis and Characterization. *ACS Omega*. doi: 10.1021/ACSOMEGA.3C00796.

Indurkar, A., Kudale, P., Rjabovs, V., Heinmaa, I., Demir, Ö., Kirejevs, M., et al. (2023c). Small organic molecules containing amorphous calcium phosphate: synthesis, characterization and transformation. *Front. Bioeng. Biotechnol.* 11, 1329752. doi: 10.3389/FBIOE.2023.1329752/BIBTEX.

Klikovits, N., Sinawehl, L., Knaack, P., Koch, T., Rgen Stampfl, J., Gorsche, C., et al. (2022). A Review on Modeling Cure Kinetics and Mechanisms of Photopolymerization. *Polym. 2022, Vol. 14, Page 2074* 14, 2074. doi: 10.3390/POLYM14102074.

Liu, J., Li, L., Suo, H., Yan, M., Yin, J., and Fu, J. (2019). 3D printing of biomimetic multi-layered GelMA/nHA scaffold for osteochondral defect repair. *Mater. Des.* 171, 107708. doi: 10.1016/J.MATDES.2019.107708.

Nallusamy, J., and Das, R. (2021). Hydrogels and Their Role in Bone Tissue Engineering: An Overview. *J. Pharm. Bioallied Sci.* 13, S908. doi: 10.4103/JPBS.JPBS_237_21.

Park, J., Kwon, S., Hwang, N. S., and Kang, B. J. (2018). Clinical Application of Bone Morphogenetic Protein-2 Microcarriers Fabricated by the Cryopolymerization of Gelatin Methacrylate for the Treatment of Radial Fracture in Two Dogs. *In Vivo* 32, 575–581. doi: 10.21873/INVIVO.11278.

Pereira, F. C., Clinckspoor, K. J., and Moreno, R. B. Z. L. (2022). Optimization of an in-situ polymerized and crosslinked hydrogel formulation for lost circulation control. *J. Pet. Sci. Eng.* 208, 109687. doi: 10.1016/J.PETROL.2021.109687.

Phogat, K., Ghosh, S. B., and Bandyopadhyay-Ghosh, S. (2023). Recent advances on injectable nanocomposite hydrogels towards bone tissue rehabilitation. *J. Appl. Polym. Sci.* 140, e53362. doi: 10.1002/APP.53362.

Sahoo, N. G., Pan, Y. Z., Li, L., and He, C. Bin (2013). Nanocomposites for bone tissue regeneration. *Nanomedicine (Lond).* 8, 639–653. doi: 10.2217/NNM.13.44.

Seetharaman, G., Kallar, A. R., Vijayan, V. M., Muthu, J., and Selvam, S. (2017). Design, preparation and characterization of pH-responsive prodrug micelles with hydrolyzable anhydride linkages for controlled drug delivery. *J. Colloid Interface Sci.* 492, 61–72. doi: 10.1016/J.JCIS.2016.12.070.

Tsanaktsidou, E., Kammona, O., and Kiparissides, C. (2019). On the synthesis and characterization of biofunctional hyaluronic acid based injectable hydrogels for the repair of cartilage lesions. *Eur. Polym. J.*

114, 47–56. doi: 10.1016/J.EURPOLYMJ.2019.02.024.

Vlachopoulos, J., and Strutt, D. (2016). Rheology of Molten Polymers. *Multilayer Flex. Packag. Second Ed.*, 77–96. doi: 10.1016/B978-0-323-37100-1.00006-5.

Yan, C., and Pochan, D. J. (2010). Rheological properties of peptide-based hydrogels for biomedical and other applications. *Chem. Soc. Rev.* 39, 3528. doi: 10.1039/B919449P.

Yan, J., Yang, H., Luo, T., Hua, F., and He, H. (2022). Application of Amorphous Calcium Phosphate Agents in the Prevention and Treatment of Enamel Demineralization. *Front. Bioeng. Biotechnol.* 10. doi: 10.3389/FBIOE.2022.853436.

Zhang, J., Liu, C., Li, X., Liu, Z., and Zhang, Z. (2023). Application of photo-crosslinkable gelatin methacryloyl in wound healing. *Front. Bioeng. Biotechnol.* 11, 1303709. doi: 10.3389/FBIOE.2023.1303709/BIBTEX.

Figure 1.JPEG

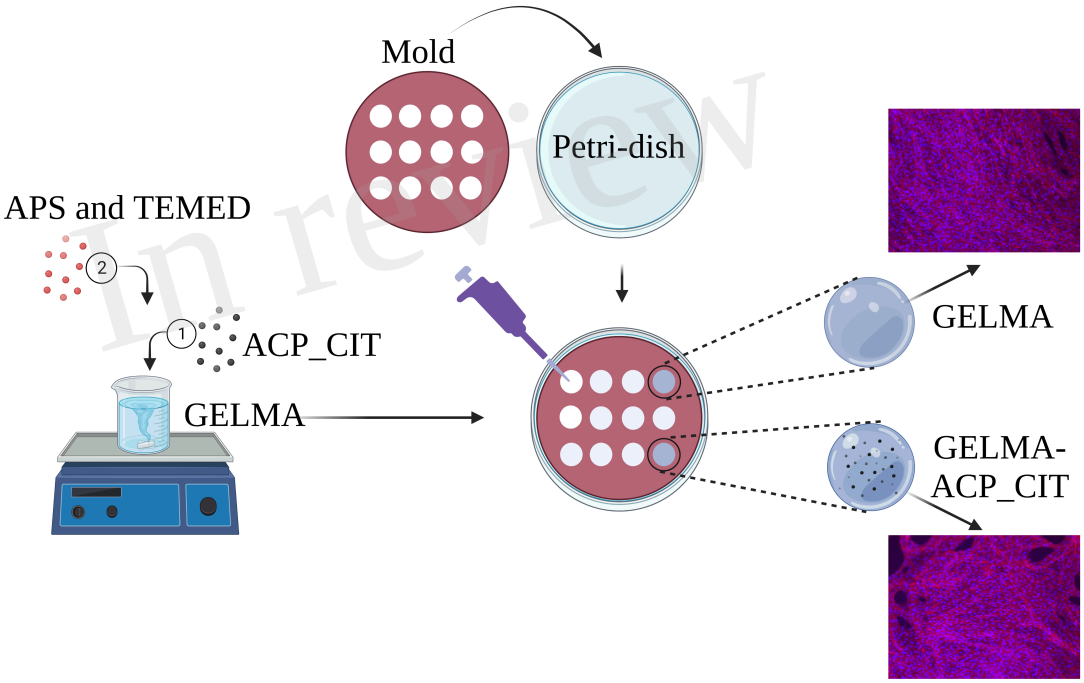

8. PIELIKUMS / APPENDIX 8

8. PUBLIKĀCIJA / PUBLICATION

Indurkar, A., Rubenis, K., A., Boccaccini, A. R., & Locs, J. Development and Characterization of Thermoresponsive Double-Network Nanocomposite Hydrogel for Bone Tissue Engineering.

The article is currently uncer peer review in Macromolecular Materials and Engineering

Macromolecular Materials and Engineering

Development and Characterization of Thermoresponsive Double-Network Nanocomposite Hydrogel for Bone Tissue Engineering

--Manuscript Draft--

Manuscript Number:	mame.202400177
Article Type:	Research Article
Corresponding Author:	Janis Locs Riga Technical University Riga, LATVIA
Corresponding Author E-Mail:	janis.locs@rtu.lv
Order of Authors (with Contributor Roles):	Abhishek Indurkar (Conceptualization: Lead; Data curation: Lead; Formal analysis: Lead; Investigation: Lead; Methodology: Lead; Writing – original draft: Lead)
	Kristaps Rubenis (Funding acquisition: Supporting; Supervision: Supporting; Validation: Supporting; Writing – review & editing: Supporting)
	Aldo R. Boccaccini (Resources: Equal; Supervision: Equal; Validation: Supporting; Writing – review & editing: Supporting)
	Janis Locs (Formal analysis: Supporting; Funding acquisition: Lead; Resources: Equal; Supervision: Equal; Validation: Supporting; Writing – review & editing: Equal)
Section/Category:	
Abstract:	The primary network of hydrogel was composed of chemically crosslinked gelatin methacrylate (GELMA) and polyacrylamide (PAM) while the secondary network was composed of physically crosslinked Pluronic P123. A systematic approach was adopted to develop DN hydrogels. Initially, the impact of P123 concentration on the mechanical properties of PAM-GELMA hydrogel was investigated. Results from the tensile strength and the oscillatory shear tests revealed that an increasing P123 concentration has a marginal effect on the storage modulus while significantly reducing the loss modulus of the PAM-GELMA hydrogel, thereby improving mechanical properties. Notably, DN3 hydrogel containing 7.5w/v% P123 exhibited the highest mechanical properties. To further enhance the mechanical properties, citrate-containing amorphous calcium phosphate (ACP_CIT) was incorporated in DN3 hydrogel at varying concentrations. It was observed that at a lower concentration of ACP_CIT (0.75w/v%), the mechanical properties of hydrogel (DN3ACP0.75) were notably enhanced. Incorporating ACP_CIT in DN3 hydrogel (DN3-ACP0.75) decreased creep strain, slowed stress relaxation, and reduced water uptake capacity while maintaining the shape memory effect. Finally, an in vitro analysis confirmed the cytocompatibility of the hydrogels with MC3T3-E1 cells, indicating the potential use in bone tissue engineering.
Suggested Reviewers:	Isha Mutreja University of Minnesota Twin Cities Department of Animal Science imutreja@umn.edu
	Dirk Grijpma Universiteit Twente d.w.grijpma@utwente.nl
	Cecilia Persson Uppsala University cecilia.persson@angstrom.uu.se
Opposed Reviewers:	
Author Comments:	
Additional Information:	
Question	**Response**
Please submit a plain text version of your	13.05.2024

cover letter here.	To, Prof. Huesmann, Editor-in-Chief, Macromolecular Materials and Engineering. Dear Prof. Huesmann, I am pleased to submit our manuscript entitled "Development and Characterization of Thermoresponsive Double-Network Nanocomposite Hydrogel for Bone Tissue Engineering" for consideration for publication in Macromolecular Materials and Engineering. In this study, we address a significant challenge in bone tissue engineering by introducing a novel approach to enhance the mechanical properties of hydrogels. Our research focuses on the development of nanocomposite double network (DN) hydrogels, combining chemically crosslinked gelatin methacrylate (GELMA) and polyacrylamide (PAM) as the primary network with a secondary network of physically crosslinked Pluronic P123. We further incorporate citrate-containing amorphous calcium phosphate (ACP_CIT) as an inorganic filler to augment the mechanical strength of the hydrogel. Our systematic approach begins with investigating the impact of P123 concentration on the mechanical properties of PAM-GELMA hydrogel, followed by the incorporation of ACP_CIT to enhance mechanical strength. Through a series of tensile strength and oscillatory shear tests, we identify optimal compositions for the DN hydrogel, demonstrating notable improvements in mechanical properties while maintaining cytocompatibility with MC3T3-E1 cells. The manuscript highlights our findings on the developed hydrogels' mechanical characterization, creep recovery, stress relaxation, water uptake capacity, and shape memory effect. We present compelling evidence supporting the potential of our composite hydrogel for applications in bone tissue engineering, backed by in vitro analysis confirming its cytocompatibility. We believe that our research contributes significantly to the field of biomaterials and tissue engineering, offering a new approach to address the limitations of current hydrogel systems in bone regeneration. This study's innovative combination of materials and systematic optimization opens new avenues for developing advanced biomaterials for clinical applications. Thank you for considering our manuscript. We believe our findings will be of great interest to your readership and contribute to advancing the field of biomaterials science. We declare that the work is original, has not been published before, and is not being considered for publication elsewhere. As a corresponding author, I confirm that the manuscript has been read and approved for submission by all the named authors. There is no conflict of interest to declare. Sincerely, Prof. Dr.sc.ing. Janis Locs Director Institute of General Chemical Engineering Riga Technical University, Latvia.
Does the research described in this manuscript include animal experiments?	No
Does the research described in this	No

manuscript include human research participants (including for experiments with sensors or wearable technologies) or tissue samples from human subjects (including blood or sweat)?	
Do you or any of your co-authors have a conflict of interest to declare?	No. The authors declare no conflict of interest.
Keywords:	- Nanocomposite; Macromolecular materials; Double network hydrogels; Amorphous calcium phosphate citrate; Shape memory hydrogel

Cover letter

13.05.2024

To,
Prof. Huesmann,
Editor-in-Chief,
Macromolecular Materials and Engineering.

Dear Prof. Huesmann,

I am pleased to submit our manuscript entitled ***"Development and Characterization of Thermoresponsive Double-Network Nanocomposite Hydrogel for Bone Tissue Engineering"*** for consideration for publication in Macromolecular Materials and Engineering.

In this study, we address a significant challenge in bone tissue engineering by introducing a novel approach to enhance the mechanical properties of hydrogels. Our research focuses on the development of nanocomposite double network (DN) hydrogels, combining chemically crosslinked gelatin methacrylate (GELMA) and polyacrylamide (PAM) as the primary network with a secondary network of physically crosslinked Pluronic P123. We further incorporate citrate-containing amorphous calcium phosphate (ACP_CIT) as an inorganic filler to augment the mechanical strength of the hydrogel.

Our systematic approach begins with investigating the impact of P123 concentration on the mechanical properties of PAM-GELMA hydrogel, followed by the incorporation of ACP_CIT to enhance mechanical strength. Through a series of tensile strength and oscillatory shear tests, we identify optimal compositions for the DN hydrogel, demonstrating notable improvements in mechanical properties while maintaining cytocompatibility with MC3T3-E1 cells.

The manuscript highlights our findings on the developed hydrogels' mechanical characterization, creep recovery, stress relaxation, water uptake capacity, and shape memory effect. We present compelling evidence supporting the potential of our composite hydrogel for applications in bone tissue engineering, backed by in vitro analysis confirming its cytocompatibility.

We believe that our research contributes significantly to the field of biomaterials and tissue engineering, offering a new approach to address the limitations of current hydrogel systems in bone regeneration. This study's innovative combination of materials and systematic optimization opens new avenues for developing advanced biomaterials for clinical applications.

Thank you for considering our manuscript. We believe our findings will be of great interest to your readership and contribute to advancing the field of biomaterials science.

We declare that the work is original, has not been published before, and is not being considered for publication elsewhere. As a corresponding author, I confirm that the manuscript has been read and approved for submission by all the named authors. There is no conflict of interest to declare.

Sincerely,
Prof. Dr.sc.ing. Janis Locs
Director
Institute of General Chemical Engineering
Riga Technical University, Latvia.

Development and Characterization of Thermoresponsive Double-Network Nanocomposite Hydrogel for Bone Tissue Engineering

Abhishek Indurkar[1,2], Kristaps Rubenis[1,2], Aldo R. Boccaccini[3], and Janis Locs[1,2*]

[1]Institute of Biomaterials and Bioengineering, Faculty of Natural Sciences and Technology, Riga Technical University, Riga, Pulka 3, LV-1007, Latvia

[2] Baltic Biomaterials Centre of Excellence, Headquarters at Riga Technical University, Kipsalas Street 6A, LV-1048 Riga, Latvia

[3] Institute of Biomaterials, Department of Material Science and Engineering, University of Erlangen-Nuremberg, 91085, Erlangen, Germany

[*] Communicating author – Janis.Locs@rtu.lv

Abstract

In this work, development of thermoresponsive double network (DN) nanocomposite hydrogel was fabricated. The primary network of hydrogel was composed of chemically crosslinked gelatin methacrylate (GELMA) and polyacrylamide (PAM) while the secondary network was composed of physically crosslinked Pluronic P123. A systematic approach was adopted to develop DN hydrogels. Initially, the impact of P123 concentration on the mechanical properties of PAM-GELMA hydrogel was investigated. Results from the tensile strength and the oscillatory shear tests revealed that an increasing P123 concentration has a marginal effect on the storage modulus while significantly reducing the loss modulus of the PAM-GELMA hydrogel, thereby improving mechanical properties. Notably, DN3 hydrogel containing 7.5w/v% P123 exhibited the highest mechanical properties. To further enhance the mechanical properties, citrate-containing amorphous calcium phosphate (ACP_CIT) was incorporated in DN3 hydrogel at varying concentrations. It was observed that at a lower concentration of ACP_CIT (0.75w/v%), the mechanical properties of hydrogel (DN3ACP0.75) were notably enhanced. Incorporating ACP_CIT in DN3 hydrogel (DN3-ACP0.75) decreased creep strain, slowed stress relaxation, and reduced water uptake capacity while maintaining the shape memory effect. Finally, an *in vitro* analysis confirmed the cytocompatibility of the hydrogels with MC3T3-E1 cells, indicating the potential use in bone tissue engineering.

Graphical abstract

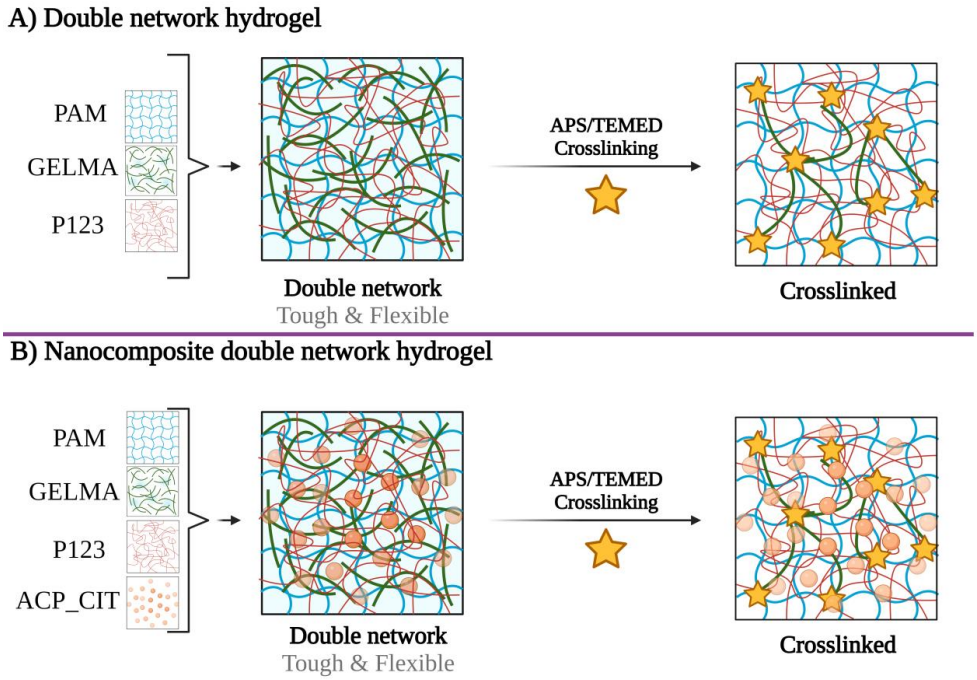

Keywords – Nanocomposite, Macromolecular materials, Double network hydrogels, Polyacrylamide, Gelatin methacrylate, Pluronic P123, Amorphous calcium phosphate citrate, Shape memory hydrogel.

1. Introduction

Bone tissue engineering has shown immense potential for the application of engineered biodegradable biomaterials that facilitate bone regeneration without acquiring the risks of metallic devices and bone grafts. In the nineteenth century, calcium phosphate (CaP) was first used as a bone substitute material [1]. Since then, bone substitute materials have aimed to replace bone defects by simply filling up the defect volume by deploying biologically active materials to facilitate bone regeneration. In subsequent years, materials such as ceramics, metal nanoparticles, bioglass, polymers, and proteins alone or in combination were utilized [2]. Today, advancements in material synthesis, biofabrication techniques, and an improved understanding of bone structural and physiological properties have opened new horizons in developing new strategies for bone regeneration [3,4].

The development of bone substitute materials intends to imitate the structural and functional role of the bone's extracellular matrix (ECM), minerals, and cellular components, providing a foundation and favorable environment for new bone growth and restoring functionality [5]. The unique mechanical properties of natural bone arise from the hierarchical nano and micro-scale arrangement of the bone ECM structure [6]. Building nanoscale and microscale materials in three-dimensional scaffolds is necessary to promote the hierarchical organization of the natural ECM. Moreover, the biophysical aspect of ECM, such as stiffness, is linked to various cellular behaviors *in vivo* and *vitro* [7,8]. The hydrogel stiffness plays a significant role in bone remodeling by 1) providing the signal to osteoblasts and osteoclasts for bone anabolism, 2) regulating mesenchymal stem cells (MSC) osteogenesis by modulating elasticity, and 3) regulating the transformation of amorphous calcium phosphate (ACP) to hydroxyapatite (HAP) [7,9].

Hydrogels are a three-dimensional network of polymer chains with excellent water absorption capacity, low friction, transparency, and ion permeability [10]. Due to such properties, hydrogels can potentially mimic the extracellular matrix (ECM). Injectable hydrogels have shown potential advantages in repairing bone defects, such as minimal invasive implantation and filling irregular bone defects [11]. However, their application in bone tissue engineering is limited due to the insufficient mechanical properties to meet the load-bearing requirements of bone tissue [12]. Additionally, scaffold fabrications have high requirements due to their non-adjustable shape.

Shape memory hydrogels (SMHs) have been gaining attraction due to their shape tuneability, which holds promise for treating irregular bone defects [13]. The reversible transition between shapes leads to the shape memory effect (SME), originating from a double network (DN) hydrogel [14,15]. DN hydrogels consist of two interpenetrating polymer networks with different physical properties [16]. One of the polymer networks consists of hard and brittle sacrificial bonds, a phase that maintains the original shape and prevents flow deformation of the DN hydrogel [17]. The second polymer provides a soft, flexible network that acts as a reversible phase to fix the temporary shape [18].

Polyacrylamide (PAM) hydrogels are used due to their easy polymerization and stable crosslinking network. In the 1980s, PAM hydrogels were first used in aesthetic surgery. Since then, this material has been widely used in ophthalmic operations, wound dressing, water treatment, food packaging products, and cell-based applications [19]. Recently, a commercial viscosupplement (Contura's Astrosemid®) was introduced, comprising PAM. A 52-week human study demonstrated the efficiency of Astrosemid® in treating knee osteoarthritis [20]. PAM hydrogels possess nearly perfect elasticity but lack cell attachment sites and shape memory function [21]. One

possibility is to deploy gelatin methacrylate (GELMA) to overcome this problem. Gelatin contains the RGD (arginine-glycine-aspartic acid) peptide sequence essential for cell adhesion [22]. Moreover, the methacrylate groups of GELMA can be crosslinked using ammonium persulfate (APS) and Tetramethyl-ethylenediamine (TEMED), which also crosslinks PAM [23,24]. Therefore, the first hydrogel network is formed by a co-polymer of GELMA-PAM. However, GELMA has weak mechanical properties and limited thermal stability; therefore, Pluronics P123 was introduced in PAM-GELMA hydrogels.

Pluronic P123 is a polymer consisting of hydrophilic polyethylene oxide (PEO) and hydrophobic polypropylene oxide (PPO) arranged in tri-block PEO-PPO-PEO, widely used in drug delivery and tissue engineering applications due to its excellent biocompatibility and thermo-sensitivity [25]. It possesses thermoreversible behavior where, below critical gelation temperature (20 to 30℃), the polymer is in the gel state due to micelles formation [26]. On heating, the gel structure breaks down, thus forming a solution. This behavior of Pluronics P123 is reversible, meaning that the solution undergoes gel formation when cooling. Amorphous calcium phosphate (ACP) was incorporated in P123-PAM-GELMA hydrogel to develop nanocomposite hydrogel.

ACP is a central precursor in biomineralization [27]. It is a biocompatible and bioresorbable calcium phosphate form widely used in biomedical applications, including bone regeneration and drug delivery. One major drawback of ACP is its metastable nature, which leads to rapid transformation to apatite [28]. The transformation of ACP to apatite can be delayed by two mechanisms: surface absorption of organic molecules (adenosine triphosphate (ATP), polyelectrolyte, citrate, and polyethylene glycol) or ionic substitution (magnesium, zinc, iron, carbonates, pyrophosphates, and fluorine) [29–34]. We have used citrate-containing amorphous calcium phosphate (ACP_CIT) to develop nanocomposite P123-PAM-GELMA hydrogels.

In this work, a systematic approach was followed for the preparation of DN hydrogels; initially, the impact of varying w/v concentrations of P123 (2.5%, 5%, 7.5%, and 10%) on mechanical and rheological properties (Young's modulus, tensile strength, elongation at break) of PAM-GELMA was evaluated. Amongst these, the DN hydrogel with 7.5 w/v% P123 in PAM-GELMA (DN3) exhibited the highest mechanical properties. Therefore, it was further utilized to develop nanocomposite DN hydrogels by incorporating different w/v concentrations of ACP_CIT (0.75%, 1.5%, and 3%). The nanocomposite DN hydrogels with 0.75 w/v% ACP_CIT (DN3-ACP0.75) exhibited the highest mechanical properties. The DN3 and DN3-ACP0.75 hydrogel's water uptake capacity, creep-recovery and stress relaxation behavior, shape memory effect, and cytocompatibility were compared with those of pristine DN3 hydrogel.

2. Materials and methods

Calcium citrate tetrahydrate (CAS 5785-44-4), trisodium phosphate (CAS 7601-54-9), sodium hydroxide (CAS 1301-73-2), ammonium persulfate (CAS 7727-54-0), and N, N, N', N'-Tetramethylethylenediamine (CAS 110-18-9) were procured from Sigma Aldrich, Germany. 30% Acrylamide/N, N′-Methylenebisacrylamide solution (37.5:1) (PAM premix) was received from Bio-Rad, USA, and ~50% methacrylate gelatin (GELMA) was obtained from Cellink, Sweden. Hanks balanced salt solution (HBSS) was acquired from Gibco Life Technologies, Germany.

2.1 Synthesis and characterization of citrate stabilized amorphous calcium phosphate.

Synthesis of ACP_CIT was performed using the previously reported protocol[35]. Briefly: The reaction was performed in a volume of 300 ml. Initially, 150 ml of 50 mM of calcium citrate solution was prepared in Milli-Q® water, followed by pH adjustment to 11.5 using 2M sodium hydroxide. Subsequently, 150 ml of 100 mM trisodium phosphate solution was rapidly added into 150 ml of 50 mM of calcium citrate solution. The precipitate was isolated by centrifuging at 3000 rpm for 5 min and washed thrice with Milli-Q® water. Centrifuge tubes containing the precipitates were immersed in liquid nitrogen for 15 min, followed by freeze-drying for 72 h. The obtained powder was preserved in airtight containers for further characterization.

The phase composition of synthesized ACP_CIT was determined using X-ray diffraction and performed with a PANalytical Aeris diffractometer (The Netherlands). The diffraction data were collected at 40 kV and 15 mA in a step mode with a step size of 0.04°, in the 2θ range from 10 to 70°.

The Fourier-transformed infrared spectroscopy (FTIR) analysis was performed using a Nicolet iS50 FT-IR spectrometer (Thermo Scientific, Waltham, MA, USA). Experiments were performed in transmission mode from the wavenumber ranging from 4000 to 400 cm^{-1} with a resolution of 4 cm^{-1} (64 scans).

The morphology and particle size of synthesized ACP_CIT were evaluated by FEG-TEM (Tecnai G2 F30, USA) operated at 300 kV. The sample preparation was as follows: a small amount of powder was dispersed in isopropyl alcohol and sonicated in an ultrasonic bath. Further, the samples were placed on a carbon-coated grid and dried before analysis.

2.2 Synthesis of DN hydrogel

The primary solution was prepared by making Pluronic's P123 prepared in Milli-Q® water at different w/v concentrations (5%, 10%, 15%, and 20%). The secondary solution was prepared by incorporating 2 w/v% GELMA in PAM premix solution and mixed at 500 rpm for 30 min to get a homogenous solution. The DN hydrogels were prepared by mixing an equal amount of primary (3 ml) and secondary solutions (3 ml). Afterward, 100µl (10 w/v%) APS and 10µl TEMED were added for crosslinking. The solution was vortexed and immediately added into the rectangular molds, which were allowed to be set for 30 min at 37°C.

Nanocomposite DN hydrogels were prepared by adding different w/v concentrations of 1.5%, 3%, and 6% of ACP_CIT in 15 w/v% Pluronic's P123 solution. The secondary solution was prepared by mixing 2 w/v% GELMA in PAM premix solution and mixed for 30 min to get a homogenous solution. The nanocomposite DN hydrogels were prepared by mixing 3 ml of primary and 3 ml of secondary solution. Afterward, 100µl APS and 10µl TEMED were added for crosslinking. The solution was vortexed and immediately added into the rectangular molds, which were allowed to be set for 30 min at 37 °C.

DN hydrogel was synthesized by mixing equal amounts of GELMA-PAM and Pluronics P123 solution; therefore, the effective concentration of the respective compounds was reduced to half. The abbreviation of hydrogels and their effective concentrations are represented in Table 1. These abbreviations were used in all the following sections.

Table 1. Abbreviations and effective GELMA, PAM, P123, and ACP_CIT concentrations in the respective DN hydrogel.

Hydrogel	**Effective concentration in hydrogel**				**Abbreviations**
	GELMA w/v%	PAM w/v%	P123 w/v%	ACP_CIT w/v%	
PAM-GELMA	1	30	-	-	PAM-GELMA
GELMA-PAM-(5 w/v%) P123	1	15	2.5	-	DN1
GELMA-PAM-(10 w/v%) P123	1	15	5	-	DN2
GELMA-PAM-(15 w/v%) P123	1	15	7.5	-	DN3
GELMA-PAM- (20 w/v%) P123	1	15	10	-	DN4
DN3-(1.5 w/v%) ACP_CIT	1	15	7.5	0.75	DN3-ACP0.75
DN3-(3 w/v%) ACP_CIT	1	15	7.5	1.5	DN3-ACP1.5
DN3-(6 w/v%) ACP_CIT	1	15	7.5	3	DN3-ACP3

2.3 Mechanical properties

The uniaxial test was performed on the fabricated hydrogels, and the mechanical properties were analyzed using the universal testing machine Instron 5967 (Instron GmbH, Darmstadt, Germany). The hydrogel was fabricated in a rectangular mold, having a 9 mm width and 20 mm length. The analysis was performed at a 5 mm/min crosshead speed at 100 N load cell. Mechanical properties such as Young's modulus, tensile strength, and elongation at break were analyzed using a tensile stress-strain curve.

2.4 Oscillatory shear tests

Oscillatory shear tests (TA HR20 rheometer, New Castle, USA) used a 20 mm parallel cross-hatched Peltier plate, and the solvent trap was used. The linear viscoelastic region (LVE) was analyzed by amplitude sweep analysis performed under a constant frequency of 1 Hz and shear strain ranging from 1–100%. The loss moduli (G") and storage moduli (G') were characterized by the frequency sweep analysis performed under 1% shear strain, and frequency ranged from 0.1 to 10 Hz. A constant static force of 10 N was applied for creep experiments, and the temperature was kept constant at 25° C throughout the experiment for 180 seconds. The stress relaxation experiments were performed at a constant strain of 1%, and shear stress of 1 kPa was applied to the hydrogel for 180 seconds. Further strain was removed, and the recovery phase was registered for 360 seconds.

2.5 Water uptake capacity

The water uptake capacity was tested using a gravimetric procedure. Initially, the weight of dry samples was recorded (W_0). Subsequently, the dry samples were immersed in 20 ml Milli-Q® water. The scaffold was removed at different time points till 720 min. The excess water from the scaffold was removed using moist filter paper, and the weight was recorded (W_1). The samples' water uptake capacity (W%) was calculated using equation (1).

$$W\% = \left(\frac{W1-W0}{W0}\right) * 100 \qquad \text{Equation (1)}$$

2.6 Shape memory behavior

Samples were prepared in rectangular molds of length of 45 mm and width of 15 mm to analyze the hydrogel's shape memory behavior. The prepared samples were swelled in Milli-Q® water for 24 h and further treated in

70° C Milli-Q® water for 2 min. Afterward, the samples were removed, and a temporary cylindrical shape was formed by wrapping the samples. The temporary shape was fixed by placing the samples in 4°C Milli-Q® water for 2 minutes. The shape recovery process from the transformed shape to the original shape was triggered by immersing samples in 70° C Milli-Q® water. Five cycles of temporary shape formation and its recovery to the original shape were performed.

2.7 In vitro analysis

2.7.1 Cell culture maintenance

An osteoblast precursor cell line derived from mouse (Mus musculus) calvaria (MC3T3-E1, Sigma Aldrich, Germany) was employed for cellular analysis after ten passages. MC3T3-E1 cells were maintained in an α-MEM medium containing 10 vol % Fetal bovine serum (Gibco Life Science, USA) and 10 vol % penicillium-streptomycin (Thermo Fisher Scientific, Waltham, MA, USA) at 37 °C in a humidified atmosphere of 95% air and 5% CO_2. The cultures of MC3T3-E1 cells were trypsinized by adding 3 ml of trypsin-EDTA solution. When the cells were detached, 9 ml of α-MEM medium was added to the T75 flask. The cells were counted, and $1x10^5$ cells/ml were inoculated into fresh T75 flasks, followed by incubation at 37 °C in a humidified atmosphere of 95% air and 5 % CO_2.

2.7.2 Cell Harvesting

Cell culture media was removed from the T75 flask, adding 5 ml of sterile Dulbecco's phosphate buffer saline (Thermo Fisher Scientific, Waltham, MA, USA) to dislodge attached cells and remove cell fractions. Then, the PBS was discarded, adding 3 ml of Trypsin-EDTA (Thermo Fisher Scientific, Waltham, MA, USA) solution for 3-5 minutes and incubating at 37 °C for 3-5 min. After detachment of cells, 9 ml of α-MEM was added and mixed well and then transferred to a centrifuge tube at 350 rpm for 2 mins to acquire cell pellet, which was further redispersed in 3 ml of α-MEM medium and mixed well. 100µl of the cell suspension was transferred to 96-well plates, 100µl of trypan blue was added, and cells were further counted using a Neubauer chamber (Neubauer-improved, Paul Marienfeld Gmbh and Co.Kg, Germany). A solution containing 25,000 cells per ml was prepared and centrifuged at 500 rpm for 2 mins to acquire a cell pellet.

2.7.3 Cell encapsulation

All the solutions were sterilized by passing through 0.22-micron filters. All operations were performed on a sterile bench. The DN and ACP-containing DN hydrogels were synthesized by procedure illustrated in section 2.2. After forming respective solutions, the cell pellet was mixed to form a cell suspension, followed by the addition of 100µl APS and 10µl TEMED. The solution was gently aspirated and immediately added into the 12-mm diameter and 2-mm height circular mold using a positive displacement pipette set for 30 min at 37°C.

CellCrown inserts (ScaffdexOy, Tampere, Finland) were placed in a 6-well plate. The circular mold was removed, and the hydrogels were transferred onto the CellCrown. 2ml of α-MEM medium was added to each well and incubated at 37°C in a humidified atmosphere of 95% air and 5 % CO_2. The α-MEM medium was changed every two days.

2.7.4 Rhodamine phalloidin/ DAPI stain

The hydrogels were washed with HBSS and treated with 4% paraformaldehyde in HBSS for 15 min, then washed thrice with HBSS. Subsequently, a permeability buffer was introduced for 5 min, after which it was removed carefully. Further, a Phalloidin-master mix (8µl Phalloidin per ml of HBSS) was added following incubation for one hour in the dark. Afterward, the Phalloidin-master mix was removed, and constructs were washed with HBSS. Then, the constructs were stained with DAPI (1µl DAPI per ml of HBSS) for 15 mins in the dark. The constructs were once again washed with HBSS and analyzed on an inverted epifluorescence microscope (Axio scope 1, Carl Zeiss, Jena, Germany). Three replicates were analyzed, and cell viability was determined.

3 Results and discussion

3.1 Characterization

X-ray amorphous ACP_CIT is shown in Figure 1(A). The functional groups of ACP_CIT were analyzed using FTIR analysis, shown in Figure 1(B). The band observed at 3250 cm^{-1} corresponds to OH asymmetric and symmetric stretching, and the band at 1670 cm^{-1} signifies the OH bending mode of water. Furthermore, the bands observed at 1600 cm^{-1} and 1446 cm^{-1} represent COO bending and COH stretching, respectively, of the carboxylic group in citrates [36]. The phosphate groups of ACP_CIT show three vibration peaks of v_1, v_3, and v_4, which were observed at 950 cm^{-1}, 1020 cm^{-1}, and 560 cm^{-1}, respectively. FTIR and XRD confirm the amorphous nature of ACP and the presence of citrate. The spherical morphology of the ACP_CIT particle was confirmed by FEG-TEM, as shown in Figure 1(C).

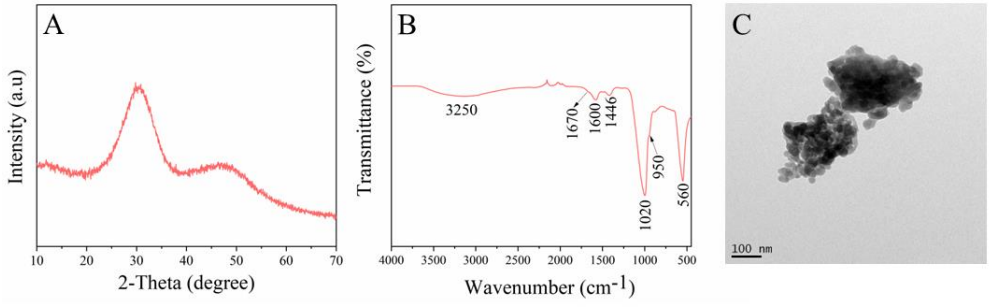

Figure 1. Characterization of ACP_CIT (A) X-ray diffraction patterns confirming the amorphous nature of ACP_CIT. (B) FTIR spectrum displaying functional groups present in the ACP_CIT. (C) FEG-TEM confirmed ~40 nm particle size of ACP_CIT nanoparticles.

3.2 Synthesized DN hydrogels

All the synthesized hydrogels are shown in Figure 2. The PAM-GELMA forms transparent hydrogels. The transparency was retained by blending 2.5% P123 (w/v) in PAM-GELMA hydrogel and increasing concentration to 5% (w/v) P123, making translucent hydrogels PAM-GELMA, further increase in P123 concentration (7.5% and 10%) results in opaque hydrogels. Therefore, at higher concentrations of P123, the transparent nature of PAM-GELMA hydrogels was compromised. At higher concentrations of P123, the intrinsic arrangement of micelles

and entanglement of the polymer chain within the PAM-GELMA hydrogel contribute to the structural complexity of Pluronic's P123, leading to light scattering and making gels opaque [37].

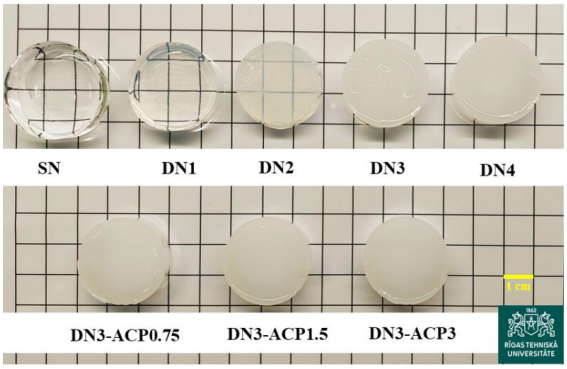

Figure 2. Photograph of synthesized hydrogels.

3.3 Mechanical analysis

Uniaxial tensile strength analysis revealed the synthesized hydrogels' mechanical properties (see Figure 3). In the PAM-GELMA hydrogel, the Youngs modulus was 446 ± 51.32 kPa, tensile strength of 44.7 ± 10 kPa, and elongation at break was 15.43 ± 2.01%, representing brittle nature [38,39]. As the P123 was blended in the PAM-GELMA hydrogel, Young's modulus gradually decreased while the tensile strength and elongation increased, which can be attributed to increased flexibility.

Under the application of tensile strain, the covalently crosslinked PAM-GELMA hydrogel's network is broken, resulting in permanent deformation. However, in DN hydrogel, the P123 offers a primary network that partially unzips under tensile strain, thus keeping the PAM-GELMA networks intact [40]. Therefore, as the concentration of P123 increased, the mechanical properties of the PAM-GELMA hydrogel were enhanced. However, at 10 w/v% P123 concentration, the elongation was reduced due to a high P123 concentration, resulting in the anisometric micellar formation, producing a large micellar core that may be responsible for this behavior [26]. The DN3 hydrogels exhibit the highest elongation of 149.45 ± 10.56% compared to other DN hydrogels (DN1, DN2, DN4); therefore, DN3 hydrogel was further utilized for making nanocomposite hydrogel by incorporating ACP_CIT.

A further effect of ACP_CIT was analyzed on the mechanical properties of DN3 hydrogel by varying the concentration of ACP_CIT. As observed in Figure 3(B), at low ACP_CIT (0.75 w/v%) concentration, the elongation of DN3-ACP0.75 hydrogel was enhanced to 181.7 ± 0.07%, while the tensile strength (63.6 ± 10 kPa) and Young's modulus (60 ± 17.32 kPa) were reduced compared to pristine DN3 hydrogels. Reducing Young's modulus and increasing elongation indicates that the DN3-ACP0.75 hydrogels were more flexible than DN3 hydrogels [41]. Further increasing concentration of ACP_CIT (1.5 w/v% and 3 w/v%) affects Young's modulus, tensile strength, and elongation.

This phenomenon results from the interplay between the molecular weight of the polymer and the ACP_CIT nanoparticles. Under the deformation, the nanoparticles absorb the applied stress, delaying the crack propagation by numerous flexible polymeric chains [42]. The concentration of 0.75 w/v% ACP_CIT provided the best stretchability results. However, 1.5 w/v% and 3 w/v% ACP_CIT concentrations may agglomerate or have formed non-crosslinked regions in the hydrogel [43]. At higher concentrations, nanoparticles can agglomerate into clusters, forming an inhomogeneous distribution within the hydrogel, hampering crosslinking between the polymer chains [44,45]. Therefore, compromised mechanical properties were observed in DN3-ACP1.5 and DN3-ACP3 hydrogels. This highlights that the desirable effect ACP_CIT was reached at a lower concentration of 0.75 w/v%.

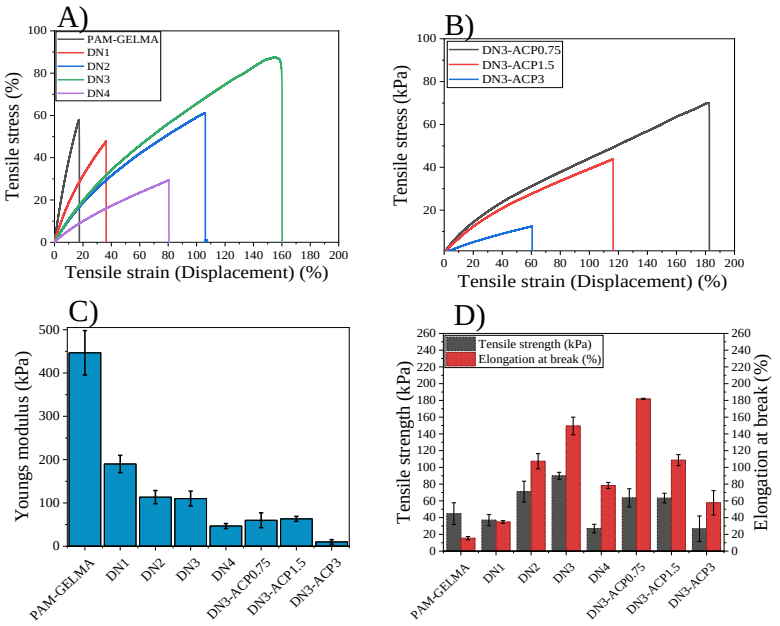

Figure 3. Tensile stress-strain curve of the prepared hydrogel. (A) Analyzing the effect of P123 concentration on the elongation of the SN hydrogel. (B) Analyzing the effect of ACP_CIT concentration on the elongation of the DN3 hydrogel. (C and D) Young's modulus, (E and F) Tensile strength, and (G and H) Elongation at break (%) of SN, DN, and NCDN3 hydrogels.

3.4 Oscillatory shear tests

Analyzing the LVE region is the first step in analyzing the viscoelastic properties of the hydrogel, as it indicates the range in which further steps need to be performed without destroying the sample structure [46]. The amplitude sweep of all the synthesized hydrogels is shown in Figure 4 (A-I). The storage modulus (G') represents the elastic behavior of the material, indicating its ability to store energy when subjected to deformation. The loss modulus (G") measured the viscous behavior of the materials, indicating dissipated energy as heat under deformation. When the G'>G", the material exhibits gel-like behavior. On the contrary, the material possesses fluid-like behavior when G'<G" [22]. All the synthesized hydrogels possess G'>G", showing gel-like behavior. After the LVE region, the breakdown of the structure starts with the formation of microcracks. However, the viscoelastic behavior of the structure was well preserved; therefore, structural breakdown is a slow process. The increasing

strain increases the micro-crack propagation and reaches where G' = G", known as the crossover point. The three-dimensional network completely ruptures after the crossover point where the hydrogel exhibits (G'<G") fluid-like behavior [47].

The crossover point of P123 hydrogel was very high (at 171.1% strain), indicating its ability to withstand strain-induced irreversible deformation. However, in the case of PAM-GELMA hydrogel, the crossover point is very low (at 2.40 % strain), which can be attributed to its brittle nature [48]. However, when the P123 blended in the PAM-GELMA hydrogels, the crossover point was enhanced, resulting in the ability to withstand strain-induced irreversible deformation. In the case of nanocomposite hydrogels, adding 0.75 w/v% ACP_CIT (DN3-ACP0.75) shows enhancement in the crossover point (at 16.15% strain) when compared to pristine DN3 hydrogel (at 12.9% strain) resulting in enhanced ability to withstand strain-induced irreversible deformation. However, as the concentration of ACP_CIT increases to 1.5 and 3 w/v%, the crossover points decrease to 12% and 5.1% strain respectively, obstructing the ability to withstand strain-induced irreversible deformation.

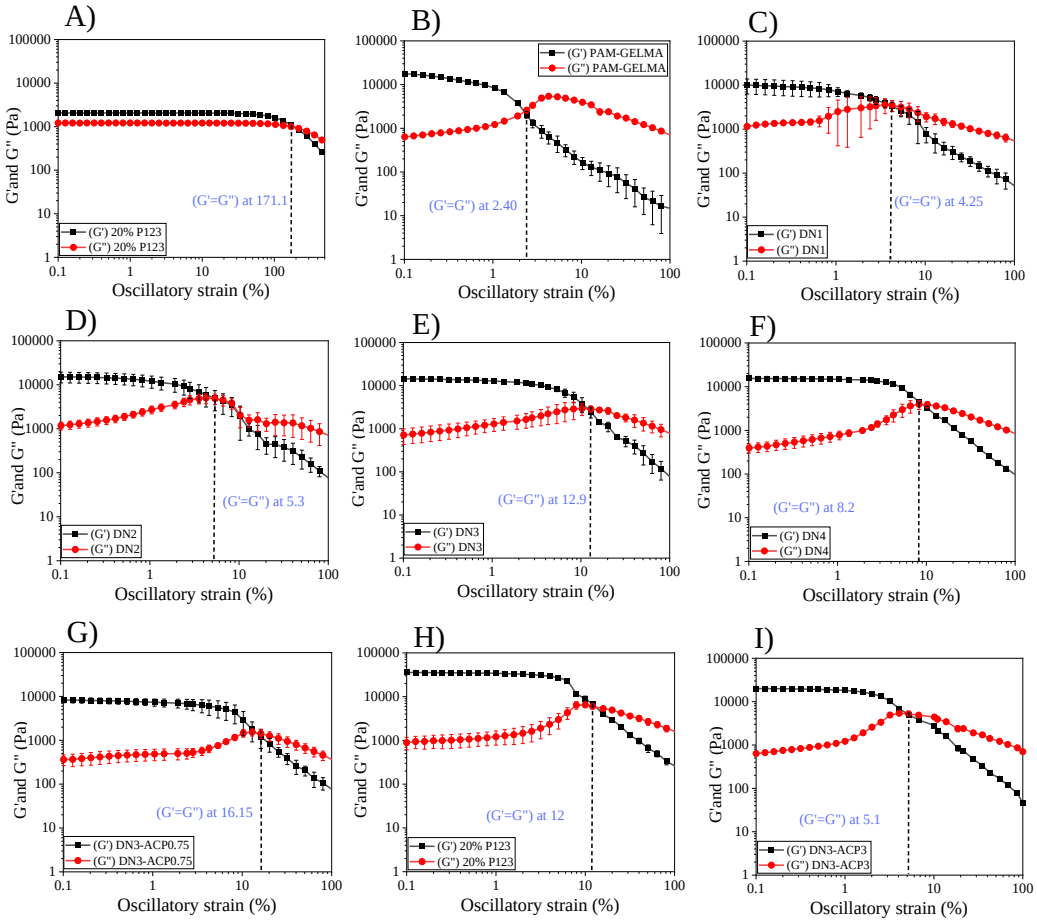

Figure 4. Amplitude sweep and crossover point of all the synthesized hydrogels.

A frequency sweep analysis was performed to evaluate the viscoelastic properties of the prepared hydrogels, as shown in Fig 5 (A-I). In Fig 5(A), the frequency sweep of 20% P123 shows G'<G" at initial frequencies corresponding to sol-like behavior; however, with an increase in frequency, the moduli sharply increase, and the crossover point is achieved, after which the G' dominates over G" ascertaining gel like behavior [22,49].

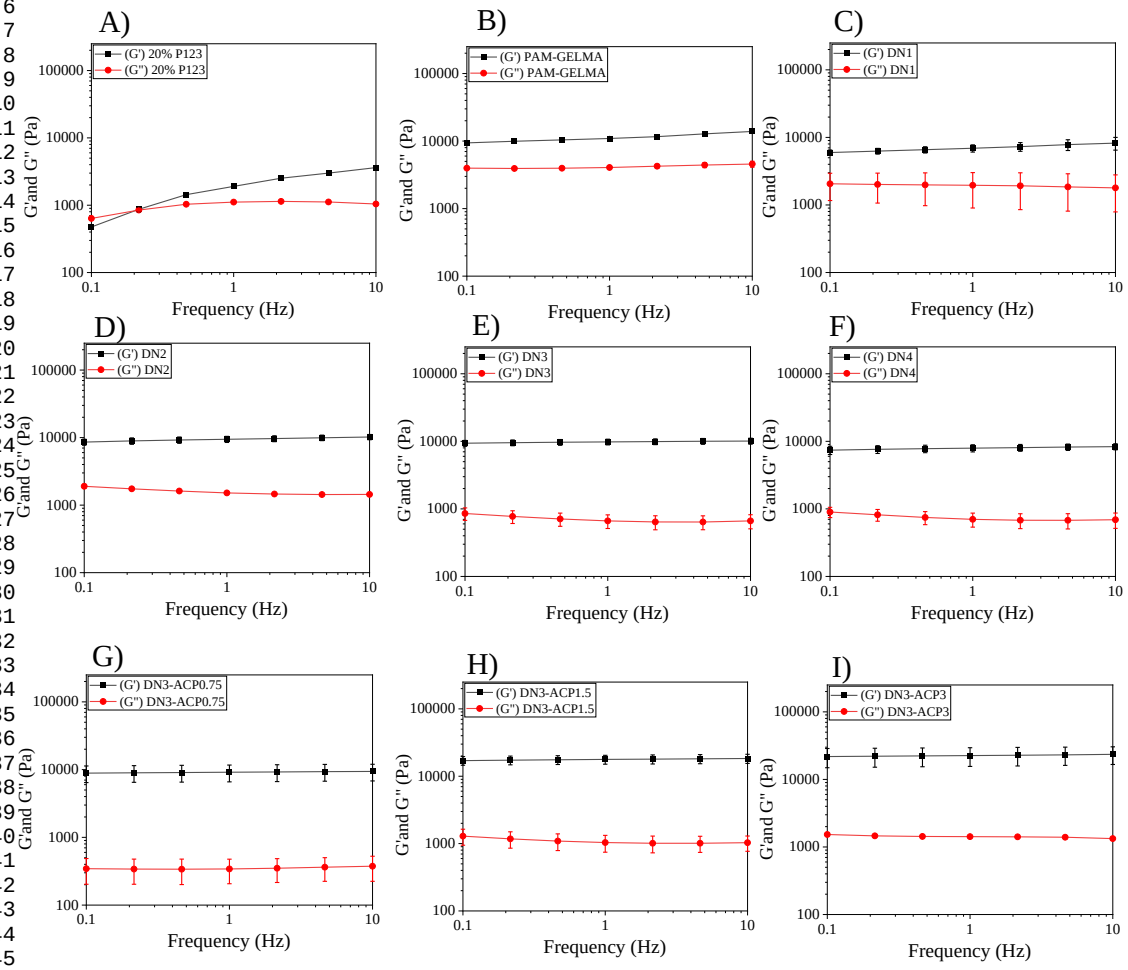

Figure 5. Frequency sweep of the synthesized hydrogels

The G' and G" of the hydrogels were analyzed against the frequency of 1 Hz shown in Figure 6A. The P123 possesses very low G' (1904 ± 50 Pa) and G" (1112.3 ± 28.5 Pa) corresponding to the characteristic of weak and soft material. On the contrary, the PAM-GELMA hydrogel has high G' (10916.6 ± 625.3 Pa) and G" (4058.6 ± 213.8 Pa), corresponding to the high strength and brittle nature. By increasing the P123 in PAM-GELMA hydrogel the G' value was less affected compared to the G" value. The reduction in G" means less energy is dissipated during deformation, indicating that the hydrogel behaves more elastically and less viscously. Therefore, as the concentration of P123 increases, the difference between the G' and G" values shows increasing elastic behavior [50]. This phenomenon was observed until the P123 concentration of 7.5 w/v% in PAM-GELMA hydrogel (DN3).

However, further increasing the P123 concentration to 10 w/v% in PAM-GELMA hydrogel (DN4), the decrease in the G' and increase in G", obstructing the elastic behavior of the hydrogel.

In the case of nanocomposite hydrogels at lower concentration of ACP_CIT (0.75 w/v%) in DN3 hydrogels (DN3-ACP0.75), reveals the G' of 9141 ± 2545 Pa and G" of 341.3 ± 134.8 Pa. The incorporation of ACP_CIT (0.75 w/v%) decreases G' and G" values, however the reduction in the G' was marginal while G" values drastically decreased which may be responsible for enhancing elastic property. However, as the concentration of ACP_CIT (1.5 w/v%) increased in DN3 hydrogels (DN3-ACP1.5) drastically increased values of G' (17766.6 ± 2689.4 Pa) and G" of (1034.9 ± 290.2 Pa) imparting rigidity to the hydrogel. A further increase in ACP_CIT concentration (3 w/v%) in DN3 hydrogels (DN3-ACP3) shows extreme enhancement on G' (22523.3 ± 6950 Pa) and G" of (1422.6 ± 47.6 Pa), which may be responsible for compromising the mechanical properties [51,52].

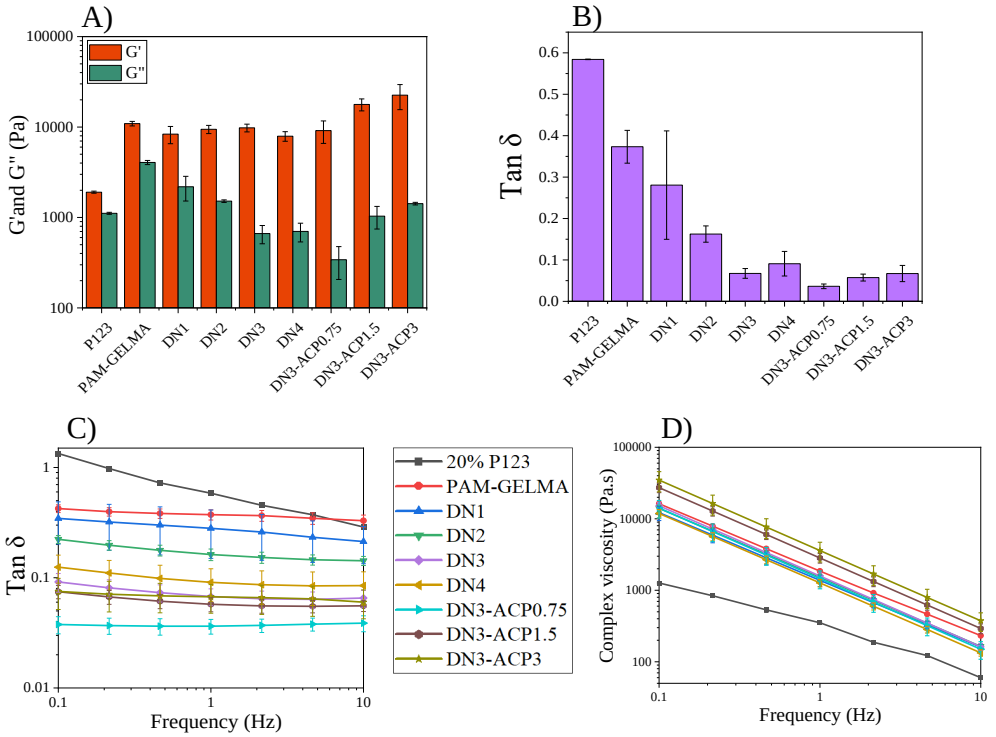

Figure 6. Analyzing storage (G') loss modulus (G") at the frequency of 1 Hz (A). Evaluation of the tan δ at 1 Hz (B). Tan δ analyzed all synthesized hydrogels at varying frequencies (C) and complex viscosity (D).

The tan δ analysis of all the synthesized hydrogels is shown in Figure 6(C). Tan δ is the ratio of G" to G' of viscoelastic material often used to analyze the damping properties of the material. It quantifies the ratio of energy dissipated as heat. In viscoelastic material, a higher tan δ value (close to 1) indicates a higher proportion of energies dissipated as heat relative to the energy stored elastically. On the other hand, a lower tan δ value indicates that more energy is elastically stored compared to dissipated energy [46].

The tan δ of PAM-GELMA hydrogel was 0.37±0.03 when analyzed at a frequency of 1 Hz, shown in Figure 6(D). Increasing P123 concentration in PAM-GELMA hydrogels shows tan δ of 0.28 ± 0.13 (DN1), 0.16 ± 0.01 (DN2), 0.067 ± 0.01 (DN3) and 0.09 ± 0.02 (DN4) respectively. This analysis observed that tan δ values decreased till hydrogel DN3, where the P123 concentration was 7.5 w/v% in PAM-GELMA (DN3), which can be attributed to increased flexibility [53]. However, when the P123 concentration was increased to 10 w/v% in PAM-GELMA (DN4), the tan δ value increased, thus hindering the damping properties, and reducing flexibility.

In the nanocomposite hydrogels, the tan δ values were 0.036 ± 0.05 (DN3-ACP0.75), 0.057 ± 0.008 (DN3-ACP1.5) and 0.067 ± 0.02 (DN3-ACP3). The tan δ value of DN3-ACP0.75 was the lowest, which can be attributed to the higher elasticity. Increasing the concentration of ACP_CIT in DN3 hydrogels to 1.5 w/v% (DN3-ACP1.5) and 3 w/v% (DN3-ACP3) increases the tan δ value, which can be attributed to the reduction in the damping properties. With the increase in the ACP_CIT concentration, the tan δ value starts to increase, which can alter the crosslinking density and polymer chain mobility within the hydrogel, thus affecting the hydrogel's overall mechanical properties.

The complex viscosity of all the synthesized hydrogel decreased with an increase in frequency, demonstrating shear thinning behavior. Variations in the complex viscosities were observed with different concentrations of P123 and ACP_CIT in PAM-GELMA hydrogel [54]. As shown in Figure 6 (D), an increase in P123 concentration in PAM-GELMA hydrogel led to a notable reduction in complex viscosity. Similarly, the addition of different ACP_CIT concentrations affected the complex viscosity of the DN3 hydrogels. The highest ACP_CIT concentration (DN3-ACP3) exhibited higher complex viscosity, followed by DN3-ACP1.5 and DN3-ACP0.75 hydrogels.

The results from tensile strength analysis go hand in hand with the oscillatory shear tests, confirming that blending of P123 enhances the elasticity and mechanical properties of PAM-GELMA hydrogels. However, the performance of P123 was concentration-dependent. In addition, the performance of ACP_CIT was also concentration-dependent. At deficient concentrations of ACP_CIT, enhancement in elasticity was observed, which may be due to pseudo crosslinking of citrate in ACP with GELMA. However, more advanced analyses are required to confirm the citrate-GELMA interaction. The DN3 and its nanocomposite DN3-ACP0.75 hydrogel have the highest mechanical properties. Therefore, further analysis was performed on these two hydrogels.

3.5 Creep recovery and stress relaxation analysis

Creep and recovery behavior helps reflect the interaction of polymeric chains of the viscoelastic material, which helps to understand and analyze the deformation mechanism of the hydrogels. Therefore, the creep recovery analysis was performed to evaluate the interaction change among the polymer chain of the one DN3 and nanocomposite DN3-ACP0.75 hydrogels, as shown in Figure 7 (A). The incorporation of ACP_CIT in DN3 hydrogel (DN3-ACP0.75) shows a positive effect on decreasing creep strain. This can be due to restricted polymer chain movements by adding ACP_CIT nanoparticles [55]. The stress relaxation curves are presented in Figure 7 (B). The DN3 and nanocomposite DN3-ACP0.75 hydrogels show rapid stress relaxations. However, the presence of ACP_CIT slowed the stress relaxation of DN3-ACP0.75 hydrogels [56,57]. Previous studies have shown hydrogel's stress relaxation dependency on water uptake capacity. Faster stress relaxation was observed,

increasing water content, which may be due to synergy of factors such as 1) migration of more water, 2) softer polymer network enhancing matrix flow, and lesser stiffness [58].

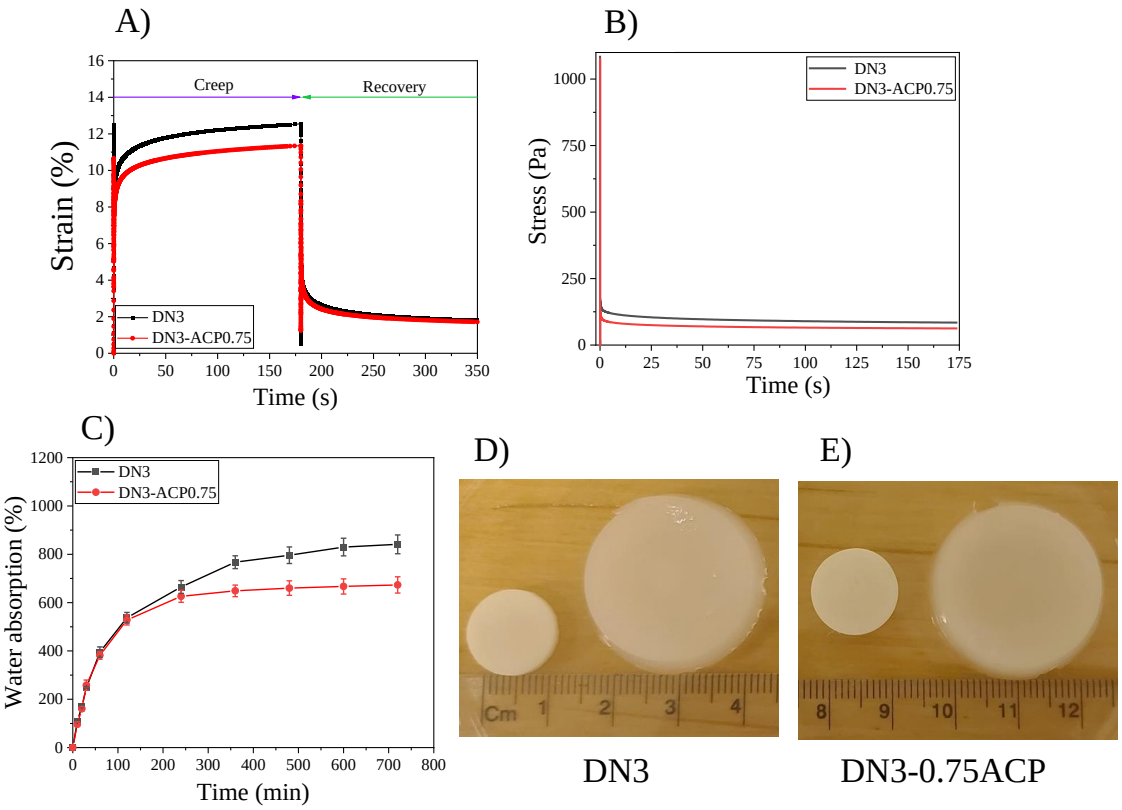

Figure 7. Analyzing creep-recovery (A), stress relaxation (B), water uptake capacity (C), and photographs of dried and swelled DN3 and DN3-ACP0.75 hydrogels (D and E).

3.6 Water uptake capacity

The water uptake capacity of DN3 hydrogels and its composite DN3-ACP0.75 is presented in Figure 8C. Both the DN3 and DN3-ACP0.75 hydrogels grow double in size after swelling, as observed in Figure 7 (D and E). The incorporation of ACP_CIT in the DN3 hydrogel affects the swelling kinetics. A reduction in the water uptake capacity of DN3-ACP0.75 hydrogels can be due to the hindrance of the free polymer chain movement by the addition of ACP_CIT [59]. Compared to DN3 hydrogel, the lower water uptake capacity of DN3-ACP0.75 hydrogel may be attributed to the slower stress relaxation.

3.7 Shape memory behavior.

The shape memory hydrogel possesses two different types of crosslinks. One of the crosslinks is composed of a covalent network, which is essential to maintaining the structural integrity of the hydrogel. On the other hand, the second crosslink is composed of a physical reversible network responsible for fixing the temporary shape. In this investigation, PAM-GELMA forms the covalently crosslinked network [60]. The thermosensitive P123 forms

reverse physical crosslinking when exposed to high temperature (70℃), triggering the temporary shape formation when exposed to (4℃), thus providing shape memory and recovery properties as shown in Figure 8. The DN3 hydrogels and its composite DN3-ACP0.75 hydrogels were immersed in Milli-Q® water for 24 h, then placed in 70℃ Milli-Q® water for 2 min, allowing shape transformation. The transformed shape was immersed in 70℃ Milli-Q® water for 2 min, allowing transformed shape fixation (temporary shape). For shape recovery, the temporary hydrogel was again immersed in 70℃ Milli-Q® (Movie provided in supplementary data). Herein, we could control and repeat shape memory and recovery for at least five cycles.

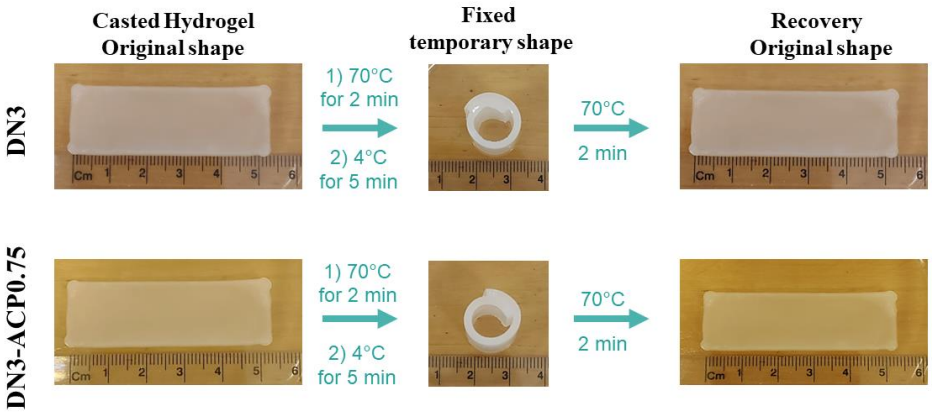

Figure 8. Temperature-induced shape memory behavior of DN3 and DN3-ACP0.75 hydrogels.

3.8 In vitro analysis

Rhodamine phalloidin and DAPI staining were performed to analyze the cytoskeleton (red) and the nucleus (blue) of MC3T3-E1 cells, as shown in Figure 9. Epifluorescent microscopy was performed on days 1, 3, and 7 to investigate the cytocompatibility of the hydrogel. The cell attachment on the hydrogel was observed on day 1. On day 3, the cells spread well and were distributed on both hydrogels. On day 7 the scaffold was densely populated with cells, confirming the cytocompatibility of developed DN3 and DN3-ACP0.75 hydrogels.

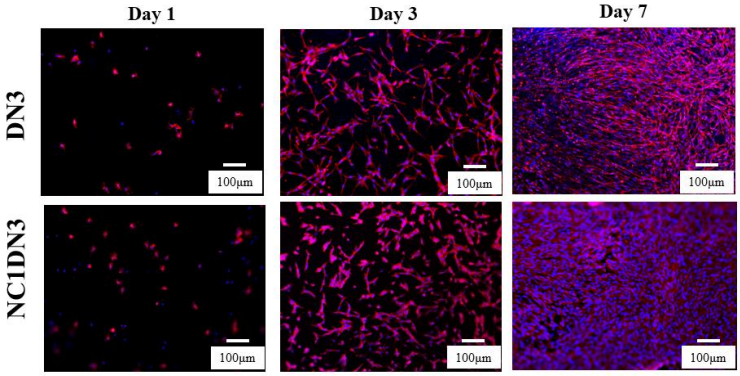

Figure 9. Fluorescent microscopy of rhodamine-phalloidin (red) and DAPI (blue) staining of MC3T3-E1 cells embedded in DN3 and DN3-ACP0.75 hydrogels.

4 Conclusion

A new thermoresponsive double-network (DN) nanocomposite hydrogel was synthesized using primary (PAM-GELMA), secondary (P123) networks, and ACP_CIT. Initially, P123 was blended in PAM-GELMA hydrogel in different concentrations, and its effect on tensile strength and viscoelastic properties was analyzed. It was observed that the increasing concentration of P123 (7.5 w/v%) in PAM-GELMA hydrogel enhanced the mechanical properties. However, a higher concentration of P123 (10 w/v%) compromised the mechanical properties of PAM-GELMA hydrogel. Similarly, the concentration-dependent trend was observed while developing nanocomposite hydrogels where a low concentration of 0.75% ACP (DN3-ACP0.75) enhanced mechanical properties beyond which the mechanical properties were negatively affected. This study has shown that PAM-GELMA hydrogel's mechanical properties strongly depend on the secondary (P123) network concentration and ACP_CIT. Therefore, the mechanical properties can be tuned per the desired applications by tuning the secondary network and ACP_CIT concentration. The temperature-induced shape memory behavior of the DN3 and DN3-ACP0.75 allows shape alteration which can be further used in developing complex architecture. The DN3 and DN3-ACP0.75 hydrogels are suitable for cell encapsulation, as evident by *in vitro* studies, thereby highlighting their potential use in tissue engineering applications requiring enhanced mechanical and biological performance.

5 Future outcome

Living organisms display unique mechanical characteristics in tissues like bone, arteries, and the brain, which are influenced by the properties of the ECM. Ex-situ measurements of the natural tissues highlight a wide range of stiffness across the different body tissues. For instance, Engler et al. revealed that the osteoid matrix surrounding the cultured has Young's modulus of 20-50 kPa, which promotes osteogenic differentiation of mesenchymal stem cells [61]. Moreover, previous studies have shown that hydrogel with faster stress relaxation promotes osteogenic differentiation and facilitates the formation of interconnected type I collagen matrix mineralized by the differentiated cells [62]. The developed DN3 and DN3-ACP0.75 hydrogels possess Young's modulus within the range of 20-50 kPa with faster stress relaxation, which can potentially be explored in bone tissue engineering applications.

6 Acknowledgment

The authors acknowledge financial support from the European Union's Horizon 2020 research and innovation program under grant agreement No. 857287 (BBCE) and Baltic Research Programme Project No. EEA-RESEARCH-85 "Waste-to-resource: eggshells as a source for next generation biomaterials for bone regeneration (EGGSHELL)" under the EEA Grant of Iceland, Liechtenstein and Norway No. EEZ/BPP/VIAA/2021/1.

7 CRediT authorship contribution statement.

Abhishek Indurkar: Conceptualization, Literature review, Methodology, Investigation, Data curation, Writing-original draft preparation. **Kristaps Rubenis:** Writing-Review and editing. **Aldo R. Boccaccini:** Supervision, Writing-Review, Resources, and Editing. **Janis Locs:** Supervision, Writing-Review, Resources, and Editing. All authors provided critical feedback and helped to shape the research, analysis, and manuscript.

8 Reference

[1] Habraken, W. et al. (2016). Calcium phosphates in biomedical applications: materials for the future? *Materials Today*. DOI: 10.1016/J.MATTOD.2015.10.008.

[2] Bai, X. et al. (2018). Bioactive hydrogels for bone regeneration. *Bioactive Materials*. DOI: 10.1016/J.BIOACTMAT.2018.05.006.

[3] Schulze, F. et al. (2023). Scaffold Guided Bone Regeneration for the Treatment of Large Segmental Defects in Long Bones. *Biomedicines 2023, Vol. 11, Page 325*. DOI: 10.3390/BIOMEDICINES11020325.

[4] Orciani, M. et al. (2017). Biofabrication and bone tissue regeneration: Cell source, approaches, and challenges. *Frontiers in Bioengineering and Biotechnology*. DOI: 10.3389/FBIOE.2017.00017.

[5] Gao, C. et al. (2017). Bone biomaterials and interactions with stem cells. *Bone Research 2017 5:1*. DOI: 10.1038/boneres.2017.59.

[6] Indurkar, A. et al. (2023). Role of carboxylic organic molecules in interfibrillar collagen mineralization. *Frontiers in Bioengineering and Biotechnology*. DOI: 10.3389/FBIOE.2023.1150037.

[7] Huebsch, N. et al. (2015). Matrix elasticity of void-forming hydrogels controls transplanted-stem-cell-mediated bone formation. *Nature Materials 2015 14:12*. DOI: 10.1038/nmat4407.

[8] Ahearne, M. (2014). Introduction to cell–hydrogel mechanosensing. *Interface Focus*. DOI: 10.1098/RSFS.2013.0038.

[9] Niu, X. et al. (2016). Shear-mediated crystallization from amorphous calcium phosphate to bone apatite. *Journal of the Mechanical Behavior of Biomedical Materials*. DOI: 10.1016/J.JMBBM.2015.09.024.

[10] Shou, Y. et al. (2023). Dynamic Stimulations with Bioengineered Extracellular Matrix-Mimicking Hydrogels for Mechano Cell Reprogramming and Therapy. *Advanced Science*. DOI: 10.1002/ADVS.202300670.

[11] Ghandforoushan, P. et al. (2023). Injectable hydrogels for cartilage and bone tissue regeneration: A review. *International Journal of Biological Macromolecules*. DOI: 10.1016/J.IJBIOMAC.2023.125674.

[12] Xu, F. et al. (2022). Hydrogels for Tissue Engineering: Addressing Key Design Needs Toward Clinical Translation. *Frontiers in Bioengineering and Biotechnology*. DOI: 10.3389/FBIOE.2022.849831.

[13] Li, T. et al. (2023). The Current Status, Prospects, and Challenges of Shape Memory Polymers Application in Bone Tissue Engineering. *Polymers*. DOI: 10.3390/POLYM15030556.

[14] Shang, J. et al. (2019). Trends in polymeric shape memory hydrogels and hydrogel actuators. *Polymer Chemistry*. DOI: 10.1039/C8PY01286E.

[15] Yang, Q. et al. (2021). Dual-responsive shape memory hydrogels with self-healing and dual-responsive swelling behaviors. *Journal of Applied Polymer Science*. DOI: 10.1002/APP.50308.

[16] Liu, S. et al. (2020). Hydrogels and hydrogel composites for 3D and 4D printing applications. *3D and 4D Printing of Polymer Nanocomposite Materials: Processes, Applications, and Challenges*. DOI: 10.1016/B978-0-12-816805-9.00014-4.

[17] Meng, Q. and Hu, J. (2009). A review of shape memory polymer composites and blends. *Composites Part A: Applied Science and Manufacturing*. DOI: 10.1016/J.COMPOSITESA.2009.08.011.

[18] Zhang, Z. et al. (2022). Hydrogel materials for sustainable water resources harvesting & treatment: Synthesis, mechanism and applications. *Chemical Engineering Journal*. DOI: 10.1016/J.CEJ.2022.135756.

[19] Nardo, T. et al. (2017). Synthetic Biomaterial for Regenerative Medicine Applications. *Kidney Transplantation, Bioengineering, and Regeneration: Kidney Transplantation in the Regenerative Medicine Era*. DOI: 10.1016/B978-0-12-801734-0.00065-5.

[20] Bliddal, H. et al. (2021). Polyacrylamide hydrogel injection for knee osteoarthritis: results of a 52 week prospective study. *Osteoarthritis and Cartilage*. DOI: 10.1016/j.joca.2021.02.366.

[21] Hassan, S. et al. (2022). Polyacrylamide hydrogels. IV. Near-perfect elasticity and rate-dependent toughness. *Journal of the Mechanics and Physics of Solids*. DOI: 10.1016/J.JMPS.2021.104675.

[22] Indurkar, A. et al. (2020). Fabrication of guar gum-gelatin scaffold for soft tissue engineering. *Carbohydrate Polymer Technologies and Applications*. DOI: 10.1016/J.CARPTA.2020.100006.

[23] Kuo, C.H.R. et al. (2014). The Facile Generation of Two-Dimensional Stiffness Maps in Durotactic Cell Platforms Through Thickness Projections of Three-Dimensional Submerged Topography. *Methods in Cell Biology*. DOI: 10.1016/B978-0-12-800281-0.00004-X.

[24] Choi, J.B. et al. (2021). Characteristics of Biodegradable Gelatin Methacrylate Hydrogel Designed to Improve Osteoinduction and Effect of Additional Binding of Tannic Acid on Hydrogel. *Polymers 2021, Vol. 13, Page 2535*. DOI: 10.3390/POLYM13152535.

[25] Birhanu, G. et al. (2019). Dexamethasone loaded multi-layer poly-l-lactic acid/pluronic P123 composite electrospun nanofiber scaffolds for bone tissue engineering and drug delivery. *Pharmaceutical development and technology*. DOI: 10.1080/10837450.2018.1481429.

[26] Zhao, Y. et al. (2019). Micellization of Pluronic P123 in Water/Ethanol/Turpentine Oil Mixed Solvents: Hybrid Particle–Field Molecular Dynamic Simulation. *Polymers*. DOI: 10.3390/POLYM11111806.

[27] Indurkar, A. et al. (2023). Small organic molecules containing amorphous calcium phosphate: synthesis, characterization and transformation. *Frontiers in Bioengineering and Biotechnology*. DOI: 10.3389/FBIOE.2023.1329752/BIBTEX.

[28] Eanes, E.D. et al. (1973). An electron microscopic study of the formation of amorphous calcium phosphate and its transformation to crystalline apatite. *Calcified Tissue Research*. DOI: 10.1007/BF02013730/METRICS.

[29] Schweikle, M. et al. (2019). Stabilisation of amorphous calcium phosphate in polyethylene glycol hydrogels. *Acta Biomaterialia*. DOI: 10.1016/J.ACTBIO.2019.03.044.

[30] Chen, S. et al. (2023). Formation Of Amorphous Iron-Calcium Phosphate With High Stability. *Advanced Materials*. DOI: 10.1002/ADMA.202301422.

[31] Jin, W. et al. (2018). Synergic Effect of Sr2+ and Mg2+ on the Stabilization of Amorphous Calcium Phosphate. *Crystal Growth & Design*. DOI: 10.1021/ACS.CGD.8B00908.

[32] Chen, Y. et al. (2014). Stabilizing amorphous calcium phosphate phase by citrate adsorption. *CrystEngComm*. DOI: 10.1039/C3CE42274G.

[33] Krogstad, D. et al. (2014). The role of polyelectrolytes in the stabilization of calcium phosphate nanoparticles for the production of biomimetic materials. *APS*.

[34] Schweikle, M. et al. (2019). Stabilisation of amorphous calcium phosphate in polyethylene glycol hydrogels. *Acta biomaterialia*. DOI: 10.1016/J.ACTBIO.2019.03.044.

[35] Indurkar, A. et al. (2023). Amorphous Calcium Phosphate and Amorphous Calcium Phosphate Carboxylate: Synthesis and Characterization. *ACS Omega*. DOI: 10.1021/ACSOMEGA.3C00796.

[36] Tarakeshwar, P. and Manogaran, S. (1994). Ground state vibrations of citric acid and the citrate trianion—an ab initio study. *Spectrochimica Acta Part A: Molecular Spectroscopy*. DOI: 10.1016/0584-8539(94)E0017-5.

[37] Pham, L. et al. (2019). A dual synergistic of curcumin and gelatin on thermal-responsive hydrogel based on Chitosan-P123 in wound healing application. *Biomedicine & Pharmacotherapy*. DOI: 10.1016/J.BIOPHA.2019.109183.

[38] Atika, N. et al. (2016). Tensile Properties of Polyacrylamide-Gelatin/Calcium Carbonate and Polyacrylamide-Chitosan/Alginic Acid Double Network Hydrogels. *Journal of Polymer Science and Technology (ISSN: 2550-1917)*.

[39] Freddi, G. et al. (1999). Structure and Physical Properties of Silk Fibroin/Polyacrylamide Blend Films. *J Appl Polym Sci*. DOI: 10.1002/(SICI)1097-4628(19990307)71:10.

[40] Bai, R. et al. (2019). Tearing a hydrogel of complex rheology. *Journal of the Mechanics and Physics of*

Solids. DOI: 10.1016/J.JMPS.2019.01.017.

[41] Gohil, M. and Joshi, G. (2022). Perspective of polycarbonate composites and blends properties, applications, and future development: A review. *Green Sustainable Process for Chemical and Environmental Engineering and Science: Green Composites: Preparation, Properties and Allied Applications*. DOI: 10.1016/B978-0-323-99643-3.00012-7.

[42] Li, S.N. et al. (2020). Chitosan in-situ grafted magnetite nanoparticles toward mechanically robust and electrically conductive ionic-covalent nanocomposite hydrogels with sensitive strain-responsive resistance. *Composites Science and Technology*. DOI: 10.1016/J.COMPSCITECH.2020.108173.

[43] Zhong, M. et al. (2015). Self-healable, tough and highly stretchable ionic nanocomposite physical hydrogels. *Soft Matter*. DOI: 10.1039/C5SM00493D.

[44] Mohammed, A.A. et al. (2022). Double-Network Hydrogels Reinforced with Covalently Bonded Silica Nanoparticles via 1-Ethyl-3-(3-dimethylaminopropyl)carbodiimide Chemistry. *ACS Omega*. DOI: 10.1021/ACSOMEGA.2C05169/ASSET/IMAGES/LARGE/AO2C05169_0010.JPEG.

[45] Boonmahitthisud, A. et al. (2017). Composite effect of silica nanoparticle on the mechanical properties of cellulose-based hydrogels derived from cottonseed hulls. *Journal of Applied Polymer Science*. DOI: 10.1002/APP.44557.

[46] Indurkar, A. et al. (2020). Optimization of guar gum-gelatin bioink for 3D printing of mammalian cells. *Bioprinting*. DOI: 10.1016/J.BPRINT.2020.E00101.

[47] Bhagavathi Kandy, S. et al. (2018). Effect of Incorporation of Multiwalled Carbon Nanotubes on the Microstructure and Flow Behavior of Highly Concentrated Emulsions. *ACS Omega*. DOI: 10.1021/ACSOMEGA.8B00579/ASSET/IMAGES/LARGE/AO-2018-00579B_0002.JPEG.

[48] Efstathiou, S. et al. (2021). Self-healing and mechanical performance of dynamic glycol chitosan hydrogel nanocomposites. *Journal of Materials Chemistry B*. DOI: 10.1039/D0TB02390F.

[49] Ashraf, U. et al. (2015). An investigation of Pluronic P123–sodium cholate mixed system: micellization, gelation and encapsulation behavior. *RSC Advances*. DOI: 10.1039/C5RA13002F.

[50] Chen, H. et al. (2016). Controlled gelation kinetics of cucurbit[7]uril-adamantane cross-linked supramolecular hydrogels with competing guest molecules. *Scientific Reports 2016 6:1*. DOI: 10.1038/srep20722.

[51] Zaragoza, J. et al. (2018). Exploring the Role of Nanoparticles in Enhancing Mechanical Properties of Hydrogel Nanocomposites. *Nanomaterials 2018, Vol. 8, Page 882*. DOI: 10.3390/NANO8110882.

[52] Levin, M. et al. (2019). Structural changes in nanoparticle-hydrogel composites at very low filler concentrations. *Journal of Chemical Physics*. DOI: 10.1063/1.5053171/198966.

[53] Jing, Z. et al. (2020). Tough, stretchable and compressive alginate-based hydrogels achieved by non-covalent interactions. *RSC Advances*. DOI: 10.1039/D0RA03733H.

[54] Kaya, G. and Oytun, F. (2021). Rheological properties of İnjectable hyaluronic acid hydrogels for soft tissue engineering applications. *Biointerface Research in Applied Chemistry*. DOI: 10.33263/BRIAC111.84248430.

[55] Shojaei, S. et al. (2019). Disclosing the role of surface and bulk erosion on the viscoelastic behavior of biodegradable poly(ε-caprolactone)/poly(lactic acid)/hydroxyapatite nanocomposites. *Journal of Applied Polymer Science*. DOI: 10.1002/APP.47151.

[56] Kaewchuchuen, J. et al. (2024). Functionalising silk hydrogels with hetero- and homotypic nanoparticles. *RSC Advances*. DOI: 10.1039/D3RA07634B.

[57] Bertsch, P. et al. (2022). Colloidal hydrogels made of gelatin nanoparticles exhibit fast stress relaxation at strains relevant for cell activity. *Acta Biomaterialia*. DOI: 10.1016/J.ACTBIO.2021.10.053.

[58] Dey, K. et al. (2021). Degradation-Dependent Stress Relaxing Semi-Interpenetrating Networks of Hydroxyethyl Cellulose in Gelatin-PEG Hydrogel with Good Mechanical Stability and Reversibility. *Gels*. DOI: 10.3390/GELS7040277.

[59] Kumar, B.Y.S. et al. (2019). Nanohydroxyapatite Reinforced Chitosan Composite Hydrogel with Tunable Mechanical and Biological Properties for Cartilage Regeneration. *Scientific Reports 2019 9:1*. DOI: 10.1038/s41598-019-52042-7.

[60] Maiti, B. et al. (2020). Thermoresponsive Shape-Memory Hydrogel Actuators Made by Phototriggered Click Chemistry. *Advanced Functional Materials*. DOI: 10.1002/ADFM.202001683.

[61] Akhmanova, M. et al. (2015). Physical, Spatial, and Molecular Aspects of Extracellular Matrix of In Vivo Niches and Artificial Scaffolds Relevant to Stem Cells Research. *Stem cells international*. DOI: 10.1155/2015/167025.

[62] Chaudhuri, O. (2017). Viscoelastic hydrogels for 3D cell culture. *Biomaterials Science*. DOI: 10.1039/C7BM00261K.

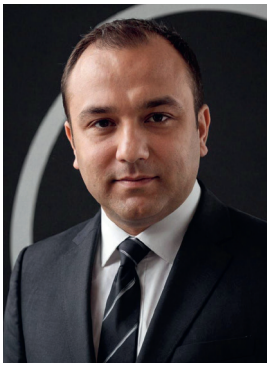

Abhishek Rajesh Indurkar was born in 1994 in Bhusawal, India. He holds a Bachelor's degree in Biotechnology Engineering (2017) and a Master's degree in Pharmaceutical Biotechnology (2019). In 2020, Abhishek began his doctoral studies under the supervision of Professor Jānis Ločs and Senior Researcher Kristaps Rubenis at Riga Technical University and the Baltic Biomaterial Centre of Excellence. During his postgraduate studies, he completed a secondment at Friedrich-Alexander-Universität Erlangen-Nürnberg, Germany, under the guidance of Professor Aldo R. Boccaccini.
His research interests focus on bioprinting, bioink formulations, and nanocomposite development to create artificial tissues and human organs.

Abhishek Rajesh Indurkar dzimis 1994. gadā Busavalā (Indija). Ieguvis bakalaura grādu biotehnoloģiju inženierijā (2017) un maģistra grādu farmācijas biotehnoloģijā (2019). 2020. gadā sācis doktora studijas Rīgas Tehniskajā universitātē (RTU), promocijas darbu izstrādājot Baltijas Biomateriālu ekselences centrā profesora Jāņa Loča un vadošā pētnieka Kristapa Rubeņa vadībā. Paralēli studijām doktorantūrā strādājis norīkojumā Fridriha Aleksandra Erlangenas-Nirnbergas universitātē (Vācija) profesora Aldo R. Bokačīni (*Aldo R. Boccaccini*) vadībā.
Zinātniskās intereses saistītas ar biodrukāšanu, biotintes preparātiem un nanokompozītu materiālu izstrādi, lai radītu mākslīgos audus un cilvēka orgānus.